



HAL
open science

Development and study of low noise laser diodes emitting at 894 nm for compact cesium atomic clocks

Nicolas von Bandel

► **To cite this version:**

Nicolas von Bandel. Development and study of low noise laser diodes emitting at 894 nm for compact cesium atomic clocks. Electronics. Université Montpellier, 2017. English. NNT : 2017MONTTS003 . tel-01683150

HAL Id: tel-01683150

<https://theses.hal.science/tel-01683150>

Submitted on 12 Jan 2018

HAL is a multi-disciplinary open access archive for the deposit and dissemination of scientific research documents, whether they are published or not. The documents may come from teaching and research institutions in France or abroad, or from public or private research centers.

L'archive ouverte pluridisciplinaire **HAL**, est destinée au dépôt et à la diffusion de documents scientifiques de niveau recherche, publiés ou non, émanant des établissements d'enseignement et de recherche français ou étrangers, des laboratoires publics ou privés.

THÈSE

Pour obtenir le grade de
Docteur

Délivré par l'**UNIVERSITÉ** de **MONTPELLIER**

Préparée au sein de l'école doctorale **Information,
Structures et Systèmes**
Et de l'unité de recherche **Institut d'Électronique et des
Systèmes**

Spécialité : **Électronique**

Présentée par **Nicolas VON BANDEL**

**Development and study of low noise laser
diodes emitting at 894 nm for compact
cesium atomic clocks**

Soutenue le 30 Juin 2017 devant le jury composé de :

Arnaud GARNACHE	DR-CNRS IES (Montpellier)	Président du Jury
Noël DIMARCQ	DR-CNRS SYRTE (Paris)	Rapporteur
Joël JACQUET	DR-EIGSI (La Rochelle)	Rapporteur
Michel GARCIA	Ingénieur - III-V Lab (Palaiseau)	Examineur
Gaetano MILETI	Professeur LTF-UniNe (Neuchâtel)	Examineur
Michel KRAKOWSKI	Chef de Projet - III-V Lab (Palaiseau)	Responsable CIFRE
Mikhaël MYARA	MC IES (Montpellier)	Co-encadrant
Philippe SIGNORET	Professeur IES (Montpellier)	Directeur de thèse
Michel BALDY	Ingénieur - Thales E. D. (Vélizy)	Invité

THÈSE

pour obtenir le titre de

DOCTEUR DE L'UNIVERSITÉ DE MONTPELLIER

École doctorale : Information Structures Systèmes

Discipline : Électronique, Composants et Systèmes

Présentée et soutenue publiquement le 30 Juin 2017 par

Nicolas VON BANDEL

**Development and study of low noise laser diodes
emitting at 894 nm for compact cesium atomic clocks**

jury

Arnaud GARNACHE	DR-CNRS IES (Montpellier)	<i>Président du Jury</i>
Noël DIMARCQ	DR-CNRS SYRTE (Paris)	<i>Rapporteur</i>
Joël JACQUET	DR-EIGSI (La Rochelle)	<i>Rapporteur</i>
Michel GARCIA	Ingénieur - III-V Lab (Palaiseau)	<i>Examineur</i>
Gaetano MILETI	Professeur LTF-UniNe (Neuchâtel)	<i>Examineur</i>
Michel KRAKOWSKI	Chef de Projet - III-V Lab (Palaiseau)	<i>Responsable CIFRE</i>
Mikhaël MYARA	MC IES (Montpellier)	<i>Co-encadrant</i>
Philippe SIGNORET	Professeur IES (Montpellier)	<i>Directeur de thèse</i>
Michel BALDY	Ingénieur - Thales E. D. (Vélizy)	<i>Invité</i>

Abstract : This PhD work deals with the design, the fabrication and the study of high-coherence semiconductor laser sources emitting at 894 nm, for application to compact, optically-pumped cesium atomic clocks in an industrial context. We are particularly interested in the electrically pumped "Distributed-Feedback" in-plane laser diodes (DFB). The aim is to obtain a low-threshold, single-mode laser with high optical efficiency and a linewidth of less than 1 MHz. We first deal with the design and first-order characterization of the DFB diodes until they are put into modules for the clock. We then carry out an in-depth study of the physical properties of the laser emission in terms of the coherence time. For that purpose, a new universal method for characterizing the optical frequency noise is introduced. Finally, we look further into the spectral properties of the emission in a servo configuration on a fluorescence line of the cesium ("Dither-Locking"). We show that the intrinsic properties of the component satisfy the requirements of the industrial system as defined in the study.

Keywords : Laser diodes, low noise, 894nm, cesium atomic clocks, frequency noise metrology, linewidth in servo

Titre: Développement et étude de diodes laser à faible bruit émettant à 894 nm pour horloges atomiques compactes au césium

Résumé : Ce travail de thèse porte sur la conception, la réalisation et l'étude de sources laser à semi-conducteur de haute cohérence, émettant à 894 nm, pour application aux horloges atomiques césium compactes, pompées optiquement. Nous nous intéressons plus particulièrement aux lasers à émission par la tranche, dits "Distributed-Feedback" (DFB), pompés électriquement. L'objectif est d'obtenir un laser monomode en fréquence, à faible seuil, à rendement optique élevé et de largeur de raie inférieure à 1 MHz. Nous traitons d'abord de la conception et de la caractérisation au premier ordre des diodes DFB, jusqu'à leur mise en modules pour horloge, puis nous effectuons une étude approfondie des propriétés physiques de l'émission laser en terme de cohérence temporelle, en introduisant une nouvelle méthode universelle de caractérisation du bruit de fréquence optique. Enfin, nous nous intéressons aux propriétés spectrales de l'émission en configuration d'asservissement sur une raie de fluorescence du césium ("Dither-Locking"). Nous montrons que les propriétés intrinsèques du composant satisfont aux exigences du système industriel tel qu'il a été défini lors de l'étude.

Mots-clés : Diodes laser, faible bruit, 894nm, horloges atomiques au césium, métrologie du bruit de fréquence, largeur de raie en asservissement

Acknowledgments

Ce travail a été effectué dans le cadre d'une collaboration CIFRE au sein du GIE Thales-Nokia III-V Lab de Palaiseau et de l'Institut d'Électronique et des Systèmes à l'Université de Montpellier. Je souhaite remercier à ce titre le Président du GIE, Monsieur François Luc et son Directeur, Monsieur Philippe Bois, ainsi que le Directeur de l'IES, Monsieur Alain Foucaran, pour m'avoir accueilli au sein de leurs structures.

Je tiens ensuite à exprimer ma profonde gratitude à l'égard de mon Directeur de thèse, le Professeur Philippe Signoret, qui a toujours été en première ligne pour défendre l'intérêt de ma candidature et son sujet et m'a procuré, tout au long de cette aventure, le soutien et l'élan nécessaires en levant, entre autres, les obstacles techniques qui se sont présentés.

J'aimerais, dans le même esprit, exprimer mon grand respect et ma reconnaissance sans faille à mon co-encadrant de thèse, le Maître de Conférence Mikhaël Myara, qui a su, grâce à son talent pour la vulgarisation, m'intéresser à la thématique du Bruit, et pour avoir suivi de très près mes travaux, en leur apportant une dimension nouvelle, riche en développements scientifiques, qui m'ont littéralement passionnés. Ce précieux encadrement m'a poussé à vouloir donner le meilleur de moi-même.

Je souhaite remercier sincèrement Noël Dimarcq, Directeur de Recherche au SYRTE et Joël Jacquet, Directeur de Recherche à L'EIGSI, pour avoir accepté de rapporter mon travail de thèse, en l'enrichissant notamment de leurs remarques pertinentes.

Également, je remercie chaleureusement Arnaud Garnache, Directeur de Recherche à l'IES, pour nos échanges scientifiques féconds et pour avoir présidé mon jury, ainsi que Gaetano Miletì, Professeur à l'Université de Neuchâtel, et son équipe, C. Affolderbach, R. Matthey et F. Gruet, pour nos nombreux échanges techniques constructifs lors du déroulement du projet.

Je remercie aussi Michel Krakowski, Chef du Programme "Lasers de Pompe" au III-V Lab et responsable du projet LAMA, qui a coordonné et conseillé les activités techniques de la thématique tout au long de la thèse, ainsi que Frédéric Van Dijk, qui m'a accueilli au sein de son équipe durant trois ans: son aide technique a été bénéfique à plus d'un titre.

Je voudrais exprimer mes remerciements professionnels et amicaux les plus sincères à Michel Garcia, Responsable de l'équipe Technologie, qui m'a transmis assidûment sa passion et son expertise avertie des techniques du semi-conducteur, ainsi que toute son équipe: Alexandre, Corinne, Fabrice, Bouzid et Eric et Yannick de l'équipe Back-end.

Je souhaite exprimer toute ma sympathie envers Roman Schmeissner, Ingénieur de Recherche du Service de l'Horloge Atomique de Thalès Electron Devices dirigé par Michel Baldy, que je remercie également, ainsi que son prédécesseur, Virgile Hermann, pour nos nombreuses interactions très constructives. L'enthousiasme communicatif de Roman et sa patience à m'expliquer les ressorts de l'horloge atomique m'ont été très bénéfiques pour la maturation de mon travail.

J'ai par ailleurs une pensée amicale pour Borge Vinter, qui a su m'expliquer avec beaucoup de pédagogie les concepts les plus fins de la Physique des semi-conducteurs durant ces trois années.

Tout comme les nombreux autres acteurs de cette thèse, que je ne peux pas tous citer: Olivier Parillaud et son équipe de l'Épitaxie, et Maryline Beguet du Secrétariat en particulier.

Enfin, je n'oublie pas, et pour cause, Joseph, Roberto, Gaël, Nathalie, Anaëlle, Peppino, Mickaël, Florian, Hugues, Andrejz, Cécil, Axel, Antonin, Inès, Lina et bien d'autres encore, qui ont beaucoup apporté à la dimension humaine et fraternelle de ce long périple.

À la mémoire de mon père

Contents

Introduction	1
I Lasers for cesium clocks: industrial requirements	3
Chapter 1 Introduction to time and frequency applications	5
1.1 Generalities on time and frequency metrology	5
1.2 The Optical Cesium Frequency Standard (OCFS)	11
1.2.1 About Cesium Frequency Standards (CFS)	11
1.2.2 Principles behind the OCFS	13
1.2.2.1 Physics package	14
1.2.2.2 Electronics package	21
1.2.3 The OCFS today	23
1.3 The need of laser modules at cesium D_1 line (894 nm)	25
1.3.1 852 nm or 894 nm ?	25
1.3.2 Industrial specifications of the laser of the OCFS	26
1.3.3 Which laser technology for the application ? The LAMA Project	27
1.3.4 Current state-of-the-art for 894 nm sources	30
1.3.5 Context of this work	30
1.4 <i>Summary</i>	31
II Laser design	37
Chapter 2 Design of the source: An overview	39
2.1 LASER sources	39
2.1.1 Introduction	39
2.1.2 Spontaneous emission and stimulated emission	40
2.1.3 Absorption and gain in the atomic medium	41
2.1.4 The feedback condition: LASER effect	44
2.1.5 Photon lifetime and laser linewidth	46
2.1.6 Spatial coherence	50
2.1.7 Deviations from an idealized laser model	51
2.1.8 Conclusion	52
2.2 About semiconductor lasers	53
2.2.1 Generalities on the gain medium	53
2.2.1.1 GaAs based materials	53
2.2.1.2 Band structures and doping	55
2.2.1.3 Carrier concentration	58
2.2.1.4 Optical transitions in a bulk semiconductor	59
2.2.1.5 Optical transitions in quantum wells	60
2.2.1.6 Case study for emission at 894 nm	62
2.2.2 Photon noise in semiconductor lasers	66
2.2.2.1 The α_H factor	66
2.2.2.2 Spontaneous emission enhancement factors	69

2.2.2.3	Non-linear behavior of the linewidth	71
2.2.3	Electrical nature of the diode laser	71
2.2.4	Carrier and photons interplay	74
2.2.5	Single-mode lasers at III-V Lab	76
2.2.5.1	Main practical parameters for the linewidth reduction	77
2.2.5.2	Choice of heterostructure materials	78
2.2.5.3	Grating technology	78
2.2.5.4	Conclusion	79
2.3	<i>Summary</i>	80
Chapter 3	Practical conception	85
3.1	Laser conception	85
3.1.1	Introduction	85
3.1.2	Heterojunction and active zone for the D_1 and D_2 lines	87
3.1.2.1	Structures	87
3.1.2.2	Electrical behavior	88
3.1.3	Optical Design	89
3.1.3.1	Components of the complex medium index	89
3.1.3.2	Transverse Design	92
3.1.3.3	Longitudinal Design	106
3.1.4	Impact of the design on noise properties	111
3.1.4.1	What is the linewidth $\Delta\nu_{S-T-H}$ of DFB lasers ?	111
3.1.4.2	Technical noise in the device: the 1/f low-frequency noise source . . .	116
3.1.5	A feedback resistant design ?	120
3.1.6	Summary of the relevant design parameters	124
3.2	Technical realization	124
3.2.1	Epitaxial growth	124
3.2.2	Technological processing	126
3.2.3	Grating processing	126
3.2.4	Ridge processing	127
3.2.5	Cleaving and mounting	130
3.2.6	Packaging	131
3.3	First characterizations and optimization	132
3.3.1	First order metrology	132
3.3.2	First run of fabrication	134
3.3.2.1	Broad-area lasers	134
3.3.2.2	Ridge-DFB lasers	139
3.3.3	Conclusion on the first run of fabrication	150
3.4	<i>Summary</i>	152
III	Laser noise study: free-running and in-loop configurations	159
Chapter 4	Electrical noise characterization	161
4.1	Noise quantification: an introduction	161
4.1.1	Introduction	161
4.1.2	RMS fluctuations and spectral density of noise	161
4.1.3	Fundamental electrical noise sources	165
4.2	Experimental setup	166

4.2.1	Digital high-quality sampling: basic rules	166
4.2.2	Acquisition chain and experimental conditions	166
4.3	Experimental results	169
4.3.1	Dynamical resistance	169
4.3.2	Electrical noise	171
4.4	Conclusion	177
4.5	<i>Summary</i>	178
Chapter 5	Study of the optical coherence of the lasers	181
5.1	Introduction	181
5.2	Noise in DFB lasers	181
5.2.1	Intensity noise	182
5.2.2	Frequency noise	183
5.3	Frequency fluctuations : Lineshape, linewidth and Power Spectral Density	184
5.3.1	Linewidth for the white noise case	184
5.3.2	Fourier limit and observation time	185
5.3.3	Case of the non-white noise	186
5.4	Standard linewidth metrology	186
5.4.1	Heterodyne setup	186
5.4.2	Self-heterodyne linewidth	189
5.4.3	Frequency noise measurements by frequency discrimination	192
5.4.4	A simple relationship between the linewidth and the frequency noise?	194
5.4.5	Conclusion	196
5.5	Experimental results of the standard metrology	197
5.5.1	RIN measurements	197
5.5.2	Linewidth in the over-coherent SHE setup	200
5.5.2.1	Setup and first results	200
5.5.2.2	Linewidth re-broadening	203
5.5.3	Frequency noise measurements by frequency discrimination	204
5.5.4	Conclusion	208
5.6	New metrology: Beat-note investigation by digital acquisition	209
5.6.1	Beat-note demodulation versus frequency discrimination: a comparison	209
5.6.2	Time-dependency of laser linewidth: final outcome	211
5.6.3	Intrinsic linewidth through experimentation	214
5.6.4	Advantages and drawbacks of this metrology	215
5.7	Spectral properties under feedback	215
5.8	Discussion and conclusion on the noise of the fabricated lasers	220
5.8.1	Schawlow-Townes-Henry limit	220
5.8.2	Frequency noise coupling to the 1/f source: a few hypothesis	220
5.8.3	External cavity for linewidth reduction	222
5.8.4	Towards more advanced designs for noise reduction ?	223
5.9	<i>Summary</i>	224
Chapter 6	Laser module in atomic clock configuration	229
6.1	Introduction	229
6.2	Generalities on servo loop theory	229
6.2.1	Laplace representation of a servo	229
6.2.2	Noise reduction in a servo	231
6.2.3	Stability of a servo	232

6.2.4	Application to the laser frequency locking	234
6.3	Laser frequency locking on cesium lines: dither-locking principle	234
6.3.1	The Cs fluorescence line in frequency discrimination	235
6.3.2	Frequency discrimination	236
6.3.3	Dither-lock setup from a servo point of view	238
6.3.3.1	Maximal gain condition	238
6.3.3.2	Minimum gain condition	241
6.3.4	Investigation of the servo requirements with a β - separation line analysis . . .	244
6.4	LAMA lasers in-loop: case studies	245
6.4.1	LAMA 852 nm modules	246
6.4.2	LAMA 894 nm modules	246
6.4.3	LAMA 894 nm modules under feedback	246
6.5	Conclusion and perspectives	250
6.6	<i>Summary</i>	251
Epilogue		255
Conclusion		257
Publications		259

Introduction

Atomic clocks are systems that deliver an incomparably more precise time-reference (millions of times more precise) than the everyday clocks based on mechanical or electronic principles, such as the Quartz oscillator. The atomic species at the heart of this device (cesium, rubidium...) has a very precise spectroscopic structure that can be exploited: the difference between two energetic levels, under certain environmental and experimental conditions, can be used as an ultra stable reference in order to correct a conventional oscillator, whose associated time-reference generally degrades in the very short-term. An atomic clock therefore consists in forcing a macroscopic oscillator to lock on an atomic reference, thus ensuring a very good long-term stability (and a very precise time-reference). To create such atomic reference, one must be able to manipulate the quantum states of the species, using for example a light source whose energy is precisely adjusted to the possible states of transitions of the atom. The greater the coherence of this source, the more efficient the process will be: this is why some modern atomic clocks use lasers for this purpose. Today, many types of such clocks exist. In particular, the industrial optically-pumped cesium beam clock, whose technological development has matured, aims to compete with other types of systems, offering more advantageous time-stability characteristics.

However, such an industrial application requires a compact single-frequency laser source of high level of spectral purity, high output power and of low power consumption, emitting in the near infrared (towards 900 *nm*).

The purpose of my PhD thesis is precisely to address this need and to develop such a source for the application, from the initial structure of the laser cavity to its industrial packaging. Beyond that, my present work also investigates the theme of the spectral purity of these sources, which is limited by noise phenomena on its output frequency. This topic is tackled both on its theoretical aspects and, more crucially, on the way to characterize experimentally this parameter. Insights on the laser design and how to improve the spectral quality of the source are given. Finally, it leads me to propose a model to predict the laser frequency characteristics when it is actively controlled in the atomic clock system.

The manuscript is divided in three distinctive parts addressing different topics:

Part I : Lasers for cesium clocks: industrial requirements

The experiments described in this part have been made in collaboration with the Atomic Clock Service of Thales Electron Devices.

The first part comprises a unique chapter. **Chapter 1** is a short introduction to the physics of frequency standards and of the cesium atomic clock. It presents the main sub-systems of this setup and the specifications asked for the laser source. From that, it is justified that semiconductor in-plane lasers electrically-pumped are well suitable for the application. The current state-of-the-art is reviewed and the industrial project linked to this work is presented.

Part II : Laser design

The results of this part are related to the engineering developments of the laser modules done within the industrial laboratory of Thales-Nokia III-V Lab.

The second part has two chapters. **Chapter 2** draws general considerations on laser cavities, the semiconductor gain medium, and how a single-mode regime is established. The main design parameters of the source are presented and their link with the fundamental laser linewidth is made. **Chapter 3** handles all the practical aspects of the semiconductor laser design: the electrical and optical confinement with the vertical design of the semiconductor layers and the lateral and longitudinal optical mode selection with the ridge-Distributed Feedback structure. Insight is given on the parameters that drive the laser linewidth in these components. The technological process of fabrication of the devices is presented. Then, a full first-order experimental study of their characteristics is realized.

Part III : Laser noise study: free-running and in-loop configurations

The work presented in this part has been conducted under the theoretical and experimental supervision of the *Waves & Terahertz* group of the Institute for Electronics and Systems (University of Montpellier).

The third part has three chapters. **Chapter 4** addresses the specific issue of the electrical noise. Useful notions used to describe quantitatively the noise in the laser parameters are given first. Then, the usual electrical noise sources are presented, as well as the experimental protocols to measure these fluctuations. Measurements are performed on the laser modules fabricated and are compared to other commercial sources. The impact of the intrinsic electrical perturbations of the devices on the frequency noise of the output beam are discussed. **Chapter 5** is dedicated to the optical noise study, both on a theoretical and experimental point of view. A new method to characterize the frequency noise in an absolute manner, unlike the traditional metrology, is brought to light. The limitations of the lasers fabricated in terms of optical noise are revealed. Finally, **Chapter 6** investigates the laser noise properties in a servo in order to stabilize the frequency on a cesium transition line in the atomic clock . The capabilities of the electronic feedback to suppress the laser frequency fluctuations are discussed. Finally, the link between the original laser specifications and what is really needed in terms of spectral purity for the application is clarified.

Epilogue

The very end of this manuscript presents the most up-to-date results of the atomic clock performances with the laser developed in this study.

Part I

Lasers for cesium clocks: industrial requirements

Introduction to time and frequency applications

1.1 Generalities on time and frequency metrology

Although the concept of time is quite intuitive in our everyday life experience, it is actually quite hard to define in the frame of theoretical physics, but it is also difficult to measure precisely [Dimarcq 2015]. Indeed, the feeling of time passing by is usually given by the observation of the action of an event, for instance, the sand flowing in an hourglass. The thing about the movement in space of such an event is that it generates a quantity –the sand in the lower part of the glass– that grows *linearly*, so that the associated time measurement unit is defined as:

$$\Delta Q = k \times \Delta t \quad (1.1)$$

where Q is the amount of the quantity observed –here the mass of sand– and k a coefficient that converts the mass to a time measurement, the most common one being the Second. The equivalent concept for distance measurement would be a ruler, with graduations equally spaced defining a distance-scale.

However, such a definition is not very practical if used with material objects as it would require to observe a growing material quantity to infinity. A more useful time measurement technique can certainly be grounded on the observation of a *periodical* phenomena. A very simple example of that is a pendulum, or the alternating between day and night. In that case, the time-scale will be the duration between the two moments when the system is in the same state. One can then define a *period* T and a *frequency* f , linked by the relation:

$$f = 1/T \quad (1.2)$$

If T or f never varies as the system evolves, one can say that it is a perfect 'time-ruler' of time-graduation T . A shorter T , or equivalently, a higher f will provide a more precise time-counter (figure (1.1)). Those very simple considerations lead us to the conclusion that a 'good clock' should have the following qualities (figure (1.2)):

- *Accuracy* (exactitude): it is the ability of the clock to give a period or frequency equal to the one chosen as time-definition without any systematic bias
- *Stability* (stabilité): it is the fact that the period or the frequency of the clock keeps the same value over a given observation time
- *Repeatability* (reproductibilité): when the period or frequency of the clock is consistent over repeated experiments (that is, independent of the operator)

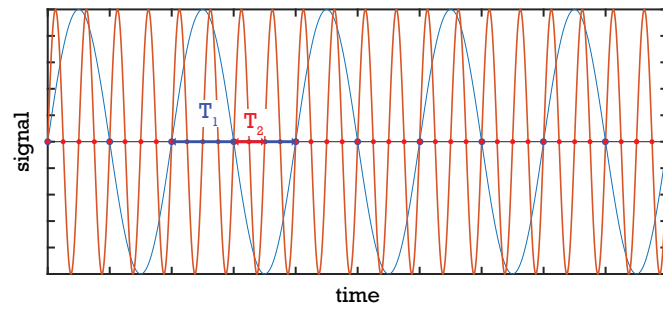


Figure 1.1: Representation of two periodic signals with $T_1 = 4T_2$. Signal in red is a better time-ruler because it has a higher frequency compared to the blue one.

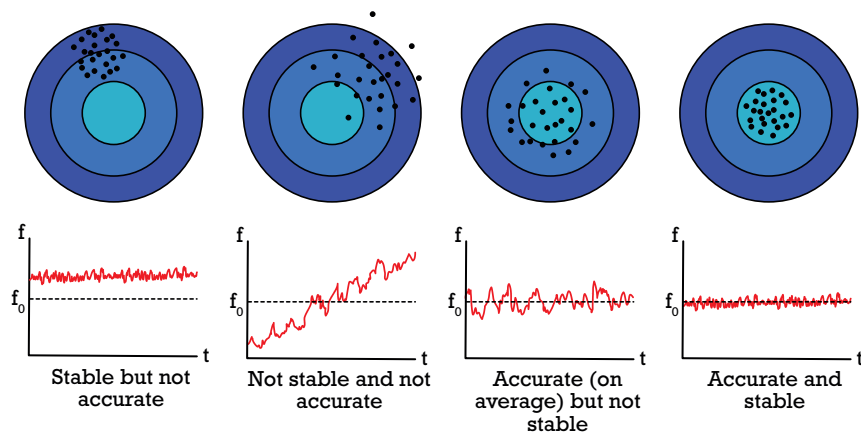


Figure 1.2: Difference between Accuracy and Stability. After an illustration of John Vig reproduced in [Dimarcq 2015]

From an historical point of view, the first instruments used to measure time were based on mechanics. The own rotation of earth with relation to the sun defines the *solar day*, which is precisely the duration between the two moments the sun illuminates the same point on earth in the same direction (the meridian). Such time-scale is not very practical as human activities take place in much smaller time-ranges. If one day is divided in 24 *hours*, which in turn accounts for 86400 *seconds*, one might have found a definition of the later unit scale, provided that the solar day is repeatable and stable.

This is actually not the case. Indeed, because the earth rotates around the sun in an elliptical orbit, the duration of the day is not the same throughout the year. Also, the axis of rotation has a small tilt, as well has a precession movement (precession of the equinoxes) which makes the day length fluctuate slowly (few *ms* per year). The solution is then to define the day as an amount of total angle of the earth rotation on itself. But this quantity is not linear. Earthquakes, tides and many other phenomena modify the angular speed so that it also varies slowly in time. One would then contemplate to ground the definition of the second on an average day time observed over a year. This is actually how it was defined till 1956. However, this was not completely satisfactory as *leap seconds* have regularly to be added to the universal time. We should also keep in mind that thanks to the Relativity of Einstein, we know that the timescale is relative to the observer, so after all, the definition of a timescale itself is arbitrary. This does not solve the issue of the stability of this

definition over time in a given physical frame.

The first step to achieve better time measurement is to use a faster periodical phenomenon, with a higher frequency. The systems that gives typically such parameters are oscillators based on crystal vibrations (sound waves) or any other electro-magnetic system from radio-frequencies (RF) to laser light (figure (1.3)).

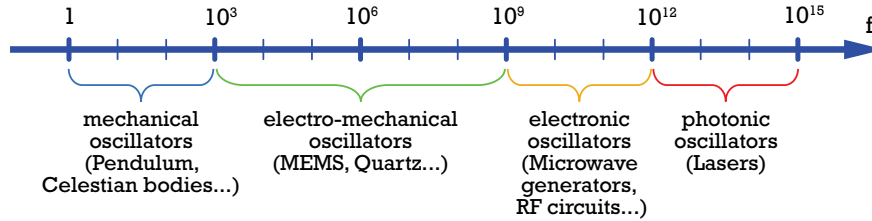


Figure 1.3: Frequency-scales given by several types of oscillators

Unfortunately, such oscillators are usually highly sensitive to the parameters they are built on as well as on external perturbations (length or mass fluctuations, thermal environment, aging...). Here comes the principle of the *atomic clock*, which is to use absolute atomic references on which the system is forced to oscillate, so that its frequency will, in theory, never vary. Having a deeper look

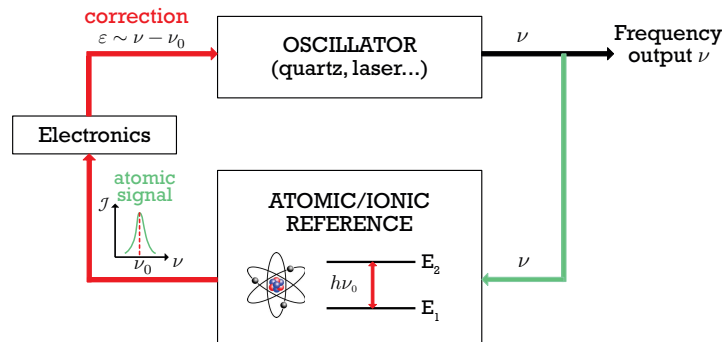


Figure 1.4: Principle of the atomic clock: a local oscillator is forced to oscillate on an absolute reference, which is the inter-space energy of two atomic or ionic levels

into the atomic clock machinery (figure (1.4)), one finds an emitting oscillator of frequency ν , usually a Quartz working in the RF domain or, possibly in the future, a laser emitting in the THz spectrum. On the other side, the energy spacing between two states of the atomic or ionic species that is used as reference is linked to a quantized electromagnetic energy of frequency ν_0 , according to *quantum mechanics* [Tannoudji 1973]:

$$h\nu_0 = E_2 - E_1 \quad (1.3)$$

where h is the Planck constant, E_i the energy level and $|i\rangle$ the corresponding quantum state. Then, the atomic system is excited when $\nu \approx \nu_0$ and has a *resonant* response with the input frequency ν . This principle is used in spectroscopy to measure energy levels in atomic species and gives the well-known fluorescence emission or absorption lines. As an atomic excited state decays, photons corresponding to the difference in energy levels with the ground state are emitted and detected. Whatever the nature of the quantity that peaks with the input frequency ν , it allows to **point out**

an absolute constant ν_0 , known to never fluctuate over time (unless the fundamental constants of the Universe are not really constant, which has never been proved to this date). Following that, an adequate electronics will allow to generate an *error signal* ε from the previous function that corrects the oscillator frequency from deviation to the atomic reference, so that $\nu \approx \nu_0$. Closing the control-loop will stabilize permanently the oscillator to the atomic reference which will provide the observer a very stable and accurate signal of frequency ν .

From that point of view, the atomic clock has been a disruptive time-counting technology compared to the former mechanical based clocks (figure (1.5)). Indeed, the first *isochronous* oscillators (Huygens pendulum in 1660, clock of Shortt in 1920, Quartz oscillators...) made time errors in the range of one second per day to one second per year/tens of years. The first accurate atomic clock, which was based on the *cesium 133* reference, was built in 1954 [Essen 1955]. Since that time, dramatic increase in precision and stability has been achieved, from the common use of compact industrial cesium clocks, to laboratory setups that take benefit from quantum effects in cold atom fountains and in direct optical interrogation of ions in optical clocks. Today, the most stable and accurate clocks make an error of one second on the horizon of the Universe's age [Huntemann 2016].

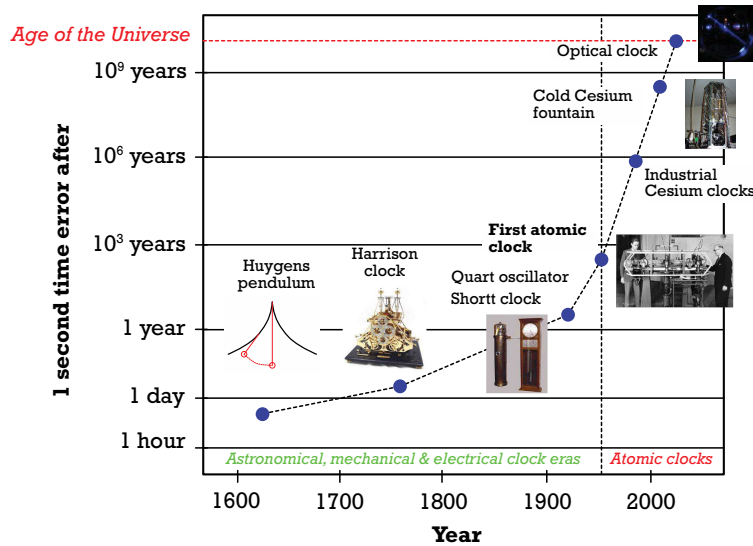


Figure 1.5: Since the 1950s, a huge progress has been made on the performances of the clocks compared to the previous centuries. After [Dimarcq 2015]

Before having a look at the applications of the atomic clocks today, we shall first see how the stability and accuracy can be defined in a rigorous way because these two parameters are crucial for the performances required in many systems. If a time-dependent signal s delivered by a frequency standard has the following form:

$$s(t) = s_0 \sin(2\pi\nu(t)t) \quad (1.4)$$

with an amplitude s_0 and a time-dependent frequency $\nu(t)$, then the latter parameter can be written as:

$$\nu(t) = \nu_0(1 + \varepsilon + y(t)) \quad (1.5)$$

with:

$$y(t) = \frac{\delta\nu(t)}{\nu_0} = \frac{1}{2\pi\nu_0} \frac{d\varphi(t)}{dt} \quad (1.6)$$

ν_0 is the *exact frequency*, ε is the systematic (constant) *frequency bias*, $\varphi(t)$ the signal phase and $y(t)$ the normalized *frequency fluctuations* in time. **A frequency standard accuracy is linked to the uncertainty on the correction of ε . A frequency standard is unstable if $y(t)$ is non-zero.**

A way to measure the frequency deviation over time is to use a statistical estimator of these frequency fluctuations. Indeed, it is not relevant to qualify a random signal by its amplitude only: the *root mean square* or variance value is rather used. In this perspective, a famous criterion for long-term stability evaluation ($\gtrsim 1s$) is the *Allan Variance* [Allan 1966], defined here for a discrete time-series:

$$AVAR(\tau) = \sigma_y^2(\tau) = \frac{1}{2} \langle (\bar{y}_{n+1} - \bar{y}_n)^2 \rangle \quad (1.7)$$

where \bar{y}_n is the n^{th} mean frequency fluctuation over the observation time τ and the brackets denote the number average over all the y_i samples of the time series. This quantity has the advantage to converge for many types of random noises affecting the y_i time series, unlike the traditional variance.

The square-root of the AVAR, called the *Allan Deviation* (ADEV), has a direct physical interpretation. The quantity:

$$\Delta t = \sigma_y(\tau) \times \tau \quad (1.8)$$

is the order of magnitude of the time deviation, in second, of the oscillator frequency of ADEV $\sigma_y(\tau)$ during an observation time τ . For instance, a clock of $\sigma_y(\tau = 1 \text{ day}) = 10^{-14}$ has a relative uncertainty of $\sim 1 \text{ ns}$ over one day. Most of the time, σ_y^2 is a changing function of τ , because the clock is perturbed by various internal factors. The slope of the AVAR reflects, in that case, the nature of the on-going frequency perturbation. As an example, a slope of -1 in a log-log ($\tau, \sigma_y^2(\tau)$) diagram shows that the oscillator is only affected by white frequency noise (that is, the power of the deviations about the mean value is constant whatever the frequency of analysis).

Consequently, the stability (the AVAR) decreases (increases) steadily as the observation time increases (decreases) (figure (1.6)). On the contrary, other effects (like thermal ones) characterized by random walk noise implies a $+1$ slope in the diagram, degrading the stability of the clock over time. Also, it is crucial to mention that such a measurement, done by sampling over time of the clock signal, has to be made with a *more stable* oscillator than the one which is probed. Indeed, the computed AVAR is always the one of the less stable oscillator. The availability of very stable clocks enables, on that point of view, to test numerous frequency standards. The AVAR has been presented here for pedagogical purposes, but many other refined schemes exist to better assess the stability trends (Modified Allan Variance, Hadamard Variance...).

It may be hard at first glance to see the point in measuring time with less than a *ns* of error. Actually, it is crucial for many technical applications of today's modern world. The three main areas where atomic clocks are intensively used are the following:

- Fundamental experiments: fundamental constants testing, fast phenomenons tracking (Large Hadron Collider or other particles accelerators for instance)
- Worldwide telecommunications: networks synchronization, radio and TV broadcasting, navigation and positioning (GPS, Galileo... which precision of localization is directly linked to the AVAR value), Coordinated Universal Time (UTC), International Atomic Time (TAI)
- Metrology: geodesy, radioastronomy

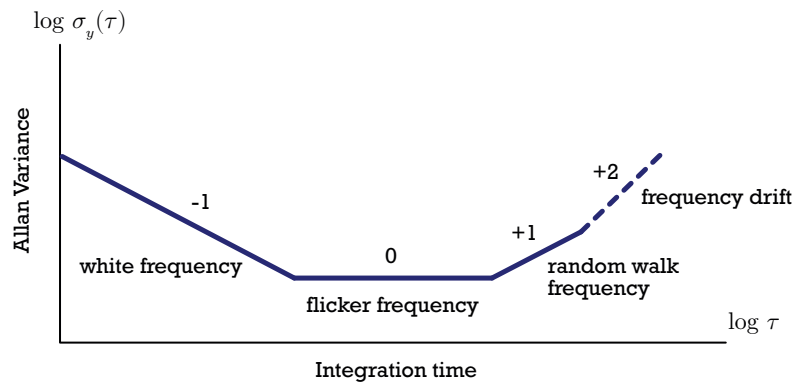


Figure 1.6: The slope of the AVAR in log-log plot vs. τ is linked to a specific type of noise. The observation time shall be measured by a more stable clock than the one tested.

Two applications are worth to mention here. The first one is the definition of the timescale TAI, and its well-known derivations UTC and GPS Time (GPST). The TAI is estimated every month by the *Bureau International des Poids et Mesures* (BIPM) in Sèvres by averaging the atomic time of nearly 450 secondary frequency standards and 13 Primary Frequency Standards (which are high accuracy atomic clocks located in few institutes of metrology in the world). This unit of measure, taken as an ultimate time-reference for scientific experiments, is as accurate as 2×10^{-16} (in 2015) and is linked to the UTC by adding or subtracting the 'leap seconds', so as to recover a time-scale close to the one given by the earth rotation on itself. GPS time definition is also grounded on TAI: they differ only from an integer number of seconds.

Another application is the geolocalization principle by the use of on-board compact atomic clocks in the Global Navigation Satellite System (GNSS). Different GNSS constellations are available, the most famous one being the Global Positioning System (GPS). Such systems enables a GNSS receiver (a cell-phone on earth for instance) to locate itself on the geoid by receiving the signals from (at least) four satellites in the sky. The first three satellites send their coordinates and their local time (given by the local atomic clock, which must be corrected from Relativistic effects before) and the fourth satellite usually give the time difference between the GPS time and the local time of the receiver. A four equations system of four unknowns then enables the receiver to recover its localization on earth. Also, the GNSS systems are an important mean to disseminate the universal time over the numerous telecommunication centers. In some cases, a local atomic clock is needed, when a network or a system cannot have physical access to the global time (submarines, isolated telecommunication centers...). In 2016, around 500 atomic frequency standards were in-orbit around the Earth.

Today, increasing attention is devoted to the development of compact and very small atomic clocks. The very first chip-scale clock was based on cesium 133 interrogation and showed very good short-term stability for its reduced sized (figure (1.7)) [Knappe 2004]. Such devices are planned to work as more stable local oscillators in isolated equipments that cannot synchronize regularly to the GNSS.

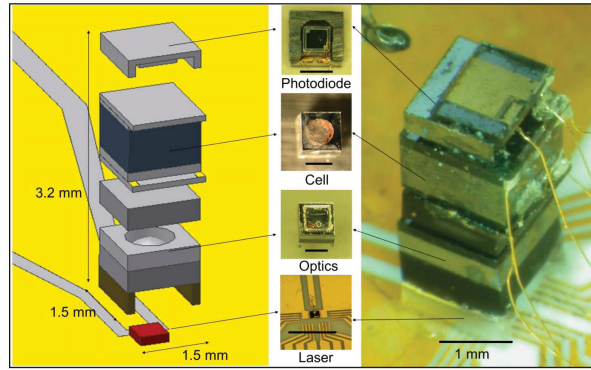


Figure 1.7: The Chip-Scale Atomic Clock (CSAC) of the National Institute of Standards and Technology targets short-haul navigation and local communications.

1.2 The Optical Cesium Frequency Standard (OCFS)

1.2.1 About Cesium Frequency Standards (CFS)

The cesium clock was the first type of stable atomic clock experimentally realized in 1955 [Essen 1955]. The cesium is an alkali of the column I of the classification which has a unique valence electron (structure is $[\text{Xe}]1s^1$). Therefore, its atomic excited structure (ES) can be rather simply described. Historically, this element was chosen for the stability of its ground state (GS) in the experimental conditions (the atomic mass is high enough for the element to be used in beams with few perturbation effects due to collisions). Having a deeper look into it, one finds a *fine structure* arising from the spin-orbit energy term, which splits into the *hyperfine structure* when the nucleus moment is taken into account. Under external magnetic field, these levels split again into the *Zeeman structure*, according to the quantum magnetic number value m [Tannoudji 1973][Steck 2008](figure (1.8)).

The cesium itself has a usable stable isotope (that is not radioactive) which is the ^{133}Cs . According to the quantum mechanics, if one excites the species thanks to the near-infrared radiations D_1 (wavelength in air $\lambda_1 = 894.4 \text{ nm}$ or $\nu_1 = 335.1 \text{ THz}$) and D_2 ($\lambda_2 = 852.1 \text{ nm}$ or $\nu_2 = 351.7 \text{ THz}$), the electron will jump to a higher energy level and the global state of the atom will change. Also, the possible sub-transitions in these lines correspond to defined state of polarization of the light (π or σ). After the average lifetime of this state, the electron will decay to lower energy levels, while emitting *fluorescence photons*. It should be noticed that because of the selection rules, only some transitions between the ground states and the excited states are allowed so that a selective fluorescence diagram is obtained if all the transitions are probed (figure (1.9)).

On the other side, regarding the atomic resonator, it is based on the difference in energy or frequency of the two hyperfine levels $F = 3$ and $F = 4$ of the ground state (GS) $6^2S_{1/2}$ [Steck 2008] (fig.1.8) which is:

$$\nu_0 = 9.192631770 \text{ GHz} \quad (1.9)$$

Such transition lies in the RF domain so it can be directly addressed using microwave generators. According to the principle of the atomic clock described earlier (figure (1.4)), some atomic peak signal has to be recovered from that excitation, according to the detuning of ν with relation to ν_0 (figure (1.10)). If we consider a large population of atoms, such signal fundamentally reflects the population difference of the atoms in GS ($F = 3$) and those in GS ($F = 4$). The problem is then how to 'count' the number of atoms that are on each level, while the ν frequency is changed.

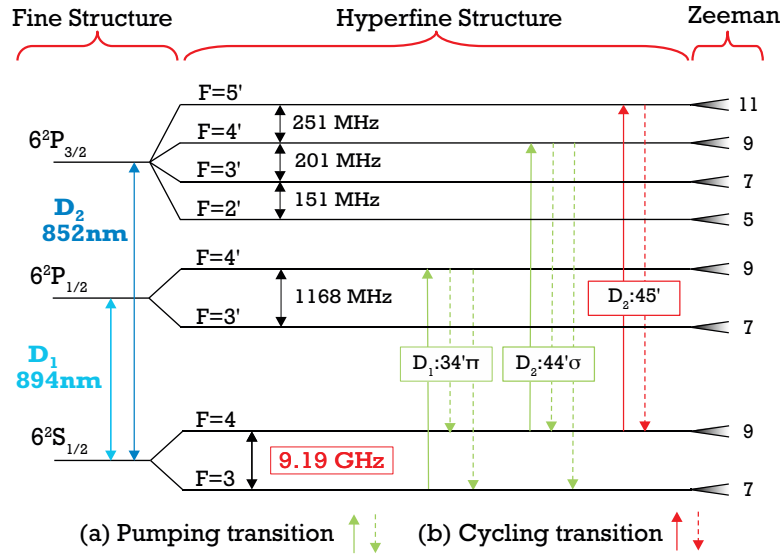


Figure 1.8: Hyperfine structure of the cesium 133. Only a few allowed transitions are represented. There are of two types: (a) The Pumping transitions: the ES can decay into the two hyperfine GS sub-levels. (b) The Cycling transitions: the ES can only decay in one of the hyperfine GS

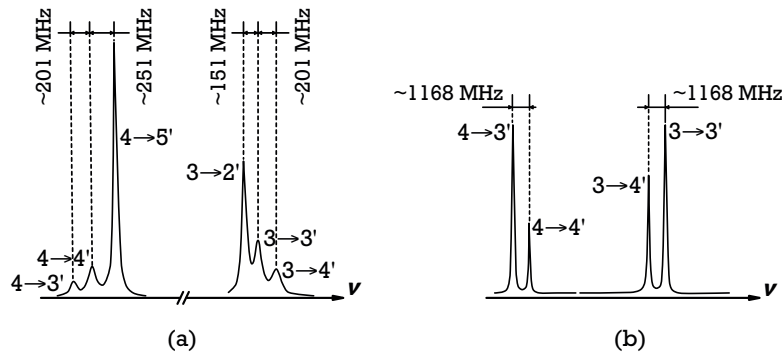


Figure 1.9: (a) The six fluorescence spectrum of the D_2 line. (b) The four fluorescence spectrum of the D_1 line. After [Dimarcq 1991].

An essential point to keep in mind is that such a signal *cannot* be recorded if the population of Cs atoms is at thermodynamic equilibrium at room temperature. Indeed, because the energy difference between the two ground states is of the order of $40 \mu eV$, versus the thermal excitation $k_B T = 25 meV$ at room temperature, one will find roughly half of the atoms in the GS ($F = 3$) and the other half in the GS ($F = 4$), so that no resonance can be retrieved because that partition will be the same after the ν_0 excitation, for symmetry purposes. That means one has to achieve *population inversion* so that all the atoms are in the same quantum state $|F = 3\rangle$ or $|F = 4\rangle$ before they can be excited to the other level and counted. There are basically two ways of doing that:

- Atomic selection: the atoms of one of the two states are discarded
- Atomic pumping: the atoms are all put in the same state

The first approach can be realized through magnetic selection, following the fundamental idea of the Stern and Gerlach experiments [Gerlach 1922]. It relies on the fact that the atoms of a

thermal atomic beam of speed v can be deviated from their trajectory using magnets which create a inhomogeneous magnetic field in the transverse direction to the beam. The deviation is tuned according to the total spin of the atom which changes depending on which state the atom is initially. Such practical mean to select the initial ground state of the cesium is at the basis of the Magnetic Cesium Frequency Standard (MCFS), since the first proof of concept by Essen [Essen 1955].

On the other hand, atomic population inversion can be achieved using the concept of pumping [Kastler 1950] where the atomic states are manipulated using laser radiations. The fundamental difference here is that, at the end of the population inversion process, no atoms are physically lost on the contrary to the magnetic selection approach where at least half of the particles are thrown away. This means that a greater number of atoms in GS can be interrogated using the RF excitation, so that the resonance signal of the clock recorded is higher for a given atomic flux. This idea grounds the principle of the Cesium Frequency Standard Optically pumped, which will be called here 'OCFS'.

Regarding the counting process, in the MCFS, the atoms that remain after magnetic selection (thus in the same state) are ionized and detected using an *electron multiplier* [Cutler 2005]. In the OCFS, the atoms are indirectly counted using a *coherent* light source i.e.: a *laser* radiation at one of the IR transitions mentioned before: when the atom state decays after the excitation, it emits photons that can be simply detected by a *photodiode* and converted to an electrical signal. All in all, the optical technology outperforms the magnetic one because it is technically simpler to operate and it provides higher atomic signal, and thus a better stability (see further).

1.2.2 Principles behind the OCFS

According to figure (1.10), the CFS has four main parts:

1. The local electronic oscillator
2. The microwave electronics for RF management
3. The atomic resonator
4. The electronics of regulation that turns the resonance signal into an error signal

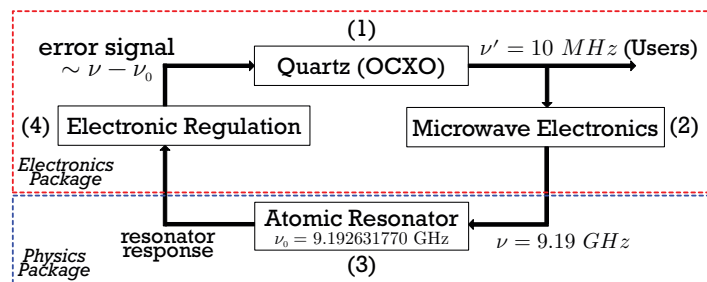


Figure 1.10: In the cesium frequency standard, the in-loop user frequency ν' at 10 MHz is up-converted to 9.19 GHz to generate the atomic resonance response

The parts (1), (2) and (4) are included in the *electronics package* while part (3) is called the *physics package*. Briefly, the oscillator of (1) is an Oven-Controlled Crystal Oscillator (OCXO) of very good short-term stability ($\sigma_y = 10^{-13}$ at $1s$) that is tuned at $\nu' = 10 \text{ MHz}$ which is also the final user's signal frequency. The signal is up-converted in (2) to a frequency $\nu = 9.19 \text{ GHz}$ by an adequate

electronics, which is turned into a resonance response at ν_0 in (3). Then, a second electronics (4) generates a signal error from the atomic resonance which can be used as a feedback in the servo-loop to stabilize (1) in the long-term. From now on, we will focus on the physics package before adding some few words about the electronics at the end of this section.

1.2.2.1 Physics package

The atomic resonator consists in a thermal cesium beam which has an intensity of flux of $I \sim 10^{10} \text{ atoms.s}^{-1}$ on a few mm^2 circular surface. The atomic speeds are given by the Maxwell-Boltzmann distribution. At 100°C , the most probable speed is $v_p = 216 \text{ m/s}$. The flux interacts several times with a laser beam at 852 nm or 894 nm perpendicular to that atomic beam through an optical bench placed along the cesium tube (figure (1.11)).

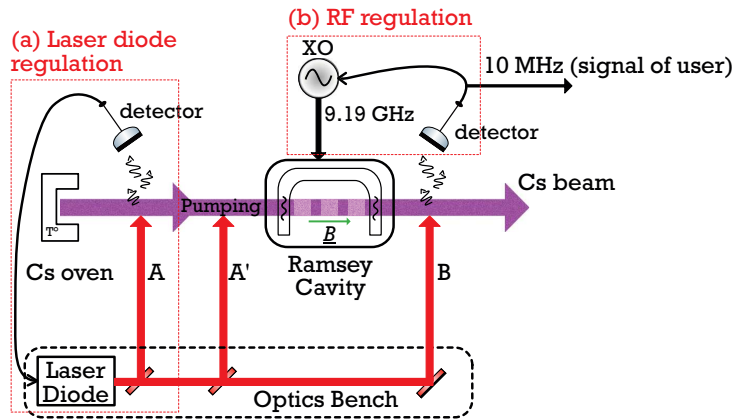


Figure 1.11: Schematic of the atomic resonator of the OCFS. The thermal Cs beam interacts several times with the laser at D_1 or D_2 transition lines

At that point, it should be mentioned that the laser used in this system is usually, for industrial application, a *laser diode*, which development is precisely the purpose of this manuscript. The topic will be addressed extensively in the coming chapters, but for the time being, it can be asserted that these devices are suiting the need of a source that can be tuned easily in the ranges of the cesium transitions around the D_1 line or the D_2 line, thanks to **temperature or current tuning of the device**.

More precisely, three main zones of Cs-light interaction can be identified. They are called zone A, zone A' and zone B. Also, a fourth zone allows the Cs beam to interact with the microwave radiation and is called the *Ramsey cavity*. On a functional point of view, part (a) in figure (1.11) regulates the laser diode frequency emission, while part (b) belonging to the electronic package handles the RF regulation and the clock-signal itself. We now have a deeper look at the physical mechanisms underlying the operation of the clock. To do that, measurements on a real prototype of OCFS (Thales Electron Devices) have been performed.

- **Zone A:** Laser diode regulation

The only function of zone A is to stabilize the diode laser wavelength on the desired Cs transition (see further section [1.2.2.2]). Indeed, the laser frequency can drift quickly with the environment perturbations (increase of the temperature of the set-up for instance). Also, random noise sources

that have various physical origins (inside or outside the laser cavity) perturb the optical frequency. These unwanted shifts with relation to ν_0 can be counteracted (to some extent only), with a careful driving of the temperature and current of the source. Ideally, these parameters must be optimized in real-time with a permanent tracking and correction of the frequency: an electronic servo loop is used to achieve that. This procedure will be described in the *electronic package*. For the moment, we will just study the physical light-atom interaction and the signal we can retrieve from it.

To highlight the fluorescence properties of Cs, one fixes the constant input current I_0 that gives the required optical power at the laser output, then the temperature of the diode is stabilized at a fixed value T_0 so that the frequency of the laser beam falls roughly at the D_1 or D_2 lines, and after that, the current of the laser is slightly modulated with modulation depth ΔI at a frequency f_I so as to scan the several transitions of each line. This is shown in figures (1.12) and (1.13). For the two transitions lines, the current of the laser diode is modulated here at low frequency ($f_I \sim 40 \text{ Hz}$) and a quite high depth ($\Delta I \sim 3 \text{ mA}$) with a sawtooth profile. The photons emitted back by the de-excitation process are then collected by a large area photodiode that turns the optical power into a voltage profile read on an oscilloscope. The tuning efficiency of the frequency (wavelength) being negative (positive) with relation to the current (around -1 GHz/mA for the laser used here), the scanning is from higher energy to lower energy with a positive slope of the current ramp, so that we recover the lines in the inverse order of figure (1.9).

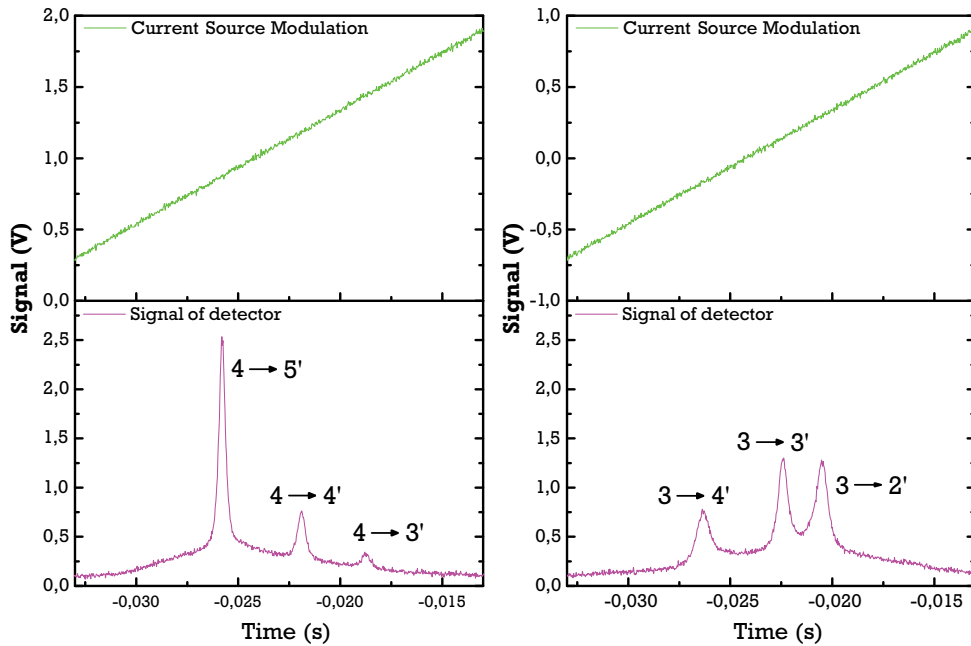


Figure 1.12: On the left: upper graph in green: Signal corresponding to the diode laser current modulation in time. Lower graph in pink: atomic fluorescence signal of the hyperfine transitions to $F = 4$ of the D_2 line recorded as a function of time in zone A detector. On the right: same as on the left but for the hyperfine transitions to $F = 3$ of the D_2 line

Later in this section, the description will be hold with the D_1 line at 894 nm . Now that the hyperfine transitions are detected, a servo loop can be implemented on one of these transitions. For instance, the $(43'\sigma)$ excitation scheme (which is the notation for a transition going from $|F = 4\rangle$ to $|F' = 3\rangle$ with a σ -state of polarization) can be used in that purpose. Before going on, it should be

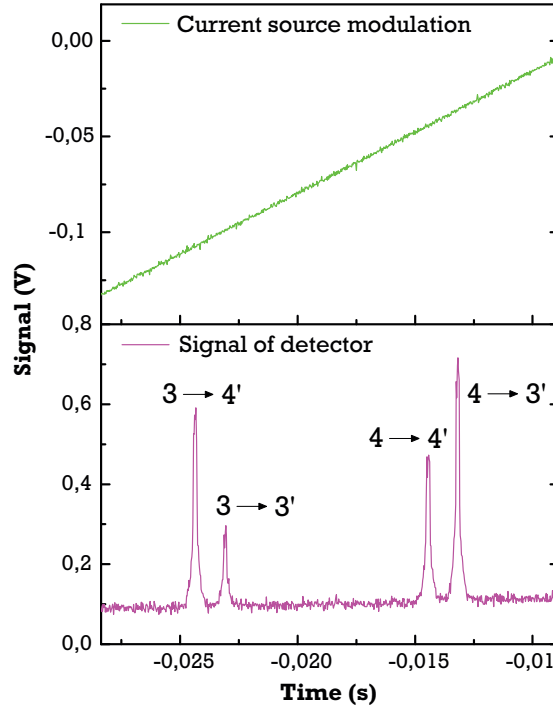


Figure 1.13: Upper graph in green: Signal corresponding to the diode laser current modulation in time. Lower graph in pink: atomic fluorescence signal of the hyperfine transitions to $F = 3$ and $F = 4$ of the D_1 line recorded as a function of time in zone A detector

mentioned that the observed fluorescence lines have a *finite linewidth*. This fact arises for two main reasons:

- The Uncertainty Principle: quantum mechanics states that the longer the decaying time of an atomic excited state, the shorter the energy/frequency broadening, according to the relation $\Delta\nu\Delta t \gtrsim h$
- Doppler broadening: in a gas, the particles have a distribution of speeds that broadens the frequency of absorption of that particles (for instance, with increasing temperature)

In a thermal Cs beam, one can expect to have negligible Doppler broadening, which is the case here, so that the fluorescence linewidth is the natural one. In the case of the D_1 lines, the transition time Δt_{dec} and the associated linewidth $\Delta\nu_{Cs}$ are [Steck 2008]:

$$\Delta t_{dec} = 35 \text{ ns} \quad (1.10)$$

$$\Delta\nu_{Cs} = 4.6 \text{ MHz} \quad (1.11)$$

For certain types of atomic clocks which work with gas cells, Doppler broadening has to be taken into account. The above value is very important because the fluorescence signal depends on how many atoms undergo the $(43'\sigma)$ transition: if the *laser linewidth* $\Delta\nu_l$ (that is, the energy broadening of the radiation) is way larger than in (1.11), the signal intensity will be less than the maximum possible value and may vary over time, creating *detection noise*. The question of the laser spectral purity (which would be perfect if $\Delta\nu_l$ was zero) is at the heart of the metrological part of this manuscript.

- **Zone A'**: Pumping of the Cs beam

When the laser is stabilized in frequency on one of the transition of the D_1 line ($43'\sigma$), the next step is to achieve population inversion regarding to what has been said before. This can be done using optical pumping (figure (1.14)). As the atoms are excited through ($43'\sigma$), the atomic population

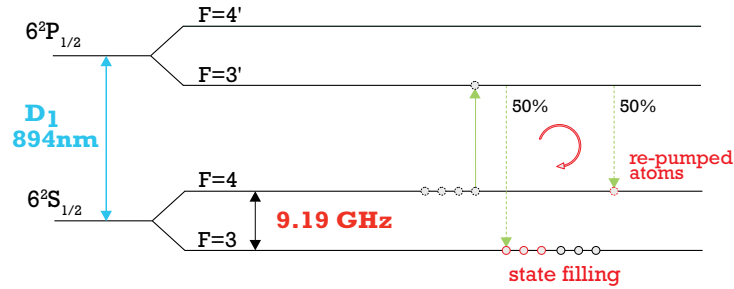


Figure 1.14: Principle of optical pumping in the $F = 3$ state. As the laser radiation acts, the level is progressively filled up with the full atomic population.

switches to the state $|3'\rangle$ and decay either in $|3\rangle$ or $|4\rangle$. But as the excitation goes on, the fraction of atoms in $|4\rangle$ undergo the same cycle as before, while the fraction in $|3\rangle$ stays in its state. If the laser power is sufficient regarding the atomic flux, after a certain time, all the atoms will populate state $|3\rangle$. Of course, we could also choose to populate the other state $|4\rangle$ with the appropriate transition.

To give some order of magnitude, the power needed for complete pumping of the Cs beam of Thales Electron Devices OCFS is about 2 mW and the time needed to do that is around a few μs . Experimentally, the pumping is realized in the zone A' of the resonator. Then, the fluorescence signal is detected in zone B, where a third laser interaction takes place, with an interrogating power of $\sim 150\ \mu\text{W}$ just as in zone A. It is interesting to look at the optical signal detected there as a function

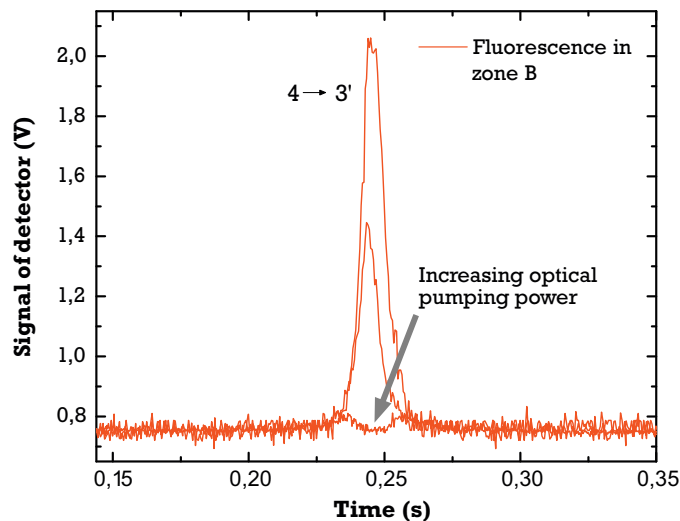


Figure 1.15: Detected fluorescence signal in zone B, using the ($43'\sigma$) transition. As laser power is increased in zone A', more and more atoms are put on $F = 3$ level, so that the fluorescence signal *decreases* in zone B, until the background noise of detection is reached

of the pumping power in A'. This is shown in figure (1.15). Now, when there is power, the signal

is high. As the pump starts to act, the maximum magnitude decreases till the peak value reaches the background noise floor. This behavior can be understood thanks to the energy diagram (1.16). Indeed, as population in state $|3\rangle$ increases to the detriment of $|4\rangle$, less and less atoms interact with

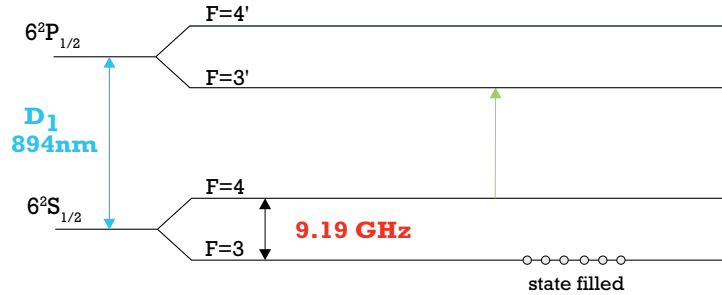


Figure 1.16: When complete pumping of level 4 is achieved, the atomic population is transparent to the $(43'\sigma)$ radiation

the laser beam and the number of photons detected in B decreases proportionally. Thus, the effective total pumping of the Cs beam is achieved when the peak signal vanishes totally. However, as it can be noticed, a little of the signal remains in the aisles, which is due to the fact that a Doppler spreading still affects the lower part of the line: some atoms of very different speeds are not influenced by the laser frequency.

Two additional points are worth to mention. The first one is that, in practice, the locking of the laser on the transition line in zone A already pumps the atomic beam, although it is not complete after the atoms have crossed that zone. It could be possible, in theory, to achieve both locking and pumping at the same time. However, this is possible only with the D_1 line because the pumping transitions of the D_2 are overshadowed by the very bright cycling one ($D_2 : 45'\sigma$, that produces at least ten times more photons than the pumping transitions) which prevents efficient fluorescence signal tracking.

The other point is that, contrary to the simple case given in [1.2.1], the efficiency of Cs pumping and fluorescence detection is not equivalent for all transitions. First, one has actually to take into account the fact that the hyperfine levels are degenerated into the $2F + 1$ Zeeman sub-levels, which split when a weak (and always present) magnetic field is applied. Indeed, when pumping is considered, it is actually into a particular $|F, m_F\rangle$ state. Because of the very small energy difference between these states, the decaying of the excited atoms usually spread over all the m_F numbers with a proportion given by the Clebsch-Gordan coefficients of the transition [Vanier 1989]. For the operation of the clock, the pumping of the level $|F, m_F = 0\rangle$ is chosen: it is indeed not sensitive to the first-order variations of the magnetic field (thus making a more stable clock with relation to environmental perturbations). Second, one should note that the maximum population achievable Δn depends on the transition used [Dimarcq 1991]. For instance, the $(43'\sigma)$ recorded above has a very good population inversion ratio $\Delta n = 16.5\%$ in $|3, m_F = 0\rangle$. Also, for this kind of pumping transition, the number of fluorescence photons emitted per atom is constant on average, whatever the detection conditions: in the previous case, $\beta = 4 /atom$. A rule of thumb is then to rank the global efficiency of transitions by their product $\beta \times \Delta n$.

- **Ramsey Cavity and Zone B:** Interrogation and Detection of the Cs beam

Once the beam is pumped into $|F = 3\rangle$, the atoms cross an electromagnetic cavity, called the Ramsey cavity [Ramsey 1950]. A static B_0 magnetic field is applied in the background, oriented

along the beam direction, so that all the Zeeman sub-levels are well separated. In the meantime, the Cs undergoes the $|3\rangle \rightarrow |4\rangle$ under RF power applied, with a frequency ν_{HF} generated by the local oscillator. This is done by using the 'Ramsey scheme'. More precisely, two HF field excitations B_{HF} at frequency $\nu_{HF} = \nu_R \approx 9.19 \text{ GHz}$ orthogonal to the beam direction, one at the entry of the resonator, the other at the exit (same interaction time τ) change the quantum state of the particle, while it is free-evolving between these two points (the free-evolution time is T). If the frequency $\nu_R = \nu_0$ of (1.9), then the whole atomic population will flip into $|4\rangle$ at the end of the resonator. If there is a little detuning from that frequency, some of the atoms will be in $|4\rangle$, while some of them will remain in $|3\rangle$ (in fact, from a quantum mechanical point of view, such intermediate Cs beam state is a *mixed superposition* of the two hyperfine states). If there is a third ($43'\sigma$) laser interaction in the zone B, it will be possible to read out the number of atoms in state $|4\rangle$, for the reason mentioned above (if one records a fluorescence signal, that means the atom was in state $|4\rangle$ with a probability given by quantum coefficients).

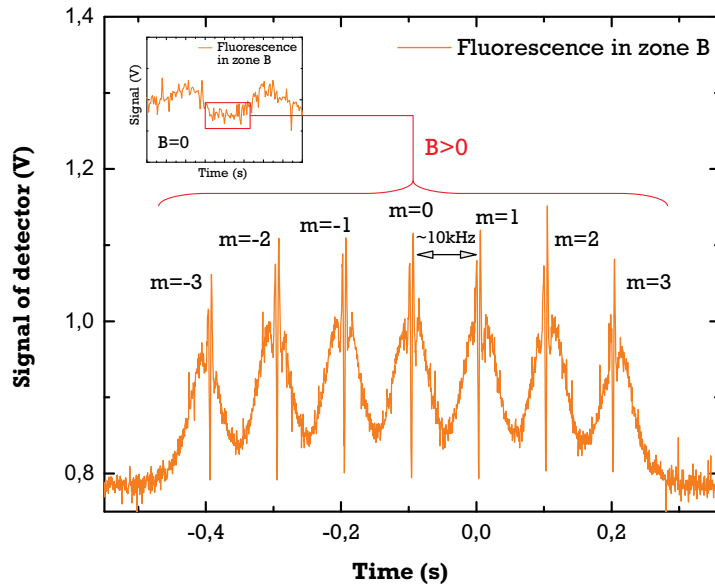


Figure 1.17: Main Graph: Under modulated frequency ν_{HF} of the RF power B_{HF} and static magnetic field B_0 , the interference pattern of the Ramsey Cavity is detected in zone B. The seven groups of fringes correspond to the seven Zeeman sub-levels which are energetically spaced of some 10 kHz in the experimental conditions. Box: at zero B -fields and no RF power, the flat zone between the aisles of the Doppler broadening has full pumping into $|F = 3\rangle$ state

Now, if the exciting ν_R is swept around ν_0 , the fluorescence in zone B will show the *interference* pattern over time of the Ramsey Cavity with this frequency detuning. This is what is highlighted in figure (1.17).

The splitting in energy into the Zeeman levels is clearly noticeable as seven groups of fringes are present. The $m = 0$ is the one of interest for the clock operation. In that group of oscillations, we are further interested in the central fringe of highest amplitude (figure (1.18)). The characteristics of that fringe gives a very important parameter of the performance of the clock, which is the *Signal-to-Noise*

Ratio (SNR)¹. It is defined as:

$$SNR = \frac{\Delta V_{flu0}}{\sqrt{S_{\delta V_{flu0}}}} \quad (1.12)$$

where ΔV_{flu0} , in *Volts*, is the detected *peak-to-valley* fluorescence signal and $\sqrt{S_{\delta V_{flu0}}}$ in *Volts*/ \sqrt{Hz} is the square root of the Power Spectral Density (PSD) of fluctuations of the fluorescence measured at half-maximum of the fringe, at the RF modulated frequency. The PSD is a (statistical) measurement of the amplitude of the noise relatively to the mean value of V in the frequency domain, in a unit bandwidth. Then, the short-term stability of the setup is given by [Vanier 1989]:

$$\sigma_y(\tau) = \frac{1}{Q\sqrt{2}} \cdot \frac{\tau^{-1/2}}{SNR} \quad (1.13)$$

where Q is the *quality factor* of the atomic resonator:

$$Q = \frac{\nu_0}{\Delta\nu_{Ramsey}} \quad (1.14)$$

Here, $\Delta\nu_{Ramsey}$ is the Half-Width at Half-Maximum (HWHM) of the central fringe. It is linked to

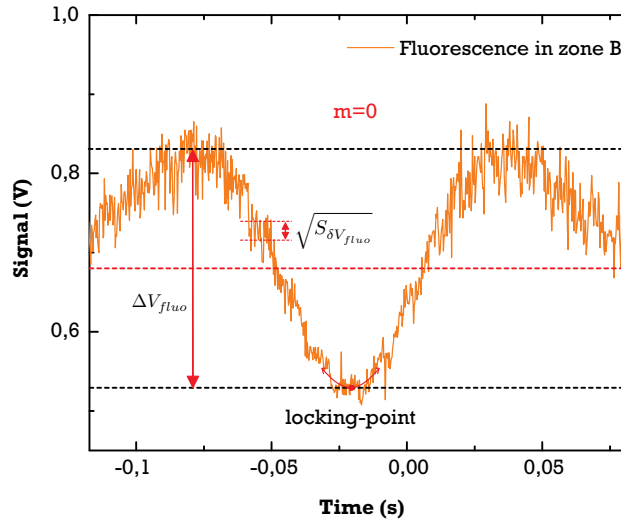


Figure 1.18: Zoom in the $m = 0$ Ramsey fringes (modulation of the RF frequency ν_R is on)

the length of the central zone of the cavity and decreases with increasing interrogation time T with the RF power. For an average atomic speed v_{at} , $T = L/v_{at}$ so that the geometry of the resonator fixes the Q factor. In the case of the Cs set-up, we have $\Delta\nu_{Ramsey} \approx 500 \text{ Hz}$ and $Q = 1.8 \times 10^7$. On the other hand, the SNR depends on many variables, including the atomic interaction parameters, the laser noise and intensity...etc. Beyond the formula (1.13), one should be aware that this model only applies to the **short-term** stability, which is supposed to be affected by white noise only, the relative magnitude of these noise fluctuations being expressed through the SNR. Such formulation of the stability of a resonator is pretty general: we will see in chapter 3 that the laser frequency noise can be characterized by a noise source term (like the inverse of the SNR here) divided by the optical cavity *Finesse* (Q here). If one wants to achieve a relative stability of 1×10^{-12} in the short-term, relation (1.13) gives immediately the $SNR \approx 40\,000$ to achieve.

¹This parameter has the dimension of \sqrt{Hz} unlike the conventional SNR. This feature can be related to a RIN (Relative Intensity Noise, see chapter 5) as defined in optics (here, it would be $1/\sqrt{RIN}$)

In the setup of Thales Electron Devices, the SNR reached with a laser at the D_1 line developed in the frame of this thesis is about 24 500 [Schmeissner 2016]. The associated relative stability of $\sigma_y(1\text{ s}) = 2.3 \times 10^{-12}$ is compatible with the Galileo requirements.

Finally, during real clock operation, the RF frequency ν_{RF} is locked by electronic means on the top of the Ramsey fringe.

1.2.2.2 Electronics package

The setup previously described enables to probe the atomic transitions. However, the signals generated and detected from the light-atoms interaction are treated by electronic schemes and the SNR can be degraded if they are not optimum. The design of the several locking servo loops of the electronics package plays an important role in the global performances of the OCFS.

- **Laser frequency locking on Cs lines**

The laser stabilization on a Cs reference line is an important step in the construction of an optically-pumped atomic frequency standard. The overall principle of this loop, which corresponds to part (a) of figure (1.11), is depicted in figure (1.19). The principle is the following: starting from

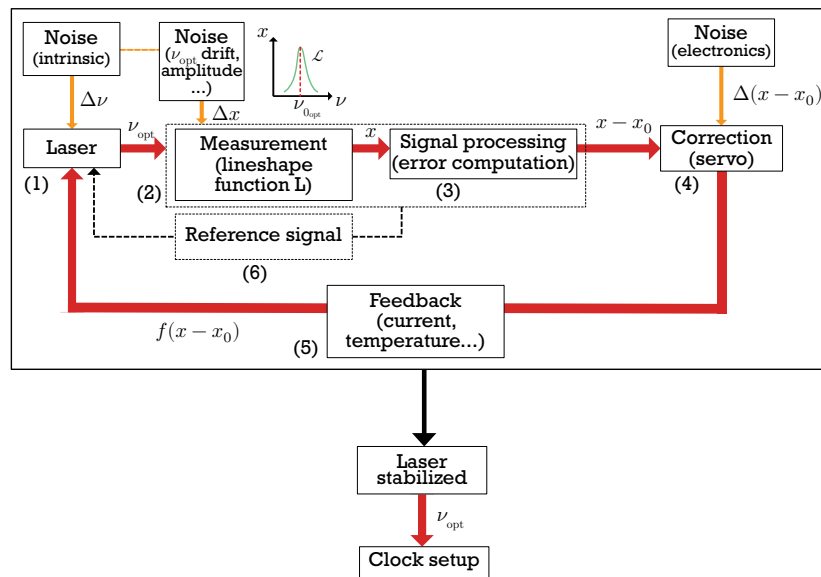


Figure 1.19: Schematic representation of the laser stabilization principle, as viewed in signal processing

le laser module (1), the source emits an optical carrier of frequency ν_{opt} which excites the atomic resonator (2). As said already, the resonator converts the laser frequency into a signal peaked on a fixed reference ν_{0opt} . This transfer function $\mathcal{L}(\nu_{opt})$ is handled by electronic means (3) and adequate signal processing to generate a *signed* error function $\varepsilon = x - x_0$ which depends on the deviation from the reference ν_{0opt} . Without going too much into details, such signal is generated by a periodical electronic excursion around \mathcal{L} maximum. The error function about ν_{0opt} is then injected into the servo part (4) which purpose is to create a correction signal $f(x - x_0)$ that will be re-injected in the driving parameters of the laser thanks to a *feedback loop* (5). The corrector itself can be a Proportional-Integrative-Derivative (PID) circuit [Astrom 1995]. This scheme is very general. A particularity of this resonator used is that the response function \mathcal{L} is actively dependent on the laser beam characteristics, on the contrary to more traditional passive resonators. Indeed, the ideal servo loop presented above

is perturbed by noise fluctuations around the nominal signals. The very first source of noise is the intrinsic noise which yields the finite laser linewidth $\Delta\nu_l$. But because of the nature of the frequency discriminator, the laser frequency fluctuations are converted and added to the useful locking signal x . Aside from that, the discriminator can have its own noise sources (for instance, an internal drift of the reference ν_{0opt}). Finally, the electronic scheme, especially the correcting electronics, may add their own noise contributions. This is why the final stabilized laser characteristics are not so easy to predict. In chapter 6, we will precise all these qualitative descriptions with an accurate model of the scheme.

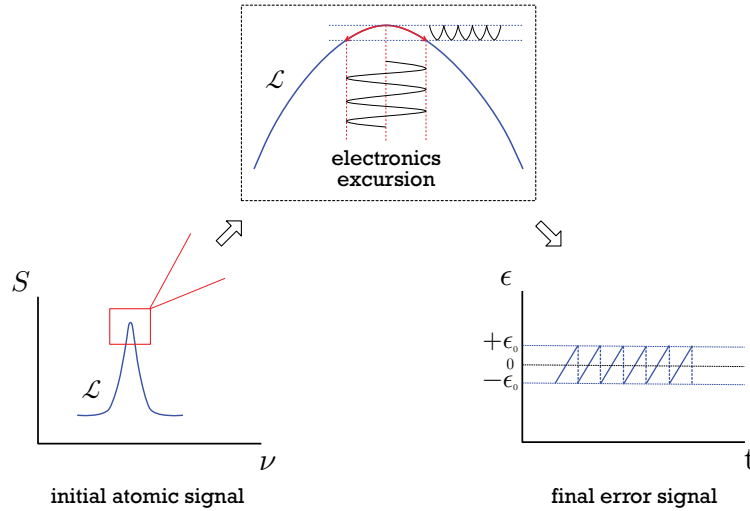


Figure 1.20: Qualitative description of the error signal generation from the atomic signal $\mathcal{L}(\nu_{opt})$

- **RF frequency locking on the central Ramsey fringe**

The other servo loop of the system (part (b) in figure 1.11, elements (1), (2), (4) in figure (1.10)) locks the RF frequency generated by the Quartz oscillator (OCXO) on the exact atomic separation ν_0 . The idea behind this procedure is very similar to the laser locking on the Cs line (figure (1.21)). A tunable Voltage Control Crystal Oscillator (VCXO) (1) oscillates closely to the hyperfine frequency $\nu_{RF} \approx 9.19 \text{ GHz}$ which generate the second atomic response function \mathcal{L}' of the setup (2). As explained in the physics package, the Ramsey fringe can be seen as a signal converter of the RF into a signal maximized at ν_0 , just like the fluorescence signal was maximized by the laser at the frequency ν_{0opt} . As for the laser locking, the signal is processed and an error function extracted (3), which is used again by a corrector (4) to act, with a feedback loop (5), on the VCXO frequency. The later is tuned by means of a voltage command. Because the VCXO has a poor stability and oscillates in the GHz range, the stability acquired by the loop is 'transferred' to a high stability OCXO (oscillating at 10 MHz) by means of a Phase Lock Loop (PLL). The PLL is a very interesting scheme which enables to correct the frequency of one oscillator with relation to another by a phase measurement difference of the two carriers: this is equivalent to a perfect integrator function on the phase. Also, in this loop, a frequency division/multiplication is realized on the carrier. It is the output of the stabilized OCXO that is finally used as the clock's signal. As before, there are sources of noise in this servo: the crucial one is the noise brought by the stabilized laser in the atomic reference signal. Indeed, we have seen that the Ramsey fringe is obtained after optical pumping of the atoms, which quality depends on the laser frequency fluctuations and output power. Of course, noise brought by the electronics occurs in (4) and the PLL in (6).

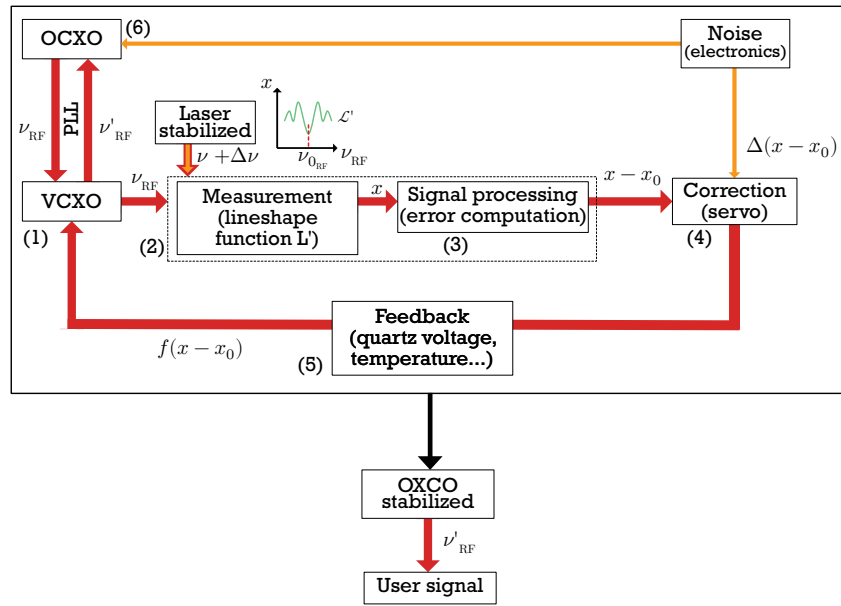


Figure 1.21: Schematic representation of the OCXO RF frequency stabilization principle, as viewed in signal processing

As a conclusion of the brief overview on the principles underpinning the OCFS, both the study of the physics going on in the Cs beam as well as the electronic regulation of the signals are fundamental to evaluate the overall clock stability. A dedicated model playing both with the atomic quantities and the regulation parameters will be presented in chapter 6 to highlight the particular role of the laser in the setup.

1.2.3 The OCFS today

Following the diffusion of the concept of optical pumping [Kastler 1950] and the onset of the development of laser diodes of various frequency emission in the near-infrared, the first OCFS prototypes appeared at the end of the 70's [Arditi 1980]. Since that time, many progresses have been made, both on theoretical and experimental point of view [Théobald 1989, Dimarcq 1991, Drullinger 1991, Dimarcq 1993, Lucas-Leclin 1998], with the pioneer work of the "Laboratoire de l'Horloge Atomique" (LHA) in Paris and the 'National Institute of Standards and Metrology' (NIST) in Boulder, Colorado.

However, the development of *industrial* OCFS was still a wishful thinking, especially because of the issue of the availability of narrow linewidth lasers required to achieve both pumping and detection. The years 2000 show the premises of such a compact clock that could be a good competitor to the aging Cs-III MCFS embarked in the GPS constellation [Lutwak 2001, Guerandel 2002, Hermann 2003, Sallot 2003, Hermann 2007, Lecomte 2007, Berthoud 2010]. Also, the lack of industrially competing European embarked clocks, versus US technologies, has pushed for the development of this new frequency standard. In the meantime, other types of clocks, namely Hydrogen Masers (HM) and Rubidium Frequency Standards (RAFS), are developed to address spatial applications [Droz 2006]. A key parameter in that case is the volume, mass and consumption (which defines an equivalent cost). For instance, such cost in 2016 for satellites launch was 20 k€/kg (source: European Space Agency). In the two previous cases, the weight is in the range of 6 to 10 kg and the volume is a few liters. Some typical current performances of those technologies are shown on graph (1.22). Commercially

available compact standards of that type are, for the time-being, US or Switzerland/France-based [Microsemi 2016a, ExcelitasTechnologies 2016, Spectratime 2016]. An essential point in these technologies is that they require *lamps* and not lasers for the operation.

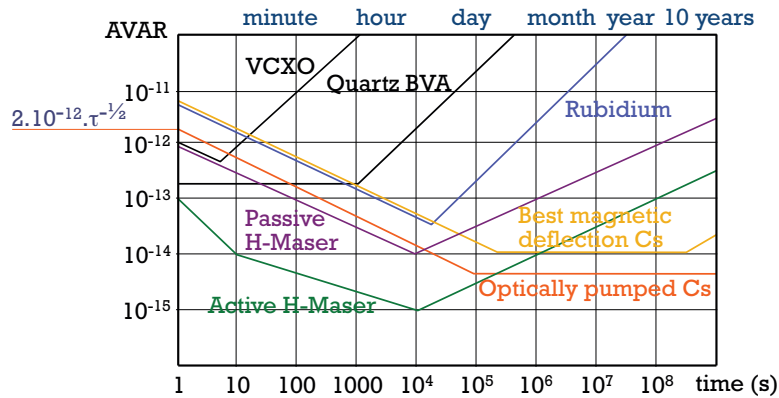


Figure 1.22: Allan Variance profiles of some industrial atomic oscillators (performances in 2015). The cesium Standards have better long term stability over RAFS. Source: Thales Electron Devices

Nevertheless, laser-based Rubidium clocks with better performances have been prototyped [Affolderbach 2011], still with the use of a gas-cell and a microwave interrogation. For atomic properties purposes, the Cs and Rb cannot be used in the same technical configurations.

Also, a huge interest is shown for the clocks using the Coherent Population Trapping (CPT) scheme. It has been said in [1.2.1] that population inversion between the ground state and the excited state has to be achieved to get contrast in the resonance signal of the clock. Actually, there is another mean to do that [Cyr 1993]. In the CPT clocks, the laser interrogates directly the atomic levels without the need of a RF cavity, usually in a gas-cell. To do that, the laser has to produce two frequencies at $\nu_{CPT1} = \nu_{D1}$ and $\nu_{CPT2} = \nu_{D1} + \nu_0$. Such excitation 'traps' the atoms in a coherent state lying in between $|3\rangle$ and $|4\rangle$, so that a pass of the laser beam in the gas-cell will show a peak of laser transmission (the atoms in the mixed state no longer absorb the radiation) if the frequencies are exactly adjusted in the previous way. This peak can be used as a locking reference for a local oscillator, just like for the classical scheme. Dramatic gain on simplicity and reduction of volume lead to the extreme case of CSACs [Microsemi 2016b] (figure 1.7), where in this case, the laser is a Vertical Cavity Surface Emitting Laser (VCSEL) used for its compactness and ease of modulation to produce the frequency side-bands. Many studies are reported (see a review in [Vanier 2005]) and finally, clocks mixing original interrogation schemes and configurations have emerged [Castagna 2009].

To sum up, the OCFS is today mature enough on an industrial point of view to compete with lamp-based Standards. Indeed, laser-based atomic interaction already showed its better efficiency against the current technologies. But a crucial point of its development is the **availability of reliable, compact and high-performances lasers modules** to operate the clock, just as many other promising technologies mentioned above. This is precisely the point addressed in the following part of the study.

1.3 The need of laser modules at cesium D_1 line (894 nm)

1.3.1 852 nm or 894 nm ?

We have seen with figure (1.8) that both Cs D_1 line (894 nm) and D_2 line (852 nm) have pumping hyperfine transitions that can be used for the atomic preparation in zone A'. Regarding the detection of Ramsey transition in zone B, both cycling (only at 852 nm) and pumping transitions (whatever the line) can be used.

For technical reasons, the first laser available at such wavelengths was the 852 nm. Indeed, it was a *Gallium Arsenide* (GaAs) diode-based laser, which energy gap is precisely in this range of frequency (around 860 nm). Thus, the first near-infrared lasers for cesium pumping commercially available were for the D_2 line. Later, the development of diodes of more complex structures using higher order ternary or quaternary alloys of III-V elements has allowed wide tunability of the frequency emission and lasers near 900 nm were commercialized.

For the OCFS industrial application, there are technical advantages to use lasers at one or the other wavelength and they are listed below:

- 1/ Laser locking on transitions

As shown in figure (1.9), the D_1 fluorescence lines have energy separations of 1.2 GHz while it is in the range of a hundred of MHz for the D_2 line. It is thus easier to lock a laser in the first case than in the second case, given the tuning coefficient of the laser frequency with temperature and current (respectively 25 GHz/K and 1 GHz/mA). The energy absorption at the targeted line is also maximum as no spilling of pumping power arises on the neighboring transitions. Moreover, the very bright cycling transition of the D_2 line gives a far higher magnitude of signal over the one of the pumping transitions, saturating easily the electronics and making more complex the locking on these transitions. On the contrary, the D_1 lines have roughly the same fluorescence level (figure 1.13). This opens the way to a unique step of locking and pumping at the same time, reducing the cesium tube complexity. Finally, cycling transitions can be affected by intrinsic saturation which leads to the line broadening. It is not the case for the D_1 lines.

- 2/ Inversion of population and photon emission

The clock's SNR is said to be proportional to the product $|\beta \times \Delta n|$ [Dimarcq 1991]. Both D_1 (with $(34'\sigma)$) and D_2 (with $(43'\sigma)$ and $(34'\pi)$) are interesting pumping and detection schemes. Especially, the case of the cycling transitions (e.g. $(45'\sigma)$) theoretically enables to collect 10-times more photons because this number is linked to the time the atom spends in the detection area, on the contrary to pumping transitions where β is fixed. However, the cycling detection scheme is far more dependent on laser's frequency noise (this can be understood intuitively as in a 2-level system, the atoms are excited and de-excited alternatively, reproducing the electrical-field fluctuations, while in a 3-level configuration, the atom is excited and de-excites in one of the two levels where it remains insensitive to the radiation, so that the population is quickly decoupled from the influence of the laser field). For ease of operation and less complex setup, in the frame of an industrial development, a one-laser operation is preferred, either at D_1 or D_2 line.

- 3/ Hanle effect

When a weak magnetic field is applied, the atoms feel the influence of the polarization of the incident light (π -polarization when it is parallel to the magnetic field, σ -polarization when it is perpendicular). In the σ configuration, quantum mechanical effects can take place, creating *coherences* (mixing of states, as evoked before for the CPT) between the Zeeman sub-levels [Théobald 1989] so that for some transitions, these 'idle-states' reduce the theoretical maximum value of population inversion (some atoms are trapped and do not see the pumping process). The solution to that is to "depolarize" the light by creating a non-homogeneously polarized laser beam [Shirley 1994, Berthoud 2010]. In the excitation schemes of interest above-mentioned, the $(3d^1\pi)$ is insensitive to Hanle effect, so that its use would leave unnecessary the depolarization step before the atomic interaction.

To sum up, the technical advantages of using a D_1 transition are valuable in the perspective of the production of simpler and cheaper OCFS.

1.3.2 Industrial specifications of the laser of the OCFS

Regarding to what has been said with relation to the development of an industrial OCFS, it is now time to specify the laser characteristics awaited by the manufacturers, here Thales Electron Devices and Oscilloquartz SA (see below). It concerns laser modules which integrates a protective *housing* and means of frequency tuning by acting on the current and temperature of the device. The list is made by order of practical importance:

1. **Emission frequency:** 894.4 nm for the D_1 line or 852.1 nm for the D_2 line measured at 25°C, with a [10°C; 40°C] maximum operation range. A tunability of ~ 1 nm around the lines is required.
2. **Mode:** The laser should be *single mode*, i.e. the output beam should be the fundamental Gaussian mode with a single frequency of emission. Also, no *mode hopping* in time or with temperature and current regulation should occur in the tuning range around the lines.
3. **Optical Power:** the setup requires at least 20 mW of laser power to address the various optical zones, taking into account the losses in the optical bench and an hypothetical loss of power with aging. This value depends also on the spectral purity of the source because more pumping power is required when the laser linewidth is broader.
4. **Side Mode Suppression Ratio:** The *SMSR* measures the ratio of the power in the main mode compared to the power of the other modes in the vicinity of the spectrum. A single mode laser is usually defined when the *SMSR* $\gtrsim 30$ dB (relation of 10^3 in power). In the present case, the criterion is a *SMSR* $\gtrsim 40$ dB.
5. **Laser linewidth and Frequency noise:** The linewidth characterizes, in the frequency domain, the spread in energy/frequency of the photons emitted by the laser. The application requires a $\Delta\nu_{laser} \leq 1$ MHz at Full-Width at Half Maximum (*FWHM*) of the spectral profile, at 40 mW output, for an observation time of 250 ms. The associated frequency noise, which characterizes the power density of frequency fluctuations per unit of Fourier frequency bandwidth, is given by its level at low frequencies ($\leq 10^{10}$ Hz²/Hz at 1 Hz for the $1/f$ flicker component), and its white noise constant floor ($\leq 10^5$ Hz²/Hz, in the range above 1 MHz). The mathematical and, more crucially, experimental relationships between these two aspects of laser frequency noise is not trivial at all and will be at the heart of the second part ("Metrology") of this manuscript.
6. **Laser relative intensity noise or RIN:** it measures the relative fluctuations of output power per unit of Fourier frequency bandwidth: *RIN* $\leq 10^{-12}$ Hz⁻¹ at 10 Hz.

7. **Threshold current:** The laser threshold should be $I_{thr} \leq 80 \text{ mA}$
8. **Sensitivity of frequency with current:** $\frac{\delta\nu}{\delta I} = -1 \text{ GHz} \pm 0.2 \text{ GHz/mA}$
9. **Sensitivity of frequency with temperature:** $\frac{\delta\nu}{\delta T} = -20 \text{ GHz} \pm 5 \text{ GHz/K}$
10. **External efficiency:** The laser efficiency of output power should be $\eta_d = 0.6 \pm 0.2 \text{ W/A}$
11. **Power budget:** Maximum 300 mW for the regulated module
12. **Optical Feedback threshold:** it measures the limit above which the relative re-injected power (in dB) in the laser cavity (for instance by a distant optical element) perturbs the laser mode so much that it cannot be used properly in the OCFS anymore. This parameter is highly sensitive and difficult to estimate (see 'Feedback' part). It should be as high as possible (perturbation for the highest possible re-injected optical power)
13. **Polarization state of the light:** linear polarization
14. **Beam far-field divergence:** the beam has to have ideally a round shape, with no divergence, with an associated beam quality characterized by $M^2 = 1$. In reality, a tolerable full divergence (at $1/e^2$ on a Gaussian profile) is 12° per 51° (more divergence would induce more technical constraints on beam shaping).
15. **Laser packaging:** The laser's housing should be as compact as possible, equipped with a Negative Temperature Coefficient thermistor (NTC) and a Peltier element for temperature regulation. The packaging should be hermetically sealed and resistant to shocks, vibrations and temperature cycling.
16. **Lifetime, Reliability, Aging:** The laser module should live at least 10 years with no detrimental degradation on the parameters mentioned above, the Mean Time Before Failure is expected to be 100 000 *hours* and laser aging should be in the range of $\leq 1 \text{ mA/year}$ of operational current drift.
17. **Cost:** Last but not least, the cost of the laser modules have to be evaluated regarding the OCFS overall budget and selling price. Technical solutions to reduce the production price of the modules can be implemented.

Some remarks can be made regarding those specifications. They were established earlier with the lasers available when the first designs of OCFS were realized (diode lasers in $TO3$ package). These specifications have evolved and will continue to do so when progress are made on their characteristics with the OCFS simplification/increase in performances they can produce. This is why a constant dialog with clock manufacturers has been conducted during the development of the sources of this work, so that both sides can adapt to the technical constraints of each others.

1.3.3 Which laser technology for the application ? The LAMA Project

- **Existing laser technologies for the OCFS**

We address now the question of which laser technology is the most relevant to comply to all the specifications required. Over the thousand of types of lasers that exist today (gas, solid-state, dye, metal-vapor, semiconductor and related diode-pumped lasers...) only semiconductor and solid-state can possibly address, for the time being, the 850–900 nm range. For the later case (e.g. Ti:Saphir), the

requirements for compactness (above the liter) and power-consumption ($\sim 1 W$, *Wall-plug efficiency* or $WPE < 0.1\%$) is not fulfilled. Within the family of laser diode based sources now, it is the same for fiber-lasers, which, though they have very narrow linewidth ($\sim 10 kHz$) must be pumped with quite high-power diodes ($\sim 200 mW$). Especially, the use of fiber Bragg gratings is interesting but increases the sensitivity to unwanted feedback, the tunability is very limited, and requires a complex packaging for light-to-fiber coupling.

In the family of semiconductor-based sources, the crystal photonic lasers are still a topic of active research while VCSELs (Vertical Cavity Surface Emitting Lasers) have very broad linewidths (100 MHz range and above) and low output power ($\sim 1 mW$). The VeCSEL (Vertical external Cavity Surface Emitting Laser) which consists in half-a-VCSEL embedded in an external cavity and optically pumped has recently shown impressive results, both in output power, consumption, beam quality and linewidth [Denet 2016]. However, for the time being, the maturity of its packaging must still be proven so as to be integrated in a commercial system. On the other side, the edge-emitting semiconductor lasers are well-known for now 40 years and have already been used in prototypes of OCFS, in external cavities or as single-mode lasers. Even though a Fabry-Perot edge-emitting diode in external cavity can reach linewidths in the range of 100 kHz, there is still the question (just like for the VeCSEL), of the stability of this cavity length over time, which usually induces strong low-frequency noise (as well as the issue of compactness). On the other side, a semiconductor laser monolithic chip does not suffer from this drawback, as the cavity length variations are negligible with temperature and current. Nevertheless, steps towards an integrated micro-platform for spectroscopy is showing promising results [Maiwald 2008].

Within the edge-emitting lasers, four types of single mode emitters (always within a given range of current and temperature windows) are of interest:

- Short Fabry-Perot cavities (FP)
- Distributed-Feedback Laser Diodes (DFB)
- Distributed Bragg Reflectors Lasers (DBR)
- Discrete-Mode Lasers (DML)



Figure 1.23: Vertical and longitudinal structure of various edge-emitting laser diodes. The light gray corresponds to the lower refractive index material (cladding), the darker gray symbolizes the core of higher index and the red material is the active zone of positive optical gain. Only the relevant layers for mode guiding are represented. Usually, the left and right mirrors are coated with either high reflectivity or anti-reflective dielectric materials. (a) a Fabry-Perot laser diode, (b) a DFB laser diode with a buried Bragg grating (c) a DBR with a single-electrode (d) a DML structured with complex periodic patterns on top of the waveguide.

For the first type, the laser is made of a bulk of semiconductor layers that defines a waveguide in the vertical direction, thanks to the use of various refractive index alloys, while it is of homogeneous

composition in the longitudinal direction. The core of the cavity embeds an *active zone* where positive optical gain is obtained under current injection. The modes are the ones that exist between the two left and right parallel mirrors, i.e. the Fabry-Perot modes, spaced out by the *free spectral range*, which gets higher for shorter cavities, so that a single mode tuning range of $\sim nm$ can be found for $\sim 100 \mu m$ -long devices. The first drawback of such a design is that it has poor thermal conductivity (which increases with a diminishing laser surface), increasing frequency tuning with current and leading to *thermal roll-over* (decrease of optical power with increasing inner temperature of the component). But the worst aspect is a quite broad laser linewidth in the $\sim 10 MHz$, which increases when the cavity is shortened, all other things being equal (see chapter on noise).

The DFB consists in a Fabry-Perot cavity which embeds a *Bragg grating* on the overall length of the component which acts like a selective wavelength filter, either in the bulk structure (buried grating) or on the top of the component (surface grating). The concept of the DFB has been widely studied for 45 years now [Kogelnik 1972], both on the theoretical mechanisms of laser emission and on practical realizations. Today, this technology is well-mastered and is a standard single-mode laser technology that is widely used for pumping applications and mid-haul telecommunications. It requires though to realize a $100 nm$ -scale corrugation in the semiconductor layers, which cannot be defined with standard Ultra-Violet light (*UV*) lithography fabrication techniques.

The DBR is made on the same principle as the DFB, but the longitudinal structure is not homogeneous: one side is made of an effective Bragg mirror (also defined in the bulk or at the top like the DFB), another side has the gain medium, so that mode selectivity is realized independently of the biasing conditions, unlike the case of the DFB. Also, some multi-electrodes configurations can be found sometimes, with an additional *phase section* between the Bragg section and the gain medium, which can be biased with an independent current so as to modify the phase of the traveling wave in the cavity (changing the lasing properties of the component). Technologically speaking, it is more difficult to fabricate compared to the DFB, as it requires a *butt-joint* epitaxial growth of the materials, that is, to stick together different vertical structures.

Finally, the DML recovers Fabry-Perot type lasers which internal modes are perturbed by discrete etching features on the top of the waveguide, so that the component can be single-mode on a wide tuning range without mode-hopping [Kelly 2007]. Their principle is not that different from the previously mentioned lasers but they are easier to fabricate. The mode selection requires however careful optical cavity simulation, which can be done using *transfer-matrix* techniques (see dedicated chapter).

- **The LAMA project**

The **LA**ser Modules for high performance **A**tomic clocks (**LAMA**) project (2014-2017) aims at providing laser modules that meets the specifications mentioned above, so as to push the OCFS to the industrial market. It gathers one Swiss atomic clock manufacturer (Oscilloquartz SA, from the ADVA group) which developed a prototype of OCFS for a project of the European Space Agency (ESA) (OSCC, [Hermann 2007]), Thales Electron Devices, a French company of the Thales Group, which develops a cesium tube for the application, the Swiss Laboratory of Time and Frequency (LTF) of the University of Neuchâtel, which as a long-standing experience in frequency standard theoretical and experimental evaluation, as well as noise characterization of laser devices for these applications. Finally, this PhD work is dedicated to the theoretical and experimental study of the lasers of the project, on the device aspect, especially on their design. The ultimate goal of LAMA is to demonstrate a fully integrated prototype of OCFS that is scalable for an industrial production. It must be in particular the case for the laser modules.

1.3.4 Current state-of-the-art for 894 nm sources

At the time of this work, few 894 nm sources were available on the market, and they did not really meet the requirements for the OCFS application. We can name the following manufacturers: Toptica Photonics AG who sells DBRs with an output power of 40 mW for a linewidth in the range of ~ 5 MHz [TopticaPhotonicsAG 2016], Nanoplus GmbH, who usually provides surface gratings DFBs, and claim to have commercially available lasers that meets the requirements at 852 nm but also at 894 nm, though no specific figures are given in their datasheets [NanoplusGmbH 2016]. Also, a seller called the Frankfurt Laser Company proposes a DFB of 10 mW output [FrankfurtLaserCompany 2016], while Vescent Photonics also provides DBRs at the desired wavelength, with a ~ 1 MHz linewidth, that is however more for lab applications given the size of their module. If some of these sources seem interesting for the application, the availability, as well as the price, have to be taken into account in the choice of the supplier. For instance, a DBR from Toptica was priced in the range of 4 000 € in 2015. Most of the time, these companies are only *packagers* of the semiconductor chips, while the semiconductor manufacturers are only a few. We can cite for instance in Europe Eagleyard Photonics, who can master the whole development chain from chip to packaging, like III-V Lab in France. To sum up, the 894 nm as become of increasing interest over the past 5 years, as demonstrated the numerous types of lasers developed around this topic. A diode-laser pumped cesium gas laser as even been developed to convert the 852 nm power to 894 nm [Zhdanov 2007].

1.3.5 Context of this work

My work is done in the frame of an "industrial thesis" (CIFRE), which is a French type of PhD work specifically oriented on R&D topics, that usually takes place in a company who has research issues, and that is supervised by an academic, here the Institute of Electronics and Systems (IES - UMR 5214) of the University of Montpellier in France. This laboratory has an historical background on electronic conception and has a department devoted to the design and study of low noise (electronic) laser sources to be integrated in optical systems. The company is a joint industrial lab of the Thales Group (formerly Thomson-CSF) and Nokia (formerly Alcatel-Lucent Bell-Labs) which works on many different topics linked to the III-V types semiconductors, from telecoms lasers, modulators and photonic integrated circuits (PICs), to GaN displays and transistors, as well as sources for species pumping.

The demonstration of a high-power laser diode with narrow linewidth at 894 nm is not new in itself [Klehr 2007, Telkkälä 2010]. At III-V Lab, its development follows the work done on the 852 nm DFB laser, that was used for optical cooling of cesium atoms in experiments of the Syrte [Ligeret 2008]. Here, we intend to show the development of adequate sources for the OCFS application, in an *industrial perspective*, with the help of the academic scientific approach. We will dwell particularly on the noise properties of the devices, which, as was said before, are very important for the application, and try to highlight theoretical and practical conception rules that lead to low noise lasers. Also, the question of the feedback sensitivity of these lasers will be addressed in a pragmatical way. Such work will highlight the intrinsic limits of the technology regarding this topic, so that the technological efforts to gain on laser performances can be adjusted in an optimized way.

Finally, the device environment (ie: the control system) must be taken into account to judge from its performances in atomic clocks. We will try to estimate the lacks (or conversely, the over-specifications) of the modules from an experimental and theoretical point of view.

1.4 *Summary*

The quest for accurate and stable clocks is going hand-in-hand with experimental and technical progresses for centuries now. It requires to find high-frequency oscillators than can be locked on high accuracy and high stability references. Since the 1950s, **the disruptive technology of the atomic clock has enabled to gain ten orders of magnitude on the stability**, measured commonly by the Allan deviation. It consists in **tuning and locking the frequency of the local oscillator (usually a Quartz) to the energy difference between two stable atomic levels**. From the laboratory to the industry, such setup has enabled numerous telecommunication technologies to emerge, one of the most famous one being the *Global Positioning System*.

The Optical Cesium Frequency Standard (OCFS) is one of these new technologies that may make its way to the market. Based on the historical Magnetic Cesium Frequency Standard, it uses **laser light instead of magnets** to efficiently manipulate atomic states before and after making the atomic transition between the two hyperfine levels of the Ground State of cesium with a radio-frequency excitation. The clock is expected to outperform the stability of its former version by at least one order of magnitude. In the meantime, several other technologies are already in-orbit to provide a local time reference for the satellites. In the case of the OCFS, **the characteristics of the laser used for atomic pumping and detection plays a crucial role in the standard performances**. Two laser lines, one at 852 *nm*, the other at 894 *nm* have been identified for use in the setup. The second one offers better technical advantages for industrialization perspectives.

Regarding the laser module itself, given the technical constraints specified by clocks' manufacturers, no sources at 894 *nm* are currently matching adequately the requirements of power, noise, volume and cost. The LAMA project, founded on a joint support of the French and Swiss Euripides consortium, is aimed at providing such sources and ending up with a prototype of commercial OCFS. **The Distributed-Feedback laser diode (DFB) technology has been chosen** for this purpose: it is well mastered at III-V Lab and offers excellent performances regarding the ease of fabrication and use.

Starting from the technical constraints on the source, the study will try to close the loop between the technological development, the deep metrological characterization and the final device integration in the system, to give a comprehensive and relevant scheme of laser conception for a high-end metrology application.

Bibliography

- [Affolderbach 2011] C Affolderbach, F Gruet, R Matthey et G Mileti. *A compact laser-pumped Rb clock with $5 \times 10^{-13} \tau^{-1/2}$ frequency stability*. In 2011 Joint Conference of the IEEE International Frequency Control and the European Frequency and Time Forum (FCS) Proceedings, pages 1–3. IEEE, 2011.
- [Allan 1966] David W Allan. *Statistics of atomic frequency standards*. Proceedings of the IEEE, vol. 54, no. 2, pages 221–230, 1966.
- [Arditi 1980] M Arditi et JL Picqué. *A cesium beam atomic clock using laser optical pumping. Preliminary tests*. Journal de Physique Lettres, vol. 41, no. 16, pages 379–381, 1980.
- [Astrom 1995] Karl J Astrom. *PID controllers: theory, design and tuning*. Instrument society of America, 1995.
- [Berthoud 2010] Patrick Berthoud et Pierre Thomann. *Optical pumping device and method*, 2010. US Patent 7,656,241.
- [Castagna 2009] Natascia Castagna, Rodolphe Boudot, Stéphane Guerandel, Emeric De Clercq, Noël Dimarcq et André Clairon. *Investigations on continuous and pulsed interrogation for a CPT atomic clock*. IEEE transactions on ultrasonics, ferroelectrics, and frequency control, vol. 56, no. 2, pages 246–253, 2009.
- [Cutler 2005] Leonard S Cutler. *Fifty years of commercial caesium clocks*. Metrologia, vol. 42, no. 3, page S90, 2005.
- [Cyr 1993] Normand Cyr, Michel Tetu et Marc Breton. *All-optical microwave frequency standard: a proposal*. IEEE Transactions on Instrumentation and Measurement, vol. 42, no. 2, pages 640–649, 1993.
- [Denet 2016] Stéphane Denet, Baptiste Chomet, Vincent Lecocq, Laurence Ferrières, Mikhaël Myara, Laurent Cerutti, Isabelle Sagnes et Arnaud Garnache. *Industrial integration of high coherence tunable VECSEL in the NIR and MIR*. Proc. SPIE, vol. 9734, pages 97340C–97340C–10, 2016.
- [Dimarcq 1991] N Dimarcq, V Giordano, G Théobald et P Cérez. *Comparison of pumping a cesium beam tube with D1 and D2 lines*. Journal of applied physics, vol. 69, no. 3, pages 1158–1162, 1991.
- [Dimarcq 1993] Noel Dimarcq, Vincent Giordano, P Cerez et G Theobald. *Analysis of the noise sources in an optically pumped cesium beam resonator*. IEEE transactions on instrumentation and measurement, vol. 42, no. 2, pages 115–120, 1993.
- [Dimarcq 2015] N Dimarcq, G Mileti, F Vernotte et al. *Introduction to Time and Frequency Standards*. In European Frequency and Time Seminar (EFTF), 2015.
- [Droz 2006] Fabien Droz, Pierre Mosset, Gerald Barmaverain, Pascal Rochat, Qinghua Wang, Marco Belloni, Liano Mattioni, Ulrich Schmidt, Francesco Emma et Pierre Waller. *The on-board Galileo clocks: Rubidium standard and Passive Hydrogen Maser-current status and performance*. In Frequency and Time Forum (EFTF), 2006 20th European, pages 420–426. IEEE, 2006.

- [Drullinger 1991] Robert E Drullinger, David J Glaze, JL Lowe et Jon H Shirley. *The NIST optically pumped cesium frequency standard*. IEEE Transactions on Instrumentation and Measurement, vol. 40, no. 2, pages 162–164, 1991.
- [Essen 1955] L Essen et JVL Parry. *An atomic standard of frequency and time interval: a caesium resonator*. Nature, 1955.
- [ExcelitasTechnologies 2016] ExcelitasTechnologies. *High-Performance Space-Qualified RAFS*. Commercial document, 2016.
- [FrankfurtLaserCompany 2016] FrankfurtLaserCompany. *DFB Laser Diode 894nm, 10mW*. Commercial Document, 2016.
- [Gerlach 1922] Walther Gerlach et Otto Stern. *Der experimentelle Nachweis des magnetischen Moments des Silberatoms*. Zeitschrift für Physik A Hadrons and Nuclei, vol. 8, no. 1, pages 110–111, 1922.
- [Guerandel 2002] S Guerandelet *al.* *Compact cesium beam frequency standard: improvements of the frequency stability towards the 10⁻¹² t-1/2 level*. In Proc. of 16th European Freq. and Time Forum, St-Petersburg, Russia, 2002.
- [Hermann 2003] Virgile Hermann. *Conception et réalisation d'une horloge atomique à jet de césium compacte et simplifiée pour des applications de télécommunication et de navigation par satellites*. PhD thesis, Université Pierre et Marie Curie - Paris VI, 2003.
- [Hermann 2007] V Hermann, M Gazard, P Berthoud, S Lecomte, R Ruffieux, C Audoin, R Barillet, E de Clercq et S Guerandel. *OSCC project: A space Cs beam optically pumped atomic clock for Galileo*. In 2007 IEEE International Frequency Control Symposium Joint with the 21st European Frequency and Time Forum, pages 77–80. IEEE, 2007.
- [Huntemann 2016] N Huntemann, C Sanner, B Lipphardt, Chr Tamm et E Peik. *Single-ion atomic clock with 3 × 10⁻¹⁸ systematic uncertainty*. Physical review letters, vol. 116, no. 6, page 063001, 2016.
- [Kastler 1950] Alfred Kastler. *Quelques suggestions concernant la production optique et la détection optique d'une inégalité de population des niveaux de quantification spatiale des atomes. Application à l'expérience de Stern et Gerlach et à la résonance magnétique*. J. phys. radium, vol. 11, no. 6, pages 255–265, 1950.
- [Kelly 2007] B Kelly, R Phelan, D Jones, C Herbert, J O'carroll, Marc Rensing, J Wendelboe, CB Watts, Aleksandra Kaszubowska-Anandarajah, Philip Perry *et al.* *Discrete mode laser diodes with very narrow linewidth emission*. Electronics Letters, vol. 43, no. 23, page 1, 2007.
- [Klehr 2007] A Klehr, H Wenzel, O Brox, F Bugge, G Erbert, TP Nguyen et G Tränkle. *High-power 894 nm monolithic distributed-feedback laser*. Optics express, vol. 15, no. 18, pages 11364–11369, 2007.
- [Knappe 2004] Svenja Knappe, Vishal Shah, Peter DD Schwindt, Leo Hollberg, John Kitching, Li-Anne Liew et John Moreland. *A microfabricated atomic clock*. Applied Physics Letters, vol. 85, no. 9, pages 1460–1462, 2004.
- [Kogelnik 1972] H Kogelnik et CV Shank. *Coupled-wave theory of distributed feedback lasers*. Journal of applied physics, vol. 43, no. 5, pages 2327–2335, 1972.

- [Lecomte 2007] Steve Lecomte, Manuel Haldimann, Robert Ruffieux, P Berthoud et P Thomann. *Performance demonstration of a compact, single optical frequency Cesium beam clock for space applications*. In 2007 IEEE International Frequency Control Symposium Joint with the 21st European Frequency and Time Forum, pages 1127–1131. IEEE, 2007.
- [Ligeret 2008] V Ligeret, S Bansropun, M Lecomte, M Calligaro, O Parillaud, D Holleville, N Dimarcq, N Michel et M Krakowski. *Narrow linewidth and demonstration of saturation spectra of the Cesium at 852 nm with high power Al-free DFB laser diodes*. In Integrated Optoelectronic Devices 2008, pages 69091F–69091F. International Society for Optics and Photonics, 2008.
- [Lucas-Leclin 1998] Gaëlle Lucas-Leclin. *Importance des propriétés spectrales des lasers pour les performances des horloges atomiques à pompage optique*. PhD thesis, Université Paris-Sud XI, Orsay, 1998.
- [Lutwak 2001] R Lutwak, D Emmons, RM Garvey et P Vlitaz. *Optically pumped cesium-beam frequency standard for GPS-III*. Rapport technique, DTIC Document, 2001.
- [Maiwald 2008] Martin Maiwald, Arnim Ginolas, André Müller, Alexander Sahm, Bernd Sumpf, Götz Erbert et Günther Trankle. *Wavelength-stabilized compact diode laser system on a microoptical bench with 1.5-W optical output power at 671 nm*. IEEE Photonics Technology Letters, vol. 20, no. 19, pages 1627–1629, 2008.
- [Microsemi 2016a] Microsemi. *MHM 2010, Active Hydrogen Maser*. Commercial document, 2016.
- [Microsemi 2016b] Microsemi. *Quantum™ LN CSAC*. Commercial document, 2016.
- [NanoplusGmbH 2016] NanoplusGmbH. *High power, narrow linewidth DFB lasers at 852 and 894 nm*. Commercial Document, 2016.
- [Ramsey 1950] Norman F Ramsey. *A molecular beam resonance method with separated oscillating fields*. Physical Review, vol. 78, no. 6, page 695, 1950.
- [Sallot 2003] C Sallot, M Baldy, D Gin et R Petit. $3.10^{12} \cdot \tau^{-12}$ *On industrial prototype optically pumped cesium beam frequency standard*. In Frequency Control Symposium and PDA Exhibition Jointly with the 17th European Frequency and Time Forum, 2003. Proceedings of the 2003 IEEE International, pages 100–104. IEEE, 2003.
- [Schmeissner 2016] R Schmeissner, A Douahi, I Barberau, P Dufreche, N Mestre, M Baldy, N von Bandel, O Parillaud, M Garcia, M Krakowski et al. *Towards an engineering model of Optical Space Cs Clock*. In 2016 European Frequency and Time Forum (EFTF), pages 1–4. IEEE, 2016.
- [Shirley 1994] Jon H Shirley et RE Drullinger. *Zeeman coherences and dark states in optically pumped cesium frequency standards*. In Precision Electromagnetic Measurements, 1994. Digest., 1994 Conference on, pages 150–151. IEEE, 1994.
- [Spectratime 2016] Spectratime. *iSource+™ Space-Qualified RAFS*. Commercial document, 2016.
- [Steck 2008] Daniel A Steck. *Cesium D line data*. Rapport technique, University of Oregon, 2008.
- [Tannoudji 1973] Cohen Claude Tannoudji, Diu Bernard et Laloë Franck. *Quantum mechanics*. volume i. Hermann, 1973.

- [Telkkälä 2010] Jarkko Telkkälä, Jukka Viheriälä, Antti Laakso, Kari Leinonen, Jari Lyytikäinen, Jukka Karinen, Mihail Dumitrescu et Markus Pessa. *Distributed feedback laser diodes emitting at 894 nm suitable for atomic clock applications fabricated using nanoimprint lithography*. In Conference on Lasers and Electro-Optics, page JTuD102. Optical Society of America, 2010.
- [Théobald 1989] G Théobald, N Dimarcq, V Giordano et P Cézé. *Ground state Zeeman coherence effects in an optically pumped cesium beam*. Optics Communications, vol. 71, no. 5, pages 256–262, 1989.
- [TopticaPhotonicsAG 2016] TopticaPhotonicsAG. *List of available DFB and DBR laser modules*. Commercial Document, 2016.
- [Vanier 1989] Jacques Vanier et Claude Audoin. *The quantum physics of atomic frequency standards*. Hilger Bristol, 1989.
- [Vanier 2005] J Vanier. *Atomic clocks based on coherent population trapping: a review*. Applied Physics B, vol. 81, no. 4, pages 421–442, 2005.
- [Zhdanov 2007] Boris Zhdanov et RJ Knize. *Diode-pumped 10 W continuous wave cesium laser*. Optics letters, vol. 32, no. 15, pages 2167–2169, 2007.

Part II

Laser design

Design of the source: An overview

2.1 LASER sources

The coming section focuses on the most important concepts of laser physics and highlights the fundamental parameters linked to the coherence of a laser source.

2.1.1 Introduction

The acronym LASER comes from Light Amplification by Stimulated Emission of Radiation. This term originates from the earlier MASER, where 'M' stands for *molecular* or *microwave*. In 1953-1954, J. Gordon, H. Zeiger and C. Townes demonstrated for the first time the possibility of microwave amplification in a cavity using transitions of hyperfine levels of ammonia [Gordon 1954, Gordon 1955]. Later, in a famous article [Schawlow 1958], A. Schawlow and C. Townes extended theoretically the principle of amplification to infrared and visible light and the very first solid state *laser* working in the visible was demonstrated a few years later by T. Maiman [Maiman 1960]. Basically, the laser is a source of highly coherent light which is very monochromatic and directional. Today, more than three hundred types of lasers are available and they use very various active species and energy sources to work. Regarding laser diodes themselves, the structure of interest is made of semiconductor layers and has a rectangular shape in which a *waveguide* can be defined (figure (2.1)). This is necessary to compensate for *diffraction* of the light inside the cavity. Also, the *gain medium* of this type of laser is very particular: in our case, it is *electrically* pumped and induces high optical losses, because of the inner structure of the material (absorption by the medium). These points are specifically addressed in chapter 3. Thus, the spectral purity of these sources, with additional specific effects, ranks these laser among the most 'noisy' ones with relation to their output light.

However, a few common grounding principles sustain their behavior, like any other 'classic' laser source. They are shortly reviewed in this chapter.

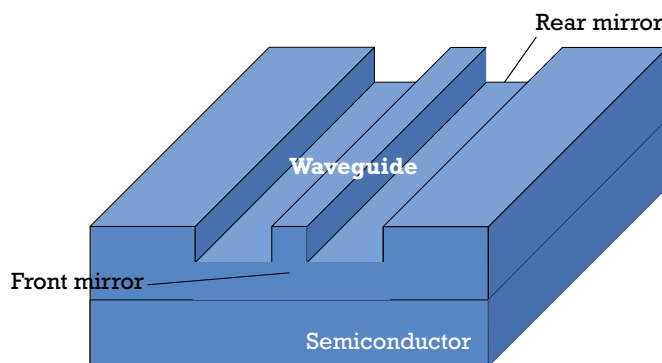


Figure 2.1: Schematic 3D view of an in-plane laser diode

2.1.2 Spontaneous emission and stimulated emission

In the nature, the vast majority of light-emitting phenomena are governed by *random statistical processes*. That is, the particles of the matter (electrons, atoms, molecules and others) emit *photons* that reflects a loss of energy or decaying from a state of higher energy to a state of lower energy with a *probability* constant. It is the fluorescence phenomenon (return to the thermodynamical equilibrium state by optical means). Such *spontaneous* emission process, is linked to a decay rate, in s^{-1} :

$$\gamma_{rad} = 1/\tau_{rad} \quad (2.1)$$

and has been evoked in chapter 1. Also, the matter state can decay through *non-radiative* transition where, in this case, the energy is lost through *phonons* (quantized vibrations) of the atomic lattice in solids (or through collisions in gas for instance), so that another corresponding rate is defined:

$$\gamma_{nrad} = 1/\tau_{nrad} \quad (2.2)$$

so that the total decay rate of the particles is $\gamma_{rad} + \gamma_{nrad}$ [Tannoudji 1973]. Basically all the bodies of finite temperature emit photons through the spontaneous decay ((c) in figure (2.2)). Meanwhile, another type of transition is related to a *coherent* process of emission. This is the *stimulated transition* that occurs in the atomic system when an incident photon interacts with the effective electric dipole formed by the electronic cloud ((a) and (b) in figure (2.2)).

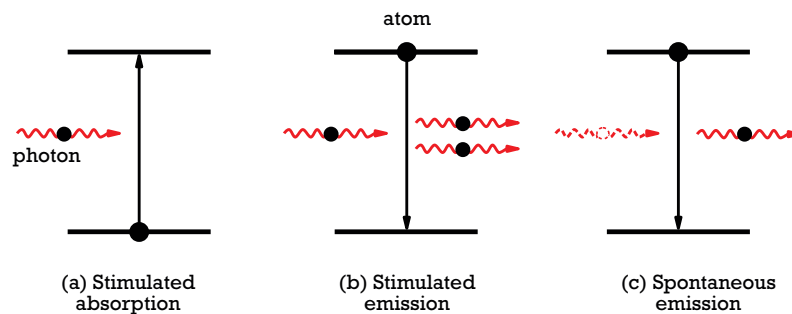


Figure 2.2: Schematic quantized representation of the three types of radiative transitions allowed in a two-level atomic system

If the atom *absorbs* the incident photon, it will jump to a higher energy state level, and the energy difference is precisely equal to the one of the incident photon (stimulated absorption). The inverse mechanism also exists, when an incident photon can provoke the decay of an atom in the excited state, so that two photons are produced on the overall. Quantum mechanics states that within such a process, this newly created photon has the same *wavevector* \vec{k} as the exciting one, so that the two particles are in an unique *coherent* state. As pointed out in [Siegman 1986], the weirdness of such phenomenon can be balanced when we consider that the photon has also a wave-like nature of an oscillating electric-field \vec{E}_k that excites the *resonant* quantized equivalent electric dipole formed by the electronic cloud, which responds in-phase for the case of stimulated emission, and out-of-phase for the absorption, just like in classical electromagnetism. Of course, in all these processes, no energy is lost or created in the closed system. The stimulated mechanism then induces a radiation *loss* (for absorption) or a radiation *gain* (for emission).

2.1.3 Absorption and gain in the atomic medium

If considering now a system of volume V (in m^3) which has a density of N_1 atoms/electrons (in m^{-3}) on level of energy E_1 and N_2 atoms/electrons on level of energy $E_2 > E_1$ that is undergoing spontaneous and stimulated transitions under a density of electromagnetic energy $\rho(\nu_0)$ in $J.m^{-3}.Hz^{-1}$ (the signal is broad-band in frequency ν but we are only looking at the useful energy $h\nu_0$ of the transition of the atomic system), then the rate equations of the atomic populations are given by (from figure (2.3)):

$$\left(\frac{dN_2}{dt}\right)_{tot} = \left(\frac{dN_2}{dt}\right)_{stim} + \left(\frac{dN_2}{dt}\right)_{spon} \quad (2.3)$$

$$\left(\frac{dN_2}{dt}\right)_{tot} = B_{12}\rho(\nu_0)N_1(t) - B_{21}\rho(\nu_0)N_2(t) - A_{21}N_2(t) \quad (2.4)$$

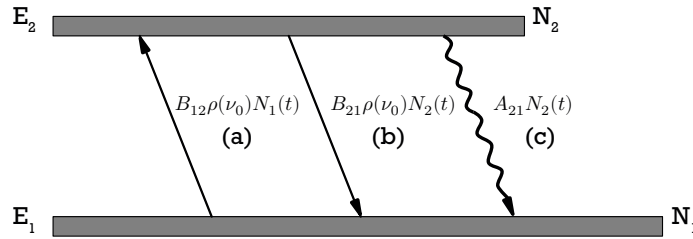


Figure 2.3: Rate of transitions involved in a two-levels atomic system. After [Siegman 1986]

In (2.4), B_{12} , B_{21} and A_{21} are the *Einstein coefficients* which accounts for the rate/the probability of transition over time, in s^{-1} for A_{21} and in $J^{-1}.s^{-2}.m^3$ for the B coefficients, of one single atom. The main difference between spontaneous emission and stimulated emission is that the latter scales with the quantity of photons in the medium. In 1917, Einstein discovered that these rates were fundamentally linked together [Einstein 1917]:

$$B_{12} = B_{21} = A_{21} \frac{\lambda_{med}^3}{8\pi h} \quad (2.5)$$

where $\lambda_{med} = \lambda_0/n_{med}$ is the wavelength of the light in vacuum divided by the refractive index of the medium. He established these relations by considering that at thermal equilibrium, the relation between N_1 and N_2 is given by:

$$\frac{N_{2, equ}}{N_{1, equ}} = e^{-(E_2 - E_1)/k_B T} \quad (2.6)$$

with k_B the Boltzmann constant and T the macroscopic temperature of the medium. Then, comparing with Planck's Black Body radiation law [Planck 1901] he deduced (2.5) way before the equations of state evolution of quantum mechanics were established. However, only the latter theories (quantized theory of electromagnetism [Loudon 2000]) gave an expression for the radiative spontaneous decay rate:

$$\gamma_{rad} \equiv \Gamma \equiv A_{21} = \frac{8\pi^2 d_{12}^2}{3\hbar \varepsilon_0 n_{med}^2 \lambda_0^3} \quad (2.7)$$

where $d_{12} = er_{12}$ is the electric dipole of the electronic cloud in the two-level system, ε_0 the vacuum permittivity and λ_0 the wavelength in vacuum of the emitted photon. Such formula assumes that

the spontaneous photons are emitted in all the wave-vectors \vec{k} of magnitude $|k| = 2\pi/\lambda$ of the space. The expression implies that **the shorter the wavelength, the higher the decay rate**. Actually, (2.7) is found when one looks at the expression of the quantized electromagnetic field when no photons are present. It appears that the probability of transition from state $|2\rangle$ to state $|1\rangle$ with such field is non-zero, so the spontaneous emission is sometimes said to be induced by the *vacuum field-fluctuations* but the very first origin of the phenomenon arises from the non-zero commutation values of the field-operators, which scale like $\sim \hbar$.

From (2.4) the total power generated by stimulated emission per unit volume in frequency ν_0 ($W.m^{-3}$) is:

$$P_V = (h\nu_0)B_{21}(N_2 - N_1)\rho(\nu_0) \quad (2.8)$$

If we consider that the production of stimulated photon changes only along one direction (the z -axis of the cavity), a small spatial change in the intensity of photons dI (in $W.m^{-2}$) verifies:

$$dI = P_V dz \quad (2.9)$$

$$= \left(\frac{hc}{\lambda_0} A_{21} \frac{\lambda_{med}^3}{8\pi h} \frac{n_{med}}{c} (N_2 - N_1) \right) I_\nu dz \quad (2.10)$$

where $I_\nu = \frac{dI}{d\nu} = \frac{c}{n_{med}} \rho(\nu_0)$ with c the speed of light (in $m.s^{-1}$), is the intensity spectral density of photons (in $W.m^{-2}.Hz^{-1}$). The dependency in the frequency bandwidth $d\nu^{-1}$ of I_ν can be reintegrated in the global term in the brackets, so that after integrating over z the well-known *Beer-Lambert's law* is recovered:

$$I(z) = I_0 e^{-\alpha_I z} \quad (2.11)$$

I_0 is just the intensity at $z = 0$ position. The α_I factor is called the *absorption* coefficient (in m^{-1}). Its opposite is the *gain* coefficient g_I . They both depend on the energy of the transition. However, quantum mechanics states that rather absorbing exactly at $\nu_0 = c/\lambda_0$, the two-level transition can occur with a Lorentzian probability distribution \mathcal{L} centered on ν_0 and of characteristic Full-Width at Half Maximum (*FWHM*) $2\gamma_{tr}$ in s^{-1} (this was evoked in the first chapter for Cesium transitions). The factor γ_{tr} stands for the global decaying rate, function of γ_{rad} and γ_{nrad} , including the collision effects for instance. Then:

$$\alpha_I(\nu) = -g_I(\nu) = \frac{\gamma_{rad}\lambda_{med}^2}{8\pi} (N_1 - N_2) \mathcal{L}(\nu - \nu_0) \quad (2.12)$$

$$\mathcal{L}(\nu) = \frac{1}{\pi} \frac{\gamma_{tr}}{\gamma_{tr}^2 + (\nu - \nu_0)^2} \quad (2.13)$$

Another convenient way to represent the absorption process is to define the absorption *cross-section* $\sigma_I(\nu)$ (in m^2) so that:

$$\alpha_I(\nu) = \sigma_I(\nu)(N_1 - N_2) \quad (2.14)$$

$$I(z) = I_0 e^{-\sigma_I(N_1 - N_2)z} \quad (2.15)$$

The conclusion is that if $N_2 > N_1$, then g_I is positive (α_I negative) and the atomic medium *amplifies* the electromagnetic energy from stimulated emission inside the volume V . Conversely, if α_I is positive (g_I is negative), the medium absorbs the traveling photons. The case $\alpha_I = 0$ is the *transparency*: light travels without any absorption or amplification. At thermal equilibrium, as $N_1 > N_2$ from (2.6),

the traveling waves decays and are usually turned into heat by the atomic population after sufficient propagation in a dense medium (the total decay rate is again $\gamma_{rad} + \gamma_{nrad}$). Also, it can be inferred that to achieve a gain effect, one needs a *population inversion* between levels $|1\rangle$ and $|2\rangle$. Of course, electromagnetic energy is not created from nowhere in a gain process: the work put to transfer the atomic population from $|1\rangle$ to $|2\rangle$ will be converted at most in the equivalent number of stimulated photons. The case of a two-level atomic system is non-physic. If the system (2.3) and (2.4) is solved, it appears that in the strong radiation regime:

$$N_1(\infty) = N_2(\infty) = \frac{N}{2} \quad \text{for } B_{21}\rho(\nu) \gg A_{21} \quad (2.16)$$

where $N = N_1 + N_2$ is the total density of atoms, meaning that $\alpha(\nu) \rightarrow 0$ in the limit of very high photon density. This is the *gain saturation* phenomenon, which is evoked in chapter 1 for cesium pumping with cycling two-level transitions. The consequence is that there can be **no population inversion in a two-level system** under optical pumping in a steady-state regime.

Actually, the large majority of the atomic/electronic systems in the nature have transitions between manifolds (and even continuum) of energy. For a three-level system, if the transition rate from level $|3\rangle$ to level $|2\rangle$ is such that $\gamma_{32} \gg \gamma_{21}$, population inversion can be achieved. However, such configurations have limited energy efficiency because the stimulated emission can be absorbed by non-inverted zones of the medium. In a four-level system, this can be avoided so that the pump wavelength used for population inversion is different from the stimulated-emission wavelength (figure (2.4)).

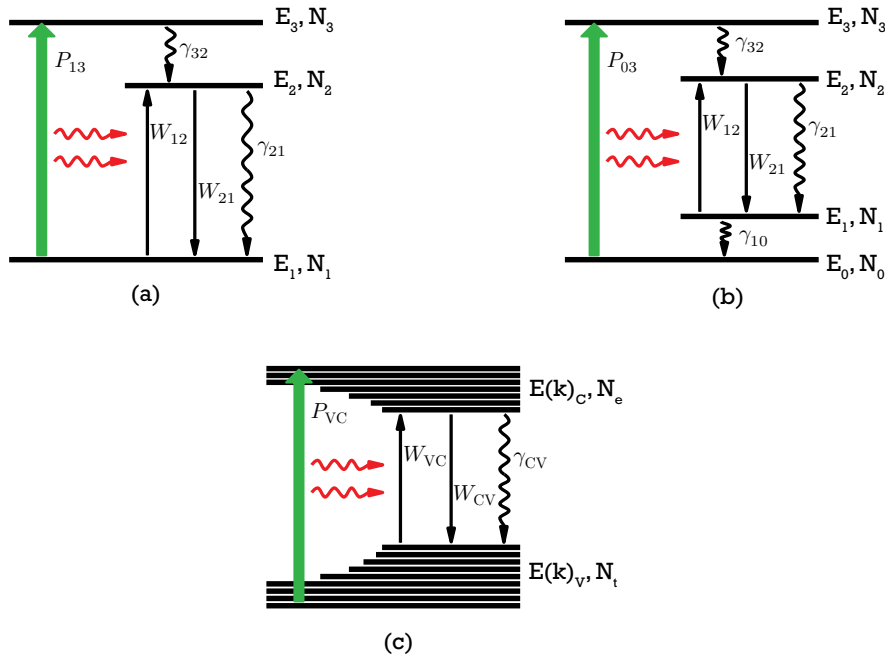


Figure 2.4: Models of transitions in high-order atomic systems: (a) Idealized three-level system, (b) Idealized four-level system, (c) Continuous-level system of the condensed matter

In the semiconductor gain medium, *carriers of charges* recombine to produce photons through spontaneous or stimulated emission. The discrete levels of the previous atomic systems are a

continuum of free electron states in the *conduction band* and of empty electron states (holes) in the *valence band* (the highest band of bound electron states), separated by the energy band-gap. But because the bands can be filled with particles with several wave vectors \vec{k} , the gain profile will be far more larger in bandwidth of frequency of the emission than that of a medium with 'distant' atoms (like a doping active ion in an amorphous matrix). In these materials, population inversion can be achieved through optical pumping (the system of dense bands is close to a three-level system) but because of electrical conduction properties, it can also be realized by *electrical pumping*, so that the pumping energy is the work of the electrons in the applied electrical potential.

Finally, it is worth to mention that whatever the order of the system, the gain always saturates with the photon density and can be written as:

$$g_I(\nu) = \frac{g_0(\nu)}{1 + I(\nu)/I_{sat}(\nu)} \quad (2.17)$$

The expression of the saturation intensity $I_{sat}(\nu)$ depends on the system studied as-well-as the low-intensity gain g_0 , which will be computed in the coming sections.

2.1.4 The feedback condition: LASER effect

The pure 'laser' state is a state of light were all photons have the same wave-vector \vec{k} , the same pulsation $\omega = 2\pi\nu$, the same polarization state, and ultimately the same state of phase. It correspond to a single mode of propagating photons and has an associated electric-field $\vec{E}_{\vec{k}}$ (forward propagation):

$$\vec{E}(\vec{r}, t) = \vec{E}_0 e^{i(\omega t - \vec{k} \cdot \vec{r})} \quad (2.18)$$

This form results from the solutions of Maxwell's equations in a non-charged and non-magnetic uniform medium of real optical refractive index $n_{med} = \sqrt{\epsilon_{med}/\epsilon_0}$ that contains a resonant active transition characterized by the *complex susceptibility* $\chi_{act}(\omega)$:

$$|\vec{k}| = \frac{\omega n_{med}}{c} |f(n_{med}, \chi_{act}(\omega))| \quad (2.19)$$

where f is a function that characterized the dispersion of the total active medium. In the linear approximation, \vec{k} can be rewritten as:

$$\vec{k} \approx \vec{k}_R + i\vec{k}_I \quad (2.20)$$

with $k_R = \omega/v_g$ with the group velocity $v_g = dk/d\omega$ and $k_I = -\alpha_I/2$. Then (2.18) is linked to the absorption expression that has been derived above, in a photon-atom interaction. A medium with active species can provide gain $g_I = g = -\alpha_I = -\sigma_I \Delta N$ which sign depends on the population inversion state ΔN , but have also absorbing species/properties characterized by *internal losses* $\alpha_i < 0$. The gain and internal losses are related again to the energy, hence a 1/2 factor in the expression of the E-field and in the general case, they are not necessarily constant over the propagation direction. Here, it has been assumed that the medium was homogeneous. If the material presents strong spatial variations of the imaginary part of χ_{act} regarding its mean value, Maxwell's equations have to be solved with such dependency $\chi_{act}(\omega, \vec{r})$. Finally, for the z-direction only:

$$\vec{E}(z, t) = \vec{E}_0 e^{\frac{g - \alpha_i}{2} z} e^{i(\omega t - k_R z)} \quad (2.21)$$

The term $g - \alpha_i$ is called the *net gain* g_{net} by some authors. Even if the net gain is positive, it is not sufficient to achieve laser effect. The radiation has to sustain itself in the mode so that all the

pumping power is transferred to this coherent state. This is why a *feedback effect* is needed.

The gain medium is embedded between two parallel mirrors of complex reflectivity r_1 and r_2 (of modulus inferior or equal to 1) to realize a *Fabry-Perot cavity* (figure (2.5)) (it is however, a schematic point of view for the sake of the simplicity: because of diffraction, two plane mirrors cannot be a valid geometry for Gaussian beams, see [2.1.5]). In practice, a rectangular *bar* of homogeneous semiconductor medium forms such a resonator. The feedback condition can be found if we consider

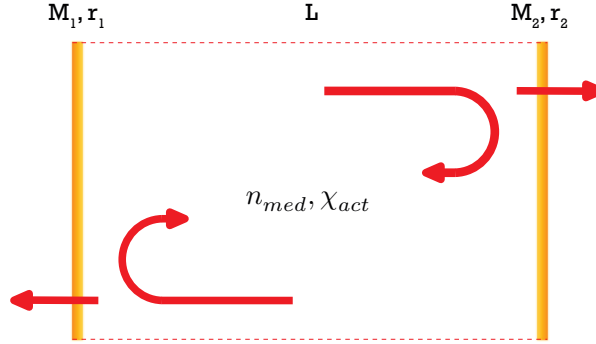


Figure 2.5: Simple (schematic) Fabry-Perot resonator of length L with reflecting mirrors perpendicular to the axis of the cavity. Optical feedback is provided by multiple round-trips of light between the two-mirrors.

that after one round-trip in the cavity of length L , the wave propagating from mirror $M1$ to mirror $M2$ and back to $M1$ (after two reflections) should have the same amplitude and phase, meaning that the cavity allows oscillations of the field:

$$\vec{E}(t) = \vec{E}(t)r_1r_2e^{g_{net}L}e^{-i2k_RL} \quad (2.22)$$

If the reflectivities introduce only a π dephasing at the mirrors (so that $r_i = -|r_i|$), the condition is written:

$$r_1r_2e^{g_{net}L}e^{-i2k_RL} = 1 = e^{2iq\pi} \quad , q \text{ integer} \quad (2.23)$$

- **Gain condition**

In (2.23), the condition that the gain and the phase should observe can be written independently. On the part of the study related to Distributed-Feedback cavities, it will be shown that it is not possible. So, the gain condition is:

$$g_{net,thr} = -\frac{1}{L} \ln |r_1r_2| = -\frac{1}{2L} \ln(R_1R_2) \stackrel{def}{=} \alpha_m \quad (2.24)$$

where the $R_i = |r_i|^2$ are the (real) intensity reflectivities. The net gain has to equalize the *mirror losses* α_m which represents the electromagnetic energy lost from the cavity. If so, the gain is said to have reached the *threshold* value for the laser effect to occur and we write:

$$g_{thr} = \alpha_i + \alpha_m \quad (2.25)$$

- **Phase condition**

In the meantime, the real-part of the wave vector k_R verifies:

$$k_R = q \frac{\pi}{L} = \frac{2\pi n_g}{\lambda_0} \quad , \text{ q integer} \quad (2.26)$$

which gives the wave-vectors of the Fabry-Perot modes in term of the *group index* n_g .

The existence of the threshold can be interpreted as follow: first, the gain is driven by the density population inversion ΔN of the active species, so it cannot amplify more energy than what is injected to make such inversion. Secondly, at threshold, any photon added in the cavity through an additional injection of a quantum of pumping energy will make, on average, a complete round trip, despite the internal absorption and the probability of leakage out. These first photons will live in a stable mode of oscillation of the cavity that complies to (2.26), and because of the dependency of the stimulated emission term in the energy density, they will transfer all the pumping energy into the coherent emission. In this regime, the laser is a *converter* of energy. Because for one photon in the cavity, we get one more photon originating from an additional quantum of energy of the pump, the stimulated power should grow *linearly* after threshold. In the same time, the density of population inversion ΔN is *clamped* and the gain saturates (condition (2.25) is a limit that is never reached exactly). Physically, it is because the very high intensity in the cavity at threshold prevents the gain to increase again (as stated by equation (2.17)). To sum up, there are three regimes in the laser onset:

1. Absorption regime: the pump power is used to start to invert the active population of the material. The spontaneous emission is re-absorbed in the medium through the stimulated absorption and the losses.
2. Amplified spontaneous emission regime (ASE): enough pumping power has inverted the population above the transparency where absorption is zero for some optical modes. The spontaneous emission is amplified in the cavity but cannot sustain in a stable mode because of the losses in and out of the volume. This is the regime where *optical amplifiers* work.
3. Laser regime: the gain compensates for the internal and mirror losses. It is clamped and any additional pump power is directly converted linearly to the laser optical modes power.

The modes that satisfy the Fabry-Perot phase condition (2.26) can potentially become the longitudinal laser mode that will consume all the pump power into a coherent emission. For a Fabry-Perot cavity, (2.25) states that these modes have the same losses. Then, there will be a sharp mode competition for the lasing effect and only one mode will be elected for lasing action. This is why an ideal laser system is always single mode. In reality, if the mode spacing is very small compared to the bandwidth of the bell-shape gain curve $g(\nu)$, the probability will be very high that the cavity jumps in time between modes, because of spatial or spectral inhomogeneities in the main parameters of the cavity (see further). In such case, the *gain margin* $\Delta\alpha$ between the two adjacent modes of highest gain is very low.

2.1.5 Photon lifetime and laser linewidth

The previous highlights on the laser behavior are very well-known and can be found in all the good books mentioned. However, it is crucial to underline the fact that the concept of losses drives deeply this behavior, on the first order characteristics of a laser cavity, but also for the second-order effects, that is, the magnitude of the small deviations to the steady-state behavior that will be called *noise*. We will try to give a complete picture of this topic in the part II of this manuscript, but for the

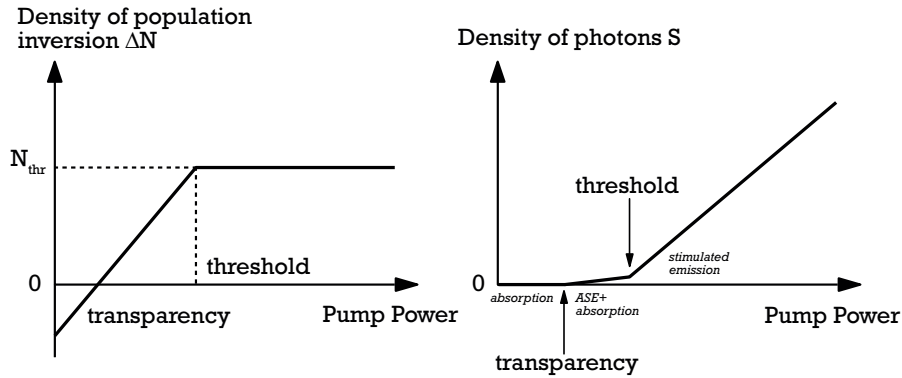


Figure 2.6: Left graph: density of population inversion as a function of the pump power. The transparency corresponds to $\Delta N = 0$. At threshold, the density is clamped. Right graph: Photon density inside the laser cavity as a function of the pump power. Above threshold, stimulated emission translates into a linear characteristics while ASE is clamped at the threshold.

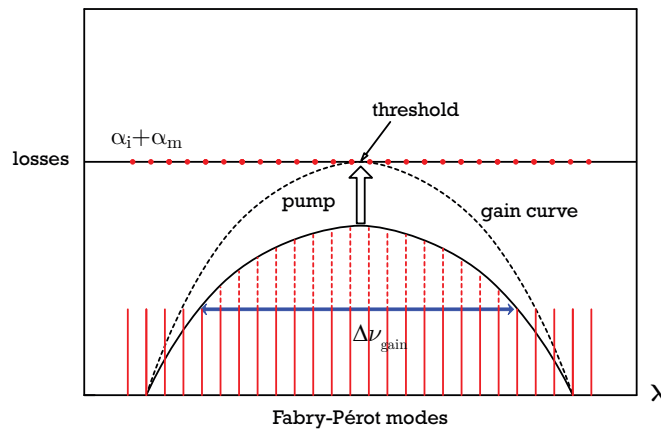


Figure 2.7: In an ideal Fabry-Perot cavity, all the modes have the same losses. If the gain grows *homogeneously* with the pump power, the mode closest to the top of the gain curve will lase

time being, it can be inferred that, because the laser effect is originally grounded on an emission of spontaneous photons with random phase and frequency in the gain bandwidth, such incoherence has to impact the spectral properties of the laser field.

A useful notion linked to that issue is the *photon lifetime*: from what has been said above, at threshold, the rate of the pump is sufficiently high to feed a stable lasing mode in the cavity. The individual photons of this mode do have a mean-lifetime before they are absorbed or they escape the resonator. Such time is given, in s , by:

$$\tau_\gamma = \frac{n_{med}}{c} \frac{1}{\alpha_{tot}} = \frac{n_{med}}{c} \frac{1}{\alpha_i + \alpha_m} \quad (2.27)$$

For example, in a Fabry-Perot cavity of length $L = 2 \text{ mm}$, with a medium of index $n_{med} = 3$, with no internal losses and mirror reflectivities $R_1 = R_2 = 0.28$, which correspond to the usual parameters of

a semiconductor cavity, the lifetime is $\tau_\gamma = 17$ ps. Also, the *transmittance* of such cavity is given by

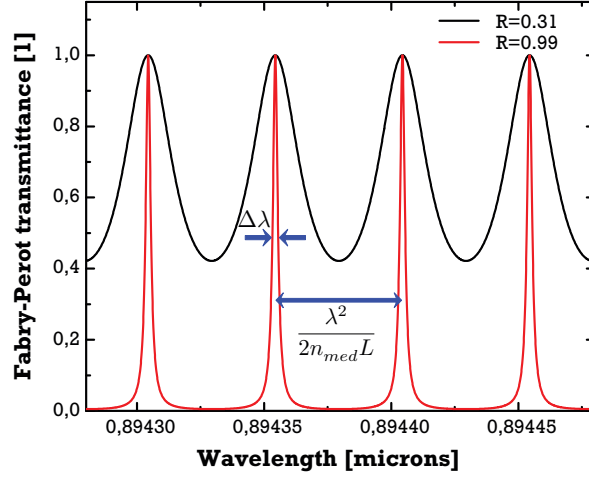


Figure 2.8: Transmittance of the Fabry-Perot cavity around the cesium D_1 line for two different reflectivities of the mirrors. As this parameter gets close to 1, the transmission peaks get thinner which corresponds to a higher cavity Finesse

the expression:

$$T = \frac{T_1 T_2}{1 + R_1 R_2 - \sqrt{R_1 R_2} \cos(\delta/2)} \quad (2.28)$$

where $\delta = 2k_{med}L$. For $R_1 = R_2 = R$:

$$T = \frac{1}{1 + \frac{4R}{(1-R)^2} \sin^2(\delta/2)} \quad (2.29)$$

This expression, also called the Airy function, is plotted in figure (2.8) for different values of the R coefficient. As R approaches 1, the peaks become thinner and thinner while the *free spectral range* $FSR_\lambda = \frac{\lambda^2}{2n_{med}L}$ stays constant as it only depends on the cavity length. The *finesse* \mathcal{F} (no unit) characterizes this behavior:

$$\mathcal{F} \stackrel{def}{=} \frac{FSR_\lambda}{\Delta\lambda} = \frac{FSR_\nu}{\Delta\nu} = \frac{\pi}{2 \arcsin(\frac{1-R}{2\sqrt{R}})} \quad (2.30)$$

where $\Delta\lambda$ is the Full-Width at Half-Maximum (FWHM) of the peaks. As $R \rightarrow 1$, $\mathcal{F} \rightarrow \infty$. On the other hand, when L increases, the FSR decreases, so that the mirror losses α_m decreases, and $\Delta\lambda \rightarrow 0$. The *cold cavity linewidth* $\Delta\nu_c$ is, by definition, the FWHM of the optical resonance of the cavity without optical gain:

$$\Delta\nu_c \stackrel{def}{=} \frac{1}{2\pi\tau_c} \stackrel{(2.30)}{=} \frac{1}{\mathcal{F}} \frac{c}{2n_{med}L} \quad (2.31)$$

In the limit where there is no internal losses in the cavity, and when $R \rightarrow 1$, the photon lifetime defined with the total losses in (2.27) is equal to the characteristic time associated to the cold cavity:

$$\tau_\gamma = \tau_c \quad (2.32)$$

$$\Delta\nu_\gamma = \Delta\nu_c \quad (2.33)$$

A more complete derivation of the Airy transfer function shows that internal losses can be taken into account through a term $e^{-2\alpha_i L} < 1$ in the reflectivities product so that (2.33) as long as the FWHM definition is meaningful relatively to the transmittance profile. A few values of the linewidth for the cavity of $L = 2 \text{ mm}$ with several reflectivities R is presented in table (2.1).

Reflectivity R	Finesse \mathcal{F}	$\Delta\nu_c$
0.31	2.4	8 GHz
0.99	313	60 MHz
0.999	3140	6 MHz

Table 2.1: Some values of the Fabry-Perot cold cavity linewidth with respect to a given R or \mathcal{F} coefficient. Here, it has been assumed no internal losses and a central frequency of $\nu = 336 \text{ THz}$

The conclusion is that, the higher the spectral filter quality (high finesse), the longer the photon lifetime (the resonator is closed and has low internal losses), the smaller the cold cavity modes linewidth. Another concept related to these quantities is the *quality factor of the cavity* Q :

$$Q \stackrel{def}{=} \omega\tau_c = \frac{\nu}{\Delta\nu_c} \quad (2.34)$$

In the case where $R = 0.31$, $Q = 4195$. To achieve cold cavity linewidths below the MHz, very long Fabry-Perot resonators with high reflectivities are required (for instance, $L = 2 \text{ m}$ and $R = 0.85$). This is clearly not possible for a compact laser source. Even for the case of resonators with distributed reflectors along the length (see the part on DFB lasers), a Q factor above 3×10^8 cannot be reached. $\Delta\nu_c$ is actually the optical filter bandwidth. On the other hand, the gain medium has itself a resonance linewidth which is linked to the spontaneous decay time of the active species:

$$\Delta\nu_{tr} = \frac{1}{\tau_{rad} + \tau_{nrad}} \quad (2.35)$$

With transition times of the order of the μs to the ms in ion-doped crystals, the transition linewidth is in the range of the MHz to the kHz. In semiconductor media, it is in the range of the ns that gives GHz, but again, the spreading in energy of the carriers leads to THz-width of the gain curve. On the overall, the effective linewidth $\Delta\nu_{eff}$ of the filtered ASE will be the FWHM of the spectral profile $g(\nu)T(\nu)$. Still, this is not what is observed in the output light of lasers. The spectral linewidth must depend on S because the more photons in the single laser mode, the spectrally 'purer' the output.

Using general considerations on resonating oscillators, Schawlow and Townes predicted the linewidth (which was written for the Half-Width at Half-Maximum HWHM of the spectral distribution) of an "optical maser" [Schawlow 1958]. However, Lax showed later, using an approach based on autocorrelation functions, that the earlier expression missed a 1/2 factor [Lax 1967], so that the FWHM this time is:

$$\Delta\nu_{S-T} = \frac{\pi h\nu(\Delta\nu_c)^2}{P_{tot}} \quad (2.36)$$

with P_{tot} the **total** radiated power of the field. Physically, this finite width of the optical resonator arises from the fact that the phase state of the field is not completely coherent because of the coupling to spontaneous emission which adds random phases. An elegant representation of Henry of this diffusion process is reproduced in figure (2.9). In the part on semiconductor lasers, it will be shown

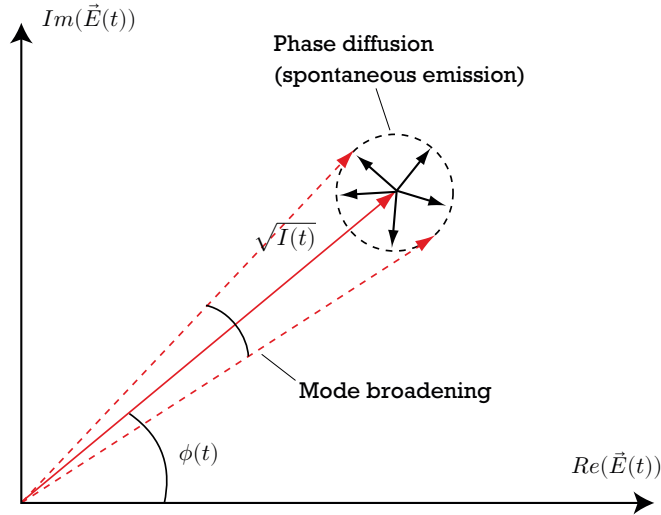


Figure 2.9: Phasor representation in the phase-amplitude plane of the electric-field phase diffusion under spontaneous emission events. After [Henry 1982]

that two factors are missing in the above expression (2.36). Also, in practice, the power measured outside the cavity is the *output power* P_{out} (in W) expressed by:

$$P_{out} \approx h\nu \frac{S}{\tau_c}, \text{ for } \alpha_i \ll \alpha_m \quad (2.37)$$

where $S = \frac{\epsilon |\vec{E}|^2 V}{2\hbar\omega}$ is the number of photons in the cavity of volume V . If the internal losses are such that $\alpha_i \ll \alpha_m$, then $P_{out} \approx P_{tot}$. If the Schawlow-Townes formula is applied for the case of the Fabry-Perot with $L = 2 \text{ mm}$, $R = 0.31$ and $P_{out} = 20 \text{ mW}$ at $\nu = 336 \text{ THz}$ we get:

$$\Delta\nu_c = 8 \text{ GHz} \quad (2.38)$$

$$\Delta\nu_{S-T} = 22 \text{ kHz} \quad (2.39)$$

The fact that there is a factor of more than 10^5 between the two values demonstrates that the output light of a laser is extremely monochromatic. The light spectrum of the cavity is typically the one depicted in figure (2.10). In that case, a single lasing mode stands out on the *ASE* background.

2.1.6 Spatial coherence

In the simple Fabry-Perot model of [2.1.3], it has been assumed that the solutions of the propagation in the medium where plane-waves bouncing between the two mirrors of the diode. This is not the case in a closed rectangular homogeneous cavity, where the propagation solutions in the *paraxial approximation* are given instead by Hermite-Gauss beams [Siegman 1986] that takes into account the diffraction properties of light. For instance, the first order transverse solution shape is given by equation (2.40) in Cartesian coordinates and is represented in figure (2.11). The minimum beam radius is the *waist*

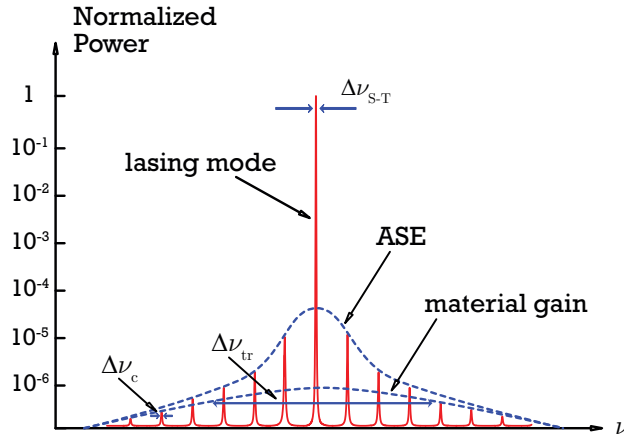


Figure 2.10: Illustration of a typical Fabry-Perot laser spectrum. At threshold, the Schawlow-Townes linewidth of the main lasing mode is a hundred times way smaller than the cold-cavity linewidth associated to the losses of the resonator

w_0 and it diverges after a distance z_R called the *Rayleigh length*.

$$\vec{E}(x, y, z) = \vec{E}_0 \sqrt{\frac{2}{\pi}} \frac{e^{-ikz + \psi(z)}}{w(z)} e^{-\frac{x^2 + y^2}{w^2(z)} - ik \frac{x^2 + y^2}{2R(z)}} \quad (2.40)$$

$$w(z) = w_0 \sqrt{1 + \left(\frac{z}{z_R}\right)^2} \quad (2.41)$$

$$R(z) = z + \frac{z_R^2}{z} \quad (2.42)$$

$$\psi(z) = \arctan\left(\frac{z}{z_R}\right) \quad (2.43)$$

For non-guiding laser cavities, such as external cavities, the compatibility of its geometrical design (mirror curvature for instance) with the Gaussian modes is essential to maintain a proper mode coherence [Laurain 2010]. Also, because of the mode shape, laser beams diverges linearly with the full-opening angle:

$$\Theta = 2\theta \simeq 2 \arctan\left(\frac{\lambda}{\pi w_0}\right) \quad (2.44)$$

The smaller the waist w_0 , the stronger the divergence. In some semiconductor lasers, the diffraction is compensated by the use of a *waveguide* defined in the cavity material itself. It can imply that the waist in the x and in the y directions do not have the same size, hence an elliptical shape of the output beam.

2.1.7 Deviations from an idealized laser model

In section [2.1.4], it was underlined that the mode competition elects one single mode which is the closest of the maximum of the gain peak. In reality, the gain can broaden *inhomogeneously* with pumping: it means that more or less independent inversions of populations coexist (spectrally or spatially), reducing the mode selection efficiency and threatening the single mode operation.

- Spectral Hole Burning

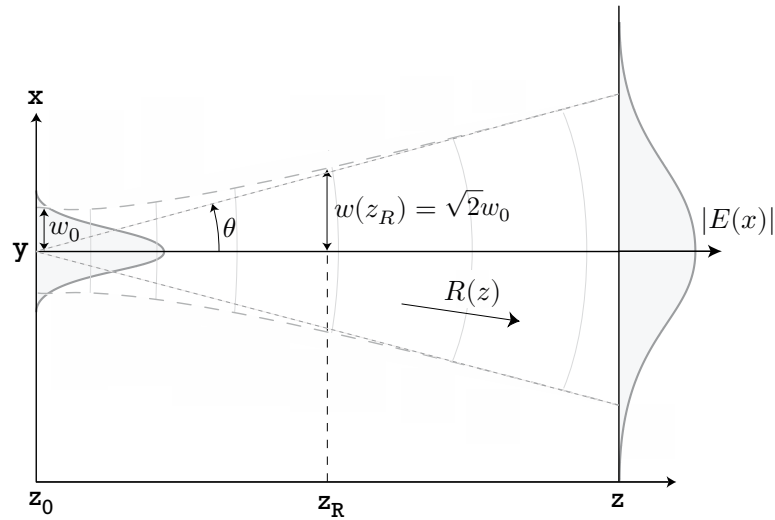


Figure 2.11: Intensity profile in the (x,z) plane of the fundamental TEM_{00} in a rectangular cavity in the paraxial approximation. After [Laurain 2010].

When several atomic sub-systems of different energy transitions are present in the active medium, they will have their own gain curve which can undergo the saturation phenomenon of (2.17). This implies that if the saturation intensities of these transitions are different, the overall gain medium will be depleted locally when the saturation level is reached, creating holes in the spectral gain profile (figure (2.12) (a)). Such inhomogeneous broadening can originate, among others, from absorbing impurities in the original matrix, from inhomogeneous thickness of the active quantum-well layer in semiconductor lasers, or simply from the inherent structure of the active medium (Quantum Dots lasers, doped-silica...) [Weisbuch 2014]. Normally, in our lasers, such phenomenon should not occur or be very limited.

- Spatial Hole Burning

In the Fabry-Perot cavity, laser oscillations create maxima that are located every $FSR_\lambda/2$, implying that the ideal model of the homogeneous gain cannot exist. Hopefully, in this case the carrier diffusion length (at least $10 \mu m$) is bigger than the FSR : it allows a re-homogenization of the gain so that no spatial hole burning occurs. However, in some cavities, the (intensity) envelop of the field, which extends on the mm scale this time, is not flat. As optical power grows, holes are created in the spatial gain because of carrier consumption by stimulated recombinations, which will eventually prevent some modes to be amplified (depending on their spatial localization), creating in turn spectral hole burning (figure (2.12) (b)). Consequently, the hole burning phenomenon can completely modify the laser dynamics, even adding chaotic mode hopping behavior. It is highly detrimental in some single-mode lasers and because of the inhomogeneous gain competition, it induces longitudinal multimode lasing as the power increases in the cavity.

2.1.8 Conclusion

In the overall section, very general considerations on lasers were put forward, without a particular focus on semiconductor lasers, which are yet the main theme of this manuscript. This was done on purpose. Indeed, besides all the particularities of such devices, which have seen constant theoretical and experimental investigations from a vast community of researchers from now more than 40 years,

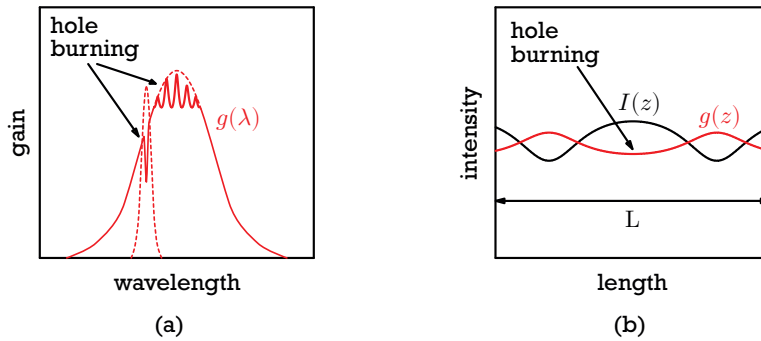


Figure 2.12: Schematics of (a) Spectral hole burning as a single depletion or periodic profile in the gain curve, (b) Spatial hole burning phenomenon. $I(z)$ is the intensity profile of the main mode while $g(z)$ is the saturated gain profile

they remain lasers, and from that point of view, are not different from a CO_2 laser in terms of the fundamental mechanisms they are built on. We tried here to underline the fact that these objects are mainly driven by the losses (internal and from mirrors), be it for the available output power or the spectral purity of light they show. As the goal is to realize low noise laser diodes for Cs pumping, we will try to keep in mind this fact in the further investigations. Also, what can differ from one type of laser to another is the pumping mechanism i.e. the way the energy is transferred to the excited population of carriers. It strongly influences the laser inner dynamics and thus can induce perturbations superimposed on the classical 'photon noise' and the associated Schawlow-Townes limit.

2.2 About semiconductor lasers

The following considerations address the case of semiconductor lasers, which gain medium and spectral properties show special properties, specific to this class of devices.

2.2.1 Generalities on the gain medium

This section focuses on the semiconductor laser itself. The very first demonstration of coherent emission from such materials dates back from 1962 [Hall 1962, Holonyak Jr 1962] and was based on *Gallium Arsenide* alloy. At that time, it could only work at $77 K$ under huge current density of injection. Later, considerable conceptual evolution in the design and the fabrication techniques led to room-temperature operation of the device with high efficiency.

2.2.1.1 GaAs based materials

In a dense solid medium like a semiconductor crystal, the optical properties of gain and propagation are far more complex to analyze than for single atomic species in a passive matrix. First, in solids, the formerly discrete levels characterized by the quantum states $|n, l, m, s\rangle$ become *quasi-continuous energy bands* of electrons separated by the energy gap E_g , where no state for the carriers are available. The gap itself can be seen as a consequence of the distance that existed between discrete levels of the individual atoms of the crystal matrix. Semiconductors or insulators have their conduction band (anti-bonding states of the orbitals *hybridization* of two neighboring atoms) empty at $0 K$ and their

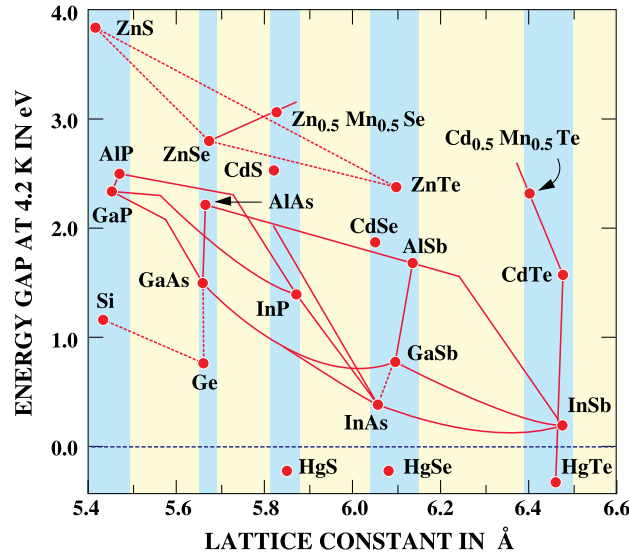


Figure 2.13: Mapping of the energy gap at 4 K of several semiconductor alloys versus their lattice constant. With the courtesy of B. Vinter in [Rosencher 2002].

valence band (bonding states of the orbitals) full. In the case of semiconductors however, at ambient temperature ($T = 300 \text{ K} \Leftrightarrow k_B T = 26 \text{ meV}$), few electrons are excited to the conduction band, making them weakly conductive [Kittel 1966].

Among the simple atomic species that are natural semiconductors, we find in the column IV of classification: Carbon (C) (Diamond in its crystalline form), Silicon (Si) (material base for transistors) and Germanium (Ge) (higher periods are metals). Actually, it is the result of hybridization of their s and p levels that give rise to their properties. Those species cannot actually be used to produce efficiently photons by free electrons de-excitation to the valence band because the minimum of energy of their conduction band does not corresponds to the maximum of energy of the valence band. The group of III-V compounds is far more interesting to make lasers: alloys of elements of the column III: Boron (B), Aluminum (Al), Gallium (Ga), Indium (In) and of column V: Nitrogen (N), Phosphorus (P), Arsenide (As) and Antimony (Sb) can be mixed to create *direct* band-gap alloys in binary, ternary, quaternary or even higher order compounds, with high versatility in the value of the gap. Figure (2.13)

III-elements	V-elements
Boron (B)	Nitrogen (N)
Aluminum (Al)	Phosphorus (P)
Gallium (Ga)	Arsenide (As)
Indium (In)	Antimony (Sb)

Table 2.2: First species of column III and column V of the classification of elements: resulting alloys have semiconducting properties.

shows some of the E_g versus the lattice constant of the crystal. For instance, GaAs has $E_g = 1.424$ at 4.2 K (equivalent wavelength emission at $\lambda_g = 870 \text{ nm}$) and a lattice constant $a_0 = 5.65325 \text{ \AA}$. The

gap dependency in temperature is usually given an empirical law:

$$E_g(T) = E_g(0) - \frac{aT^2}{b + T} \quad (2.45)$$

where a , b and $E_g(0)$ are determined from the material (for GaAs, $a = 5.41 \times 10^{-4} \text{ eV/K}$, $b = 204 \text{ K}$). A change of temperature can then be used to tune the energy transition of the material. Also, some basic properties of alloys are usually calculated using *Vegard's law* [Vegard 1921] for the lattice constant (2.46) while the energy gap is approximated by quadratic combinations of binaries [Adachi 2009] (2.47):

$$a_{0,A_x B_{1-x} C_y D_{1-y}} = x a_{0,A} + (1-x) a_{0,B} + y a_{0,C} + (1-y) a_{0,D} \quad (2.46)$$

$$E_{g,A_x B_{1-x} C_y D_{1-y}} = x E_{g,AC} + x(1-y) E_{g,AD} \quad (2.47)$$

$$+ (1-x)y E_{g,BC} + (1-x)(1-y) E_{g,BD} \quad (2.48)$$

where A, B, C and D are the III-V alloys, x and y the proportions of III and V elements respectively (for electro-neutrality purposes, half of the mass is III-type and the other is V-type). Most of the time, *bowing parameters* have to be taken into account to correct these approximations. Then, the energy transitions can be also tuned by changing the relative compositions of alloys. However, a stringent constraint should be observed: the materials have to keep their full crystal properties to get the desired band transitions, which is never the case with 'natural' growth in nature where they are found as poly-crystalline or amorphous media. Such alloys are grown artificially on different length scales:

1. Industrial growth of giant crystals: Si, GaAs, InP, GaSb and other simple alloys are grown in ingots of several inches of diameter (1 *inch* = 2.54 *cm*). It is then sliced in round *wafers* of hundreds of microns of thickness
2. Epitaxial growth on buffer substrates: several techniques are used to grow other complex materials on the previous basis, with thickness ranging from a few atomic layers to several microns

To keep the crystal properties without any defects in its structure (dislocations), the alloys grown on their substrate have to keep the same lattice parameter: this is why, depending on the original substrate, a family of compounds and then of band-gaps are imposed, depending on the targeted optical transitions: for GaAs, it is in the 500 – 1100 *nm* range (visible and Near-Infrared NIR), for InP, 1.2 to 1.6 μm (Telecom range), and for GaSb, between 2 to 3 μm . The GaN family, which is still on its way for mature processing methods, covers the blue (400 *nm*) to the near Ultraviolet (NUV). To reach transitions between 850 to 900 *nm*, we see that the GaAs related alloys are the good choice for the gain medium. The use of higher order compounds is interesting: while the gap of GaAs and its lattice constant have fixed values at a given temperature, ternary alloys introduce an additional degree of freedom so that the gap can be changed with a matching lattice constant to GaAs when playing with the x ratio. For instance, Al, which has pretty much the same electronic structure as the one of Ga, can be introduced to give the well-known $\text{Al}_x\text{Ga}_{1-x}\text{As}$. Usually, this Al substitution increases the energy gap.

2.2.1.2 Band structures and doping

The band structures of solids are extremely complex and their calculation is a complex area of research. Simple models can be used to get the physical behavior of the motion of electrons: for instance, the

quasi-free electron model assumes that the carriers see an average periodic potential of energy created by the fixed nuclei of atoms. It starts by solving the stationary Schrödinger equation in the atomic potential V :

$$\hat{H}|\Psi(\vec{r})\rangle \stackrel{def}{=} \left(\frac{\hat{p}^2}{2m_e} + V(\vec{r}) \right) |\Psi(\vec{r})\rangle = E_{\vec{k}} |\Psi(\vec{r})\rangle \quad (2.49)$$

with $\hat{p} = \hbar\hat{k}$ the momentum operator and m_e the mass of the electron. The equation is a classical eigenvalue one that calls for a diagonalization of the Hamiltonian H on a complete basis of wavefunctions $|\Psi\rangle$ to find the eigen-energies $E_{\vec{k}}$. A classic derivation shows that the solutions are the Bloch vectors which are plane waves propagating with a position-dependent amplitude which have the same periodicity as the one of the crystal: $\Psi_{n,\vec{k}}(\vec{r}) = u_{n,\vec{k}}(\vec{r})e^{i\vec{k}\cdot\vec{r}}$. Their energies are discretized in dense n bands with the following dispersion relation in the first *Brillouin* zone (reciprocal representation in wave-vector of an elementary cell of the crystal in real \vec{r} -space), [Kittel 1966]:

$$E_{\vec{k},e} = E_c + \frac{\hbar^2 k^2}{2m_e^*} \quad (2.50)$$

Expression (2.50) is only valid near $|\vec{k}| = 0$ and is called the approximation of the **parabolic bands**. The term m_e^* is the *effective mass*, that takes into account the average variation of energy with propagation in the periodic potential. For GaAs, $m_e^* = 0.067m_e$. This expression implies that the iso-energy surfaces in the \vec{k} -space are spheres centered on $\vec{0}$. In the reality, all the directions are not necessarily equivalent in a crystal. For Zinc-Blende crystal structures, the (\vec{k}, E) diagram is represented in the plane defined by $\vec{k} = [110]$ and $\vec{k} = [111]$ (figure (2.14)).

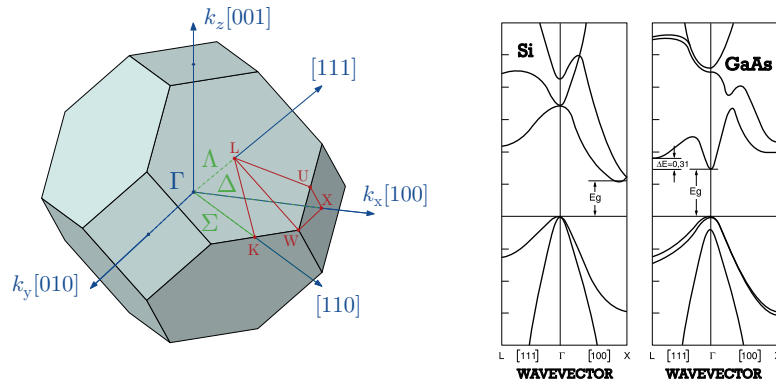


Figure 2.14: On the left: Representation of the first Brillouin zone of Zinc-Blende crystals with its axis of symmetry (adapted from Wikipedia.org). On the right: First Brillouin zones of Si and GaAs in the $([110], [111])$ plane. With the courtesy of B. Vinter in [Rosencher 2002].

When an electron is excited from the valence band to the conduction band, it releases a unoccupied bonding state in this band: the theory of solids demonstrates that this state behaves like a particle of positive charge e , of negative energy $-E_{\vec{k}}$ and is called a *hole*. The parabolic band model, with an effective mass m_h^* , can also be applied, such that:

$$E_{\vec{k},h} = E_v - \frac{\hbar^2 k^2}{2m_h^*} \quad (2.51)$$

Further analysis shows that there is actually three valence bands: the corresponding pseudo-particles are called *heavy-holes*, *light-holes* and *split-off holes*. The greater the effective mass of the holes, the smaller the curvature of the energy bands $\frac{d^2E}{dk^2}$. The parabolic band model is in the vicinity of the Γ -valley only. Otherwise, the band structures are computed using perturbative theories, one of which, the Kohn-Luttinger-Kane model ('*k.p*' theory) enables to predict the effective masses of electrons and of the holes in complex band structures. It can be shown that the dispersion relation for the conduction band can be written as in (2.50) with an effective mass given by:

$$m_e^* = m_e \left(1 + \frac{E_P}{E_g} \right)^{-1} \quad (2.52)$$

$$E_P = 2 \frac{|\langle u_{c,\vec{0}} | \vec{e} \cdot \vec{p} | u_{v,\vec{0}} \rangle|}{m_e} \quad (2.53)$$

E_P (in eV) is the Kane energy and the matrix element in (2.53) translates the coupling that exists between the conduction band and the valence band Bloch vectors for an electron wave-vector along \vec{e} . The E_P can be experimentally determined and is rather constant in most of the III-V, IV and II-VI semiconductors:

$$E_P \approx 25 \text{ eV} \quad (2.54)$$

So the effective mass of the electron is mainly determined by the gap E_g of the material. For the LH and HH, the problem is far more complex (the three types of valence bands influence each others), and the theory shows that three parameters are sufficient to determine the dispersion relations [Peter 2010]:

$$E_{\vec{k},hh/lh} = E_{v,\vec{0}} + \frac{\hbar^2 k^2}{2m_e^*} \left[(1 - \gamma_1) \vec{k}^2 \pm \sqrt{4\gamma_2^2 \vec{k}^4 + 12(\gamma_3^2 - \gamma_2^2)(k_x^2 k_y^2 + k_y^2 k_z^2 + k_z^2 k_x^2)} \right] \quad (2.55)$$

The γ_1 , γ_2 and γ_3 are the Kohn-Luttinger parameters and can be, again, measured for a given material. Alternatively, for complex compounds like quaternaries, the γ_i parameters can be expressed in terms of the HH and LH effective masses along some symmetry directions of the k -space, by using Vegard's law and inverting (2.55). For GaAs, $\gamma_1 = 6.85$, $\gamma_2 = 2.1$ and $\gamma_3 = 2.9$ so that $m_{hh}^* = 0.38m_e$ and $m_{lh}^* = 0.09m_e$ in the Γ valley. In some cases, mechanically *strained* materials (see further for the quantum-wells) are used, which modifies both the energy gap and the effective masses of the electron and holes. One of the first effect of strain is to lift the degeneracy of the valence bands so that the energy of LL and LH at the Γ center are separated. It also causes the effective mass to decrease, so that the band curvature increases.

Semiconductors are weakly conducting at ambient temperature. This is an issue for them to be used as an active optical medium in the case of electrical pumping. This is why most of the semiconductors are *doped*, that is, a controlled number of impurities is introduced in the original lattice to add either electrons or holes states aside from the ones naturally available in the material. Two types of doping exist:

- N-type: *Donor* species releases free electrons in the conduction band of the host material (e.g. Si (group IV) in GaAs)
- P-type: *Acceptor* species releases holes in the valence band of the host material (e.g. Zn (group II) in GaAs)

- Intrinsic: No doping

At ambient temperature, the dopants are generally ionized because their energy levels lie a few tens of meV apart from the top of the bands (less than $k_B T$). In GaAs, N-type doping can go up to $N_d = 2 \times 10^{18} cm^{-3}$ and for P-type, up to $N_a = 2 \times 10^{19} cm^{-3}$. Higher order alloys are more difficult to enrich in dopants because high concentration of impurities modify deeply the order of the lattice.

2.2.1.3 Carrier concentration

The probability for an electron or a hole to occupy an energy level E in its band is given by the well-known *Fermi-Dirac* statistics:

$$f_c(E) = \frac{1}{1 + e^{\frac{E-E_F}{k_B T}}} \quad (2.56)$$

$$f_v(E) = 1 - f_c(E) \quad (2.57)$$

where the Fermi level E_F (or chemical potential) is the energy of the highest level occupied by the particles. The number of states per unit energy (in $J^{-1}cm^{-3}$), i.e. the density of states, is expressed using the band dispersion relations (2.50) and (2.51), at a distance $|\vec{k}|$ from the center of an isotropic sphere, taking into account the spin degeneracy :

$$\rho_{c,v}(E) = \frac{1}{2\pi^2} \left(\frac{2m_{c,v}^*}{\hbar^2} \right)^{3/2} |E - E_{c,v}|^{1/2} \quad (2.58)$$

Finally, the density of electrons (in cm^{-3}) in the conduction band and of holes in the valence band are given by:

$$n = \int_0^{+\infty} \rho_c(E) f_c(E) dE = N_c F_{1/2} \left(\frac{E_c - E_F}{k_B T} \right) \quad (2.59)$$

$$p = \int_0^{+\infty} \rho_v(E) f_v(E) dE = N_v F_{1/2} \left(\frac{E_F - E_v}{k_B T} \right) \quad (2.60)$$

where the *effective* density of states $N_{c,v}$ in the bands and the Fermi integral $F_{1/2}$ are:

$$N_{c,v} = \frac{1}{4} \left(\frac{2m_{c,v}^* k_B T}{\pi \hbar^2} \right)^{3/2} \quad (2.61)$$

$$F_{1/2}(y) = \frac{2}{\sqrt{\pi}} \int_0^{+\infty} \frac{x^{1/2}}{1 + e^{(x-u)}} dx \quad (2.62)$$

In GaAs, $N_c = 4.4 \times 10^{17} cm^{-3}$ and $N_v = 8.7 \times 10^{18} cm^{-3}$. For an intrinsic semiconductor, $n = p$ and in the Boltzmann regime, $E - E_F \gg k_B T$, then (2.59) gives the intrinsic carrier concentration $n_i = \sqrt{N_c N_v} e^{-\frac{E_g}{2k_B T}} = 2 \times 10^6 cm^{-3}$ at ambient temperature. In case of doping, $n = n_i + N_d \simeq N_d$ and the same for the holes. On the other side, the Fermi levels are given easily by the inversion of (2.59):

$$E_{F,c} = E_c - k_B T \cdot F_{1/2}^{-1} \left(\frac{N_c}{N_d} \right) \approx E_c - k_B T \ln \left(\frac{N_c}{N_d} \right) \quad (2.63)$$

$$E_{F,v} = E_v - k_B T \cdot F_{1/2}^{-1} \left(\frac{N_v}{N_a} \right) \approx E_v + k_B T \ln \left(\frac{N_v}{N_a} \right) \quad (2.64)$$

The conclusion is that with a high level of doping, the Fermi levels enter the bands: the semiconductor is said to be degenerated. Equivalently, the Fermi-levels govern the level of population in an intrinsic semiconductor that is injected with electrical current.

2.2.1.4 Optical transitions in a bulk semiconductor

The rules of optical transitions between the conduction band and the valence band are specified by quantum mechanics: the total momentum (wave-vector) of the electron must be conserved:

$$\vec{k}_e^{before} = \vec{k}_e^{after} \quad (2.65)$$

$$= \vec{k}'_e + \vec{k}_{opt} \quad (2.66)$$

where \vec{k}_{opt} is the emitted photon wave-vector. As $\vec{k}_{opt} \sim 1/\lambda_{opt} \ll \vec{k}'_e \sim 1/a_0$ for $\lambda_{opt} \sim 1 \mu m$, the transition is nearly vertical in the \vec{k} -space. The photon energy is then:

$$E_{opt}(\vec{k}) = h\nu_{c,v} = |E_c(\vec{k}) - E_v(\vec{k})| = E_g + \frac{\hbar^2 \vec{k}^2}{2m_r} \quad (2.67)$$

$$m_r = \frac{1}{m_c^*} + \frac{1}{m_v^*} \quad (2.68)$$

associated to the *reduced* density of states available for optical transitions (in $J^{-1}cm^{-3}$):

$$\rho_{r,opt}(E) = \frac{1}{2\pi^2} \left(\frac{2m_r}{\hbar^2} \right)^{3/2} |E - E_g|^{1/2} \quad (2.69)$$

which is very similar to (2.58). As in section [2.1.1], the gain of the semiconductor medium can be expressed with Einstein's relations:

$$g(\hbar\omega) = -\alpha(\omega) = B_{cv}\rho_r(\hbar\omega)[f_c(E_c) - f_v(E_v)] \quad (2.70)$$

$$= g_{max}(\hbar\omega)[f_c(E_c) - f_v(E_v)] \quad (2.71)$$

and the spontaneous emission rate in ($cm^{-3}.s^{-1}.J^{-1}$):

$$R_{spon}(\hbar\omega) = A_{cv}\rho_r(\hbar\omega)f_c(E_c)[1 - f_v(E_v)] \quad (2.72)$$

$$A_{cv} = \frac{1}{\tau_{rad}} = \frac{8\pi^2 e^2 |r_{cv}^{eff}|^2}{\hbar \varepsilon_0 n_{med}^2 \lambda_0^3} \quad (2.73)$$

where A_{cv} is again the radiative decay constant. This time, the dipole element $|r_{cv}^{eff}|$ is directly linked to the transitions available between the conduction band and the HH and LH bands (the S-O is too far apart to interact) and to the Kane energy [Rosencher 2002]:

$$|r_{cv}^{eff}|^2 = 2/3 |r_{cv}|^2 = \frac{\hbar^2 E_P}{2m_e E_g} \quad (2.74)$$

In GaAs, $\tau_{rad} = 0.7 ns$. The interesting thing is that **the radiation lifetime depends strongly on the gap**.

Both g and R_{spon} are driven by the quasi Fermi-levels separation, which are in turn dependent on the carriers densities in the material. The condition of amplification of a photon of energy $h\nu$ needs a positive gain, so:

$$E_g < h\nu < \Delta E_F = E_{F_c} - E_{F_v} \quad (2.75)$$

Below the gap, the material is transparent. For any photon of energy above the Fermi levels separation, it is absorbed. An other form of $R_{spon}(\hbar\omega)$ is interesting to write by integrating on all the spectrum of energy:

$$R_{spon} = Bnp \quad (2.76)$$

The bimolecular recombination coefficient $B = \frac{1}{\tau_{rad} N_c} \left(\frac{m_r}{m_v} \right)^{3/2}$ is around $10^{-10} cm^{-3}.s^{-1}$ in GaAs.

2.2.1.5 Optical transitions in quantum wells

Few years later after the first demonstration of lasing in GaAs, the concept of multiple *heterostructures* that create jumps in the bandgap of a semiconductor crystal made of different alloys along the direction of growth was the object of intense research. It was recognized that such structures could help to confine electrons and holes in the specific areas of the bulk, reducing the threshold current for the lasing effect (Alferov, Panish et al. [Panish 1970]). Then, theoreticians like C. Henry of the Bell Labs and Esaki and Tsu from IBM showed that for very thin layers 'sandwiched' between materials of higher gap, quantum effects should occur with the discretization of the semiconductor bulk bands in sub-levels [Esaki 1970]. In 1974, the first realization of *quantum-well lasers* (QW) gave the proof-of-concept [Dingle 1974].

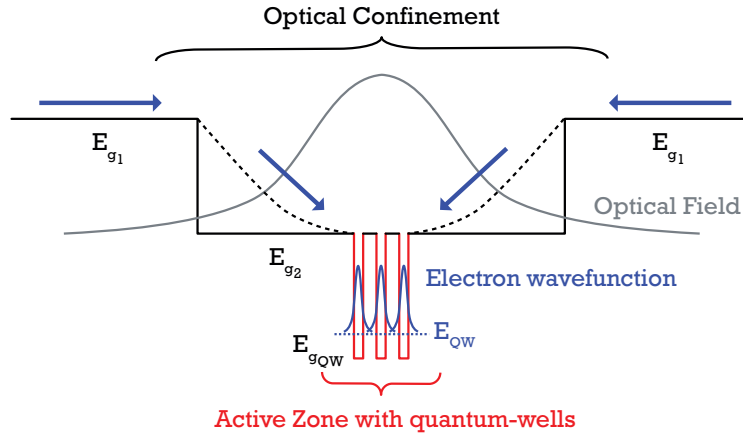


Figure 2.15: Double heterostructure using quantum-wells for carrier confinement and a large optical cavity for intensity confinement

Today, the majority of semiconductor lasers produced are Separate Confinement Heterostructure (SCH) with an active zone made of multiple and multidimensional quantum-wells (figure (2.15)). In such a configuration, the advantages are two-fold: first, the barriers $\Delta E_g = E_{g2} - E_{g1}$ retain the carriers in the active zone, were they are strongly confined in a lower gap material $E_{g,QW}$. Also, because the refractive index of the semiconductor n_{SC} increases with a decreasing energy gap, the SCH plays the role of an optical cavity that guides the laser mode. The overlap of the field-intensity that spread in the volume V_{SCH} with the volume of the active zone V_{QW} defines the *confinement factor* Γ . The effective amplifying gain seen by the optical mode is referred to as the *modal gain* g_{mod} :

$$g_{mod} = \Gamma g \quad (2.77)$$

$$\Gamma = \frac{\int_{QW} |E(z)|^2 dz}{\int_{SCH} |E(z)|^2 dz} \quad (2.78)$$

The active zone can be built with N_{QW} non-coupled quantum-wells. This is usually the case for low band-gap emissions ($\lambda = 1.3 \mu m$ and above) where carriers can escape more easily the local potential. The total material gain is multiplied by N_{QW} if the wells are filled uniformly.

To recover the expression of the gain in the QW case, both the reduced density of states $\rho_r(\hbar\omega)$ and the band coupling element $|r_{cv}^{eff}|$ must be changed depending on the geometry of the confined volume. For a 2D QW (thin planar layer of $5 - 15 nm$), the energy levels can be determined using the

technique of the *envelope function*: one considers that the Bloch functions in (2.49) can be separated in the transverse direction of the quantum-well, so that they are written as the product of the bulk amplitudes $u_{n,\vec{k}}$ times the envelopes $\xi_n(\vec{r}_{\perp QW})$. Then, the Hamiltonian can be solved for the envelopes only, which is the very well-known problem of the simple square-well potential. The results are the following, in the parabolic bands approximation:

$$\rho_{2D}(E) = \frac{m_{QW}^*}{\pi\hbar^2} \sum_n \theta(E - \varepsilon_n) \quad (2.79)$$

$$E_n(\vec{k}) = E + \varepsilon_n + \frac{\hbar^2 \vec{k}^2}{2m_{QW}^*}, \quad \varepsilon_n \approx n^2 \frac{\hbar^2 \pi^2}{2m_{QW}^* d_{QW}} \quad (2.80)$$

with n the considered band, E the energy of the edge of the band in the bulk case, m_{QW}^* the effective mass of the carrier in the material of the well, d_{QW} the thickness of the well, θ the Heaviside function and ε_n the energy of confinement showing the fact that there is a positive shift (*blue shift*) in occupied energy compared to the bottom of the well (which is at the energy of the bulk). Only if the well is considered as 'infinite' (which is true if there are many quantized levels and $n = 1, 2$ is considered), a simple formula gives ε_n as a function of n^2 . Figure (2.16) shows the profile of the density of states in a QW compared to the bulk. If the optical transitions are considered, the symmetry of the wavefunctions allows only some transitions at constant sub-band number $n \rightarrow n$. Usually, the confinement energy for the HH band is higher than that of the LH band, so the degeneracy of those bands in the bulk case is *lifted*. The *inter-band* gain is given by the sum of the contributions of each pair of

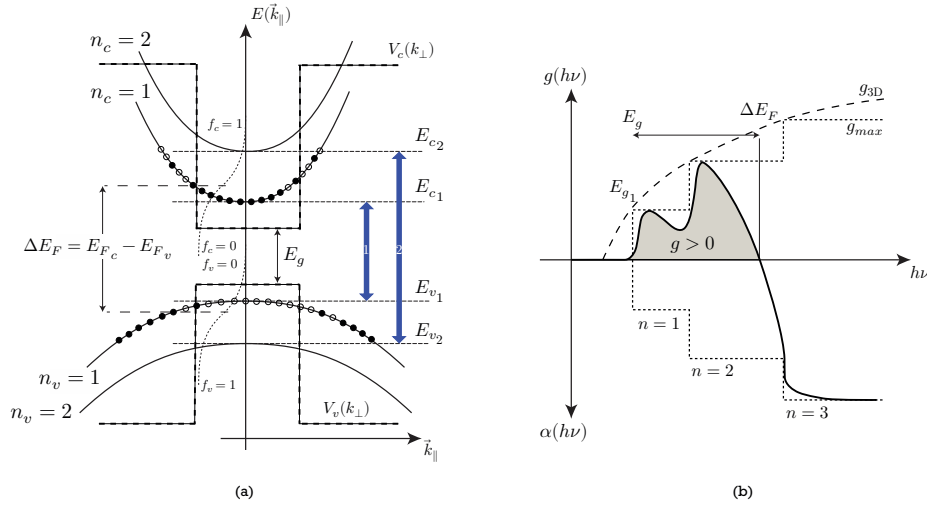


Figure 2.16: (a) Representation of the first energy bands in the parabolic approximation in the (E, \vec{k}_{\parallel}) plan, as well as their occupancy state. (b) Representation of the gain curve as a function of the transition energy $h\nu$ for a quantum well structure

inter-band transitions:

$$g_{QW}(\hbar\omega) = \alpha_{QW} \sum_{n,m} |\langle \xi_n | \xi_m \rangle|^2 \theta(\hbar\omega - (E_g + \varepsilon_n^c + |\varepsilon_n^v|)) [f_n^c(\hbar\omega) - f_m^c(\hbar\omega)] \quad (2.81)$$

$$\alpha_{QW} = \frac{2\pi e^2 |r_{cv}^{eff}|^2 m_r}{\lambda_0 n_{med} \varepsilon_0 \hbar^2 d_{QW}} \quad (2.82)$$

If the transition $C \rightarrow HH$ from $n_c = 1$ to $n_v = 1$ is considered only, the envelop function term $|\langle \xi_n | \xi_m \rangle|$ is 1 and expression (2.81) is simplified. In practice, the gain function is approximated at its

maximum value (whatever the corresponding energy transition) for a given *surface density* of electrons $n_s = n/d_{QW}$ in the quantum well by the following expression:

$$g_{QW}^{max} = \alpha_{QW} \left(1 - e^{-n_s \frac{\pi \hbar^2}{m_e^* k_B T}} - e^{-n_s \frac{\pi \hbar^2}{m_h^* k_B T}} \right) \quad (2.83)$$

$$g_{QW}^{max} \approx g_0 \ln \left(\frac{n}{n_{tr}} \right) \quad (2.84)$$

Close to the transparency density $n_{tr} = m^* k_B T / d_{QW} \pi \hbar^2$, the gain curve can be fitted with the above expression, which is very practical to evaluate the threshold of the laser with an analytical formula.

Note on strained quantum-wells

With the development of quantum-well structures, it appeared that mechanically *strained* layers were particularly interesting. Such strain ε is defined, in the transverse direction to the QW layer:

$$\varepsilon = \frac{a_0 - a_{QW}}{a_0} \quad (2.85)$$

where a_0 is the lattice constant of the substrate (GaAs in our case) and a_{QW} is the lattice constant of the material of the well, for instance, *Gallium Indium Arsenide Phosphide* ($\text{Ga}_x\text{In}_{1-x}\text{As}_y\text{P}_{1-y}$). If $\varepsilon > 0$, the well is said to be in *compressive* strain while $\varepsilon < 0$ means that it has *tensile* strain. Such definition implies that the material stays in the linear elastic deformation approximation, otherwise the crystal will undergo irreversible deformations (dislocations) undermining the gain properties (dark-lines). For a given QW strain, there exist a critical length l_c (that depends on the material) beyond which lattice degradation occurs. For a 8 nm thick QW made of GaAs based materials, the critical strain is of the order of $\varepsilon_c \sim 2.5\%$.

The strain induces shifts in the band energies, which can be computed using the sub-matrix of the Kohn-Luttinger Hamiltonian. The theory shows that the degeneracy of the valence band is strongly lifted depending on the sign of the strain: if compressive, the fundamental HH sub-level lies at the highest energy, while it is the LH is the case of tensile strain. Also, the effective masses of the valence bands are reduced (the curvature increases), so (2.83) shows that for a given transparency density, the gain is higher than in the non-strained quantum-well. Furthermore, the effective optical matrix element $|r_{cv}^{eff}|^2$ is strongly affected depending on the polarization of the amplified electric field: for *transverse magnetic* (TM, orthogonal to the plan of the quantum-well) transition, the element is zero for $C \rightarrow HH$. This means that a compressively strained QW favors deeply the gain of the TE mode, making the laser beam strongly polarized in this mode.

2.2.1.6 Case study for emission at 894 nm

The previous little reminder of the gain properties in semiconductors gives relations that can be practically implemented to predict the gain spectrum of the active zone, depending on the pumping parameters (density of carrier) needed to create enough positive gain to compensate for the losses of the optical cavity and achieve lasing condition. A model, called *Esaki Heterojunction Diode* has been implemented in *Fortran*, thanks to the work of E. Chirlias, A. Fily and B. Vinter among others, in the former group of Thomson-CSF-Thales, belonging now to the III-V Lab. The first part of this program (*CALBAND*), does precisely what has been described above: it computes the discrete levels of energies (as well as the wavefunctions) of the conduction band and the valence band (LH and HH, the S-O band being far enough to be neglected) in a quantum-well of arbitrary form, based on the bulk

profiles of bands (this part only requires the effective masses of binary alloys and the Kohn-Luttinger γ_{is} , plus some additional parameters to take into account the behavior under strain). Then, it evaluates all the envelope elements $|\langle \xi_n | \xi_m \rangle|^2$ between the chosen sub-bands and the effective density of states (DOS) $\rho^r(\hbar\omega)$ in both [100] and [110] directions. The population inversion part in (2.81) depends on the Fermi levels position, so on the electrons and holes densities. It will be evaluated by another piece of the model, *EsakiHTD*, a transport model of carriers through an heterojunction in 1D.

The structure studied is a 2D quantum-well made of GaInAsP with Gallium Indium Phosphide barriers (GaInP). These barriers are considered thick enough to have the bulk properties of the material. Figure (2.17) is the result of the potential energy diagram for the first electron, heavy-hole and

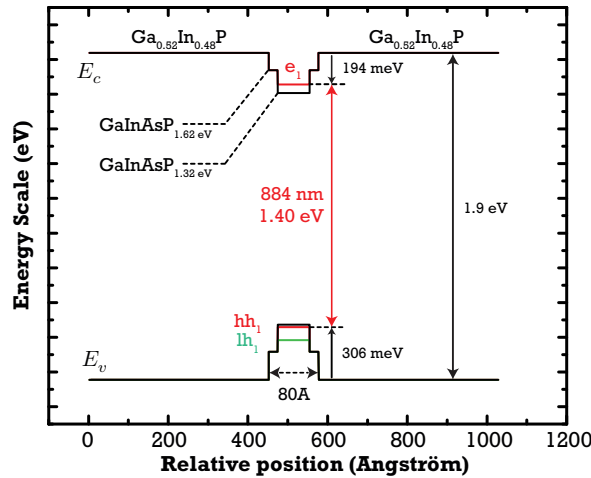


Figure 2.17: Band diagram of the quantum-well first transitions given by the *CALBAND* program.

Layer	Alloy	Strain ε
Optical Cavity	Ga _{0.516} In _{0.484} P	0%
Matching Interface	Ga _{0.733} In _{0.267} As _{0.544} P _{0.456} (Q(1.62 eV))	0%
QW	Ga _{0.7} In _{0.3} As _{0.331} P _{0.669} (Q(1.32 eV))	+1%

Table 2.3: Alloys used in the active zone of the laser for emission at 894 nm and their lattice matching to the GaAs buffer

light hole bands. The high GaInP barriers ($E_g = 1.9$ eV) are lattice-matched to GaAs, but because of the ternary composition, it allows a degree of freedom on the energy gap. Growth techniques can maintain its energy in the 1.6 – 1.63 eV range (depending on the ordering of the alloy that is subject to strong variations [Adachi 2009]). The QW itself is a 8 nm thick layer of quaternary of intrinsic gap energy equal to 1.32 eV (Q(1.32 eV)). Its advantages are that both gap energy and strain can be adjusted independently compared to the ternaries. In the present case, it has compressive strain of about +1%. The computation shows that the degeneracy between the HH and LH band is lifted, the HH lying at higher energy, so that this well will have gain for *TE* polarized photons. Finally, 2 nm interfaces of Q(1.62 eV) are necessary to manage the energy transition from the well to the barriers. In reality, it is a linear change of composition and it is critical to obtain a very steep transition so that the energy levels of the well are not affected (unlike in a GRINSCH structure). The *photoluminescence*

energy of the main transition is $1.40 \text{ eV} = 884 \text{ nm}$ (transition for non-filled well). The choice of such a structure is quite unusual for these wavelengths, and it will be justified at the end of the chapter. The emission has been tuned 10 nm below the targeted lasing wavelength because many effects shift the energy of the emission with material pumping:

- Gap shrinking effects (*redshift*)
 - Temperature: the gap is reduced according to the empirical law (2.45) ($a = 4.3 \times 10^{-4} \text{ eV/K}$, $b = 224 \text{ K}$). The local temperature usually increases with current injection that creates a *Joule* heating effect in the heterostructure.
 - Coulomb screening: with increasing density of electrons n , the distance between particles reduces, the ionic positive charges of the lattice are more screened out, and the band-gap reduces according to the approximation $\Delta E_g = -cn^{1/3}$ for an intrinsic semiconductor. In the case of the quantum-well, using the carrier sheet density, the coefficient is of about $c = 25 \text{ meV}/(10^{18} \text{ cm}^{-3})^{1/3}$ [Bennett 1990] for GaAs and alloys of close effective masses and dielectric constants.
- Effective Gap expansion effect (*blueshift*)
 - Band-filling: as the density of carriers increases in the material, Fermi levels separate away and higher energy electrons fill in the bands so that the mean energy of the spontaneous emission photons evolves according to (2.74). The tendency is $\Delta E_{\text{spont}} \propto n^{2/3}$.

In practice, it is observed that the photoluminescence is abruptly shifted by $+15 \text{ nm}$ at high injection near the transparency density n_{tr} and it decreases until the density n_{thr} is reached at laser threshold, where it remains constant. Then, local heating with current injection produces a steady rise of the wavelength of emission.

With the above band diagram, the DOS can also be computed as a function of the wave-vector \vec{k} in the two directions of symmetry of the lattice. For the conduction band, it is simply the step-function (2.79) that includes three electron discretized sub-bands. For the holes, because of band mixing effects between the HH sub-levels and LH sub-levels, eleven levels of each band are considered. Finally, there are $3 \times (11 + 11)$ matrix elements $|\langle \xi_n | \xi_m \rangle|$ in (2.81) to compute to reconstruct the gain curve. For the present case, it is given in figure (2.18). It is assumed that the density of carriers in the well is the intrinsic one.

It is worth to mention that, in addition to the many-body effects, an effective broadening of the optical absorption lines is taken into account (equivalent of the $\mathcal{L}(\nu)$ in (2.12)) through the heavy-holes collisions with the *optical phonons* of the lattice [Fily 1998]. The model has been confronted to the experiments with good agreement. It reveals that the density at transparency for this active zone is:

$$n_{tr} = 1.8 \times 10^{18} \text{ cm}^{-3} \quad (2.86)$$

We will see later that the density at threshold (that depends on the profile of the electric field in the cavity as well as the losses, conversely to n_{tr}) is roughly equal to $n_{thr} = 2n_{tr}$ in our designs. The corresponding gain curve, in red, indicates that the theoretical maximum is at around $\lambda_g^{max} = 900 \text{ nm}$. Above n_{thr} , the effects of the higher order transitions between the sub-bands of the well start to shift the maximum of gain to the lower wavelengths. It is important then to stay close to the transparency to avoid a too deep blueshift in the spectrum. If the maximum of gain is plotted against the carrier density in the well, curve (2.19) is obtained. Then, the material gain can be fitted around transparency

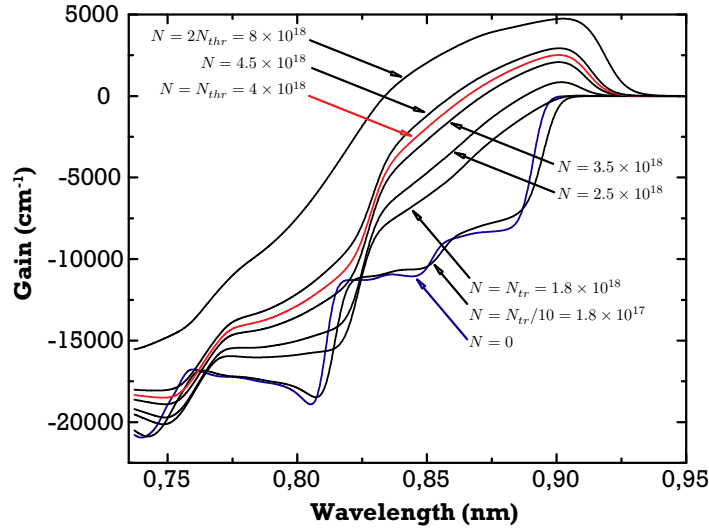


Figure 2.18: Material gain curve as a function of transition wavelength as computed by the *CALBAND-EsakiHTD* model. The transparency is reached for $N_{tr} = 1.8 \times 10^{18} \text{ cm}^{-3}$ and the threshold is typically around $N_{thr} = 4 \times 10^{18} \text{ cm}^{-3}$ for the targeted cavity.

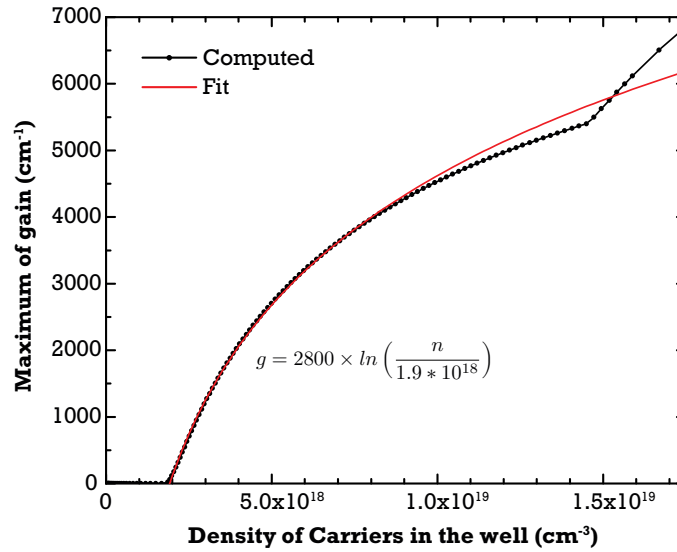


Figure 2.19: Maximum material gain curve as a function of carrier density in the well as computed by the *CALBAND-EsakiHTD* model. The curve can be fitted around transparency with a log law of the carrier density.

according to (2.83) with:

$$g_0 = 2800 \text{ cm}^{-1} \quad (2.87)$$

Beyond $n = 7 \times 10^{18} \text{ cm}^{-3}$, the gain deviates from the fit, and at $1.5 \times 10^{19} \text{ cm}^{-3}$, another transition stops the gain saturation. The value of g_0 is higher than what is presented in [Coldren 2012] for

InGaAs-GaAs structures. This is because InGaAs has a strain of lattice mismatch of about 0.44% to GaAs. The benefits of high strain in the present structure will be linked to a consequent reduced threshold current following the lower transparency current.

2.2.2 Photon noise in semiconductor lasers

2.2.2.1 The α_H factor

In section [2.1.4], the Schawlow-Townes linewidth of an optical resonator was presented. Additional factors have to be taken into account for semiconductor lasers. The phase-amplitude coupling factor (or Henry's factor) is one of them. In a famous article, C. Henry explained why the linewidth of the modes of semiconductor lasers was one order of magnitude higher than what was observed in solid-state lasers for instance [Henry 1982]. The following form for the linewidth was pointed out:

$$\Delta\nu_{S-T-H} = \frac{R_{spon}}{4\pi I} (1 + \alpha_H^2) \quad (2.88)$$

with R_{spon} the rate of spontaneous emission in the mode of interest as given in (2.76) for instance, I the *number* of photons in the laser cavity, and α_H the *linewidth enhancement factor*. The formula is very general and it may seem hard to see at first glance the link between (2.36) and (2.88). It will be made clear in section [2.2.2.2] when writing the expression of R_{spon} : we can just mention that the rate of spontaneous emission saturates at laser threshold at a value that depends on the cavity losses, yielding an intimate link with the cold cavity linewidth $\Delta\nu_c$. Actually, M. Lax was the first to wrote the above form for the linewidth, but Henry linked the enhancement factor to a true physical parameter specific of semiconductor lasers to explain the observed early measurements of laser diode linewidths. It is related to the fundamental optical properties of the medium:

$$\alpha_H(\hbar\omega_0, N) \equiv -\frac{\partial n_R/\partial N}{\partial n_I/\partial N} = -\frac{4\pi}{\lambda} \frac{\partial n_R/\partial N}{\partial g/\partial N} \quad (2.89)$$

where $n(\hbar\omega_0) = n_R + jn_I = n_R(\hbar\omega_0) + j\frac{\lambda_0}{4\pi}g(\hbar\omega_0, N)$ is the complex refractive index of the medium that depends both on the carrier density N and on the transition energy. Definition (2.89) states how a gain change $\Delta g(N)$ (due to a carrier density deviation from equilibrium) is related to a refractive index change of the medium: $\Delta n_R(N) = \alpha_H \times \Delta g(N)$. The interpretation of the modified linewidth is the following: the spontaneous emission of photons being a random process, this will cause the carrier density to be affected by random forces that will, in turn, cause the gain to fluctuate. Because of the previous relation, the refractive index of the medium fluctuates, enhancing the *diffusion* of the phase of the laser field. If $\alpha_H = 0$, we recover the S.-T. formula in a form that states that the total magnitude of the frequency/phase fluctuations is proportional to the source rate of spontaneous emission R_{spon} .

The relation (2.89) has no exclusive link to the issue of linewidths in semiconductor lasers, but is rather a particular case of non-linear optics in physics: as soon as there is a change in absorption of a medium, a corresponding change in the dispersion occurs. If the complex susceptibility $\chi = \chi_R + j\chi_I$ is used to describe the medium, the following relations holds [Hutchings 1992, Lucarini 2005]:

$$\chi_R(\omega) = \frac{2}{\pi} \mathcal{P} \int_0^{+\infty} \frac{\omega' \chi_I(\omega')}{\omega'^2 - \omega^2} d\omega' \quad , \text{Kramers-Krönig relations} \quad (2.90)$$

$$= \frac{1}{\pi} \mathcal{P} \int_{-\infty}^{+\infty} \frac{\chi_I(\omega')}{\omega' - \omega} d\omega' = \mathcal{H}(\chi_I) \quad , \text{Hilbert transform} \quad (2.91)$$

where \mathcal{P} denotes the principal value of the integral, that is the limit:

$$\mathcal{P} \int_{-\infty}^{+\infty} \cdot \equiv \lim_{\varepsilon \rightarrow 0} \left(\int_{-\infty}^{-\varepsilon} \cdot + \int_{+\varepsilon}^{+\infty} \cdot \right) \quad (2.92)$$

Such equivalent formulas arise from the fact that physically, the susceptibility is a *causal* function (it is zero before the excitation by the electric-field of the atomic medium) so the theory of analytical functions requires such constraints on the real and imaginary part. A more practical form for a perturbation to the complex refractive index is:

$$\Delta n_R(\hbar\omega, \zeta) \stackrel{def}{=} \frac{\partial n_R}{\partial \zeta}(\hbar\omega, \zeta) d\zeta = \mathcal{H}(\Delta n_I(\hbar\omega, \zeta)) \quad (2.93)$$

In our case, $\zeta = N$ but any other independent source of fluctuations can be considered. Finally, it is possible to estimate, theoretically, the α_H factor from the *material differential gain* curves $\frac{dg}{dN}(h\nu, N)$ extracted from the *EsakiHTD* model (figure (2.20)). The relations (2.90) have been implemented either with the 'hilbert' function of MatlabTM or with an algorithm of discrete integration given in [Lucarini 2005]. The results are almost the same in the range of energy of interest and are shown in figure (2.21): graph (c) displays that at the fixed wavelength of interest $\lambda = 894 \text{ nm}$, the factor barely varies with the injected carrier density of transparency. On the other side, graph (d) gives a well-known tendency of the factor to decrease on the lower-wavelength/higher energies side of the gain curve.

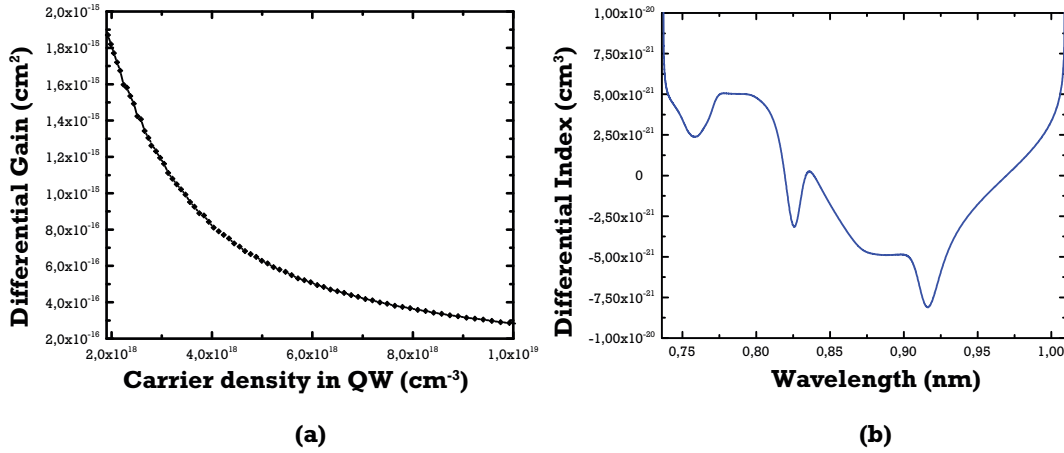


Figure 2.20: (a) Differential gain as a function of the carrier density in the well, at a fixed transition of 894 nm. (b) Differential refractive index as a function of the transition wavelength, at a fixed carrier density $n = 4 \times 10^{18} \text{ cm}^{-3}$. *EsakiHTD* model.

The value itself is found at $\alpha_H \approx 0.7$ for $N = 2N_{tr} = 4 \times 10^{18} \text{ cm}^{-3}$. It is very small, at least 3 or 5 times from what has been reported in the literature for 2D quantum-wells [Kikuchi 1985]. Some comments can be made:

- In [Balle 1998], a simple model of relations between the susceptibility, the differential gain and the α_H curves is outlined. The author gives the following approximate analytical formula:

$$\alpha_H = 2D - \sqrt{2D^2 - 1} - \frac{\sigma}{3} D^{1/3} \quad (2.94)$$

$$D = \frac{N}{N_{tr}} \quad (2.95)$$

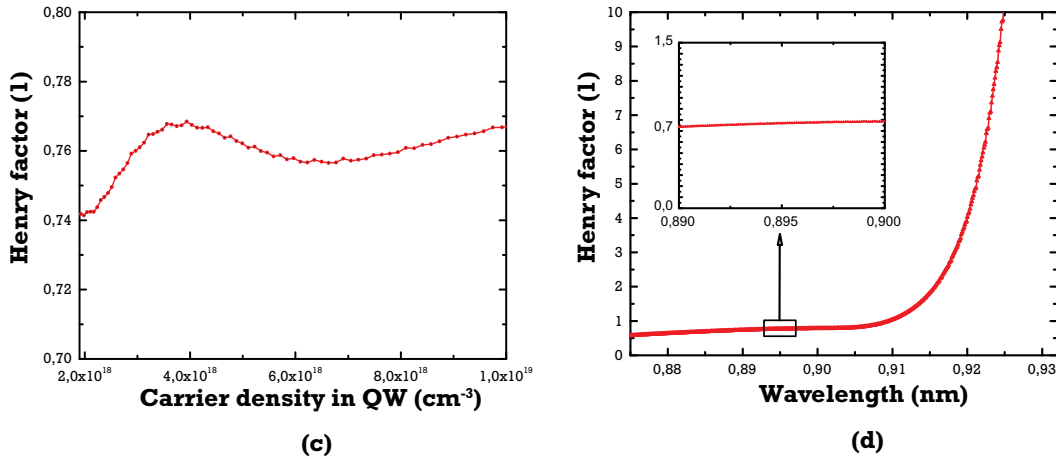


Figure 2.21: (c) Henry factor as a function of the carrier density in the well, at a fixed transition of 894 nm. (d) Henry factor as a function of the transition wavelength, at a fixed carrier density $n = 4 \times 10^{18} \text{ cm}^{-3}$. *EsakiHTD* model.

where σ is a parameter which tunes the gap shrinkage/expansion as in section [2.2.1.6]. Depending on this value, the factor can easily range from 0.5 to 3 as one has just to 'shift' the (λ, α_H) curve to the right to increase the factor. However, for the case $N_{thr} = 2N_{tr}$, the maximum value is $\alpha_H = 1.75$. The value computed above is not so absurd. Also, it should be noticed that close to the transparency, the differential gain is higher and the α_H reduced.

- Aside from the theoretical value given above, the question of the measurement of the enhancement factor should be asked: several techniques can be used, for instance by the historical recording of several gain curves with the Hakki-Paoli method [Hakki 1975], which accuracy is questionable here, to more recent sophisticated setups where the laser is modulated at high-frequencies and an analysis of the induced 'chirp' of the laser spectrum is made. A good summary and presentation of such techniques can be found in [Provost 2011].
- The α_H factor not only depends on the value of the differential gain in the denominator of (2.89), but also strongly on the form of differential gain curve. While it is rather the same profile in heterostructures with 2D quantum-wells, the gain curves are more close to the Lorentzian of a discrete atomic two-levels in quantum-dot (QD) lasers (which can be seen as 'super-atomic' systems). The Hilbert transform of such line being zero at the maximum of gain (due to the symmetry of the curve and of the transformation), the alpha factor is close to zero. This is why there is no enhancement of the linewidth in solid-state lasers made of discrete transitions energy levels. In the case of QDs, the values reported for α_H are also quite variable depending on the excitation of the quasi-discrete energy levels with injection [Grillot 2008].

In conclusion, we will not go further in the study of this topic. First because, as said above, no simple, universal and accurate technique of direct measurement of the α_H exists in SC lasers above threshold, secondly, the value of the factor is rather the same from one structure to another, though the strain in QW's are said to have contributed to its reduction with the development of laser diodes. It will be taken *a priori* between 2 and 3, giving a maximum enhancement of the order of $1 + \alpha_H^2 \approx 10$. Nevertheless, a rough estimation will be made out of frequency noise measurement on the dedicated section of this manuscript. To conclude, as we have seen, a positive detuning of the

lasing frequency from the maximum of gain $\Delta\lambda = \lambda_g - \lambda_l$ can decrease the factor. This is why an effective maximum of gain at 900 nm, compared to the targeted 894 nm, has been chosen when tuning the photoluminescence of the well. However, a stronger detuning can have other detrimental effects on the frequency stability in single-mode lasers (see further).

2.2.2.2 Spontaneous emission enhancement factors

- Intrinsic enhancement factor

In (2.88), the linewidth is written in terms of the total rate of spontaneous emission R_{spont} . In his article, Henry develops the term as follow (longitudinal direction of the cavity):

$$R_{spont} = \Gamma v_g g n_{sp} \quad (2.96)$$

where n_{sp} is the *population inversion factor*:

$$n_{sp}(h\nu) = \frac{f_c(E_c)(1 - f_v(E_v))}{f_c(E_c) - f_v(E_v)} = \frac{1}{1 - e^{-\left(\frac{\Delta E_F - h\nu}{k_B T}\right)}} \quad (2.97)$$

The factor goes to 1 when the Fermi-levels spacing is far greater than the energy of the transition considered i.e. when *complete* inversion of the population of the band is achieved. Conversely, the factor increases to infinity with no inversion of population. This comes from the fact that the semiconductor medium is not an ideal 4-levels system: the transparency is not immediately reached at the start of the population inversion and the rates of spontaneous and stimulated emission cannot be equal. With Henry's expression (2.96) the gain g can be written in terms of the losses at threshold, for the **particular case of the (homogeneous) semiconductor laser cavity**:

$$\Delta\nu_{S-T-H} = h\nu \frac{\Gamma v_g^2 \alpha_m g}{4\pi P_{out}} (1 + \alpha_H^2) n_{sp} \quad (2.98)$$

- Astigmatism factor

In an edge-emitting laser diode, the optical mode is always a guided mode in transverse, lateral and longitudinal directions. K. Petermann was the first to show that depending on the type of guiding, an additional enhancement factor K_P had to be taken into account in the case of gain-guided laser diodes, where the transverse phase-front is strongly curved [Petermann 1979]. Physically, it means that the spontaneous emission is enhanced by increased coupling and amplification. Later, a more general form of its expression was given [Petermann 2012]:

$$K_P = \left| \frac{\iiint |E(x, y, z)|^2 dx dy dz}{\iiint E(x, y, z)^2 dx dy dz} \right|^2 \quad (2.99)$$

$$K_P = K_t K_z \quad (2.100)$$

which can be decomposed in a transverse and longitudinal terms. The transverse term takes into account the mode amplitude in the (x, y)-plane (figure (2.22)). For instance, if the far-field and near-field of the lasing mode are reduced in the transverse x direction, the corresponding K_t will be reduced. Indeed, as the spontaneous emission is radiated in all directions of the space, with a strictly planar wave-front of mode, no enhancement of recoupling is created. For the longitudinal direction,

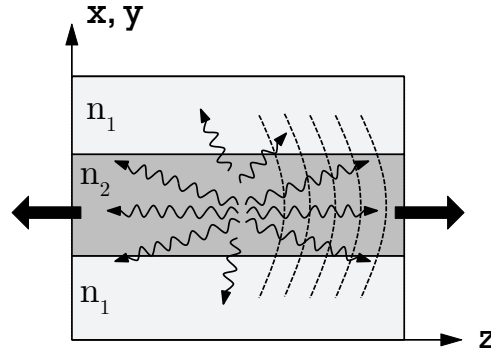


Figure 2.22: Schematic representation of the spontaneous emission recoupling and amplification in a waveguide of an edge-emitting laser diode

[Henry 1986] shows that in the case of a Fabry-Perot cavity, for $R_1 = R_2 = 0.3$, $K_z = 1.13$. For a DFB laser with distributed mirrors along the cavity, [Wang 1987] showed that $K_z \approx 2$ for a conventional DFB laser with no facet reflection and a normalized *coupling coefficient* of ~ 2 .

Another more explicit form of the spontaneous rate can be used instead of (2.96), depending directly on the carrier density:

$$R_{\text{spont}} = \Gamma \beta_m B n p \quad (2.101)$$

The β_m is the so-called *spontaneous emission factor into the lasing mode m*. It is a useful form to use in rate equations of the semiconductor laser which tells that only a fraction β_m of the total spontaneous emission goes to the perturbation of the linewidth of the mode m of interest. However, its theoretical evaluation is complicated and barely reliable, and it is practically used as a fitting parameter of the electro-optics characteristics. With such simple procedure, it can be assessed whether a change in the conception of mode guiding in the laser decreases the overall coupling of spontaneous emission.

To sum up, taking into account all the correcting factors for the Schawlow-Townes linewidth, the following form is useful to remember, both for the sake of the clarity of the physical meaning and its practical use in laser physics:

$$\Delta\nu_{S-T-H} = \frac{\pi h \nu (\Delta\nu_c)^2}{P_{\text{out}}} \xi (1 + \alpha_H^2) \quad (2.102)$$

$$\xi = K P n_{\text{sp}} \quad (2.103)$$

Again, it works as (2.36) in the regime of low internal losses compared to the power radiated outside the cavity. It can be derived from (2.98) for instance by considering the threshold condition: $g = \alpha_m + \alpha_i$, so $\alpha_m g \approx (\alpha_m + \alpha_i)^2$ when $\alpha_i \ll \alpha_m$ and the cold cavity linewidth is recovered (remember (2.27)). To go further, we should await a maximum total enhancement factor of the semiconductor laser linewidth of $\xi(1 + \alpha_H^2) \sim 4 \times 10 = 40$. Those factors will be evaluated more precisely in chapter 3 and chapter 5 for the real lasers.

2.2.2.3 Non-linear behavior of the linewidth

Above threshold, the gain is clamped and the S-T-H linewidth is proportional to $1/P_{out}$. In a real component this ideal regime holds only in the vicinity of the threshold at low power. At high power, several non-linear phenomenons can occur. As an example, the spatial-hole burning of section [2.1.6] in the longitudinal direction of the cavity will modify locally the gain profile:

$$g(z) = \frac{g}{1 + \varepsilon_s s(z)} \quad (2.104)$$

where $\varepsilon_s \sim 2 \times 10^{17} \text{ cm}^3$ is the coefficient of gain saturation by the photon density $s(z)$. As said above, any change of gain induces a corresponding change in the refractive index (equation (2.93)) so the linewidth will experience an enhancement factor just like in Henry's theory. In [Girardin 1996], the authors add another mechanism to spatial hole burning in DFB lasers which is called *carrier heating* and originates from the local change of temperature T instead of the photon density s . They express the linewidth as follow:

$$\Delta\nu_{S-T-H}^{NL} = \frac{R_{spon}}{4\pi I} \left(1 + (\alpha_{eff}^{dfb})^2 \right) \quad (2.105)$$

The effective enhancement factor is shown to rapidly increase at a certain level of output power. Even worse linewidth broadening can take place when the laser shows multimode dynamic: then several modes are competing on an equal foot, exchanging gain between their reservoirs of carriers (*partition noise*). The spontaneous emission is not clamped anymore, and deviation from the linear case are unavoidable [Petermann 2012].

An other important case of deviation from the Schawlow-Townes formula is the presence of *technical noise* in the laser diode. This term recovers all types of fluctuations (modulation) of the grounding parameters of the laser: length of the cavity, pumping conditions, external acoustical or thermal perturbations that induce fluctuations of the local refractive index... For instance, the $1/f$ or *flicker noise* which is present in all semiconductors electrically pumped, gives a contribution to the linewidth that is not power dependent (see chapter 5).

The graph (2.23) summaries the linewidth behavior commonly encountered in edge-emitting single mode laser diodes.

2.2.3 Electrical nature of the diode laser

A simple mean to create a high density of electrons and holes available for optical recombination is to build a *P-I-N junction* where the undoped active zone is sandwiched between N-doped and P-doped barriers of semiconductor as in figure (2.15). At equilibrium, the Fermi levels are equal throughout the structure and the electrons and holes do not have enough energy to cross the built-in potential that arise between the P-side and the N-side (figure (2.24)).

When a *forward bias is applied*, quasi-Fermi levels separate away, the potentials seen by the carriers on each side are smoothed so that they can reach the undoped area, where they are likely to recombine, leading the condition (2.75) to be fulfilled. Barriers on the minority carrier side after the active region will prevent the particles to escape this (forced) recombination process. This is only to some extent as the height of potential is finite so that a potential of *carrier leakage* (mainly of electrons) ΔE_{leak} exists. The relations between the injected current in the diode, the local potential and the densities of electrons and holes can be found thanks to the following coupled equations, derived

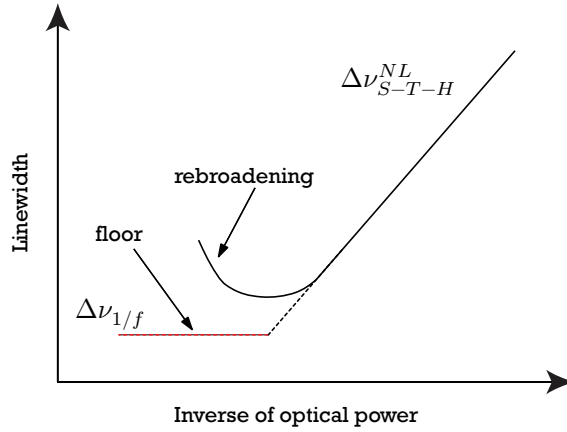


Figure 2.23: Linewidth as a function of the inverse of the optical power. In the general case, it does not follow a proportionality law at high-power.

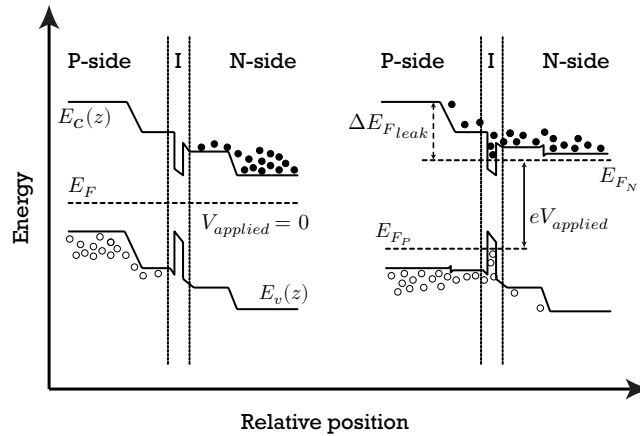


Figure 2.24: On the left: P-I-N junction at zero-bias. Electrons and holes are maintained in their respective majority carrier regions. The intrinsic zone has *space-charges*. On the right: P-I-N junction in forward bias. The barriers of potential are lowered on both sides and carriers diffuse into the active region where they can recombine.

from Boltzmann's transport equation, under the assumption of a non-magnetic medium:

$$\frac{\partial n}{\partial t} = \frac{1}{e} \nabla \cdot \vec{J}_n + (G_n - R_n) \quad (2.106)$$

$$\frac{\partial p}{\partial t} = \frac{1}{e} \nabla \cdot \vec{J}_p + (G_p - R_p) \quad (2.107)$$

$$\vec{J}_n = e\mu_n(\vec{E})n\vec{E} + eD_n\nabla n \quad (2.108)$$

$$\vec{J}_p = e\mu_p(\vec{E})p\vec{E} + eD_p\nabla p \quad (2.109)$$

$$\vec{E} = -\nabla V \quad (2.110)$$

$$\nabla \cdot \vec{E} = \frac{\rho}{\varepsilon}, \quad \rho = e(p - n + N_d - N_a) \quad (2.111)$$

$$\nabla \cdot \left(\vec{J}_p + \vec{J}_n + \varepsilon \frac{\partial \vec{E}}{\partial t} \right) = 0 \quad (2.112)$$

Where ∇ is the *nabla* operator, G and R are respectively the generation and recombination rates (G-R) of carriers, \vec{J} is the density current vector, D the diffusion constant, μ the electrical mobility that is generally a function of the electric field and doping N_a and N_d , V the electric potential and ρ the total local charge. Equations (2.106) are the *continuity equations* (conservation of the total charge), (2.108) the sum of the phenomenological laws of Joule and Fick and (2.110) the Maxwell-Poisson equations. All the five independent variables \vec{J}_n , \vec{J}_p , V , n and p are functions of the position \vec{r} and time t . The stationary continuity condition can be written in a simplified form using the flux-divergence theorem for a z -dependent current only, directed in the z direction:

$$\frac{1}{e} \frac{dJ_{tot}}{dz} = R_{tot}(n, p) \quad (2.113)$$

with the total density of current $J = J_n + J_p$ and the sum of the all the rates of change R_{tot} . In the particular case of the homogeneous undoped quantum-well of length d , the relation is just $J = edR_{tot}(n)$. The main mechanisms of G-R below the laser threshold are the following [Rosencher 2002]:

- Spontaneous emission recombination

It is the mechanism described by (2.76) which allows optical recombinations of an electron and a hole for direct band-gap semiconductors:

$$R_{spon} = Bn^2 = \frac{n}{\tau_{rad}} \quad (2.114)$$

- Non-radiative recombinations

Defect and impurities in the crystal lattice can act as *traps* of electrons or holes, especially when they are located in the middle of the gap of the optical transition. The Shockley-Read-Hall mechanism states that for high densities of carriers, the recombination is:

$$R_{nr} = An = \frac{n}{\tau_{nr}} A = \frac{n}{\tau_e + \tau_h} \quad (2.115)$$

Where τ_e and τ_h are the electrons and holes trapping constants. They values range between 0.1 to 10 *ns* depending on the density of traps in the matrix.

Another mechanism called the Auger recombination involves the collision of particles within the conduction band and the valence band. The form for the rate is:

$$R_{Auger} = Cn^3 \quad (2.116)$$

In materials with transitions below 1 μm , this rate is negligible compared to the two others and will not be taken into account.

If the current that feeds radiative recombination mechanisms from the active zone is separated from the total current injected in the diode, an *internal (or injection) quantum efficiency* η_i can be defined (after the definition of [Coldren 2012]):

$$\eta_i = \frac{\tau_{rad}^{QW} + \tau_{nr}^{QW}}{\tau_{rad}^{tot} + \tau_{nr}^{tot}} \quad (2.117)$$

Aside from the possible radiative and non-radiative recombinations in the barriers of the heterostructure, leakage through the active zone (carriers escape the quantum-well) should also be taken into account. The internal-quantum efficiency is generally temperature-dependent in addition to the carrier density: $\eta_i = \eta_i(n, T)$. The relation between the current in the structure and the local density of carriers in the quantum-well is explicit and the total current can be written as a polynomial of degree two in n :

$$J_{QW} = ed(An_{QW} + Bn_{QW}^2) \quad (2.118)$$

$$J_{tot} \sim a + bn + cn^2 \quad (2.119)$$

Practically, the *EsakiHTD* model solves the above problem in 1D: for small initial increments of the bias V , it finds the solution $(V, n, p, J_n, J_p)(z)$ given the rates of recombination $R_{spn}(z)$ and $R_{nr}(z)$ specified in each layer of the junction. Thanks to relations (2.63), Fermi levels are computed as a function of z . The quantum-well itself is treated as a simple point of recombination given its dimensions, with a radiative rate above the transparency following (2.74) which is E_F -dependent. It should be noted that above threshold, the rate of stimulated emission is $R_{st} = v_g g(n)s$ with s the photon density.

2.2.4 Carrier and photons interplay

To complete the model of the diode laser, the photon density s must be added to the rate equations of the carrier density. A simplified non-thermal model (including only the continuity equation) for the active zone is reproduced here (2.120):

$$\begin{cases} \frac{\partial n}{\partial t} = \eta_i \frac{J}{ed} - (An + Bn^2) - v_g g(n)s \\ \frac{\partial s}{\partial t} = \Gamma v_g g(n)s - \frac{s}{\tau_c} + \beta \Gamma Bn^2 \end{cases} \quad (2.120)$$

with Γ the modal gain and τ_c the photon lifetime as in (2.27). At threshold: $\dot{n} = 0$

$$\Gamma g(n_{thr}) = \frac{1}{v_g \tau_c} = \alpha_i + \alpha_m \quad (2.121)$$

So that, from (2.87):

$$n_{thr} = n_{tr} \exp\left(\frac{\alpha_i + \alpha_m}{\Gamma g_0}\right) \quad (2.122)$$

The photon density in the steady-state above threshold is:

$$s = \eta_i \frac{J - J_{thr}}{(ed)g(n_{thr})v_g} \quad (2.123)$$

and the Light-Current characteristics (L-I) in terms of output power is (2.37):

$$P_{out} = \eta_{q,ext} \left(\frac{h\nu}{e}\right) (I - I_{thr}) \quad (2.124)$$

$$\eta_{q,ext} = \eta_i \frac{\alpha_m}{\alpha_m + \alpha_i} \quad (2.125)$$

With $I = J \times S$ the injected current on the section of surface S . The *external quantum efficiency* $\eta_{q,ext}$ accounts for the rate of photons that effectively escape the cavity. The *external efficiency* η_{ext} (in $W.A^{-1}$) can be defined as:

$$\eta_{ext} = \frac{dP_{out}}{dI} \quad (2.126)$$

It is a function of the photon energy, and to some extent, of T through $\eta_i(T)$. The threshold current can be written in terms of simple experimental parameters by fitting the (n, J) and (J, g) characteristics with a log dependency:

$$J_{thr} = J_{tr} \exp\left(\frac{\alpha_i + \alpha_m}{\Gamma g_{0,J}}\right) \quad (2.127)$$

where $g_{0,J}$ is the material gain parameter with respect to current density. As the transparency $n_{tr}(T)$ depends on the temperature (it is explicit in relation (2.83)), the threshold current depends on it. Also, because the Fermi level is also depending on the temperature, carrier heating can lead to stronger leakage above the active zone. Empirical laws are used to describe such dependency:

$$J_{thr}(T') = J_{thr}(T) \exp\left(\frac{T' - T}{T_0}\right) \quad (2.128)$$

$$\eta_i(T') = \eta_i(T) \exp\left(\frac{T' - T}{T_1}\right) \quad (2.129)$$

The temperatures T_0 and T_1 characterize the resistance of the parameters to a change of temperature.

Relation with noise in the laser output

The above relations are useful to discuss about the linewidth in semiconductor lasers. In the form (2.102), it is inversely proportional to P_{out} , so from (2.124), it is inversely proportional to the pump current efficiently injected above threshold $\Delta I = \eta_i(I - I_{thr})$. However, this relation can lead to the wrong conclusion that with a higher external efficiency, the linewidth is reduced. As it depends on the losses, form (2.98) highlights that the linewidth is actually proportional to the square of the modal gain $(\Gamma g)^2$ which is the square of the total losses at threshold (which gives the cold cavity linewidth). Even if it is an approximate formulation, **it points out the true physical meaning of the laser linewidth**. Indeed, (2.98) is sometimes misleading, because **one can think that the gain g drives the spectral purity. This is wrong, it is only driven by the losses (and the coherent energy stored in the laser cavity)**.

If we think to reduce the mirror losses α_m , one might intuitively think, at first, that it will be an irreversible trade-off with a reduction of the output power available for the application: this is not true, because when the internal losses α_i is zero in the expression of the external quantum efficiency, such parameter is equal to 1, whatever the value of the mirror losses α_m . This is possible because **the laser cavity acts like a converter of the pump energy**: when the mirror losses are decreased, the density of photons in the cavity increases, but the rate of energy injected that must go out is still the same (for instance, solid-state lasers can have high external efficiency with high-reflectivity mirrors because of low internal losses). So, at a given pump current, a joint reduction of internal and mirror losses is necessary to gain on the linewidth, without degrading too much the output power available. In the meantime, with lower losses, the threshold current is reduced, so is the threshold

current, and more pump power is available at a given bias to produce photons.

Mirror losses can be decreased by longer cavity lengths L or higher mirror reflectivities R in a Fabry-Perot resonator. In a DFB laser, it is mainly with the increase of the normalized equivalent reflectivity $\kappa \times L$ where κ is the *coupling coefficient* to the grating (in cm^{-1}). It should be noticed that an increase in the length of the device is at the expense of a potential increase of the threshold current, while the density at threshold decreases. The internal losses are mainly *free-carrier absorption* arising from the dopants: their contribution will be evaluated in the next chapter. Also, there are propagation losses, such as diffraction losses for the grating of the DFB.

Paradoxically, a lower threshold means that the laser operates closer to the transparency, so that n_{sp} increases. From (2.83) and (2.63), it was clear that either an increase of carrier densities in the bands (higher electrical pumping) or a reduction of the effective densities of states in the bands would increase ΔE_F and decrease n_{sp} . The later condition can be helped by the use of strained quantum-wells that induce the desired reduction of effective masses in the bands. The indirect advantage of that is to decrease the spontaneous emission enhancement factor.

The writing of the system (2.120) is useful to highlight the central place of the pump source $\eta_i J/e$ in the equation of carrier density. Above threshold, the stimulated emission rate $v_g g(n)s$ sets a negative feedback on the carrier density which is clamped. Meanwhile, the photon density s is not clamped. If the source J is modulated in time, either intentionality or because of external or internal fluctuations before it reaches the active zone, it will imprint the corresponding pattern on the fluctuation of laser's frequency, via the coupling of s , n and other parameters like the local temperature. The standard approach to deal with stochastic fluctuations around the equilibrium of the system is to introduce *Langevin noise sources* $F_X(t)$ which is a mean to reintroduce the random nature of the microscopic processes described by quantum mechanics in the classical rate equations [Henry 1982, Turrenc 2005]. It turns out that the diode laser can be treated as an equivalent electrical circuit [Daulasim 1994, Signoret 1995], a model that enables to take into account the electrical nature of the pump. This will be studied further in chapter 4 on electrical noise.

2.2.5 Single-mode lasers at III-V Lab

Historically, within the industrial laboratory, the development of single-mode sources emitting between 780 nm and 1080 nm for pumping applications is based on monolithic electrically-pumped edge emitting lasers, integrating a buried Bragg grating on the overall length of the cavity (Distributed-Feedback laser: DFB) or not (Fabry-Perot type). The goal of the DFB cavity is to select a specific longitudinal mode by increasing deeply the losses between this mode and the first other adjacent modes (figure (2.25)).

In practice, the development of the current source at 894 nm will be grounded on previous results regarding the design and fabrication of high-power lasers at the D_2 line 852 nm for Cs atomic cooling application (among others), following a project founded by the National Center for Spatial Studies (CNES). It was demonstrated the potential for high-power ($> 100 mW$) single-mode emission, with reliability in time of the chip [Vermersch 2005, Ligeret 2008], using heterostructures with Aluminum-free materials in the region of the active zone. We discuss here briefly what are the main choices behind such designs.

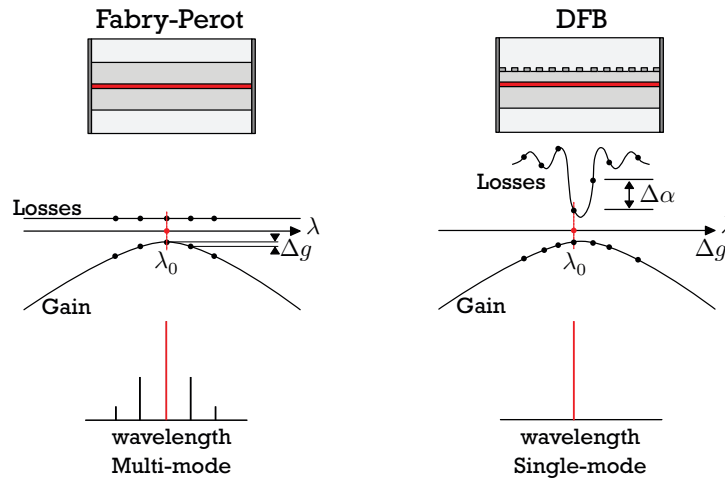


Figure 2.25: Illustration of the mode selection in Fabry-Perot lasers (left) and DFB cavities (right). For the second, the grating feedback effect ensures (if well designed) a high loss margin $\Delta\alpha$ between the two modes of lowest losses. It yields in practice to a longitudinal single-mode behavior above threshold with a high SMSR. Adapted from [Buus 2005]

2.2.5.1 Main practical parameters for the linewidth reduction

In practice, linewidth reduction is increased with the cavity length, the values of the facet reflectivities and the coupling factor κ of grating as discussed above. The later is determined by the geometry of the corrugation and its localization in the optical cavity. Usually, the normalized coupling coefficient κL is taken close to 1, values targeted in the previous development of DFBs for atomic cooling, with lengths of devices between 1 and 2.5 mm. Such choice is not the optimum for high-power applications: excellent results have been demonstrated with vanishing coupling coefficients on 780 nm DFBs for rubidium pumping (κ close to 1 cm^{-1} , in contrast to a value of 5 cm^{-1} for the same length of 2 mm) [Nguyen 2010]. Small coupling coefficients are justified to increase the cavity length without increasing too much the equivalent reflectivity that can lead to strong inhomogeneities of optical power in the laser, leading further to earlier spatial hole burning effects and linewidth rebroadening. Also, diffractions losses in second-order gratings, as the one used for near infrared wavelength, may be increased with higher coupling strength. Concerning the values of the reflectivities at the facets, the high-reflectivity one being commonly 95% (higher values can be reached with an expense of technical difficulties), the front low-reflectivity facet can be optimized with a trade-off of linewidth reduction vs. single-mode stability. A systematic study of [Nguyen 2010] comes to the conclusion that for the low coupling case, an optimal value at the front facet is close to 5% for efficient linewidth reduction. In our case, there may be an interest of keeping a high coupling factor and low reflectivity at the front facet, given the low power required for the final application.

An increase in the mirror losses should be followed by an optimization of internal losses, namely the previous diffraction losses plus the *free-carrier* losses, proportional to the level of doping in the optical cavity. The absorption coefficient of the p-type semiconductor being roughly two-times higher than for the n-type, the vertical design of the layers should optimally limit the overlap of the optical mode on the p-side.

2.2.5.2 Choice of heterostructure materials

This topic will not be much discussed. The choice of a GaInAsP quantum-well with GaInP barriers forming the *Large Optical Cavity* (LOC) where most of the optical power is located and AlGaInP surrounding cladding layers has been historically based on publications showing the resistance of such active zone to Catastrophic Optical Mirror Damages (COMD) for emission at 808 *nm* and the benefits of Indium in the active zone to prevent dark lines [100] growth with aging [Yi 1995, Wade 1998]. Though, most of the structures in the near-infrared range elsewhere are based on the AlGaAs/GaAs/InGaAs system, which is very-well mastered and has proved its robustness [Wenzel 2004, Klehr 2007], unlike the AlGaInP alloys, which are difficult to dope with high concentration of impurities in thick layers during the phase of material epitaxy. Also, ramps of dopants concentration are difficult to stabilize, preventing smooth GRINSCH heterostructures to be implemented. The literature also highlights the fact that such alloy has poor mobility and thermal resistance [Martin 1992]. However, the sturdiness of the solution employed for the D_2 line emission contrasts with the previous remarks. Moreover, the targeted performances for the D_1 line are not related to the usual issues of high-power lasers. The use of such a system of alloys will ask to reverse the core/cladding mode localization if one wants to improve the vertical beam quality of the device (see Super-LOC section).

2.2.5.3 Grating technology

The grating in the DFB structure itself consists in a periodic pattern of corrugation of characteristic size 100 *nm*. One of the major change to take into account in the fabrication process that occurred between the results previously mentioned and that of the lasers of the LAMA project is the way the laser is fabricated. Indeed, such structure cannot be realized with standard *photolithography techniques* that imprint the chosen pattern in a *photoresist* with *masks* illuminated with *UV* light. The wavelength at around 450 *nm* limits the definition of the features to the same scale. Before, a widespread technique called *holographic grating* definition was used to shape the photoresist with a sinusoidal profile thanks to the interference of a laser beam in the near-*UV* and the distance between two fringes could be adjusted with the angles formed by the beams. Although the definition is instantaneous and very uniform on a large surface, the shape and the distance between the corrugations could not be varied on small area of the same wafer. Instead, III-V Lab is using *electron-beam lithography* (e-beam) which consists in writing the desired pattern directly in the photoresist with a focused beam of electrons of high resolution (spot size of around 8 *nm*). The technique is very versatile, allowing virtually any pattern to be defined on scales as large as 2 and 3 inches wafers. Meanwhile, the conception and process of the grating is completely redefined. The redefinition of such a parameter is critical, especially because the grating properties are directly linked to the mirror and scattering losses entering the Schawlow-Townes linewidth. As mentioned in chapter 1, the corrugation can be either located within the heterostructure (*buried* grating), or outside, on the top or on the flanks of the lateral waveguide (figure (2.26))

If the corrugation is buried, as it is usually done, the process needs to first grow the layers from the buffer to the grating layer (called '1st epitaxy'), then to define and etch the corrugation, followed by a *regrowth* of material to complete the structure up to the top contact. Both *nm* definition, etching and regrowth are critical steps that need complex and expensive technologies, and is above all time-consuming. Furthermore, the grating zone must be made of Aluminum-free materials, falling that a quick oxidation occurs in oxygen rich environments, preventing any regrowth of material. This is why we use a sequence of GaInP-GaInAsP-GaInP in the grating to avoid the previous drawback. In contrast, increasing attention is devoted to alternative solutions like external gratings etched directly in the top contact [Telkkälä 2010]. Moreover, by using higher-order gratings, the size of the corrugation



Figure 2.26: (a) Buried Bragg grating (darkest gray pattern). (b) Surface Bragg grating etched directly at the top of the cavity.

is made bigger, allowing standard photolithography to be used, reducing drastically the cost of the overall process. All in all, such developments need to switch from the buried proven technology, that has showed very low losses and high-performances, to a very different concept requiring careful optical studies, new etching processes... If the future of cheap monolithic single-mode lasers may certainly go in that direction, for the time being, the small series and performances asked for the compact OCFS application make that paradigm not urgent. It was also not the objective of this work.

2.2.5.4 Conclusion

On the overall, the whole process of fabrication of the device, from the very start of the initial epitaxy of the heterostructure, has been completely revamped. In those modifications, we sought reproducibility and consistency of the results of one chip to another, that is, homogeneity in the process, to increase strongly the yield of fabrication of lasers with the required performances for the application, that was limited before. This is also the meaning of the LAMA project: building a complete chain of fabrication, characterization and packaging of the laser that makes it compatible with the production of small series of lasers for a direct use in the OCFS. In this new approach, some choices have been made, other parameters that could have been improved have been let so. Instead of looking for the single performance, the re-engineerings were targeted on the critical points that directly serves the laser module performances in the system.

2.3 *Summary*

Throughout this introduction to the design of the source, we tried to highlight which governing phenomena of the laser diode act on the frequency noise of the device. **The first component of the frequency broadening is related to the quantum 'photon noise', expressed by the modified Schawlow-Townes-Henry linewidth:** it is directly linked to the square of the **optical losses** in the cavity (concept of cold-cavity linewidth), multiplied by enhancement factors, and inversely proportional to the pump current that feeds the radiative transitions in the active zone, or, equivalently, the total coherent energy stored in the cavity. Additional correcting factors, one taking into account the properties of the gain medium (Henry's factor), and one taking into account the coupling of the spontaneous emission source term to the output power, do not vary so much in 2D-quantum wells with a broad index-guiding waveguide. The other component of the noise, **intimately linked to the electronic nature of the diode**, states how much perturbation on the field is induced by the pump current transport across the junction. As for the other performances, the basis of the previous development of the 852 *nm* sources will be used, with the required modifications accounting for the change of the process of fabrication of the lasers. Such task will be assumed through the '1st run' of fabrication, which will confront the theory to the reality, before a second run will target what is required to make a good module for the Optical Cesium Frequency Standard application.

Bibliography

- [Adachi 2009] Sadao Adachi. Properties of semiconductor alloys: group-iv, iii-v and ii-vi semiconductors, volume 28. John Wiley & Sons, 2009.
- [Balle 1998] Salvador Balle. *Simple analytical approximations for the gain and refractive index spectra in quantum-well lasers*. Physical Review A, vol. 57, no. 2, page 1304, 1998.
- [Bennett 1990] Brian R Bennett, Richard A Soref et Jesus A Del Alamo. *Carrier-induced change in refractive index of InP, GaAs and InGaAsP*. IEEE Journal of Quantum Electronics, vol. 26, no. 1, pages 113–122, 1990.
- [Buus 2005] Jens Buus, Markus-Christian Amann et Daniel J Blumenthal. Tunable laser diodes and related optical sources. Wiley-Interscience New York, 2005.
- [Coldren 2012] Larry A Coldren, Scott W Corzine et Milan L Mashanovitch. Diode lasers and photonic integrated circuits, volume 218. John Wiley & Sons, 2012.
- [Daulasim 1994] Khamphanh Daulasim. *Caractérisation et modélisation des bruits blancs et en $1/F$ des diodes lasers à semiconducteur*. PhD thesis, Université Montpellier II, 1994.
- [Dingle 1974] Raymond Dingle, William Wiegmann et Charles H Henry. *Quantum states of confined carriers in very thin $Al_x Ga_{1-x} As-GaAs-Al_x Ga_{1-x} As$ heterostructures*. Physical Review Letters, vol. 33, no. 14, page 827, 1974.
- [Einstein 1917] Albert Einstein. *Zur quantentheorie der strahlung*. Physikalische Zeitschrift, vol. 18, 1917.
- [Esaki 1970] Leo Esaki et Ray Tsu. *Superlattice and negative differential conductivity in semiconductors*. I B M J RES DEVELOP, vol. 14, no. 1, pages 61–65, 1970.
- [Fily 1998] Arnaud Fily. *Modèles pour Diodes Laser de Puissance*. PhD thesis, 1998.
- [Girardin 1996] F Girardin, Guang-Hua Duan et P Gallion. *Linewidth rebroadening due to nonlinear gain and index induced by carrier heating in strained quantum-well lasers*. IEEE Photonics Technology Letters, vol. 8, no. 3, pages 334–336, 1996.
- [Gordon 1954] James P Gordon, Herbert J Zeiger et Charles H Townes. *Molecular Microwave Oscillator and New Hyperfine Structure in the Microwave Spectrum of NH_3* . Physical Review, vol. 95, no. 1, page 282, 1954.
- [Gordon 1955] James P Gordon, Herbert J Zeiger et Charles H Townes. *The maser—new type of microwave amplifier, frequency standard, and spectrometer*. Physical Review, vol. 99, no. 4, page 1264, 1955.
- [Grillot 2008] Frédéric Grillot, Béatrice Dagens, Jean-Guy Provost, Hui Su et Luke F Lester. *Gain compression and above-threshold linewidth enhancement factor in $1.3\text{-}\mu\text{m}$ -gaas quantum-dot lasers*. IEEE Journal of Quantum Electronics, vol. 44, no. 10, pages 946–951, 2008.
- [Hakki 1975] Basil W Hakki et Thomas L Paoli. *Gain spectra in GaAs double-heterostructure injection lasers*. Journal of Applied Physics, vol. 46, no. 3, pages 1299–1306, 1975.
- [Hall 1962] Robert N Hall, Gunther E Fenner, JD Kingsley, TJ Soltys et RO Carlson. *Coherent light emission from GaAs junctions*. Physical Review Letters, vol. 9, no. 9, page 366, 1962.

- [Henry 1982] Charles Henry. *Theory of the linewidth of semiconductor lasers*. IEEE Journal of Quantum Electronics, vol. 18, no. 2, pages 259–264, 1982.
- [Henry 1986] C Henry. *Phase noise in semiconductor lasers*. Journal of Lightwave Technology, vol. 4, no. 3, pages 298–311, 1986.
- [Holonyak Jr 1962] Nick Holonyak Jr et SF Bevacqua. *Coherent (visible) light emission from Ga (As_{1-x}P_x) junctions*. Applied Physics Letters, vol. 1, no. 4, pages 82–83, 1962.
- [Hutchings 1992] D Crichton Hutchings, M Sheik-Bahae, David J Hagan et Eric W Van Stryland. *Kramers-Krönig relations in nonlinear optics*. Optical and Quantum Electronics, vol. 24, no. 1, pages 1–30, 1992.
- [Kikuchi 1985] K Kikuchi et T Okoshi. *Estimation of linewidth enhancement factor of AlGaAs lasers by correlation measurement between FM and AM noises*. Rapport technique, Department of Electronic Engineering, University of Tokyo, Bunkyo-ku, Tokyo, 1985.
- [Kittel 1966] Charles Kittel. *Introduction to solid state physics*. John Wiley and Sons, 1966.
- [Klehr 2007] A Klehr, H Wenzel, O Brox, F Bugge, G Erbert, TP Nguyen et G Tränkle. *High-power 894 nm monolithic distributed-feedback laser*. Optics express, vol. 15, no. 18, pages 11364–11369, 2007.
- [Laurain 2010] Alexandre Laurain. *Sources laser à semiconducteur à émission verticale de haute cohérence et de forte puissance dans le proche et le moyen infrarouge*. PhD thesis, Université Montpellier II-Sciences et Techniques du Languedoc, 2010.
- [Lax 1967] Melvin Lax. *Classical noise. V. Noise in self-sustained oscillators*. Physical Review, vol. 160, no. 2, page 290, 1967.
- [Ligeret 2008] V Ligeret, S Bansropun, M Lecomte, M Calligaro, O Parillaud, D Holleville, N Dimarcq, N Michel et M Krakowski. *Narrow linewidth and demonstration of saturation spectra of the Cesium at 852 nm with high power Al-free DFB laser diodes*. In Integrated Optoelectronic Devices 2008, pages 69091F–69091F. International Society for Optics and Photonics, 2008.
- [Loudon 2000] Rodney Loudon. *The quantum theory of light*. OUP Oxford, 2000.
- [Lucarini 2005] Valerio Lucarini, Jarkko J Saarinen, Kai-Erik Peiponen et Erik M Vartiainen. *Kramers-kronig relations in optical materials research*, volume 110. Springer Science & Business Media, 2005.
- [Maiman 1960] Theodore H Maiman. *Stimulated optical radiation in ruby*. 1960.
- [Martin 1992] Olivier JF Martin, G-L Bona et Peter Wolf. *Thermal behavior of visible AlGaInP-GaInP ridge laser diodes*. IEEE journal of quantum electronics, vol. 28, no. 11, pages 2582–2588, 1992.
- [Nguyen 2010] Phong Thanh Nguyen. *Investigation of spectral characteristics of solitary diode lasers with integrated grating resonator*. PhD thesis, Technischen Universität Berlin, Fakultät IV - Elektrotechnik and Informatik, 2010.
- [Panish 1970] MB Panish, I Hayashi et S Sumski. *Double-heterostructure injection lasers with room-temperature thresholds as low as 2300 A/cm²*. Applied Physics Letters, vol. 16, no. 8, pages 326–327, 1970.

- [Peter 2010] YU Peter et Manuel Cardona. *Fundamentals of semiconductors: physics and materials properties*. Springer Science & Business Media, 2010.
- [Petermann 1979] Klaus Petermann. *Calculated spontaneous emission factor for double-heterostructure injection lasers with gain-induced waveguiding*. *IEEE Journal of Quantum Electronics*, vol. 15, no. 7, pages 566–570, 1979.
- [Petermann 2012] Klaus Petermann. *Laser diode modulation and noise, volume 3*. Springer Science & Business Media, 2012.
- [Planck 1901] Max Planck. *Über das Gesetz der Energieverteilung im Normalspectrum*. *Annalen der Physik*, vol. 309, no. 3, pages 553–563, 1901.
- [Provost 2011] Jean-Guy Provost et Frederic Grillot. *Measuring the chirp and the linewidth enhancement factor of optoelectronic devices with a Mach-Zehnder interferometer*. *IEEE Photonics Journal*, vol. 3, no. 3, pages 476–488, 2011.
- [Rosencher 2002] Emmanuel Rosencher et Borge Vinter. *Optoelectronics*. Cambridge University Press, 2002.
- [Schawlow 1958] Arthur L Schawlow et Charles H Townes. *Infrared and optical masers*. *Physical Review*, vol. 112, no. 6, page 1940, 1958.
- [Siegman 1986] Anthony E Siegman. *Lasers*. University Science Books, Mill Valley, CA, 1986.
- [Signoret 1995] Philippe Signoret, Bernard P. Orsal, Jean-Marie Peransin et Robert M. Alabedra. *Analysis of white optical and electrical noises of a DFB laser with optical feedback*. *Proc. SPIE*, vol. 2382, pages 187–199, 1995.
- [Tannoudji 1973] Cohen Claude Tannoudji, Diu Bernard et Laloë Franck. *Quantum mechanics. volume i*. Hermann, 1973.
- [Telkkälä 2010] Jarkko Telkkälä, Jukka Viheriälä, Antti Laakso, Kari Leinonen, Jari Lyytikäinen, Jukka Karinen, Mihail Dumitrescu et Markus Pessa. *Distributed feedback laser diodes emitting at 894 nm suitable for atomic clock applications fabricated using nanoimprint lithography*. In *Conference on Lasers and Electro-Optics*, page JTuD102. Optical Society of America, 2010.
- [Tourrenc 2005] Jean-Philippe Tourrenc. *Caractérisation et modélisation du bruit d’amplitude optique, du bruit de fréquence et de la largeur de raie de VCSELs monomodes émettant autour de 850 nm*. PhD thesis, Montpellier 2, 2005.
- [Vegard 1921] Lars Vegard. *Die konstitution der mischkristalle und die raumfüllung der atome*. *Zeitschrift für Physik A Hadrons and Nuclei*, vol. 5, no. 1, pages 17–26, 1921.
- [Vermersch 2005] F.-J. Vermersch. *Etude*. PhD thesis, Université Paris-Sud XI, 2005.
- [Wade 1998] JK Wade et JA Morris. *8.8 W CW power from broad-waveguide AI-free active-region ($3L = 805\text{nm}$) diode lasers*. 1998.
- [Wang 1987] J Wang, N Schunk et K Petermann. *Linewidth enhancement for DFB lasers due to longitudinal field dependence in the laser cavity*. *Electronics Letters*, vol. 14, no. 23, pages 715–717, 1987.

-
- [Weisbuch 2014] Claude Weisbuch et Borge Vinter. Quantum semiconductor structures: Fundamentals and applications. Academic press, 2014.
- [Wenzel 2004] H Wenzel, A Klehr, M Braun, F Bugge, G Erbert, J Fricke, A Knauer, P Ressel, B Sumpf, M Weyers *et al.* *Design and realization of high-power DFB lasers*. In Optics East, pages 110–123. International Society for Optics and Photonics, 2004.
- [Yi 1995] HJ Yi, J Diaz, LJ Wang, I Eliashevich, S Kim, R Williams, M Erdtmann, X He, E Kolev et M Razeghi. *Optimized structure for InGaAsP/GaAs 808 nm high power lasers*. Applied physics letters, vol. 66, no. 24, pages 3251–3253, 1995.

Practical conception

3.1 Laser conception

The aim of this first section is to address the theoretical conception of a single-mode semiconductor (in-plane) diode laser, both on the electrical and optical points of view.

3.1.1 Introduction

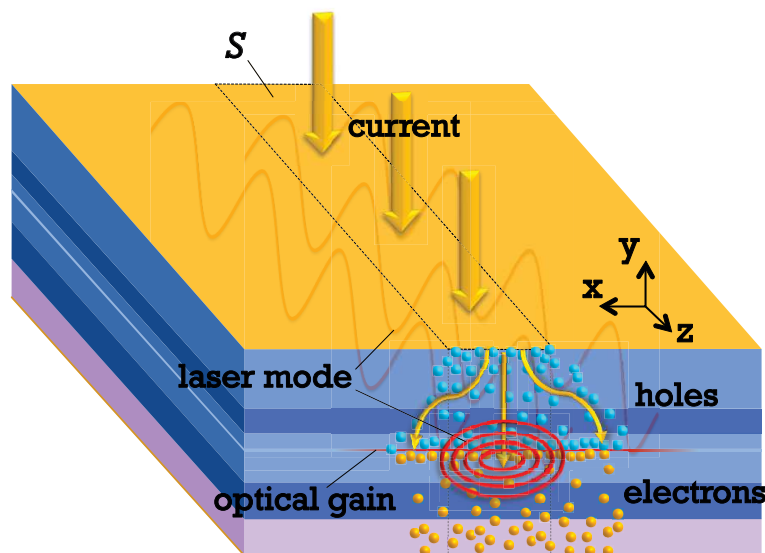


Figure 3.1: 3D representation of a Fabry-Perot type semiconductor laser diode. The current is injected perpendicularly to the epitaxial layers (y -direction) through a surface S . Electrons and holes recombine mainly in the quantum well at the P-N junction to generate optical gain. At laser threshold, a standing wave is generated between the two longitudinal semiconductor mirror facets (z -direction) but the modes have also a lateral extension (x -direction)

This section on the laser practical conception will address the design of the heterojunction itself. The electrical injection of the gain medium and the transport of the carriers to the active zone are made easier by the use of dopants in the barriers of the heterostructure. The electronic confinement is ensured by the height of the barriers, down to the well where most of the optical recombinations occur. However, concentrations of impurities are one of the main source of optical losses (and of the series resistance of the device), and barriers heights are related to the real refractive index, which profile defines the guiding and the optical mode overlap on the layers. This is why, in a separate confinement heterostructure, optimization must usually be carried out on both aspects at the same time.

Though, some degrees of freedom in the conception remain within each domain, so that the vertical structure can be modified with relation to optical considerations, in both transverse, longitudinal and vertical directions without affecting too much carriers transport. Thus, we will

present first the vertical structures inherited from the previous design at the D_2 line, then study the optical confinement of light in the cavity to design new structures with more interesting properties. Then, the fabrication process will be reviewed for the single-mode DFB lasers, as well as the new packaging approach in TO3. Preliminary 'broad-area' laser results will enable to confirm experimentally the predictions of the *EsakiHTD* model. Finally, a first-order characterization of the 1st run of fabrication will give hints for the optimizations to implement on the 2nd run.

Before that, we should underline what are the main design considerations under such laser design. The first point is to achieve optical gain thanks to the electrical injection of a semiconductor medium which allows a high density of optical recombinations of electrons and holes in the quantum well, as described in the previous chapter. Second, the medium must be a valid optical resonator (a very simple one being the Fabry-Perot cavity) to allow a stable standing wave at laser threshold. This situation is depicted in figure (3.1). Finally, the optical mode of interest for the application must have sufficient overlap with the active zone to be amplified. For the first two points, an effective design implies:

- To achieve the electrical confinement perpendicularly to the layers in y (see section [3.1.2]) but also in the lateral direction x ([3.1.3.2]). Indeed, the electrical bias over the top contact of surface S does not guaranty that the carriers will be injected strictly over this area in the active zone.
- To achieve the optical confinement in the three spatial directions x , y and z to obtain a **single-mode** behavior in laser operation. The semiconductor medium cannot, for technological reasons, be processed to create arbitrary shapes of monolithic cavities. Usually, it is used as rectangular bars that are cleaved along the crystal natural axis. But as indicated in section [2.1.6], two plan mirrors cannot realize a stable resonator for the Hermite-Gauss modes. This is why optical **waveguides** are used instead to achieve mode confinement, in the (x,y) plane for instance, over the μm distance (transverse electric or transverse magnetic modes in the case of a rectangular guide, see section [3.1.3.2]). Vertically, the heterojunction structure creates a 'natural' guide through the refractive index change with the material of the layers. Hence, delicate considerations are often required to modify the vertical optical properties without affecting too much the electrical ones. In the lateral direction, the material homogeneity requires to induce an (real) index change, if one is to create *index guiding*. In the longitudinal direction, the characteristic length being way greater than the wavelength, optical **filters** can be used to select a mode against the many others (section [3.1.3.3]).

Regarding now the third point, it is essential to highlight that two strategies allow to achieve single-mode laser operation above threshold:

1. Make the design such that **modal competition occurs and a single threshold is reached**, that is, only the threshold of the optical mode of interest is reached over the total power range of operation of the laser. This is a stringent condition requiring that the ratio of the total mode losses to the modal gain $\alpha_{tot}/\Gamma g$ for the mode of interest must be the highest for the selected mode (remember (2.127)). If the condition is to be satisfied in the three spatial directions, it is more or less simple to implement in practice: when the **gain is localized** (for instance in the well in y) one can try to play with the waveguide geometry to increase the gain/decrease the absorption losses on the mode of interest, even if several other modes can exist otherwise in the waveguide. In the lateral x direction, the **gain is not localized**: carrier spreading implies a difficult control over the area of amplification so that an **intrinsic single-mode real refractive index guiding** is preferred.

2. Make the design in an **intrinsic multi-mode configuration with modal competition and a unique threshold is reached**. In this case, the stable single-mode behavior above threshold can be ensured, again, if the gain is localized: even if the intrinsic threshold current of another mode is reached after lasing of the fundamental one, no energy exchange or mode switching occurs, simply because **the carrier density (and thus the gain) is clamped** at the lowest threshold. If several modes with approximately the same optical gain are competing, single-mode operation can occur in some particular cases with the **help of non-linear effects** (four-waves mixing...etc). It explains, for instance, observed stable (longitudinal) operation of a Fabry-Perot laser with a cavity length way longer than the *FSR*. In some other cases, spatial gain inhomogeneity (caused for instance by carrier spreading in the structure or by spatial hole burning) induces **no modal competition so that several thresholds are reached in a multi-mode design** : in other words the modes are amplified (almost) independently by several (almost) independent carrier reservoirs. Then, it is extremely difficult to achieve a stable single-mode operation over a large range of current injection.

In our case, the first method will be used with the realization of a multi-mode vertical waveguide in y which allows however modal competition with a unique threshold, an intrinsic single-mode guiding with the shallow ridge waveguide for the transverse confinement in x, and the use of an intrinsic single-mode Bragg filter in the longitudinal direction. This is is pretty standard for the type of in-plane laser under study.

3.1.2 Heterojunction and active zone for the D_1 and D_2 lines

3.1.2.1 Structures

According to [Ligeret 2008a], the structures chosen for the 1st run of single-mode lasers are displayed in figure (3.2). These material configurations, one for each line of the cesium, comprise three main

D ₁ line: 894 nm (XXL2029)			D ₂ line: 852 nm (XXL2020)		
Layer	Alloy	Thickness (μm)	Layer	Alloy	Thickness (μm)
Contact	GaAs (P++)	0.25	Contact	GaAs (P++)	0.25
Ridge	GaN (P+)	~ 1	Ridge	GaN (P+)	~ 1
Cladding up.	AlGaInP (P+)	~ 0.5	Cladding up.	AlGaInP (P+)	~ 0.5
Planarity	GaN (P+)	~ 0.1	Planarity	GaN (P+)	~ 0.1
Interface	GaN (P+)	~ 0.1	Interface	GaN (P+)	~ 0.1
Grating core	Q(1.62) (P+)	0.035	Grating core	Q(1.62) (P+)	0.05
Interface	GaN (P+)	~ 0.1	Interface	GaN (P+)	~ 0.1
Spacer	AlGaInP (P+)	~ 0.1	Spacer	AlGaInP (P+)	~ 0.1
LOC	GaN (P)	0.45	LOC	GaN (P)	0.45
Interface	Q(1.62)	23Å	Interface	Q(1.62)	23Å
QW	GaNAsP	80Å	QW	GaNAsP	80Å
Interface	Q(1.62)	23Å	Interface	Q(1.62)	23Å
LOC	GaN (N)	0.45	LOC	GaN (N)	0.45
Cladding low.	AlGaInP (N+)	~ 1	Cladding low.	AlGaInP (N+)	~ 1
Optical barrier	GaN (N+)	~ 1	Optical barrier	GaN (N+)	~ 1
Buffer	GaAs (N++)		Buffer	GaAs (N++)	

Figure 3.2: LAMA 1st run structures for a DFB at 894 nm (XXL2029) and for a DFB at 852 nm (XXL2020)

areas:

- **Contact layers:** Made of GaAs, it is highly p-doped with Zn on the p-side (around $N_a = 10^{19} \text{ cm}^{-3}$) and highly n-doped for the buffer on the n-side with Si ($N_d = 2 \times 10^{18} \text{ cm}^{-3}$). With additional deposit of metals, it ensures that the current is correctly injected in the semiconductor with minimum *contact resistance* and no Schottky barrier

- **Optical cavity:** the 8 nm-thick quantum-well and its adaptation layers are embedded in a symmetrical $2 \times 0.45 \mu\text{m}$ -wide GaInP optical cavity, surrounded by an upper and lower cladding layer in AlGaInP(25%). The composition of the well varies, depending on the targeted wavelength, but has the same properties as described in chapter 2. The compressive strain is higher than expected for the 894 nm case (1.2% versus 1% expected) and is in line with what has been done before at 852 nm. The level of doping in each layer cannot be precisely indicated, however, it is on the order of $N_a = 10^{17} \text{ cm}^{-3}$ on the p-side, and $N_d = 2 \times 10^{17} \text{ cm}^{-3}$ on the n-side
- **Grating layers:** A sequence of GaInP/GaInAsP(1.62 eV)/GaInP (regrown) defines a waveguide where a corrugation can be processed

The wells are tuned in composition to target a photoluminescence of respectively $\lambda_{PL_1} = 884 \text{ nm}$ and $\lambda_{PL_2} = 842 \text{ nm}$.

Additional structures, made for broad-area lasers of 90 μm -wide lateral waveguides, are worth to study. Indeed, although it is multimode lasers, it has very little propagation losses other than free-carrier absorption of the doping species, as well as little current spreading effects. Thus, it is useful to test experimentally to extract the internal parameters of the design, such as the transparency current J_{tr} , the modal gain parameter $\Gamma g_{0,J}$, the current density at threshold J_{thr} , the internal quantum efficiency η_i and the internal losses α_i^{fc} . The simpler designs, free of any grating layers, are presented in figure (3.3).

D ₁ line: 894 nm (XXL2028)			D ₂ line: 852 nm (XXL2022)		
Layer	Alloy	Thickness (μm)	Layer	Alloy	Thickness (μm)
Contact	GaAs (P++)	0,25	Contact	GaAs (P++)	0,25
Ridge	GaInP (P+)	~ 1	Ridge	GaInP (P+)	~ 1
Cladding up.	AlGaInP (P+)	~ 1	Cladding up.	AlGaInP (P+)	~ 1
LOC	GaInP (P)	0,45	LOC	GaInP (P)	0,45
Interface	Q(1.62)	23Å	Interface	Q(1.62)	23Å
QW	GaInAsP	80Å	QW	GaInAsP	80Å
Interface	Q(1.62)	23Å	Interface	Q(1.62)	23Å
LOC	GaInP (N)	0,45	LOC	GaInP (N)	0,45
Cladding low.	AlGaInP (N+)	~ 1	Cladding low.	AlGaInP (N+)	~ 1
Optical barrier	GaInP (N+)	~ 1	Optical barrier	GaInP (N+)	~ 1
Buffer	GaAs (N++)		Buffer	GaAs (N++)	

} **Optical cavity & Active zone** }

Figure 3.3: LAMA 1st run structures for broad-area lasers at 894 nm (XXL2028) and for broad-area lasers at 852 nm (XXL2022)

3.1.2.2 Electrical behavior

The above junctions have been tested in the *EsakiHTD* model. Figure (3.4) displays the results of the transport simulation for the DFB structures. The analysis shows that the huge majority of recombinations, be they from Shockley-Read-Hall mechanisms (SRH) or from radiative recombinations below and above threshold, occurs in the well while a fraction only of the current feeds other recombinations in the barriers. The internal quantum efficiency reaches $\eta_i = 99\%$ at an injection level of $J = 240 \text{ A/cm}^2$ for the SRH constants of $\tau_e + \tau_h = 2 \text{ ns}$ in the well, and 6 ns elsewhere in the other layers, while the bimolecular coefficient is taken at $B = 5 \times 10^{11} \text{ cm}^3 \cdot \text{s}^{-1}$, except in the well where it is calculated using the considerations of chapter 2. Such a value, lower than that of GaAs, is justified by the higher gap of the material that decreases B , but again, as very few recombinations occur in the barriers, it is not so important to evaluate exactly. All this procedure of adjustments can be seen as arbitrary, but we will see that, despite any direct measurements of those recombination coefficients

(as done in [Laurain 2010] for instance), the predictions agree quite well with what is observed. The

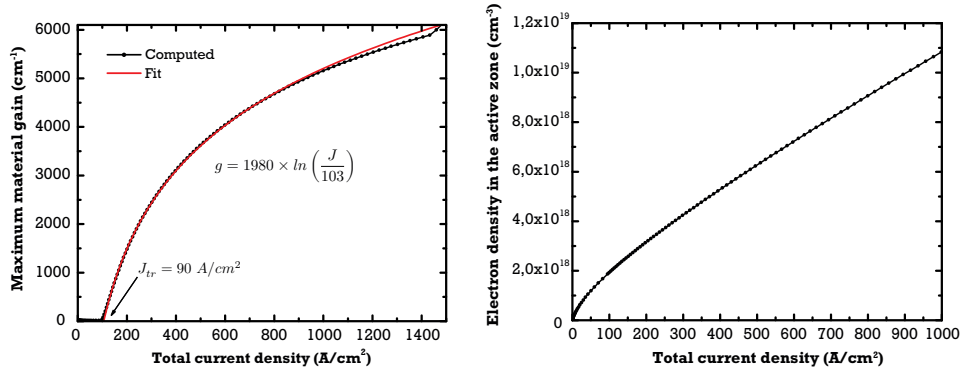


Figure 3.4: Left: Theoretical material gain g of structure XXL2028 as a function of the current density J and a log fit of the curve in red. The transparency current is evaluated at $J_{tr} = 90 \text{ A.cm}^{-2}$. Right: Theoretical electron density n in the well as a function of the current density J . The function is almost linear above transparency

transport model gives the direct relations between the injected current and the carrier density in the well. We find also a relation between the injected current and the material gain g :

$$g = g_{0,J} \ln \left(\frac{J}{J_{tr}} \right) \quad (3.1)$$

$$g_{0,J} = 1980 \text{ cm}^{-1}, \quad J_{tr} = 103 \text{ A/cm}^2 \quad (3.2)$$

where $g_{0,J}$ is the material gain parameter with respect to the current density and J_{tr} the density of current at transparency. The fit is very useful to estimate the effective current threshold of the optical modes against their respective losses and confinement factor Γ on the well. Also, we can notice that the $n(J)$ characteristics of figure (3.4) shows a quadratic dependency in J which ends up in a linear law. This results from the choice of the different recombination constants, as pointed out in chapter 2.

3.1.3 Optical Design

The goal of the section on the optical design is to evaluate the optical mode properties in the three directions of the optical cavity. First, the mode profile in the transverse direction, perpendicular to the z -axis of propagation is evaluated. Then, the longitudinal mode losses dependent on the Bragg grating parameters are computed. In practice, the transverse and longitudinal optical profiles can be evaluated separately due to the very different length scales of propagation. In the transverse direction, the decoupling in the x and y directions can also be used to some extent, to make the analysis easier. However, the computation of the effective refractive index of the structure must be performed with a 2D analysis.

3.1.3.1 Components of the complex medium index

Prior to any analysis on the optical behavior of the structure, one should know the real refractive index of the structure as well as the absorption of the materials both at 852 nm and 894 nm . These data, especially the refractive index, are maybe the most sensitive parameters of the design because it directly determines the optical parameters of the laser and the lasing wavelength of the DFB cavity

among others. While it is well-known for InP/GaInAsP-based materials at $1.55 \mu m$ and GaAs/AlGaAs at $850 nm$, it is not the case for the AlGaInP/GaInP cavity at $800 - 900 nm$. Moreover, the index of complex alloys can vary depending on the material phase ordering, the epitaxy technique... Hopefully, the previous results for the DFB D_2 line give a starting point to evaluate the optical properties at the D_1 line. The refractive index of the GaInP LOC is critical because most of the field is located in the core of the cavity. On that point of view, the corresponding refractive indices have been adjusted in the simulations to agree with the far-field measurements and the Bragg lasing wavelength obtained experimentally at both lines (see results at the end of the chapter). For that, the ellipsometry measurements of [Schubert 1995] have been preferred to the extrapolation formula of Adachi for the GaInAsP alloys. Table (3.1) recaps the optical indices used for simulations and their bibliographical origins. The refractive index undergo changes with various parameters:

Material	E_g^Γ (eV)	$n_R^{894 nm}$	$n_R^{852 nm}$	Origin
GaInP	1.88	3.2492	3.2758	[Schubert 1995]
GaInAsP	1.62	3.4167	3.4452	[Adachi 2009]
GaInAsP ($\epsilon = +1\%$)	1.32	3.6070	3.5560	[Adachi 2009]
AlGaInP (Al= 25%)	2.02	3.2022	3.2228	[Moser 1994]
AlGaInP (Al= 12%)	1.94	3.2371	3.2584	[Moser 1994]
GaAs	1.42	3.6070	3.5560	[Jellison 1992]
SiO ₂	–	1.4716	1.4721	[Gao 2013]

Table 3.1: Refractive indexes used for the simulations of the D_1 and D_2 lines structures (given at room temperature) as a function of the alloy composition and energy gap in the Γ valley E_g^Γ . The composition of the AlGaInP alloy is given for an Al percentage of the total cationic mass

- Energy of the gap E_g : Many authors have put forward more or less complicated models to write an explicit link between the refractive index and the gap below and above the band-edge of absorption. From chapter 2, it is generally linked to the absorption by the Kramers-Krönig-Hilbert relations. A simple approximate formula working for a vast majority of materials is deduced in [Herve 1994]:

$$n_R^2 = 1 + \frac{13.6^2}{(E_g + 3.4)^2} \quad (3.3)$$

With the gap energy in eV. More precise derivations include higher order terms [Afromowitz 1974].

- Temperature T : from (2.45), the gap decreases with temperature so with (3.3), the refractive index increases. Experiment shows that on average, for the above active zone:

$$\frac{\partial n_R}{\partial T} = 2 \times 10^{-4} K^{-1} \quad (3.4)$$

Which is close to the value found using (3.3) and the gap dependency with temperature (2.45).

- Intra-band absorption (plasma effect): Within the energy bands, free carriers can absorb photons which leads to a corresponding change in refractive index. This mechanism explains the

source of losses with doping of the passive cavity layers, and the index change can be approximated by Drude's model [Bennett 1990]:

$$\Delta n_R = - \left(\frac{e^2 \lambda^2}{8\pi^2 c^2 \epsilon_0 n_R} \right) \left(\frac{n}{m_e^*} + \frac{p}{m_h^*} \right) \quad (3.5)$$

with m^* the effective masses of the material. In our case, the indices changes are given in table (3.2):

Material	Δn_R
GaInP	$-(4.5 \times 10^{-4}) \frac{\lambda^2}{n_R} \left(\frac{n/10^{18}}{0.09} + \frac{p/10^{18}}{0.53} \right)$
AlGaInP	$-(4.5 \times 10^{-4}) \frac{\lambda^2}{n_R} \left(\frac{n/10^{18}}{0.14} + \frac{p/10^{18}}{0.52} \right)$

Table 3.2: Refractive index shift formula for intra-band transitions as a function of the transition wavelength (in μm) and the carrier density (in cm^{-3}).

Given that the effective masses for holes are five times greater than for electrons, the effect is predominant for electrons injection and n-type doping. For a n-type GaInP LOC with up to $n = N_d = 10^{18} cm^{-3}$, the index shift is $\Delta n_R = -1.2 \times 10^{-3}$ at 894 nm and $\Delta n_R = -1.4 \times 10^{-3}$ at 852 nm. The change is appreciable but is not meaningful given the uncertainties on the alloys compositions and refractive indexes, so it will not be taken into account in the simulations of modes properties, because the core where 85% of the field is located is only doped in the range of 10^{17} , so one order of magnitude below the previous values. It is even lower for the cladding region in AlGaInP. Moreover, the waveguide does not use a confinement based on *doping ramps*, unlike some high-power structures of the literature. For the quantum-well, with an intrinsic $n = p \sim 3.5 \times 10^{18} cm^{-3}$ at threshold, the change is $\Delta n_R \sim -8.4 \times 10^{-3}$, which can induce a mode de-confinement for the injected area to the non-injected areas of the well.

- Other inter-band effects: as pointed out in [Bennett 1990], the refractive index also shifts with band-filling and gap shrinkage, because again of the Kramers-Krönig relations. According to their model, the authors find either positive or negative index changes for the two effects, depending on the position below or above the gap of the material. In chapter 2, we have evaluated the differential index behavior of the well with injection in the 900 nm range thanks to the gain model of *EsakiHTD*. It gave $\Delta n_R = (-2.5 \times 10^{-21})(3.5 \times 10^{18}) = -8.8 \times 10^{-3}$. For the case of doping, both conduction-band filling and gap shrinkage with Coulomb screening of the dopants are present: the article gives $\Delta n_R = 4 \times 10^{-3}$ for n-doped GaAs at 1060 nm at $N_d = 10^{18} cm^{-3}$ (the three effects are included).

In conclusion, we will adopt a pragmatical approach by using directly the refractive index of (3.1) if it agrees well with the experiment which, given the uncertainties, will not give more precision than the 2×10^{-3} level on the effective index of the whole structure. Then, relation (3.4) shows that the refractive index shift can be corrected on the 10^{-3} level by tuning the temperature of the device of a few degrees, without degrading too much the laser performances. However, mode de-confinement in the area of the active zone must be anticipated as a detrimental mechanism for light amplification and modal competition.

Concerning the free-carrier absorption now, empirical laws are used, instead of complicated models of intra-band quantum absorption processes. It can be written as a function of the trapping cross-sections c_c , with α_i^{fc} the total free-carrier absorption (in cm^{-1}):

$$\alpha_i^{fc} = c_p p + c_n n \quad (3.6)$$

$$c_p = 11 \times 10^{-18} \text{ cm}^2 \quad \text{and} \quad c_n = 3 \times 10^{-18} \text{ cm}^2 \quad (3.7)$$

The relation shows that the optical power is four-times more absorbed on the p-side of the cavity (because of heavier effective masses of holes). This is why modern designs are focused on asymmetric vertical confinement with a field mainly confined in the n-region. Formula (3.6) gives the losses in the transparency regions of the materials of the heterostructure. However, in the outer barriers of the top and buffer layers of GaAs, the D_1 and D_2 lines are close to the band-gap edge. Then, targeted experimental data are needed for this case because the doping level influences the band-gap position. At $852 \text{ nm} = 1.455 \text{ eV}$, the absorption is very high, whatever the doping level: $n_{I,GaAs} = 0.074 \Leftrightarrow \alpha_{GaAs} = 11000 \text{ cm}^{-1}$ [Jellison 1992] which allows to create single mode vertical structures by leakage of higher order modes on the substrate for instance. In the case of $894 \text{ nm} = 1.387 \text{ eV}$, the band edge is too far away to obtain such absorption level. Instead, we take the values $\alpha_{GaAs(N++)} = 30 \text{ cm}^{-1}$ on the n-side and $\alpha_{GaAs(P++)} = 750 \text{ cm}^{-1}$ on the p-side [Casey Jr 1975].

3.1.3.2 Transverse Design

In this section, the mode properties will be evaluated in the (x, y)-plane (figure (3.5)).

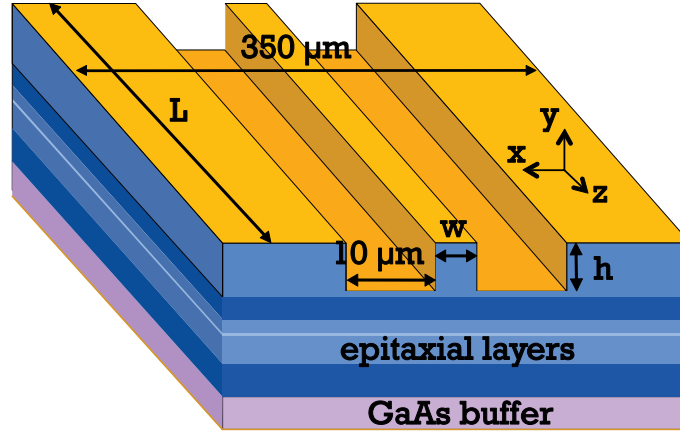


Figure 3.5: Schematic 3D view of a 'ridge' semiconductor laser

A/ In the perpendicular direction to the layers (y-axis)

The heterostructures (3.2) and (3.3) define a varying profile of materials energy gaps. Thus, it is associated with a real refractive index of propagation $n_R(\vec{r})$. In the present (non-magnetic and neutral) medium, the Maxwell equation for the electric field propagation $\vec{E}(\vec{r}, t) = \Re(\vec{E}(\vec{r})e^{j\omega t})$ in the stationary regime is written:

$$\nabla^2 \vec{E}(\vec{r}) + k^2 n_{med}^2(\vec{r}) \vec{E}(\vec{r}) = 0 \quad (3.8)$$

with, as in chapter 2, the complex refractive index $n_{med} = n_R + jn_I$. If the field is only considered to propagate in the z-direction (it is confined in the transverse plane), the propagation constant β along

z is introduced, so that it writes $\vec{E}(\vec{r}) = \vec{E}(x, y)e^{j\beta z}$. Then, for a 1D analysis, there is an amplitude dependency along y only, so:

$$\frac{\partial^2}{\partial y^2} \vec{E}(y) + (k^2 n_{med}^2 - \beta^2) \vec{E}(y) = 0 \quad (3.9)$$

In a 'linear' medium, the electric-field can either be oriented in the (x, z) plane of the layers (s polarization) giving the transverse electric (TE) solutions, or with the B -field orthogonal to that plan (p polarization) giving the transverse magnetic (TM). From what has been said in chapter 2 about the amplification of TE waves in a compressively-strained quantum-well, the rest of the analysis will only be conducted with the solutions $\vec{E}(y) = E_x(y)$. The classical wave-equation (3.9) can be solved, for instance, by discretization of the y -axis and matching step-by-step the continuity conditions on the E -field and B -field at the virtual interfaces. The procedure is realized internally by a program called *CINEMA*, which computes all the 1D modes of the vertical structure given the real and imaginary part of n_{med} of section [3.1.3.1].

- Structure XXL2029

The simulation results for the DFB structure at 894 nm are given below. They do not differ a lot from what was estimated before for the earlier D_2 line structure, because apart from the slight change in the LOC index, the layers have the same composition in both cases. Figure (3.6) shows the electric profile of the fundamental TE_0 Gaussian mode in the cavity. It is obviously maximum at the position of the quantum-well because of the symmetry of the cavity and the high value of the local index. The field has also a local maximum at the location of the grating layer. The confinement factor Γ on this layer will be used in the next section to compute the coupling coefficient to the grating. The total losses are estimated by the sum of the losses on each layer times the confinement factor of the field:

$$\alpha_i^{fc} = \sum_k \Gamma_k \alpha_{i,k} \quad (3.10)$$

$$\Gamma_k = \frac{\int_{layer\ k} |E(y)|^2 dy}{\int_{-\infty}^{\infty} |E(y)|^2 dy} \quad (3.11)$$

Regarding the losses of the well which has no doping, we consider the carrier densities at threshold ($\sim 4 \times 10^{18} \text{ cm}^{-3}$) to be a source of free-carrier losses (both electrons and holes). The confinement factor on the well Γ_{QW} and the total losses are summarized in table (3.3) for the two DFB structures. The accurate values of the two parameters are not so important at this stage because it will be evaluated more precisely in the 2D computation of next section (they depend on the lateral confinement as well). However, they allow to estimate the threshold density currents of lasing of all the modes of the vertical structure, which are numerous in the present case. The total mode overlap on the n-side is about 34% compared to 65% on the p-side: this configuration could be optimized to achieve lower free-carrier losses.

According to (2.127), the threshold of the mode number j is:

$$J_{thr,j} = J_{tr} \exp \left(\frac{\alpha_{i,j} + \alpha_{m,j}}{\Gamma_{QW,j} \times g_{0,J}} \right) \quad (3.12)$$

which is easy to determine with the fit (3.1). For example, the mirror losses are the Fabry-Perot one for the case $R_1 = R_2 = 0.28$, which corresponds to the reflectivity of cleaved semiconductor facets in

Structure	Γ_{QW}	α_i^{fc}
XXL2029	1.06%	2.5 cm^{-1}
XXL2020	1.1%	2.6 cm^{-1}

Table 3.3: Computation (*CINEMA*) of the confinement factor on the well and the resulting free carrier losses from a 1D optical modeling in the y-axis

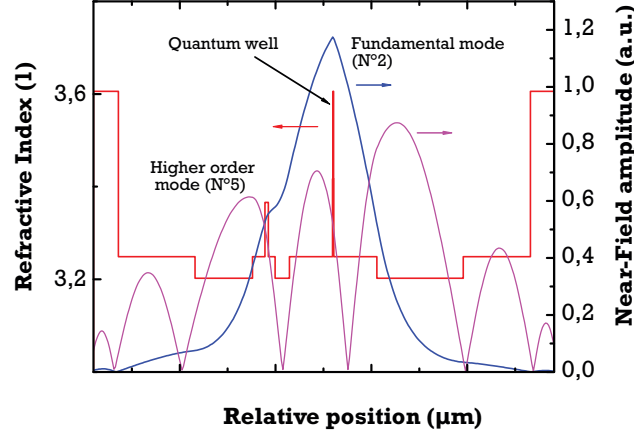


Figure 3.6: Profile of the fundamental mode TE_0 centered on the well (in blue) and of a higher-order mode (in pink). The material refractive index is also plotted against the position in the cavity. The electrical field is trapped in the regions of higher indices

N°	Γ_{QW}	α_i^{fc}	α_m	J_{thr}
1	1,1E-14	35,3	6,4	>10000
2	1,1E+00	2,0	6,4	155
3	3,1E-04	4,1	6,4	>10000
5	2,1E-01	7,0	6,4	2933
6	5,1E-02	20,8	6,4	>10000
7	9,9E-02	25,6	6,4	>10000
8	1,8E-01	18,3	6,4	>10000
9	1,5E-01	32,7	6,4	>10000
10	2,6E-01	30,6	6,4	>10000
11	1,6E-01	35,8	6,4	>10000
12	2,1E-01	67,2	6,4	>10000
13	7,0E-02	42,6	6,4	>10000
14	2,1E-01	68,2	6,4	>10000
15	4,3E-02	62,6	6,4	>10000
16	2,7E-01	69,0	6,4	>10000
17	2,1E-02	77,7	6,4	>10000
18	3,2E-01	63,9	6,4	>10000
19	1,7E-02	66,6	6,4	>10000
20	3,3E-01	68,1	6,4	>10000
21	4,1E-03	64,3	6,4	>10000
22	3,2E-01	67,4	6,4	>10000
23	1,0E-03	61,0	6,4	>10000
24	3,2E-01	62,9	6,4	>10000
25	6,5E-03	68,0	6,4	>10000
26	3,2E-01	67,4	6,4	>10000
27	2,2E-02	75,7	6,4	>10000
28	2,9E-01	77,9	6,4	>10000
29	4,4E-02	88,9	6,4	>10000
30	2,5E-01	105,7	6,4	>10000
31	8,1E-02	119,4	6,4	>10000
32	2,0E-01	131,4	6,4	>10000

Figure 3.7: 1D mode list as computed by *CINEMA*. The fundamental Gaussian cavity mode with the lowest current density at threshold is highlighted in yellow, the second lowest gain higher-order mode in orange. The very first mode is located in the GaAs buffer

air. Even if some modes have very low losses, they have also very little overlap with the well: any little difference will be amplified exponentially by (3.1) and repel the higher order mode threshold.

Figure (3.7) lists all the modes sustained by the cavity as-well-as their current densities at threshold. The evaluation is made from the mode of higher refractive index to the lower index mode. The very first result of the list is not the fundamental Gaussian TE_0 but a buffer mode which propagates in the buffer layer of high refractive index. Otherwise, **it is clear that no mode competition is possible within standard injection condition**. Indeed, as soon as the driving current is high enough to provide the gain required to compensate for the losses of the less-lossy mode, the carrier density and the gain are clamped, so that any additional injected current feeds the stimulated emission of the winner only. Furthermore, there is no possibility of 'vertical spatial hole burning' given the transverse dimensions of the well ($\sim nm$) versus the mode dimensions ($\sim \mu m$): all the modes see the same material gain (gain localization in the well), only their confinement factor changes. For the fundamental mode, the threshold density of $155 A/cm^2$ represents a current of $I_{thr} = 12 mA$ for a surface of injection of $S = 2 \mu m \times 2 mm$.

The far-field emission can be computed from the near-field profile. The mode near-field width in the perpendicular direction to the layers (as denoted by ' \perp ' for easier reading) is of about $w_{y\perp} \sim 0.5 \mu m$, which gives an approximate far-field full divergence of $\Theta_{y\perp} \sim 59^\circ$ (after (2.44)) which is quite large. Usually, high divergence of the beam in free space is detrimental for coupling applications into lenses, fibers... All the more so since the divergence in the other lateral x-axis (parallel to the layers, as denoted by ' \parallel ' this time) is three to four time lower, inducing beam astigmatism [Siegman 1986] (it is however common for edge-emitting lasers, unlike VCSEL which have very high-quality beams [Denet 2016]). Energy is lost, and beam-shaping optical benches (use of cylindrical lenses) have to be set up to obtain a round spot. In the frame of the free-space application of the OCFS, it would be valuable to have a reduced divergence in the fast-axis, at least to decrease the ratio of the elliptical shape. This can be achieved, after relation (2.44), by an increase of the local waist. This is what is looking for in the so-called 'Super-LOC' cavities, which have been studied for the D_1 line structure.

- Extension: Super-LOC design

The design of enlarged vertical structures is not an easy task in edge emitting lasers: with increasing cavity width, more and more modes are sustained and enough gain margin for single mode behavior between the fundamental Gaussian mode and the others have to be maintained. In the meantime, with the objective to reduce the losses of the cavity, one tries to decrease the overlap of the mode on the p-side, heading the design toward an asymmetric cavity, which is now quite standard in the development of monolithic high-power laser diodes. Pushing further this concept leads to original structures called 'slab-coupled waveguides' where the mode travels in the n-side region only (the guiding properties have been theorized very early in [Marcatili 1974]): practical realizations have demonstrated almost Gaussian and circular beam-shapes with a standard 'deep-ridge' etching of the layers [Huang 2003, Plant 2005], called SCOWLs, with internal losses as low as $0.5 cm^{-1}$. However, these structures need a complete re-engineering of the vertical and lateral cavity process, which was going beyond the scope of this work. Instead, we tried a compromise by extending the vertical mode width without deviating too much from the original design, which would have been risky given the lack of time on both the epitaxial developments allowed for the project, or on the other aspects of device processing and characterization.

The general scheme followed was to increase the mode width with a thicker GaInP-LOC cavity on the n-side. While only the fundamental and the higher-order modes with *odd* numbers of maxima were favored in the symmetrical LOC design (TE_0, TE_2, \dots), now the modes with *even* number of maxima have the highest confinement factor on the well, because of the symmetry breaking of the

refractive index profile of the cavity. To 'kill' these higher-order modes, a useful technique is to increase their leakage on the highly n-doped layers beyond the n-cladding by lowering the refractive index of the latter material. For instance, if the proportion of Aluminum is reduced from 25% to 12% in AlGaInP, a difference of refractive index of $\Delta n_R = +0.035$ is achieved which is closer to the index of GaInP LOC. In the meantime, because of mode expansion in the cavity, the confinement on the well will mechanically decrease if the well width is kept constant (it is actually halved), which will increase the threshold, then the carrier leakages... This is why the GaInAsP $Q(1.62 \text{ eV})$ interfaces have been made thicker (9 nm on each side) as true barriers to act as an 'optical trap' to keep the confinement back at a value comparable to that in the LOC design. If it is too thick, it will cancel the benefits of the extended cavity by increasing the confinement in the cavity as well as the far-field divergence. We have also verified that the thinning of the spacer does not induce too much electron leakage in the grating, which otherwise acts like a confining trap: at such thickness (close to 100 nm), it is still an efficient carrier barrier, but allows more optical leakage towards the well.

D₁ line: 894 nm (Super-LOC)

Contact	GaAs (P++)	0.25	}	Epitaxial régrowth
Ridge	GaInP (P+)	~ 0.5		
Cladding up.	AlGaInP 25%(P+)	~ 0.2		
Planarity	GaInP (P+)	~ 0.2		
Interface	GaInP (P+)			
Grating core	Q(1.62) (P+)	0.035	}	Grating layers
Interface	GaInP (P+)	0.1		
Spacer	AlGaInP 25%(P+)	~ 0.1	}	Optical cavity & Active zone
LOC	GaInP (P)	0.5		
Interface	Q(1.62)	90Å		
QW	GaInAsP	80Å		
Interface	Q(1.62)	90Å		
LOC	GaInP (N)	1.8		
Cladding low.	AlGaInP 12%(N+)	~ 0.2		
Optical barrier	GaInP (N+)	~ 0.5		
Buffer	GaAs (N++)			
Layer	Alloy	Thickness (μm)		

Figure 3.8: Super-LOC cavity designed according to the principles described. Better beam shape properties and reduced optical losses can be theoretically expected from this type of structure

Figure (3.8) is the actual design for the super-LOC cavity defined with the previous considerations. Simulation (3.9) shows the fundamental mode profile. The 1D mode analysis reveals that this oscillation has a threshold current of $J_{th} = 164 \text{ A.cm}^{-2}$, versus $J'_{th} = 1133 \text{ A.cm}^{-2}$ for the higher order mode just above. The difference is less than in the case of the LOC cavity, but we should remember that it has been computed with an ideal gain curve. In reality, the gain parameter will be lower, which, given the exponential relation between the threshold current and the gain, will increase a lot the threshold margin. Moreover, even if the second threshold is reached, gain localization and carrier density clamping at the first threshold will prevent modal competition *above* the first threshold. Finally, the expected losses and confinement for the fundamental mode are presented in table (3.4). The absolute losses reduction can seem very tiny with respect to the LOC design. Though, it has been

Structure	Γ_{QW}	α_i^{fc}
Super-LOC	0.89%	1.8 cm^{-1}

Table 3.4: Super-LOC fundamental mode confinement on the well and free-carrier losses as computed using CINEMA

lowered by 1 cm^{-1} and this reduction will benefit on the laser linewidth and external efficiency.

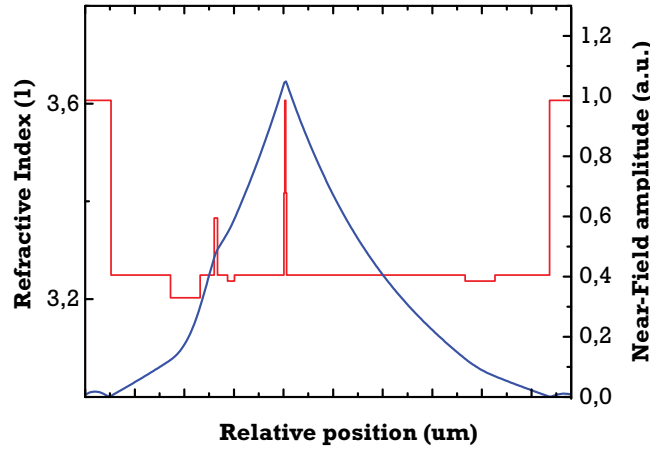


Figure 3.9: Profile of the fundamental mode TE_0 centered on the well (in blue) in the Super-LOC structure. Confinement is reduced in the active zone when the mode spreads along the cavity

B/ In the parallel direction to the layers (x-axis)

The lateral confinement is a key feature of the optical design. Not only it does ensure a single mode behavior in the x-direction, but it also provides the injection current confinement. Two main mode-guiding techniques can be used:

- *Gain-guided waveguides*: mode selection is ensured by the lateral gain localization: the fundamental mode has the higher overlap on the positive-gain part of the active zone below the contacts, so that an intrinsic multimode waveguide becomes single-mode in laser operation (providing all other losses are being equal for all the modes)
- *Index-guided waveguides*: the lateral mode confinement is ensured by a physical change of lateral real refractive-index, like in a fiber. By construction, only one lateral mode can exist in the guide

The first technique was popular in the 90's in edge-emitting lasers, because it does not require any physical etching of the layers. However, because of *lateral current spreading*, if no insulation is provided in the bulk outside of the contact area the gain is not localized anymore, the threshold current increases and potential higher order modes excitation can occur. Today, in high-power lasers, index-guiding is systematically used because of its stability : mode confinement does not depend on the injection if the design is done properly. In our case, the waveguide is a *shallow ridge* which provides lateral refractive index change by etching two trenches on the p-side of the layers without crossing the active zone (see figure (3.5)).

The effective refractive index jump between the central part and the two adjacent lateral sides is a crucial parameter $\Delta n_R^{lat} = n_{R,eff}^c - n_{R,eff}^l$ which value reflects the mode confinement strength in this direction. The effective refractive index itself is defined as the refractive index associated to the mode propagation constant $\beta = 2\pi n_{R,eff}/\lambda$ and can be evaluated as:

$$n_{R,eff} = \sum_k \Gamma_k n_{R,k} \quad (3.13)$$

Thanks to the etch of depth h , the upper semiconductor layers of lower refractive index (cladding) is removed and replaced by air and an insulator (SiO_2). Given (3.13), the 'mean' effective index decreases on the lateral sides, so that $\Delta n_R^{lat} > 0$. Of course, such lateral index step depends on h . A method to evaluate such a parameter is to compute the 1D effective refractive index in the y -direction in the central part, below the top contact, then in the lateral sides (that are equivalent by symmetry purposes), as explained in figure (3.10). The ridge-waveguide is then made equivalent to a 1D guide with an index step Δn_R^{lat} in the x -direction, which modes can be studied without any difficulties, taking into account the ridge width w .

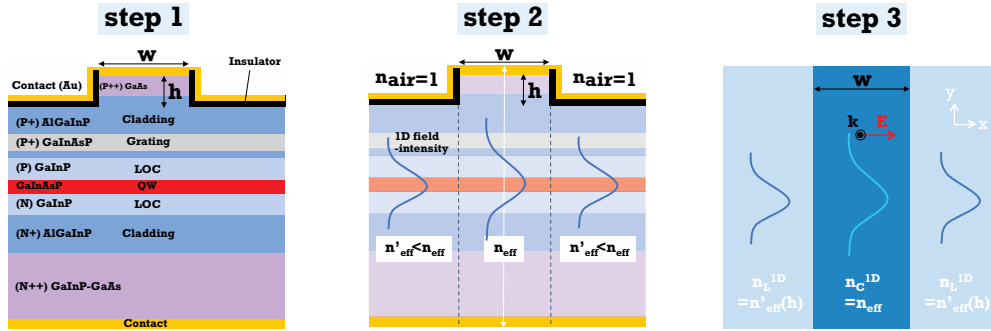


Figure 3.10: Principle of the transverse mode confinement study, using a 1D modeling. The structure is separated into a central part below the ridge with an effective refractive index $n_{R,eff}^c$ and lateral parts of index $n_{R,eff}^l$

The results of the above procedure of index step computation are summarized in tables for the relevant structures under study: XXL2029 (3.5), XXL2020 (3.6) and Super-LOC (3.7).

Etching depth h	$n_{R,eff}^c$	$n_{R,eff}^l$	$\Delta n_R^{lat}(h)$
$h = 1.66 \mu\text{m}$ (to top of planarisation)	3.24203	3.24044	1.6×10^{-3}
$h = 1.70 \mu\text{m}$ (below the planarisation)	3.24203	3.23997	2.1×10^{-3}
$h = 1.79 \mu\text{m}$ (to top of grating)	3.24203	3.23928	2.8×10^{-3}
$h = 1.895 \mu\text{m}$ (to top of spacer)	3.24203	3.23811	3.9×10^{-3}
$h = 1.995 \mu\text{m}$ (to top of spacer+100 nm)	3.24203	3.23630	5.7×10^{-3}
$h = 2.045 \mu\text{m}$ (to top of LOC)	3.24203	3.23493	7.1×10^{-3}

Table 3.5: Effective indices computation (1D model) for several etch depths h and the resulting effective index step created by the ridge guide for XXL2029

Depending on the value of h , there exists a *ridge-width cutoff value* w_c beyond which the lateral effective waveguide supports more than one mode. This appears when, for a given lateral index step, one varies the ridge width w and solve for all the 1D existing *TM* modes (indeed, in this modeling, the electric-field is now orthogonal to the virtual layers boundaries of different effective index). Figure (3.11) shows the fundamental mode and the first-order symmetrical mode in the case of an etching $h = 1.79 \mu\text{m}$ in XXL2029 and a ridge width $w = 4 \mu\text{m}$ which is beyond the cutoff value, for a $\Delta n_R^{lat} = 2.5 \times 10^{-3}$. Also, the number of intrinsic modes of the ridge versus w allows to compute all these cutoff values (figure (3.12)).

Etching depth h	$n_{R,eff}^c$	$n_{R,eff}^l$	$\Delta n_R^{lat}(h)$
$h = 1.66 \mu m$ (to top of planarisation)	3.26788	3.26672	1.2×10^{-3}
$h = 1.79 \mu m$ (to top of grating)	3.26788	3.26586	2×10^{-3}
$h = 1.86 \mu m$ (to top of spacer)	3.26788	3.26528	2.6×10^{-3}
$h = 1.96 \mu m$ (to top of spacer+100 nm)	3.26788	3.26409	3.8×10^{-3}
$h = 2.06 \mu m$ (to top of LOC)	3.26788	3.26180	6.1×10^{-3}

Table 3.6: Effective indices computation (1D model) for several etch depths h and the resulting effective index step created by the ridge for XXL2020

Etching depth h	$n_{R,eff}^c$	$n_{R,eff}^l$	$\Delta n_R^{lat}(h)$
$h = 1.8 \mu m$ (in the LOC)	3.24	3.24	4.2×10^{-3}

Table 3.7: Effective indices computation (1D model) for one etch depth h and the resulting effective index step created by the ridge for the Super-LOC design

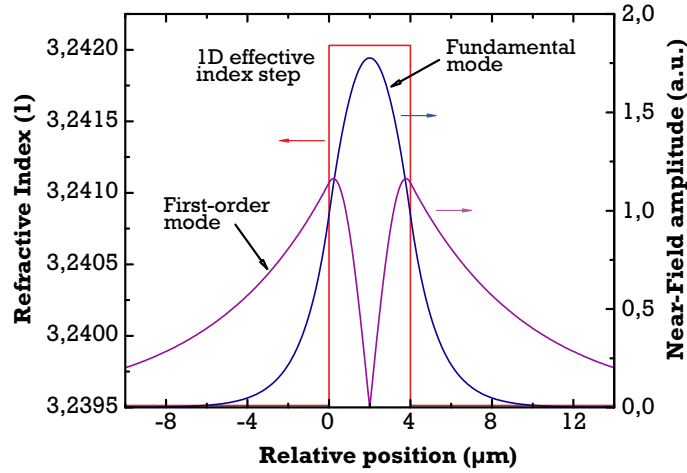


Figure 3.11: Profile of the fundamental TE_0 mode and onset of the first-order TE_1 centered on the ridge waveguide. The effective refractive index is also plotted against the position in the cavity. Guiding parameters are $w = 4 \mu m$ and $\Delta n_R^{lat} = 2.5 \times 10^{-3}$

One thing to be noticed is that the overlap of the modes on the central part of the ridge is around 88% for the fundamental one while it is 27% for the first order mode. So even if the waveguide is multimode in this precise case (it is very close to the cutoff because the second mode leaks away from the center part), it has a lower modal gain than the fundamental one if we consider that only a portion of length w of the well is injected below the guide. As a consequence, it should not be an issue in single-mode operation. **In practice, it is not the case.** First because there is always **current spreading in the lateral direction**, so that a bigger area is injected, defining an *effective ridge width* $w_{eff} > w$. Such extended gain is not clamped (only the central part, where the optical losses equal the optical gain, is) and will overlap more efficiently with the second mode. Also, a 2D analysis (see next) will show that the second mode is more confined in the LOC than the fundamental one, and has then lower losses on the overall. **These two facts explains why it is easy to switch from**

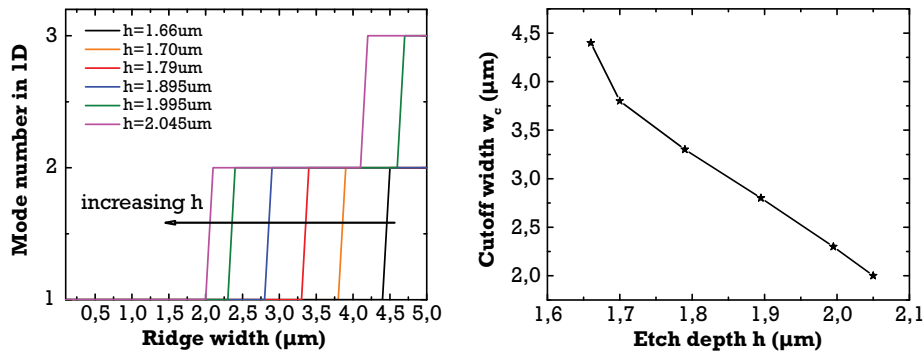


Figure 3.12: Case of XXL2029. Left: Number of intrinsic lateral modes as a function of the ridge width w , for several etch depths h . With increasing w , the waveguide stands more and more lateral modes, for a given h . Right: cutoff ridge width w_c above which the waveguide is multimode, as a function of the etch depth h

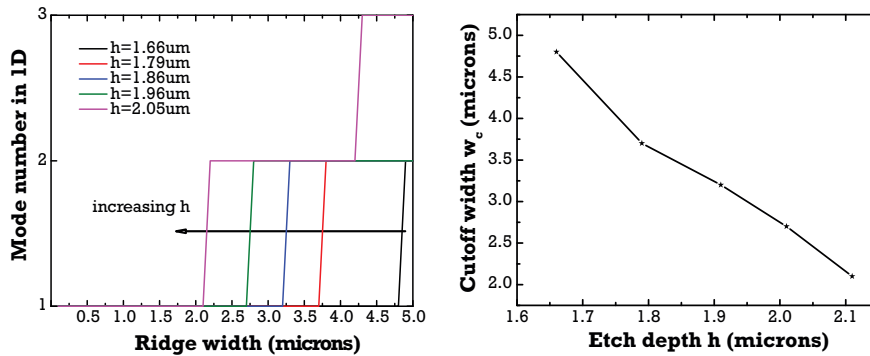


Figure 3.13: Case of XXL2020. Left: Number of intrinsic lateral modes as a function of the ridge width w , for several etch depths h . With increasing w , the waveguide stands more and more lateral modes, for a given h . Right: cutoff ridge width w_c above which the waveguide is multimode, as a function of the etch depth h

single to multimode operation in the shallow ridge technology. From the above graphs, we learn that for an etch depth $h = 1.7 \mu\text{m}$, the ridge width w should be less than $3.7 \mu\text{m}$ to ensure an intrinsic single-mode behavior in XXL2029. To avoid very thin ridge that would degrade the beam divergence, one could think to keep wide waveguides ($4 - 5 \mu\text{m}$) and decrease the index step below 10^{-3} . This is what was done on the previous realizations of ridge lasers at 852 nm . However, **this value is not sufficient to achieve proper index-guiding.** This is what is discussed now.

★ *Lateral mode confinement vs. lateral current spreading*

Two drivers may induce lateral spreading of the carrier density in the active zone: **carrier diffusion**, which is created by gradients of carrier density (Fick's law), modifying the gain and refractive index, and **current spreading**, for which the current lines diverge out from the injection area in the highly-doped layers, before reaching the active zone.

Regarding the first aspect, as early as 1984, Agrawal looked at the issue of lateral mode stability, putting forward that two effects control the mode behavior in quasi-index guided (QIG) devices [Agrawal 1984]. The first term is the refractive index step as defined above, while the second is an *anti-guiding* negative change of the local refractive index with the gain, due, again, to the Kramers-Krönig relations:

$$\Delta n_{R,tot} = \Delta n_{R,eff} - \Gamma_{AZ} \left(\frac{dg}{dn} \right) \frac{R}{k_0} n \quad (3.14)$$

$$R = \frac{\alpha_H}{2} \quad (3.15)$$

The confinement factor Γ_{AZ} is defined for the active zone, which is the quantum-well in our case, so $\Gamma_{AZ} = \Gamma_{QW}$. The second term is what we have tried to evaluate in section [3.1.3.1] and is $\Gamma_{QW} \times (dn_R/dn) \sim 0.01 \times (-9 \times 10^{-3}) \sim 10^{-4}$. Unlike to the case studied by Agrawal, who was working with simple heterostructures, the low optical confinement on the thin well induces low anti-guiding effect. Moreover, the high differential gain which probably induces low Henry factor also explains the difference in index change encountered. The interesting part is on the lateral diffusion of carriers and associated gain profile seen by the modes: from (2.106), the lateral component of the current can be clarified, in the stationary regime:

$$\frac{J_{x\parallel}(x)}{ed_{QW}} = \frac{n(x)}{\tau(n)} + v_g g(n(x)) s(x) - D_a \frac{\partial^2 n}{\partial x^2} \quad (3.16)$$

where D_a is the *ambipolar* diffusion coefficient (in $m^2.s^{-1}$) of the active zone taking into account both electrons and holes diffusion. By solving such equation consistently with the field that gives the power density $s(x)$, Agrawal shows that the overlap of the lateral carrier density with the intensity gives an optimum for the refractive index step $\Delta n_{R,tot}$ to choose: indeed, if this value is too low, the field spreads laterally and eventually reaches the lateral areas where there is no injection, thus inducing additional absorption (the material of the well is not transparent at zero injection). Conversely, if the index step is too strong, the field is very confined in the central part and does not benefit from the gain that spreads in x. Thus, he finds an optimum value of:

$$\Delta n_{R,opt} = 4.5 \times 10^{-3} \quad (3.17)$$

which minimizes the threshold current and maximizes the external efficiency. The only point which holds caution is the value of $D_a = 10 \text{ cm}^2.s^{-1}$ taken by the author, which seems a bit small for the case of quantum-wells. In [Hu 1994], the authors measured $D_a = 22 \text{ cm}^2.s^{-1}$ because of the high densities in a 8 nm InGaAs well similar to our active zone.

Regarding the other aspect of lateral effects, using qualitative, experimental results, as well as 2D modelings, [Achtenhagen 2006] and [Laakso 2008] give an intuitive view of the effects of spreading in the lateral direction for single-mode behavior of ridge lasers. With an effective index step above 2×10^{-3} , the first group of authors notice that their devices shows intrinsic and stable behavior of the lateral fundamental mode. A lower index step corresponding to a decreasing etch-depth leads to quasi

index guiding, which is very unstable against de-focusing and focusing (for instance, with increasing temperature in the ridge, the index rises) occurring at increasing injected current. They observe initial unstable near-field, followed by self-stabilization at higher current, giving very non-linear L-I characteristics. On the other side, [Laakso 2008] have solved the 2D transverse injection model. They show that depending on the etch-depth and ridge width, there exist an optimum area of (w, h) values: if the etching does not provide enough mode confinement, fundamental and higher order modes extend strongly in the lateral direction and the overlap of the modes increases, which are more likely to be fed simultaneously by the spreading gain (the gain margin between two lateral modes is reduced). If the ridge width is too high, higher order modes will not be cutoff. They conclude that the range of stable single-mode operation of the small etch/wide ridge configuration is very limited.

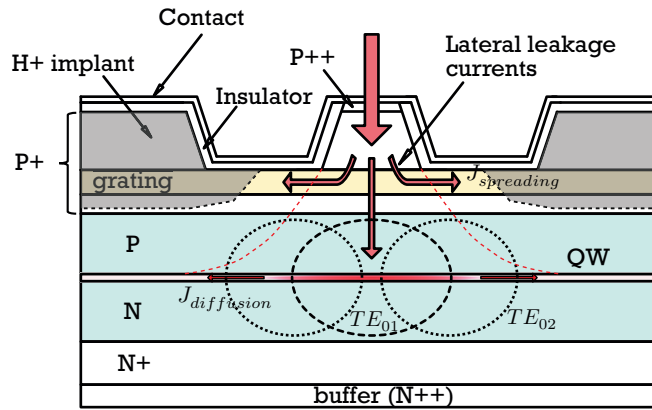


Figure 3.14: Schematic representation of a lateral cut of the laser cavity in the transverse (x,y) plan. Both lateral current spreading in the highly p-doped cladding and carrier diffusion in the well are responsible for lateral carrier concentration inhomogeneity

The question of current *spreading* in the upper part of the p-side region (see figure (3.14)) can be addressed qualitatively. Because of the high p-doping of these layers, they have low resistivities ρ_p :

$$\rho_p = \frac{1}{ep\mu_p} \quad (3.18)$$

The mobility μ_p decreases with increasing doping concentration but ρ_p decreases faster on the overall. The applied external electric-bias is oriented vertically in the y -direction, but it is also the direction of the gradient of resistivity toward the active-zone so a transverse component of the current will preferably drift in the lateral sides below the trenches (this is no diffusion because this would require a gradient of carrier density). Especially, the region of the grating which is etched and regrown, will probably induce additional interface resistivity so that the carriers flow preferably in the x -direction. In [Achtenhagen 1999], an approximate profile of the current flowing downwards to the active region is given, after the model of [Yonezu 1973], by:

$$J_{y_\perp}(x) = \frac{J_s}{1 + \frac{|x| - w/2}{l_s}} \quad \text{if } -w/2 \leq y \leq w/2 \quad (3.19)$$

$$= J_s \quad \text{below the ridge stripe} \quad (3.20)$$

where J_s is the density current below in the central ridge part of length w . The existence of a characteristic *spreading length* l_s forces to inject more current than the nominal J_s to reach this value below the guide, so that the total current J_t to inject is (3.21):

$$J_t = J_s \left(1 + \frac{2l_s}{w}\right) \quad (3.21)$$

$$l_s = \sqrt{\frac{2nk_B T d}{e\rho_p J_s}} \quad (3.22)$$

with n the ideality factor of the diode (between 1 and ~ 2.5 for a laser diode) and d the thickness of the spreading layer. This simple model gives an intuitive behavior of the spreading phenomenon: with increasing layer thickness and decreasing resistivity, the spreading length increases, so that J_t increases. Figure (3.15) plots the normalized current profile for the case of a spreading in the upper highly-doped p-layers (grating) at $N_a = 10^{18} \text{ cm}^{-3}$ ($\rho_p = 0.2 \text{ } \Omega \cdot \text{cm}$) of thickness $d_1 = 0.235 \text{ } \mu\text{m}$ versus the case of the LOC-p layer only at $N_a = 10^{17} \text{ cm}^{-3}$ ($\rho_p = 2 \text{ } \Omega \cdot \text{cm}$) of same thickness $d_1 = 0.2 \text{ } \mu\text{m}$. It is clear that the spreading is much lower if the current is only flowing in the second layer, after an etching depth through the highly-doped materials for instance. If we use the simple gain model (3.1)

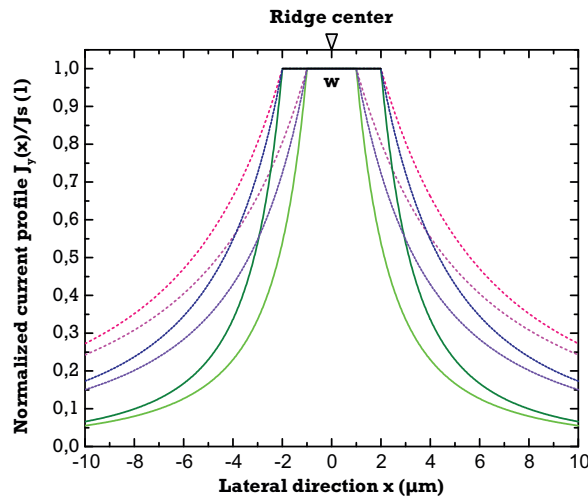


Figure 3.15: Current spreading profile as a function of various parameters, with a common $J_s = 160 \text{ A} \cdot \text{cm}^{-2}$. Green plain: $\rho_p = 2 \text{ } \Omega \cdot \text{cm}/d = 0.2 \text{ } \mu\text{m}/l_s = 2.5 \text{ } \mu\text{m}$, Purple dotted: $\rho_p = 0.4 \text{ } \Omega \cdot \text{cm}/d = 0.235 \text{ } \mu\text{m}/l_s = 5.7 \text{ } \mu\text{m}$, Pink with spaced dots: $\rho_p = 0.2 \text{ } \Omega \cdot \text{cm}/d = 0.235 \text{ } \mu\text{m}/l_s = 8.7 \text{ } \mu\text{m}$

together with the above distribution with the parameters $w = 2.3 \text{ } \mu\text{m}$, $\rho_p = 2 \text{ } \Omega \cdot \text{cm}$ and $d = 0.65 \text{ } \mu\text{m}$ (values for a 'mean' cladding region below the etching), we get the lateral gain profile (3.16). In this rough model, beyond $\sim 2.3 \text{ } \mu\text{m}$ away from the ridge center, the gain turns to absorption. It is then very important for the design that the near-field profile of the mode has maximum overlap with the positive gain profile.

Of course, this simple picture does not take into account the multiple layers below the etching (spacer and LOC-p) but it gives an idea of the magnitude of the resulting spreading when injecting a total current density $J_t = 816 \text{ A} \cdot \text{cm}^{-2}$ to obtain an effective $J_s = 160 \text{ A} \cdot \text{cm}^{-2}$ below the stripe which corresponds to the calculated threshold current of XXL2029 (relation of more than five between the two currents). If the etching goes through the grating plus the spacer, up to 200 nm above the active zone in the lightly doped GaInP, with a ridge width of $w = 2.2 \text{ } \mu\text{m}$, the positive gain area extends

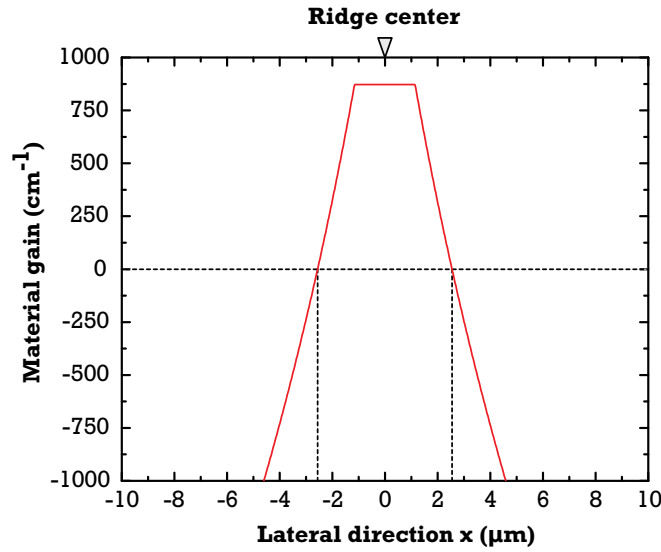


Figure 3.16: Material gain spreading profile, with $J_s = 160 \text{ A.cm}^{-2}$ and $w = 2.3 \text{ } \mu\text{m}$, $\rho_p = 1.3 \text{ } \Omega.\text{cm}/d = 0.65 \text{ } \mu\text{m}/l_s = 5.7$

on $3.8 \text{ } \mu\text{m}$ and the relation between J_t and J_s decreases to 3.8: this is precisely the parameters that would be of interest to limit current leakage for the Super-LOC structure.

The last point to mention is that Agrawal and [Hu 1994] have treated the case of lateral diffusion in the well with scaling relations that leads to similar conclusions as (3.19): if $w \gg l_s, l_{D_a}$, then the current behaves as if there was no lateral drift or diffusion. This is why accurate measurements of threshold currents and optical losses are preferably realized on broad-area lasers with $w = 90 \mu\text{m}$, which will be done first in the coming device results.

To conclude this part on the 1D transverse confinement of the mode, we will keep in mind that **a sufficient lateral index step in the range of $\Delta n_{R,eff} \sim 3.5 - 4 \times 10^{-3}$ must be first achieved** to ensure correct quasi-index guiding of the mode. Then, **the lateral waveguide should be intrinsically single-mode** with $w = 2 - 2.5 \text{ } \mu\text{m}$ to keep a security margin against positive-lensing effects with device heating at high power. This is necessary to **avoid lateral mode competition above threshold**. On the overall, one try to etch the ridge deep enough to remove the highly-doped upper layers (this is commonly done for high-power lasers, see [Wenzel 2004]), without confining too much the current and decreasing the overlap with the field and the gain. In fact, the later criterion is stringent, because it is the main source of lateral gain inhomogeneities. The analysis of Agrawal and Hu can apply: if the spreading is too strong, the external efficiency will drop because of a factor $\eta_t < \eta_i$ to take into account the lateral losses which do not feed the gain seen by the mode, nor the current further injected: **the L-I characteristics linearity is thus bias-dependent above threshold**. All the previous points cannot be structurally achieved with the XXL2020 and XXL2029 structures because an etching to the LOC layer would give a too strong index step (going through the spacer of low index changes rapidly the mode confinement). Though, for the Super-LOC, the new design should enable the full optimization. Table (3.9) summarizes those conclusions. The very last conclusion of that would be the fact that the laser noise is driven deeply by the mode fluctuations in amplitude and refractive index: **a first step toward noise reduction is to work in a very stable guiding regime**. Ultimately, a comprehensive 2D-model, mixing both carrier transport and optical behavior

(an *EsakiHTD* program extended in the y -direction) would be very useful to better understand the electro-optic parameters under high current injection (some commercial codes exist) and would spare speculative models like the above.

Structure	Etching depth h	$\Delta n_{R,eff}$	w
XXL2029	$h = 1.9 \mu m$ (spacer)	4×10^{-3}	$2.2 \mu m$
XXL2020	$h = 1.96 \mu m$ (spacer+100 nm)	3.8×10^{-3}	$2.2 \mu m$
LOC(0.55 μm)	$h = 2 \mu m$ (spacer+100 nm)	3.7×10^{-3}	$2.2 \mu m$
Super-LOC	$h = 1.6 \mu m$ (in the LOC)	4×10^{-3}	$2.2 \mu m$

Table 3.8: Summary of the main guiding parameters retained in the structures under study

C/ 2D optical modeling

A real 2D computation of the field intensity is necessary to estimate accurately the effective refractive indices of the fundamental mode of the several structures, as-well-as their near-field and far-field properties. This simulation is realized here using FimmWaveTM, a commercial software of PhotonDesignTM. The algorithm used is the Film Mode Matching technique (FMM), which consists in computing all the 1D modes of each part of the waveguide (just as in the previous section) and propagating laterally the modes by matching the continuity properties of the field at the virtual interfaces. The advantage is that the modes can be computed step-by-step, instead of the more classical Finite Difference Method (FDM) which requires the modes to be computed simultaneously after meshing the 2D structure. Figure (3.17) shows the fundamental and the onset of the second order mode of XXL2029, for a small etching depth, when enlarging the ridge w .

We have verified that the previous 1D simulation tool as-well-as the FimmWaveTM model give the same estimation of the 1D effective indices of the vertical structure. However, the estimation of the '2 \times 1D' effective index of the previous section and the real 2D effective index differ from $\sim 3 \times 10^{-4}$ for small w values. This is not much, but the transition at the ridge cutoff width w_c is sharp in the 1D model by construction, while it is smooth and leads to hybrid situations for a 2D computing. We could have led all the study of the transverse modes and their confinements on the well with CINEMA, but it is not possible for the layers etched in the ridge, because both h and w modify deeply the mode position in the cavity and influence the grating properties (figure (3.17)). Also, a proper near-field and far-field estimation can only be done in 2D. Table (3.9) summarizes all the theoretical relevant parameters of the LAMA structures according to this study. A comparison with experimental values

Structure	h/w	$n_{R,eff}^{2D}$	α_i^{fc}	$w_{y\perp}^{1/2}/w_{y\perp}^{1/e^2}$	$w_{x\parallel}^{1/2}/w_{x\parallel}^{1/e^2}$	$\Theta_{y\perp}^{1/2}/\Theta_{y\perp}^{1/e^2}$	$\Theta_{x\parallel}^{1/2}/\Theta_{x\parallel}^{1/e^2}$
XXL2029	1.65/4	3.2415	2.4	0.68/1.31	3.47/6	26.9/51.6	7/12.1
XXL2029	1.9/2.2	3.2403	2.1	0.65/1.29	2.07/3.87	28.4/56.2	8.6/17.1
XXL2020	1.65/4	3.2673	2.6	0.66/1.3	3.54/6.3	27.6/52.1	6.7/10.5
XXL2020	2/2.2	3.2659	2.3	0.63/1.25	2/3.7	29/56.8	8.7/17.2
LOC(0.55 μm)	2/2.2	3.2419	1.7	0.68/1.36	2.1/4	28/54	8.5/16.4
Super-LOC	1.6/2.2	3.2485	1.3	1.22/2.25	2.07/3.87	18.9/31.9	8.3/15.7

Table 3.9: Transverse 2D optical study of the fundamental TE_{00} mode, as computed by FimmWaveTM will be made in section [3.3.2.2]. It can be noticed that with a narrowed ridge width and higher

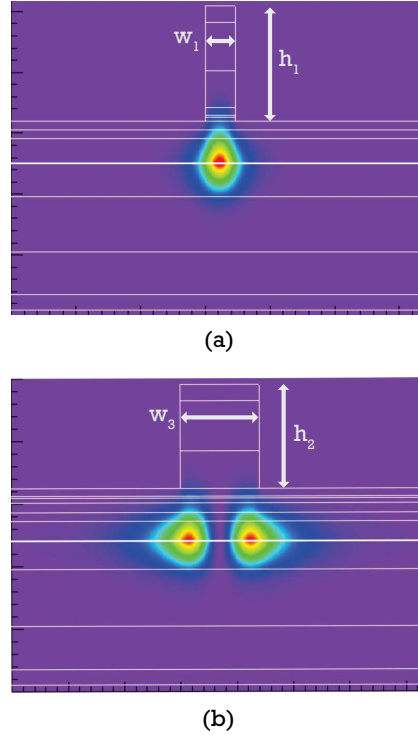


Figure 3.17: Structure XXL2029: (a) Fundamental TE_{00} Gaussian mode ($w_1 = 2.2 \mu\text{m}/h_1 = 1.9 \mu\text{m}$), (b) TE_{01} Gaussian mode ($w_3 = 7 \mu\text{m}/h_2 = 1.65 \mu\text{m}$)

etching depth h , the losses are reduced because the mode leaves the central highly-doped part of the waveguide. The far-field divergences are way smaller in the case of the Super-LOC compared to the historical structures, with ratios of far-field total amplitude at $1/e^2$ of $\Theta_{y_{\perp}}^{1/e^2}/\Theta_{x_{\parallel}}^{1/e^2} = 1.7$ for the first versus $\Theta_{y_{\perp}}^{1/e^2}/\Theta_{x_{\parallel}}^{1/e^2} = 4.3$ for the simple LOC. Thus, the Super-LOC would adequately release beam-shaping constraints in the OCFS prototype.

3.1.3.3 Longitudinal Design

Once a single mode behavior in the transverse section of the optical cavity is ensured, one has to deal now with the longitudinal mode behavior. Because of the cavity dimension $L \gg \lambda$, a huge number of Fabry-Perot modes can oscillate between the two mirrors. As pointed out in chapter 2, these modes have theoretically the same mirror losses α_m which makes the Fabry-Perot ridge laser highly multimode in practice (for a FWHM of gain bandwidth of 15 nm and a FSR of $\sim 0.050 \text{ nm}$, more than 300 modes are competing longitudinally). A way to select one of these mode against the others is to induce wavelength-dependent losses in the cavity: this can be done by introducing a periodical refractive-index perturbation in the cavity which will acts (intuitively speaking) as a diffraction grating filter that reflects some wavelengths in a specific bandwidth. Such Bragg reflector is a concept widely used in optics: alternating layers of materials of different dielectric constant are used to create energy *stop-bands* in which light cannot propagate/is reflected. For instance, dielectric mirrors that are deposited on semiconductors laser facets are used to create anti-reflective/high-reflectivity coatings. Fiber Bragg Grating are a type of single-mode fiber that uses a periodical variation of silica index, just as Distributed-Feedback lasers (DFB) and Distributed-Bragg Reflectors lasers

(DBR) [Buus 2005]. In these devices, the corrugation extends on a limited vertical dimension parallel to the layers, whereas in VCSELs, the whole structure is made of alternating thin material layers [Tourenco 2005, Laurain 2010]. In our case, the grating of the DFB is presented more in details in figure (3.18). The DFB behavior is well-understood for now 40 years, from the first

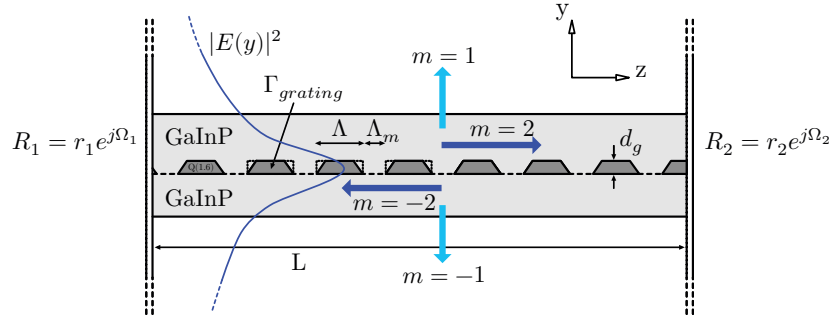


Figure 3.18: Schematic view of the 2nd-order grating area in the (y,z) plane.

theoretical description [Kogelnik 1972] and first practical realization [Nakamura 1975], it has become a widespread technology in the design of efficient single-mode lasers.

A/ Theoretical basis

Though simple at first glance, the modal behavior is complex and cannot be properly described by approximate general formula. Here, a single uniform grating of thickness d_g made of high refractive index Q(1.62 eV) buried in a GaInP waveguide is considered. It has a *period* Λ , an opening length Λ_m and the field has a local confinement Γ_g on the quaternary, small enough to consider the whole corrugation has a *perturbation* of the total field $E(y)$ in the cavity. The local y and z -dependent real refractive index writes:

$$n_R^2(y, z) = n_{R,eff}^2 + \Delta n_R^2 \times f(y)g(2\beta_0 z + \Omega) \quad (3.23)$$

where $n_{R,eff}$ is the mean effective index of the (transverse) mode with the corrugation replaced by an uniform layer, Δn_R the amplitude of the mean index change in the grating, f a function of x and g a periodic function of z , scaled by the Bragg propagation constant β_0 , with m the order of the periodic corrugation and $\Omega = \Omega_1 + \Omega_2$ a constant phase arising from the boundary phase conditions at each of the mirrors. The function $n_R^2(y, z)$ can be Fourier-expanded to give:

$$n_R^2(y, z) = \sum_{q=-\infty}^{\infty} A_q(y) e^{\frac{2jq\pi z}{\Lambda} + j\Omega} \quad (3.24)$$

which yields $\beta_0 = q\pi/\Lambda$, q an integer characterizing the order of the diffraction. The associated Bragg wavelength is:

$$\lambda_B = \frac{2\Lambda n_{R,eff}}{q} \quad (3.25)$$

One then looks for solving the 1D wave equation along z , with an expansion of the wave-vector $k(z) = kn_R(z)$ limited to the first Fourier terms thanks to (3.24):

$$\frac{\partial^2}{\partial z^2} \vec{E}(z) + k^2(z) \vec{E}(z) = 0 \quad (3.26)$$

$$k^2(z) = k_0^2 n_R^2(z) \approx \beta^2 + 2j\alpha\beta + 4\kappa_q\beta \cos(2\beta_0 z + \Omega) \quad (3.27)$$

In the above expression, α accounts for the net gain (reduced from the internal losses). The factor κ_q (in m^{-1}) is the so-called real *coupling factor* to the grating and scales the magnitude of the periodic corrugation influence on the unperturbed longitudinal mode solution. It is defined at order q by:

$$\kappa_q = \frac{k_0^2 \int_{grating} A_q(y) E_x(y) dy}{2\beta \int_{\infty} E_x(y) dy} \quad (3.28)$$

with k_0 the free-space wave-vector. In [Ghafouri-Shiraz 2004], the coupling factor is expressed with A_q for various corrugation shapes, thanks to a corrugation function $Z(y)$:

$$\kappa_q = \frac{k_0^2(n_2^2 - n_1^2)}{2q\pi\beta \int_{\infty} E_x(y) dy} \left| \int_{grating} \sin\left(\frac{2\pi q Z(y)}{\Lambda}\right) E_x^2(y) dy \right| \quad (3.29)$$

Usually, the corrugation is not strictly rectangular (see dotted shape in figure (3.18)) but rather trapezoidal due to the (dry) etching process that induces lateral attack of the material. For gratings realized by wet chemical etching, the shapes can even be triangular. This is why a more complete derivation of the coupling factor is presented here. In our case (figure (3.19)), the corrugation function is given by $Z(y) = w_T/2 + (w_z/d_g)(d_g - y)$. The κ_q expression can be simplified if considering that

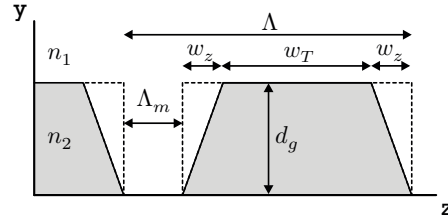


Figure 3.19: Schematic detail of the trapezoidal grating corrugation, defining the geometrical parameters d_g, w_z and w_T

the electric-field is almost constant in the layers. It is then straight-forward to integrate (3.29):

$$\kappa_q = \frac{k_0^2(n_2^2 - n_1^2)\Gamma_g}{2q\pi\beta} \left(\frac{\Lambda}{2q\pi w}\right) \left| \cos\left(\frac{q\pi w_T}{\Lambda}\right) - \cos\left(\frac{q\pi(w_T + 2w_z)}{\Lambda}\right) \right| \quad \text{if } w_z \neq 0 \quad (3.30)$$

$$= \frac{k_0^2(n_2^2 - n_1^2)\Gamma_g}{2q\pi\beta} \left| \sin\left(\frac{q\pi\Lambda_m}{\Lambda}\right) \right| \quad \text{if } w_z = 0 \quad (3.31)$$

The coefficient can be assimilated to a linear amount of reflection per unit length. To obtain coupling to the grating, we require a value of κ_q so that $\kappa_q \times L \sim 1$, meaning that the wave is completely reflected in the laser cavity after one trip. The only modes which are influenced by the grating are then those close to the Bragg condition (3.25) so that **the Bragg pitch Λ governs the single-mode emission frequency**. In practice, for near-infrared wavelength, at a grating order of $m = 2$, for an effective index of $n_{R,eff} \sim 3.24$, the corrugation pitch Λ is in the range of 275 nm . If $w_z = 0$ and $k_0^2(n_2^2 - n_1^2)/(2\beta) \approx (n_2 - n_1)/\lambda_B$ and for an *opening ratio* of the grating $r_g = \Lambda_m/\Lambda = 0.25$:

$$\kappa_{q=2} = \frac{\Gamma_g(n_2 - n_1)}{\lambda_B} \quad (3.32)$$

which is a classical formula for the square-shaped grating at maximum coupling efficiency. Nevertheless, in case of strong w_z value, the above formula is not accurate.

Finally, once the structural definition of κ is given, the resolution of (3.26) is easy (it is a very classical derivation there is no point to reproduce here): after [Streifer 1975], the solution has to be found as the sum of two counter-propagating plane-waves with z -dependent amplitudes S and R :

$$E_x(z) = S(z)e^{-j\beta_0 z} + R(z)e^{j\beta_0 z} \quad (3.33)$$

With:

$$R(z) = a_1 e^{\gamma z} + a_2 e^{-\gamma z} \quad (3.34)$$

$$S(z) = b_1 e^{\gamma z} + b_2 e^{-\gamma z} \quad (3.35)$$

$$\gamma^2 = (\alpha - j\delta)^2 + \kappa^2 \quad (3.36)$$

where a_1 , a_2 , b_1 and b_2 are complex constants, γ is the *complex propagation constant* of the mode and $\delta = \beta - \beta_0$ the *deviation* from the Bragg propagation constant. These parameters are found by imposing the boundary reflection conditions (defining implicitly the threshold condition). First, the propagation constant obeys the following complex transcendental equation in [Streifer 1975] (for an homogeneous grating only):

$$(\gamma L)^2 \left\{ (1 + r_1 r_2)^2 - 4r_1 r_2 \cosh^2(\gamma L) \right\} + (\kappa L)^2 \sinh^2(\gamma L) (1 - r_1^2)(1 - r_2^2) \quad (3.37)$$

$$+ 2j\kappa L(r_1 + r_2)(1 - r_1 r_2)(\gamma L) \sinh(\gamma L) \cosh(\gamma L) = 0 \quad (3.38)$$

As the left hand-side is helpfully an explicit holomorphic function $W(\gamma L)$, it remains to find the roots of W in the complex plan. The Newton-Raphson method can be used on both the real and imaginary parts of W , but MATLAB[®] has the powerful 'fsolve' function which handles complex roots. One has just to guess starting points in the plane, which are in practice disseminated to draw a 'star' centered on zero, so that we will converge to all the solutions of (3.37) within a given disc. It is worth to note that the gain and the phase conditions are one single intrinsic condition so the modal behavior of the DFB is not easily predictable at first sight. If $\kappa = 0$, we recover the Fabry-Perot condition which gives usually the starting trial points to solve for the general non-zero coupling equation. When all the sets of solutions $\{\gamma_i\}$ are found given the parameters (r_1, r_2, κ) , an inversion gives all the couples $\{(\beta_i, \alpha_i)\}$, that is, the wavelength and the net losses of each DFB mode around the Bragg wavelength λ_B . Also, the complex amplitudes R and S can be computed with relation to a unique constant, and so is the case for $E_x(z)$ and the intensity in the cavity $I(z) = |E_x E_x^*|$. This work is done to address the special case of the LAMA DFBs, where reflection coefficients and κ values are specific, and to give an estimation of the losses that will be used to compute the laser linewidth.

B/ Practical choice of the grating properties

At the beginning of this PhD work, a first fabrication of DFB at the D_1 and D_2 lines was based on the structures XXL2029 and XXL2020, with previous experimental well-known parameters for the latest. The effective index of the fundamental mode at $25^\circ C$ was experimentally found, thanks to the Bragg relation: $n_{R,eff} = 3.2645$ was guessed from the laser wavelength with a Bragg pitch of $\Lambda = 261 \text{ nm}$. However, with the previous data of material refractive indices for the optical cavity, the effective computed index was close to 3.29. Together with J. Lobé [Lobé 2015], we tried to find more accurate data that would fit better the experimental results, especially for the GaInP-LOC index which is critical. The use of Schubert's [Schubert 1995] measurements allowed to **reach a new accuracy on the 10^{-3} level** regarding the predicted value of the effective index and the measured one, which was also confirmed by far-field measurements close to the simulated one. As a consequence, particular attention had to be paid on grating's real coupling factor value, given that:

1. The GaInP index influences strongly the local confinement factor on the grating
2. The eBeam process of the grating leads to stronger coupling factors than for an holographic process, because of the aspect ratio of the Q(1.62 eV) material (see below)

Traditionally, within an holographic process, the second-order grating opening factor is equal to $r_g = 0.75$ while in the case of the III-V Lab e-Beam process, $r_g = 0.25$. This is bound to modify the local confinement Γ_g which is stronger in the second case. Figure (3.20) is the computation of the $\kappa_{q=2}$ for several structures and ridge w and etching h values. The formula of the ideal rectangular corrugation (3.32) was used in which the confinement factor was computed for an average refractive index $\bar{n}_g = n_{GaInP} * r_g + n_{Q(1.62\text{ eV})} * (1 - r_g)$. First, we can notice that the coupling factor is larger on the side $r_g < 0.5$ and maximum at around $r_g^{max} = 0.23$. Second, for the traditional structures, the prediction shows that $\kappa^{max} > 12\text{ cm}^{-1}$, which, in the worst case (XXL2020) corresponds to a confinement factor on the grating of $\Gamma_g = 1.2\%$ at the top of the arch. For the LOC(0.55 μm) which has a 0.55-thick half LOC cavity to reduce the confinement on the grating, and for the Super-LOC design, the maximum confinement is of $\sim 0.4\%$ which yields $\kappa \sim 7 - 8\text{ cm}^{-1}$. In the first case, for 2 mm-long devices, the normalized reflectivity $\kappa L = 2.4 - 4.8$ resulting in an over-coupling, while in the second case, $\kappa L = 1.2 - 1.6$, which is a more reasonable value to ensure proper single mode operation.

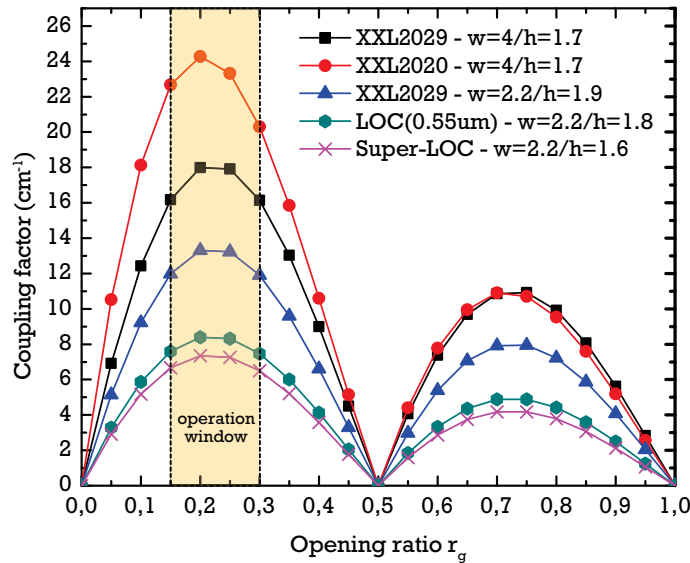


Figure 3.20: Computation of the coupling factor $\kappa_{q=2}$ for several structures and geometrical configurations of the waveguide, after the simple formula (3.32). The coupling value is higher for $r_g = 0.25$ compared to $r_g = 0.75$. A reduction of the ridge width w reduces the overlap of the fundamental mode on the grating, thus reducing the coupling

Finally, if an over-etching of the flanks of the corrugation leads to a trapezoidal form as in figure (3.19), we can expect that the coupling will drop of around 65% (not negligible) if $w = 20\text{ nm}$ and $r_g = 0.23$. This is why the etching process should keep the rectangular shape, or at least one should anticipate this drop in coupling by increasing the optical confinement on the corrugation: an increase of grating's thickness, or grating's cladding, and also a decrease of the distance from the grating to the active layer allow to play on this value. To conclude, if this model is correct, the traditional DFB

structures are not optimized to give reasonable coupling values with the e-Beam process: this is why the two new structures have been modified to correct this parameter. Of course, there remain an uncertainty on the $Q(1.62 \text{ eV})$ value of the refractive index of the grating, so a measurement of the coupling factor would be necessary to verify this prediction.

C/ Extension: optical matrices theory

The case of the conventional uniform DFB gives explicit and relatively simple analytical equations. Though, when non-uniformly periodic reflectors are used in the cavity, like in multi-section lasers, or multiple phase-shifted gratings, a more general technique is needed to find the threshold condition. The technique of the optical matrices can be employed: it consists in modeling all the longitudinal homogeneous sections by a two-by-two transfer matrix (two entries for incoming waves and two others for outgoing waves, as it is done classically in linear optics) and then multiply all these matrices between them to reconstruct the optical medium global transfer function. Such approach has not been used here because it was not necessary. However, a number of interesting examples of compound cavities, as well as sub and above threshold behavior modeling of single mode lasers can be found in [Ghafouri-Shiraz 2004]. It is also very useful for the design of DBR mirrors [Tourrenc 2005]. These last years, new optical designs have emerged in which strong perturbations in the longitudinal propagation are created by means of deep localized surface etching of Fabry-Perot lasers. It enables very efficient single mode emission, at a very reduced cost (Discrete Mode Lasers) [O'Brien 2005]. Such designs can be typically handled by the previous techniques.

3.1.4 Impact of the design on noise properties

We examine now the impact of the main DFB laser parameters (length, coupling factor, internal losses...) on the linewidth of the laser output. We will address first the photon noise (Schalow-Townes-Henry linewidth) and then the low-frequency technical noise which is predominant for the 'long-term' linewidth. No non-linear behavior has been taken into account (spatial hole burning), more complete treatments of the device like in [Wunsche 1993] would be required in that case.

3.1.4.1 What is the linewidth $\Delta\nu_{S-T-H}$ of DFB lasers ?

The linewidth of conventional DFBs has been predicted notably in [Kojima 1985, Ogita 1987, Ogita 1988]. If the resonator losses (equivalent to the mirror losses of the Fabry-Perot) are $\alpha_r = 2\alpha_{th}$ where α_{th} are the net threshold losses (the factor two comes from the definition of the gain relatively to the intensity, not the amplitude of the field), the linewidth is from (2.36):

$$\Delta\nu_{S-T-H} = K_P n_{sp} h\nu \frac{v_g^2 \alpha_r g}{4\pi P_{out}} (1 + \alpha_H^2) \quad (3.39)$$

On the other hand, the losses evolve like:

$$\alpha_r \sim \frac{1}{(\kappa L)^2 L} \quad (3.40)$$

which is valid in the limit $\kappa L \gg 1$. This (rough) global tendency shows that the linewidth decreases with increasing coupling and device length. However, these parameters cannot be too high, because they influence both the modal discrimination through the gain margin and drive the value of the external efficiency η_d of the device.

A/ Case with no reflectivities

Following what has been said in the previous section, the case with $R_1 = R_2 = 0$ and $\kappa L = 1.5$ is solved numerically. Figure (3.21) gives the useful (λ, α_r) diagram of the resonator losses in cm^{-1} versus the mode wavelength, derived from the (δ, α_{thr}) solutions of (3.37) for two cases:

1. $\kappa L = 0, R_1 = R_2 = 0.03$ which is the Fabry-Perot case with equal 3% reflectivities
2. $\kappa L = 1, R_1 = R_2 = 0$ corresponding to the conventional DFB laser in the limit of zero reflectivities

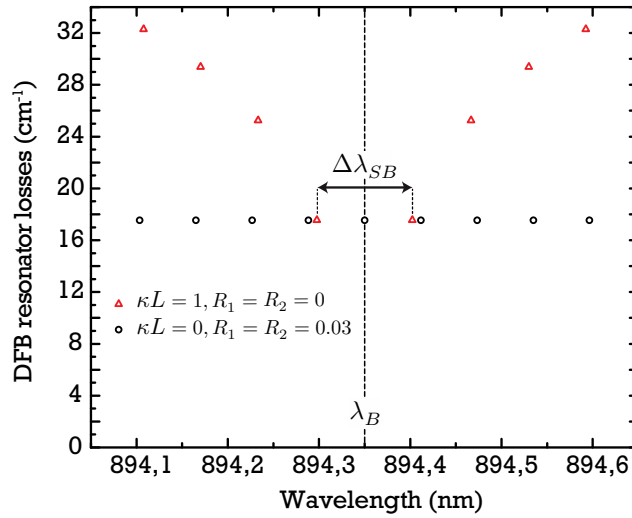


Figure 3.21: (λ, α_r) diagram of the modal solutions of the DFB equation (3.37), with $L = 2 \text{ mm}$, for a non-zero normalized coupling value κL (triangles), and for zero coupling (circles)

The solutions for the DFB illustrate the well-known result that single mode behavior cannot be achieved in this configuration: the modes have symmetrical locations by pairs of same resonator losses on each sides of a forbidden region centered on the Bragg wavelength, which can be defined as the 'stop-band' of length $\Delta\lambda_{SB}$. Outside this region, the DFB modes spacing is getting closer to the free spectral range of the equivalent Fabry-Perot of same mirror losses $\alpha_m = 17.5 \text{ cm}^{-1}$. A quantity called the *normalized stop-band* can be defined as:

$$NSB = \frac{\Delta\lambda_{SB}}{\Delta\lambda_{FP}} \quad (3.41)$$

Here, $NSB = 1.5$, giving a wavelength jump of around $\sim 0.1 \text{ nm}$ between the two edges of the stop-band. Solutions to achieve high gain margin between the two stop-band modes is for instance to break the symmetry of the solutions by applying different reflectivities on each sides of the cavity, or to allow a mode in the stop-band by introducing one or several phase-shifts in the cavity [Glinski 1986].

B/ General case

The high-reflectivity/anti-reflective configuration is chosen because it allows to collect more output power for the application. Though, the control over the emitted wavelength is more

difficult than in the telecom approach of a phase-shift in the middle of the cavity with symmetrical anti-reflective coatings that allow lasing at the Bragg wavelength. In the present case, the mode propagation constant can be very sensitive to the residual total phase Ω introduced by the grating. Figure (3.22) is the result of the mode computation from (3.37) for $\kappa L = 1 = 5 \text{ cm}^{-1} \times 0.2 \text{ cm}$, with $r_2 = \sqrt{0.95}$, $\Omega_2 \in [0, 2\pi[$ and a fixed $r_1 = 0$ in the first case, and $r_1 = \sqrt{0.03}$, $\Omega_1 = 0$ in the second case.

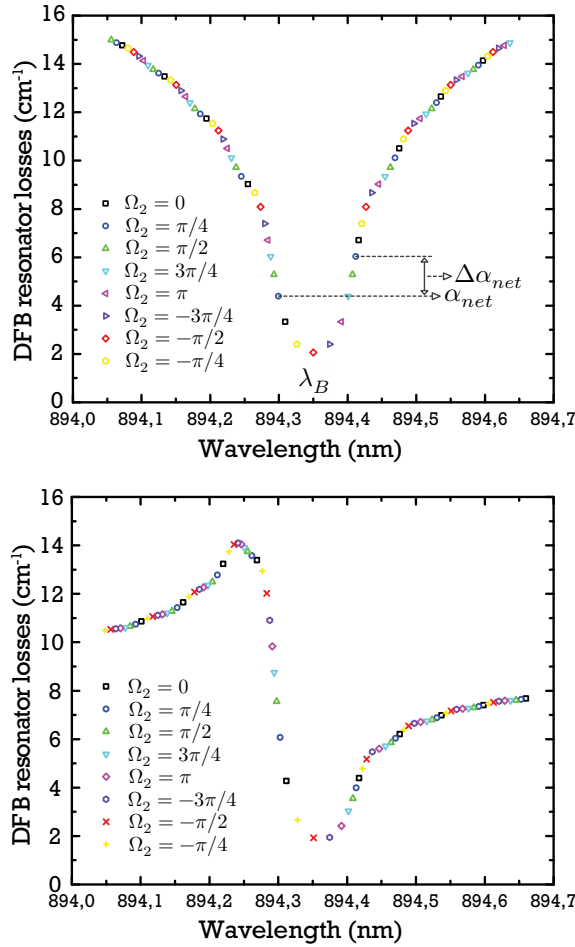


Figure 3.22: On top: Modal solutions for the case ($r_2 = \sqrt{0.95}$, $r_1 = 0$, $\Omega_1 = 0$) with various $\Omega_2 \in [0, 2\pi[$. Bottom: Modal solutions for the case ($r_2 = \sqrt{0.95}$, $r_1 = \sqrt{0.03}$, $\Omega_1 = 0$) with various $\Omega_2 \in [0, 2\pi[$

For the case with ideal (zero reflectivity) AR coating at the front facet, we can see that the solutions distribute along a symmetrical curve with relation to the Bragg wavelength. The worst configuration here is the case $\Omega_2 = \pi/2$ since then two symmetrical modes with the lowest equal mirror losses are situated on either sides of the stop-band. In contrast, the case $\Omega_2 = -\pi/2$ is very favorable to single mode operation with a loss margin of 6 cm^{-1} between the Bragg-centered solution and the next lower losses modes. Because the residual phase cannot really be controlled at the working wavelength (this requires to realize facet cleaving at a few tens of nm of precision in the grating), the yield of single mode DFBs with the required $SMSR$ is always less than 100%. A criterion for the net

gain margin $\Delta\alpha_{net}$ to reach a given $SMSR$ is [Buus 2005]:

$$\Delta\alpha_{net} \simeq \frac{SMSR(h\nu v_g)n_{sp}\alpha_r(\alpha_r + \alpha_i)}{P_{out}} \quad (3.42)$$

with $SMSR = 10^4$, $h\nu = 1.386$ eV, $v_g = c/n_g$, $n_g = 3.7$, $n_{sp} = 1.4$, $\alpha_r = 4$ cm⁻¹ and $\alpha_i = 2$ cm⁻¹, we get $\Delta\alpha_{net} = 0.08$ cm⁻¹ which is easy to obtain in the above configuration. In reality, the AR coating cannot be perfectly zero. For $R_1 = |r_1|^2 = 0.03$ which starts to be a high value, figure (3.22) shows clearly that the symmetry is broken and that the modes of lower energy, on the right of λ_B , have lower losses. For $\lambda \gg \lambda_B$ or $\lambda \ll \lambda_B$, the modes converge to the Fabry-Perot solutions of the cavity without the grating ($\alpha_m = 8.9$ cm⁻¹).

We can also vary the normalized coupling κL and examine both losses of the first lasing mode, the normalized stop-band around this mode and the net gain/loss margin. The results are summarized in table (3.10).

Parameters	α_{net} (cm ⁻¹)	$\Delta\alpha_{net}$ (cm ⁻¹)	\overline{NSB} (1)
$\kappa L = 0.5, R_1 = 0$	7.9 – 11.9 * 9.1	0 – 6.2 * 3.5	1.3
$\kappa L = 0.5, R_1 = 0.001$	7 – 10.9 * 9.2	0 – 5.7 * 3.1	1.3
$\kappa L = 0.5, R_1 = 0.03$	4.8 – 8.9 * 8.7	0 – 3.4 * 1.2	1.2
$\kappa L = 1, R_1 = 0$	3.8 – 7.3 * 5.3	0 – 6.5 * 3.6	1.5
$\kappa L = 1, R_1 = 0.001$	3.5 – 7.6 * 5.3	0 – 6.6 * 3.6	1.5
$\kappa L = 1, R_1 = 0.03$	2.6 – 7.2 * 6.1	0 – 4.5 * 2	1.2
$\kappa L = 1.5, R_1 = 0$	2 – 5.5 * 3.4	0 – 6 * 3.3	1.7
$\kappa L = 1.5, R_1 = 0.001$	2 – 5.5 * 3.5	0 – 6.1 * 3.3	1.6
$\kappa L = 1.5, R_1 = 0.03$	1.5 – 5 * 3.5	0 – 4.6 * 2.4	1.3

Table 3.10: Results of the computation of modal properties of the DFB for several coupling parameters. For the net resonator losses α_{net} (lowest resonator modal losses for a given configuration) and the net gain margin $\Delta\alpha_{net}$ (losses difference between α_{net} and the second lowest modal losses for a given configuration), the minimum, maximum and mean values are indicated [*min – max * average*], the NSB is the mean value of the quantity. The average is done on 8×8 phases configurations

The above study is modest compared to the analysis of the grounding articles cited, with relation to the various configurations of the DFB. Nevertheless, it highlights some interesting points with this AR-HR configuration:

- At a given κL product, the net losses amplitude decreases with higher reflectivity at the AR facet, lowering the probability of high SMSR (which can be explained roughly by the fact that Fabry-Perot modes competes more strongly with the grating modes, perturbing the single mode behavior)
- With a higher AR reflectivity, the amplitude of the fundamental mode losses decreases
- With decreasing κL , the mode losses increase and are more influenced by the AR reflectivity
- The normalized stop-band varies widely between 1 and 2

The effective yield is computed for each configuration (by averaging the above quantities on 8×8 couples (Ω_1, Ω_2)). [Jacquet 1990] looked comprehensively at the single mode properties of various DFB

configurations and predicted that the optimum to maximize $\Delta\alpha_{net}$ for the AR-HR is for $\kappa L \in [1, 1.5]$. The previous table gives at least the most interesting point which is an estimate of the resonator losses attainable. For $\kappa L = 1.5$ with $L = 2 \text{ mm}$, $\alpha_r \sim 3.5 \text{ cm}^{-1}$: this value starts to be quite low, given the estimated theoretical magnitude of the internal losses $\alpha \sim 2 \text{ cm}^{-1}$. To reduce the losses further, a product κL kept constant with lower coupling and higher length is more interesting. In our case, the actual 2 mm will be chosen, because higher lengths are not necessarily a good option for a high fabrication yield on the wafer... Also, a new structure as the Super-LOC makes sens in this context, because the reduction of internal losses from 2 cm^{-1} to 1.3 cm^{-1} could help to achieve roughly +16% on the external efficiency.

To evaluate the linewidth, we set the same parameters as in (3.42) with $\alpha_H = 2.5$ and $K_P = K_{tr}K_z$. The transverse astigmatism factor is equal to 1 for perfect index guiding (but increases in gain guiding mechanisms, for instance with a weak lateral index confinement in the ridge: this is an additional argument for optimized etching of the waveguide) which is the case we are looking for, and the longitudinal factor can be computed with the formula [Petermann 1979]:

$$K_{tr} = 1 \quad (3.43)$$

$$K_z = \left| \frac{\int |E(z)|^2 dz}{\int E(z)^2 dz} \right|^2 \quad (3.44)$$

For $\kappa L = 7.5 \text{ cm}^{-1} \times 2 \text{ mm} = 1.5$ we get $K_z \in [1, 3.4]$ and $\overline{K_z} = 1.38$ with $R_1 = 0.03$ and $R_2 = 0.95$ (table (3.11)). Petermann's enhancement factor increases with decreasing coupling coefficient value and decreasing AR reflectivity. It is also slightly enhanced with shorter cavity lengths. This observations are in agreement with [Wang 1987]. If the enhancements factors are set to $n_{sp}K_z =$

Parameters	$\overline{K_z}$
$\kappa = 2.5 \text{ cm}^{-1}, L = 2 \text{ mm}, R_1 = 0.03$	1.93
$\kappa = 5 \text{ cm}^{-1}, L = 2 \text{ mm}, R_1 = 0.03$	1.72
$\kappa = 7.5 \text{ cm}^{-1}, L = 2 \text{ mm}, R_1 = 0.03$	1.38
$\kappa = 7.5 \text{ cm}^{-1}, L = 2 \text{ mm}, R_1 = 0.001$	1.75
$\kappa = 10 \text{ cm}^{-1}, L = 1.5 \text{ mm}, R_1 = 0.03$	1.4

Table 3.11: Theoretical values of the longitudinal K_z factor computed with (3.43) from the values of the electrical field according to the coupled-mode theory ($R_2 = 0.95$). The average value is taken on 8×8 phases configurations

$1.4 \times 1.38 \sim 2$ for $\kappa L = 1.5$ and $(1 + \alpha_H^2) = (1 + 2.5^2) = 7.25$, the numerical expression of the linewidth is then:

$$\Delta\nu_{S-T-H} = 16.8 \text{ W.cm}^2.\text{Hz} \times \frac{\alpha_r(\alpha_r + \alpha_i)}{P_{out}} \quad (3.45)$$

If $\kappa = 7.5 \text{ cm}^{-1}$, $L = 2 \text{ mm}$, $\alpha_r \in [1.5, 5] \text{ cm}^{-1}$, $\alpha_i = 2 \text{ cm}^{-1}$ and $P_{out} = 40 \text{ mW}$, $\Delta\nu_{S-T-H} \in [2.5, 15.8] \text{ kHz}$. Such values are very low. We will see in the chapter on linewidth metrology that for 2 mm-XXL2029 DFB lasers, an intrinsic linewidth of 90 kHz is found from the white noise floor of the frequency noise measurements at 40 mW output power, with an estimated $\kappa L = 1$. Thus, the previous figures are under-estimated, but the order of magnitude is roughly consistent. If the α_H is closer to 3.5, or the n_{sp} factor higher, or the coupling factor less than computed, the linewidth will be

closer to the experimental value. Though, it is usually difficult to predict with a factor better than 2. If we adopt the other point of view with the cold-cavity linewidth, we can define an equivalent $\Delta\nu_{c,eq}$ (the internal losses are not negligible compared to the resonator losses so the definition must be adapted):

$$(\Delta\nu_{c,eq})^2 = \left(\frac{1}{2\pi\tau_{c,eq}} \right)^2 = \frac{1}{\pi} \frac{v_g^2 \alpha_r (\alpha_r + \alpha_i)}{4\pi} \quad (3.46)$$

which yields $\Delta\nu_{c,eq} = 6.3 \text{ GHz}$ (for the same parameters as before and $\alpha_r = 4 \text{ cm}^{-1}$), a value close to the one of a Fabry-Perot laser with cleaved facets. What is worth to notice is that the linewidth scales with the square of the losses, while it decreases only linearly with the power. Rather opposite strategies can be used to reduce $\Delta\nu$: either we stay in the 'high' κ regime to decrease the resonator losses, at the expense of a lower longitudinal spatial hole burning threshold which will prevent us to reach high single mode output power (both for questions of external efficiency decrease and stability of longitudinal carrier distribution clamping) or conversely, we keep low κ values and try to store more photons in the cavity with higher output power. In all cases, long devices favor a low noise operation, with a total dependency of the S-T-H linewidth $\propto L^3$. The intermediate optimization would be to keep reasonable cavity length around $2 - 2.5 \text{ mm}$ while trying to reduce the internal losses to prevent the external efficiency decrease. From that point of view, the Super-LOC design would help to win on all counts.

We choose to keep a normalized coupling at around 1.5. Indeed, we believe that such value of the parameter could help to strengthen the device's resistance to perturbative *feedback* (see dedicated section).

3.1.4.2 Technical noise in the device: the 1/f low-frequency noise source

A/ Theoretical background

In chapter 2, we have seen that a linewidth floor is observed at 'high' output powers, in contradiction with the Schawlow-Townes-Henry model. Apart from spatial hole burning implying to take into account an effective linewidth enhancement factor, it is usually due to 'technical' noise sources, meaning that it originates from the technical realization of the laser. In our monolithic cavities, they are of three types. These sources usually turn into frequency noise through more or less complex mechanisms that will be described in chapter 4 and 5. For the time-being, they are just given as such:

- The fundamental thermal noise (or Johnson-Nyquist's noise) due the series resistance of the device R_S of temperature T , has a spectral density of voltage fluctuations (in $V^2.Hz^{-1}$):

$$S_V = 4k_B T R_S \quad (3.47)$$

Before going back precisely to the definition of S_x , we can roughly state that the dispersion Δx of the quantity x during a time Δt due to random fluctuations is given by $\Delta x \sim \sqrt{S_x \Delta f}$ with f the Fourier frequency of observation and $\Delta f \sim 1/\Delta t$, for a small bandwidth Δf . This white noise source is very quiet in a semiconductor laser given the magnitude of the resistance ($\sim 1\Omega$) and the other noisier sources: it will be neglected (see chapter 4 where the relationship between the electrical noise and the frequency noise is clarified).

- Mechanical fluctuations of the cavity length: they recover all the perturbations of the optical path $n_g L$. The intrinsic fluctuations of the semiconductor length with temperature is negligible:

for a *coefficient of thermal expansion* for GaAs of $CTE_{GaAs} = 6.9 \text{ ppm.K}^{-1}$ and a length of 2 mm , the expansion is $\Delta L \sim 14 \text{ nm.K}^{-1}$. For a Fabry-Perot configuration, this yields a change of *FSR* of $\Delta\nu = 14 \text{ kHz.K}^{-1}$. In practice, the temperature is controlled at better than 10^{-3} which makes this change non-significant. However, another configuration is critical: when the laser is put intentionally or non-intentionally (parasitic back-reflexions in the optical setup) in a longer external cavity for which the total length fluctuates (for instance, by acoustic waves which modulate locally the refractive index, or by physical vibrations of the output mirrors) then noise in the long-time scales (1 to 10 *ms*) is added. This will be addressed further on the optical feedback section [3.1.4].

- External thermal perturbations: the tuning coefficient of the refractive index with temperature is high enough to drive strongly the output laser frequency at $\sim 25 \text{ GHz.K}^{-1}$. In fact, an active control of the temperature at better than 10^{-4} is required for the targeted applications.
- The intrinsic electronic noise of the semiconductor junction: it is the purpose of this section

The very first fundamental mechanism of electronic noise is the *shot-noise* arising from the discontinuous nature of the carrier injection in the crystal lattice (its spectral density characteristics will be given in chapter 4). Then, other local current flow modulation exists, and originates from the properties of the conductive medium. We address briefly the topic of low-frequencies perturbations in solids, a vast issue which encompasses different noise mechanisms and is still controversial. We will show in the second part of the manuscript that it is the limiting source of noise in our DFB lasers.

This source is named so because it has a time-dependent magnitude of its fluctuations which grows as the time-scale becomes larger. It is superficially explained as an effect of carrier current modulation through the heterojunction as a whole for the case of the p-n junction, including all its conductive parts (with the contacts). In the early 70's, the group of Eindhoven and others have highlighted the broad presence of this noise in the voltage fluctuations in thin film metals, transistors or simply in semiconductors bulks. Extensive reviews of these experiments can be found in [Hooge 1981, Dutta 1981]. The first controversy appeared when they tried to discriminate whether it was a surface phenomenon (McWhorters's theory) or a bulk effect. In the first case, a trapping/detrapping effect of carriers at the surface states (created for instance in oxidized surfaces) was put forward. In the other case, the bulk conductivity σ is said to be affected by low-frequency noise. As it writes $\sigma = en\mu$, the question of whether it is the carrier density n that fluctuates or the mobility μ itself is an opened question and still not resolved, though proofs are accumulated in favor of the second option [Chen 1997]. F.N. Hooge was the first to summarize the experimental results of the literature on the topic by proposing an empirical law (3.48) which reads [Hooge 1994]:

$$\frac{S_R}{R^2} = \frac{S_V}{V^2} = \frac{S_I}{I^2} = \frac{\varepsilon_H}{Nf^a} \quad (3.48)$$

It states that the normalized spectral densities of the dynamical resistance R , voltage V or current I are all proportional to $1/f$, f being the Fourier frequency. The power law exponent is generally in the range $a \in [0.8, 1.4]$. The two constants ε_H (it was originally named ' α ' by Hooge but we change this denomination here to avoid confusion with Henry's factor) and N are respectively the so-called Hooge's constant and the *number* of electrons in the sample observed. The last point is crucial: it implies that the magnitude of the noise is inversely proportional to the volume of the device. The above relation is to be used as a fitting law of electrical noise measurements, as it will be done in

chapter 4. The measured Hooge's constant ε_H has a further expression (3.49):

$$\varepsilon_{H,meas} = \left(\frac{\mu_{meas}}{\mu_{latt}} \right)^2 \varepsilon_{H,latt} \quad (3.49)$$

The constant $\varepsilon_{H,latt}$ is material-dependent and captures the crystalline quality of the semiconductor lattice. It is usually in the range of 10^{-5} to 10^{-3} , decreasing with increasing epitaxial quality. The mobility μ_{latt} is the one of the crystal lattice alone, while μ_{meas} is the total mobility measured (lattice+doping impurities). As Hooge underlines, in the mobility fluctuation model, it is only the lattice, through some fluctuations of the phonon numbers, that is responsible for the noise, not the doping (a high purity lattice will have a reduced number of phonon modes). We can notice also that **the noise will decrease with decreasing mobility of carriers**, which is the case when the doping level is increased. There is in particular no theoretical or experimental dependency of the factor with the temperature.

The other model, the number fluctuation one, is worth to mention because it is based on a well-identified noise mechanism called *generation-recombination* noise (*G-R* or telegraphic noise). Basically, it occurs when a trapping-detrapping process with a constant τ , in deep impurity levels for instance, modulates in a binary way the current flow, that would be otherwise *shot-noise* limited (figure 3.23): The associated spectral density of noise has a Lorentzian form [Hooge 1994]:

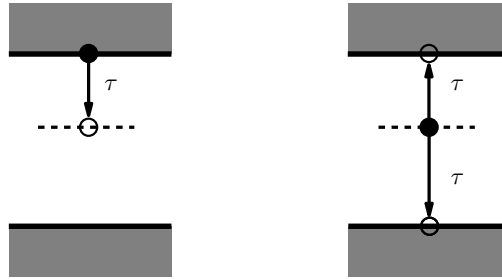


Figure 3.23: Illustration of the Generation-Recombination mechanism in a deep (in the middle of the gap for instance) discrete electronic level

$$\frac{S_R}{R^2} = \frac{\overline{\Delta N^2}}{N^2} \frac{4\tau}{1 + (2\pi\tau f)^2} \quad (3.50)$$

$$\frac{1}{\overline{\Delta N^2}} = \frac{1}{N} + \frac{1}{X_n} + \frac{1}{X_p} \quad (3.51)$$

with X_n the average number of occupied traps and X_p the average number of empty traps. This noise can be detected quite easily in the spectral density of noise because it provokes a 'bump' at the characteristic frequency $f_0 = 1/\tau$. The number theory assumes that the $1/f$ slope arises from the sum of several of these G-R spectra, created on a wide range of τ constants of independent traps which would be linked to a broad range of trapping energies. No clear experimental evidence of that has been brought to light though. Whatever the origin of (3.48), a puzzling consequence of the relation is that the magnitude of the noise does not converge when $t \rightarrow \infty$! Actually, this would also imply that the time of the observation is infinite, which is never the case, so we are bound to cutoff the long-time limit in the computation of laser noise. This will have profound consequences on the linewidth estimation from the frequency noise, as we will see in chapter 5. Also, the a

priori non-stationary behavior of this noise raises also issues in the way the literature computes this linewidth. To conclude, we shall mention that the $1/f$ phenomenon is not limited to this topic, but extends to the physics of criticality, where a scale-invariance takes place, like in phase-transitions as described in statistical mechanics [Christensen 1992]. According to these speculations, the $1/f$ in the semiconductor matrix would involve a memory process in which the further behavior of the electrons is dependent on its history in the crystal. On the specific issue of $1/f$ noise in lasers, the work of the group of the university of Montpellier [Signoret 1994, Signoret 1995, Daulasim 1994, Orsal 1994] used the equivalent noise circuits to explain the experimental characteristics of electrical and amplitude noise of various types of lasers.

Practically, for us, we will keep in mind the following facts about the above:

- The $1/f$ spectra in *unavoidable*, but its magnitude can be reduced by high-quality epitaxy and a clean technological process (perfect ohmic contacts), and deep-center free materials (for the G-R noise)
- An increasing volume of the device should decrease the magnitude of this noise (this point is seen in more details now)
- Hopefully, the low-frequency noise can be suppressed partly by actively regulating the device current with servo loops (see chapter 6)
- The noise models presented concern the *electrical* characteristics of a device. For the laser, the impact of these fluctuations on the frequency noise of the output is not trivial and requires a model with grounding hypothesis of the exact origin of the modulation in the device, which can change from one type of technology to another

Experimentally speaking, we will try to extract the Hooge parameter from the electric noise characterizing our technology quality.

B/ Effects of device's dimensions

According to Hooge's law, the spectral density of current noise should evolve like $1/N \propto 1/V$. The volume V being equal to $V = (w \times d) \times L$ with d the layer thickness, the number of electrons is $N = n \times V$ (the mobility of holes is at least ten times smaller than for electrons so the Hooge constant of the p-side will be neglected). If the thickness of the active zone is $d_{QW} = 8 \text{ nm}$ and the thickness of the SCH n-side is $d_{SCH} \sim 1 - 2 \text{ }\mu\text{m}$ which we assume homogeneous, the electron surface density is respectively $N_{QW} = 4.10^{18} \times d_{QW} = 3.2 \times 10^{12} \text{ cm}^{-2}$ and $N_{SCH} = 10^{17} \times d_{SCH} = 1.8 \times 10^{13} \text{ cm}^{-2}$. Also, the mobility in the active zone is estimated to be six-times the one of the SCH, as there is no doping (so the Hooge's constant is the lattice constant, while the SCH constant is multiplied by 6^2). Roughly, the noise magnitude in the active zone can be supposed to be two orders higher than in the SCH. This holds only if the lattice constant $\varepsilon_{H,latt}$ is the same for all materials, which is not evident, the GaInP/AlGaInP layers are said to have disordered phases that could enhance this factor. Also, there still could be the issue of excess noise in the Schottky contact on the n-side. If we examine the effects of the geometry on the power of the fluctuations, if the mirror losses are kept constant in the DFB, the current threshold density J_{th} stays constant for the active zone and so is the electron number N , whatever the length. This is the same for the guide width w . As a consequence, **increasing L is beneficial to reduce the $1/f$ effects** (w is set by the higher lateral modes cutoff, and because of the lateral current spreading, it is not clear that a ridge widening would be efficient to increase the active zone volume).

3.1.5 A feedback resistant design ?

The issue of the perturbations of the laser operation induced by optical back-reflections in the device is of enough importance for the OCFS to dedicate a section about it. It has been observed during tests of the clock's prototypes that it could cause the laser to de-lock abruptly from the cesium line, when the optical bench was submitted to acoustical perturbations with commercial 852 nm modules from other providers for instance. External optical feedback effects in semiconductor sources is a complex topic that involves all the fundamental statical and dynamical parameters of the device in the case of a laser. We will consider only a 'weak' coupling, where unwanted small-magnitude back-reflections of light into the cavity occurs from distant reflecting surfaces along the optical setup for instance (figure (3.24)). The strong-coupling configuration corresponding to intentional external cavities used to increase deeply the photon lifetime and narrow the spectral linewidth will not be treated here. Here

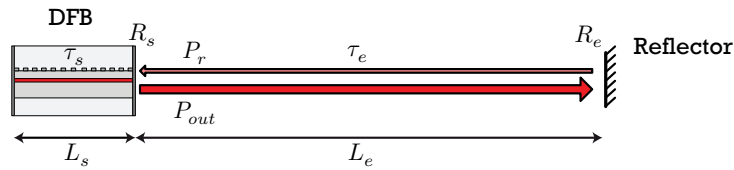


Figure 3.24: Schematic representation of the weak feedback configuration. The photon round-trip internal round-trip τ_s is way smaller compared to the external parasitic cavity round-trip time τ_e

we consider that an amount of reflected power P_r from a distance L_e of a reflector of R_e is re-injected into the laser cavity of length L_s , front-facet reflectivity R_s that has an output power P_{out} . The feedback ratio is defined as:

$$f_{FB} = \frac{P_r}{P_{out}} \quad (3.52)$$

If the re-injection is made with no losses, then $f_{FB} = R_e$ simply, but it is usually not the case. It is often given in dB , which is done from now on. Due to the non-zero value of the external reflectivity R_e and length L_e , there exists a photon round-trip time τ_e in the external cavity different from the laser photon round-trip time τ_s and, because of the non-one reflectivity R_s , the photon laser-lifetime (linked to the losses) is changed to an effective lifetime $\tau_{\gamma,eff}$, which depends also on the *phase* ϕ_e of the reflection. For the case of a DFB laser, the front facet reflectivity $R_s = R_{eff,DFB}$ is the effective reflectivity, that depends both on the AR coating and κL . Then, the effective resonator losses of the laser $\alpha_{r,eff}$ are modified, impacting in turn the threshold gain. So at first order, the effect of the feedback is to modify the threshold current, hence the optical power. Experimentally, we find variations of about 2 – 3% in the power. Further, at the second order, the statical noise properties are modified, i.e. the laser linewidth is impacted.

The feedback dynamics is well described by the Lang-Kobayashi model [Lang 1980]. Later, [Tkach 1986] found that five distinct regimes could be identified in monolithic semiconductor lasers, that appear at growing f_{FB} values:

- Regime I: The linewidth increases or decreases with the feedback phase, it is sensitive to both L_e and ϕ_e , in a range of very low f_{FB} values down to -80 dB . However, the laser remains single mode
- Regime II: The same behavior as for regime I is observed, however, the laser suffers now from mode hopping

- Regime III: The laser stabilizes back to a single-mode regime with a narrower linewidth, independently of L_e or ϕ_e
- Regime IV: The laser enters the *coherent collapse* regime where it loses a lot of its coherence properties: the linewidth broadens up to several GHz .
- Regime V: Intentional feedback: the laser is single mode, operating in the usual external cavity regime, with a very narrow linewidth proportional to the inverse of the total photon lifetime (so of length L_e).

Figure (3.25) reproduces the feedback regimes map. It shall be noticed that the f_{FB} values at the frontiers are only indicative of the order magnitude and changes with the geometry and type of laser. The crossing of the boundary from region I to region II is given by the condition $X > 1$, with X

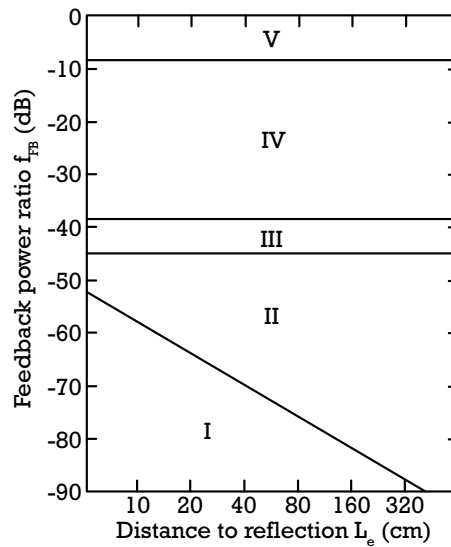


Figure 3.25: Mapping of the feedback regimes in the (L_e, f_{FB}) diagram. After [Tkach 1986]

expressed by (3.53):

$$X = 2|C| \frac{\tau_e}{\tau_s} \sqrt{f_r} \sqrt{1 + \alpha_H^2} \quad (3.53)$$

The round-trip time coefficients are also written $\tau_e = 2L_e/c$ and $\tau_s = 2n_g L_s/c$. Thus, it is clear that the limit from the single-mode domain to the instable mode-hopping one is strongly driven by the distance to the external reflector. If the optical bench has a maximum length of L_e , the boundary of instability can be repelled with the use of longer lasers. The coefficient C is called the complex feedback coefficient (which can be defined for each facet, but we are interested on the AR side) which only depends of the internal parameters of the device. For a Fabry-Perot laser, it has been explicated in [Tkach 1986]. Later, with the work of F. Favre and F. Grillot, it has been expressed theoretically in [Favre 1987] and generalized in [Grillot 2004] for DFB lasers:

$$C_{FP,s} = -\frac{1 - R_s}{2\sqrt{R_s}} \quad (3.54)$$

$$C_{DFB,s} = \frac{2(1 - |r_s|^2)e^{-j\Omega_s(\kappa^2 + q^2)L^2}}{j\kappa L(1 + r_s^2) - 2r_s q L} \left[2qL - \sum_{k=s,2} \frac{(1 - r_k^2)\kappa L}{2jqLr_k + \kappa L(1 + r_k^2)} \right]^{-1} \quad (3.55)$$

For the DFB, the writings are the same as in the previous section, with $r_k = \sqrt{R_k} e^{j\Omega_k}$ the amplitude reflectivity of the facet k . The reduced propagation constant is $q = \alpha - j\delta$. The coefficients have been expressed here for $k = s = 1$ (AR facet) which is the most sensitive to feedback effects. For instance, the cleaved-cleaved Fabry-Perot has a feedback coefficient of $C_{FP} = 0.68$. For the DFB, one has just to use the propagation solutions of the previous section to compute the $C_{DFB,s}$ number. From a qualitative point of view, we learn that a device is all the more (intrinsically) feedback resistant so since it has high mirror reflectivities, which is intuitively satisfactory (the cavity is closed to external re-injection). With (3.53), it is clear that the region II boundary is repelled with decreasing C , shorter external parasitic cavities, smaller Henry's factors and longer devices. The C parameter also drives the boundary of the coherent collapse regime Γ_c [Grillot 2003]:

$$\Gamma_c = 10 \log \left(\frac{\omega_r^4 \tau_s^2}{16|C_s|^2(1 + \alpha_H^2)\omega_d^2} \right) \quad (3.56)$$

Two important quantities appear in this expression: the carriers resonance pulsation ω_r and the damping pulsation ω_d given by [Coldren 2012]:

$$\omega_r^2 = \frac{\Gamma v_g}{e} \frac{dg}{dn} \eta_i \frac{(I - I_{th})}{V} \quad (3.57)$$

$$\omega_d = K\omega_r^2 + \gamma_0 \quad (3.58)$$

with V the volume of the active region, $K \in [0.1, 0.5]$ ns and γ_0 (neglected) two constants : the first characterizes the damping at the resonance frequency (it scales with the photon lifetime τ_γ) while the second is an offset parameter essentially important at low optical power (proportional to the inverse of the differential carrier lifetime $\tau_{\Delta N}$ and the number of photons in the cavity). The formula (3.56) holds for $\Gamma_c < 30$ dB and $\omega_r \tau_s, \omega_d \tau_s \ll 1$. For $L_s = 2$ mm, $\tau_s = 49$ ps and experimentally we find ω_r, ω_d in the range of ~ 12 GHz. So the value of Γ_c is mainly driven by the internal round-trip time τ_s and the magnitude of C_s . Another interesting formula states that the minimum and maximum excursion of the linewidth below the coherent collapse regime and the maximum linewidth in the collapse regime are given respectively by:

$$\Delta\nu_{R<IV} \in \left[\frac{\Delta\nu_0}{(1 + X^2)}; \frac{\Delta\nu_0}{(1 - X^2)} \right] \quad (3.59)$$

$$\Delta\nu_{R=IV} = \ln 4 \sqrt{1 + \alpha^2} f_r \quad (3.60)$$

with $\Delta\nu_0$ the non-perturbed linewidth. The conclusion is the following: increasing the device length L_s and decreasing the C_s value reduce the linewidth fluctuations in the weak feedback regimes. It also allows to repel the coherent collapse threshold.

Two configurations shall be discussed: first, the effects of the coupling coefficient value κL on the C_s value, all other things being equal. Second, the effects of the random value of the phase at the AR facet, for a given value of R_s . The two points have been addressed in [Grillot 2003, Grillot 2009]:

- For the first point, the C_s coefficient and the collapse threshold Γ_c are respectively decreased and increased with growing values of κL . For a $R_s = 0$ configuration, the threshold is increased by 25 dB from the value $\kappa L = 0.3$ to $\kappa L = 1.2$. Also, the authors note that the threshold is maximum at the Bragg wavelength. Any deviation $|\delta| > 0$ decreases symmetrically the Γ_c on each sides of the stop-band (up to 5 dB for $|\delta| > 2$), especially for high κL

- On the other side, the random facet phases spread the threshold values in a certain range, which extends for increasing R_s values. For instance, the authors shows that for $\kappa L = 0.3$ and $R_s > 10^{-3}$, the threshold varies in a range of 5 dB. Though, for higher couplings, such variation seems to be less pronounced

We would have intuitively thought that choosing a high AR coating $R_s = 0.03$ would have provided additional immunity to external feedback. To test this hypothesis, the above parameters have been computed for our DFB. The results are summarized in table (3.12): The conclusion is

Parameters	$\overline{C_s}$
$\kappa L = 0.5, R_s = 0$	3.7
$\kappa L = 0.5, R_s = 0.001$	3.9
$\kappa L = 0.5, R_s = 0.03$	3.1
$\kappa L = 1, R_s = 0$	1.5
$\kappa L = 1, R_s = 0.001$	1.5
$\kappa L = 1, R_s = 0.03$	2.7
$\kappa L = 1.5, R_s = 0$	0.8
$\kappa L = 1.5, R_s = 0.001$	0.8
$\kappa L = 1.5, R_s = 0.03$	0.9

Table 3.12: Computation of mean the feedback coefficient C_s over 8×8 phases configurations, for several DFB parameters configurations using (3.37) and (3.54). A lower C_s characterizes a higher resistant to external feedback

that increasing the R_s value in the range indicated does not increase the resistance to feedback, which stays quite constant, especially for the case $\kappa L = 1.5$, for which the feedback coefficient is almost 5-times less than for $\kappa L = 0.5$. For instance, from (3.53), the $X > 1$ boundary is set by $f_{FB} > -47$ dB for $L_e \sim 10$ cm, $\alpha_H = 2.5$ in the strong coupling case, while it is $f_{FB} > -60$ dB for the weaker κ .

To conclude, the relevance of the above could be called into question if considering that it could be simply solved using *optical isolators* that can extinct back-reflections up to -70 dB. First, those elements are costly and bulky at the wavelengths of interest. Furthermore, they proved to be difficult to use in practice in the optical bench, a slight misalignment inducing light reflections from the isolator's surface, perturbing the locking on the atomic lines ! One then could think to 'tilt' all optical elements of the bench, as it is usually done in noise measurement setups, up to the very first collimating lens right after the laser module. This is not optimum though. Thus, we believe that keeping high coupling factor and laser length values, which works, after all, for the reduction of the resonator losses, is an additional point in favor of this parameter for the application. Also, when the laser is integrated in the housing of the module, the beam goes out from a small window that has and AR coating, which does not go below 0.1%. Back-reflections can then influence the linewidth of the device. If the facet is 100 μm away from the window and if the feedback ratio is of about $f_{FB} = 0.5\%$, the X coefficient is very small, so no real influence of the feedback is observed because the external cavity is very small. Aside from the theoretical study, we can imagine simply why it was observed, as said at the beginning, de-locking of the electronics. With a distant reflector $L_e = 100L_s$, the linewidth can broaden in the best case, which results in a loss of signal from the Cesium and a break-out of the servo loop, or more catastrophically a multimode operation in region II. If the coherent collapse regime is reached, it is

obvious that the clock cannot be operated anymore. A low C_s value can avoid the critical boundaries to be crossed.

3.1.6 Summary of the relevant design parameters

To sum up, table (3.13) recaps the main laser design parameters chosen for the application as well as their typical values to implement.

Parameter	Index step	Ridge width	Length	Grating Coupling	Facets Reflectivities	Feedback coefficient
Symbol	Δn_R	w	L	κL	$R_2 - R_1$	C_s
Value	4×10^{-3}	$2 - 2.5 \mu m$	$2 - 2.5 mm$	1.5	95% - 0.1%	< 1
Effect	Lateral mode stability	Lateral single mode	Low resonator losses / Reduced electronic noise	High SMSR	High SMSR	Resistance to feedback
Section reference	[3.1.3.2]	[3.1.3.2]	[3.1.4]	[3.1.4.1]	[3.1.4.1]	[3.1.5]

Table 3.13: Summary of the main design parameters highlighted in chapter 3, with the corresponding values recommended for the application

3.2 Technical realization

This section focuses on the practical aspects of the laser module fabrication regarding the design that has been previously investigated and defined.

3.2.1 Epitaxial growth

All the semiconductor structures have been realized using Metalorganic Vapor Phase Epitaxy (MOVPE) [Stringfellow 1999]. This technique consists in growing III-V materials on a heated GaAs buffer wafer with a mix of gas flows regulated in pressure. The typical precursors are TMGa (trimethylgallium), TMIIn (trimethylindium) and TMAI (trimethylaluminum) for the V-group and AsH₃ (arsine) and PH₃ (phosphine) for the III-group. The dopants are added with the injection of TMZn (p-type doping) and TMSi (n-type doping). All the species are transported with the help of an hydrogen vector flow. The typical temperature of growth is 600°C, but it varies with the alloy to grow (figure (3.26)).

The MOCVD technique is a standard one which is suitable for an industrial production of wafers, with its capacity to grow many satellites at the same time with excellent reproducibility. The growth is also fast compared to other techniques like Molecular Beam Epitaxy (MBE) (it scales in μm per hours). The technological process is realized, in our case, on 2'-wafers, in a Aix200/4 series of AIXTRON. Aside from the bulk materials, it allows also to realize the quantum well structure which needs sharp transition at the interfaces. As a first step, calibration structures of these wells are realized to target the desired photoluminescence wavelength. Figure (3.27) shows the characterization, under low optical

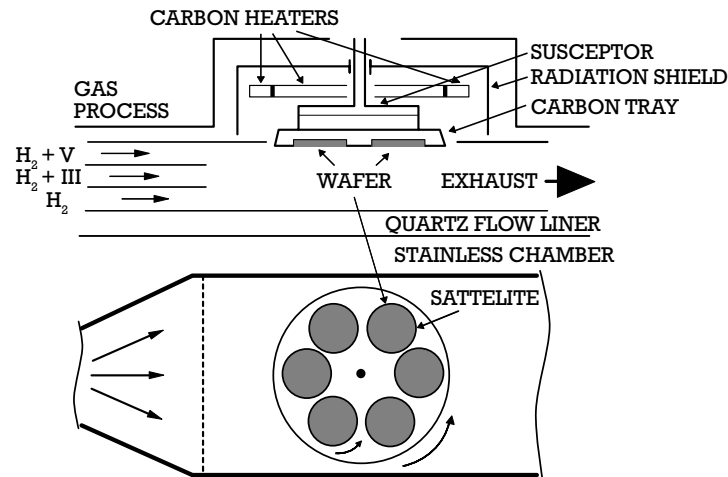


Figure 3.26: Schematic representation of the inside of the grow chamber of a multi-satellites MOVPE bati. Inspired from [Stringfellow 1999]

pumping, of the active zones of XXL2029 and XXL2020. The photoluminescence mapping shows a good homogeneity of the emission, in the range of 885 nm for the first structure (target at $895\text{--}900\text{ nm}$) and 840 nm for the second (target at $852\text{--}857\text{ nm}$) (again, the positive PL shift in laser operation must be taken into account). Also, another standard characterization of the well structure is the X-ray diffraction measure (figure (3.27)). The main peak is the substrate signal, while the smaller maxima are linked to the well. It should be noticed that a 5 mm crown from the wafer's border cannot be used due to the layer inhomogeneous strain.

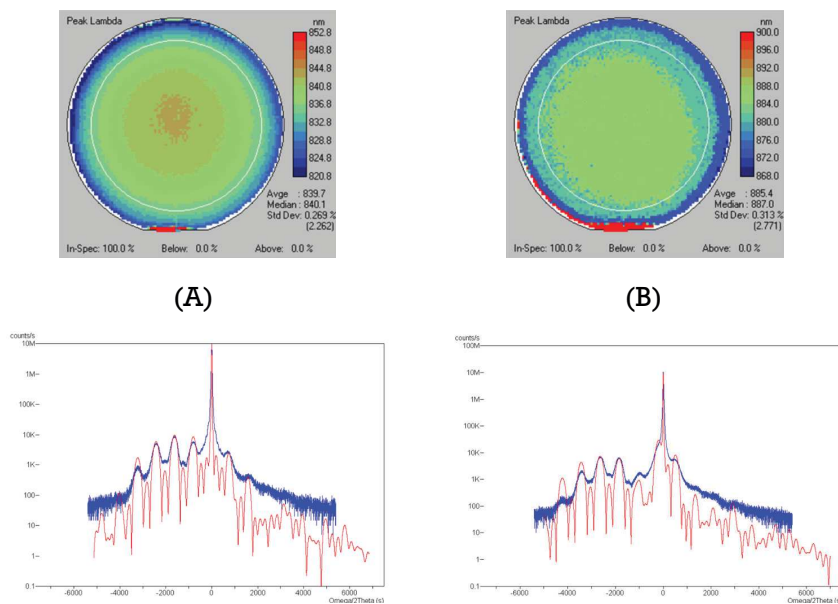


Figure 3.27: (A) Photoluminescence mapping (on top) and X-ray spectrum (bottom) of the quantum well structure of XXL2020. (B) Same as (A) but with XXL2029

The epitaxial realization is (the first and) one of the corner stone of high performances lasers. Defects, unwanted impurities (oxygen in Al-layers, passivating H...) are additional non-radiative recombination centers, light-traps and electronic noise sources that hinders performances. The author of the manuscript has not taken part in these technical realizations, however, the quality of the several runs of fabrication will be assessed through the experimental measures.

3.2.2 Technological processing

The second corner stone of the laser realization is the technological process of the geometrical shaping of the semiconductor layers. It is divided in two main steps for the ridge-DFB: the realization of the Bragg grating in the '1st epitaxy' followed by a regrowth up to the contact layer, and the realization of the ridge waveguide in the p-side.

3.2.3 Grating processing

The process of the grating, as it has been shown, is a key element to obtain good single-mode behavior. The corrugation is defined after the 1st epitaxy of the cavity to the quaternary Q(1.62 eV) grating layer. The global process is the following (figure (3.28)):

1. After the 1st epitaxy, a SiO₂ layer of a few tens of *nm* is deposited using Plasma-Enhanced Chemical Vapor Deposition (PECVD). A positive photoresist is spin-coated. It will be used as the matrix for the definition of the grating
2. The resist is insulated with spot size in the range of 8 *nm* (focused beam of electrons). The pattern is written on bands of several *mm* length per μm width, on the whole 2' surface. The resist is exposed to solvents to leave a mask with the grating features
3. The hard mask of SiO₂ undergoes a Reactive-Ion-Etching (RIE) process (O₂ gas), which imprints the features of the resist in the silica. The etching depth is tracked in real-time by interferometry (a laser perpendicular to the surface of the wafer tracks the optical signature of the several material layers and draws an interferogram) which gives an accuracy of 30 *nm* in practice the depth.
4. Then the grating features are transferred, in turn, in the semiconductor Q(1.62 eV) layer using again RIE, with a stronger plasma (H₂ gas)
5. The grating is buried by a GaInP regrowth (2nd epitaxy), followed by all the layers up to the top contact

In this process, the physical etching of the grating layers is allowed by the Aluminum-free content of this zone. Indeed, for layers containing Al, an exposure to air, even brief, leads to rapid oxidization of the surface. At best, the oxygen atoms incorporated created light recombination centers, inducing higher optical losses in the material. In the worst case, the layers swell and eventually delaminate. The use of in-situ chemical etching of the grating in an oxygen-free environment is an alternative to the process described above. The global cleanness state of the surface before the regrowth is of crucial importance to allow proper material regrowth and to obtain good electrical properties. Additional series resistance can be induced by the impurities absorbed at the interface (sulfur for instance). Picture (3.29) shows a Scanning Electron Microscopy (SEM) image of a band of several μm width of a grating, after SiO₂ etching.

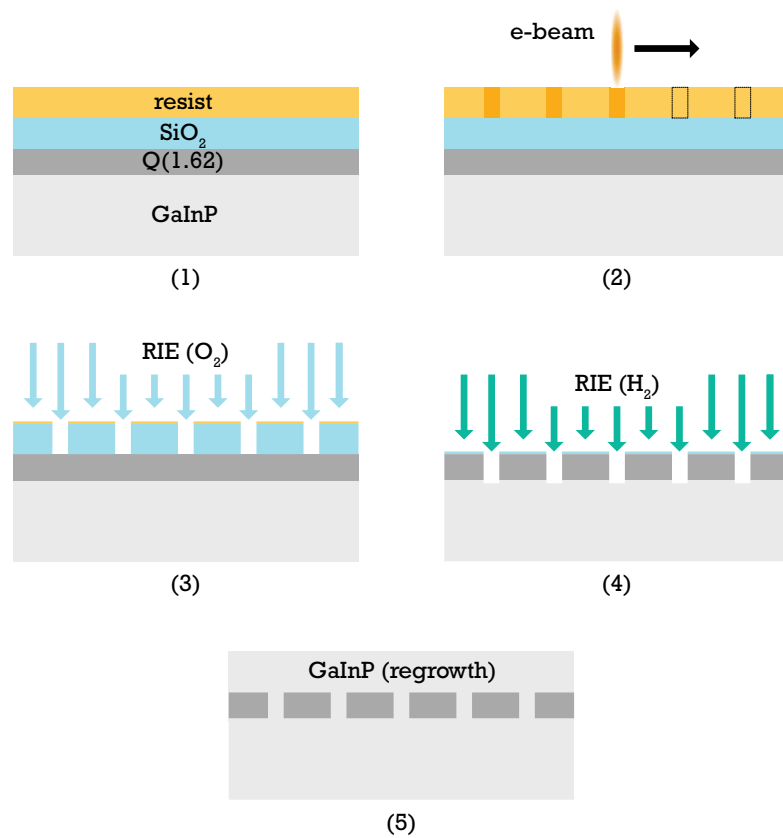


Figure 3.28: The five main steps of the process of the grating using e-beam lithography

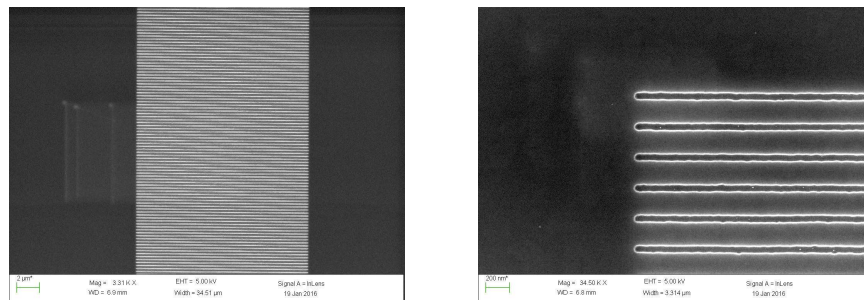


Figure 3.29: Right: SEM picture of a band of the grating. Left: zoomed view of the previous

3.2.4 Ridge processing

All the physical masks (five levels) have been realized using the commercial software L-EDIT[®] which enables to design GDSII layers. Picture (3.30) shows a typical complete mask of the DFB fabrication: lasers are located in cells which have been designed to ensure the best compatibility with relation to further cleaving process, manipulation, storage without oxidization of the facets...etc. It also includes several alignment marks to ensure quick and reproducible alignment on the features from one level to another. The design has been created with the help of M. Garcia, who is responsible for the technology process and back-end group in III-V Lab-Thales. Once the design is achieved, the physical

masks are realized by an external company who will define the patterns on slabs of quartz, covered by Chromium on the dark areas.

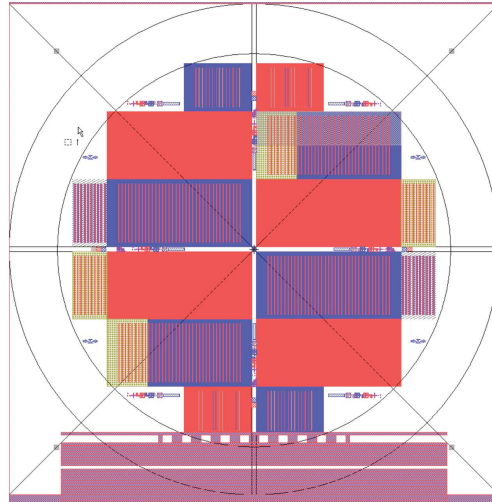


Figure 3.30: Example of a virtual mask coded with L-EDIT[®] for the processing of the lasers. Five levels of layers are superimposed

The steps to define the waveguide and to realize the electric contacts are listed below:

1. Definition of the alignment marks in the wafer. They will serve to align all the further layer levels on a common point of reference
2. Implantation of protons H^+ in the lateral sides next to the waveguide. It is supposed to prevent current spreading below the ridge in the highly doped layers (see previous section)
3. Etching of the waveguide (see further) and realization of the top contact on the stripe. An insulating layer of SiO_2 is deposited, then opened on the width of the ridge by the 'creep' technique, followed by the deposition of the metallic (ohmic) contact in Ti/Pt/Au on the highly p-doped GaAs layer
4. Reduction of the thickness of the wafer by polishing and deposition of the n-side contact: a standard Au/Ge/Ni/Au sequence, which is annealed to suppress the intrinsic Schottky barrier with n-type GaAs
5. Separation of the contacts between the chips with a deep ion etching. Labels on the lasers are imprinted in the meantime

The ridge definition is described in more details in picture (3.31). The step number 3 above can be decomposed in seven sub-steps:

- 3.1. After the complete epitaxy, a SiO_2 mask of a few tens of nm is deposited using PECVD. A positive resist is spin-coated
- 3.2. The resist is exposed with a standard UV source through the quartz mask to define the double trenches which will form the ridge waveguide

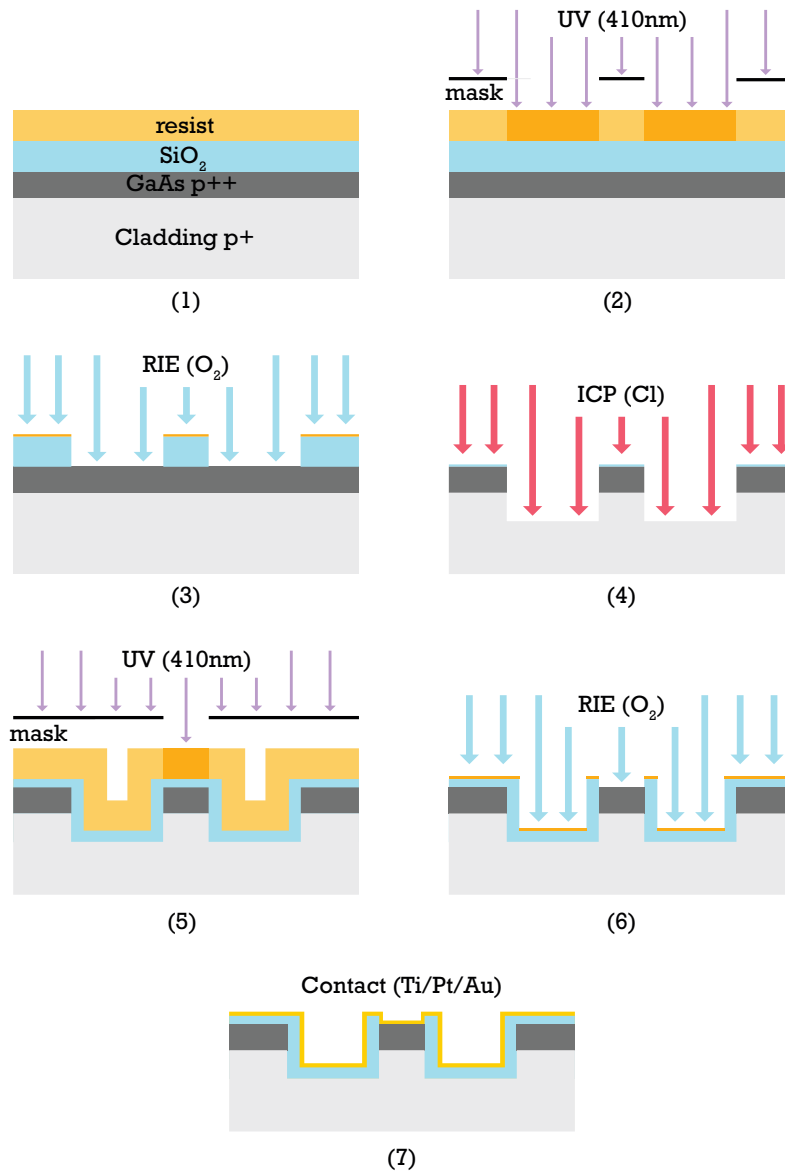


Figure 3.31: The seven main steps of the process of the ridge waveguide using conventional UV-lithography

- 3.3. The resist is revealed and the pattern transferred to the silica mask by means of RIE etching
- 3.4. The semiconductor top GaAs and cladding layers are etched further, to a depth h which has been defined in section [3.1.2.1] using Inductive Coupled Plasma (ICP). The etching depth is tracked, again, by laser interferometry. The Chloride (Cl) plasma parameters are crucial to obtain the physical removal of the material, but also to ensure a 'smooth' chemical attack (due to the reactivity of the ions), avoiding unwanted corrugations that induce mode diffraction and losses in the guide. The silica mask is hard enough to protect the other surfaces from the attack
- 3.5. A thin insulating SiO₂ layer is deposited afterwards. The surface is spin-coated again and an other quartz mask is used to expose the top of the waveguide for further removal of the resist

on this surface

3.6. The silica is removed on the top of the guide with RIE

3.7. The final metal contact is evaporated in the sequence Ti/Pt/Au. Titanium is used for its adhesion properties

Picture (3.32) displays a SEM picture of a typical realization of the above. One can notice the trapezoidal form of the waveguide. This can be enhanced because the desired cutting-width of the ridge w at the top is not equal to that at the bottom. Actually, this process, which was implemented for the 1st run, was corrected afterwards for the 2nd run.

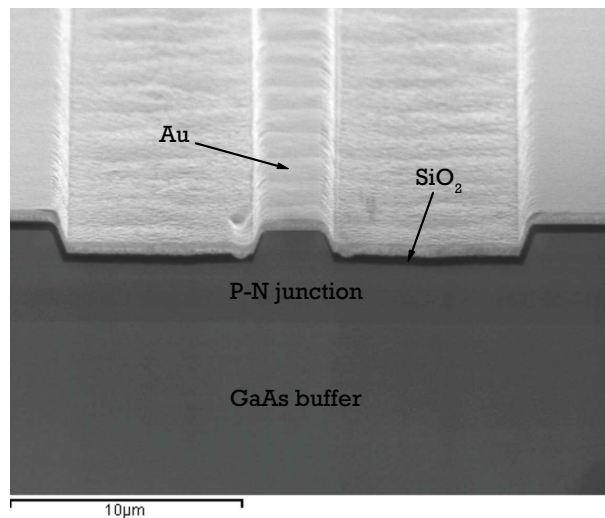


Figure 3.32: SEM picture of the facet of a ridge-DFB realization, showing the waveguide on the top contact

3.2.5 Cleaving and mounting

After the contact separation and substrate polishing, the wafer is thin enough to be cleaved along the GaAs natural crystal planes. A diamond peak locally presses the material to induce local strain which will act as the starting point of the cleaving. In that way, we can generate all the laser facets, perpendicularly to the waveguides, in a first step, from which a laser *bar* of cavity length L is obtained and chips of $350 \mu m$ width are separated individually by a cleaving parallel to the guide (figure (3.33)).

The mounting of the laser is of special importance, in particular for applications which require drastic thermal management (high-power broad area lasers at 975 nm for instance). Conservation of the electrical properties of the interface between the laser and the mount through aging requires a careful choice of the mount materials and metal coating. For the application, the *C-mount* has been chosen. This mount has a hole to be screwed, ensuring robust electrical and thermal contact with the heat-sink (figure (3.34)). This mount is compatible with all the test setups of the lab, including the multi-slots aging test bay. The mount is made of Cu, metalized with a special mix of Au and other metals to avoid oxidization over time. A rectangular (grey color) piece of copper-tungsten (CuW) is inserted between the heatsink and the chip. The integration is such that the interface between the two pieces is continuous, avoiding a source of failure. The mix of alloys has a CTE that matches the one of

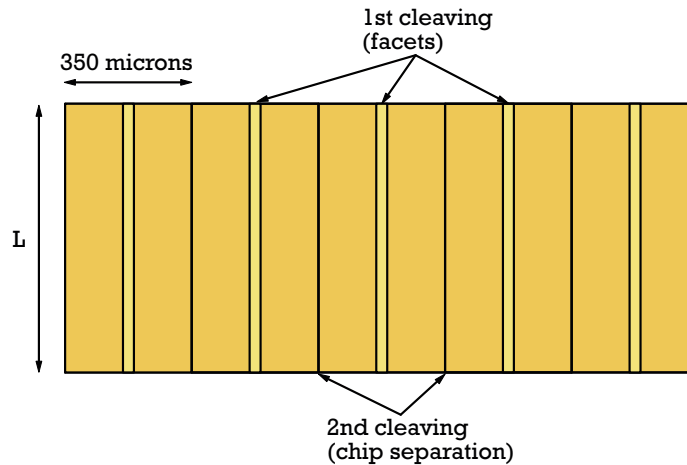


Figure 3.33: Principle of the laser bars cleaving into individual chips of length L and width $l = 350 \mu m$

GaAs, so that under temperature cycles, no mechanical stress will alter the interface between the two. The chip itself is soldered at $\sim 200^\circ C$ on the n-side (mounting 'up', the mount is the ground) with a precise cycle of temperature, with a Au-Sn hard solder on the CuW. Finally, the mount comprises a metallic band for the upper p-contact. Regarding the top contact, the ball-bonding technique is employed on the p-side of the chip to connect the laser to the metallic band with $30 \mu m$ diameter Au wires terminated with a $50 \mu m$ Au ball, for further testing.

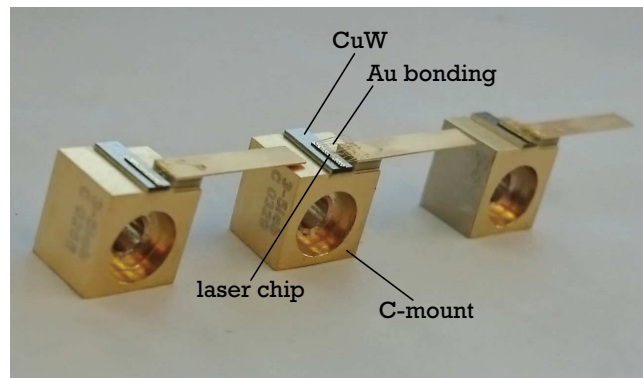


Figure 3.34: Laser chips soldered and connected to the C-mount, with an integrated CuW

3.2.6 Packaging

The laser packaging consists in an hermetic housing called *TO3* made of a Cu header with 8 contact pins, originally designed for high-power transistors, and a lid, with a transparent window for the laser beam output (figure (3.35)). The window is anti-reflective coated at $850 - 900 nm$. This housing has standard dimensions that have been adopted by the manufacturers of clocks.

A crucial point for the application is the integration of an efficient temperature monitoring and regulation of the laser. The two points are addressed with the soldering of a $10 k\Omega$ CTN on the C-mount (this element sees a change in its resistivity with the temperature, so an absolute measure of the latter is easily done by injecting a constant current at its two ends), and a peltier element on



Figure 3.35: TO3 final module

the C-mount hole side to either heat or cool the device (by injecting current in the peltier junction). The temperature regulation over time of a target value is done with a servo loop between the current read at the CTN and the current injected in the peltier. It should be noticed that the laser and the CTN have separated grounds to minimize crosstalk and electronic noise, as required by the clock manufacturers.

Precise requirements on the laser positioning tolerance with relation to the output window, as long as the wish to work to the very end of the process with the C-mount, has led us to look for a mean to integrate directly the mount in the TO3 can. Figure (3.36) shows a mechanical drawing of such an integration. Several advantage of this packaging design can be mentioned. Again, the use of the C-mount enables to use directly lasers characterized from the lab and burned-in in aging tests in the final module, which saves the cost of mounting on different platforms (Aluminum Nitride for instance). Also, the depicted process allows to align the laser facet at $\pm 100 \mu m$ from the geometrical center of the header. Then, the peltier and the C-mount can be soldered (with a low melt temperature alloy) at once within the tolerance specified by the end-user. On the other side, such packaging may not be suitable for applications where the laser is modulated at several GHz , because of the ground volume for instance. Towards qualifying the module for spatial applications, it is also very important to avoid the so-called epoxy conducting glues, which are otherwise used to attach all the pieces together, with a sufficient electrical and thermal conductivity. Indeed, the specifications put forward by the spatial agencies prevent their use (H20E for instance) to avoid the risk of contamination inside the can. Once the assembly is fixed, the can is sealed under an Ar atmosphere. An hermetic module is required for at least 10 years (no humidity inside that could induce condensation on the inner side of the window and perturb the laser beam).

Standard industrial approval also requires the module to undergo mechanical stress tests in which the resistance of the mechanical parts to strong vibrations are assessed.

3.3 First characterizations and optimization

In this section, we present the first order characterizations of the devices that have been fabricated at III-V Lab. The measures are mainly related to the first, non-optimized, run of fabrication.

3.3.1 First order metrology

Experimentation has dwelt on the majority of the time of this work. The first order metrology comprises mainly Light and Voltage vs. Current measurements (L-I-V) as well as low-resolution spectrum analysis. The accuracy and reproducibility of these measurements are essential, otherwise



Figure 3.36: Mechanical assembly for TO3, peltier and C-mount soldering. Left: exploded view. Right: mounted assembly

they can lead to wrong interpretation and decisions on the laser parameters to optimize. In the line of the renewal of the laser fabrication process, new test benches have been built up. Figure (3.37) shows a test platform designed for the lasers made of a golden Cu plate where different mounts can be screwed. A peltier Thermo-Electric Cooler (TEC) is inserted between the platform and the Al heat sink below and the temperature is tracked directly in the plate with a NTC. A golden spring-tip is fixed in an elevator to ensure the same contact pressure at each measure. The current source is a Thorlabs ITC4001/4005 which allows bias up to 1 A or 5 A (accuracy of $\pm 0.1\%$ on reading $+0.5\text{ mA}$). It integrates a multimeter (accuracy of $\pm 10\text{ mV}$), The measurement of the resistance of the device is made out of the I-V characteristic, so it has an accuracy of $\pm 0.1\ \Omega$ for a measurement at 100 mA . The calibration is made with a first measurement of the resistance of a mount without any chip, in short-circuit, so that the real series resistance of a mount with a laser is $R_s = R_{meas} - R_p$, with R_p the *parasitic resistance* which includes the resistance of all the circuitry of the laser bias wires plus the mount only. However, in the case of very small resistance measurements, for instance with broad-area lasers where $R_s < 100\text{ m}\Omega$, a *4-points probe* setup should be used, where an independent precise voltmeter measures the impedance directly at the laser ground and plus [Mostallino 2017].

For the temperature measurement, the ITC integrates a TEC and a NTC controller with an electronic servo loop, which PID parameters can be adjusted. The temperature stability is on the order of $\sim 10\text{ mK}$ for an hour. It is not a low-noise current source, but this has no consequence for these characterizations. The optical power is measured with two different setups, depending on the level of output power. For $P_{out} < 1\text{ W}$, an integrated optical head (ILX OMH-6742B), based on a Silicon photodiode suitable for the $400 - 1100\text{ nm}$ range detection, is linked to an optical powermeter (ILX OMM-6810B) auto-calibrated at the desired wavelength. Power reading is claimed by the constructor to be reproducible at $\pm 3\%$. For powers above 1 W , a bigger integrating sphere (Thorlabs IS236A) is used: it includes a large area Silicon photodiode (Thorlabs SM05PD2A) which can be biased for purposes of the linearity of the detector's response at very high power. To detect the optical spectrum, a fibered lens is placed close to the laser facet (not too close to avoid back-reflections in the chip), with a 3-stages axis that enable to control the positioning in the μm range. The fiber connector is connected to an Advantest Q8384 Optical Spectrum Analyzer (OSA) which has a wavelength resolution of 2 pm and a detection floor of -85 dBm . The instrument is based on a rotating diffraction grating that

separates the light components during the scanning period (the resolution is linked to the number of *grooves* or corrugations per unit length of this grating). The resolution capacities are not enough to measure the linewidth (which is below the fm) so a more powerful spectrometer will be used in the device study, but the OSA allows to resolve the Fabry-Perot modes spacing of the lasers which have a $FSR \sim 60 pm$. A LABVIEW[®] program has been created to compile the L-I-V measures in real-time by GPIB communication with the measuring devices. Automatic threshold, external efficiency, series resistance and junction corner voltage are fitted and the data are rendered in Excel[®] sheets reports, as a basic tool to give consistent form of the data and to spare experimental time.

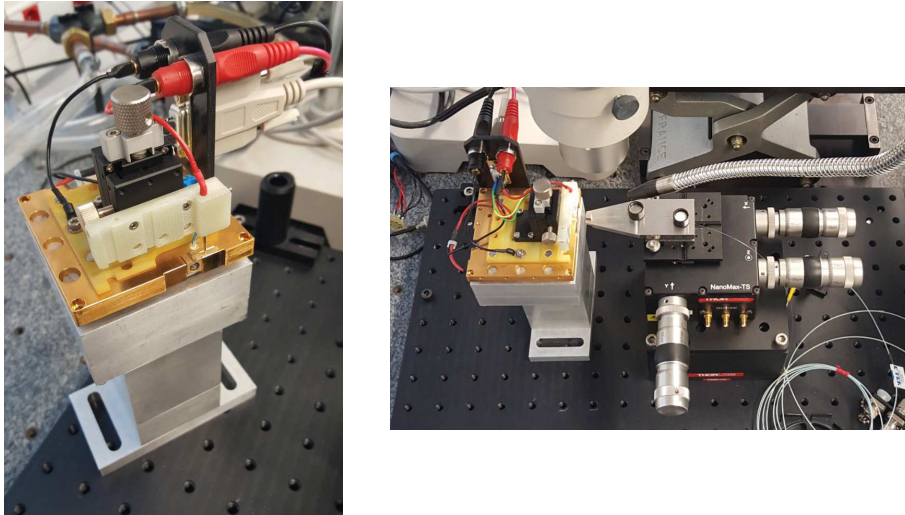


Figure 3.37: Pictures of the test platforms designed for C-mounts (left) and probing of the laser output beam with a fibered lens, mounted on a three-stages axis (right)

3.3.2 First run of fabrication

The first run of lasers has been fabricated in a same epitaxial calibration, one for DFB emission at $894 nm$ (XXL2029) and the other at $852 nm$ (XXL2020). The broad-area structure at each wavelength has also been realized at the same time (respectively XXL2028 and XXL2022), this is why the material properties are pretty homogeneous for each type of quantum well, whatever the structure.

3.3.2.1 Broad-area lasers

The broad area laser is realized by a shallow etching of two trenches, similarly to the ridge, but the width of the guide is $w = 90 \mu m$ and $h < 1 \mu m$. The technological process is slightly different from the one presented before and will not be described here. For more informations on high-power broad area lasers, see [Mostallino 2017].

As pointed out in section [3.1.2.1], due to the very small lateral current spreading, the current density distribution at FWHM is localized in a band of $100 \mu m$ below the ridge. We can then assume that the effective current density in the active layer is the injected one at the top contact. To extract the internal parameters of the structures, chips of cavity length of 2, 3, and 4 mm were cleaved and mounted p-side down without any facet treatment, with a soft In solder, on a lab submount different from the C-mount. Figure (3.38) shows a typical L-I characteristic at different temperatures for a

2 mm-long cavity, for the 894 nm. The threshold current ($I_{thr} = 380 \text{ mA}$ at 20°C) increases with increasing temperature, while the slope of the linear output power (external efficiency η_d) decreases. Tables (3.14) (XXL2028) and (3.15) (XXL2022) summarizes the mean values found for each cavity length, as long as the measurement of the dispersion (standard deviation). From these figures, one can extract all the internal parameters of the structures, namely the internal losses α_i , the internal quantum efficiency η_i , the current density at transparency J_{tr} and the modal gain parameter (with relation to the current density) ΓG_0 . The values are recapped in table (3.16). Also, the T_0 and T_1 characteristic temperatures of threshold and external efficiency evolution with temperature can be extracted from an exponential fit (table 3.17).

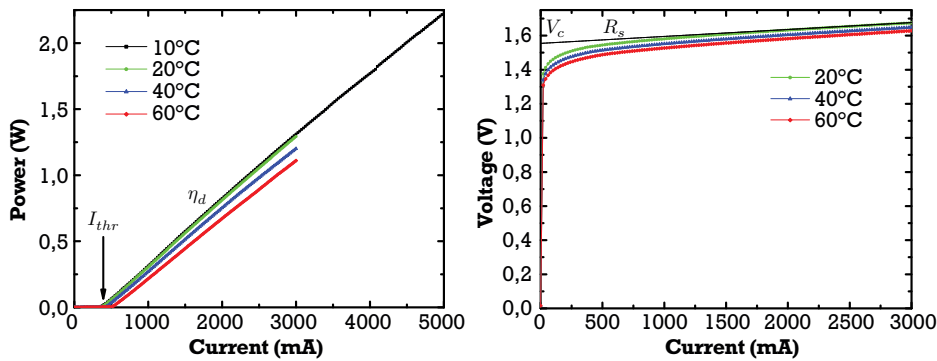


Figure 3.38: Left: L-I characteristic of a 2 mm long broad area laser with cleaved facets, at several temperatures. Right: V-I characteristics of the same laser at several temperatures

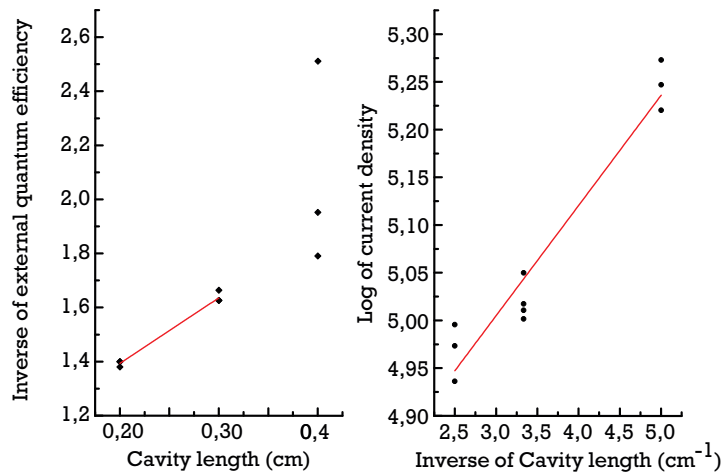


Figure 3.39: Fitting procedure to extract the internal parameters α_i , η_i , J_{tr} and ΓG_0

Some comments can be made on these results. First, the L-I-V parameters found for 4 mm-long devices were too spread to give a reasonable fit of the internal parameters, so they have been omitted when the threshold and efficiency was obviously too far apart from the linear tendency. From a technical point of view, those lasers have been fabricated using an old process, and mounted on a lab submount, different from the C-mount. The soldering process employed was not robust for such cavity lengths (the mounting robustness is increasingly difficult to achieve with longer cavities,

Internal parameters		$I_{thr} (mA)$			$\eta_d (W/A)$			$R_s (\Omega) @ 1 A$			$V_c (V)$			$\lambda_{thr} (nm)$		
		$20^\circ C$	$40^\circ C$	$60^\circ C$	$20^\circ C$	$40^\circ C$	$60^\circ C$	$20^\circ C$	$40^\circ C$	$60^\circ C$	$20^\circ C$	$40^\circ C$	$60^\circ C$	$20^\circ C$	$40^\circ C$	$60^\circ C$
2 mm	av.	380	424	509	0.51	0.48	0.46	0.052	0.053	0.054	1.53	1.49	1.48	884	889	894
	stdv.	10	11	4	0.01	0.006	0.01	0.001	0.001	0.001	0.01	0.01	0.01	0.3	0.3	0.2
3 mm	av.	454	537	634	0.43	0.40	0.37	0.039	0.039	0.040	1.51	1.48	1.46	887	892	897
	stdv.	10	14	34	0.01	0.01	0.02	0.005	0.004	0.004	0	0.003	0	0.2	0.4	0.5
4 mm	av.	575	666	795	0.34	0.32	0.31	0.031	0.030	0.03	1.50	1.47	1.44	888	893	898
	stdv.	17	21	42	0.06	0.06	0.06	0.04	0.05	0.01	0	0	0	0.5	1	1

Table 3.14: XXL2028: summary of the main parameters extracted from the L-I-V characteristics and OSA measurements

Internal parameters		$I_{thr} (mA)$			$\eta_d (W/A)$			$R_s (\Omega) @ 1 A$			$V_c (V)$			$\lambda_{thr} (nm)$		
		$20^\circ C$	$40^\circ C$	$60^\circ C$	$20^\circ C$	$40^\circ C$	$60^\circ C$	$20^\circ C$	$40^\circ C$	$60^\circ C$	$20^\circ C$	$40^\circ C$	$60^\circ C$	$20^\circ C$	$40^\circ C$	$60^\circ C$
2 mm	av.	393	459	541	0.52	0.51	0.48	0.050	0.051	0.048	1.53	1.51	1.48	857.5	863	867.5
	stdv.	7	15	16	0.02	0.02	0.02	0.004	0.004	0.004	0.01	0.02	0.01	0.2	0.9	0.9
3 mm	av.	491	600	688	0.46	0.43	0.40	0.045	0.048	0.042	1.5	1.49	1.47	861.2	866.3	870.2
	stdv.	8	37	14	0.03	0.03	0.02	0.02	0.01	0.02	0.01	0.01	0	0.7	0.6	0.3
4 mm	av.	624	719	820	0.43	0.41	0.39	0.024	0.027	0.027	1.51	1.48	1.47	862.2	-	-
	stdv.	23	24	7	0.01	0.01	0	0.005	0.002	0.002	0.01	0	0	0.2	-	-

Table 3.15: XXL2022: summary of the main parameters extracted from the L-I-V characteristics and OSA measurements

Structure	α_i (cm^{-1})	η_i (1)	J_{tr} ($A.cm^{-2}$)	ΓG_0 (cm^{-1})
XXL2028	2.3	95%	94	13.8
XXL2022	2.2	95%	110	15

Table 3.16: Extraction of the internal parameters of the two structures XXL2028 and XXL2022

Structure	T_0 ($^{\circ}C$)	T_1 ($^{\circ}C$)
XXL2028	138	500
XXL2022	127	600

Table 3.17: Experimental evaluation of the characteristic temperatures T_0 and T_1 of the two structures XXL2028 and XXL2022

for homogeneity and mechanical strain purposes), which may explain the variability of the lasers parameters. Also, the fitting technique assumes that the losses are independent of the length, which is in general not true, as it has been discussed in the previous sections. Nevertheless, the values found for the internal losses are close to the one estimated using the results of section [3.1.2.1] (around $2.1 cm^{-1}$ for the broad-area lasers) and the transparency currents are matching the *EsakiHTD* predictions (respectively $J_{tr} = 85 A.cm^{-2}$ and $J_{tr} = 110 A.cm^{-2}$), with a lower value for the quantum-well with higher strain. The internal efficiency is high, which is usually the case for broad-area lasers, however, the modal gain parameters are quite low. Indeed, with an estimated confinement on the well $\Gamma_{QW} = 1.4\%$, the material gain parameter does not exceeds $G_0 = 1000 cm^{-1}$. These figures must be put in the perspective of the accuracy of such experimental fitting procedure, which leaves quite a lot of margin on the parameters values, as they all depend on each others, especially for this limited range of cavity length investigation. The G_0 depends also on the threshold values, so on non-radiative recombinations, hence a possible deviation from the predicted value of $1980 cm^{-1}$ for these wells. Finally, the values are coherent with what was expected (losses close to $\alpha_i = 2 cm^{-1}$), but one should not ask to much from this limited study. These structures have been investigated more thoroughly in the past [Ligeret 2008b]. To comment on the figures found for the characteristic temperatures, they are quite standard for this type of lasers: in the near-infrared, the barriers in the active zone are high so carriers escape less easily the well with growing temperature, compared to the $1.55 \mu m$ case. The external efficiency always shows higher resistance to a temperature variation.

Regarding now the light properties of these lasers, the output spectra revealed by the beam collection to the OSA are displayed in figure (3.40). The $852 nm$ structure emits a typical multimode Fabry-Perot spectrum at $20^{\circ}C$ centered at $\lambda_g \sim 856.5 nm$. Recalling that the photoluminescence wavelength of the well was $\lambda_{PL} = 840 nm$, there is an emission shift of $16 nm$ in this structure, in agreement with the predictions of the model used. The peak of emission red-shifts with increasing temperature, according to the energy gap narrowing with temperature. The wavelength behavior is more complex to analyze with the change of cavity length: with increasing L , the mirror losses decrease, so the current density at threshold is reduced and the lower band-filling induces lower blue-shift. In the meantime, it does not compensate for the increase of the injection surface which increases on the overall the quantity of current to inject, creating more Joule effect that heats the active zone. Globally, the wavelength emission increases with the cavity length.

Turning now to the $894 nm$ structure, the emission peak was surprisingly found at $\lambda_g \sim 882.5 nm$ for all the laser tested, despite the calibration of the well at $\lambda_{PL} = 885 nm$. In fact, **all the structures**

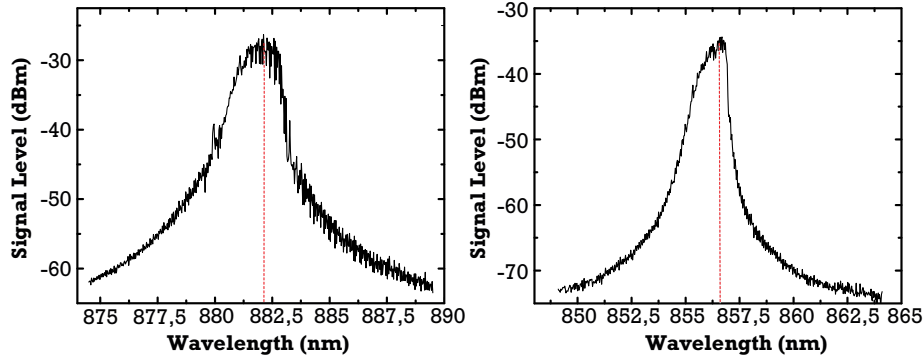


Figure 3.40: Right: XXL2029 OSA spectrum of a typical multimode broad-area laser ($L = 2 \text{ mm}$, $T = 20^\circ\text{C}$) centered at $\lambda_g \sim 882 \text{ nm}$. Left: XXL2020 OSA spectrum of a typical multimode broad-area laser ($L = 2 \text{ mm}$, $T = 20^\circ\text{C}$) centered at $\lambda_g \sim 856 \text{ nm}$

of the 1st run for this wavelength were blue-shifted, including the DFB ones. We see that the desired wavelength can only be reached at $60 - 70^\circ\text{C}$. This had serious consequences on the whole results obtained in this work. We tried to find explanations of the discrepancy between the PL measured on calibration structures by the epitaxy team and the emission wavelength of the lasers. The well is pretty similar to that of the 852 nm structure, so it is very unlikely that it is due to intrinsically different well behavior. The calibration of the reactor may have shifted during the process, or the interfaces boundaries in the well may not be sharp enough (species segregation) to ensure the good confinement properties. The PL measurement is done by a weak optical pumping (UV lamp or LEDs at 530 nm for instance) of a test structure: the real properties of laser emission under strong electrical injection can be different with the band-filling, as it seems to be the case here. The 2nd run of fabrication will address this mis-calibration. The polarization state of the beam has also been tested. The amount of TE radiation (polarization parallel to the epitaxial layers) versus the TM one (orthogonal to the layers) can be measured with a Glan-Thompson setup. The output beam goes through the two half-prisms at the interface of which the s and p components of the polarization are separated, one continues straight further, the other is reflected with a 90° angle (1st polarizer). A second linear polarizer (the analyzer) right after can be oriented by rotation around the optical axis to select a linear polarization. The rate of polarization in a mode is defined, for the TE mode, as:

$$t_{TE} = \frac{P_{TE}}{P_{TE} + P_{TM}} \quad (3.61)$$

with P_{TE} the optical power measured on the straight light pass.

Structure	t_{TE}	
	500 mA	1500 mA
XXL2028	97.4%	97.8%
XXL2022	97.1%	99.5%

Table 3.18: Experimental rates of polarization of the laser output for the two structures XXL2020 and XXL2020

The light is strongly polarized in the TE mode (close to 100 %), as expected, due to the compressive strain of the well which favors this polarization mode (table (3.18)). This rate increases with the

current injected, though, it is almost constant for the XXL2028 structure. Actually, the relation in optical gain between the TE mode and the TM is predicted around 100 in the quantum well simulations. This means that the light above threshold is certainly almost completely in TE mode, so that the ratios in power observed experimentally are probably biased, because of the limited resolution of the Glan prism. Finally, the OCFS specification that requires as much as possible of linearly polarized light is well satisfied.

3.3.2.2 Ridge-DFB lasers

The 1st run of fabrication consists in one wafer of each DFB structure XXL2029 (894 nm) and XXL2020 (852 nm). The first step of fabrication, the definition of the grating by e-beam, was based on a range of five grating pitches Λ for each wavelength, in order to scan the target wavelength around the computed refractive index n_{eff} (corresponding pitch ' Λ_0 ') which may be subject to errors of estimation. The pitches implemented are recapped in table (3.19). It should be noticed that the choice of these parameters was based on an older material refractive index base, and do not reproduce well the experimental results to come. Indeed, the respective effective index computed were $n_{eff,XXL2029} = 3.2691$ and $n_{eff,XXL2020} = 3.2898$. Additionally, three ridge widths $w = 3 \mu m$,

Structure	XXL2029	XXL2020
Λ_{-2}	272 nm	259 nm
Λ_{-1}	273 nm	259.5 nm
Λ_0	273.5 nm	260 nm
Λ_{+1}	274 nm	260.5 nm
Λ_{+2}	275 nm	261 nm

Table 3.19: Pitches Λ used in the 1st run of fabrication for each DFB structure

$w = 3.5 \mu m$ and $w = 4 \mu m$ were implemented and the etching depth was chosen to be $h = 1.6 \pm 0.1 \mu m$, so above the grating layer, yielding an effective refractive index step of $\Delta n_{R,eff} \sim 1 \times 10^{-3}$. Cavity lengths of $L = 1.5 mm$, $L = 2 mm$ and $L = 2.5 mm$ cleaved, depending on the structure and a AR-HR facet treatment of 3%-95% was applied. All these parameters were chosen prior to the device analysis of this manuscript, to stick to the previous design of the CNES 852 nm lasers. Tables (3.20) and (3.21) summarizes, as in the previous section, the relevant results of the L-I-V and spectrum characterization of the devices.

First observations

- It is clear that the threshold increases and the external efficiency, resistance and characteristic voltage decreases with increasing temperature, just as for broad-area lasers. The current density threshold that was of about $190 A.cm^{-2}$ for 2 mm broad-area lasers of XXL2028 is now in the range of $J_{th} = 625 A.cm^{-2}$ for 2 mm and $w = 4 \mu m$ lasers of XXL2029 at 20°C which indicates clearly a current spreading and decrease of the injection efficiency η_i (enhanced non-radiative recombinations in the SCH may also act), according to section [3.1.2.1]. No distinction has been made between the different ridge width because there was no clear experimental evidence of the threshold reduction in the sample with reduced w
- The threshold increases with the cavity length and the external efficiency decreases, which is linked to the decrease of the resonator losses for the latest. If we compare Fabry-Perot lasers

Internal parameters	$I_{thr} (mA)$			$\eta_d (W/A)$			$R_s (\Omega)$			$V_c (V)$			$\lambda_{thr} (nm) @120 mA$		
	20°C	40°C	60°C	20°C	40°C	60°C	20°C	40°C	60°C	20°C	40°C	60°C	20°C	40°C	60°C
1.5 mm av.	56	68	79	0.66	0.65	0.57	1.3	1.3	1.1	1.57	1.53	1.51	874.5*	877.7*	893.7
275 nm stdv.	3	1	1	0.01	0.01	0.1	0.2	0	0.2	0.02	0.01	0.02	1.4	1.9	0.1
1.5 mm av.	55	66	80	0.72	0.70	0.69	1.3	1.1	1.1	1.57	1.55	1.51	873*	875.5*	879.3*
F-P stdv.	2	2	4	0.01	0.02	0.01	0.1	0	0	0.01	0.01	0.02	1.2	1.1	0.1
2 mm av.	70	82	105	0.58	0.57	0.50	1	1	0.9	1.55	1.51	1.49	875.1*	880.8*	893.8
275 nm stdv.	5	-	21	0.07	-	0.07	0.1	0	0.08	0.02	-	0.01	0.3	0.3	0.2
2 mm av.	63	65	72	0.45	0.37	0.38	1	1	0.9	1.54	1.52	1.48	887.3	888.6	889.7
273.5 nm stdv.	5	-	-	0.07	-	-	0.1	-	0.07	0.02	-	-	0.7	0.2	-
2 mm av.	60	63	73	0.52	0.51	0.48	1	1	0.9	1.54	1.50	1.48	883.1	884.2	885.4
272 nm stdv.	4	-	-	0.01	-	-	0.01	-	-	0.08	-	-	0.1	-	-

Table 3.20: XXL2029: L-I-V parameters of DFB lasers. No figure for the 'stdv.' parameter indicates that the sample is reduced to one device. The '*' indicates that the laser emission is of Fabry-Perot type.

Internal parameters	$I_{thr} (mA)$			$\eta_d (W/A)$			$R_s (\Omega)$			$V_c (V)$			$\lambda_{thr} (nm) @120 mA$		
	20°C	40°C	60°C	20°C	40°C	60°C	20°C	40°C	60°C	20°C	40°C	60°C	20°C	40°C	60°C
1.5 mm av.	45	54	64	0.47	0.45	0.44	1.6	1.4	1.3	1.56	1.54	1.52	851.95	853.10	854.20
261 nm stdv.	-	-	-	-	-	-	-	-	-	-	-	-	-	-	-
1.5 mm av.	41	49	60	0.47	0.45	0.43	1.4	1.3	1.2	1.56	1.54	1.52	850.55	851.66	852.80
260.5 nm stdv.	4	5	6	0.07	0.07	0.08	0	0.1	0	0	0.01	0	0.1	0.1	0.1
2 mm av.	53	61	73	0.39	0.36	0.33	1.3	1	1	1.55	1.53	1.51	851.88	853.00	854.15
261 nm stdv.	2	2	3	0.05	0	0	0	0.1	0.1	0	0.01	0	0.12	0.12	0.07
2 mm av.	60	69	83	0.47	0.46	0.45	1.2	1.1	1	1.56	1.53	1.51	850.48	851.90	852.7
260.5 nm stdv.	5	2	4	0.06	0.03	0.04	0.1	0	0	0.01	0	0	0.1	0.1	0.09
2.5 mm av.	61	72	88	0.32	0.31	0.29	1.1	0.9	0.8	1.53	1.52	1.51	850.50	851.61	852.71
260.5 nm stdv.	4	4	7	0.07	0.06	0.06	0.2	0	0.1	0.02	0.01	0.01	0.07	0.09	0.07

Table 3.21: XXL2020: L-I-V parameters of DFB lasers. No figure for the stdv. parameter indicates that the sample is reduced to one device. The '*' indicates that the laser emission is of Fabry-Perot type.

and the DFB of XXL2029 for $L = 1.5 \text{ mm}$ and $\Lambda = 275 \text{ nm}$, the thresholds are almost the same, while the efficiency is reduced for the DFB. Though, up to 55°C , the DFB is not single mode, as indicated by the OSA measurement: at 20°C , the Fabry-Perot modes dominate with a wavelength at the gain peak of $\lambda_g = 876 \text{ nm}$! It is simply explained by the gain detuning which was evoked in the previous section, which maximum is too far from the Bragg wavelength to give gain to the DFB modes. When the temperature is high enough to feed these DFB modes of lower losses (above 890 nm), the lasing switches to a single-mode behavior and the external efficiency is reduced accordingly. Still, the external efficiency of the DFB in the multimode lasing is lower than that of real F-P lasers, which may indicate higher optical losses because of the grating. For lower grating pitches, the Bragg wavelength filter lies at lower λ_B and single-mode regime is effective at 20°C

- Regarding the 852 nm structures, all the lasers are single-mode in DFB regime from 20°C to 60°C

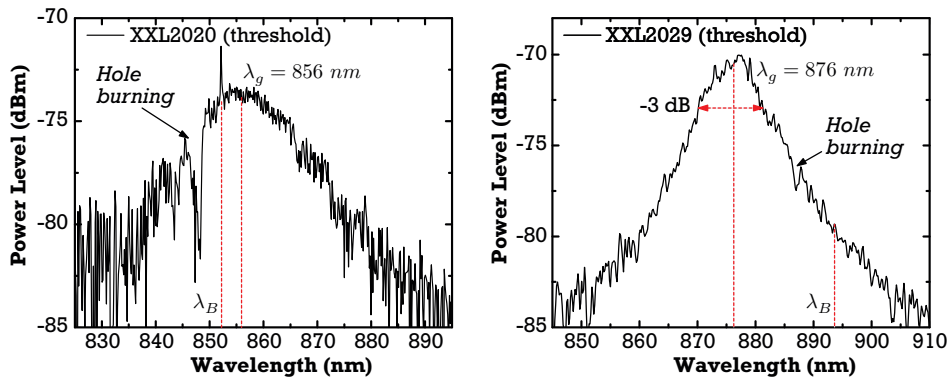


Figure 3.41: Sub-threshold spectra (just before efficient lasing) of 2 mm lasers of each structure. For XXL2029, $\lambda_g = 876 \text{ nm}$ (at 25°C) and for XXL2020, $\lambda_g = 856 \text{ nm}$ (at 25°C). The gain curves have a width $\Delta\lambda_g \sim 12 - 15 \text{ nm}$ at FWHM.

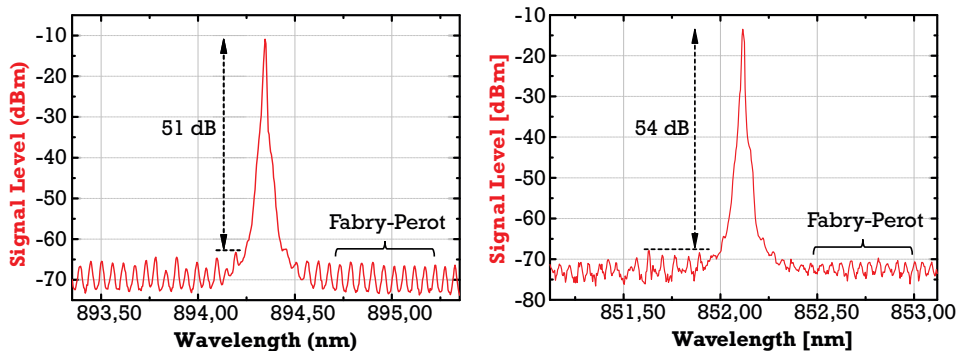


Figure 3.42: OSA sample of the output of laser C0208 (XXL2029/ $\Lambda = 275 \text{ nm}/67^\circ\text{C}/155 \text{ mA}$) (left), and of laser C0176 (XXL2020/ $\Lambda = 261 \text{ nm}/25.8^\circ\text{C}/120 \text{ mA}$) (right). A SMSR of more than 50 dB can be reached in both cases.

A proper single mode behavior with a high SMSR (at least 40 dB) at the D_1 and D_2 is the very first criterion to meet for the lasers. Figure (3.42) shows typical DFB spectra for each structure, at

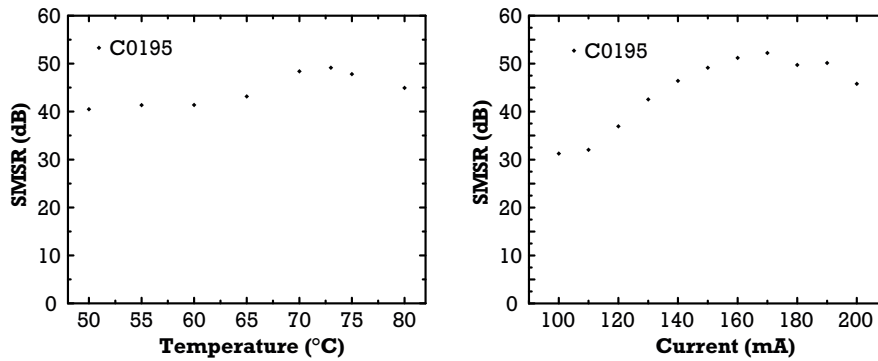


Figure 3.43: SMSR at the single-mode operation of laser C0195 ($XXL2029/\Lambda = 275 \text{ nm}/165 \text{ mA}$) as a function of the mount temperature (left) and current injection ($T = 70^\circ\text{C}$) (right)

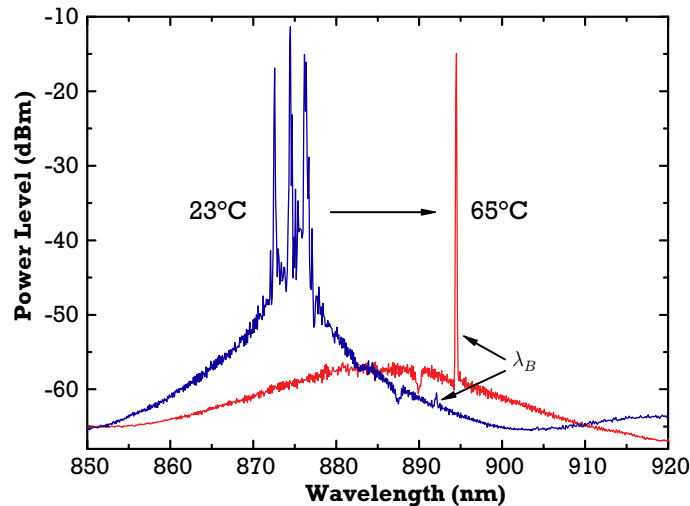


Figure 3.44: OSA sample of the output of laser C0208 ($XXL2029/\Lambda = 275 \text{ nm}$) at 140 mA : with the increase of the temperature of the mount, emission switches from a multimode Fabry-Perot behavior to single-mode DFB. At ambient temperature, the effective refractive index can be estimated from the perturbation of the local optical gain around the stop-band.

the two cesium lines. We can see that the previous requirement is satisfied (output powers above 20 mW). The Fabry-Perot modes are clearly distinguishable at the ground of the spectrum, with a more pronounced presence in the case of $XXL2029$, because of the non-zero front facet reflectivity. Also, typical SMSR plots versus the injected current at a fixed temperature, or versus the temperature at a fixed current, are reproduced in figure (3.43). In the case of $XXL2029$, both parameters enhance the SMSR, which was expected with a linear behavior of the L-I characteristics, because at threshold, the ASE is clamped, the DFB mode wins the competition and absorbs all further injected pumping energy. Mode hops and non-linear behavior degrades this high SMSR regime (see further).

Still for $XXL2029$, the line is only reached at high temperature (around 70°C) because there is otherwise not enough gain at 894 nm for the DFB mode to win this gain competition (and we are still far from the gain peak at such temperature, where $\lambda_g \sim 884 \text{ nm}$) as shown in graph (3.44). Another point is that the index computation of table (3.19) has over-estimated the effective index, but finally,

with the temperature rise, the pitch $\Lambda = 275 \text{ nm}$ allows to reach the D_2 line in an optimal way, despite the structure mis-calibration. Inspection of the laser spectrum at ambient temperature allows to localize the DFB mode among the Fabry-Perot ones and to give a value of the structure effective index, which is probably the most important data of this run of fabrication:

$$n_{eff,25^\circ C} = \frac{\lambda_{B,25^\circ C}}{\Lambda} \quad (3.62)$$

Table (3.22) gives the experimental measurement of the index and compares to the predictions of the 2D index computation of section [3.1.2.1] based on rebuilt material indexes collection. The agreement is good at both wavelength, which plays in favor of this model for the optical structure. The index of the XXL2020 structure corresponds to what was found in previous experimentation on the 852 nm [Ligeret 2008b], indicating that the material indices hardly change during successive epitaxial processes (degree of GaInP ordering for instance). Further look for accuracy on the effective index prediction would be difficult given the uncertainties on the exact temperature of the active zone, the exact optical indices, doping effect, lasing on the stop-band mode etc. Precise ellipsometry measurements of materials samples can be used to get an experimental value if the indexes of the structure but it is often delicate in practice and requires expertise. Here, we are looking to reach precisely the D_2 line at ambient temperature for the next run of well-calibrated structures. We thus know that we have to use a pitch of $\Lambda_{eff} = 275.8 \text{ nm}$ on the next run to get the D_2 line at $25^\circ C$.

Structure	XXL2029	XXL2020
$n_{eff,exp}$	3.2425	3.2645
$n_{eff,theo}$	3.2415	3.2673
Λ_{eff}	275.8 nm	261 nm

Table 3.22: Effective index of the structures: comparison between theory and experiment and the theoretical Bragg pitch to use to reach the cesium lines at $25^\circ C$

The pulling coefficients of the output frequency versus temperature (f-T) and current (f-I) have also to be determined: they are **the direct link between the laser internal frequency tuning and the outer electronics of the atomic clock**. The two coefficients can be extracted from graphs (3.45). Table (3.23) summarizes their values in GHz.K^{-1} (which is of more practical use in the field of spectroscopy and noise than the nm.K^{-1}) for both types of lasers. All these characterizations have been lead once in III-V Lab and another time at LTF-UniNe in the frame of the LAMA project (and agreement has been found). The later figures are presented with their authorization. Regarding

Structure	XXL2029	XXL2020*
$\partial\lambda_B/\partial T$	20.5 GHz.K^{-1}	22 GHz.K^{-1}
$\partial\lambda_B/\partial I$ ($L = 2 \text{ mm}$)	1.2 GHz.mA^{-1}	1 GHz.mA^{-1}

Table 3.23: Pulling coefficients of the lasers linearized around the Cs point. *Denotes measurements from LTF-UniNe (reproduced with the authorization of G. Miletì)

the f-T coefficient, relations (3.3) and (2.45) indicates that the refractive index decreases with the band-gap of the well, which follows itself an inverse relation with the temperature, so on the overall the refractive index rises with temperature. One can write, with an excellent approximation (2nd order

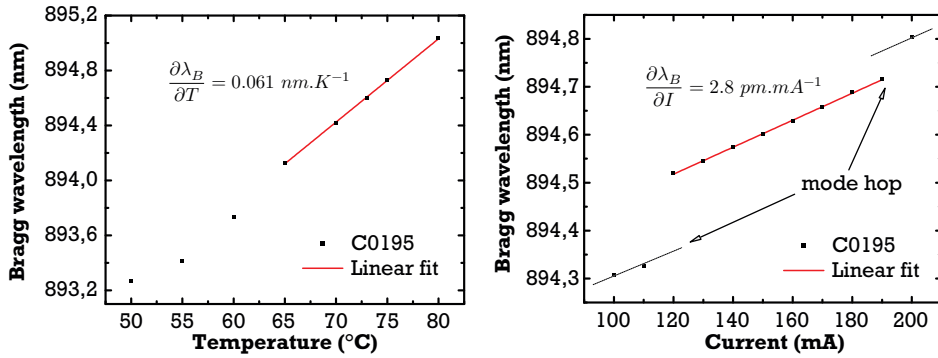


Figure 3.45: OSA sample of the output of laser C0208 (XXL2029/ $\Lambda = 275 \text{ nm}$) at 140 mA : with the increase of the temperature of the mount, emission switches from multimode Fabry-Perot behavior to single-mode DFB. At ambient temperature, the effective refractive index can be estimated from the perturbation of the local optical gain around the stop-band.

grating):

$$\frac{\partial \lambda_B}{\partial T} = \Lambda \frac{\partial n_{R,eff}}{\partial T} \quad (3.63)$$

So it was easy to determine $\partial n_{R,eff}/\partial T = 2.10^{-4} \text{ K}^{-1}$ from the linear regressions. For a given well material and Bragg pitch, the f-T coefficient is rather fixed and hardly depends on the wavelength. Looking at the f-I dependency now, the case is different. If we assume that above threshold this so-called 'chirp' results from a rise of the temperature of the active zone by dissipative mechanisms in the p-n junction (Joule heating mainly, in the lightly p-doped cladding layer), one can write that the heating power is $P_J = V \times I - P_{out}$ where P_{out} is the output optical power. Then, a chain-rule gives:

$$\frac{\partial \lambda_B}{\partial I} = \frac{\partial \lambda_B}{\partial T} \times \frac{\partial T}{\partial P_J} \times \frac{\partial P_J}{\partial I} \quad (3.64)$$

The $\partial T/\partial P_J$ can be considered to be the thermal resistance of the device $R_{th} = \sum_i \rho_{th,i} d_i / S_{eff}$ with $\rho_{th,i}$, and d_i the thermal resistivity and thickness of layer number i of the mounted laser and $S_{eff} = L \times w_{eff}$ the effective surface of injection of the device. Finally:

$$\frac{\partial \lambda_B}{\partial I} = \Lambda \frac{\partial n_{R,eff}}{\partial T} \times R_{th} \times (2R_s I + V_c - \eta_d) \quad (3.65)$$

The f-I coefficient depends on many parameters, especially on the operating point of the laser. The above writings give a method to estimate quickly the thermal resistance with a plot and slope extraction of the $\left(I, \frac{\partial P_J}{\partial I} \right)$ graph:

$$R_{th} = \frac{\partial \lambda_B}{\partial I} \times \left(\frac{\partial \lambda_B}{\partial T} \right)^{-1} \times \left(\frac{\partial P_J}{\partial I} \right)^{-1} \quad (3.66)$$

$$= \frac{1.2 \times 10^3}{20.5 \times 1.268} \quad (3.67)$$

$$= 46 \text{ K.W}^{-1} \quad (3.68)$$

for a 2 mm laser (C0195) of XXL2029. In graph (3.45), we can see two mode switchings (or 'hop') where the laser jumps to a wavelength distant from approximately a stop-band ($\sim 150 \text{ pm}$). The

hop is induced by the mismatch of the maximum of the gain curve (roughly parabolic at the peak) which evolves at a rate of 0.25 nm.K^{-1} and the discrete DFB modes which wavelength follows the above pulling coefficients. When the gain of the second lowest losses mode equals that of the first lasing mode, hopping occurs. It is advantageous to reduce the f-I pulling value to extend the range of hopping-free operation: a thermal or series resistance decrease (longer device) acts favorably for that.

★ Further analysis

A/ SEM analysis

The lasers of the 1st run of fabrication were analyzed under SEM. Picture (3.46) represents the waveguide transverse cut of a XXL2020 $w_n = 3.5 \mu\text{m}$ nominal (mask-coded) ridge width. We can notice that the etching process gives a trapezoidal form to the waveguide. The non-vertical flanks induce deviations from the nominal desired width, with a top effective width of $w_T = 3.5 \mu\text{m}$ and bottom width of $w_B = 4 \mu\text{m}$. This aspect ratio is representative of all the waveguides realized at each of the two wavelengths for this 1st run: $w_T \sim w_n - 0.5 \mu\text{m}$ and $w_B \sim w_n + 1 \mu\text{m}$ in the effective realization. The etch depth h is not homogeneous along the lateral direction, with deeper etching away from the contact stripe.

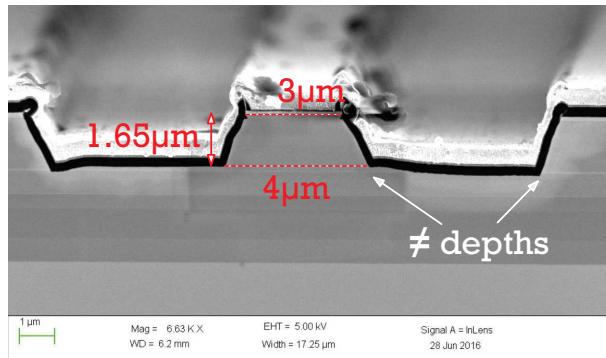


Figure 3.46: SEM picture of the waveguide of laser C0215

The etching depths for each of the structure are respectively $h = 1.75 \mu\text{m}$ for XXL2029 and $h = 1.65 \mu\text{m}$ for XXL2020 (just above the grating layer) as measured by Atomic-Force Microscopy (AFM). According to tables (3.5) and (3.6), the effective index steps are respectively $\Delta n_R = 2.3 \times 10^{-3}$ and $\Delta n_R = 1.6 \times 10^{-3}$. Thus, the ridge cutoff widths of higher order lateral modes are respectively $w_c = 4 \mu\text{m}$ and $w_c = 4.75 \mu\text{m}$. The ridge widening at the bottom of the guide is then a serious issue, because we are close to the onset of the second order mode. Aside from the fact that the index step is weak with relation to what has been analyzed before, it is not robust to keep w close to the cutoff, because in practice, a too-deep etching depth is not reversible and may hinder completely the single-mode properties of the batch of lasers.

Pictures (3.47) have been taken along the laser (y,z)-plane, in the grating layer. They allow to see the real shape of the corrugation after the technological process. In the case of XXL2029, while the grating pitch seems to correspond to the coded scheme, the opening ratio is $r_g \sim 46\%$! This value is far from the 25 – 30% expected to reach the top of the coupling factor curve (3.20). This implied that we have (theoretically) a value for the coupling factor of $\kappa = 4.5 - 5 \text{ cm}^{-1}$ if the

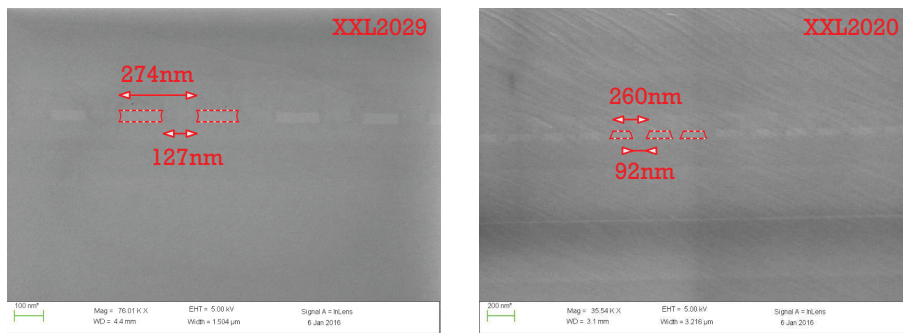


Figure 3.47: SEM picture of a grating (pitch $\Lambda = 273.5 \text{ nm}$) of a laser at 894 nm (left) and of a grating (pitch $\Lambda = 260.5 \text{ nm}$) of a laser at 852 nm

observed sample is representative of the whole wafer, which may not be necessarily the case, given the inhomogeneities observed on the other grating teeth. What counts is the average value of the geometry over the thousands of corrugations in the z -axis. Moreover, the teeth ends are 'curved'. In the case of XXL2020, the ratio $r_g \sim 35\%$ is closer to what would be expected, given a coupling value of maximum $\kappa = 16 \text{ cm}^{-1}$, which is probably reduced further in the 10 cm^{-1} range due to the trapezoidal shape.

B/ Non-linear L-I characteristic

The L-I characteristics of the 1st run present systematic non-linearities depending on the level of injected current. Graph (3.48) displays such typical curve, showing the deviations from the theoretical linear output power with current, for the laser C0220 of XXL2020 (2.5 mm -long cavity and nominal ridge width $w_n = 3.5 \mu\text{m}$).

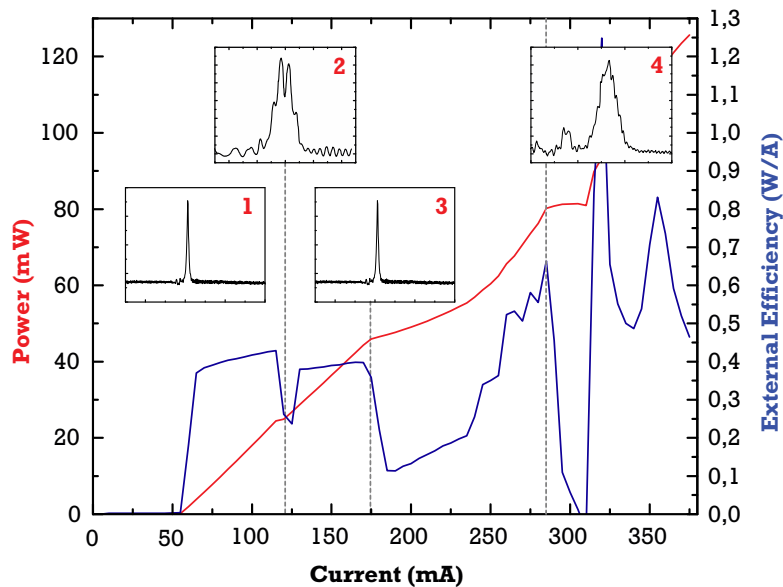


Figure 3.48: L-I characteristic (left scale) and external efficiency (right scale) of a XXL2020 DFB laser showing several modal behavior at OSA inspection with current injection

1. From the threshold current at 55 mA to around 125 mA, the power is almost linear (flat external efficiency). At OSA inspection, the spectrum is single mode with high SMSR
2. At 125 mA, the curve is marked by a typical 'kink' linked to longitudinal mode hop, which cannot be avoided. After the internal switching, the curve is linear, with a slightly lower slope. This observation is explained by the change in mirror losses which change in turn the statical external efficiency value. The OSA picture reveals that the two longitudinal modes compete at equal output power because the gain margin is very low between the two configurations
3. Above 175 mA, the external efficiency decreases abruptly and recovers its initial value at 275 mA. The spectrum is single-mode though, with still a high SMSR. Noise measurements in part II of this work will reveal that the linewidth of the laser *broadens substantially* in this range (it is multiplied by a factor 4 or more)
4. Finally, above 275 mA, the L-I curve is very kinky and OSA measurements show that the laser is now multimode and characterized by a persistent altered Bragg peak. Several side modes modulated by Fabry-Perot combs appear randomly

The behavior of this laser is also found for 894 nm devices, but it is shifted at higher current injection. The observation can be potentially linked to three phenomenons, which may act all-together:

- Perturbation of the injection by current spreading at point (3) and decrease of the efficiency because of lower overlap of the stimulated recombination term on the carrier density (as depicted in (3.1.3.2))
- Higher lateral modes excitation at higher current, which revives mode competition and creates a high level of noise (we have seen that we are close to the ridge cutoff value)
- Spatial-hole burning at high power: because the coupling factor value is quite high, the field envelop is particularly inhomogeneous in the cavity, allowing above-threshold competition for gain for several longitudinal modes and destroying the single-mode operation.

At this point, it is hard to identify precisely which mechanism is at stake. Even for low power, it is very important to remove any non-linear behavior in the range of operation, just because it can have serious consequences on the long-term aging of the device (displacement of kinks over time for instance). It should be said that similar observations were found in the previous generation of 852 nm lasers, with systematic smooth kinks in the L-I curves. The same geometrical parameters being applied here, it is not that surprising that the same behavior is observed.

C/ Far-field and near-field profiles

The far-field and near-field profiles are standard measurements of the laser beam properties. The principle of the two measurements are depicted in figure (3.49). The near-field one consists in the magnification of the beam waist w_0 with a microscope objective that collimates the diverging beam on a CCD matrix, which is used to image the vertical and lateral optical intensity. The system used is a CINOGY CinCamTM beam profiler for the VIS-IR range that makes calibrated waist measurements with adequate image processing to extract the characteristic beam widths. The far-field setup, on the other side, consists in measuring the beam intensity at a distance $d \gg z_R$ with a HAMAMATSU radiogonometer: it is based on a bar of photodiodes that rotates in the plan perpendicular to the optical axis, so that the beam profile can be recorded in the fast and slow axis of the diode (or any

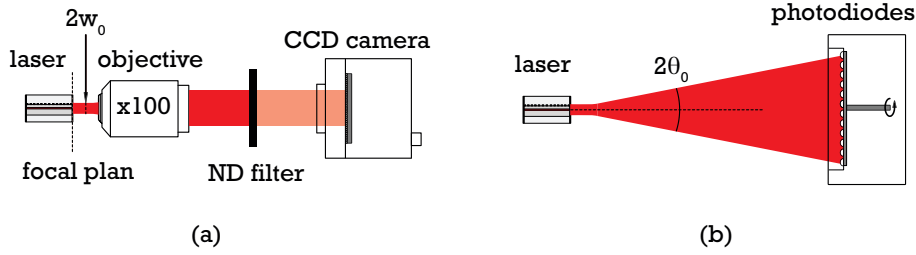


Figure 3.49: Schematic representations of (a) the near-field measurement setup, (b) the far-field measurement setup

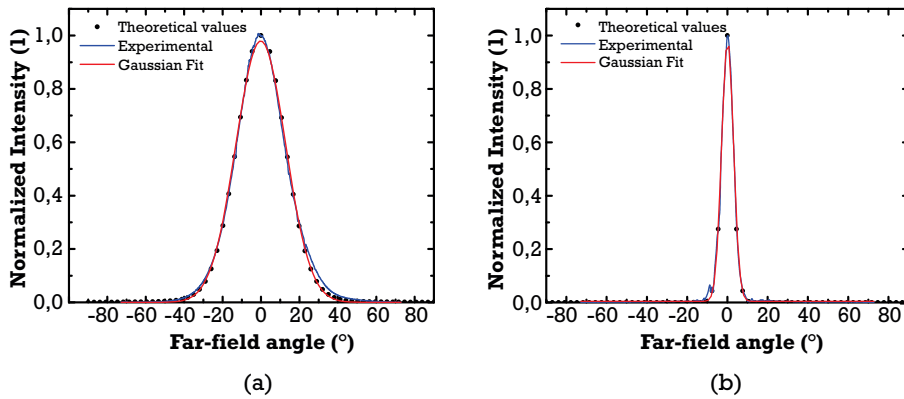


Figure 3.50: Far-field experimental profiles in (a) the fast-axis and (b) the slow-axis, of a XXL2029 DFB laser (C0165) of ridge $w_n = 4 \mu m$ and $h = 1.75 \mu m$

other axis).

Figure (3.50) presents the fast-axis and slow-axis far-field of a XXL2029 DFB laser. By comparison, predicted far-field profiles using FimmWaveTM (section [3.1.2.1]) are plotted against these results. Both theory and experiment agree quite well. Table (3.24) recaps the relevant figures. A Gaussian fit

XXL2029	Theory	Experiment
$\Theta_y^{1/2} / \Theta_y^{1/e^2}$	28.7°/52.1°	[31.5°/53.8°] \pm 2°
$\Theta_x^{1/2} / \Theta_x^{1/e^2}$	7°/12.1°	[6.8°/11.8°] \pm 2°

Table 3.24: Far-field divergence values of the laser C0165 ($L = 2 mm$, $w_n = 4 \mu m$ and $h = 1.75 \mu m$) at 883 nm at 20°C: comparison between optical computation and experiment

of the experimental data for each axis of divergence reveals that the beam deviates slightly from the ideal Gaussian profile in the fast axis.

Turning now to the near-field observation, figure (3.51) displays the profile of a XXL2029 laser in the slow-axis y -direction. We can notice that under current injection, such optical profile changes: while it is more or less Gaussian above threshold up to 300 mA, the shape modifies deeply above this current to reveal another mode which is probably the second-order TE₀₁ mode.

Also, even below 300 mA, the maximum of the peak shifts to the right: **this beam steering**

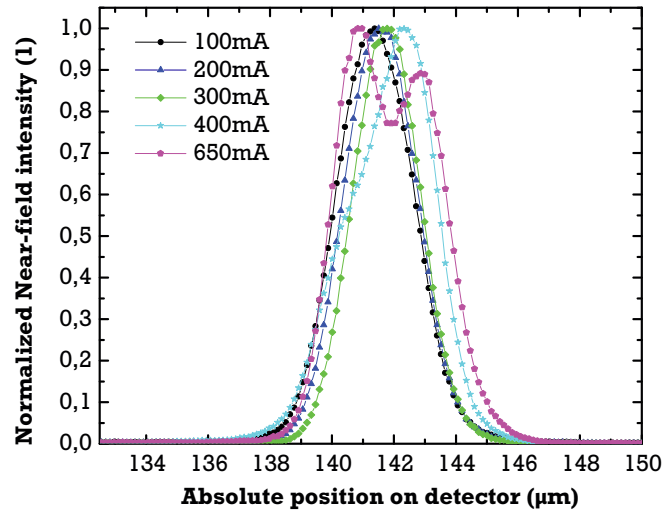


Figure 3.51: Near-field experimental profiles of laser C0237 ($L = 2 \text{ mm}$, $w_n = 4 \text{ } \mu\text{m}$ and $h = 1.75 \text{ } \mu\text{m}$) at several levels of current injection. Modification of the modal geometry is clearly visible

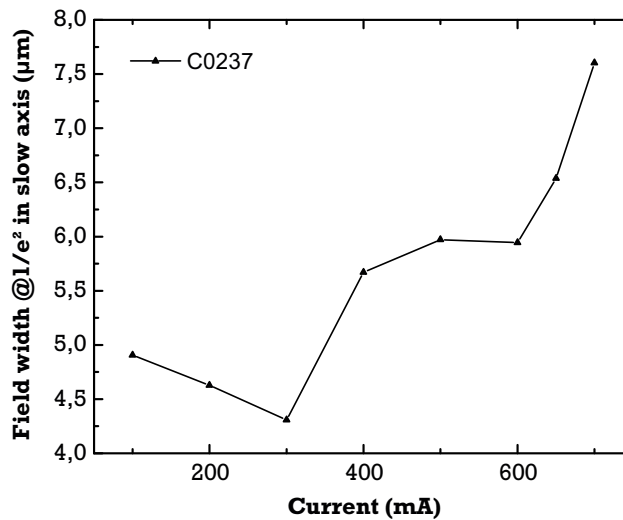


Figure 3.52: Near-field $1/e^2$ width of laser C0237 ($L = 2 \text{ mm}$, $w_n = 4 \text{ } \mu\text{m}$ and $h = 1.75 \text{ } \mu\text{m}$) versus the injected current. Above $I = 300 \text{ mA}$, the near-field width broadens substantially

phenomenon is characteristic of lateral mode instability. It may result from the relatively weak lateral optical confinement which is perturbed by gain-guiding with current spreading. A plot of the $1/e^2$ near-field width w_x^{1/e^2} versus the injected current (figure (3.52)) shows that up to 300 mA the mode width reduces (probably because of a thermal-lens effect under Joule heating) then the mode broadens abruptly for the onset of the higher order lateral mode. The optical theory gives (for an index-guided model) $w_x^{1/e^2} = 5.5 \text{ } \mu\text{m}$ for a cold optical cavity. All devices investigated show the same behavior, which is more pronounced for XXL2020 lasers. The decrease in external efficiency highlighted in the previous section may be linked to mode instabilities here.

D/ Stop-band evaluation

In section [3.1.3.1], we have seen that the normalized stop-band value (NSB) of a DFB laser in a given configuration can be predicted and is related to the normalized coupling strength to the grating κL . Though, in practice, because of the random phase at facets, the NSB has a dispersion in values which prevents to find precisely the coupling value with this single data. If one uses a DFB in a strong AR-AR configuration with $R_1 = R_2 < 0.5\%$ and measures the NSB, it is possible to give a quite precise value of κL [Jacquet 1990]. Figure (3.53) plots precisely the theoretical prediction of the coupled-modes theory for the NSB values versus κL . For $\kappa L \geq 1$, which is precisely our case, the coefficient can be determined with good accuracy, despite the phase dispersion. For $\kappa L < 1$, the dispersion is high, and one requires a (too) low facet reflectivity value to draw a conclusion (below 0.01% for instance). A more general method to find all the optical parameters, including the experimental phases, is to perform a numerical fit based on a sub-threshold ASE model with a parametrized regression [Wenzel 2003, Wenzel 2004]. This would go to far in the frame of this study.

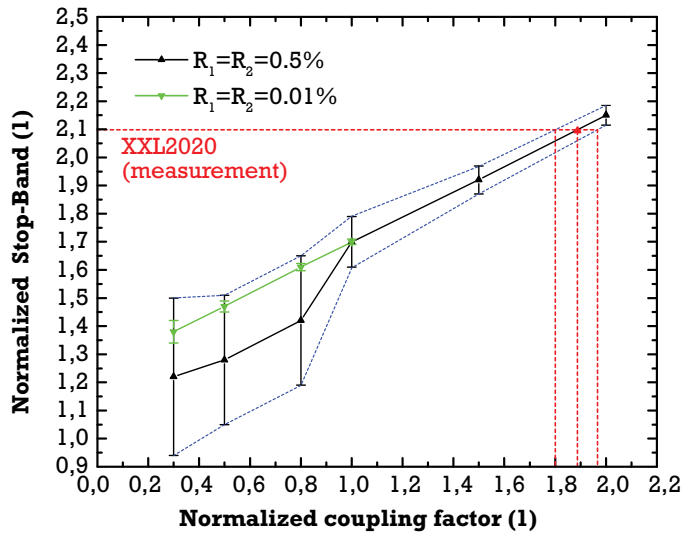


Figure 3.53: NSB versus κL for $R_1 = R_2 = 0.5\%$ (black triangles) and for $R_1 = R_2 = 0.01\%$ (green reversed triangles). The error bars are related to the NSB dispersion from the random phases at the front-facet. Computed from (3.37)

For XXL2020, with a treatment $R_1 = R_2 = 0.5\%$ (a lower value was not achievable for technical reasons), one measures a stop-band $\Delta\lambda_{SB} = 0.1 \pm 0.05$ for a $L = 2 \text{ mm}$ laser, and $\Delta\lambda_{FP} = 0.048 \pm 0.01$ for a Fabry-Perot laser of same length, which yields $NSB = 2.1 \pm 0.1$. According to the above simple model, if the NSB was exactly equal to 2.1, the normalized coupling strength value would be between 1.8 and 1.95. Because of experimental uncertainties, the value is more $\kappa L \in [1.6; 2.15]$. This is why it is interesting to have very low AR values on the facets to perform these estimations. Despite the possible range of coupling values (for the worst case of uncertainty), **it corroborates the hypothesis made earlier on the high built-in coupling strength of the grating**, which is far from being at its highest theoretical value, because of the aspect ratio of the grating.

3.3.3 Conclusion on the first run of fabrication

The conclusion on the 1st run of fabrication can be the following: as a first try, the 894 nm lasers present good enough spectral characteristic to address the D_1 line, with sufficient single-mode optical

power. However, because of the gain detuning for the targeted wavelength, the lasers are only operable at high-temperature. This is non-optimum for a low Henry's factor or for the resistance to optical feedback. Also, a shorter tuning range between two mode hops is not favorable to obtain safe operation margin around the D_1 line. We have also seen that the technological process deserves improvements on the rendered geometrical shape of the waveguide and of the Bragg corrugation, to avoid multimode behavior of the ridge guide and a dangerous decrease of the coupling factor to the grating.

Despite the drawbacks mentioned, we want to point out the good yield of fabrication of single-mode lasers in this 1st run. Graphics ((3.54)) precisely show this technological yield for the two wafers of each wavelength, on two populations of C-mounted lasers, originating from chips collected from the central part of the wafers (the statistics includes the yield from the fabrication of the cleaving and mounting). The population in each case is of around 60 lasers.

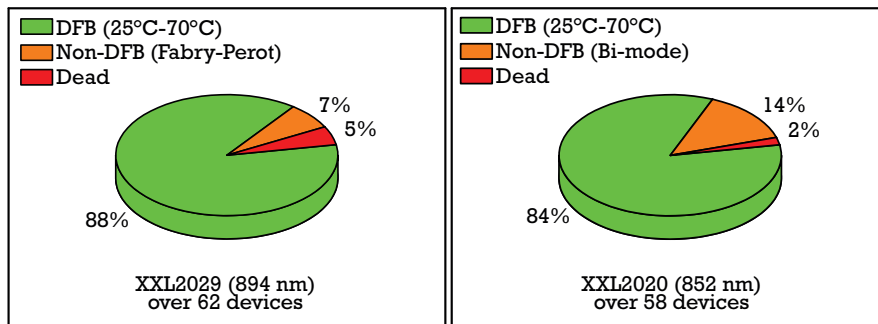


Figure 3.54: Left: statistics of the effective technological yield of DFB (single-mode) lasers on C-mount over a population of 62 devices, for XXL2029. Left: same analysis for XXL2020

One can notice that the yield exceeds 80% of functional lasers that have the first-order characteristics to be used as efficient single-mode lasers. Then, for XXL2029, 7% of the mounts showed a Fabry-Perot type spectrum. This is due to the gain detuning, which is not homogeneous and prevents in some cases single-mode operation below $70^\circ C$. For XXL2020, 14% of the lasers have stable bi-mode spectrum in the targeted range of operation. This can be linked to the high coupling factor of this fabrication which was underlined before. Otherwise, respectively 5% and 2% of the devices had no laser behavior, emitting only ASE. The mounting itself was not at the origin of the failure, but rather damages at the facets, coming from improper cleaving of the mirrors during bars separation (it was noticed that the wafers did not spontaneously broke along the designated crystal planes in many cases). Also, the packaging concept [3.2.6] was successfully implanted. As a first batch of prototypes, 8 modules of each wavelength (based first on epoxy glued parts), and then 25 others (fully soldered) were fabricated out of the 1st run. They gave start-of-the-art operation of the OCFS during the first implementations (see last chapter).

3.4 Summary

In this chapter, the theoretical and experimental realization of single-mode DFB laser modules at the D_1 and D_2 cesium lines have been addressed in practice. With the previous vertical structure of 852 nm lasers as a background, simulations of the electro-optics properties of laser cavities have allowed us to examine the properties of the modes to ensure a vertical single-mode behavior and an estimation of the optical losses of the cavities. This has led to the design of **a new cavity with a less divergent beam in the fast axis and lower losses**, acting favorably for the application requirements. Then, a more in-depth look at the transverse optical and electrical confinement in a ridge-waveguide allowed us to formulate a rule on the adequate choice of the ridge width w and the etching depth h to obtain robust transverse single-mode behavior and current confinement. Concerning the Bragg grating properties, a more accurate prediction of the crucial coupling factor value showed that, due to the new fabrication process, the built-in value of this factor was not optimum and led to an over-coupling to the grating, decreasing the probability to obtain single-mode lasers. More generally, thanks to the coupled-modes theory, the longitudinal modal properties with relation to the laser optical parameters were highlighted: **an increasing κL value lowers the resonator losses and confers a relative immunity to external parasitic optical feedback**. Regarding noise now, it was clear that **the length of the device is a key lever to reduce the magnitude of the Schawlow-Townes-Henry linewidth, and to further extent the 'technical' electronic noise**.

The effective technological realization of the lasers is an art in itself: from the epitaxy to the grating and cavity processing, deviations from the ideal computed parameters are easy, and one has to understand then the consequences on the device behavior. The 1st run of fabrication, (which optical parameters were based to a great extent on the former laser design) allowed to confront the theory to the reality: a renewed technological process, new designs of the masks and of the process, up to the mounting of the chip were conducted in the perspective of reproducibility and homogeneity of the lasers properties. **The first order characterizations of the devices showed that this goal was partly achieved, with more than 80% of yield on single-mode DFB lasers**. The basic beam and spectral properties were analyzed and they agree well with what was expected. Similar characterizations from LTF-UniNe confirmed these results [von Bandel 2016].

Though, an epitaxial mis-calibration in the well of the 894 nm lasers led to a high detuning of the gain with relation to the Bragg wavelength, forcing the devices to be **single-mode at high temperatures**. Also, the technological mis-realization of the ridge-waveguide, together with loose guiding parameters w and h gave, with high probability, a quick (lateral) multimode behavior with increasing injected current. In spite of those negative points, **the lasers were integrated in a home-made TO3 module and tested successfully in different OCFS prototypes**. For the 894 nm DFBs of the 1st run, the 40 mW of output power are reached at around 165 – 180 mA and $T = 65 - 70^\circ C$. This high temperature of operation is not favorable for the electronic stabilization of the source in a control loop, this is why **a 2nd run of fabrication was necessary to correct that**, along with more adequate optical parameters, as computed in the study.

Bibliography

- [Achtenhagen 1999] Martin Achtenhagen et Amos Hardy. *Lateral current spreading in ridge waveguide laser diodes*. Applied physics letters, vol. 74, no. 10, pages 1364–1366, 1999.
- [Achtenhagen 2006] Martin Achtenhagen, Amos Hardy et Christoph S Harder. *Lateral mode discrimination and self-stabilization in ridge waveguide laser diodes*. IEEE photonics technology letters, vol. 18, no. 3, pages 526–528, 2006.
- [Adachi 2009] Sadao Adachi. Properties of semiconductor alloys: group-iv, iii-v and ii-vi semiconductors, volume 28. John Wiley & Sons, 2009.
- [Afromowitz 1974] Martin A Afromowitz. *Refractive index of Ga 1- x Al x As*. Solid State Communications, vol. 15, no. 1, pages 59–63, 1974.
- [Agrawal 1984] G Agrawal. *Lateral analysis of quasi-index-guided injection lasers: transition from gain to index guiding*. Journal of lightwave technology, vol. 2, no. 4, pages 537–543, 1984.
- [Bennett 1990] Brian R Bennett, Richard A Soref et Jesus A Del Alamo. *Carrier-induced change in refractive index of InP, GaAs and InGaAsP*. IEEE Journal of Quantum Electronics, vol. 26, no. 1, pages 113–122, 1990.
- [Buus 2005] Jens Buus, Markus-Christian Amann et Daniel J Blumenthal. Tunable laser diodes and related optical sources. Wiley-Interscience New York, 2005.
- [Casey Jr 1975] HC Casey Jr, DD Sell et KW Wecht. *Concentration dependence of the absorption coefficient for n- and p- type GaAs between 1.3 and 1.6 eV*. Journal of Applied Physics, vol. 46, no. 1, pages 250–257, 1975.
- [Chen 1997] XY Chen, PM Koenraad, FN Hooge, JH Wolter et V Aninkevicius. *1/f noise in δ -doped GaAs analyzed in terms of mobility fluctuations*. Physical Review B, vol. 55, no. 8, page 5290, 1997.
- [Christensen 1992] Kim Christensen, Zeev Olami et Per Bak. *Deterministic 1/f noise in nonconservative models of self-organized criticality*. Physical Review Letters, vol. 68, no. 16, page 2417, 1992.
- [Coldren 2012] Larry A Coldren, Scott W Corzine et Milan L Mashanovitch. Diode lasers and photonic integrated circuits, volume 218. John Wiley & Sons, 2012.
- [Daulasim 1994] Khamphanh Daulasim. *Caractérisation et modélisation des bruits blancs et en 1/F des diodes lasers à semiconducteur*. PhD thesis, Université Montpellier II, 1994.
- [Denet 2016] Stéphane Denet, Baptiste Chomet, Vincent Lecocq, Laurence Ferrières, Mikhaël Myara, Laurent Cerutti, Isabelle Sagnes et Arnaud Garnache. *Industrial integration of high coherence tunable VECSEL in the NIR and MIR*. Proc. SPIE, vol. 9734, pages 97340C–97340C–10, 2016.
- [Dutta 1981] Pulak Dutta et PM Horn. *Low-frequency fluctuations in solids: 1/f noise*. Reviews of Modern physics, vol. 53, no. 3, page 497, 1981.
- [Favre 1987] Francois Favre. *Theoretical analysis of external optical feedback on DFB semiconductor lasers*. IEEE journal of quantum electronics, vol. 23, no. 1, pages 81–88, 1987.

- [Gao 2013] Lihong Gao, F Lemarchand et M Lequime. *Refractive index determination of SiO₂ layer in the UV/Vis/NIR range: spectrophotometric reverse engineering on single and bi-layer designs*. Journal of the European Optical Society-Rapid publications, vol. 8, 2013.
- [Ghafouri-Shiraz 2004] H Ghafouri-Shiraz. Distributed feedback laser diodes and optical tunable filters. John Wiley and Sons, 2004.
- [Glinski 1986] J Glinski et T Makino. *Mode selectivity in DFB lasers with a second-order grating*. Electronics letters, vol. 22, no. 12, pages 679–680, 1986.
- [Grillot 2003] F Grillot, B Thedrez, O Gauthier-Lafaye, MF Martineau, V Voiriot, JL Lafragette, JL Gentner et L Silvestre. *Coherence-collapse threshold of 1.3- μ m semiconductor DFB lasers*. IEEE Photonics Technology Letters, vol. 15, no. 1, pages 9–11, 2003.
- [Grillot 2004] Frédéric Grillot, Bruno Thedrez et Guang-Hua Duan. *Feedback sensitivity and coherence collapse threshold of semiconductor DFB lasers with complex structures*. IEEE Journal of Quantum Electronics, vol. 40, no. 3, pages 231–240, 2004.
- [Grillot 2009] Frédéric Grillot. *On the effects of an antireflection coating impairment on the sensitivity to optical feedback of AR/HR semiconductor DFB lasers*. IEEE Journal of Quantum Electronics, vol. 45, no. 6, pages 720–729, 2009.
- [Herve 1994] P Herve et LKJ Vandamme. *General relation between refractive index and energy gap in semiconductors*. Infrared physics & technology, vol. 35, no. 4, pages 609–615, 1994.
- [Hooge 1981] FN Hooge, TGM Kleinpenning et LKJ Vandamme. *Experimental studies on 1/f noise*. Reports on progress in Physics, vol. 44, no. 5, page 479, 1981.
- [Hooge 1994] FN Hooge. *1/f noise sources*. IEEE Transactions on Electron Devices, vol. 41, no. 11, pages 1926–1935, 1994.
- [Hu 1994] SY Hu, SW Corzine, K-K Law, DB Young, AC Gossard, LA Coldren et JL Merz. *Lateral carrier diffusion and surface recombination in InGaAs/AlGaAs quantum-well ridge-waveguide lasers*. Journal of applied physics, vol. 76, no. 8, pages 4479–4487, 1994.
- [Huang 2003] Robin K Huang, Joseph P Donnelly, Leo J Missaggia, Christopher T Harris, Jason Plant, Dan E Mull et William D Goodhue. *High-power nearly diffraction-limited AlGaAs-InGaAs semiconductor slab-coupled optical waveguide laser*. IEEE Photonics Technology Letters, vol. 15, no. 7, pages 900–902, 2003.
- [Jacquet 1990] J. Jacquet. *Etude*. PhD thesis, 1990.
- [Jellison 1992] GE Jellison. *Optical functions of GaAs, GaP, and Ge determined by two-channel polarization modulation ellipsometry*. Optical Materials, vol. 1, no. 3, pages 151–160, 1992.
- [Kogelnik 1972] H Kogelnik et CV Shank. *Coupled-wave theory of distributed feedback lasers*. Journal of applied physics, vol. 43, no. 5, pages 2327–2335, 1972.
- [Kojima 1985] Keisuke Kojima, Kazuo Kyuma et Takashi Nakayama. *Analysis of the spectral linewidth of distributed feedback laser diodes*. Journal of lightwave technology, vol. 3, no. 5, pages 1048–1055, 1985.

- [Laakso 2008] Antti Laakso, Mihail Dumitrescu, Pasi Pietilä, Mikko Suominen et Markus Pessa. *Optimization studies of single-transverse-mode 980 nm ridge-waveguide lasers*. Optical and quantum electronics, vol. 40, no. 11-12, pages 853–861, 2008.
- [Lang 1980] Roy Lang et Kohroh Kobayashi. *External optical feedback effects on semiconductor injection laser properties*. IEEE journal of Quantum Electronics, vol. 16, no. 3, pages 347–355, 1980.
- [Laurain 2010] Alexandre Laurain. *Sources laser à semiconducteur à émission verticale de haute cohérence et de forte puissance dans le proche et le moyen infrarouge*. PhD thesis, Université Montpellier II-Sciences et Techniques du Languedoc, 2010.
- [Ligeret 2008a] V Ligeret. *Etude*. PhD thesis, Université Pierre et Marie Curie - Paris VI, 2008.
- [Ligeret 2008b] V Ligeret, S Bansropun, M Lecomte, M Calligaro, O Parillaud, D Holleville, N Dimarcq, N Michel et M Krakowski. *Narrow linewidth and demonstration of saturation spectra of the Cesium at 852 nm with high power Al-free DFB laser diodes*. In Integrated Optoelectronic Devices 2008, pages 69091F–69091F. International Society for Optics and Photonics, 2008.
- [Lobé 2015] J Bébé Manga Lobé. *Développement de diodes laser à faible largeur de raie pour le pompage atomique et d'un MOPA (Master Oscillator Power Amplifier) à 780 nm pour le refroidissement d'atomes de Rubidium et la réalisation de capteurs inertiels*. PhD thesis, 2015.
- [Marcatili 1974] EAJ Marcatili. *Slab-Coupled Waveguides*. Bell System Technical Journal, vol. 53, no. 4, pages 645–674, 1974.
- [Moser 1994] M Moser, R Winterhoff, C Geng, I Queisser, F Scholz et A Dörnen. *Refractive index of $(Al_xGa_{1-x})_0.5In_{0.5}P$ grown by metalorganic vapor phase epitaxy*. Applied physics letters, vol. 64, no. 2, pages 235–237, 1994.
- [Mostallino 2017] Roberto Mostallino. PhD thesis, 2017.
- [Nakamura 1975] M Nakamura, K Aiki, J Umeda et A Yariv. *CW operation of distributed-feedback GaAs-GaAlAs diode lasers at temperatures up to 300 K*. Applied Physics Letters, vol. 27, no. 7, pages 403–405, 1975.
- [O'Brien 2005] Stephen O'Brien et EP O'Reilly. *Theory of improved spectral purity in index patterned Fabry-Perot lasers*. Applied Physics Letters, vol. 86, no. 20, page 201101, 2005.
- [Ogita 1987] S Ogita, M Hirano, H Soda, M Yano et H Ishikawa. *Dependence of spectral linewidth of DFB lasers on facet reflectivity*. Electronics Letters, vol. 23, pages 347–349, 1987.
- [Ogita 1988] S Ogita, Y Kotaki, K Kihara, M Matsuda, H Ishikawa et H Imai. *Dependence of spectral linewidth on cavity length and coupling coefficient in DFB laser*. Electronics Letters, vol. 24, no. 10, pages 613–614, 1988.
- [Orsal 1994] Bernard Orsal, Philippe Signoret, J-M Peransin, Khamphanh Daulasim et Robert Alabedra. *Correlation between electrical and optical photocurrent noises in semiconductor laser diodes*. IEEE Transactions on electron devices, vol. 41, no. 11, pages 2151–2161, 1994.
- [Petermann 1979] Klaus Petermann. *Calculated spontaneous emission factor for double-heterostructure injection lasers with gain-induced waveguiding*. IEEE Journal of Quantum Electronics, vol. 15, no. 7, pages 566–570, 1979.

- [Plant 2005] Jason J Plant, Paul W Juodawlkis, Robin K Huang, Joseph P Donnelly, Leo J Missaggia et Kevin G Ray. *1.5- μm InGaAsP-InP slab-coupled optical waveguide lasers*. IEEE photonics technology letters, vol. 17, no. 4, pages 735–737, 2005.
- [Schubert 1995] Mathias Schubert, V Gottschalch, Craig M Herzinger, Huade Yao, Paul G Snyder et John A Woollam. *Optical constants of GaIn1- x P lattice matched to GaAs*. Journal of applied physics, vol. 77, no. 7, pages 3416–3419, 1995.
- [Siegman 1986] Anthony E Siegman. Lasers. University Science Books, Mill Valley, CA, 1986.
- [Signoret 1994] Philippe Signoret. *Analyse des bruits optique-électriques et étude de leur corrélation. Application à une tête optique d'émission laser à réaction répartie*. PhD thesis, Université Montpellier II, 1994.
- [Signoret 1995] Philippe Signoret, Bernard P. Orsal, Jean-Marie Peransin et Robert M. Alabedra. *Analysis of white optical and electrical noises of a DFB laser with optical feedback*. Proc. SPIE, vol. 2382, pages 187–199, 1995.
- [Streifer 1975] William Streifer, D Scifres et R Burnham. *Coupling coefficients for distributed feedback single-and double-heterostructure diode lasers*. IEEE Journal of Quantum Electronics, vol. 11, no. 11, pages 867–873, 1975.
- [Stringfellow 1999] Gerald B Stringfellow. Organometallic vapor-phase epitaxy: theory and practice. Academic Press, 1999.
- [Tkach 1986] R Tkach et AR Chraplyvy. *Regimes of feedback effects in 1.5- μm distributed feedback lasers*. Journal of Lightwave technology, vol. 4, no. 11, pages 1655–1661, 1986.
- [Tourenç 2005] Jean-Philippe Tourenç. *Caractérisation et modélisation du bruit d'amplitude optique, du bruit de fréquence et de la largeur de raie de VCSELs monomodes émettant autour de 850 nm*. PhD thesis, Montpellier 2, 2005.
- [von Bandel 2016] N von Bandel, M Garcia, M Lecomte, A Larrue, Y Robert, O Driss, O Parillaud, M Krakowski, F Gruet, R Matthey et al. *DFB-ridge laser diodes at 894 nm for Cesium atomic clocks*. In SPIE OPTO, page 97552K. International Society for Optics and Photonics, 2016.
- [Wang 1987] J Wang, N Schunk et K Petermann. *Linewidth enhancement for DFB lasers due to longitudinal field dependence in the laser cavity*. Electronics Letters, vol. 14, no. 23, pages 715–717, 1987.
- [Wenzel 2003] Hans Wenzel. *Green's function based simulation of the optical spectrum of multisection lasers*. IEEE Journal of selected topics in quantum electronics, vol. 9, no. 3, pages 865–871, 2003.
- [Wenzel 2004] H Wenzel, A Klehr, M Braun, F Bugge, G Erbert, J Fricke, A Knauer, P Ressel, B Sumpf, M Weyers et al. *Design and realization of high-power DFB lasers*. In Optics East, pages 110–123. International Society for Optics and Photonics, 2004.
- [Wunsche 1993] HJ Wunsche, U Bandelow et H Wenzel. *Calculation of combined lateral and longitudinal spatial hole burning in $\lambda/4$ shifted DFB lasers*. IEEE journal of quantum electronics, vol. 29, no. 6, pages 1751–1760, 1993.

-
- [Yonezu 1973] Hiroo Yonezu, Isamu Sakuma, Kohroh Kobayashi, Taibun Kamejima, Masayasu Ueno et Yasuo Nannichi. *A GaAs-AlXGa1-XAs double heterostructure planar stripe laser*. Japanese Journal of Applied Physics, vol. 12, no. 10, page 1585, 1973.

Part III

Laser noise study: free-running and in-loop configurations

Electrical noise characterization

4.1 Noise quantification: an introduction

4.1.1 Introduction

The aim of the noise study is to have access to the coherence time of the laser. A possible definition of this time, which will be referred as τ_c , has been given in (2.31), pointing out that it is inversely proportional to the linewidth of the source, which is intuitive: after a few τ_c , the laser-field sees changes in its fundamental parameters (jump of phase, reorientation of polarization...) or, from a photon point of view, the particles have changed their wave-vector \vec{k} . For instance, the random spontaneous emission depicted at the beginning of chapter 2 produces decorrelated photons that add to the stimulated (coherent) emission. Before looking further into this so-called quantum-originated *frequency noise* that induces the Schawlow-Townes Henry limit, one must first study the noise created by the pump power (the electrical injection into the semiconductor) which perturbs the quantum noise picture. We will prove here that this noise has a non-negligible magnitude compared to the other sources of fluctuations and that it is intrinsic to the noise of the device, unlike it is sometimes read in the literature (where it is only attributed to noisy external current supplies: it can be the case but it is not systematic). It is then bound to have an impact on the frequency noise and the linewidth of the source, which in turn has an impact on the performances of the atomic clock. For these reasons, it is worth to study further this thematic. Also, these measurements can give additional interesting informations on the semiconductor crystal quality and the reliability in time of the device, which is an essential parameter for the lifetime of the whole system.

The study will be structured as follow: first, the key notions and criteria for noise quantification will be introduced. Then, the experimental set-ups and their principles will be described: care must be taken to calibrate the experimental data and to interpret correctly what is measured. Measurements carried out on the 1st manufacturing run of modules, in the frame of the LAMA project, will allow to draw quantitative conclusions on the magnitude of the electric noise in these devices and its possible origins. This will be used in chapter 5 to give an interpretation of the trends of the frequency noise at low-frequencies, after a systematic study of the optical coherence of the sources. For that, the methods developed here are valuable, even if they address a different type of fluctuations of the laser parameters.

4.1.2 RMS fluctuations and spectral density of noise

Let consider $x(t)$, a time-dependent signal which is generated with a probability P , out of a *random* variable X parametrized by t . By definition, the outcomes $\{x_i(t)\}$ are unpredictable: they define a *noisy* signal. Figure (4.1) represents a 'single shot' of this realization in the time domain, on $\Delta t = 1$ s starting at $t = 0$ s.

Because of the previous characteristics, its properties can only be described in terms of *statistical* quantities (the *moments*) derived from the law P . The *mean* value $\overline{x(t)}$ and the *variance* $\Delta x(t)^2$ are

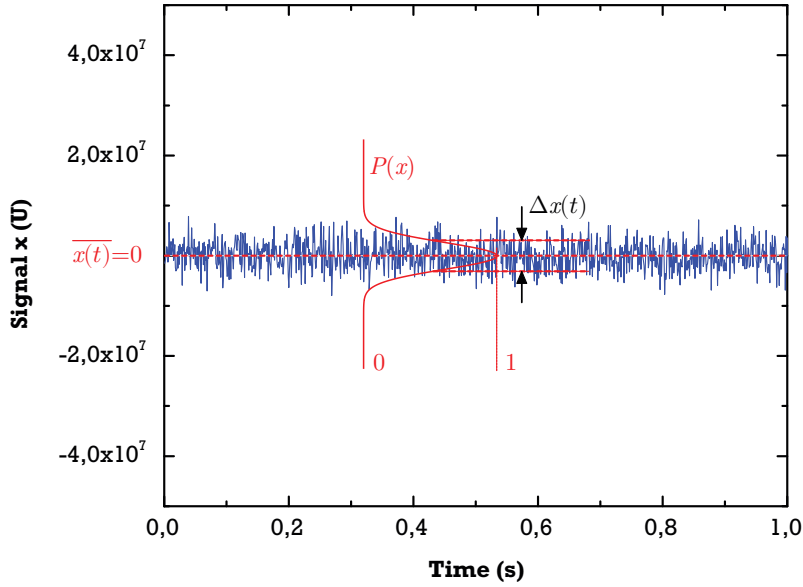


Figure 4.1: Example of a stationary signal x as a function of time t , result of one outcome of a random variable distributed with a probability P . Its mean value $\overline{x(t)} = 0$ and standard deviation $\Delta x(t)$ over the interval $\Delta t = 1$ s can be defined

some of them: they can be defined if the signal is *stationary* over the range of observation (its moments do not depend on t). Usually, the signal x is known through *samples* distant from the same *period* $T = t_{i+1} - t_i$ (4.1), so:

$$\overline{x(t)} = \frac{1}{\Delta t} \int_{t_1}^{t_2} x(t) dt = \frac{1}{N} \sum_{i=1}^N x(t_i) \quad (4.1)$$

$$\Delta x(t)^2 = \frac{1}{\Delta t} \int_{t_1}^{t_2} (x(t) - \overline{x(t)})^2 dt = \frac{1}{N} \sum_{i=1}^N (x(t_i) - \overline{x(t)})^2 \quad (4.2)$$

where $\Delta t = t_2 - t_1$, $t_i \in [t_1, t_2]$ and $N = \Delta t/T$ is the number of samples in the interval. If x is also *ergodic*¹, the temporal mean $\overline{x(t)}$ is equal to the mean computed on multiple random realizations of X at t : this is how it is retrieved in practice, from an experimental point of view. Indeed, **a physical measurement process cannot last an infinite time**: we can just hope that the noise characteristics are well represented over Δt and try to work on a limited set of data. Also, $\overline{x(t)}$ is the macroscopic value observed at first order on this time-scale: the output power measured with an integrating sphere for instance, or the mode wavelength measured with a low-resolution OSA. On the other side, this mean value fluctuates locally, with a very tiny dispersion quantified by $\Delta x(t)$. Though, these parameters do not help to identify, *a priori*, a regular pattern from the direct temporal observation of x . The *auto-correlation function* R_x highlights those similarities. It is defined as (4.3):

$$R_x(\tau) = \lim_{\Delta t \rightarrow \infty} \frac{1}{\Delta t} \int_0^{\Delta t} x(t)^* \times x(t + \tau) dt \quad (4.3)$$

where '*' stands for the complex conjugate operator. It can be seen as a convolution product in time of x by itself. It is maximized when repetitions in the signal are found. However, working in the time

¹The ergodicity hypothesis will always be assumed, because it is a classical hypothesis of the thermodynamical systems which we are dealing with here. Physically speaking, it means that the space of states of the system is homogeneously scanned (all the possible outcomes x_i are accessible) with the time parameter

domain is not always practical: if the signal has always the same level of fluctuations on a time scale Δt , this will be pointed out simply in the frequency domain $f = 1/t$. Thus, it is interesting to have a look at the *Fourier transform* \hat{x} of x (4.4):

$$\hat{x}(f) = \mathcal{F}[x(t)] = \int_{-\infty}^{\infty} x(t)e^{-i\omega t} dt \quad (4.4)$$

where $\omega = 2\pi f$. The corresponding *power* of the fluctuations of x are noted $\Delta\hat{x}(f)^2$ on an interval/a bandwidth $\Delta f = f_2 - f_1$ and can be computed, if $\overline{x(t)} = 0$, as (4.5):

$$\Delta\hat{x}(f)^2 = \frac{1}{\Delta f} \int_{f_1}^{f_2} \hat{x}(u)^* \times \hat{x}(u) du \quad (4.5)$$

If the bandwidth $\Delta f \rightarrow 0$ and $f \rightarrow \pm\infty$, it can be shown that the related energy is equal in the frequency and in the time domain. One can define the *Root Mean Square* (RMS) value of x (4.6):

$$x_{RMS} \equiv \Delta\hat{x}(f) = \sqrt{\lim_{\Delta t \rightarrow \infty} \frac{1}{\Delta t} \int_{-\frac{\Delta t}{2}}^{+\frac{\Delta t}{2}} x(t)^2 dt} = \sqrt{\int_{-\infty}^{+\infty} S_x(f) df} \quad (4.6)$$

$$S_x(f) \equiv \hat{x}(f)^* \hat{x}(f) = |\hat{x}(f)|^2 \quad (4.7)$$

S_x is the *double-sided power spectral density* (PSD) of x . It measures the mean power (on an infinite horizon of time) of the signal fluctuations at a frequency $f \in]-\infty, +\infty[$ in a unit bandwidth. In practice, there is no access to the negative frequencies (because of causality) so the *single-sided* PSD is defined on $]0, +\infty[$ and has *twice* the magnitude of its double-sided counterpart. If x has the unit U , S_x has the unit of $U^2 \cdot Hz^{-1}$. The well-know Wiener-Khintchine theorem links the PSD to the auto-correlation function (4.8):

$$S_x(f) = \mathcal{F}(R_x(\tau)) = \int_{-\infty}^{+\infty} R_x(\tau) e^{-i\omega\tau} d\omega \quad (4.8)$$

It is important to underline that there is a major conceptual step in (4.6): **we can now have an equivalent frequency picture of the noise provided S_x is known**, and the link between the two is the *RMS* value of x . If it is true that the experimentalist cannot have access to all the frequencies of the spectrum, it is still possible to compute this quantity on a limited bandwidth. The PSD has then the same status as x at the beginning of this introduction: in stationary and ergodic conditions, it is *estimated* experimentally by ensemble means over repeated measurements: $S_x(f) = \overline{|\hat{x}(f)|^2}$. **We will assume from now on and in all the coming chapters that it is effectively this quantity when talking about the PSD for experimental results.**

In practice, there are basically two ways to recover the power spectrum in the frequency domain:

1. Sweeping spectrum analyzers: a bandpass filter of finite bandwidth scans a limited band of frequencies of the spectrum and measures the corresponding power (Electrical Spectrum Analyzers or ESA, for instance)
2. FFT-analyzers: The signal is sampled once in the time-domain (with a time-scope for instance or any other type of sampler) and Fourier transformed to the frequency domain using numerical *fft-algorithms*

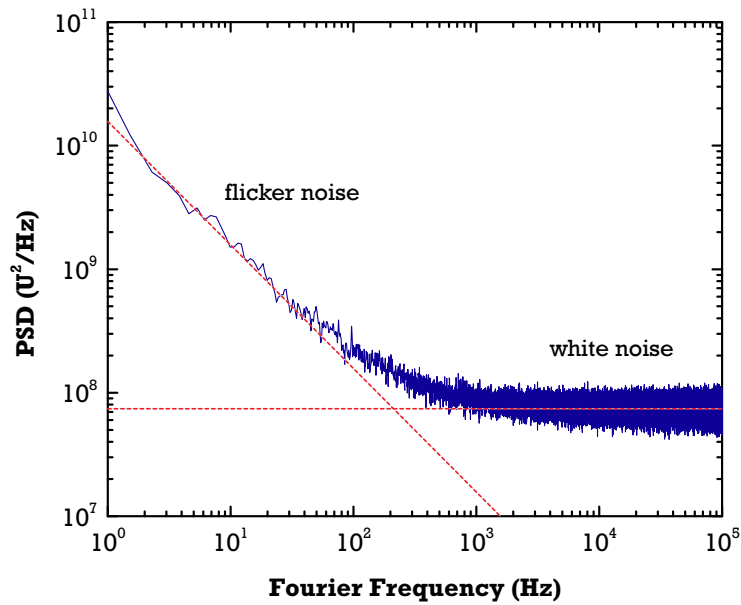


Figure 4.2: Example of the PSD computation of signal x in figure (4.1). At high frequencies, the noise is 'white', while a $1/f$ 'flicker' noise stands out at low frequencies

If the two methods give equivalent results in the majority of the cases encountered, it is preferable to use the second one for reasons that will be made clear in the next chapter. Roughly speaking, ESA apparatus are very limited to provide an accurate picture of the low-frequency noise (when is just not limited to reach this frequency range), for intrinsic reasons of their conception (the resolution of the sweeping filter around a frequency f is inversely proportional to f , so at $\sim 1 \text{ Hz}$, each point needs 1 s . One has then to wait a very long time to acquire the spectrum, which may exceed the time over which the signal is really stationary. This is not the case when the signal is acquired by single-shots). When the frequency-domain signal is retrieved, formula (4.6) can be used.

Be that as it may, this procedure of reaching S_x is far less costly in terms of computation time than estimating R_x first. If the later is needed, it is still better to obtain the function from the frequency domain (the computation time of the autocorrelation is $\sim N^2$ while it is $\sim N \ln_2 N$ for a N -points samples).

Figure (4.2) shows an example of the physical PSD computation of signal x , using a MATLAB[®] 'fft' function. It is very often represented in a log-log plot to identify trends more easily. The function reveals that the noise power components are not equal on the whole spectrum: at high frequencies, there is a constant white noise floor of amplitude $S_0 = 7.5 \times 10^7 \text{ U}^2 \cdot \text{Hz}^{-1}$, at low frequency, $S_x(f) = S_{-1}/f$, with $S_{-1} = 1.5 \times 10^{10} \text{ U}^2$. The later trend is called 'flicker noise'.

The PSD representation is convenient, however it does not tell anything about the *probability distribution* P of the outcomes $x_i(t)$. On this point, for theoretical investigation, one is often led to draw **hypothesis on how the signal is generated**. The Gaussian distribution $P = \mathcal{N}(\mu, \sigma)$ (or *normal* distribution) of X is assumed if it is thought that the physical on-going process in noise generation results from a very high number of independent events. The *density* of probability function

p is then given by (4.9):

$$p(x) = \frac{1}{\sqrt{2\pi\sigma^2}} e^{-\frac{(x-\mu)^2}{2\sigma^2}} \quad (4.9)$$

with μ and σ^2 the mean and variance of the realizations of X . In particular, σ is the RMS value of the signal that would be generated out of P . Another useful modelling law is the discrete *Poisson distribution* $P = \mathcal{P}(k, \lambda)$ in which the probability $p(k)$ of k events to occur in an interval (of time for instance) where λ events have been counted *on average* is given by:

$$p(k) = \frac{\lambda^k e^{-\lambda}}{k!} \quad (4.10)$$

For $\lambda \gg 1$, the distribution converges towards the normal law \mathcal{N} . The electronic shot-noise is for instance well-modeled by this distribution.

★ Note on the experimental averaging

It should be mentioned that because the PSD of x is measured with a statistical uncertainty, we can expect to reduce this dispersion by making a number average over N samples. Indeed, a consequence of the Law of Large numbers implies:

$$\Delta x(t) \sim \frac{1}{\sqrt{N}} \quad (4.11)$$

Thus, with $N = 100$ successive measures, it yields $\pm\sqrt{100} = 10\%$ of the mean. This is systematically done in all the experimental measurements presented further. Of course, a higher N is possible, but it leads first to lengthy experimental manipulations if the low frequency domain is explored, and second, the set-up has to be stable enough to give consistent results over time (in the case of mechanical noise in optical coherence measurements, this can be tricky).

★ Note on the Allan deviation

When the signal is not stationary over the horizon of observation (drift of the mean value $x(t)$), the meaningful quantity to use is the Allan variance (or its derivatives), which is always defined, unlike the RMS value. As a reminder of chapter 1:

$$AVAR = \sigma_y^2(\tau) = \frac{1}{2(N-1)} \sum_{i=1}^{N-1} [\bar{x}(t_{i+1}) - \bar{x}(t_i)]^2 \quad (4.12)$$

with $\bar{x}(t_i)$ the i^{th} mean of x over the timescale τ . For a temporal step of 1 (in the sampling procedure), the AVAR is equal to the variance of the sample.

4.1.3 Fundamental electrical noise sources

The first very fundamental noise encountered in all electronic systems is the thermal noise that was already presented in chapter 3, section [3.1.3.2]. As a reminder, a resistor R_S of temperature T , has a PSD of voltage fluctuations (in $V^2 \cdot Hz^{-1}$) [Johnson 1928]:

$$S_V = 4k_B T R_S \quad (4.13)$$

This noise is white and has a level of $S_V = 1.6 \times 10^{-20} \text{ V}^2 \cdot \text{Hz}^{-1}$ at room temperature, for $R_S = 1 \Omega$.

Another type of noise, the shot-noise, is particularly important in the study of the device because it is the fundamental quantum limit brought by the electrical injection in a conductive matrix. More generally, it occurs for any *partition* process of the electronic population. The spectral density of current noise, detected in a conductor where a current of magnitude I is flowing, is [Schottky 1918]:

$$S_I(f) = 2eI \quad (4.14)$$

which magnitude is linear in I . For $I = 50 \text{ mA}$, $S_I(f) = 2eI = 2 \times (1.6 \times 10^{-19}) \times 0.05 = 1.6 \times 10^{-20} \text{ A}^2 \cdot \text{Hz}^{-1}$. This current injection generates the same PSD of voltage noise in a resistor of 1Ω as the thermal noise at room temperature.

4.2 Experimental setup

4.2.1 Digital high-quality sampling: basic rules

As mentioned above, the signal recorded is always a sample of the physical quantity measured. In terms of signal processing, this has concrete consequences on the validity of the data after Fourier operations in the frequency domain. A few rules have to be followed:

- *Sampling rate*: the sampling unit time dt_s defines a *sampling frequency* $f_s = 1/dt_s$. Let consider a sinusoidal signal of frequency f . It can be for instance a Fourier component of the physical signal x . The phase information in the signal can be reconstructed if there is at least one point per period of the sine in the time domain. More generally, the Shannon theorem states that an acceptable sample of signal x should be such that the sampling frequency f_s verifies:

$$f_s \geq \frac{f_{max} - f_{min}}{2} \quad (4.15)$$

where f_{max} and f_{min} are the maximum and minimal frequency of the spectrum of \hat{x} . If this condition is not realized, the *aliasing* phenomenon occurs: all the power components of the frequencies above f_s are mirrored back to the useful signal which must be then low-pass filtered. In practice, if we want to analyse the signal up to $f_{max} = 10 \text{ MHz}$, $f_s \geq 20 \text{ MHz}$.

- *Sample size*: For a sampling frequency f_s that satisfies the Shannon criterion, we can choose f_{min} in the low-frequencies that determines the total number of samples required. If $f_{min} = 1 \text{ Hz} \iff t_{max} = 1 \text{ s}$, then $N_s = f_s \times t_{max} \geq 20 \text{ MS}$. Thus, the acquisition capabilities need at least that amount of recording memory.

4.2.2 Acquisition chain and experimental conditions

The experimental setup of electric noise measurement is depicted in figure (4.3). It consists in measuring the *voltage* fluctuations at the laser diode (DUT) terminals under DC bias. This electric scheme is required because the diode has a variable and high dynamical resistance R_d around the laser threshold (in the range of $[1; 100] \Omega$). The voltage amplifier of gain G has itself a much higher entry impedance ($R_e \sim M\Omega$) so if the voltage at the laser terminals is v_{DL} , the output voltage of the amplifier is $v_{out} = G \times v_{LD}$ [Myara 2003]. The output signal is sent to a digital sampler which records the time domain voltage fluctuations $v(t)$. The data are then processed using a computer. This noise measurement is extremely sensitive to any electromagnetic perturbation (RF emissions, 50 Hz of the sector...). In practice, to avoid any additional external source of electrical perturbations, the diode

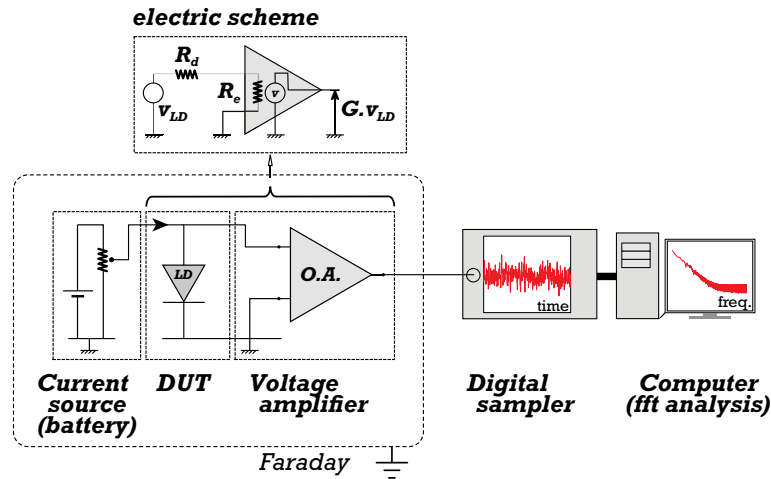


Figure 4.3: Measurement setup of the electric noise of the laser diode. After [Myara 2003]

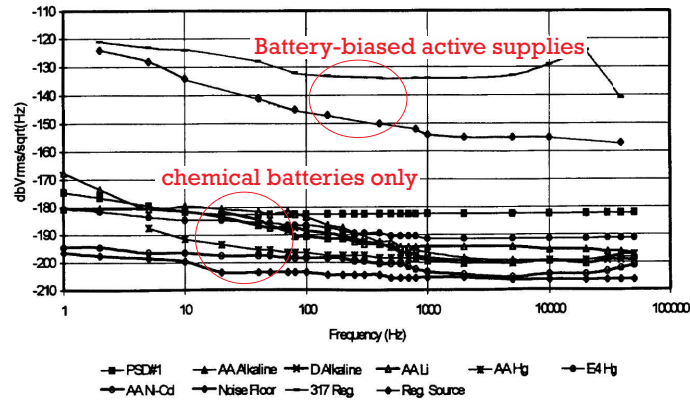


Figure 4.4: Voltage noise measurements of the output of several types of battery-biased supplies. The fluctuations at the terminals of the batteries alone are thermal noise limited, with almost no $1/f$ noise. Reproduced from [Boggs 1995]

is supplied with autonomous chemical batteries (+24 V) completely isolated from the sector, which is a very low-noise configuration [Boggs 1995] (figure (4.4)). Then, with a home-made current supply using low-noise resistors (coil resistors), the output is only thermal noise-limited with no significant $1/f$ fluctuations. All the connections are realized with coaxial cables to provide a relative immunity to external RF perturbations and the whole set-up is placed in a *Faraday cage*. Also, the modules are characterized at ambient temperature without any electronic regulation to avoid the introduction of a modulated signal in the cage. The signal amplifier is a Brookdeal EG&G 5004, supplied again by a ± 15 V battery. It realizes first a DC-filtering to amplify only the AC component. It has a voltage gain of $G = 10^3$ (so the gain on the PSD is G^2), a cutoff frequency of 1 MHz and a white noise floor (in short-circuit) of $S_{floor} = 5.5 \times 10^{-19} \text{ V}^2 \cdot \text{Hz}^{-1}$ (figure (4.5)). The low-frequency chain noise at 100 Hz is $S_v(f = 100 \text{ Hz}) = 1.5 \times 10^{-18} \text{ V}^2 \cdot \text{Hz}^{-1}$ which will be considered regarding the measurements made in this range of frequencies. In terms of equivalent thermal noise that would be generated at ambient temperature in a resistor R_{eq} , $S_v(f = 100 \text{ Hz}) = 4k_B T R_{eq} \iff R_{eq} = 91.2 \Omega$. If the resistance of the current supply is higher than this value, we are limited by the later in terms of noise floor. This is the case for currents on the order of $\sim 50 \text{ mA}$ ($\Rightarrow R = 480 \Omega$). On the other side, the sampling is

done with an acquisition card M3I, 50 MHz analog at 100 MS.s⁻¹ with 128 MB on-board memory, which sends the data through a high-speed link to a PC station with 32 Go of RAM. The signal is processed with an home-made MATLAB[®] GUI program ('fft-Scope' of M. Myara) that simulates a high-quality fft-analyzer (see below).

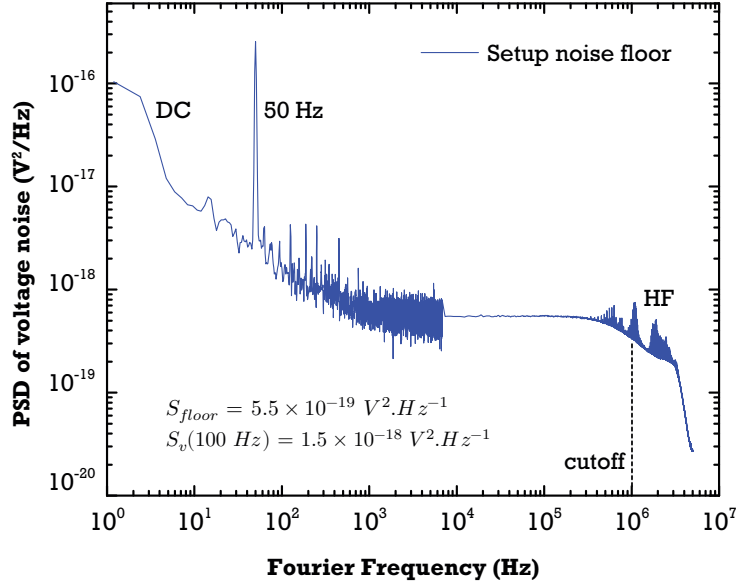


Figure 4.5: Measurement of the voltage noise floor S_v/G^2 of the acquisition chain with a short-circuited voltage amplifier ($I = 0$ mA). At low-frequencies, the trace of the DC component is still visible. Also a 50 Hz sector peak can be noticed. At high frequencies, the signal is cut by the amplifier above 1 MHz. The sampling rate is $f_s = 10$ MS.s⁻¹ for a total number of $N_s = 4$ MS.

Going back to the measurements of the electronic noise of the component, one can retrieve the *noise in current* in the diode S_I in A².Hz⁻¹ by considering that the voltage is transformed through the dynamic resistance R_d of the device:

$$S_I(f) = \frac{S_{v,measured}}{G^2 R_d^2} \quad (4.16)$$

This is why it is necessary to record precisely the $R_d(I)$ function before making this conversion.

★ *Note on the signal processing*

To obtain the PSD of the noise of a signal, MATLAB[®] fft algorithms are used. However, one has to apply them with caution. Indeed, because the physical signal x is truncated in the time-domain (the observation time is finite), it is equivalent to a multiplication with the *door* function Π (which is 1 on the recording interval $[-\Delta t/2; \Delta t/2]$ and zero elsewhere). In the frequency domain, this leads to *convolute* the Fourier transform of the signal to the *cardinal sine function* (4.17):

$$\mathcal{F}(\Pi \times x(t)) = \Lambda * \hat{x}(f) \quad (4.17)$$

$$\Lambda(f) = \Delta t \times \text{Sinc}(\pi \Delta t f) = \frac{\sin(\pi \Delta t f)}{\pi f} \quad (4.18)$$

This function converges to the *Dirac* distribution when $t \rightarrow \pm\infty$ and decreases relatively slowly to zero away to the peak maximum. This is not favorable for the spectral resolution of the computed

PSD because we want the noise peaks to be well-separated from the background noise: usually, *fft-windows* are used to modify the spectral profile of this apparatus function. For instance, the spectrum shown above have been multiplied in the time-domain with the **Blackmann-Harris window** before transformation to the frequency domain [Heinzel 2002]. In this case, the corresponding *fft* falls-off much faster to zero away from the central peak. Now, for computational time reasons, some 'tricks' have been used in the *fft* procedures. Because we are recording a unique (long) sample in the time-domain, the low-frequency and high frequency domain can be addressed separately to avoid a lengthy time of processing for the second range. To do that, the sample is sub-divided (in $\Delta N = 10^4$ samples interval for instance) and the PSD is computed on each of them. Averages made out of the results allow to smooth out the curve and reveal precisely the noise floor. At low-frequencies, the sample is reduced in number of points and is Fourier transformed with the pre-required Shannon low-pass filtering of the data.

4.3 Experimental results

The electric noise has been studied on four TO3 laser modules: one 852 *nm* and two 894 *nm* devices of III-V Lab that integrate chips of the 1st run of fabrication and one 852 *nm* commercial module of EagleYard Photonics (EYL). A comparison of our technology to another one makes an interesting benchmark of the electrical performances of the devices. Table (4.1) recaps the main laser characteristics.

Module reference	Type	Structure	Cavity length L	T_{meas}
C0195	DFB 894 <i>nm</i>	XXL2029	2 <i>mm</i>	27°C
C0308	DFB 887 <i>nm</i>	XXL2029	2 <i>mm</i>	27°C
C0314	DFB 852 <i>nm</i>	XXL2020	1.5 <i>mm</i>	27°C
EYL	DFB 852 <i>nm</i>	-	1.5 <i>mm</i>	27°C

Table 4.1: Summary of the main characteristics of the modules tested in the electric noise investigation

4.3.1 Dynamical resistance

The measurement of the dynamical resistance of the diodes is made first to identify any deviation from the ideal junction model. The I-V characteristic is recorded with high precision from 1 *nA* to 0.2 *A*. The result is shown in figure (4.6).

While the III-V Lab modules have very similar characteristics, the EYL I-V curve shows a different behavior below 10 μA . It is actually a *leakage current* which means that the *shunt resistance* R_{shunt} (the resistance of the parallel parasitic path to the diode) is lower in this technology than in our fabrication (this should, however, have virtually no consequences on the laser performances above threshold. It is important to know however so as to interpret correctly the electrical noise measurements). The characteristic can be modeled under threshold by (4.19) [Myara 2003]:

$$I = I_s \left[\exp \left(\frac{eV}{mk_B T} \right) - 1 \right] + \frac{V}{R_{shunt}} \quad (4.19)$$

where I_s is the saturation current and m the ideality coefficient.

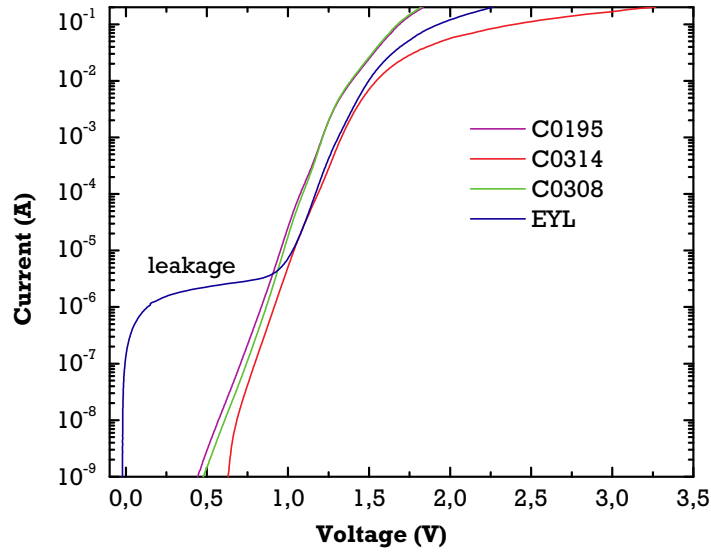


Figure 4.6: I-V characteristics of four laser modules (III-V Lab: C0195, C0314 and C0308 and Eagle-Yard Photonics: EYL)

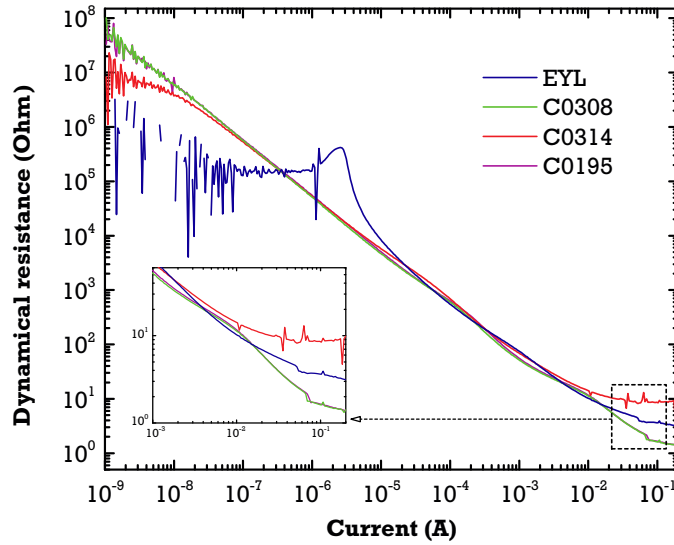


Figure 4.7: R_d characteristics of four laser modules (III-V Lab: C0195, C0314 and C0308 and Eagle-Yard Photonics: EYL)

Graph (4.7) shows the dynamical resistance $R_d = \partial V / \partial I$. Between $10 \mu A$ and $10 mA$, all the curves follow a I^{-1} law (4.20):

$$R_d = \frac{mk_B T}{eI} + R_s \quad (4.20)$$

At high injection, $R_d \rightarrow R_s$, the constant series resistance of the layers of the junction. Regarding this latter value, it is theoretically better for the C0195 device ($2 mm$ -long chip) versus the C0314 and the EYL, which is confirmed by the experiment. Between the two, the EYL has a lower resistance, which can be attributed to many causes, including the composition of the vertical structure of the

junction. However, the packaging connections are probably failing for module C0314 (see further). We can notice that around $50 - 70 \text{ mA}$, R_d falls-off abruptly: this is due to the laser threshold and the onset of the stimulated emission in the device that modifies the electric dynamics [Katz 1981, Harder 1982, Myara 2003]. The ideality coefficient m is found to be close to $\sim 2 - 2.4$, in accordance to the models of the authors.

4.3.2 Electrical noise

The noise from the electric characteristics of the type of devices under study exhibits two main components: a white noise at high frequencies, and a $1/f$ flicker type at low frequencies. The first one is well-known and has been precisely investigated by some authors [Myara 2004]. Figure (4.8) reproduces the white noise level of the PSD of current noise at high frequencies, as a function of the bias of the component. Apart from the threshold case where the noise is enhanced, the overall level is quite low (around $10^{-20} \text{ A}^2 \cdot \text{Hz}^{-1}$) and close to the shot-noise level. A series peaks of parasitic radio-frequencies (the fundamental and the harmonics) can be seen at 20 kHz and above. Accordingly, we have not looked further in the investigation of these fluctuations which have virtually no impact on the frequency noise, and require complicated techniques (measurements by correlations). Instead, we will investigate the low frequency noise part, which is greater of several orders of magnitude.

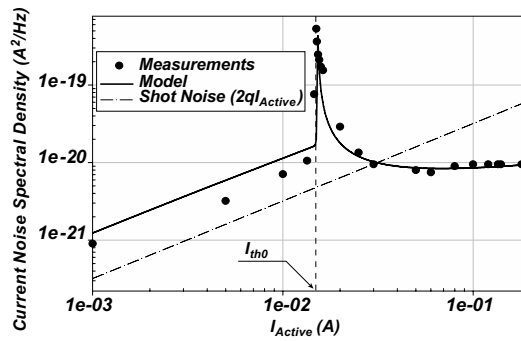


Figure 4.8: PSD of current white noise of an edge-emitting device, as a function of the bias of the active zone only. Reproduced from [Myara 2004]

The electrical noise was only evaluated on modules C0195, C0314 and EYL. Figure (4.9) and (4.10) shows respectively the PSD of voltage noise and the PSD of current noise at several levels of bias I of the laser C0195 at 27° C . Each curve is the average \bar{S} over 30 acquisitions of the PSD.

On the voltage noise first, we identify clearly a white noise range above 1 kHz . External parasites at 18.9 kHz and its higher harmonics are noticeable for low bias. A fit of the curve for $I = 5 \text{ mA}$ gives $S_v(f) = 2.7 \times 10^{-15} \cdot f^{-1} + 7.5 \times 10^{-19} \text{ V}^2 \cdot \text{Hz}^{-1}$, so the white noise level is close to the detection noise floor S_{floor} which would have to be subtracted from the previous fit to recover the signal of the diode only (but it is not done here). At 100 Hz , the signal level is 18-times above the detection noise which is enough to forget these considerations. We can notice that the white noise is stable with the bias I , but in the vicinity of the threshold for $I = 80 \text{ mA}$ where the PSD grows by 4. It then goes back to its sub-threshold value. The interpretation of this behavior would require a comprehensive model of the electric noise that goes far beyond this study [Daulasim 1994, Signoret 1995, Myara 2004]. It can be simply mentioned that the white noise is linked to the thermal noise from the series resistance and from the spontaneous emission in the active zone (hence the enhancement of fluctuations at threshold where the photon regime changes drastically). The low frequency fluctuations, by contrast, show a

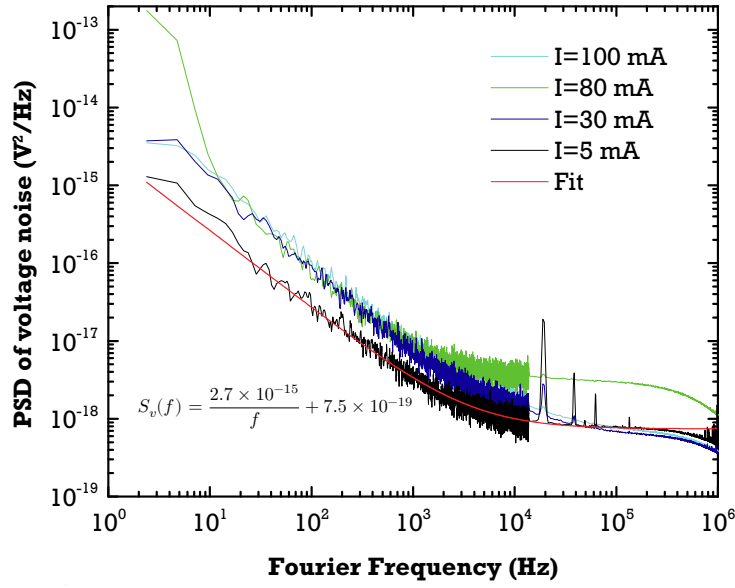


Figure 4.9: PSD of voltage noise of the laser module C0195 for several levels of bias. The fit for $I = 5 \text{ mA}$ yields $S_v(f) = 2.7 \times 10^{-15} \cdot f^{-1} + 7.5 \times 10^{-19} \text{ V}^2 \cdot \text{Hz}^{-1}$

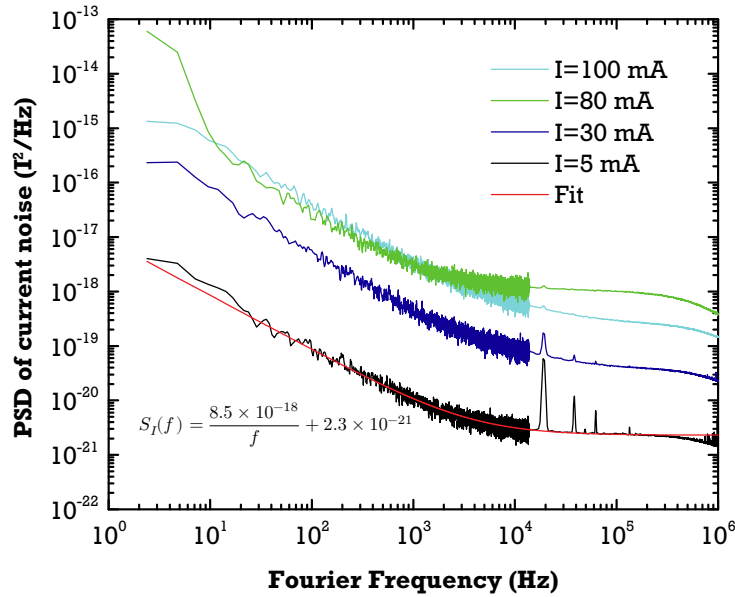


Figure 4.10: PSD of current noise of the laser module C0195 for several levels of bias. The fit for $I = 5 \text{ mA}$ yields $S_I(f) = 8.5 \times 10^{-18} \cdot f^{-1} + 2.3 \times 10^{-21} \text{ V}^2 \cdot \text{Hz}^{-1}$

perfect -1 slope in the log-log plot at low bias. For increasing current I , the slope is a bit steeper and the curve shifts of about half-a-decade, but it is still 'flicker' noise.

Regarding the current noise now, figure (4.10) is simply deduced from (4.9) with (4.16). Here, the amplitude at low frequencies grows with I , until the threshold is reached. It stays constant above this bias point.

As a comparison, figure (4.11) gives the PSD of voltage noise measured on the EYL laser. The behavior of the fluctuations is not the same when the diode is polarized: first, the shape of the spectrum is different in the high-frequencies range. Second, the noise is not 'clamped' above threshold in the low frequency range: the trend completely departs from the flicker -1 slope (the origin of that is not identified).

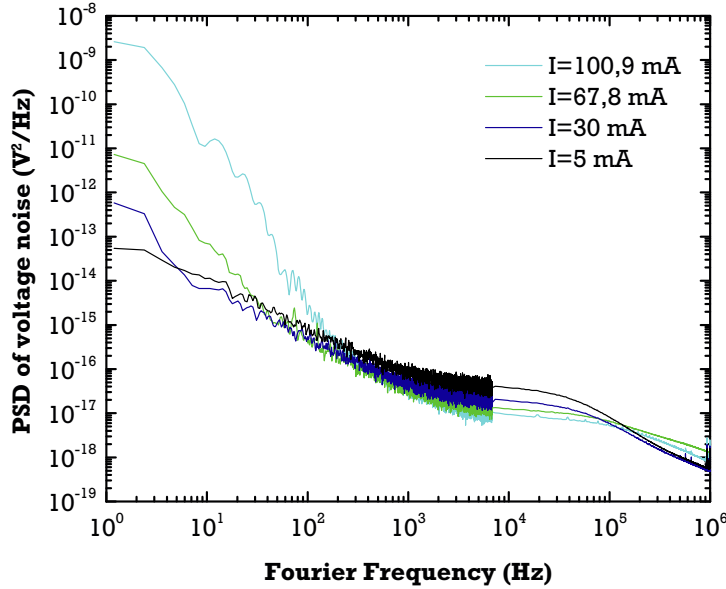


Figure 4.11: PSD of voltage noise of the laser module EYL for several levels of bias

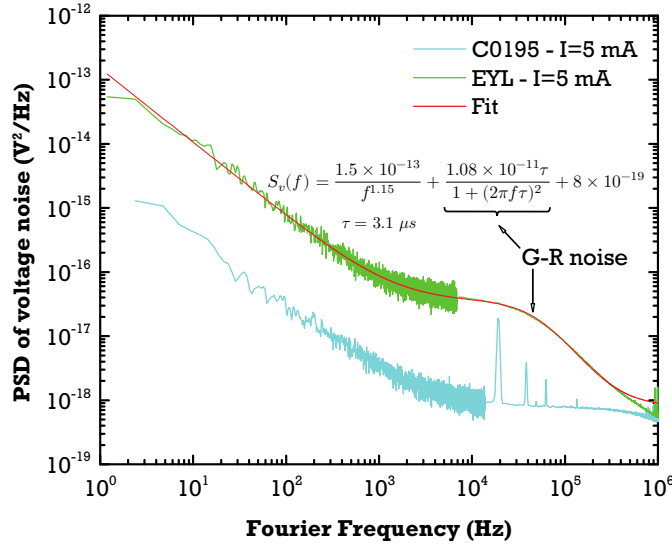


Figure 4.12: Comparison of the PSD of voltage noise of the laser module C0195 and EYL at $I = 5 \text{ mA}$. The fit of the latter characteristic yields $S_v(f) = \frac{1.5 \times 10^{-13}}{f^{1.15}} + \frac{1.08 \times 10^{-11}\tau}{1 + (2\pi f\tau)^2} + 8 \times 10^{-19}$

When we compare the two previous modules at $I = 5 \text{ mA}$, it appears that the noise of EYL in the low-frequencies is almost two decades higher than for C0195. Also, there may be the signature

of a generation-recombination (G-R) mechanism (3.52) in the $10 - 100 \text{ kHz}$: the signal is well-fitted by a $1/f$ law with a white floor and an additional Lorentzian spectrum [Hooge 1981]: $S_v(f) = 1.5 \times 10^{-13} \cdot f^{-1.15} + 1.08 \times 10^{-11} \tau \cdot (1 + (2\pi f \tau)^2)^{-1} + 8 \times 10^{-19} \text{ V.Hz}^{-1}$ with $\tau = 3.1 \text{ } \mu\text{s}$. This value is linked to the average trapping-detrapping time associated to the defect in the material that creates the noise. We notice that the 'bump' in the PSD decreases with increasing injection in (4.11), in accordance with the $\overline{\Delta N}/N$ dependence of the law. If we fit now the PSD of noise level at 100 Hz versus the normalized injected current (with relation to the electric threshold of each laser) in log-log, graphs (4.13) and (4.14) are obtained. Those curves are interesting because they enable to infer a low-frequency noise model for the device:

- ★ **C0314** : The analysis for this module is particular: indeed, from the I-V characteristic, we notice that the series resistance at high injection (above 10 mA) is excessively high ($\sim 8 \text{ } \Omega$). From the previous study of XXL2020 lasers, the series resistance of a 1.5 mm laser on a C-mount was in the range of $\sim 1.6 \text{ } \Omega$. So the packaging adds a high parasitic resistance on this module: it was indeed verified after the experiments that this former version of the packaging which used conductive epoxy had a failing contact on the ground of the C-mount. Thus, the noise results are hardly explainable because this (probably non-perfectly ohmic) contact pollutes the intrinsic noise of the diode. The PSD S_v is first constant, at the level of the C0195 and evolves further in I^2 , to exceed rapidly the two other PSD magnitudes (2 to 3 decades above at twice the threshold). The PSD S_I shows the same trend, which is not surprising. Indeed, from (4.20) it is clear that if $R_d \simeq R_s$ on the whole current range, $S_I = S_v/R_d^2 \propto S_v$.
- ★ **C0195** : For this module, we observe that $S_v \sim 8 \times 10^{-17} \text{ V}^2 \cdot \text{Hz}^{-1}$ is low and approximately constant on the whole range of current investigated. As for S_I , the trend is $S_I \propto I^{0.8}$ in the range of the mA and follows then a perfect I^2 law up to the threshold.
- ★ **EYL** : In this case, $S_v \sim 8 \times 10^{-16} \text{ V}^2 \cdot \text{Hz}^{-1}$ is approximately constant, just like for C0195 on the whole range of current investigated. The trend of S_I is $\propto I^{1.1}$ in the range of the mA . Then, it is flat up to the threshold where it increases.

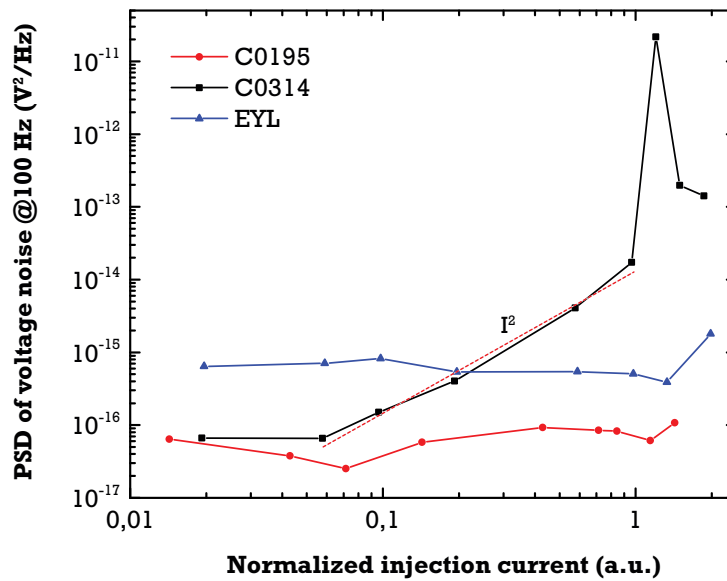


Figure 4.13: PSD of voltage noise magnitude at 100 Hz versus the normalized injected current (with respect to the laser threshold) for three laser modules

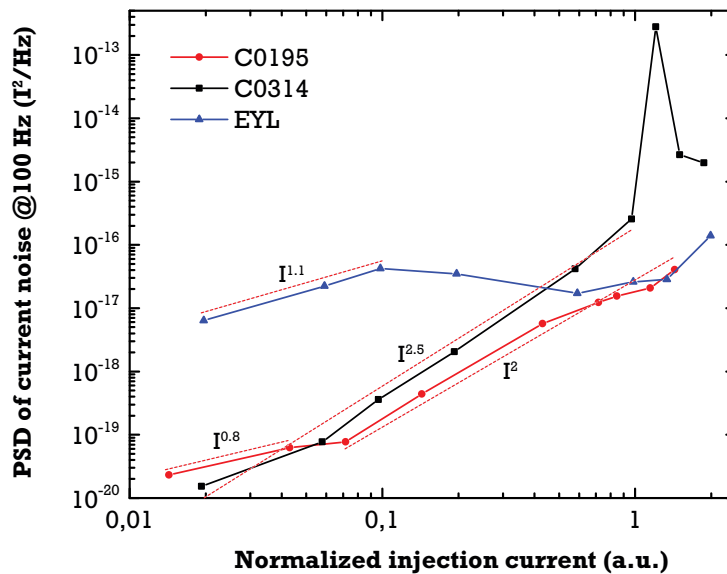


Figure 4.14: PSD of current noise magnitude at 100 Hz versus the normalized injected current (with respect to the laser threshold) for three laser modules

The interpretation of the previous trends is difficult: indeed, the early and more recent literature on the $1/f$ noise dealt with experiments on very basic samples, with delimited geometries and homogeneous materials [Hooge 1981, Hooge 1993, Chen 1997]. Some investigations have been led in transistors, and models proposed for p-n junctions, but a laser diode is a complex component made of several layers of compound alloys which may, first, not have the same crystalline quality. Also, the transport conditions define areas of very different carrier concentrations: for instance, the profile is intrinsic with the highest concentration in the quantum-well at threshold. More precisely, three zones

where potential electronic noise can occur are identified:

1. Schottky/ohmic contacts on n and p-sides (interface semiconductor-metal)
2. The optical heterojunction (optical barriers in the n and p-sides + electrical barriers of the well)
3. The active zone (quantum well bulk)

For high quality contacts, which can be assumed if the technological process is 'clean' (and the packaging as well), point 1 can be put aside of the discussion. The separation between the two other points is quite artificial: actually, we distinguish zone 2 from zone 3 because in the heterojunction, the mobilities of the materials are reduced (due to the doping impurities) and the free carrier concentration is the extrinsic one N_d or N_a . For the active zone, the carrier concentration is the intrinsic one and the mobility is *a priori* very high. Kleinpenning has proposed a mobility-fluctuation model for p-n junctions where the diffusion process of carriers at the junction predicts $S_I \propto I$ [Hooge 1981]. This model is grounded on the fact that the ambipolar diffusion coefficient $D_a = \mu k_B T / e$ fluctuates with the mobility μ . On the other side, we have seen in chapter 4, section [3.1.3.2] that mobility-fluctuations based Hooge's law scales with I^2 for a pure resistivity bulk of material. Many of the authors that studied the electric characteristics of laser diodes put forward very speculative models based directly on these relations : this literature is far from being clear, when it is not completely confusing. We can just mention [Chen 2001] who studied multi quantum-well laser diodes and found similar trend as for C0195: at low bias, the optical generation-recombination in the junction is low, and the transport is dominated by diffusion of carriers in the well: thus, the PSD evolves in I . Then, at higher currents, the $1/f$ noise arises from the bulk series resistances in which case $S_I \sim I^2$.

In our case, we can develop the following reasoning: because the PSD is $\sim I^2$ above $I = 10 \text{ mA}$, we are probably in the series resistance regime. How Hooge's law can be applied for the non-homogeneous material of the diode ? If we remember the expression $S_I/I^2 = \varepsilon_H/fN$, we can notice that the ratio ε_H/N represents the average power of noise induced by one carrier. This value depends on the local environment of the particle through the relation $\varepsilon_H = \varepsilon_{H,meas} = (\mu_{meas}/\mu_{latt})^2 \varepsilon_{H,latt}$: the ratio of the effective mobility of the carriers in the doped-material to the intrinsic mobility in the 'pure' lattice alone (ratio ≤ 1) scales down the measured Hooge's constant $\varepsilon_{H,meas}$, compared to the value $\varepsilon_{H,latt}$ which is linked to the crystal quality only. So on the overall, the total PSD of noise will be dominated by the noisiest layers of the heterostructure which commits electrons in low quality alloys, with virtually no doping, at low concentrations/confined in small volumes. If we admit that the section $S = L \times w$ of the laser is the same for all carrier populations, the thinnest layers are the quantum-well and its adaptation layers on the n and p sides ($\sim 12 \text{ nm}$). A numerical computation of the profile of carriers in the z direction (as in chapter 3) reveals that the number of electrons N_e is minimum in the active zone for which $N_e = 3 \times 10^8$ ($L = 2 \text{ mm}$ and $w = 7 \text{ }\mu\text{m}$). If we make the simple assumption that $\mu_{meas} = \mu_{latt}$ in this region, we are left with the relation $S_I/I^2 = \varepsilon_{H,latt}/fN_e$. The regime of interest is valid above $I = 10 \text{ mA}$, and at this value of the injection, the PSD is fitted as $S_I(f) = 6 \times 10^{-17} \cdot f^{-1.05} + 5.3 \times 10^{-21}$. Thus, $\varepsilon_{H,latt}/N_e = 6 \times 10^{-17}/0.01^2$ which yields $\varepsilon_{H,latt} = 6 \times 10^{-13} N_e$. If our assumption of the source of the noise is correct, we get (4.21):

$$\varepsilon_{H,latt} = 1.8 \times 10^{-4} \quad (4.21)$$

According to the review of Hooge [Hooge 1994], the $\varepsilon_{H,latt}$ values ranges from 10^{-5} to 10^{-3} in the literature. Our value here is then quite standard. Nevertheless, given the number of bold assumptions we have made, we should not give an excessive importance to this result.

4.4 Conclusion

To conclude this short chapter, the first aim of these measurements was to prove that **the flicker slope on the PSD of electric noise measured in the low-frequencies comes intrinsically from the electronic transport in the device and has nothing to deal with the noise of the current supply**, when the latter has very low fluctuations in the current delivered. This is proved by the several decades of amplitude between the acquisition chain noise floor and the PSD of voltage noise measured at the terminals of the modules. Also, the characteristics from one device to another are quite different, which excludes a common origin from the supply. Though, it is crucial in general to have a low noise source so not to add fluctuations in the characteristics of the laser.

The interesting point is that we can compare the performances of the III-V Lab technology to another independent fabrication: our DFBs are free of G-R parasites, unlike the EYL module. This conclusion must be tempered by the fact that the two modules C0195 and C0314 did not undergo a deep *burn-in* before the measurements (they have been running for less than 50 *hours*): with such aging, the electric characteristics can change, with the modification of the noise levels, defect migrations in the active zone... with external stress (current, temperature...) [Chen 2001]. A complementary study with aged modules would be required to conclude definitively. The Hooge parameter of the lattice extracted is $\varepsilon_{H,latt} = 1.8 \times 10^{-4}$ which expresses a good, but standard, epitaxial realization of the active zone. It also appeared clearly that low-quality connections in the packaging have serious consequences on the level of the electric noise. Finally, this study allows to say that the intrinsic structure/conception of the device can turn the quiet noise source of the supply into a noisy one, which behaves in $1/f$. This noise in the pumping mechanisms, not negligible at all, will have a negative impact on the other optical fluctuations: amplitude, frequency... Indeed, if the flicker modulation of the current is located in the passive regions, this may perturb the refractive index of the cavity, hence the frequency noise/the linewidth. If it is only in the active region, we will see intensity noise fluctuations first. In chapter 5, simple models will be outlined on these considerations.

4.5 Summary

In this chapter, useful conceptual tools for the noise study were settled and applied to the case of these 2nd order fluctuations of the electric characteristics of laser diodes. In particular, **the Power Spectral Density (PSD) was used to quantify the stationary amplitude of the power of the noise as a function of the frequency components of the signal.** In practice, one must care to sample properly the physical signal so not to induce aliasing when using Fast-Fourier transform algorithms. Regarding the study of the electric noise, a simple setup allows to measure the PSD of voltage S_v and current fluctuations S_I using a low-noise current supply and acquisition chain. These two quantities are simply converted to each others by the dynamical resistance of the device.

Three DFB lasers modules were studied. For the first one (III-V Lab), it was found that a failing contact to the ground of the sub-mount in the packaging created an excess low-frequency noise. The other III-V lab module showed two distinct profiles of PSD: at high frequencies, the amplitude is flat: this white noise arises mainly from the thermal noise from the series resistance. Below 10^4 Hz, a $1/f$ flicker slope characterizes the so-called intrinsic low-frequency noise. The third module (other technology from EagleYard Photonics) showed the same trends in frequencies, with a somewhat higher level of noise on the overall and a signature of generation-recombination noise. At a given frequency, below 1 kHz, the observation of the S_v and S_I magnitudes as a function of the current injection reveals different trends. For the III-V Lab module, the PSD is proportional to I at very low current and evolves in I^2 at higher bias. The first trend usually reveals characteristics of the active zone: here, it could be the signature of diffusion mechanisms scaling in $1/f$. The second, which dominates rapidly, may be linked to the bulk mobility fluctuation modeled by Hooge's law. From the later, **we estimate Hooge's lattice constant to be in the range of what is commonly accepted in the literature**, revealing a fairly good material quality and a clean process of fabrication. Though, the description is limited by unverified assumptions. Nevertheless, it proves that **the p-n junctions are intrinsically noisy**, even when injected by very quiet current sources. The impact of this internal modulation of the current should still be modeled adequately to go beyond this quick overview of the complex and controversial $1/f$ noise topic. Still, the data will help to understand the deviations from the Schawlow-Townes linewidth in our lasers.

Bibliography

- [Boggs 1995] Chadwick K Boggs, Alan D Doak et FL Walls. *Measurement of voltage noise in chemical batteries*. In Frequency Control Symposium, 1995. 49th., Proceedings of the 1995 IEEE International, pages 367–373. IEEE, 1995.
- [Chen 1997] XY Chen, PM Koenraad, FN Hooge, JH Wolter et V Aninkevicius. *1/f noise in δ -doped GaAs analyzed in terms of mobility fluctuations*. Physical Review B, vol. 55, no. 8, page 5290, 1997.
- [Chen 2001] XY Chen, A Pedersen et AD Van Rheeën. *Effect of electrical and thermal stress on low-frequency noise characteristics of laser diodes*. Microelectronics Reliability, vol. 41, no. 1, pages 105–110, 2001.
- [Daulasim 1994] Khamphanh Daulasim. *Caractérisation et modélisation des bruits blancs et en 1/F des diodes lasers à semiconducteur*. PhD thesis, Université Montpellier II, 1994.
- [Harder 1982] Christoph Harder, Joseph Katz, S Margalit, J Shacham et Amnon Yariv. *Noise equivalent circuit of a semiconductor laser diode*. IEEE Journal of Quantum Electronics, vol. 18, no. 3, pages 333–337, 1982.
- [Heinzel 2002] Gerhard Heinzel, Albrecht Rüdiger et Roland Schilling. *Spectrum and spectral density estimation by the Discrete Fourier transform (DFT), including a comprehensive list of window functions and some new at-top windows*. Technical Report, 2002.
- [Hooge 1981] FN Hooge, TGM Kleinpenning et LKJ Vandamme. *Experimental studies on 1/f noise*. Reports on progress in Physics, vol. 44, no. 5, page 479, 1981.
- [Hooge 1993] FN Hooge et M Tacano. *Experimental studies of 1/f noise in n-GaAs*. Physica B: Condensed Matter, vol. 190, no. 2, pages 145–149, 1993.
- [Hooge 1994] FN Hooge. *1/f noise sources*. IEEE Transactions on Electron Devices, vol. 41, no. 11, pages 1926–1935, 1994.
- [Johnson 1928] John Bertrand Johnson. *Thermal agitation of electricity in conductors*. Physical review, vol. 32, no. 1, page 97, 1928.
- [Katz 1981] J Katz, S Margalit, Ch Harder, D Wilt et Amnon Yariv. *The intrinsic electrical equivalent circuit of a laser diode*. IEEE Journal of Quantum Electronics, vol. 17, no. 1, pages 4–7, 1981.
- [Myara 2003] Mikhaël Myara. *Caractérisation et modélisation de lasers accordables à DBR émettant autour de 1.55 [micromètres]: étude des bruits d’amplitude et de la largeur de raie*. thesis, Montpellier 2, Université des Sciences et Techniques du Languedoc, 2003.
- [Myara 2004] Mikhaël Myara, Philippe Signoret, J-P Turrenc, J-P Perez, Bernard Orsal et Joël Jacquet. *Strongly sub-Poissonian electrical noise in 1.55- μ m DBR tunable laser diodes*. IEEE journal of quantum electronics, vol. 40, no. 7, pages 852–857, 2004.
- [Schottky 1918] Walter Schottky. *Über spontane Stromschwankungen in verschiedenen Elektrizitätsleitern*. Annalen der physik, vol. 362, no. 23, pages 541–567, 1918.
- [Signoret 1995] Philippe Signoret, Bernard P. Orsal, Jean-Marie Peransin et Robert M. Alabedra. *Analysis of white optical and electrical noises of a DFB laser with optical feedback*. Proc. SPIE, vol. 2382, pages 187–199, 1995.

Study of the optical coherence of the lasers

5.1 Introduction

The optical coherence can be grasped across several types of indicators. First through noise, notably phase or frequency noise, which are **quantified in a similar way to that described in chapter 4** on electrical noise. However, it is common practice to use other indicators, such as the Allan variance, traditionally used for the study and quantification of the long-term coherence, or the linewidth, more commonly used for the evaluation of the short-term one. In this chapter, we first introduce the fundamental and technical limits of noise in lasers. Then, we give the relations between the various indicators described above –essentially linewidth and spectral density– both at the theoretical level and using the traditional metrology, and apply it to the lasers developed in the framework of this thesis. Finally, we show that this metrology is limited and we propose new improvements that we apply again to the sources under study. To go further, we quickly investigate the optical noise characteristics under external feedback. This helps to evaluate the specifications required for the module in a servo-control of the frequency fluctuations (chapter 6).

5.2 Noise in DFB lasers

In this section, the fundamental limits of laser noise will be addressed. To highlight the nature of the fluctuations, we go back to the fundamental dynamical equations describing the laser state over time [Petermann 2012]:

$$\begin{cases} \frac{\partial n}{\partial t} = \eta_i \frac{J}{ed} - (An + Bn^2) - v_g g(n)s + f_n(t) \\ \frac{\partial s}{\partial t} = \Gamma v_g g(n)s - \frac{s}{\tau_\gamma} + \beta \Gamma B n^2 + f_s(t) \\ \frac{\partial \phi}{\partial t} = \frac{\alpha_H}{2} \left(\Gamma v_g g(n) - \frac{1}{\tau_\gamma} \right) + f_\phi(t) \end{cases} \quad (5.1)$$

As in chapter 2–[2.2.3], the main parameters are the photon lifetime τ_γ , the spontaneous emission coefficient β , Henry’s factor α_H , the confinement factor on the quantum-well Γ and its thickness d . On top of the additional equation describing the phase evolution, *Langevin noise sources* $f_i(t)$ have been added to take into account the fact that random fluctuations forces the temporal deterministic system for each t . The goal of the noise models are precisely to associate a power spectrum to these forces and study their impact on the dynamics of the system. It can be shown for instance that due to carrier density clamping at threshold, the force f_n can be neglected (the feedback on the carrier fluctuations is so strong that they are squeezed in the laser regime) and only f_s and f_ϕ are taken into account. We are then confronted to **two types of noise in practice**: the amplitude noise (in the photon density or, equivalently, in the output power if the cavity losses are not perturbed) and the phase/frequency noise on the optical carrier. The coherence properties themselves are quasi-exclusively linked to the

second contribution, but for extreme cases (strong modulation of the amplitude for instance), the two noise dynamics are coupled and it raises experimental issues to make a distinction between them. This is why we will focus first on the Relative Intensity Noise (RIN) and prove experimentally that its magnitude does not impact the (experimental) evaluation of the frequency noise.

On an analytical point of view, when the system is linearized about the mean values of each variable: $\phi = \bar{\phi} + \tilde{\phi}$, the PSD of \tilde{s} and $\tilde{\phi}$ can be retrieved in theory. We will not dwell on the analysis of these expressions, unless there is a conceptual pitfall in their use. This is precisely the case for the PSD of amplitude noise, which value has indeed to be considered relatively to the experimental conditions.

5.2.1 Intensity noise

The intrinsic fluctuations of the optical power $P(t)$ of a laser source can be defined and measured in the Fourier domain, just as for the electric noise of chapter 4. Graph (5.1) represents the typical PSD components of the output of an in-plane semiconductor laser. The white noise, visible at high

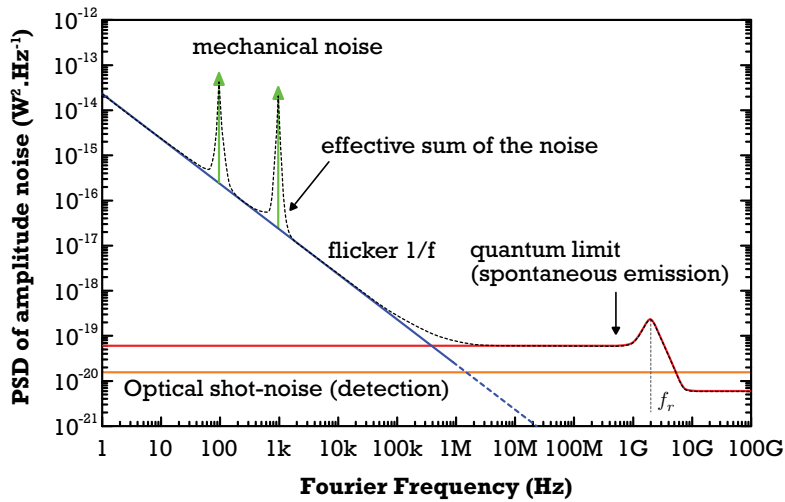


Figure 5.1: Representation of the typical single-sided PSD of amplitude noise of a LAMA-like in-plane laser ($P_{out} \sim 20 \text{ mW}$), with several noise sources added to give the spectrum that could be experimentally measured

frequencies, originates from the spontaneous emission. A flicker low-frequency component is typically linked to a $1/f$ source. Also, mechanical perturbations arise in the $100 \text{ Hz} - 1 \text{ kHz}$ range. We will look further into these trends in the section dedicated to the frequency noise. However, to judge from the noise magnitude from one source to another, it is better to *normalize* the corresponding PSD with relation to the output power. One can define the Relative Intensity Noise or RIN, with the following expression (5.2) [Schimpe 1983, Jérémie 1997]:

$$RIN(f) = \frac{S_P(f) - 2h\nu\overline{P_{out}}}{\overline{P_{out}}^2} \quad (5.2)$$

where S_P is the PSD of the laser output power and $\overline{P_{out}}$ the mean optical power reaching the detector. This definition is not trivial because it allows to measure the power fluctuations *independently* of the experimental conditions. Indeed, first, the normalization by $\overline{P_{out}}^2$ scales the power-dependent amplitude variations of the field with relation to the absolute power. Second, it would not be

meaningful to ground a 'universal' definition on the previous term only: the process of power detection creates its own *detection shot-noise* (section [4.1.3]) which PSD is $S_{shot} = 2h\nu\overline{P_{out}}$ (this noise arises from the possibility for a photon to be detected or not) and must be subtracted to the total magnitude [Donati 1997, Baney 2000]. In practice, a current i_{ph} is detected at the photodiode of efficiency η_{ph} (it includes the coupling efficiency). It implies that the attenuation of the beam power decreases the ratio of the magnitude between $S_{i_{ph}}$ and the shot-noise: **if it is too low, the laser noise will be eventually drowned in the detection noise**. This is why the beam injection in the photodetector must be optimized.

Some RIN measurements on laser modules of the 1st run will be presented in section [5.5.1] and will show that this amplitude noise is negligible in front of the phase fluctuations.

5.2.2 Frequency noise

In this section, we clarify the link between the linewidth, which can be seen as the power spectrum of the laser of frequency $\nu = (2\pi)^{-1}d\phi/dt$, and the Power Spectral Density (PSD) of the fluctuations of this frequency $S_{\delta\nu}$. After the Langevin sources $f_i(t)$ have been expressed with an adequate noise model, the **double-sided** PSD of frequency noise is approximated by [Henry 1983, Turrenc 2005b, Laurain 2010, Coldren 2012]:

$$S_{\delta\nu}(f) = \frac{1}{2\pi}\Delta\nu_{S-T} \left\{ 1 + |H(f)|^2 \alpha_H^2 \right\} \quad (5.3)$$

$$\Delta\nu_{S-T} = \frac{R_{sp}}{4\pi\bar{s}} \quad (5.4)$$

In this expression, we recognize the Schawlow-Townes linewidth $\Delta\nu_{S-T}$, and the modulus of a complex function H of the frequency f that describes the carrier noise, scaled by Henry's factor. In the frame of the ideal model of the laser diode (5.1), the pump source is shot-noise limited. H is a second-order transfer function with $|H(f)|^2 \rightarrow 1$ when $f \rightarrow 0$ and $|H(f)|^2 \rightarrow 0$ when $f \rightarrow +\infty$, so that $S_{\Delta\nu}(f) = \Delta\nu_{S-T-H}/2\pi$ at low frequencies. *This value is multiplied by two if the single-sided PSD representation is chosen*. In this range, the spectrum is a flat (white) noise, proportional to the Schawlow-Townes-Henry linewidth (2.96) (figure (5.2)).

At high frequencies, H usually peaks at the *carrier resonance frequency* f_r (3.57). Above this limit, the carrier density cannot follow anymore the fluctuations of the electric-field so only the spontaneous emission noise remains, with the Schawlow-Townes floor. Figure (5.2) also represents common noises profiles found in the output frequency of the in-plane lasers studied: there is the flicker 1/f slope (just as for the amplitude noise) that extends from the very low frequencies, up to the *MHz* at least. It finds again its source in the electric pumping of the semiconductor medium. External perturbations are seen through mechanical noise peaks in the $100 \text{ Hz} - 1 \text{ kHz}$ range, when the laser is put in an external cavity, on purpose or because of unwanted feedback. Also, the laser frequency follows external thermal perturbations (here, we assume a peltier regulation with maximum temperature excursions of $100 \mu\text{K}$) at a (low-frequencies) rate of $\partial\lambda/\partial T = 25 \text{ GHz}\cdot\text{K}^{-1}$ which are usually cutoff above 10 kHz . Finally, the resulting PSD spectrum is the sum of all these spectra (the PSD adds, unlike the square roots of the magnitudes). The intrinsic thermal fluctuations, from the series resistance of the laser for instance, have not been represented because they are very low.

Even though there are a lot of similarities between the amplitude noise and the frequency noise, the metrology used to characterize the second one is far from being obvious and accessible in the liter-

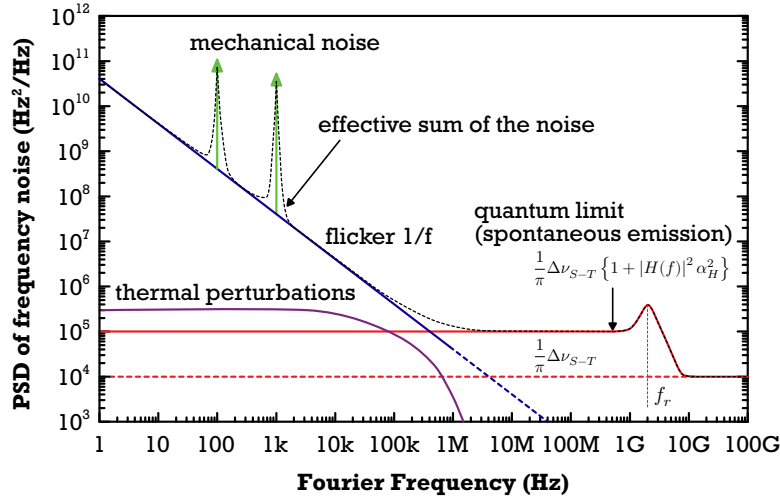


Figure 5.2: Representation of the typical single-sided PSD of frequency of LAMA lasers, with several noise sources adding to give the spectrum that could be experimentally measured

ature. First because a **frequency fluctuation is not a physical quantity directly measurable**, second because **it can be evaluated through at least three indicators (spectrum linewidth, PSD of the fluctuations, Allan variance)** requiring each different measurement setups. Moreover, the results are not always coherent between each other. In the first place, we will describe the theoretical relations between these representations, before turning to the metrology itself.

5.3 Frequency fluctuations : Lineshape, linewidth and Power Spectral Density

5.3.1 Linewidth for the white noise case

From (5.3), there is obviously a link between the PSD of frequency noise and the linewidth. Historically, the later was expressed first, before more rigorous analyses based on the Langevin forces were derived. The *intrinsic* linewidth can be defined more generally as the *spectrum of the autocorrelation function* of the laser electric-field. If the temporal part of the later is considered only, it is written in its complex form (5.5):

$$E(t) = E_0 \sqrt{1 + \alpha_l^2(t)} e^{i(2\pi\nu_0 t + \phi(t))} \quad (5.5)$$

The function $\alpha_l(t)$ describes the amplitude variations, which are assumed now to be negligible in front of the phase fluctuations $e^{i\phi(t)}$. If the autocorrelation Γ_E of this function (4.3) is computed, we end up with:

$$\Gamma_E(\tau) \equiv R_E(\tau) = \overline{E(t)^* E(t + \tau)} \equiv \lim_{\Delta t \rightarrow \infty} \frac{1}{\Delta t} \int_0^{\Delta t} E(t)^* E(t + \tau) dt \quad (5.6)$$

$$= E_0^2 e^{i2\pi\nu_0 \tau} \overline{e^{i\Delta_\tau \phi(t)}} \quad (5.7)$$

Here $\Delta_\tau \phi(t) = \phi(t) - \phi(t + \tau)$. The evaluation of the mean value $\overline{e^{i\Delta_\tau \phi(t)}}$ requires further derivations (see [Tourenco 2005b] or [Petermann 2012]). One important assumption made is that **the phase ϕ**

is driven by independent, normally distributed processes, as in (4.9). This yields $\overline{e^{i\Delta\tau\phi(t)}} = e^{-\frac{1}{2}\overline{\Delta\tau\phi(t)^2}}$ with (5.8):

$$\overline{\Delta\tau\phi(t)^2} \equiv \Delta\tau\phi(t)_{RMS}^2 = \int_{-\infty}^{+\infty} S_{\Delta\tau\phi(t)}(f)df \quad (5.8)$$

On the other side, it is shown also that:

$$\overline{\Delta\tau\phi(t)^2} = 4 \int_0^{+\infty} \frac{\sin^2(\pi\tau f)}{f^2} S_{\delta\nu}(f)df \quad (5.9)$$

Finally:

$$\Gamma_E(\tau) = E_0^2 e^{i2\pi\nu_0\tau} \exp \left[-2 \int_0^{+\infty} \frac{\sin^2(\pi\tau f)}{f^2} S_{\delta\nu}(f)df \right] \quad (5.10)$$

By definition, the laser spectrum \mathcal{L} is the Fourier transform of this expression (5.11):

$$\mathcal{L}(f) = \mathcal{F}(\Gamma_E(\tau)) = E_0^2 \delta(f - \nu_0) * \mathcal{F} \left\{ \exp \left[-2 \int_0^{+\infty} \frac{\sin^2(\pi\tau f)}{f^2} S_{\delta\nu}(f)df \right] \right\} \quad (5.11)$$

We can see that the **single-sided** PSD of frequency noise $S_{\delta\nu}$ and the lineshape \mathcal{L} are linked in a very complex way. Moreover, the transformation $S_{\delta\nu}(f) \rightarrow \mathcal{L}(f)$ is obviously not reversible. In the case of the white noise $S_{\delta\nu}(f) = S_0$, we have the simple Lorentzian shape:

$$\mathcal{L}(f) = E_0^2 \frac{2\pi^2 S_0}{(\pi^2 S_0)^2 + 4\pi^2(f - \nu_0)^2} \quad (5.12)$$

The integration of this expression on the whole spectrum yields an energy E_0^2 . The associated FWHM linewidth is:

$$\Delta\nu_{FWHM} = \pi S_0 \quad (5.13)$$

If $S_0 = \frac{1}{\pi} \Delta\nu_{S-T}(1 + \alpha_H^2)$ then $\Delta\nu_{FWHM} = \Delta\nu_{S-T-H}$.

5.3.2 Fourier limit and observation time

Expression (5.11) raises a certain number of issues linked to the fact that the phase fluctuations $\overline{\Delta\tau\phi(t)^2}$ entering the computation of the lineshape have been considered on an infinite bandwidth going from $t_{obs1} = 0$ to $t_{obs2} = +\infty$. In reality, the experimental observation time $T_{obs} = \Delta t$ is always limited so that $f_0 = 1/t_{obs2} \neq 0$. This means that the autocorrelation function $\Gamma_E(\tau)$ is certainly multiplied by a door function of time Π . After the Fourier transform, the lineshape is convoluted by a cardinal sine as explained in chapter 4-[4.2.2]:

$$\mathcal{F}(\Pi \times \Gamma_E(\tau)) = \Lambda * \mathcal{L}(f) = \frac{\sin(\pi T_{obs} f)}{\pi f} * \mathcal{L}(f) \quad (5.14)$$

Unfortunately, Λ has an incompressible FWHM of $\Delta f_\Lambda \simeq 1.2/T_{obs}$. The FWHM of the convolution of the lineshape with this apparatus function being roughly $\Delta f_\Lambda + \Delta\nu_{FWHM}$, we are obviously making a serious error when $T_{obs} \lesssim \tau_c = 1/2\pi\Delta\nu_{FWHM}$, in which case it is only the Fourier limit that is measured.

We are now in the case $T_{obs} \gg \tau_c$. If the PSD of frequency noise $S_{\delta\nu}$ is constant, it is quick to see that the summation of this function on a limited bandwidth has no consequence on the value of the linewidth, because then $\overline{\Delta\tau\phi(t)^2}$ does not depend on the observation time T_{obs} .

5.3.3 Case of the non-white noise

When the PSD spectrum is 'colored' (there are other non-white components), what has been said before is not necessarily true. For instance, if the noise is the sum of a flicker $1/f$ noise with some additional white noise ('pink' noise) defined from $f_0 = 0$ to $+\infty$, the integral in the brackets of (5.11) diverges when $f_0 \rightarrow 0$. According to the preceding, this is not an issue from a physical point of view because the linewidth is observed during a finite time $1/f_0 > 0$. If this lower frequency is set such that $f_0 = 1/\tau$ and the PSD of frequency noise model is taken to be $S_{\delta\nu} = S_0 + S_{-1}/f$, the authors of [Stéphan 2005] showed that the lineshape is a *Voigt profile* (5.15):

$$\mathcal{L}(f) = G(f) * L(f) = \int_{-\infty}^{+\infty} G(f', \nu_0, \sigma) L(f - f', \nu_0, \gamma) df' \quad (5.15)$$

$$G(f, \nu_0, \sigma) = \frac{E_0}{\sqrt{2\pi\sigma^2}} e^{-\frac{(f-\nu_0)^2}{2\sigma^2}} \quad (5.16)$$

$$L(f, \nu_0, \gamma) = \frac{E_0}{\pi} \frac{\gamma}{\gamma^2 + (f - \nu_0)^2} \quad (5.17)$$

It results from the convolution product of a Gaussian arising from the $1/f$ noise, and a Lorentzian, from the white noise. The distribution parameters are linked to the noise factors through $\gamma = \pi S_0/2$ and $\sigma^2 = 1.78S_{-1}$. Though, **it is only an approximation to associate the $1/f$ solely to a Gaussian distribution**. Moreover, the lower cutoff frequency f_0 is arbitrary and changes the FWHM of the linewidth profile. If a $1/f$ noise is considered only, an approximate linewidth for the lineshape is (5.18) [Mercer 1991]:

$$\Delta\nu_{1/f} \simeq \sqrt{(8 \ln 2) S_{-1} \left[1 + \ln(2\sqrt{S_{-1}} T_{obs}) \right]} \quad (5.18)$$

The conclusion is that, except for the pure white noise case, the laser linewidth always depends on the observation time T_{obs} . If an additional $1/f$ is taken into account, the laser lineshape is very close to the Voigt profile. In the general case of an arbitrary $1/f^\alpha$ noise, or with additional technical noise sources, those analysis are obsolete [Tourenç 2005a].

5.4 Standard linewidth metrology

We review now the main standard experimental setups used to measure the linewidth, and more generally, the PSD of frequency noise. Briefly, as already mentioned, Optical Spectrum Analyzers (OSA) can be used to analyze the spectrum of the output light. They can be based for instance on a diffraction grating that scans the input radiation: usually, the resolution of these devices does not exceed 8 GHz for the standard ones (however, recent OSA can go down to 10 MHz). It can also rely on an interferometric setup: mainly the Fabry-Perot cavity and the Michelson interferometer, in which case the resolution is on the order of 10 MHz . The drawback of the first technique is that it cuts-off high frequencies of the noise spectra (this upper frequency is equal to the half of the Fabry-Perot cold-cavity linewidth [Tourenç 2005b]). For the second technique, it can reconstruct the autocorrelation function of the field, which is then Fourier transformed. However, it cannot localize the absolute value of the central frequency ν_0 [Agilent 2000b]. Moreover, **those techniques cannot resolve correctly a laser linewidth below 1 MHz .** The coming optical setups can go way beyond this limit.

5.4.1 Heterodyne setup

The most simple metrology of the linewidth on a conceptual point of view relies on the so-called heterodyne set-up: the beams of two identical lasers are superimposed spatially, and the frequency of

the lasers is adjusted to generate a beating at a frequency which is low enough to be observable with radio-frequency (RF) instrumentation (figure (5.3)). The resulting beam then falls on a photodetector that generates a beat-note in the radio-frequency domain, which is in turn analyzed thanks to a sweeping (super-heterodyne) RF electrical spectrum analyzer or ESA [Agilent 2000a]. This apparatus is based on the mixing of the RF-input signal with a tunable (reference) RF-oscillator (a VCO for instance). The resulting signal is bandpass filtered, which allows to detect the amplitude as a function of the Fourier frequency. On the overall, it is equivalent to scan the response to a Dirac function on the whole spectrum (but this peak has actually a finite linewidth, which depends on the sweeping time, as already mentioned).

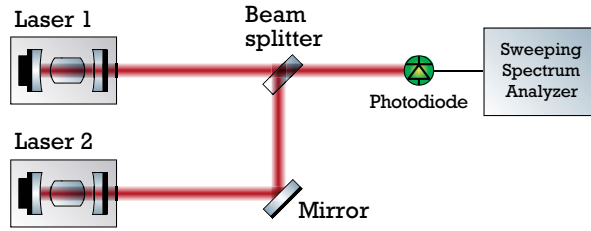


Figure 5.3: Standard heterodyne setup. The beams of two laser cavities are superimposed thanks to a beam-splitter/recombiner and the resulting radiation is sent on a photodiode which photo-current is analyzed by an ESA

Mathematically speaking, if the electric-fields of the two lasers $E_1(t) = E_{0,1}e^{i(2\pi\nu_{0,1}t+\phi_1(t))}$ and $E_2(t) = E_{0,2}e^{i(2\pi\nu_{0,2}t+\phi_2(t))}$ are added, an electrical *beat-note* is formed after the recombination. The current detected on the photodiode $i_{ph}(t)$ is proportional to the optical power generated $P_{opt}(t)$: $i_{ph}(t) = \eta_{ph}P_{opt}(t)$, with η_{ph} the conversion efficiency of the photodiode (in $A.W^{-1}$). The total power itself is proportional to the magnitude of the Poynting vector:

$$P_{opt}(t) \propto |E_1(t) + E_2(t)|^2 = P_{0,1} + P_{0,2} + b(t) \quad (5.19)$$

$$b(t) = 2\sqrt{P_{0,1}P_{0,2}} \cos[2\pi\Delta\nu_{12}t + \Delta\phi_{12}(t)] \quad (5.20)$$

$$\Delta\nu_{12} = \nu_{0,1} - \nu_{0,2} \quad (5.21)$$

$$\Delta\phi_{12}(t) = \phi_1(t) - \phi_2(t) \quad (5.22)$$

If $\Delta\nu_{12} \in [0; \sim 10 \text{ GHz}]$, the beat can be detected by a photodiode of adequate bandwidth. The fluctuations of phase (and thus of frequency) are contained in the term $\Delta\phi_{12}(t)$. We can see how fruitful is this concept: the beat-note translates all the noise information contained in the phases into a single carrier of RF frequency $\Delta\nu_{12}$ which can be easily analyzed with RF instrumentation. It can be shown that the lineshape of the beat-note is a convolution of the two lasers individual lineshapes. If the lasers have an ideal pure white noise, the PSD of their frequency noise $S_{\delta\nu_1}$ and $S_{\delta\nu_2}$ are constant, their lineshape are Lorentzian of FWHM $\Delta\nu_1$ and $\Delta\nu_2$. Then, the beat-note linewidth, by the property of the Lorentz function, will be $\Delta\nu_b = \Delta\nu_1 + \Delta\nu_2$. If the linewidth of laser #2 is such that $\Delta\nu_2 \ll \Delta\nu_1$, $\Delta\nu_b = \Delta\nu_1$. In practice, this can be realized with the beat-note of the laser under test (LUT) and a narrow linewidth laser in external-cavity (ECDL) for instance, which lineshape can be assimilated to a Dirac function compared to the one of the LUT. Otherwise, if the two lasers are equivalent, $\Delta\nu_1 = \Delta\nu_2 = \Delta\nu_b/2$. If not, one can still use a third laser, record three beat-notes (one laser against the two others), and solve the simple system to recover the three linewidths. If the two lasers had a perfect Gaussian linewidth, the convolution would also give a Gaussian of variance

$\sigma_b^2 = \sigma_1^2 + \sigma_2^2$. A beat-note with two identical lasers would have $\sigma_b = \sqrt{2}\sigma_1$ so the FWHM of a single source would be $\Delta\nu_1 = \Delta\nu_2 = \Delta\nu_b/\sqrt{2} = 2\sqrt{\ln 2}\sigma_b$.

This way of measuring the purity of a source has several drawbacks. First, in the case of semiconductor lasers, the frequency noise always shows a $1/f$ component, and today's laser cavities have a high enough quality factor for the white noise power to be on the same order of the flicker one, or even less in the case of our lasers (see later). Thus, **the lineshape is a very close to the Voigt profile**. An approximate useful formula for the FWHM linewidth is in this case [Olivero 1977]:

$$\Delta\nu_V \approx 0.5346\Delta\nu_L + \sqrt{0.2166\Delta\nu_L^2 + \Delta\nu_G^2} \quad (5.23)$$

where $\Delta\nu_L$ and $\Delta\nu_G$ are the corresponding FWHM of the Lorentzian and the Gaussian of the function. On the other hand, by the commutativity properties of the convolution product, the lineshape of a beat of two identical Voigt lines of FWHM $\Delta\nu_{V_1} = \Delta\nu_{V_2}$ is a Voigt profile of components $\Delta\nu_{L_b} = 2\Delta\nu_{L_1}$ and $\Delta\nu_{G_b} = \sqrt{2}\Delta\nu_{G_1}$. Obviously, in the general case, $\Delta\nu_{V_b} \neq \Delta\nu_{V_1} + \Delta\nu_{V_2}$ but rather $\Delta\nu_{V_b} = \zeta\Delta\nu_{V_1}$, $\zeta \in [\sqrt{2}, 2]$ which means that **making the systematic assumption of a Lorentzian line can lead to underestimate the experimental linewidth** (up to 41%).

The solution to realize the beat-note with a narrow laser (to have, let's say, $\Delta\nu_2 = \Delta\nu_1/50$) is also not an easy task: it should be tunable, stable and centered on the LUT frequency. For the telecom range, excellent solid-state sources exist for that purpose. For more exotic wavelengths (NIR or MIR) on-the-shelf probing lasers are rare. Moreover, home-made ECDLs are difficult to set up, stabilize over time, and one needs first a broad-band (Fabry-Perot) laser with gain at the targeted wavelength. They are also very often affected by low-frequency peaks which may perturb the analysis in this range of frequencies.

Beyond that, there is still the issue of the linewidth dependency on the observation time, which is, to our sens, not accurately addressed with an ESA, as it was explained in the previous section. Indeed, the sweeping time of these devices does not go below 1 *ms* in practical cases. So not only the spectrum cannot be retrieved for very short observation times, but not all the points will be estimated on the same timescale ! This is what is illustrated in picture (5.4).

The acquisitions obtained with this kind of analyzer assume that the spectrum remains stable during the whole sweeping, which is not true with laser lines perturbed by technical noise sources. Thus, the profile is distorted by the highly non-linear transfer function of the spectrum analyzer, loosing accuracy on the spectral shape itself. More crucially, in some cases, the time-limited linewidth will change at each acquisition, even for a constant time-frame of observation. A telling example is the case of frequency fluctuations originating from mechanical resonances, which are typically sine-wave shaped in time. One will easily see that **the linewidth is not constant between repeated experiments**, given that the RMS frequency fluctuations intercepted in the corresponding time window changes in figure (5.5). Put in another way, the quantity (5.24):

$$\sqrt{\frac{1}{\Delta T} \int_{T_i}^{T_i+\Delta T} \sin^2(2\pi f_M t) dt} \quad (5.24)$$

with f_M the mechanical frequency, is not a constant function of T_i , nor of ΔT . This is why only statistical values of the linewidth over repeated measurements makes sens. **As a conclusion, these limitations of the traditional heterodyne setup does not provide an accurate and universal mean to retrieve the time-dependent linewidth of lasers.**

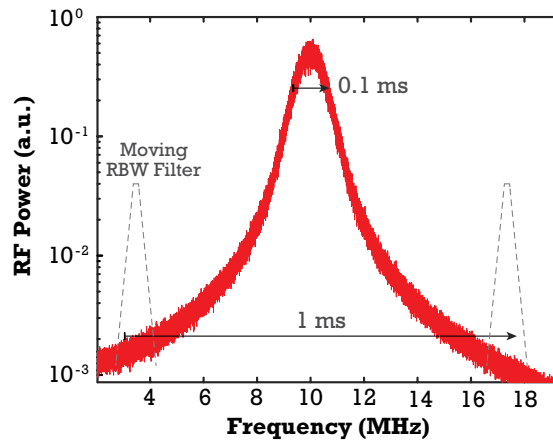


Figure 5.4: Sweeping (superheterodyne) RF spectrum analyzer at work: the resolution filter sweeps in time across all the frequencies to obtain the whole spectrum. Hence, such a spectrum does not reflect a specific timeframe

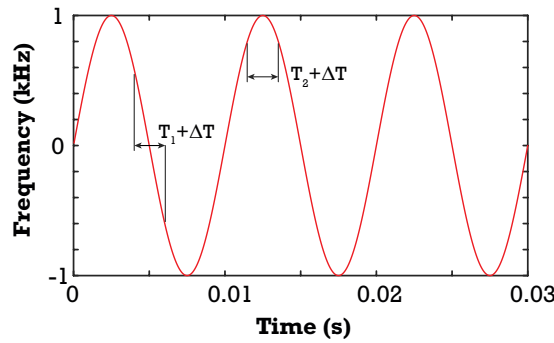


Figure 5.5: Frequency variations induced by typical mechanical noise. In this case, the RMS value is not stable as a function of the starting time T_i of the experiment

5.4.2 Self-heterodyne linewidth

As an alternative to the basic heterodyne setup, the self-heterodyne technique is very often used: it has the major advantage to give an estimate of the linewidth with a laser only and to be barely sensitive to the experimental conditions (no perfect stabilization of the laser required). However, the results of these measurements can be very difficult to interpret, as we will see. The general principle of the self-heterodyne beat-note is to use a Mach-Zehnder interferometer in the *over-coherent* regime, that is, to realize a self-interference of a laser beam with a delayed part of itself, such that the delay $\tau_d \gg \tau_c$, the coherence time of the laser [Okoshi 1980, Gallion 1984].

The setup is depicted in figure (5.6). The laser beam is collimated thanks to an aspherical lens of focal length $f_L = 8 \text{ mm}$ (Thorlabs C610-TMB) and goes through an optical isolator (Isowave) that attenuates back-reflections up to 70 dB, with maximum efficiency at 894 nm. After attenuation, the light path is divided by a non-polarizing cube beam splitter (BS) (Thorlabs BS011). One ray is injected into a reel of fiber (780HP type) of length L_d with a mirror M and a packaged lens of focal length $f_L = 8 \text{ mm}$ (Thorlabs F240APC-780) and reached finally the 50/50 coupler. Sometimes, a polarization controller is added on one arm to adjust the polarization matching, but it is not crucial

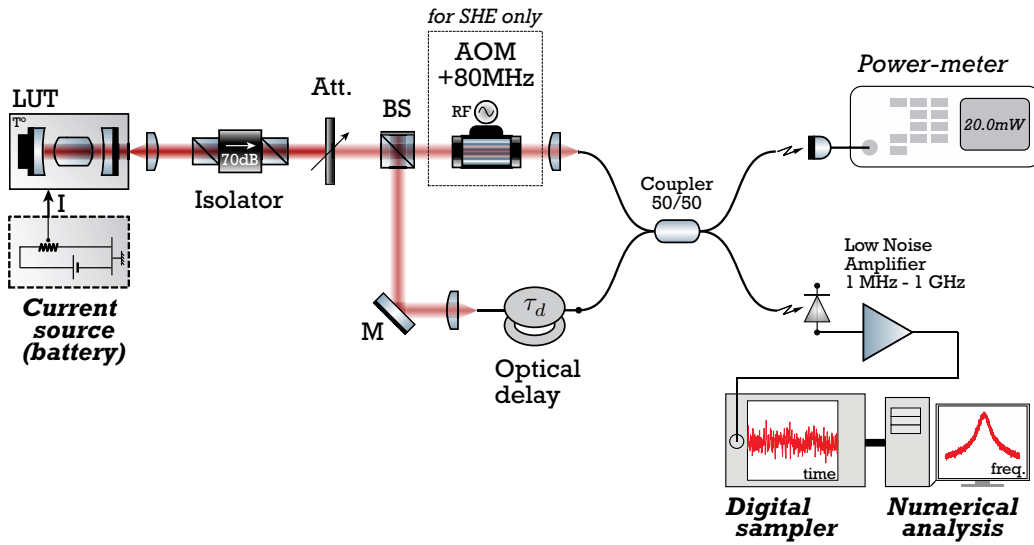


Figure 5.6: Schematic of the SHO/SHE optical bench used to estimate the (self-heterodyne) laser linewidth

in over-coherent regimes. If the second beam is simply recombined in the coupler after the delay, the configuration is called *self-homodyne* (SHO). Thus, the beat central frequency lies precisely at $\nu_{12} = 0 \text{ Hz}$. This can lead to an issue after the Fourier analysis if the acquisition chain does not remove correctly this DC component, which may pollute the lineshape spectrum. The same comment can be done with the low-frequency noise. This is why, a frequency shifter is often added on one of the arm: it can be for instance an *Acousto-Optic Modulator* (AOM). This device is able to shift, by diffraction, the laser beam carrier frequency by $\Delta\nu_{AOM}$ when the optical wave crosses a non-linear medium excited by acoustic waves. This configuration is called *self-heterodyne* (SHE). However, the laser intrinsic linewidth must be way below $\Delta\nu_{AOM}$ otherwise the aisles of the lineshape may be affected by the DC, preventing a proper numerical fit of the data. In our case, the AOM (Crystal Technology Inc. type 3000-122, with its RF driver 1080-AF-DIFO-1.0) has a $\Delta\nu_{AOM} = 80 \text{ MHz}$, so the beat-note will be centered at $\nu_{12} = 80 \text{ MHz}$, far enough from the DC to avoid the previous issue. The first output is sent on the fibered low-noise photodiode-amplifier ($DC - 100 \text{ MHz}$) which photocurrent goes to the usual acquisition chain, while the other output is sent to the power-meter to track the beam injection efficiency.

Some authors have studied the expression of the autocorrelation of the field in the SHO/SHE schemes [Mercer 1991, Signoret 1994, Turrenc 2005b] when the PSD of noise has a white and a flicker component. If the total SHE electric-field after the recombination is $E_T(t) = E(t) + \gamma E(t + \tau_d) e^{i\Omega t}$, with γ the recombination efficiency and $\Omega = 2\pi\Delta\nu_{AOM}$ the SHE pulsation shift, it can be shown that the autocorrelation function of this intensity of this expression is, under some reasonable approximations [Ludvigsen 1998, Turrenc 2005b]:

$$\Gamma_I^{SHE}(\tau) = \overline{I(t) * I(t + \tau)} = E_0^4 \left\{ (1 + \gamma^2)^2 + 2\gamma^2 \cos(\Omega\tau) \exp[-2s(\tau, \tau_d)] \right\} \quad (5.25)$$

$$s(\tau, \tau_d) = 4 \int_0^{+\infty} \sin^2(\pi\tau_d f) \frac{\sin^2(\pi\tau f)}{f^2} S_{\delta\nu}(f) df \quad (5.26)$$

which is very close to (5.10) if we set $\gamma = 1$ and $\Omega = 0$, with an additional delay-dependent modulation

term in $\sin^2(\pi\tau_d f)$ in the integral. The definition of the linewidth can be applied so that (5.27):

$$\mathcal{L}_{SHE}(f, \tau_d) = \delta(f - \Omega/2\pi) * \mathcal{F} \left\{ \exp \left[-8 \int_0^{+\infty} \sin^2(\pi\tau_d f) \frac{\sin^2(\pi\tau f)}{f^2} S_{\delta\nu}(f) df \right] \right\} \quad (5.27)$$

The amplitude has been normalized to 1. Depending on the theoretical form of the frequency noise $S_{\delta\nu}$ inserted in (5.27), different lineshape profiles are obtained, depending on the value of τ_d [Tourrenc 2005b]. This expression solves the issue of the lower bound of integration: setting a delay defines an implicit lower frequency cutoff (mathematically, the integral converges even for $1/f$ noise when $f \rightarrow 0$). On the other hand, the lineshape now depends on τ_d . **This is why talking about the SHE linewidth of a source without referring to this parameter makes no sense.** The only case for which $\Delta\nu_{SHE}$ is independent of the delay is for a pure white frequency noise, in which case $\mathcal{L}(f)$ is Lorentzian of FWHM linewidth:

$$\Delta\nu_{SHE} = 2\pi S_0 \quad (5.28)$$

which is **twice the intrinsic linewidth** (5.13). The SHE technique is very popular and widely used to measure easily and quickly the linewidth. Among others, it is completely insensitive to long term *drifts* of the central frequency ν_0 (like thermal ones) that are canceled out in the beating. It is traditionally recorded with an ESA, because there is no integration time pitfall. Though, we use (at the University of Montpellier) the same setup of acquisition as for the frequency noise to obtain very high-resolution in the spectra.

If this on-the-shelf method is very practical, it is not very satisfactory on a metrological point of view. Indeed, if one has to record the 'full' spectral broadening of a laser, the interferometer must be in the over-coherent regime to avoid *correlations* between the two arms of the setup. This condition writes again $\tau_d \gg \tau_c = 1/2\pi\Delta\nu$. It can be verified by computation that it is in practice $\tau_d \sim 10\tau_c$ for white noise. When the source is very narrow, it leads to add tens of *km* of delay fiber. In the meantime, if the laser is affected by flicker noise, the resulting measured linewidth will keep on growing with the delay ! What then could be the most relevant figure to highlight: the white noise part only ? The delay-constrained total linewidth ? More generally, the link (or the absence of a link) between the SHO linewidth and the intrinsic one for a given delay has never been clearly brought to light to our knowledge. These facts calls for a more general method to extract the noise components of lasers and express their spectral width. Still, we can use the SHE method to give a first estimation of the order of magnitude of the coherence time: it is especially interesting to make a first calibration of frequency discriminators in frequency noise measurements (see further).

To conclude, it shall be mentioned that the self-heterodyne technique can also be used in the *sub-coherent* regime ($\tau_d \ll \tau_c$). In these conditions, the correlations are seen in the spectrum through waves in the flanks while the central peak turns much to a Dirac function. The interference patterns are characteristic to a type of noise and a delay τ_d . Thanks to the theoretical autocorrelation functions, it is possible to estimate the white noise level S_0 and the flicker coefficient S_{-1} out of these spectral shapes.

In the frame of the noise investigation, these methods are too approximate to give a precise picture of the noise and will not be exploited further, unless for the experimental demonstration of the above.

5.4.3 Frequency noise measurements by frequency discrimination

The frequency noise discrimination is probably the most difficult, but also the most fruitful method of characterization of the light coherence. Instead of the laser power spectrum, it aims at **retrieving directly the frequency variations over time of the field**. Because it cannot be measured as such, an optical device is used to convert the fluctuations into light power variations to be measured directly by a detector. More formally, we want to record the phase fluctuations of the source E-field $\Delta\phi(t) = \phi(t) - \phi_0$ (with $\phi_0 = \overline{\phi(t)}$) by a *linear* conversion of such phase to amplitude fluctuations of a measurable electrical variable, that can be Fourier transformed to the PSD (figure (5.7)).

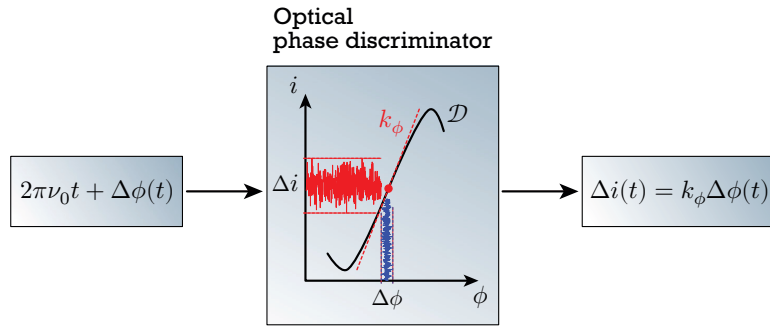


Figure 5.7: Principle of the optical carrier frequency discrimination with the use of phase discrimination

The conversion is operated by an optical *frequency discriminator* which transfer function $i(t) = \mathcal{D}(\phi(t))$ has a **linear domain of slope** k_ϕ (at least locally): this point of operation can be used to convert the phase into an (electrical) amplitude given by the photodiode: the photocurrent i for instance. Most of the time, the converter is an interferometer with two arms where the radiation travels with a *delay* τ_d between the two paths. Because this delay is way smaller than the coherence time τ_c of the field, the phase difference is proportional to the frequency variation: $\Delta\phi(t) = \tau_d \times (d\phi/dt) = 2\pi\tau_d\delta\nu(t)$. So we are able to retrieve the frequency noise from the converter with the relation $S_{\delta\nu}(f) = S_i(f)/k_\nu^2$ with $k_\nu = 2\pi\tau_d k_\phi$ (in $A.Hz^{-1}$). Some common interferometers are:

- Fabry-Perot interferometer: the linear conversion is realized along the flanks of the resonance 'fringes', which local slope can be tuned from the mirror reflectivities and cavity length, while the operation point is changed by a slight variation of the FSR [Tourenco 2005b]
- Mach-Zehnder interferometer: this simple interferometer is based on the splitting and imbalanced recombination of a beam with a delay τ_d
- Atomic references: The natural fluorescence line of a species can be used as a discriminator; while the central atomic line frequency ν_0 is an absolute reference point, the flanks of the line provides an absolute conversion slope k_{at} . It should be highlighted that the atomic transfer function has a simple Lorentzian form if the exciting laser has itself a Lorentzian spectral shape
- Michelson interferometer: equivalent to a Mach-Zehnder setup where the beam is separated and recombined at the same point thanks to the use of Faraday mirrors (see next section)

Two important criteria must be observed to use these setups:

1. The converter must remain in its zone of linearity during the measurements: if the slope k_ν is too high regarding the RMS frequency fluctuations of the laser, the amplitude excursions Δi will exceed the range of validity and the data will be corrupted (more simply, the laser frequency can drift during the experimental time)
2. The signal converted from the laser frequency noise must stand out of the laser RIN noise and the background noise of the interferometer, so k_ν cannot be too low

Thus, the choice of the discriminator slope is always a **compromise between the linearity of the response and the measurement sensitivity**. To conclude, we used a (fibered) Michelson to make the traditional frequency noise measurements instead of the other apparatus: the Fabry-Perot, for instance, is relatively complex to set-up (on-the-shelf benches can be found, but one has to inject carefully the laser beam into the cavity, so not to excite higher order modes of the resonator and be close to the theoretical finesse of the setup). The atomic references have the drawback that the single-mode laser has to be exactly at (or very close to) the atomic frequency transition, so the operation point in current is fixed, for a given temperature (because of the frequency tuning with current). Finally, a basic Mach-Zehnder with a classic fiber may be sensitive to low-frequency perturbations: conversely to the Michelson with Faraday mirrors, fluctuations of the fiber refractive index with ambient temperature for instance are not canceled out in the interferometer.

Aside from these constraints, whatever the discrimination process, the main issue is that the conversion factor must be carefully calibrated or assessed to recover the true magnitude of frequency noise. This is why it is required, paradoxically, to have an estimate of the coherence time of the laser before setting-up the measurements ! Sometimes, the laser is put in a *servo* to stabilize its operation point (see chapter 6), before measuring the noise at higher frequencies. But it is not obvious to ensure that the 'high-frequency' noise is not affected. Several discriminators of different sensitivities can also be used.

In section [5.2.2], we will establish an alternative method, easy to set-up and overriding those limits.

★ The Michelson setup

Figure (5.8) represents our Michelson setup used to measure the frequency noise of the LAMA lasers.

After collimation and passing the isolator, the laser beam is attenuated and injected into the first arm of a 50/50 broadband (850 nm) fibered coupler (Thorlabs TW850R5A2) with APC terminations (to avoid back-reflections). The radiation crosses the optical junction point before splitting into the two output paths. On the first arm, the beam is reflected back by a Faraday mirror centered at 894 nm (Isowave). The aim of this mirror is to rotate the field polarization by 90° after the reflection. The consequence is that any random variation of the polarization in the fiber after the coupler is canceled out when the radiation comes back, so the interference efficiency is maximum at the beam recombinations [Kersey 1991]. On the second arm, a delay is added with a fiber of length $L_d = \tau_d \times c / 2n_{fiber}$ between the coupler and the second Faraday rotator (the light makes a double-pass in the delay in this configuration). Once the beams have been recombined, the light can make its way through the fourth arm where it reaches a photodiode and a signal amplification/analysis chain.

Theoretically, it can be shown [Stéphan 2005, Tow 2013] that if the detected current at the photodiode is written $i_{ph}(t) = i_0(1 + \cos(\phi(t, \tau_d))) \approx i_0(1 + 2\pi\tau_d\delta\nu(t))$ the PSD of frequency noise is:

$$S_{\delta\nu}(f) = \frac{1}{\sin^2(\pi\tau_d f)} \frac{S_i(f)}{(2\pi\tau_d i_0)^2} \quad (5.29)$$

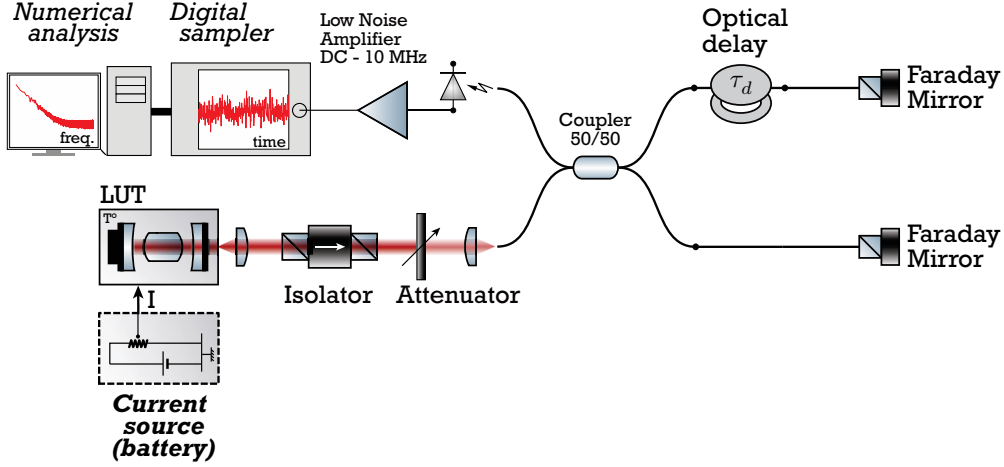


Figure 5.8: Michelson setup of the frequency noise measurement in the classical approach

Contrary to the simple analysis of [5.4.3], the apparatus function of the Michelson is taken into account in (5.29) with an additional *sinc* function. This indicates that the measure is valid into a limited bandwidth set by the condition $\text{sinc}(\pi\tau_d f) \approx 1 \Rightarrow f \ll f_{max} = 1/\pi\tau_d$. For a delay induced by a length $L_d = 1 \text{ m}$, with $n_{fiber} = 1.47$, this upper cutoff frequency is $f_{max} = 65 \text{ MHz}$, which is enough for the high frequency analysis of the noise, up to approximately 6 MHz . Longer delays will decrease this value. In practice, we rather measure the voltage noise fluctuations that have been amplified with a gain G . Below f_{max} we get:

$$S_{\delta\nu}(f) = \frac{S_v(f)}{G^2 v_0^2} \times \frac{1}{(2\pi\tau_d)^2} \stackrel{1}{=} RIN_{Michelson} \times FSR'_\nu{}^2 \quad (5.30)$$

$$\stackrel{2}{=} \frac{S_v(f)}{G^2 k_v^2} \quad (5.31)$$

The experimental PSD of frequency noise can be interpreted in two different ways: either it is the direct conversion (5.31) from the voltage noise through the slope $k_v = 2\pi\tau_d v_0$ (in $V.Hz^{-1}$), or it is more generally (5.30) **the RIN of the interferometric setup multiplied by its (pseudo) free spectral range** $FSR'_\nu = (2\pi\tau_d)^{-1}$. Because the flicker noise induces growing frequency excursions over time, it is likely that the setup will shift from its optimal point of operation during the measurement: the properties of the sine function allows however to make an acceptable error on the absolute value of the slope of the discriminator: if we set this margin to a deviation lower than 10% from the exact PSD of frequency noise, this means that the error on the determination of $1/k_v$ must be below 32%. This range is pinpointed in graph (5.9). Otherwise, it is still possible to reduce the slope with a smaller L_d . For $L_d = 0.3 \text{ m}$, $k_v = v_0/FSR'_\nu$ with $FSR'_\nu = 1.08 \times 10^8 \text{ Hz}$.

5.4.4 A simple relationship between the linewidth and the frequency noise?

In section [5.3.1], we have written explicitly a mathematical relationship between the lineshape $\mathcal{L}(f)$ and $S_{\delta\nu}(f)$ with (5.11). This complicated formula was used as such until the work of G. Di Domenico et al. [Di Domenico 2010] really clarified the physical meaning behind it using concepts of signal processing and modulation theory. Basically, the log-log $(f, S_{\delta\nu})$ domain can be separated into two areas where the frequency noise has a very different contribution to the total **FWHM** (or -3 dB) linewidth: in the 'high-modulation' area, defined by $S_{\delta\nu}(f) < f$, the lineshape is Lorentzian and

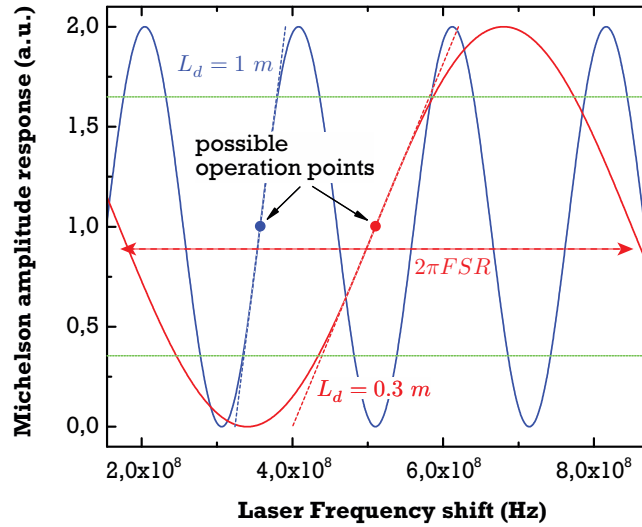


Figure 5.9: Plot of the Michelson amplitude response function for the two cases $L_d = 1\text{ m}$ and $L_d = 0.3\text{ m}$. The operations points where the response is locally linear is indicated by plain circles. The acceptable range of excursion to have less than 10% of error on the conversion slope is indicated in small green dotted lines

most of the fluctuation energy is contained in the wings of the distribution. On the other side, the 'slow-modulation' area $S_{\delta\nu}(f) > f$ gives a Gaussian contribution, which FWHM is larger than that of the Lorentzian of same total energy. These two different behaviors are separated by the frontier of equation $y = 0.56x$ called the β -separation line. All the frequency noise above this line contributes to the FWHM linewidth, while the noise under this limit can be neglected in the computation. The authors give then a simple formula to estimate the linewidth:

$$\Delta\nu_{FWHM} = \sqrt{8 \ln 2 \times \mathcal{A}} \quad (5.32)$$

where \mathcal{A} is the area, under $S_{\delta\nu}$, delimited by $f_0 = 1/T_{obs}$ and f_c , the corner frequency where $S_{\delta\nu}(f)$ and the β -separation line cross each others (see figure (5.10)).

The concept is fruitful because it allows to identify quickly the relevant bandwidth for a noise-reduction servo loop (it will be used intensively in chapter 6). However, because it is based on (5.11), it still relies on an arbitrary lower frequency cutoff in the frequency domain.

To summarize in a bird's-eye view the connections between the noise quantities used up to now, graph (5.11) is useful. We have represented the equivalences between the frequency noise and the phase noise, the latter been more commonly encountered in the field of RF electronics. If some paths are reversible, some others are not: what we learn here is that if there is not exact transformation going from the PSD of frequency noise $S_{\tilde{\nu}} \equiv S_{\delta\nu}$ to the lineshape \mathcal{L} , if one starts from an heterodyne beat-note of equivalent lasers (or, of course, from the field $E(t)$ itself), all the other noise representations can be computed. In particular, we will show later that the phase variations $\tilde{\varphi}(t) \equiv \Delta\phi(t)$ can be retrieved, using the Hilbert transform \mathcal{H} .

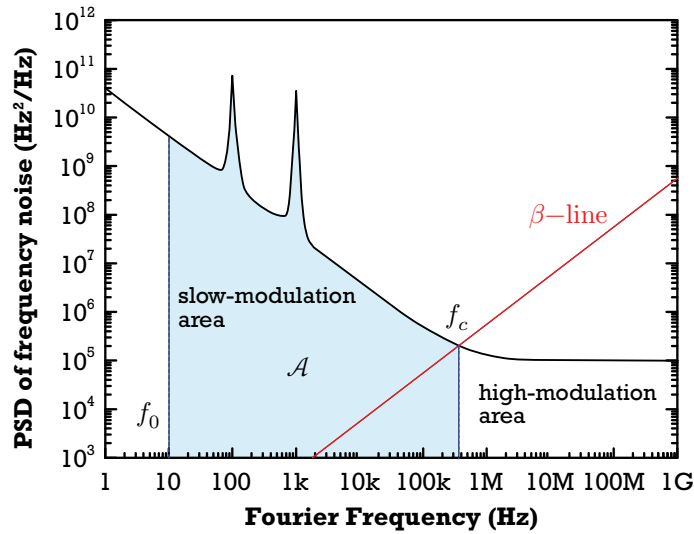


Figure 5.10: Concept of the β -separation line. Inspired from [Di Domenico 2010]

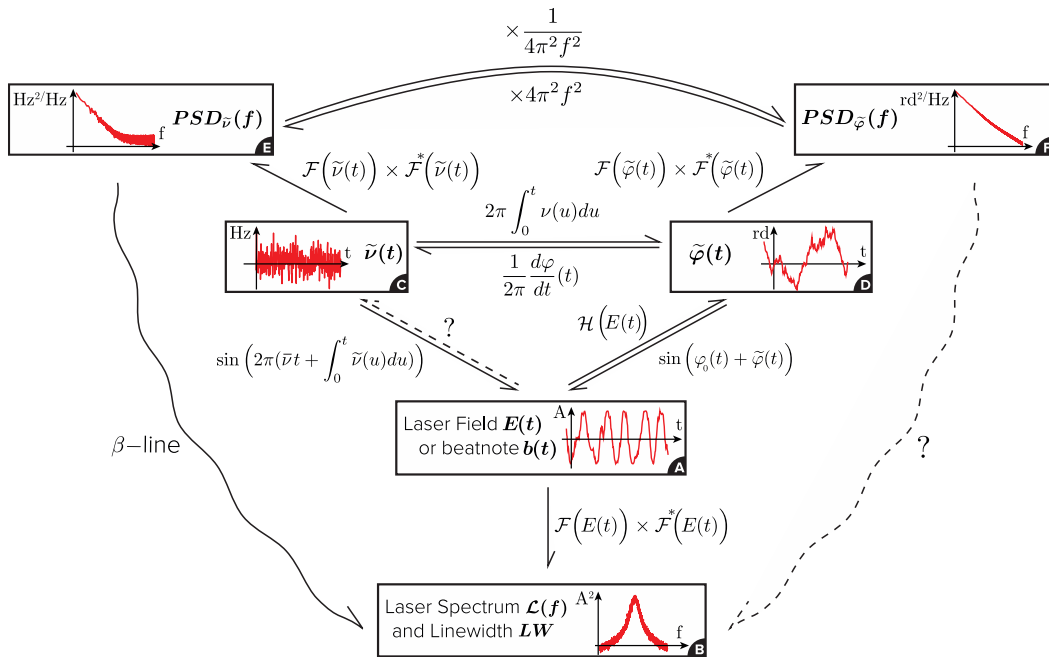


Figure 5.11: Summary of the relevant signals and the mathematical relationships between them. No arrow is for no possible path. Dashed arrow is for no conceptual impossibility but not reported in the literature. Wavy arrow is for a possible path with numerical approximations. After [von Bandel 2016b]

5.4.5 Conclusion

Regarding to what has been said about the traditional linewidth metrology, **nor the heterodyne or the self-homodyne/heterodyne techniques are completely satisfying to study the laser frequency noise, in the way they are traditionally used.** Also, the frequency noise measured from frequency discrimination have to be converted to the FWHM linewidth (β -line or direct integration) with the opened question on its relation with the observation time T_{obs} . An extensive method

of practical characterization of a laser technology that makes no particular assumptions on the noise components of the spectrum, with an access to the intrinsic time-dependent linewidth of a laser, as well as its PSD of frequency noise, would be suitable. These two aspects of the frequency fluctuations are required to either identify the type of noise in the device, or to give a more practical aspect of the latter through the single $\Delta\nu$ figure that is often directly linked to the optical system performances (for instance, to address an atomic line of a given natural linewidth in atomic clocks).

5.5 Experimental results of the standard metrology

In this section, the principles and experimental setups previously presented are used to study the noise of the 1st run of LAMA sources.

5.5.1 RIN measurements

The RIN must be priorly estimated in the semiconductor lasers to validate a frequency discrimination technique. Figure (5.12) is an example of the most simple measurement setup of this quantity. After collimation, passing the isolator and the attenuation-step, the output beam reaches directly the

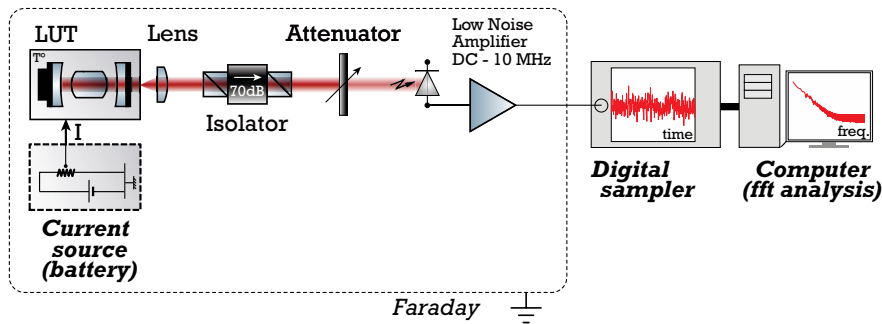


Figure 5.12: RIN measurement setup

detector (5.12). It is the combination of a photodiode and a home-made low-noise transimpedance amplifier (TIA) biased with a 9 V chemical battery. The TIA is used first to avoid self-polarization of the photodiode and to keep the linear relation between the collected optical power and the photocurrent output. Then, the current is converted to a voltage through the relation $v_{ph} = R_f i_{ph}$, where the feedback resistor $R_f = 10 \text{ k}\Omega$ sets the gain $G_{TIA} = R_f$. The AC output has an additional gain $G_{AC} = \sqrt{1000}$ relatively to the DC. The ensemble has a band of 10 MHz (cutoff frequency). **Because of impedance adaptation (50 Ω), this gain has to be divided further by two.** The first input is used to measure the photocurrent (read in Volts) to compute the shot-noise, while the AC records the amplitude fluctuations. The signal is sent to the digital sampler and to the home-made fft-scope, as described in chapter 4, to retrieve the PSD of photocurrent noise. Then, the formula (5.2) is applied. In darkness, the background detection floor is $S_{floor} = 1.1 \times 10^{-22} \text{ A}^2 \cdot \text{Hz}^{-1}$ (figure (5.14)). We can observe that the DC component is not completely filtered out by the electronics: it could be removed by a manipulation on the signal before applying the fft.

The low-frequency RIN is, like the electric noise, extremely sensitive to external perturbations: it follows in particular all the current fluctuations (1/f, parasites...) [Myara 2003] and the free space coupling to the photodiode makes it sensitive to mechanical vibrations (coupling fluctuations). For these reasons, the optical bench is placed on a stack of inner (air) tubes and wood slabs that act

like a low-pass filter for mechanical resonances, and the assembly is placed itself in the Faraday cage (picture (5.13)). The LUT is biased by the same low-noise battery current source as before.

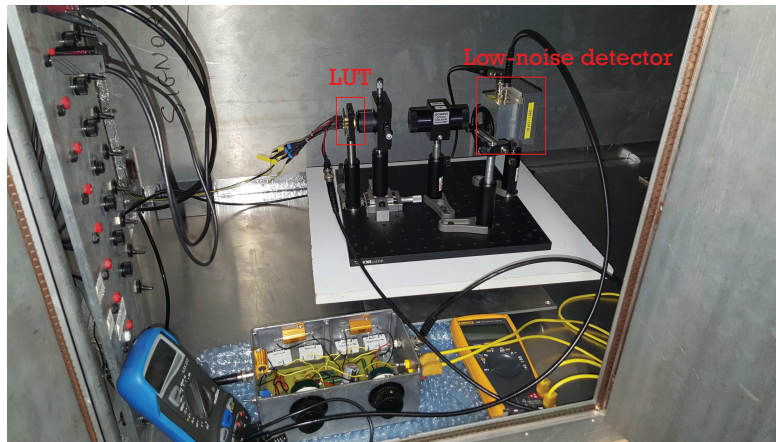


Figure 5.13: Picture of the RIN measurement setup (IES, University of Montpellier)

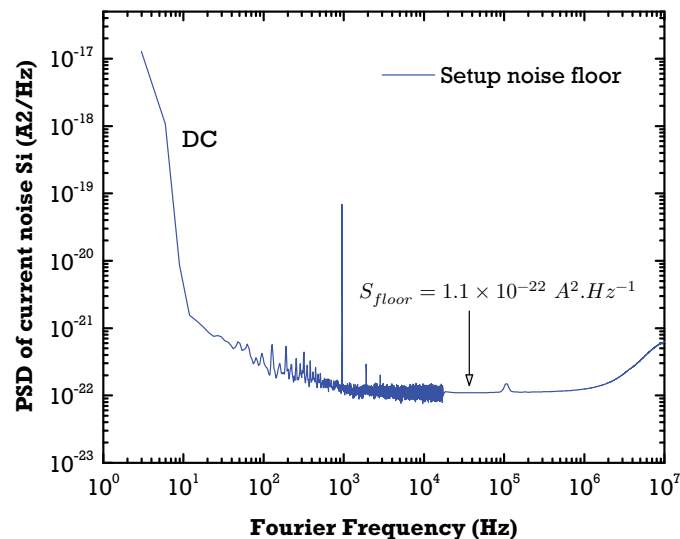


Figure 5.14: PSD of current noise of the RIN setup in darkness (average over 100 measurements)

★ Device C0195 (894 nm)

The first RIN evaluation is made on the device C0195 (XXL2029, $L = 2 \text{ mm}$, TO3 package). The quantity is plotted as a function of the Fourier frequency for several output power levels in figure (5.15).

It is clearly observed that the RIN decreases with increasing power, with a minimum in the white noise at $P_{out} = 60 \text{ mW}$. This value corresponds to a measured PSD of photocurrent noise of $S_i = 2.5 \times 10^{-21} \text{ V}^2 \cdot \text{Hz}^{-1}$: it is more than one decade above the detection floor which confirms the validity of the setup to measure correctly the RIN from DC to 1 MHz . To read more clearly the behavior at high power in the high-frequency range, figure (5.16) plots the white level at 3 MHz versus the optical power.

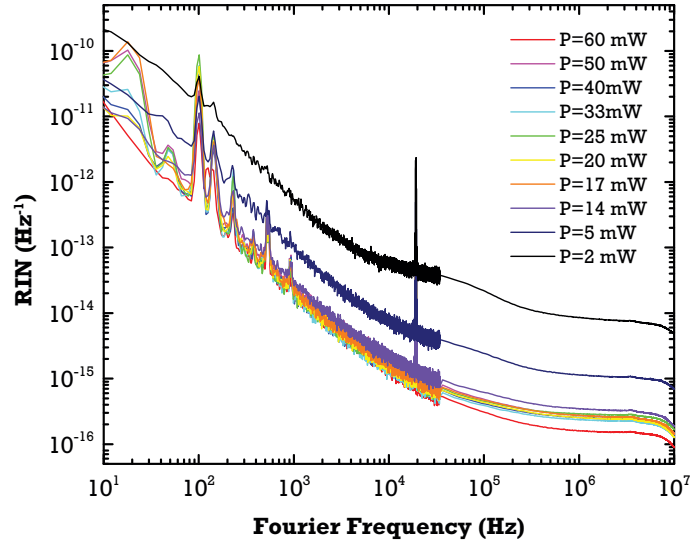


Figure 5.15: RIN as a function of the Fourier frequency, for several output powers of device C0195 ($T = 67^\circ C$)

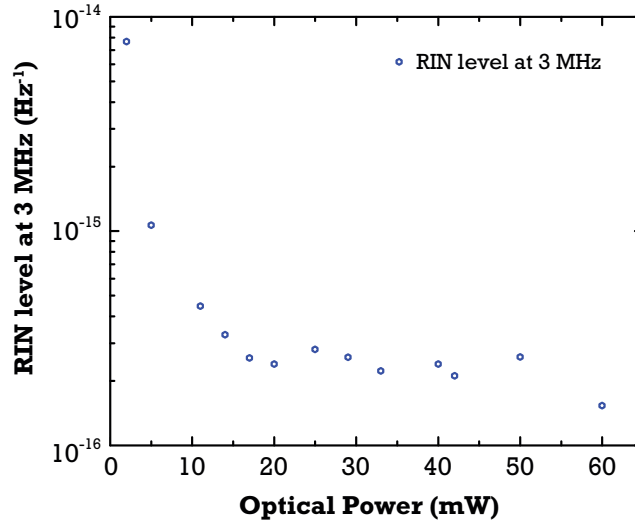


Figure 5.16: RIN level at $f = 3 \text{ MHz}$ versus the optical output power of laser module C0195

The theory states that for modulation frequencies way below the carrier resonance frequency $f_m \ll f_r$, the amplitude white noise is $RIN \propto 1/P_{out}^3$ [Petermann 2012]. Here, no similar trend is observed, even in the low power regime. Whatever the origins of this behavior, above $P_{out} = 30 \text{ mW}$, the RIN evolution is not steady, with a higher noise at 40 mW followed by a deeper decrease above 60 mW . **This may be associated to the beam lateral instabilities already observed in chapter 3.** When the mode is not stable in the cavity, the photon noise is affected and does not follow the quantum limit anymore. Regarding the low-frequency part, **the $1/f$ slope stands out clearly and originates from the (independent) electronic noise source that was studied in chapter 4.** Indeed, if we consider that the current noise of the device is converted directly to the amplitude noise through the external efficiency $S_P = \eta_a^2 S_I$, then at 1 kHz above threshold, we have from section [4.3.2]: $S_{P, @1 \text{ kHz}} = (0.5 \text{ W.A}^{-1})^2 \times (8.7 \times 10^{-18} \text{ A}^2 \cdot \text{Hz}^{-1}) = 2.2 \times 10^{-18} \text{ W}^2 \cdot \text{Hz}^{-1}$. In the meantime, the direct

RIN measurement gives $S'_P = P^2 \times RIN = (0.014 W)^2 \times (2.7 \times 10^{-14} Hz^{-1}) = 5.3 \times 10^{-18} W^2.Hz^{-1}$. The values of S_P and S'_P are close enough, given the uncertainties on the experimental values, to consider the direct current noise conversion in stimulated emission in the quantum well.

★ Device C0314 (852 nm)

The RIN has also been evaluated in the device C0314 (XXL2020, $L = 1.5 mm$, TO3 package). The quantity is plotted as a function of the Fourier frequency for several output power levels in figure (5.17). As before, the RIN level decreases with increasing P_{out} . Between 14 mW and 40 mW, the white

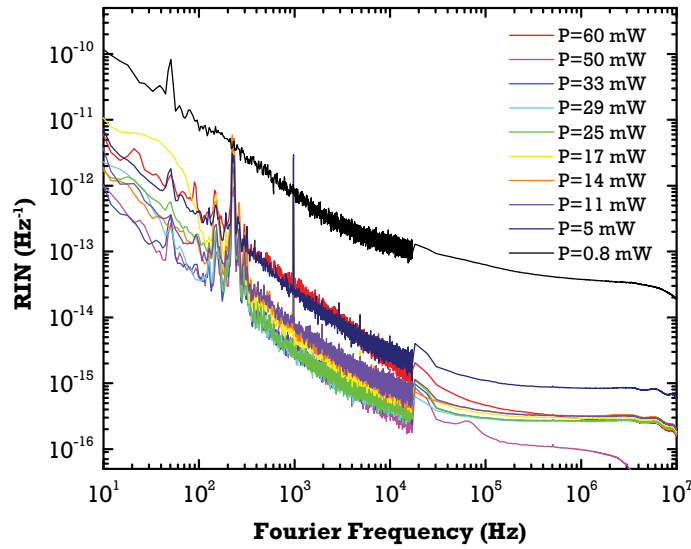


Figure 5.17: RIN as a function of the Fourier frequency, for several output powers of device C0314 ($T = 27^\circ C$)

noise is relatively stable, before decreasing abruptly at 50 mW (the measure is probably corrupted at high frequencies for this bias because the level gets close to the shot-noise limit) and coming back to the stagnation level at 60 mW. In the meantime, the $1/f$ level, which was stable above 5 mW increases by almost one decade for this level of power, going back to the 5 mW level where the noise is high. This is probably linked to the packaging defect mentioned in chapter 4 that amplifies the flicker magnitude, converted directly to the RIN.

5.5.2 Linewidth in the over-coherent SHE setup

5.5.2.1 Setup and first results

The linewidth of the 894 nm and 852 nm lasers (C-mounts and TO3 package) has been investigated first with a SHE bench of III-V Lab (the scheme with the AOM has already been described), which has been upgraded to the D_1 line (figure (5.18)). In this setup, the detection system is a commercial integrated photodiode+amplifier (Thorlabs PDA10BS) of range $DC - 100 MHz$. The acquisition is realized with an ESA (Agilent E4411B 9 KHz – 1.5 GHz) which principle has been described before. The current source is a commercial low-noise one that can switch from sector to autonomous batteries (ILX Lightwave LDX-3620) with an announced Noise Equivalent Power (NEP) of $NEP = 0.8 pA.Hz^{-1/2}$ at 1 kHz. This level (square root of the corresponding PSD of current noise) is low enough to add negligible noise to the laser output but it is not as efficient as the home-made source

used for the electric noise setup and the other frequency noise measurements made at the University of Montpellier.

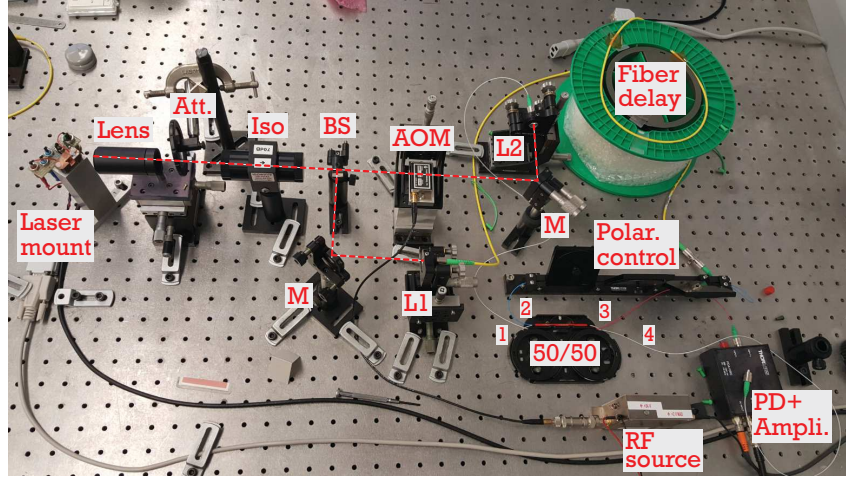


Figure 5.18: Picture of III-V Lab SHE bench

We already know from preliminary measurements that the intrinsic linewidth of the LAMA lasers are in the range of $0.5 - 2 \text{ MHz}$. Thus, the coherence time is on the order of $\tau_c = (2\pi \times 1 \text{ MHz})^{-1} = 0.16 \mu\text{s}$ and the delay must be at least $\tau_d \gtrsim 10 \times \tau_c \Leftrightarrow L_d \gtrsim 10 \times 0.16 \mu\text{s} \times (3 \times 10^8 \text{ m.s}^{-1} / 1.47) = 325 \text{ m}$. The reel of fiber used has $L_d = 2 \text{ km}$ which is theoretically sufficient to reach linewidths down to $\sim 160 \text{ kHz}$.

Figure (5.19) is a typical measurement of the lineshape as given by the ESA, for one laser at 852 nm and another at 894 nm , with the same reference output powers of respectively 20 mW and 40 mW . The central beat frequency is at 80 MHz . The data is the result of a point average over 300 successive acquisitions. The resolution bandwidth is 100 kHz . The sweeping time has no importance in this configuration (except to increase the resolution bandwidth of the analyzer) if we assume that the laser PSD of frequency noise is stationary for $t < \tau_d$ (this is not the case if a chaotic behavior takes place, under optical feedback for instance). The curves have been fitted with a Voigt profile with ORIGIN LAB[®].

We can notice that the linewidth behavior with the output power is completely different in each case: for the laser at 894 nm , the total FWHM SHE linewidth decreases slightly from 1.92 MHz to 1.72 MHz with P_{out} , while it is multiplied by four, from 960 kHz to 4.1 MHz for the 852 nm laser. However, these observations are homogeneous for each technology. Regarding the lineshape itself, the profile is Lorentzian for C0171 and a true Voigt profile for C0190: in this case, the fit reveals a $\Delta\nu_{L,20\text{mW}} = 860 \text{ kHz}$ and $\Delta\nu_{G,20\text{mW}} = 300 \text{ kHz}$ versus $\Delta\nu_{L,40\text{mW}} = 3.1 \text{ MHz}$ and $\Delta\nu_{G,40\text{mW}} = 2.1 \text{ MHz}$. It means that the ratio of the 'Gaussian' noise with relation to the Lorentzian one has increased with the optical power. It can be seen from direct visual inspection that the profile at high power is departing from the Lorentzian with a broadening of the central peak. The difficulties of interpretation of the SHE linewidth are well illustrated here:

- The Lorentzian profile of C0171 suggest that the Schawlow-Townes-Henry limit dominates largely over other sources of technical noise ($1/f$). Theoretically, we should have a decrease of the linewidth by a factor two with the doubling of the optical power, which is not the case here. This suggest that either the laser has not a 'linear' behavior, or that the technical noise is not as

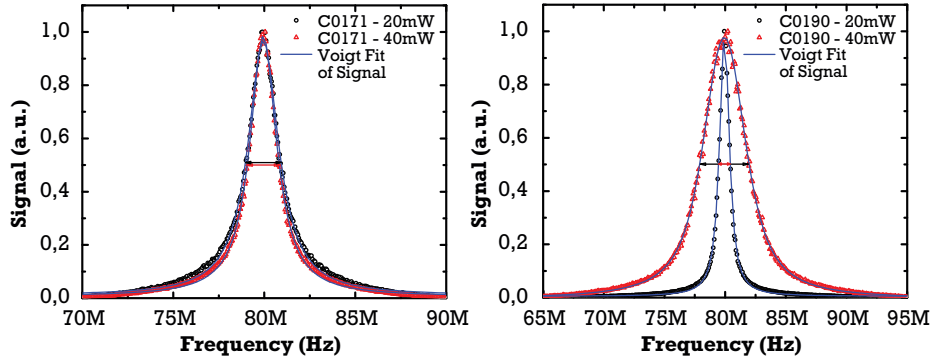


Figure 5.19: Left: experimental measurement of the spectrum of the laser output with the SHE setup, for a power of 20 *mW* and 40 *mW* (DFB device C0171 of length 2 *mm* at $T = 67^\circ C$ at 894 *nm*). The SHE linewidth at FWHM is respectively $\Delta\nu_{20mW} = 1.92 \text{ MHz}$ and $\Delta\nu_{40mW} = 1.72 \text{ MHz}$. Right: same measure, for a power of 20 *mW* and 40 *mW* (DFB device C0190 of length 2 *mm* $T = 27^\circ C$ at 852 *nm*). The SHE linewidth at FWHM is respectively $\Delta\nu_{20mW} = 960 \text{ kHz}$ and $\Delta\nu_{40mW} = 4.1 \text{ MHz}$

low as expected and the SHE delay τ_d value is too low to reveal sufficiently this low-frequency noise component

- As it has already been highlighted, if one wants to give a value of the intrinsic linewidth of the lasers, one has to make a reasonable assumption on the noise that dominates: for C0171, if we assume that the white noise dominates largely, then $\Delta\nu_{C0171,40mW} = 860 \text{ kHz} \pm 100 \text{ kHz}$. For C0190, we have at most $\Delta\nu_{C0190,20mW} = 960/\sqrt{2} \text{ kHz} = 679 \text{ kHz} \pm 100 \text{ kHz}$ and $\Delta\nu_{C0190,40mW} = 4.1/\sqrt{2} \text{ MHz} = 2.9 \text{ MHz} \pm 100 \text{ kHz}$

All in all, the values given here are quite arbitrary so we should not give too much credit to the SHE linewidth as such. It is useful though to give an order of magnitude of the spectral broadening of the source in laser data-sheets for instance: if a source measured with a given delay τ_d has satisfying performances in a system, this configuration can be set as a reference for further laser fabrication and testing. Aside from these values, it is clear that a strong non-linear behavior takes place in the XXL2020 852 *nm* technology, which is rather linked to the level of current injected than an effect coming from the optical power itself (see below).

Module reference	C0171 (DFB 894 <i>nm</i>)		C0190 (DFB 894 <i>nm</i>)	
Profile @20 <i>mW</i>	Lorentzian $\Delta\nu_L = 1.92 \text{ MHz}$	Max. linewidth $\Delta\nu = 960 \text{ kHz}$	Voigt $\Delta\nu_V = 960 \text{ kHz}$ $\Delta\nu_L = 860 \text{ kHz}$ $\Delta\nu_G = 300 \text{ kHz}$	Max. linewidth $\Delta\nu = 680 \text{ kHz}$
Profile @40 <i>mW</i>	Lorentzian $\Delta\nu_L = 1.72 \text{ MHz}$	Max. linewidth $\Delta\nu = 860 \text{ kHz}$	Voigt $\Delta\nu_V = 4.1 \text{ MHz}$ $\Delta\nu_L = 3.1 \text{ MHz}$ $\Delta\nu_G = 2.1 \text{ kHz}$	Max. linewidth $\Delta\nu = 2.9 \text{ MHz}$

Table 5.1: Summary of the main characteristics of the modules tested in the electric noise investigation

5.5.2.2 Linewidth re-broadening

The lasers of the 1st run of LAMA are characterized by a FWHM linewidth re-broadening with increasing current injection, in contradiction with the Schawlow-Townes-Henry theory. This is more precisely illustrated by graph (5.20) showing the 'intrinsic' SHE linewidth (the SHE experimental linewidth has been arbitrary divided by two) of two DFB lasers of each Cs line versus the output power.

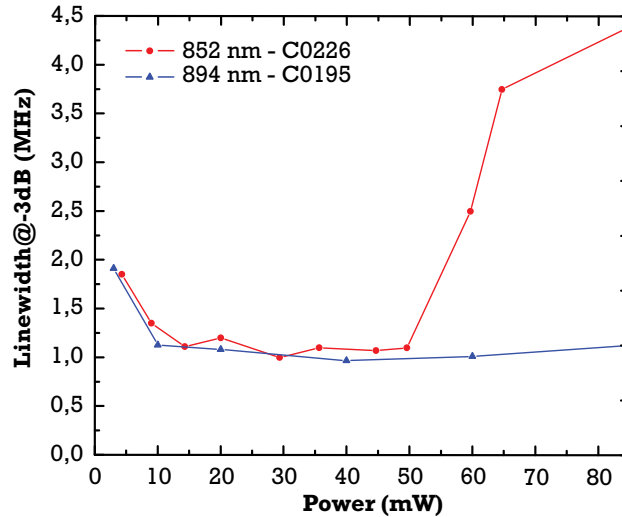


Figure 5.20: SHE linewidth divided by two versus the output power, for the laser C0226 (XXL2020, length of 1 *mm*) and for the laser C0195 (XXL2029, length of 2 *mm*)

Simply, we observe a stabilization and a net increase of the linewidth in both cases, especially for C0226. Further inspections on other lasers of different lengths show the same trends: the re-broadening is sharper for the device of the fabrication XXL2020. The phenomenon does not depend clearly on the device's length but changes from a device to another. Two main hypothesis can be put forward to explain it:

1. Longitudinal spatial-hole burning takes place with increasing optical power inside the cavity (see chapter 2): the experimental coupling factor κ being higher for XXL2020, the intensity profile in z is more inhomogeneous in the cavity, which leads to local carrier consumption and de-clamping and the loss of the single-mode behavior with no longitudinal mode competition
2. The devices instable lateral mode confinement in the ridge: if the guide is multimode, lateral carrier spreading and gain non-localization in the x -axis will cause a transverse mode competition with increasing current injection. In these conditions, the single-mode behavior cannot be stable. Feeding of the higher order modes creates first a linewidth floor (the current further injected does not create more stimulated photons of the main mode in the cavity), then a transfer of energy between the oscillations.

Hypothesis number 2 is more reasonable, all the more so since it has been observed in section [3.3.2.2] that the XXL2020 devices had lateral beam-steering precisely in the range where the linewidth re-broadens. Moreover, the coupling factor values to the grating are not that high to create a deep longitudinal spatial hole burning: this behavior is more commonly observed for output powers above 150 *mW* (but this is relative, one must take into account the mirror losses of the structure to evaluate

the power level inside the cavity). At this stage, we cannot conclude. The practical solution in the first case would be to have lower coupling factors at the expense of higher losses. Some exotic solutions (multiple phase-shift cavities or distributed coupling cavities [Okai 1991, Ghafouri-Shiraz 2004]) exist to reduce the field inhomogeneities of the cavity but it is rather complex to implement, especially for AR-HR DFB configurations. On the other side, the issue of lateral instabilities relies on the guiding parameters which have been extensively defined in chapter 3. Whatever the origin of the linewidth uncommon behavior, a technical solution must be found to avoid any detrimental effect in the atomic clock setup: even if the laser is used in the stable regime below the re-broadening, we can perfectly imagine that the non-linear behavior might be amplified with the laser aging, especially if it results from current injection. Frequency noise measurements will provide more insight into these mechanisms.

5.5.3 Frequency noise measurements by frequency discrimination

The frequency discrimination is a useful mean to recover the frequency fluctuations of the source, as it was discussed in section [5.4.3]. To remind the reader of the position of this technique in the summary of picture (5.11), the discriminator allows to recover the instantaneous frequency fluctuations \textcircled{C} $\tilde{\nu}(t) = \delta\nu(t)$ from amplitude fluctuations conversion and the numerical treatment computes the power of the Fourier transform, i.e. the PSD (it is simply the path $\textcircled{C} \rightarrow \textcircled{E}$).

To illustrate first this concept, the Michelson interferometer described in section [5.4.3] is used. The linewidth measurements have shown that the RMS frequency fluctuations up to a 1 Hz integration limit are on the order of $\Delta\nu \sim 1 \text{ MHz}$. For a delay of $L_d = 30 \text{ cm}$, $FSR_\nu = 54.1 \text{ MHz} \gg \Delta\nu$. Also, the temperature RMS fluctuations of the package can be estimated to $\Delta T = 1 \text{ mK}$ over 1 s which yields a frequency drift of $\Delta\nu_T = 25 \text{ MHz}$: the delay allows to keep the laser around the point of operation with comfort. On the other side, the voltage fluctuations are related to the frequency ones by $\Delta V = k_v \times \delta\nu = (Gv_0/FSR'_\nu) \times \Delta\nu$. The amplifier has a gain $G = 10^3$, the DC voltage (total amplitude of the interferometric oscillations, see figure (5.22)) is $v_0 \sim 1 \text{ V}$ so $\Delta V \sim 0.1 \text{ V}$ which is three decades above the detection floor. Thus, the delay chosen is a good compromise between sensitivity and stability of the operation point. The last point to check is linked to the conversion of the laser intrinsic amplitude noise by the optical setup. Thanks to the previous section, we know that the RIN white noise is on the order of $5 \times 10^{-16} \text{ Hz}^{-1}$ so the associated PSD of 'artifact' frequency noise is, after (5.30), $S_{art} = RIN \times FSR'_\nu{}^2 = 1.5 \text{ Hz}$. Such level is completely negligible in front of the intrinsic white noise floor ($\sim 10^5 \text{ Hz}^2 \cdot \text{Hz}^{-1}$).

Picture (5.21) shows the interferometer. The part situated after the coupler is very sensitive to external perturbations (fiber twisting or vibrations): the bench is placed on an isolating cork and covered by a wooden box. When the setup is operational, the signal of the Michelson can be tracked in the time domain with an oscilloscope. It is this signal that is Fourier transformed with the fft-scope. The conversion factor to calibrate the PSD requires the knowledge of v_0 and the value of the FSR. The first parameter is measured by the maximum voltage amplitude excursion of the Michelson. The second can be determined either theoretically with the exact knowledge of the delay (exact L_d and refractive index of the fiber) or one can fit the interferometer response to a current ramp in the laser, with a precise knowledge of the pulling coefficient $\delta\nu/\delta I$.

★ Device C0314 (852 nm)

The first result of frequency noise discrimination is shown in figure (5.23) which presents cali-

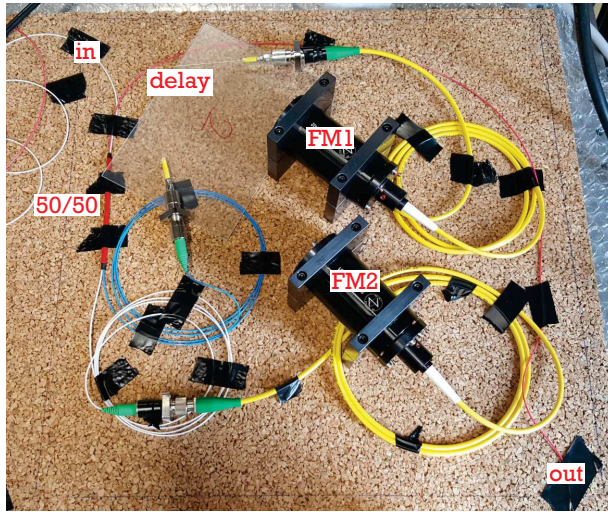


Figure 5.21: Picture of the Michelson interferometer

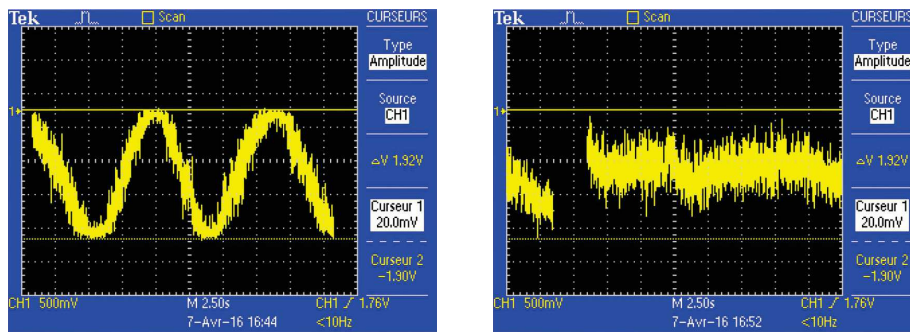


Figure 5.22: Michelson signal visualized with an oscilloscope. Left: constant drift of the laser frequency that draws the transfer function of the setup. Right: stabilization at the operation point where the conversion is linear. The signal total amplitude gives the v_0 parameter

brated $S_{\delta\nu}$ curves for the device C0314 at several output powers. As for the RIN in figure (5.15), the white noise floor and the flicker $1/f$ stand out clearly. The first level decreases steadily with the optical power, while the second varies over one decade, with no clear relationship with the power. This is highlighted more precisely in figure (5.24) where both types of noise are plotted against a function of the output power P_{out} .

As for the white noise, a linear trend with the inverse of the power is noticed. The fit parameters gives $S_0 = (2.3 \times 10^6 \text{ Hz.mW})P_{out}^{-1} - 11.8 \times 10^3 \text{ Hz}$. The negative ordinate is non-physical and due to the uncertainty of the fit: removing one or two points gives a positive ordinate of same magnitude. Thus, we can infer that **the white noise is proportional to the inverse of P_{out} , as described by the Schawlow-Townes-Henry limit**, except at low power above threshold, where the laser is not exactly in this regime (single mode behavior with high SMSR is not reached), but also above 50 mW, where an abrupt re-broadening is measured. Similar behavior was observed for the RIN, along with the noise instability in the region of 29 mW, where no mode hop was observed though. We should however be careful with the data at high power: in this range, the white noise is low and barely readable between the $1/f$ trend and the excess noise at the amplifier cutoff. On the other hand,

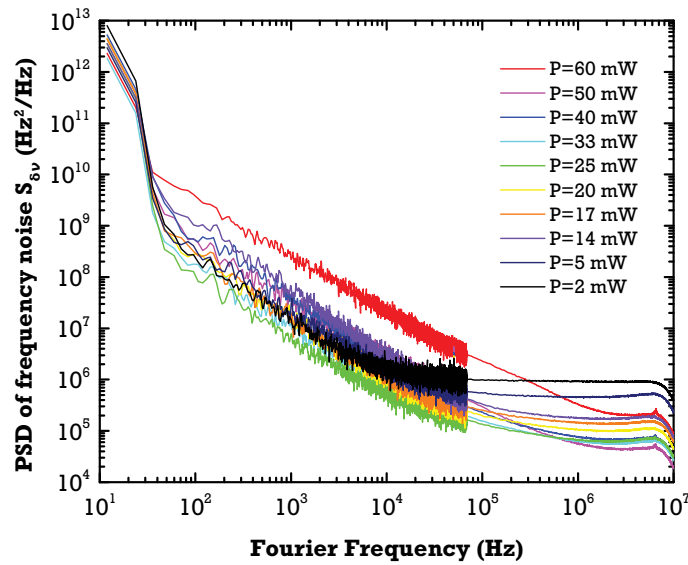


Figure 5.23: Frequency noise from Michelson at different output powers of device C0314

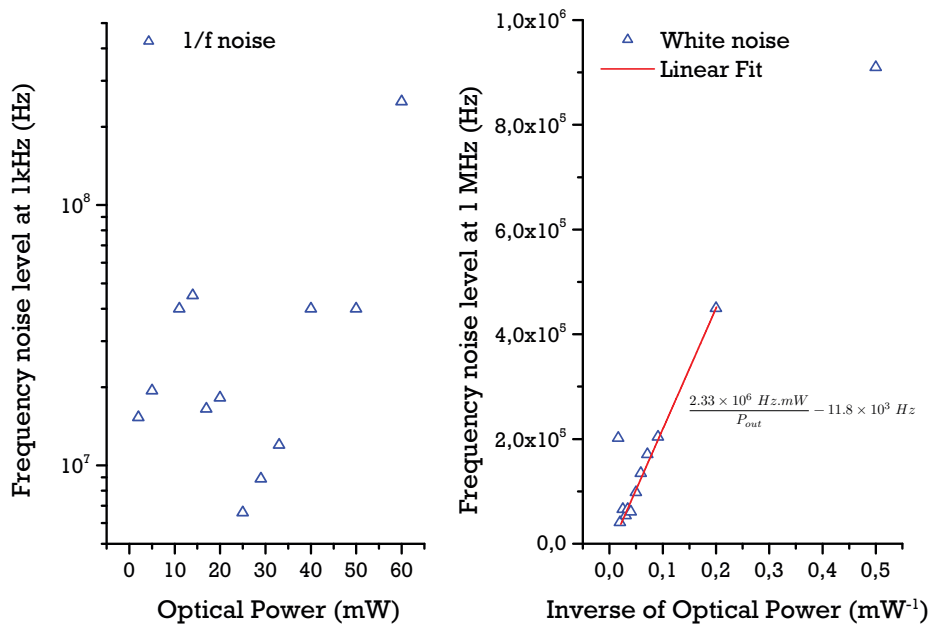


Figure 5.24: Frequency noise levels from Michelson at different output powers of device C0314. Right: White noise levels taken at 1 MHz as a function of P_{out}^{-1} . Between 5 mW and 50 mW, the fit is linear, with a slope of $2.3 \times 10^6 \text{ Hz}\cdot\text{mW}$. Left: Flicker 1/f noise levels taken at 1 kHz as a function of P_{out}

the flicker noise decreases and is strongly enhanced for some values of the power (up to 38 times!). This may be correlated to the white noise floor instabilities.

★ Device C0195 & C0294 (894 nm)

The same data as above is reproduced for device C0195 (XXL2029, $L = 2 \text{ mm}$, TO3 package) and C0294 (XXL2029, $L = 1.5 \text{ mm}$, TO3 package).

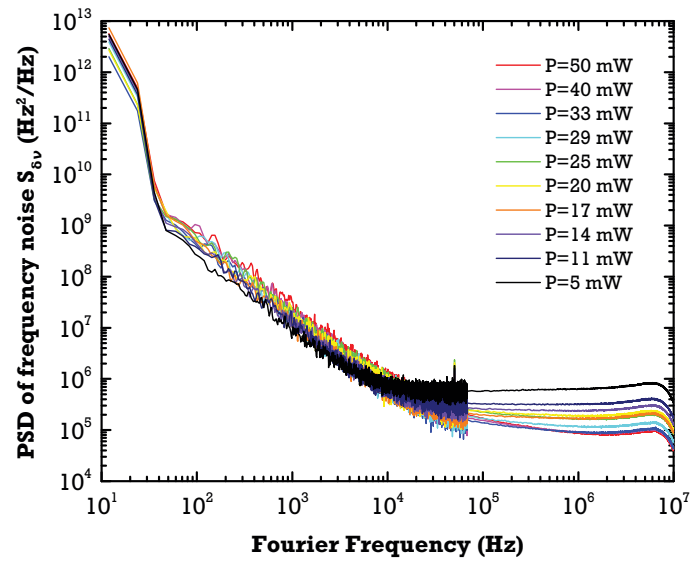


Figure 5.25: Frequency noise from Michelson at different output powers of device C0195

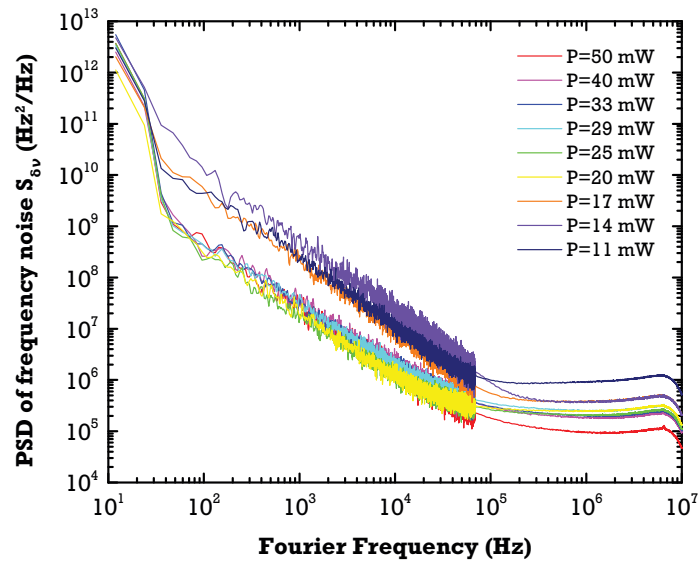


Figure 5.26: Frequency noise from Michelson at different output powers of device C0294

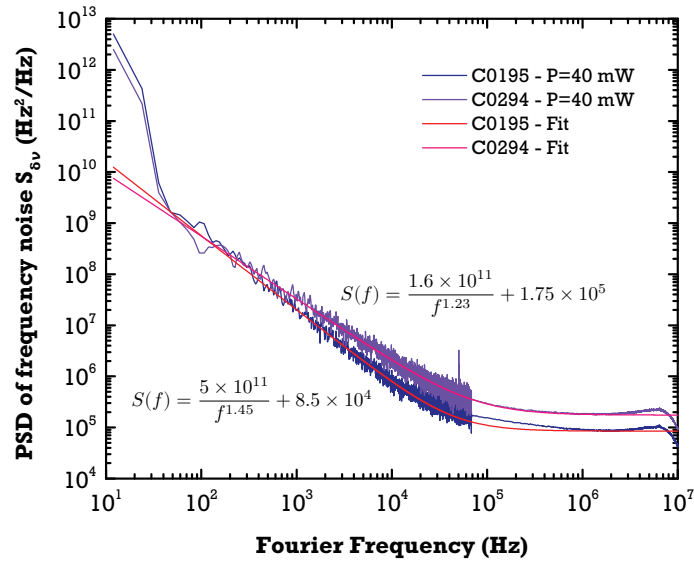


Figure 5.27: Frequency noise PSD of device C0195 and C0294 at $P_{out} = 40 \text{ mW}$. The fit give respectively $S_{\delta\nu}(f) = 5 \times 10^{11} \cdot f^{-1.45} + 8.5 \times 10^4$ and $S_{\delta\nu}(f) = 1.6 \times 10^{11} \cdot f^{-1.23} + 1.8 \times 10^5$

Similarly as for C0314, a decrease in the white noise floor is observed in C0195 with increasing injection, the flicker noise magnitude being more stable, with a slight increase with the current. The 1.5 mm laser C0294 has a more exotic behavior: two distinct flicker slopes are visible in the 11–17 mW range and above, for 20–50 mW. If we compare now the two lasers (figure (5.27)) at 40 mW, a simple fit reveals that **the white noise (S-T-H) limit is lower for the longest laser**: this was expected since then the DFB resonator losses α_r are lower. The power coefficient α of the $1/f^\alpha$ is far from being equal to one in both cases.

5.5.4 Conclusion

With the measurements done so far, a good picture of the coherence properties of the lasers has already been depicted. In particular, the lasers of the 1st run seem to fulfill the specifications of the end user, with a linewidth $\sim 1 \text{ MHz}$. Though, some ambiguity remains on how the real observation time of the frequency fluctuations is linked to this figure.

5.6 New metrology: Beat-note investigation by digital acquisition

This section is based extensively on the work described in [von Bandel 2016b]. The traditional use of a frequency discriminator is compared to a pure numerical treatment of a laser beat-note to recover the PSD of the frequency noise as well as the true time-dependent linewidth. To begin with, let go back to the heterodyne setup which realize the beat between two (ideally) identical lasers (5.28). Thanks to the use of time-sampling and numerical analysis of the signal, the relations reminded in (5.11) can be exploited in practice to recover the frequency noise with a simpler (and absolute) method compared to the standard metrology, and also the time-dependent intrinsic linewidth. There are two objectives in this section: first, to validate the metrology since it is a new one, then to apply the technique to the lasers of the LAMA project.

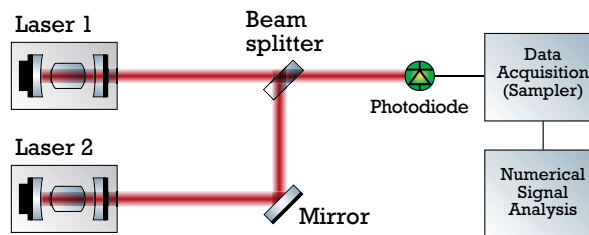


Figure 5.28: Upgraded heterodyne setup. The beams of two laser cavities are superimposed thanks to a beam-splitter/recombiner and the resulting radiation is sent on a photodiode which photo-current is sampled in the time-domain and analyzed by numerical means

5.6.1 Beat-note demodulation versus frequency discrimination: a comparison

The other way to retrieve the frequency noise information, without using any frequency discrimination, is described again in figure (5.11). If we start from a laser beat-note, the lasers phase noises that affect the sinusoidal RF carrier can be retrieved mathematically by applying a Hilbert transform \mathcal{H} in path (A)→(D), using MATLAB[®] for instance [von Bandel 2016b]. Then, the frequency noise PSD results from an integration and a Fourier transform (D)→(C)→(E). With such a demodulation process, if the lasers are similar, the resulting PSD has twice the magnitude of a single-laser because of the summation of the PSD of independent noise sources.

In practice, the beat is realized according with the high-quality digital sampling. For a record over 1 s of a carrier at 50 – 100 MHz, the sampling frequency is at least $f_s = 100 - 200 \text{ MS.s}^{-1}$ to meet the Shanon criterion, so the memory needed on the board (Agilent U1084A-001) is at least 200 MS. Of course, the detector/amplifier cutoff frequency must be adapted to this RF domain (a 3 GHz photodiode coupled to a MiniCircuit[™] ZFL-1000LN+ of gain 10^3 is used). The beat frequency is tracked on an ESA to check that it does not drift too much (figure (5.29)).

To test this procedure, a beat is realized with the module C0195 and with C0171, an equivalent laser of same length and same characteristics (ridge width for instance) as the first one. The result is shown in figure (5.30). The PSD of frequency noise given by signal processing is very close to the total noise for the two lasers recorded with the Michelson setup. However, because **the demodulation does not require any calibration process, it can be considered as an absolute measurement**. The little discrepancy between the two methods can then be attributed to a miscalibration of the Michelson which is about 16% on the frequency conversion coefficient for this specific point. Figure (5.31) gives

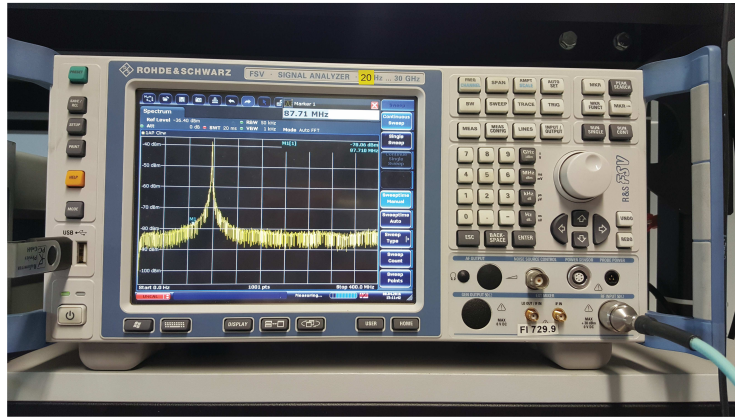


Figure 5.29: Two-lasers beat-note stabilization at 87 MHz visualized with a classical ESA

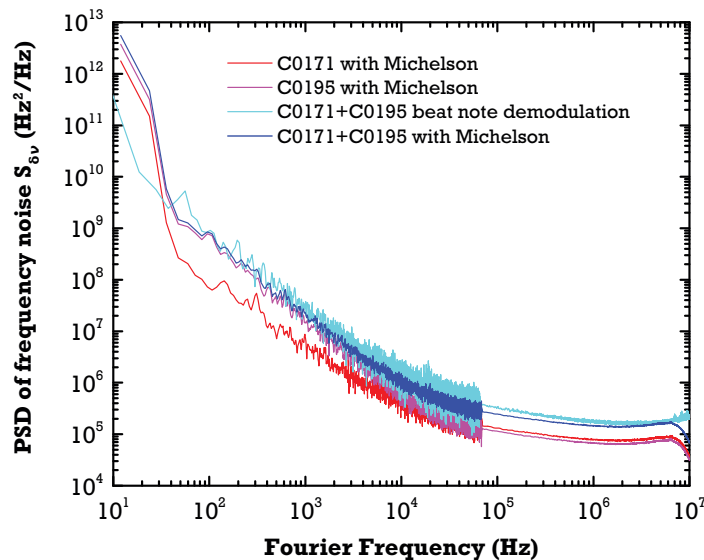


Figure 5.30: Beat note demodulation versus direct frequency noise measurement for modules C0195 and C0171. After [von Bandel 2016b]

the flicker level and white noise level comparison between the two methods after recalibration of the data acquired with frequency discrimination, for several levels of power. Again, the agreement is satisfying, showing that, beyond a global scaling factor, the physical trend is identical in both cases.

In [von Bandel 2016b], we also demonstrate that this method can be used on virtually any type of laser source. If a laser beats with another one which noise level is far lower (a fiber laser for instance), the demodulation gives directly the frequency noise of the first source. Regarding the sensitivity of the demodulation, the limits are set by the acquisition card jitter clock noise and the background amplitude noise (laser RIN, amplifier, card jitter...) but at high Fourier frequencies only. In the typical setup used, **frequency noise levels down to $1 \text{ Hz}^2 \cdot \text{Hz}^{-1}$ can be measured over a 100 kHz Fourier span.**

Finally, we can add that the results presented here are in fair agreement with what was investigated by our colleagues of LTF-UniNe during the LAMA project, with a cesium-based frequency discrimination [von Bandel 2016a, Matthey 2016].

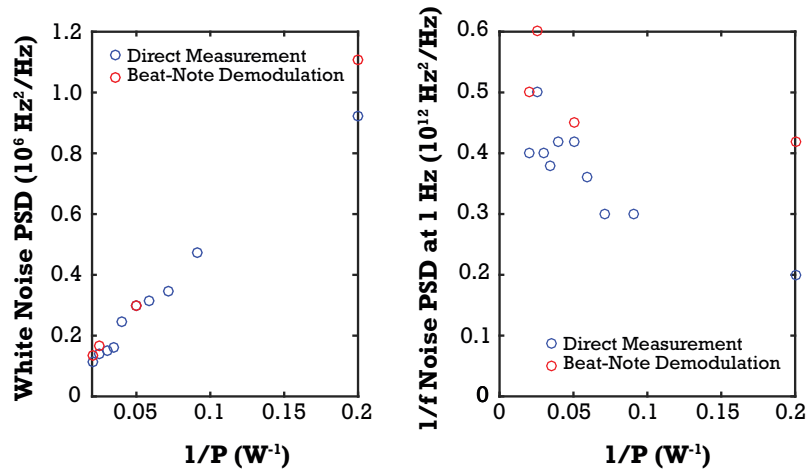


Figure 5.31: White noise level (left) and flicker noise at 1 Hz as a function of the inverse of the optical power, as given by the beat-note demodulation of C0195 and C0171

5.6.2 Time-dependency of laser linewidth: final outcome

Section [5.3] was mainly devoted to show the limits of the standard metrology to recover the accurate intrinsic laser linewidth for a source affected by arbitrary noises. Nor the self-heterodyne setup, nor a direct integration in the frequency domain are able to render properly the time-dependency of this parameter. In the frame of the description (5.11), this issue can be solved. Indeed, the path $\textcircled{A} \rightarrow \textcircled{B}$ can be exploited advantageously (figure (5.32)): If a beat-note $b(t)$ (that codes for the phase information

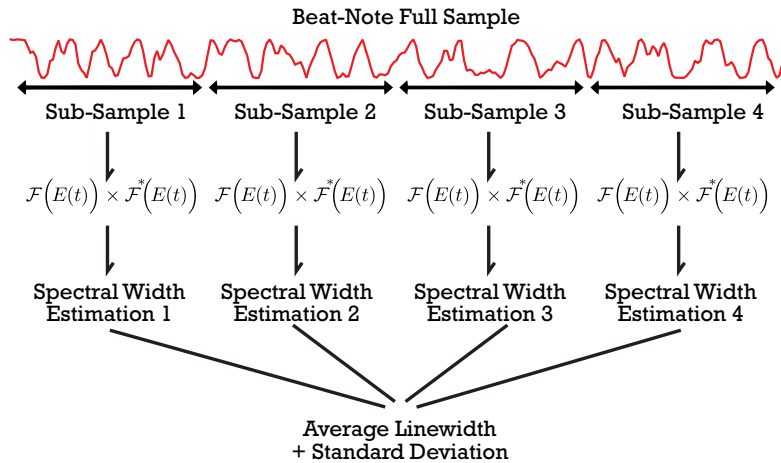


Figure 5.32: Procedure of time-dependent heterodyne linewidth estimation

of the two lasers) is acquired on a length Δt_i , it can be subdivided in $N = t/\Delta t_i$ sub-samples on which the Fourier transform \mathcal{F} can be applied. By definition, the exact heterodyne lineshape is recovered each time, on the observation time Δt_i :

$$\mathcal{L}_{\Delta T_i}(f) = \mathcal{F}(b_{\Delta T_i}(t)) \times \mathcal{F}^*(b_{\Delta T_i}(t)) \quad (5.33)$$

Moreover, the FWHM linewidth can be estimated by a proper fit, and a statistical average $\overline{\Delta\nu_{\Delta T_i}}$ and standard deviation computed over the sub-samples population. To identify the Lorentzian and

Gaussian components of the linewidth, a robust and efficient algorithm is used [McLean 1994]. To make this analysis practical, a GNU MATLAB[®] interfaced script has been implemented (figure (5.33)). The program is available under free BSD license [Myara 2016].

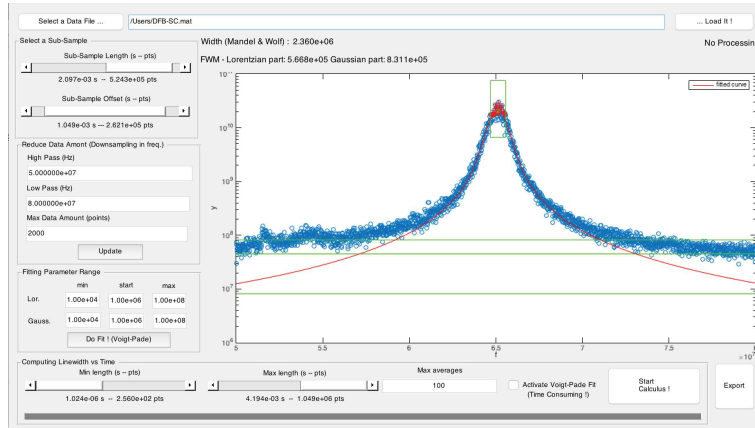


Figure 5.33: Interface of the LinewidthExplorerGUI allowing the time-dependent computation of the linewidth. Here, a snapshot of the lineshape of the C0195-C0171 beat-note is shown for $\Delta T_i = 2.1 \text{ ms}$

The beat-note of the module C0195 and C0171 has been analyzed with this method. Figure (5.34) shows the linewidth as a function of the observation time, for $P_{out} = 40 \text{ mW}$, in four different cases: a Voigt fit and FWHM of the beat-note, the Lorentzian and the Gaussian linewidths associated and a new definition, $\Delta\nu_c$ which meaning is explained below. We can notice that the data treatment renders the physical limitation of the linewidth: below $10 \mu\text{s}$, the Fourier limit appears and set a lower value to the quantity. We also find again that the Lorentzian component is rather independent of the observation time, while the Gaussian one increases, and so is the total Voigt linewidth. The value is of about 2 MHz at $\Delta T_i = 1 \text{ ms}$.

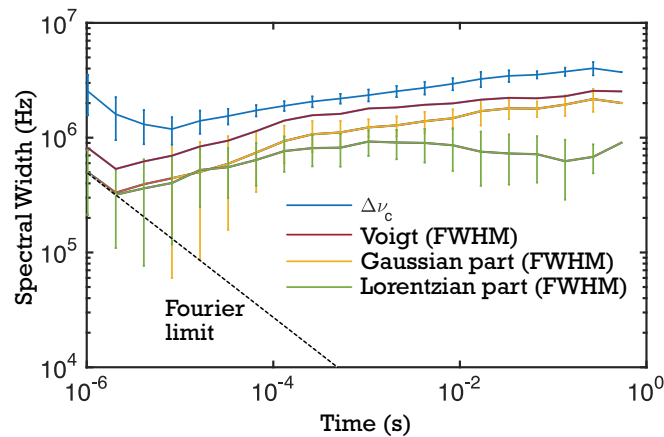


Figure 5.34: Interface of LinewidthExplorerGUI showing the time-dependent ($\Delta T_i = 2.1 \text{ ms}$) linewidth of the C0195-C0171 beat-note

★ *A universal criterion for the spectral width of laser lines ?*

The relevance of the FWHM criterion to give a single figure that characterizes the spectral broadening of a source has not been called into question up to now. This definition is practical because it can be easily estimated at first sight by visual inspection of the lineshape on the ESA screen in the traditional metrology. However, it is far from being an universally relevant definition on a physical aspect: the Gaussian and Lorentzian FWHM are not equivalent, simply because it does not encompass the same spectral energy in each case (although some people are willing to compare one laser to another with such parameters). Also, some cases where the source is affected by mechanical noise show that this definition cannot stand anymore: for these lineshapes, we found a 'top-hat' profile for which it is very difficult to use the FWHM (figure (5.35)).

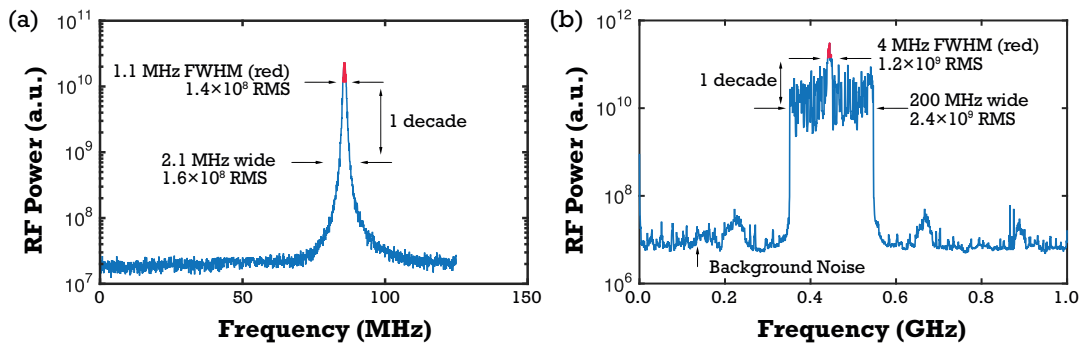


Figure 5.35: Relevance (a) and irrelevance (b) of the FWHM depending on the spectral shape. a) case of a semiconductor DFB: the width and the associated RMS value do not change too much over one decade of magnitude. b) case of an ECDL: the width and associated RMS value change dramatically in the same conditions. After [von Bandel 2016b]

Still, higher order statistical moments could be used, like the variance, the kurtosis... Unfortunately, none of these parameters exist for a Cauchy-Lorentz distribution, which is always found with white noise. Thus, after the work of L. Mandel and E. Wolf [Mandel 1995] and B. E. Saleh [Saleh 1991], a spectral width derived from the coherence time definition is worth to study:

$$\Delta\nu_c = \Delta\nu_{\Delta T_i} = \frac{\left(\int_0^{+\infty} \mathcal{L}_{\Delta T_i}(f) df\right)^2}{\int_0^{+\infty} \mathcal{L}_{\Delta T_i}^2(f) df} \quad (5.34)$$

In this quantity, the denominator strengthens the spectrum magnitude variations with $\mathcal{L}_{\Delta T_i}^2$ while the numerator is simply the square of the total energy. The ratio is then related to a measure of the concentration of this energy. We believe that this definition has many advantages. First, **it is based on the fundamental definition of the coherence time**. Also, **all the points of the spectrum are taken into account in the linewidth estimation**, which is not the case for the FWHM. Put in another way, $\Delta\nu_c$ gives a physical quantification to the width of a source, while the FWHM is more a simple engineer tool, which, in some cases, cannot be used. A practical consequence of the above definition is that the linewidth is way **easier to compute numerically** (an integral summation is always more comfortable than finding a proper fit of statistical data) and it is closely linked to the traditional linewidth for usual noises (it is shown in [von Bandel 2016b] that $\Delta\nu_c = \Delta\nu_{FWHM}/\pi$ for white noise for instance). In the case of the semiconductor lasers beat-note of (5.34), $\Delta\nu_c$ is almost

twice the FWHM. We have seen that a single laser source has a FWHM close to 1 MHz so the new definition gives twice the energy for such lasers for the beat, which is satisfactory.

★ *Time-domain signal processing vs. β -line approach*

It is interesting to compare the linewidth derivation as described above to the β -line theory of section [5.4.4]. Figure (5.36)(a) gives the PSD of frequency noise from demodulation of three types of beat-notes: modules C0195+C0171, a commercial (noisy) tunable ECDL at $1.55\ \mu\text{m}$ and a home-made fiber laser at $1.55\ \mu\text{m}$ pumped by a $980\ \text{nm}$ DFB laser ('DFB-FL'), and finally two fiber lasers of the previous kind. The variety of the noise and PSD magnitude recorded shows that it is a powerful technique: no calibration has been made to adjust the setup to the nature of the source. Because the DFB-FL noise is very low compared to the ECDL, we can consider that it is directly its frequency noise that is recorded. Figure (5.36)(b) gives the spectral width of the ECDL and of the two DFB

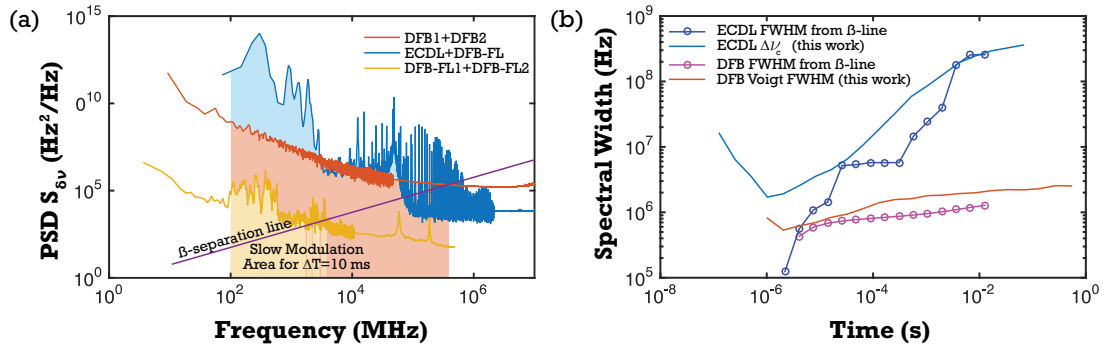


Figure 5.36: (a) β -separation line illustration on three types of laser beat-notes. The shaded area below the curves delimits the upper observation time $\Delta T = 10\text{ ms}$ and the crossing with the β -line. (b) Time-dependent linewidth computed thanks to the numerical methods proposed here, compared to the β -separation line approach. After [von Bandel 2016b]

lasers at $894\ \text{nm}$. For the first one $\Delta\nu_c$ is used, for the reasons explained previously. On the other hand, the FWHM of the Voigt profile is taken for the DFBs. These linewidths are compared to the result of the β -line theory. What we see first is that the β -line does not take into account the Fourier limit, which was expected. Second, for the ECDL, the two methods can be compared directly above $1\ \text{ms}$ where the lineshape is close to a top-hat. It results that the β -line underestimates by a factor five the linewidth, which finally reaches $\Delta\nu_c$ abruptly, when the mechanical peaks are integrated. For the DFBs, we notice that the FWHM also underestimates by a factor two the spectral width. This time, it is the $1/f$ noise that is not fully taken into account at low frequencies.

5.6.3 Intrinsic linewidth through experimentation

The final concept which is fruitful to develop is the intrinsic linewidth, which was already described in [5.3.1]. Because we have now access to the time-domain phase noise, it is easy to recover this fundamental lineshape. For that, we inject the frequency fluctuations $\delta\nu(t)$ in a virtual carrier b (a pure sine wave that mimics the beat-note carrier) and apply naturally the definition (5.11) (equivalent to follow the path $\textcircled{C} \rightarrow \textcircled{A} \rightarrow \textcircled{B}$ in (5.11)):

$$\mathcal{L}(f) = \mathcal{F}(\Gamma_b(\tau)) = \mathcal{F}^*(b(t)) \times \mathcal{F}(b(t)) \quad (5.35)$$

Again, for computation efficiency, it is the Fourier transform that is evaluated. The fluctuations can be retrieved by frequency discrimination. The result is shown in figure (5.37) for the laser module C0195, with the data of the Michelson interferometer. With decreasing observation time,

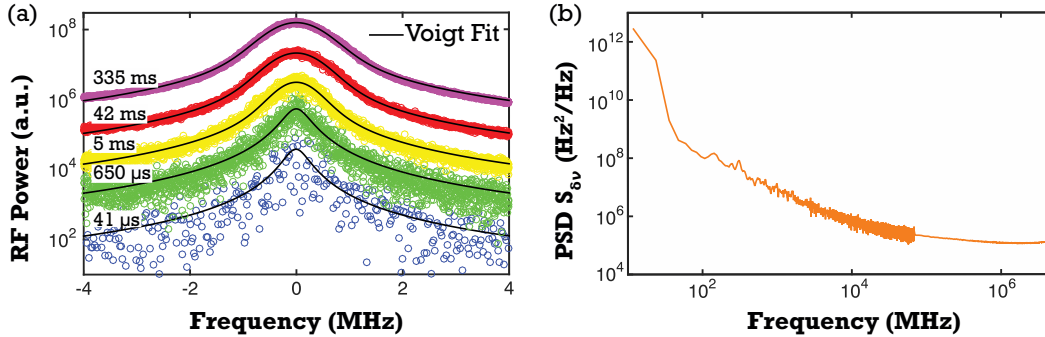


Figure 5.37: (a) Intrinsic linewidth computed from time-domain frequency noise signal using a 'virtual' carrier. (b) Frequency noise spectrum computed from the time-domain frequency noise signal. After [von Bandel 2016b]

less points are present in the spectrum and the statistical uncertainty increases (we are getting closer to the Fourier limit). For $\Delta T = 3 \text{ ms} \Leftrightarrow f_{obs} = 333 \text{ Hz}$, we find $\Delta\nu_c = 1.5 \pm 0.275 \text{ MHz}$. For the FWHM, $\Delta\nu_{FWHM} = 1,05 \text{ MHz}$. The related Lorentzian and Gaussian parts are respectively $\Delta\nu_{FWHM,L} = 218 \pm 126 \text{ kHz}$ and $\Delta\nu_{FWHM,G} = 826 \pm 346 \text{ kHz}$.

It is interesting here to underline that **the above procedure allows to recover the true intrinsic linewidth by experimental means**. Moreover, with the use of the 'coherence' intrinsic linewidth, a more fundamental picture of the noise is available, compared to the FWHM.

5.6.4 Advantages and drawbacks of this metrology

The relative merits and limits of this metrology are discussed in [von Bandel 2016b] [6.6], the aim here being first to characterize lasers in noise.

5.7 Spectral properties under feedback

In section [3.1.5] of chapter 3, we have investigated theoretically the influence of unwanted feedback reflections on the linewidth of monolithic DFB lasers. Here, we intend to present a few experimental results of measurements of the PSD of frequency noise in this configuration. This is especially important for the atomic clock setup configuration with no optical isolator. The traditional metrology have been used, for simplicity purposes (but we could have realized the beat-note of two lasers, with one perturbed by feedback, to make this study: it is less appropriate though to interpret the results without any ambiguity). The setup is presented in figure (5.38). Right after the laser module, a cube beam splitter (BS) divides the beam in two paths: one is reflected approximately by 90° and reaches a system of polarizer/analyzer ($\lambda/2$ plate) to tune precisely the beam attenuation, and a further movable mirror (with $\sim nm$ sensitivity) generates the optical feedback, so that the beam will follow back the preceding path and return to the laser cavity. On the opposite side, a power-meter is used to measure precisely the power re-injected. On the second path, the light going straight from the laser crosses the isolator, a neutral density (ND) filter and is injected in the Michelson that was previously

used for frequency noise measurements. The overall external feedback cavity has a physical length of $L_e = 60 \text{ cm}$. It is important to tilt the beam-splitter to avoid additional back-reflections in the optical element that would not be controlled by the operator.

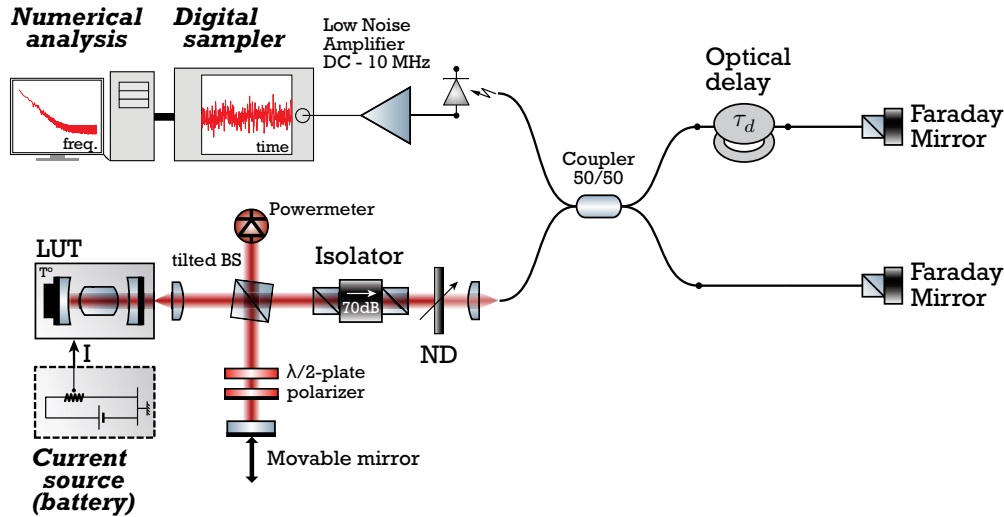


Figure 5.38: Setup for feedback investigation. The output of a laser module perturbed by controlled feedback reflections is analyzed in the Michelson interferometer

★ Device C0314 (852 nm)

A first illustration of the effects of optical feedback is given in figure (5.39) where the module C0314 (852 nm) is perturbed by various amount of back-reflections power (rate of feedback f_{FB} as defined in chapter 3). Experimentally, it is hard to ensure a perfect injection of the light in the facet of the laser. First, the laser is set to the current that gives 20 mW of output power. The procedure is then to adjust the returning beam trajectory to induce maximum variation of the power: indeed, we have seen that the feedback leads to a change in the effective photon lifetime, implying a change in the laser threshold (of a few percents). We first observe, for low feedback rates ($< -22 \text{ dB}$) that the white noise level decreases steadily with increasing back-injection in the cavity, with an insensitivity to the feedback phase (when the mirror is translated over a distance below the wavelength). With no feedback, $S_0 = 10^5 \text{ Hz}$, which decreases down to $S_0 = 2 \times 10^3 \text{ Hz}$ (factor of 50). Also, the $1/f$ level is also dramatically affected: from $S_{-1} = 8.6 \times 10^3 \text{ Hz}$ to $S_{-1} = 2 \times 10^6 \text{ Hz}$ at 3 kHz (factor of 230!). In the meantime, the laser becomes noisier in the $10^2 - 10^3 \text{ Hz}$ range. These peaks are due to the mechanical vibration of the external cavity (reflecting mirror for instance) which induces a Doppler shift in the light that is re-injected, and a beat inside the cavity which frequency is precisely in the range where the perturbations in the spectrum arise.

Now, for $f_{FB} > -22 \text{ dB}$, the white noise floor regrows of almost one order of magnitude. At this stage, another regime is observed: the spectrum becomes completely flat (with no $1/f$ noise) on the whole spectrum. We have actually reached **the coherent collapse regime, where the source has lost its fine coherence properties**. The linewidth is extremely broad (several GHz) so that the coherence time of the laser is shorter than the coherence time of the interferometer $\tau_c < \tau_d$. The setup works in the over-coherent regime, that is, can be assimilated to a self-homodyne configuration. What is observed is the top of the SHO lineshape, which seems 'flat' given the order of magnitude

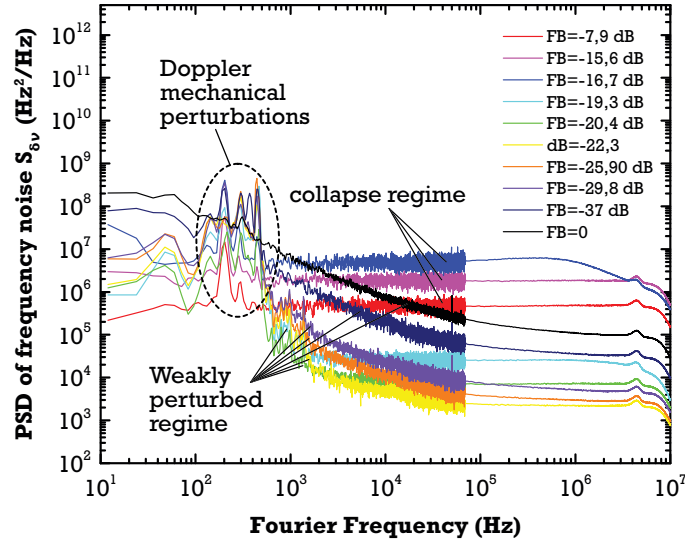


Figure 5.39: PSD of frequency noise of device C0314 as a function of the Fourier frequency for various feedback ratios f_{FB}

of the linewidth. The transition from a coherent to an incoherent regime is an interesting point of reference for the study.

★ EagleYard device at 852 nm

To make some qualitative comparisons, the EYL device at 852 nm which was already studied in chapter 4 in the frame of the electronic noise has been tested under the same conditions. First, a classical frequency noise study as a function of the output power is shown in figure (5.40). We can notice that the white noise level is way higher than for C0314 (for e.g. $S_0 = 2.5 \times 10^6 \text{ Hz}$ at $P_{out} = 40 \text{ mW}$, which gives a minimum linewidth of $2.5 \times 10^6 \times \pi = 7.9 \text{ MHz}$ at this level). On the other hand, the $1/f$ level is lower ($S_{-1} = 2.8 \times 10^6 \text{ Hz}$ at $P_{out} = 40 \text{ mW}$ and $f = 1 \text{ kHz}$ versus $S_{-1} = 7 \times 10^7 \text{ Hz}$ for C0314). At lower frequencies, huge peaks of noise stands out in the range of the mechanical frequencies. The origin of this behavior is unknown.

In the feedback regime, we obtain the result (5.41) for a fixed $P_{out} = 20 \text{ mW}$. Again, below $f_{FB} \sim -22 \text{ dB}$, the laser is still coherent and we observe a decrease in the white noise floor, but in a lower extent compared to the module C0314. At low frequencies, the flicker is also affected. As for the peaks of noise, it is hard to draw any conclusion, though it seems that the re-injection changes the PSD dynamics in this region. The mechanical vibrations are probably seen at $f = 200 \text{ Hz}$, just as for C0314. At higher rate of feedback, the PSD is flat which tells that the coherent collapse regime is reached.

It is worth to do the same measurements for $P_{out} = 150 \text{ mW}$ (which is not possible for C0314 because it loses its single mode properties at this level of power). In figure (5.42), we notice that there is no clear predictable behavior of the white floor, which magnitudes changes randomly with the level of feedback, probably with the phase of the perturbation. Interestingly, no coherent collapse regime is observed on a large range of feedback rate. But another impressive phenomenon occurs: for $f_{FB} \in [-28, -18] \text{ dB}$, the laser switches abruptly and unexpectedly from a coherent regime to a very noisy one, with a deep resonance at high frequencies. This behavior can be said to be chaotic: a slight perturbation in this regime makes the laser mode behavior unpredictable. For instance, we

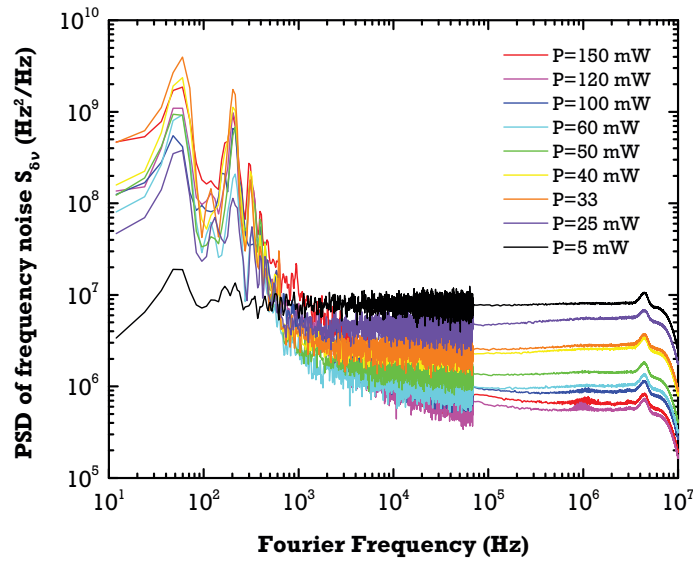


Figure 5.40: Frequency noise PSD of the EYL device as a function of the Fourier frequency for various output power levels ($f_{FB} = 0$)

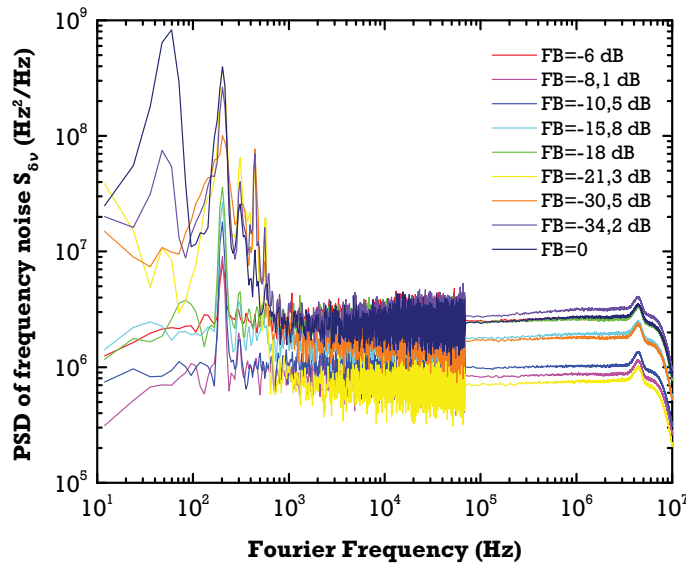


Figure 5.41: Frequency noise PSD of the EYL as a function of the Fourier frequency for various feedback ratios f_{FB} for a fixed $P_{out} = 20 \text{ mW}$

see an enhancement of the white noise at $f = 1.25 \text{ MHz}$ which reflects the characteristic time of the dynamics.

As a conclusion, we have indeed verified that for the same operation conditions ($P_{out} = 20 \text{ mW}$), **the III-V Lab laser C0314 is 4-times more resistant** to feedback than the EYL laser, if the transition from coherent (single mode) to incoherent (collapse) is considered. When the power of operation increases, the EYL laser does not show the transition, but the operation point is unstable: multiple modes are observed with the optical spectrum analyzer. On the overall, it is hard to make quantitative conclusions with such a rough study. On a qualitative point of view, we can put forward

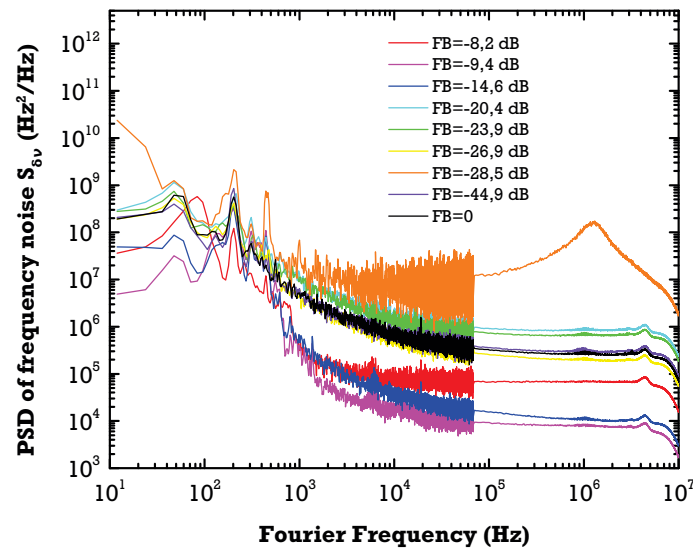


Figure 5.42: PSD of frequency noise of the EYL device as a function of the Fourier frequency for various feedback ratios f_{FB} for a fixed $P_{out} = 150 \text{ mW}$

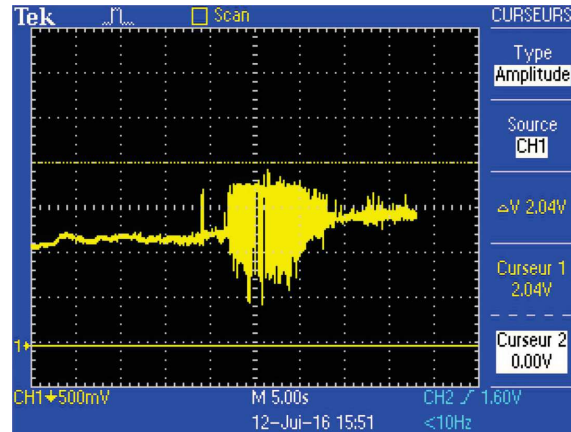


Figure 5.43: Example of the time-domain signal of the Michelson switching spontaneously to a chaotic behavior

that parasitic feedback induces low frequency perturbation peaks that can lead easily to a de-locking of a servo loop, if it is not designed to absorb these huge fluctuations of the source. Less pronounced in the case of the III-V Lab laser, this may be the reason why our laser has shown better behavior in an OCFS up to now.

5.8 Discussion and conclusion on the noise of the fabricated lasers

5.8.1 Schawlow-Townes-Henry limit

According to chapter 3–(3.39), the Schawlow-Townes-Henry linewidth times the output power for an (ideal) DFB laser is given by:

$$\Delta\nu_{S-T-H} \times P_{out} = K_P n_{sp} h\nu \frac{\Gamma v_g^2 \alpha_r g_{th}}{4\pi} (1 + \alpha_H^2) \quad (5.36)$$

We can test experimentally this limit with the results of frequency noise in the high frequency range by fitting the white noise level as a function of P_{out} : $S_0 \times P_{out} = \Delta\nu_{S-T-H}/\pi \times P_{out}$. For instance, with the results on the white noise of the beat-note of figure (5.31) we get $S_0 \times P_{out} = 5.4 \pm 0.2 \text{ MHz.mW}$, so approximately half of this value for a single laser of XXL2029 with $L = 2 \text{ mm}$. On the other hand, if we set $K_P n_{sp} = 1.72 \times 1.4$ for $\kappa L = 5 \text{ cm}^{-1} \times 0.2 \text{ cm} = 1$, $h\nu = 1.386 \text{ eV}$, $v_g = c/n_g$ with $n_g = 3.7$, $g_{th} = \alpha_r + \alpha_i + \alpha_s = 7 + 2 + 1 \text{ cm}^{-1}$ and $\alpha_H = 3.5$, the theory yields $\Delta\nu_{S-T-H}/\pi \times P_{out} = 0.81 \text{ MHz.mW}$. This latter value is at least three times more optimistic than the experimental measure. This is also the case for the other lasers. If we perform the same calculus for the module C0314 with the data of figure (5.24), it gives $K_P n_{sp} = 1.4 \times 1.4$ for $\kappa L = 9.5 \text{ cm}^{-1} \times 0.15 \text{ cm} = 1.4$, $h\nu = 1.422 \text{ eV}$, $v_g = c/n_g$ with $n_g = 3.7$, $g_{th} = \alpha_r + \alpha_i + \alpha_s = 4.7 + 2.5 + 1.5 \text{ cm}^{-1}$ and $\alpha_H = 3.5$, the theory yields $\Delta\nu_{S-T-H}/\pi \times P_{out} = 0.4 \text{ MHz.mW}$ versus the fit $S_0 \times P_{out} = 2.33 \pm 0.1 \text{ MHz.mW}$. Again, the theory is six times too optimistic.

These conclusions can be put into perspective of the little knowledge we have on the true laser parameters. For instance, Petermann's factor is probably enhanced because of lasing operation in a mode where it has a broader value. Also, there may be a transverse component K_{tr} arising from the gain guiding properties of the cavities of the 1st run where index guiding is weak. As for the resonator losses, given the random phase of the grating at the AR facet, the real value can depart from the mean that as been used in the calculus, as it was shown in table (3.10) of chapter 3. Regarding Henry's factor, a 'standard' value has been used because no direct experimental measure has been made. In reality, it is highly probable that it is **an effective value taking into account the lateral gain inhomogeneity in the ridge waveguide**. All in all, it is difficult to predict (with high accuracy) the linewidth in complex cavities like in the Distributed-Feedback design.

5.8.2 Frequency noise coupling to the 1/f source: a few hypothesis

If it is clear that the 1/f noise source arising from the electronic transport in the laser induces a 1/f perturbation on both the RIN and the PSD of frequency noise, no mechanism of this perturbation generation has been put forward. This is what we intend to do here but first, it is useful to remind the causality relationships between the various types of fluctuations found in the semiconductor lasers under study in figure (5.44).

A/ Direct perturbation of the cavity refractive index: Joule heating

The first 'naive' but most simple reasoning to explain the magnitude of $S_{\delta\nu}$ at low frequencies is to consider that it is linked to the *direct conversion of the current noise* through the current-to-frequency pulling coefficient:

$$S_{\delta\nu}(f) = \left(\frac{\partial\nu}{\partial I} \right)^2 S_I(f) \quad (5.37)$$

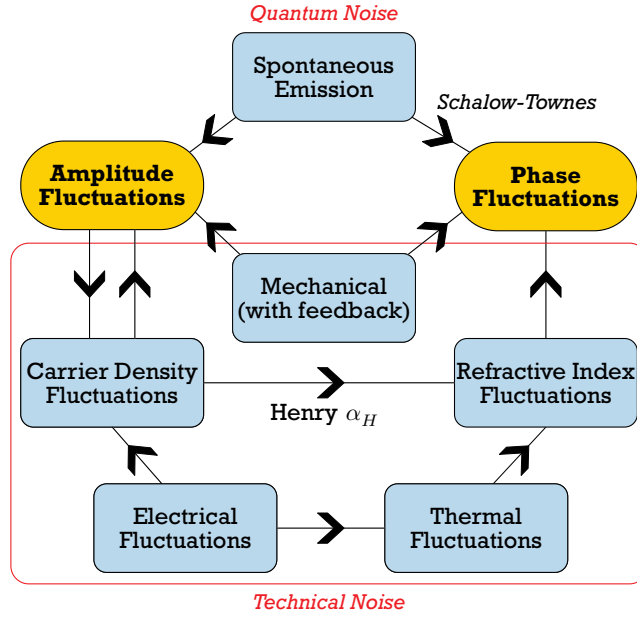


Figure 5.44: Summary of the causality relationships between the different types of fluctuations found in the lasers of the study. Inspired from [Laurain 2010]

In chapter 4, electric noise measurements on module C0195 gave above threshold, for $I = 100 \text{ mA}$, $S_I(1 \text{ kHz}) = 3 \times 10^{-18} \text{ A}^2 \cdot \text{Hz}^{-1}$. Also, $(\partial\nu/\partial I)_{C0195} = 1 \text{ THz} \cdot \text{A}^{-1}$, so that from (5.37) above, $S_{\delta\nu}^{theo}(1 \text{ kHz}) = 2.8 \times 10^6 \text{ Hz}^2 \cdot \text{Hz}^{-1}$. This can be compared to the experimental value of $S_{\delta\nu}^{exp}(1 \text{ kHz}) = 7 \times 10^6 \text{ Hz}^2 \cdot \text{Hz}^{-1}$ of section [5.5.3]. The theoretical value is close to the experimental one within a factor 2.5. If the model is correct on a physical point of view, this means that the low-frequency noise is mainly generated by the temperature fluctuations from (current) Joule effect in the p-doped layers. There are some doubts however that this model fully explains what we observe. For instance, for the device C0314, $S_I(1 \text{ kHz}) = 9.2 \times 10^{-15} \text{ A}^2 \cdot \text{Hz}^{-1}$ and $(\partial\nu/\partial I)_{C0314} = 1.5 \text{ THz} \cdot \text{A}^{-1}$ which yields $S_{\delta\nu}^{theo}(1 \text{ kHz}) = 2.1 \times 10^{10} \text{ Hz}^2 \cdot \text{Hz}^{-1}$ versus $S_{\delta\nu}^{exp}(1 \text{ kHz}) = 6.6 \times 10^6 \text{ Hz}^2 \cdot \text{Hz}^{-1}$! We cannot rule out that the packaging degradation that was noticed in chapter 4 induces some peculiar effects but still, the model does not explain why the slopes of S_I and $S_{\delta\nu}$ are not the same ($f^{-1.1}$ in the first case and $f^{-1.4}$ in the second).

B/ Indirect perturbation of the cavity refractive index : phase-amplitude coupling

Another (simple) model can be used to explain the flicker noise in frequency fluctuations: it was put forward first by [Fukuda 1993] to ground the experimental results of linewidth broadening with aging of the semiconductor lasers. Fukuda et al. noticed that the residual non-power dependent linewidth (which is just linked to the flicker noise) was growing when the component was stressed at high temperature and high injection for some time. They built a model in which the frequency fluctuations can be due to gain perturbations through the phase-amplitude coupling (actually just like in Henry's first derivation [Henry 1982]):

$$\delta\nu = \frac{v_g}{4\pi} \alpha_H \delta g \quad (5.38)$$

Taking into account a gain model $g = \Gamma G_0 \ln(I/I_0)$, we can write $\delta g = \Gamma G_0 \delta I/I$ so that:

$$S_{\delta\nu}(f) = \left(\frac{\Gamma G_0 c}{4\pi n_g} \alpha_H \right)^2 \frac{S_I(f)}{I^2} \quad (5.39)$$

In the article, the expression of S_I is based on Kleinpenning's model because the 1/f noise source is described by non-radiative recombinations at the heterojunction interface. In our case, if we use Hooge's law (3.48) for a bulk 1/f noise, we get:

$$S_{\delta\nu}(f) = \left(\frac{\Gamma G_0 c}{4\pi n_g} \alpha_H \right)^2 \frac{\varepsilon_H}{N f^a} \quad , \quad a \in [0.8, 1.4] \quad (5.40)$$

For C0195, the parameters are $n_g = 3.7$, $\Gamma G_0 = 13.5 \text{ cm}^{-1}$, $\alpha_H = 3.5$ and $S_I(1 \text{ kHz})/I^2 = 3 \times 10^{-16} \text{ Hz}^{-1}$ at $I = 100 \text{ mA}$. Then, $S_{\delta\nu}^{theo}(1 \text{ kHz}) = 2.8 \times 10^5 \text{ Hz}^2 \cdot \text{Hz}^{-1}$. Clearly, this contribution does not explain the full magnitude (factor 25) of the experimental noise. On the other hand, there is no current dependency in the relation (5.40) which means that the 1/f level is always constant whatever the injection. Of course, above threshold, the gain is ideally clamped. Because of lateral gain inhomogeneity, some areas away from the waveguide in the ridge-DFB laser are not in this regime and even in this case, no increase of noise should be observed. In the case of C0195, figure (5.25) proves the contrary: the flicker level increases slightly with the injection. For the other modules, the behavior is even erratic for some operation points, with an increase of magnitude of one decade with a somewhat higher current. It cannot be explained by the first model (A). If we imagine that the lateral (un-clamped) carrier spreading goes along with lateral modal instabilities, an effective Henry factor $\alpha_{H,eff}$ may take into account the total perturbation of the mode, in particular when it overlaps on weakly injected parts of the quantum-well: then, the phase-amplitude factor can have very high values ($\alpha_H > 10$).

C/ Direct re-coupling of the spontaneous emission: un-clamped populations

Finally, a third path can lead to what is observed in the lasers. It is closely linked to the previous model (B) and probably the most simple explanation to the white noise floor instabilities and increase, together with the increase of the 1/f level itself, especially in 852 nm lasers. If we imagine that because of lateral current spreading with injection, some un-clamped reservoirs of carriers keep on growing on the lateral sides of the waveguide, this will first perturb the single-mode behavior (because of the multi-modal properties of the ill-designed waveguides). Then, **the un-clamped 1/f noise associated to this carriers is transferred to the spontaneous emission that re-couples to the first lasing mode with the intermediate of the spontaneous emission factor**. It would explain why we do not observe a constant frequency noise magnitude at low-frequencies with increasing current injection.

To conclude, in both models, it is possible to reduce the 1/f level either by designing low thermal resistance devices (longer cavity for instance), making very 'clean' technology and packaging (contacts and epitaxial layers) or ensuring very stable modal behavior by strong index-guiding.

5.8.3 External cavity for linewidth reduction

In the section on the experimentation of feedback, we have seen that the frequency noise could be reduced on both the white noise part and on the flicker one by re-injection of the laser beam in the cavity, in the 'weak-coupling' regime (where the mode behavior of the laser diode dominates over

the total cavity). If this was expected for the first type of fluctuations, which magnitude is inversely proportional to the square of the global photon lifetime τ_γ^2 , it is less obvious that an additional external cavity helps to decrease the electronic noise. This leads us to imagine that here, **the 1/f noise in the frequency fluctuations is strongly correlated to the *photon* fluctuations, which are directly driven by τ_γ** . If the noise was simply created by an external perturbation of the cavity refractive index (temperature for instance), there would be no reason for this technical noise to decrease with the external photon lifetime, just because the external cavity stocks more photon described by the same electric-field phase fluctuations. This speaks in favor of the model (C) of the previous section to explain what is observed, at least on III-V Lab lasers. In practice, external cavities are built in the strong-coupling configuration where the Fabry-Perot diode plus the external cavity are considered to be a unique resonator. Then, all the fluctuations are reduced according to:

$$\Delta\nu_{ECDL} \simeq \left(\frac{n_{eff}L_s}{n_eL_e} \right) \Delta\nu_{LD} \quad (5.41)$$

with the notations of chapter 3, section [3.1.4].

5.8.4 Towards more advanced designs for noise reduction ?

To go further on the noise reduction in monolithic semiconductor lasers, we can mention that today, light is shed on new designs to achieve cavities of very quality factors, thus enhancing the output coherence. Silicon photonics is one of this path. It hybridizes III-V gain media with low-losses silicon waveguides with very low coupling between the active zone and the Si cavity modes. Thus, it can be expected to reduce strongly the total losses (or equivalently the gain at threshold) in the laser regime [Santis 2014] with very long Si filtering cavities. This is a promising way to overcome the intrinsic limitations in noise of the present DFB chips.

5.9 Summary

Traditionally, laser frequency fluctuations can be quantified thanks to the intrinsic linewidth $\Delta\nu$ or to a more complete picture with the Power Spectral Density (PSD) $S_{\delta\nu}$ of the frequency noise. On a physical point of view, the quantum photon noise limit is a pure white noise which gives rise to the Schawlow-Townes-Henry linewidth: for this ideal case, the lineshape is Lorentzian in the frequency domain and its full width at half-maximum (FWHM) is directly proportional to the PSD constant magnitude: $\Delta\nu_{S-T-H} = \pi S_0$. However, in the general case of noise components of arbitrary forms, especially for 1/f fluctuations, the integration of $S_{\delta\nu}$ to recover the linewidth cannot be done without setting a lower frequency cutoff, leading to an additional approximation in the $\Delta\nu$ estimation. Thus, **the linewidth depends on the observation time.**

On an experimental point of view, the traditional metrology underlines this dichotomy: on one hand, the linewidth can be estimated by self-heterodyne setups where the laser beats with a delayed version of itself. Despite the ease of the technique, the (arbitrary) delay of the interferometer induces a non-trivial relation between the linewidth and the noise components which is not necessarily close to the intrinsic definition of the linewidth. On the other hand, the PSD of frequency noise can be retrieved using a frequency discriminator: an optical setup (Michelson, Fabry-Perot or Mach-Zehnder interferometers, atomic line signal...) converts linearly the frequency fluctuations into a voltage signal which is Fourier transformed. The true physical level of noise is estimated by evaluating or measuring the conversion slope. This method is complex and requires a careful calibration.

Now, **if a standard beat-note is realized** between two identical lasers, thanks to the modern instrumentation, all the noise parameters can be recorded in the time domain with high quality digital sampling and adequate signal processing. **This solves the issue of the link between $\Delta\nu$ and $S_{\delta\nu}$ by providing a mean to compute the exact time-dependent linewidth and PSD of frequency noise, without any calibration process.** Additionally, a new definition of the linewidth is presented. Based on the work of Mandel, Wolf and Saleh on the coherence time of the electric-field, it gives, to our sens, more insight into the laser noise properties than the FWHM when the source is affected by various noises in a complex way.

On the experimental results themselves, the typical 894 nm laser of the 1st run has a FWHM of $\Delta\nu_{FWHM} \approx 1 \text{ MHz}$ and a M-W-S equivalent $\Delta\nu_c$ of the same order of magnitude, for a few ms of observation time. The Gaussian component arising from 1/f noise dominates over the Lorentzian one of the white noise. Indeed, the Schawlow-Townes-Henry limit is mainly driven by the low losses of the cavity, even if the theoretical value is a bit too optimistic compared to what is really measured. Some simple mechanisms to explain the flicker trend at low frequencies were put forward. A reasonable model involves an amplitude to phase conversion, through the α_H Henry's factor, of the current noise fluctuations to the frequency ones. Another model, built to explain the excess low-frequency noise above threshold, is based on the modulation and re-coupling to the laser mode of the spontaneous emission generated by un-clamped carriers.

As a conclusion, the lasers designed and fabricated so far meet the specification for the current OCFS clock on a linewidth point of view. However, it remains to be seen how the different noises of the source affect the real system.

Bibliography

- [Agilent 2000a] Agilent. *8 hints for making better spectrum analyzer measurements, Agilent Application Note 1550-4*. Rapport technique, 2000.
- [Agilent 2000b] Agilent. *Optical Spectrum Analysis, Agilent Application Note 1550-4*. Rapport technique, 2000.
- [Baney 2000] Douglas M Baney, Philippe Gallion et Rodney S Tucker. *Theory and measurement techniques for the noise figure of optical amplifiers*. Optical fiber technology, vol. 6, no. 2, pages 122–154, 2000.
- [Coldren 2012] Larry A Coldren, Scott W Corzine et Milan L Mashanovitch. Diode lasers and photonic integrated circuits, volume 218. John Wiley & Sons, 2012.
- [Di Domenico 2010] Gianni Di Domenico, Stéphane Schilt et Pierre Thomann. *Simple approach to the relation between laser frequency noise and laser line shape*. Applied optics, vol. 49, no. 25, pages 4801–4807, 2010.
- [Donati 1997] Silvano Donati et Guido Giuliani. *Noise in an optical amplifier: Formulation of a new semiclassical model*. IEEE journal of quantum electronics, vol. 33, no. 9, pages 1481–1488, 1997.
- [Fukuda 1993] Mitsuo Fukuda, Takuo Hirono, Takeshi Kurosaki et Fumiyoshi Kano. *1/f noise behavior in semiconductor laser degradation*. IEEE photonics technology letters, vol. 5, no. 10, pages 1165–1167, 1993.
- [Gallion 1984] P Gallion et Guy Debarge. *Quantum phase noise and field correlation in single frequency semiconductor laser systems*. IEEE Journal of Quantum Electronics, vol. 20, no. 4, pages 343–349, 1984.
- [Ghafouri-Shiraz 2004] H Ghafouri-Shiraz. Distributed feedback laser diodes and optical tunable filters. John Wiley and Sons, 2004.
- [Henry 1982] Charles Henry. *Theory of the linewidth of semiconductor lasers*. IEEE Journal of Quantum Electronics, vol. 18, no. 2, pages 259–264, 1982.
- [Henry 1983] C Henry. *Theory of the phase noise and power spectrum of a single mode injection laser*. IEEE Journal of Quantum Electronics, vol. 19, no. 9, pages 1391–1397, 1983.
- [Jérémie 1997] Francine Jérémie, Jean-Luc Vey et Philippe Gallion. *Optical corpuscular theory of semiconductor laser intensity noise and intensity squeezed-light generation*. JOSA B, vol. 14, no. 2, pages 250–257, 1997.
- [Kersey 1991] AD Kersey, MJ Marrone et MA Davis. *Polarisation-insensitive fibre optic Michelson interferometer*. Electronics letters, vol. 27, no. 6, pages 518–520, 1991.
- [Laurain 2010] Alexandre Laurain. *Sources laser à semiconducteur à émission verticale de haute cohérence et de forte puissance dans le proche et le moyen infrarouge*. PhD thesis, Université Montpellier II-Sciences et Techniques du Languedoc, 2010.

- [Ludvigsen 1998] Hanne Ludvigsen, Mika Tossavainen et Matti Kaivola. *Laser linewidth measurements using self-homodyne detection with short delay*. Optics Communications, vol. 155, no. 1, pages 180–186, 1998.
- [Mandel 1995] Leonard Mandel et Emil Wolf. *Optical coherence and quantum optics*. Cambridge university press, 1995.
- [Matthey 2016] Renaud Matthey, Florian Gruet, Christoph Affolderbach, Gaetano Mileti, Nicolas von Bandel, Michel Garcia, Michel Krakowski et Patrick Berthoud. *Development and spectral characterisation of ridge DFB laser diodes for Cs optical pumping at 894 nm*. In 2016 European Frequency and Time Forum (EFTF), pages 1–4. IEEE, 2016.
- [McLean 1994] AB McLean, CEJ Mitchell et DM Swanston. *Implementation of an efficient analytical approximation to the Voigt function for photoemission lineshape analysis*. Journal of Electron Spectroscopy and Related Phenomena, vol. 69, no. 2, pages 125–132, 1994.
- [Mercer 1991] Linden B Mercer. *1/f frequency noise effects on self-heterodyne linewidth measurements*. Journal of Lightwave Technology, vol. 9, no. 4, pages 485–493, 1991.
- [Myara 2003] Mikhaël Myara. *Caractérisation et modélisation de lasers accordables à DBR émettant autour de 1.55 [micromètres]: étude des bruits d’amplitude et de la largeur de raie*. thesis, Montpellier 2, Université des Sciences et Techniques du Languedoc, 2003.
- [Myara 2016] Mikhaël Myara, Mohamed Sellahi et Nicolas von Bandel. *Laser Coherence Analyser - DOI:10.5281/zenodo.162952*, 2016.
- [Okai 1991] M Okai, T Tsuchiya, K Uomi, N Chinone et T Harada. *Corrugation-pitch modulated MQW-DFB lasers with narrow spectral linewidth*. IEEE journal of quantum electronics, vol. 27, no. 6, pages 1767–1772, 1991.
- [Okoshi 1980] T Okoshi, Ki Kikuchi et A Nakayama. *Novel method for high resolution measurement of laser output spectrum*. Electronics letters, vol. 16, no. 16, pages 630–631, 1980.
- [Olivero 1977] John J Olivero et RL Longbothum. *Empirical fits to the Voigt line width: A brief review*. Journal of Quantitative Spectroscopy and Radiative Transfer, vol. 17, no. 2, pages 233–236, 1977.
- [Petermann 2012] Klaus Petermann. *Laser diode modulation and noise*, volume 3. Springer Science & Business Media, 2012.
- [Saleh 1991] Bahaa EA Saleh, Malvin Carl Teich et Bahaa E Saleh. *Fundamentals of photonics*, volume 22. Wiley New York, 1991.
- [Santis 2014] Christos Theodoros Santis, Scott T Steger, Yaakov Vilenchik, Arseny Vasilyev et Amnon Yariv. *High-coherence semiconductor lasers based on integral high-Q resonators in hybrid Si/III-V platforms*. Proceedings of the National Academy of Sciences, vol. 111, no. 8, pages 2879–2884, 2014.
- [Schimpe 1983] R Schimpe. *Theory of intensity noise in semiconductor laser emission*. Zeitschrift für Physik B Condensed Matter, vol. 52, no. 4, pages 289–294, 1983.

- [Signoret 1994] Philippe Signoret. *Analyse des bruits optique-électriques et étude de leur corrélation. Application à une tête optique d'émission laser à réaction répartie*. PhD thesis, Université Montpellier II, 1994.
- [Stéphan 2005] GM Stéphan, TT Tam, Stéphane Blin, Pascal Besnard et Michel Têtu. *Laser line shape and spectral density of frequency noise*. Physical Review A, vol. 71, no. 4, page 043809, 2005.
- [Tourrenc 2005a] J-P Tourrenc, Philippe Signoret, Mikhaël Myara, Marc Bellon, J-P Perez, J-M Gosalbes, Robert Alabedra et Bernard Orsal. *Low-frequency FM-noise-induced lineshape: a theoretical and experimental approach*. IEEE journal of quantum electronics, vol. 41, no. 4, pages 549–553, 2005.
- [Tourrenc 2005b] Jean-Philippe Tourrenc. *Caractérisation et modélisation du bruit d'amplitude optique, du bruit de fréquence et de la largeur de raie de VCSELs monomodes émettant autour de 850 nm*. PhD thesis, Montpellier 2, 2005.
- [Tow 2013] Kenny Hey Tow. *Laser Brillouin à fibre microstructurée en verre de chalcogénure*. PhD thesis, Université Rennes 1, 2013.
- [von Bandel 2016a] N von Bandel, M Garcia, M Lecomte, A Larrue, Y Robert, O Driss, O Parillaud, M Krakowski, F Gruet, R Matthey *et al.* *DFB-ridge laser diodes at 894 nm for Cesium atomic clocks*. In SPIE OPTO, page 97552K. International Society for Optics and Photonics, 2016.
- [von Bandel 2016b] Nicolas von Bandel, Mikhaël Myara, Mohamed Sellahi, Tahar Souici, Rémi Dardaillon et Philippe Signoret. *Time-dependent laser linewidth: beat-note digital acquisition and numerical analysis*. Opt. Express, vol. 24, no. 24, pages 27961–27978, 2016.

Laser module in atomic clock configuration

6.1 Introduction

In chapter 1, we described the main sub-systems of the atomic clock. The first brick of this architecture is the laser in a servo that allows to adjust precisely its frequency to one of the transition lines of the cesium (D_1 or D_2 lines) [1.2.2.2].

With this electronic package, it is intended to control the noise (including the drift) of the laser source, i.e. to oppose the frequency variations of the laser by a steady comparison with the instantaneous frequency at the central position of the laser cesium line. We will therefore deal with a system which **measures** the frequency of the laser in real time, deduces an **error** on the laser spectral position, and this error will be processed (with a **corrector**) to inject an adequate signal on the laser current. Thus, because of the frequency tuning with current (or *chirp*), it allows to **counter-act** (with an electronic **feedback**) on the laser frequency to compensate for the shift from the cesium line with internal/external **perturbations**. This process will be limited, of course, by the global **frequency bandwidth** of the response of the system to the perturbations. Similarly, the same reasoning can be applied to stabilize the laser frequency by a control on the absolute temperature of the chip. However, because there is not much degree of latitude on this parameter in practice, the temperature is stabilized first close to the desired point of operation, and then the current is used as a locking parameter to the cesium frequency. We will only investigate this second loop. The limit of these systems is that under certain conditions, if excessive noise correction is required, they may become unstable. In this chapter, we begin by describing the general criteria that allow a servo to reduce noise and its associated limits. Next, we model a realistic *dither-locking* servo as they are used in atomic clocks to check if the lasers developed in this work meet the industrial requirement in terms of system performance and stability.

6.2 Generalities on servo loop theory

This section presents briefly some useful concepts of electronic control theory that will be used to describe the electronics package of the clock.

6.2.1 Laplace representation of a servo

If we consider a system g that transforms an input signal x (a target output parameter of s for instance) into an output y , the transformation can be considered in the time-domain, or we can adopt a frequency representation. If we assume that the system is linear (which is usually not the case in reality, but in noise processing, we can always assume that it can be linearized around the operation point), it is described by a linear combination of various derivative (and integrative) orders of the

input. By applying the Laplace transform¹ \mathcal{L}_T to the representation $y(t) = g * x(t)$ (g is the impulse response of the system), we obtain a new picture $Y(s) = G(s)X(s)$, where the transfer function G is now a rational fraction of the variable s , which simplifies deeply the mathematical analysis (6.1).

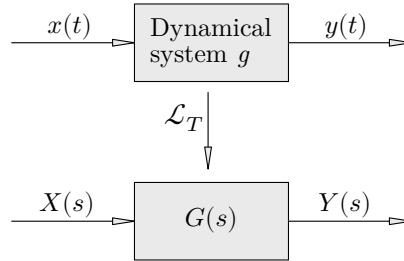


Figure 6.1: Representation of the transfer function of the system in the time and (Laplace) frequency domain

When some output parameters of the system are to be controlled tightly, a *servo-loop* can be used. The principle of this scheme is depicted in figure (6.2) and an equivalent description of the transfer functions in the Laplace frequency domain in (6.3). Concretely speaking, in our case, X is

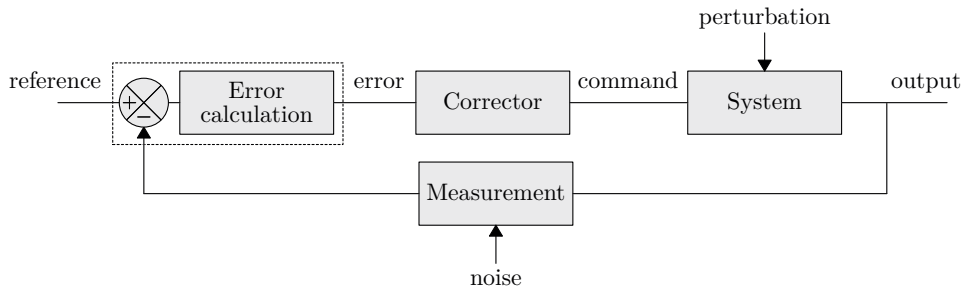


Figure 6.2: Diagram block scheme of a generic servo

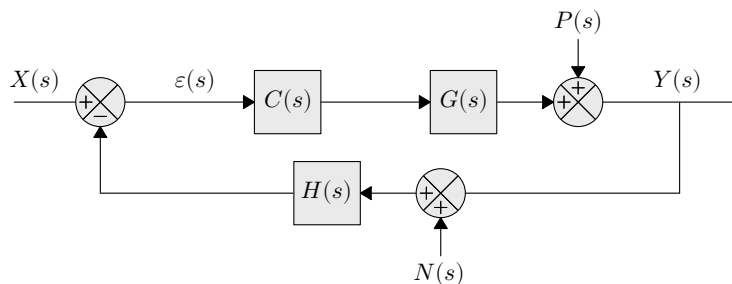


Figure 6.3: Detailed diagram block of the generic system in a servo-loop. X : reference signal, Y : regulated output, C : corrector, P : output perturbation, G : system, N : input detection noise and H : measurement process

the central frequency of the Cs line ν_0 (in Hz), ν' is the 'in-loop' laser frequency ν' (in Hz), ε the

¹The Laplace transform is similar to the Fourier transform which in practice allows to study the transient regimes, which is not possible with the Fourier representation. If $s = \rho + j\omega$ is the Laplace variable, setting $\rho = 0$ brings back to the Fourier domain

signal error (in V) between the two frequencies (it can be generated by a specific electronics), C an active corrector (a PID circuit for instance), G the laser that turns the current into the frequency, P can be seen as a perturbation on the output of the laser frequency (it is typically the frequency noise in Hz) and finally, the measurement system H detects the optical frequency and converts it to an amplitude (electrical) signal (in V) used to generate the error. This detection process can be affected by an *entry* noise (for instance, parasitic light on the photodiode).

6.2.2 Noise reduction in a servo

The goal of the servo of interest is to reduce the noise of the output Y arising from the perturbation P of the system [Sellahi 2011]. If the input reference X is set to zero and the diagram (6.3) is rearranged to set the perturbation as the reference signal, we can explicit the expression of Y in the dynamical regime after a few reduction operations on the diagram (6.1):

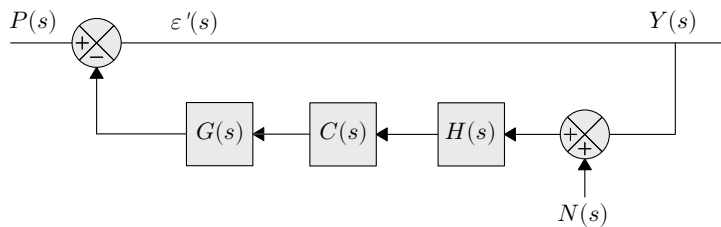


Figure 6.4: Detailed diagram of the generic system in servo-loop, rewritten with the perturbation P as the initial input only ($X = 0$). It shows that the perturbation P completely bears the total gain of the loop

$$Y(s) = \frac{P(s) + GCN(s)}{1 + GCH(s)} = Y_P(s) + Y_N(s) \quad (6.1)$$

Y_P and Y_N are components of the output that dependent respectively on P and on N . Y_P/P is the capacity of the system to reject the perturbation whereas Y_N/N is the limit of this rejection by the noise that exists on the detection. Since this noise is independent of Y_P and the feedback does not impact this noise, it cannot be corrected. The only way to minimize it is to optimize the noise of the measurement system. We will focus on the ability of the system to suppress the perturbation (the frequency noise of the laser in our case), the limit posed by the detection noise is not the issue of this chapter. More into details, if Y_P is considered, (6.1) yields:

$$\frac{Y_P(s)}{P(s)} = \frac{1}{1 + GCH(s)} \quad (6.2)$$

so the minimization of this expression leads to have $|GCH| \gg 1$. The conclusion is that a correction and/or a measurement conversion function of arbitrary high modulus (or high gain), are able to **squeeze completely the perturbations** on the system. Considering Y_N now, we get:

$$\frac{Y_N(s)}{N(s)} = \frac{GC(s)}{1 + GCH(s)} \quad (6.3)$$

If $|GCH| \gg 1$, $Y \rightarrow N/H$: in the limit of very high open-loop gain, the output error will be limited by the relative magnitude of the detection noise-to-signal ratio. These relations are very general: **a good servo loop must have high feedback gain for each frequency s to reduce the**

fluctuations. In this case, the ultimate limit will be the noise of the measurement chain though.

This is however not sufficient. Intuitively, if the sign of the feedback that is re-injected at the entry point changes, the loop will obviously switch from a damping behavior to an amplification, leading to an oscillator instead of a locking system. In many usual systems, this scenario occurs when we want to increase too much the gain in order to reduce the noise : this is the issue of the **stability** of the system.

6.2.3 Stability of a servo

To illustrate the stability issue, let us take a simplified servo loop with unitary feedback (6.5):

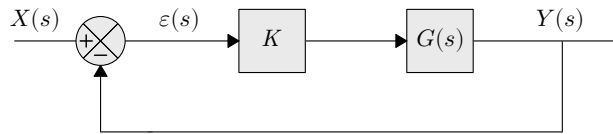


Figure 6.5: Simplified diagram block of the generic system in servo-loop with unitary feedback

The transfer function of the closed loop is:

$$G_{cl}(j\omega) = \frac{Y(j\omega)}{X(j\omega)} = \frac{KG(j\omega)}{1 + KG(j\omega)} \quad (6.4)$$

with K a variable gain. The function $G_{ol}(j\omega) = KG(j\omega)$ is often called the *open-loop* gain. The loop will be instable if $1 + KG(j\omega) = 0$, i.e. the modulus and the phase verify:

$$|KG(j\omega)| \geq 1 \quad (6.5)$$

$$\angle[KG(j\omega)] = -180^\circ \quad (6.6)$$

For *low-pass* transfer functions, which are very often found in physical systems (there are combinations of 1st and 2nd order low-pass), the criterion is illustrated in figure (6.6). The goal in making a stable servo for noise reduction is to inject a maximum of gain in the loop without crossing the critical phase point. There are particular servo systems for which this condition is always satisfied (Routh-Hurwitz criterion):

- 1st order system: unconditionally stable (the critical phase point cannot be reached whatever the gain value because $0 \leq \angle[KG(j\omega)] < 90^\circ$)
- 2nd order system: unconditionally stable in practice (the critical phase point is reached in the asymptotic limit of infinite gain because $0 \leq \angle[KG(j\omega)] < 180^\circ$). However, it is not reliable if small phase variations have not been taken into account in the model
- nth order system, $n > 2$: no general conclusion can be drawn without examining the *poles values* of G_{cl}

These rules have a very practical consequence for the electronic design of a servo: in reality, such a system cannot be of 1st or 2nd order (simply because the existence of the corrector, the system and the measurement process creates at least a 3rd order). We look then at the *dominant pole* of the transfer function: very often, the global transfer function behavior will be determined by a 1st or 2nd

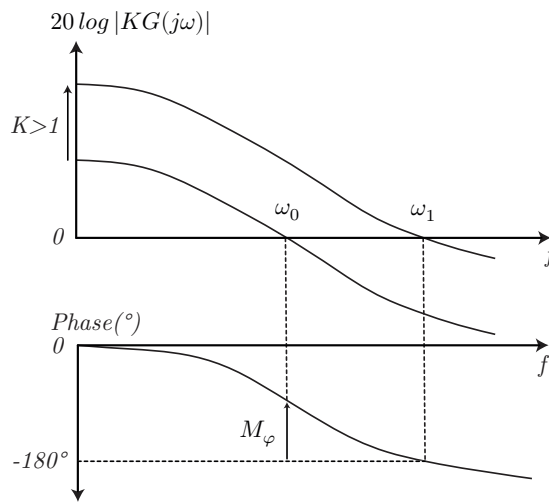


Figure 6.6: Bode diagrams of G_{ol} showing the crossing possibilities at the phase critical point of -180°

order in the frequency range of interest, before turning to higher order at higher frequencies. The gain can then be increased until the higher order slope in the Bode diagram (6.6) crosses the critical phase point (with a security margin M_φ). Therefore, when designing a servo loop, one has better to **reduce the system to a first order (where possible) on the widest bandwidth** achievable.

This simple reasoning allows to size the parameters of the servo. Then, more refined criteria are used to test the sturdiness of the final conception (actually, the real transfer functions of the *operational amplifiers* can be modeled accurately with modern codes): the *Nyquist criterion* is one of them. A simplified version (valid for systems that are already stable in open-loop configuration) tells that: *a linear system is stable if its open-loop function G_{ol} represented in the Nyquist diagram ($\Re(G_{ol}); \Im(G_{ol})$) draws a curve that is always (strictly) at the right of the point $(-1, 0)$ for a growing frequency parameter.* Illustration of this principle is given in figure (6.7).

The Nysquist criterion is generally used at the end of the conception to validate the stability on its

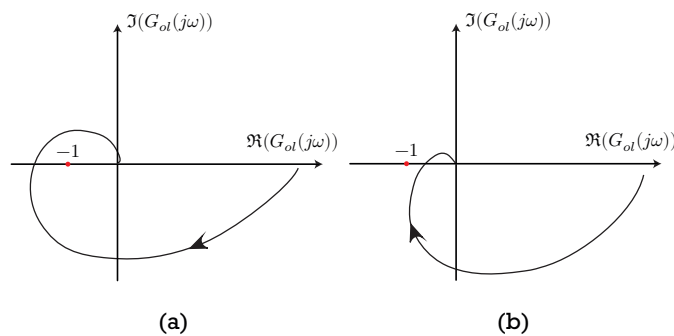


Figure 6.7: Nyquist diagrams of the open-loop function G_{ol} . Case (a): the loop is unstable. Case (b): the loop is stable

fine characteristics.

6.2.4 Application to the laser frequency locking

To illustrate the above theory, let us consider a laser source affected by frequency noise/frequency drift and Y the deviation from the laser reference frequency to maintain. A servo system allows to reject some of these fluctuations. The Power Spectral Density (PSD) of the corrected output in this loop is linked to the PSD of the (free-running) laser frequency noise $S_{\delta\nu}$ through:

$$S_Y(f) = \left| \frac{1}{1 + G_{ol}(f)} \right|^2 S_{\delta\nu}(f) \quad (6.7)$$

$G_{ol}(f)$ is again the open-loop gain, product of all the transfer functions of the system. Let assume that $G_{ol}(f)$ has a dominant pole. It can then be approximated by a first-order low-pass transfer function over a limited bandwidth:

$$G_{ol}(f) = \frac{H_0}{1 + j\tau f} \quad (6.8)$$

with H_0 the statical gain and $f_c = 1/\tau$ the -3 dB cutoff frequency. The principle of noise rejection of (6.7) is illustrated in figure (6.8) with the model (6.8) ($f_c = 100 \text{ Hz}$). With increasing gain, the

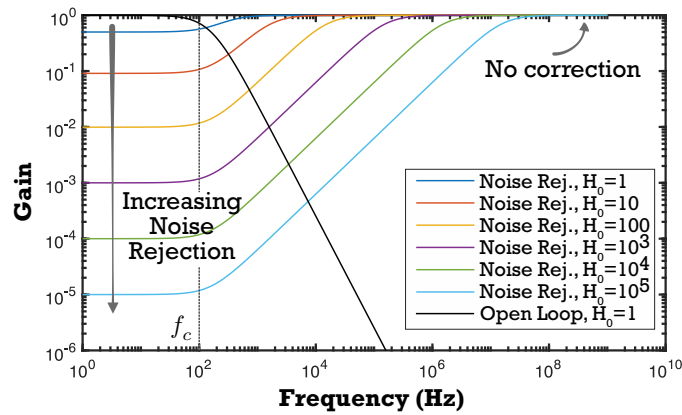


Figure 6.8: Noise rejection principle illustrated by the gain plot vs frequency of (6.8) (black line) for $f_c = 100 \text{ Hz}$ and of (6.7) for $S_{\delta\nu} = 1$ and several values of the statical gain H_0

low-frequency noise is squeezed by a flat coefficient below f_c , while the noise reduction decreases with a slope of 2 in the log-log representation until it reaches the unitary gain. Also, as said above, far from the dominant pole, the system has a higher order behavior that has to be carefully assessed to define a gain margin before instability.

6.3 Laser frequency locking on cesium lines: dither-locking principle

The prerequisite to use the DFB laser modules in the atomic clock setup is to stabilize precisely the optical frequency on the (D_1) or (D_2) line, as it was mentioned in chapter 1, section [1.2.2.1]. That is, to lock in an absolute way the laser frequency on the atomic transitions. For that, we need first to understand the dynamical response of the atomic system (Cs versus light interaction). In the electronic package description, we gave a general picture (1.19) to describe the locking process from a signal processing point of view. This scheme, called *dither-locking*, will be investigated in details by giving a quantitative description of each element of the setup and their interactions.

6.3.1 The Cs fluorescence line in frequency discrimination

The spectral profile of a Cs line can be obtained theoretically from a quantum mechanical description of light-atom interaction. Let consider an individual atom: its structure can be simplified to a *two-level* or *three-level* configuration, depending on the type of transition chosen (respectively cycling or pumping, see chapter 1) as depicted in figure (6.9). It interacts with a laser beam field $\vec{E}(t)$.

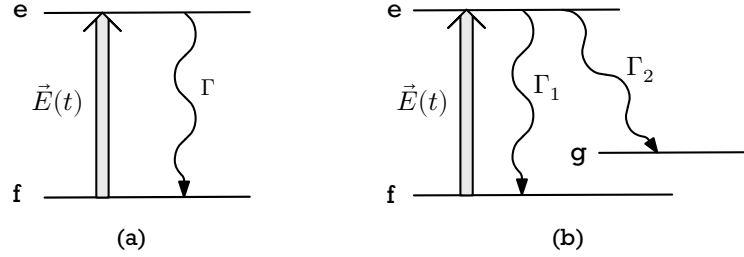


Figure 6.9: (a) Two-level system excited by a radiation $\vec{E}(t)$ between the ground state f and the excited state e that decays with a rate Γ . (b) Three-level system excited by a radiation $\vec{E}(t)$ between the ground state f to the excited state e that decays either towards f or g with the branching ratios Γ_1 and Γ_2 .

A population of such N independent atoms will be characterized by the *time-dependent densities of probability* $\rho_{ee}(t)$, $\rho_{ff}(t)$ and $\rho_{gg}(t)$ (no dimension) to be respectively in state e , f or g . If we consider the **two-level case only**, it can be shown that these terms are the solutions of the set of coupled differential equations [Tannoudji 1973, Lucas-Leclin 1998]:

$$\frac{d\rho_{ee}}{dt} = \frac{i\Omega_R}{2}(\rho_{ef} - \rho_{fe}) - \Gamma\rho_{ee} \quad (6.9)$$

$$\frac{d\rho_{ef}}{dt} = i2\pi\Delta\nu_T(t)\rho_{ef} - \frac{i\Omega_R}{2}(\rho_{ff} - \rho_{ee}) - \frac{\Gamma}{2}\rho_{ef} \quad (6.10)$$

$$\frac{d\rho_{fe}}{dt} = -i2\pi\Delta\nu_T(t)\rho_{fe} + \frac{i\Omega_R}{2}(\rho_{ff} - \rho_{ee}) - \frac{\Gamma}{2}\rho_{fe} \quad (6.11)$$

$$\rho_{ee} + \rho_{ff} = 1 \quad (6.12)$$

The additional cross-terms $\rho_{ef}(t)$ and $\rho_{fe}(t)$ ($\rho_{ef} = \rho_{fe}^*$) are typical from the quantum mechanical description in that they account for the *coherence* that appears between the excited and fundamental states (oscillation of probabilities through the superposition of these states under applied field). The system (6.9) without these terms is just the classical spontaneous decay one. The Rabi frequency Ω_R gives the strength of the atomic dipole-to-field coupling:

$$\Omega_R(t)^2 = \frac{3\Gamma\lambda_0^3}{2\pi\hbar c} I_l(t) \quad (6.13)$$

It is tuned by the laser *intensity* $I_l(t)$ (in $W.m^{-2}$), the transition wavelength λ_0 and the rate Γ . The laser total frequency shift from the exact transtion is $\Delta\nu_T(t) = \nu_l(t) - \nu_0 + \delta\nu_l(t)$ where the laser frequency noise $\delta\nu_l(t)$ can eventually be taken into account. The instantaneous flux of photons per second $I_\gamma(t, t_d)$ emitted by one atom at time t , which has interacted during t_d with the laser beam is:

$$I_\gamma(t, t_d) = \Gamma\rho_{ee}(t, t_d) \quad (6.14)$$

with $\rho_{ee}(t, t_d)$ solution of the above system. If the Cs beam configuration is considered, the atoms have a unique velocity component v_{at} . The mean number of photons emitted by one atom and detected at

time t in the interaction zone of length L_d is then:

$$\beta(v_{at}, t) = \int_{t_d=0}^{L_d/v_{at}} I_\gamma(t, t_d) dt_d \quad (6.15)$$

Finally, the mean (statistical) value of the fluorescence detected at time t in the zone of length L_d for the beam of constant flux $I_{at}^{lf}(t)$ (in *atom/s*) of the atoms on level f before the interaction, whatever their speed, is:

$$\overline{I_{at}(t)} = \int_{v_{at}=0}^{\infty} \beta(v_{at}, t) I_{at}^{lf}(t) p(v_{at}) dv_{at} \quad (6.16)$$

where $p(v_{at})$ (in $s.m^{-1}$) is the speed distribution of the atoms in the thermal beam. More simply, we consider that all the particles have a constant speed $\overline{v_{at}}$. So the mean fluorescence of the population is $\overline{I_{at}(t)} \propto \rho_{ee}(t)$. In figure (6.10) (top figure), a simulation of a Cs fluorescence line is represented. This profile has been plotted thanks to a resolution in the time domain (using the 'ode' function of MATLAB[®] for instance) of the two-level system with $\Gamma = 28.7 \text{ MHz}$ and $\Delta\nu_T(t) = \alpha \times t - \nu_0$ which corresponds to a linear ramp of the laser frequency. The profile is a Lorentzian, as predicted by a steady-state resolution of the system [Lucas-Leclain 1998], with a FWHM of $\Delta\nu_{Cs} \approx 4.6 \text{ MHz}$. It should be noticed that the fluorescence characteristics of a three-level system are complicated to recover from a numerical point of view (although we know experimentally that it is also a Lorentzian profile): physically, after a transitory regime in the pumping laser beam, a single atom will be stored in the level g after the emission of a mean number of photons (equal to Γ/Γ_2), hence it does not take part to the fluorescence signal anymore [Lucas-Leclain 1998]. In a Cs beam with several atom velocities, this individual rate of pumping changes from one atom to another, so the overall fluorescence will be a statistical mean of the real-time fluorescence emission of all the atoms. Thus, we cannot expect to recover easily the line profile like in a two-level system. This case will not be treated in the frame of this document.

★ *Note on the small-signal response function of the two-level configuration*

It will be useful for the coming analysis to derive a Cs line transfer function in the frequency domain (harmonic regime) out of equations (6.9) for a small pulsation $\omega = 2\pi f$ (which has nothing to do with the laser own pulsation) variation about the steady state value:

$$H_{Cs}(\omega) = \frac{\left(\frac{\Omega_R}{\Gamma}\right)^2}{1 + 4\left(\frac{\Delta}{\Gamma}\right)^2 + 2\left(\frac{\Omega_R}{\Gamma}\right)^2} \times \frac{2\Delta(\Gamma + j\omega)}{\left(\frac{\Gamma}{2} + j\omega\right)\Omega_R^2 + (\Gamma + j\omega)\left(\Delta^2 + \left(\frac{\Gamma}{2} + j\omega\right)^2\right)} \quad (6.17)$$

with $\Delta = \Delta\omega_T = 2\pi\Delta\nu_T$. The first non- ω dependent term is the (normalized) magnitude of the fluorescence which *saturates* for very high intensities, i.e. approaches 1/2 for $\Omega_R \gg \Delta$. This was expected because there is always a saturation intensity in the two-level system:

$$\left(\frac{\Omega_R}{\Gamma}\right)^2 = \frac{I}{I_{sat}} \quad (6.18)$$

The second term of (6.17) is clearly of 3rd order in $j\omega$.

6.3.2 Frequency discrimination

The servo requires at least a **monotonic** measurement function (or discriminator) that will turn a laser frequency variation into a voltage amplitude read by the detection. With a Cs profile as such, it is

only possible on the flanks of the line (see chapter 5) where the relationship is almost linear (constant discrimination slope). However, it does not provide any reference to adjust the laser frequency on the line transition ν_0 (possible drift of ν_l).

Now, if we follow out again the idea behind (1.20), we can go further by examining the response of the atomic reference to a small modulation of the laser frequency $\Delta\nu_m(t) = \tilde{\nu}_m \sin(\omega_d t)$ with $\tilde{\nu}_m \ll \Delta\nu_{Cs}$.

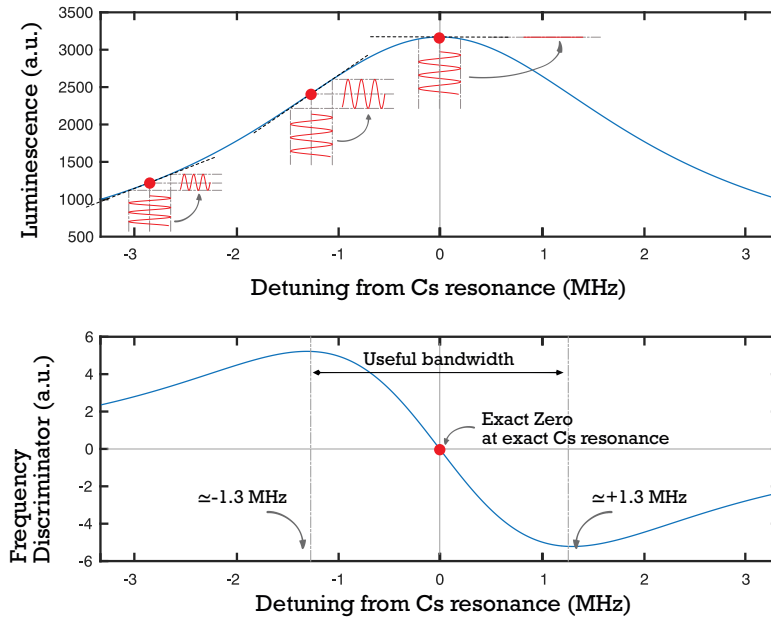


Figure 6.10: Principle of the frequency discrimination on an atomic fluorescence line using a constant modulation of the laser central frequency. Top: blue line: simulated Cs D_1 line profile (based on the unsaturated two-level system) when the laser frequency is tuned linearly with time around the Cs transition ($\Gamma = 28.7 \text{ MHz}$). Bottom: first order derivative of the top Cs profile. The useful range of operation is approximately equal to $\Delta\nu_{lin} = 2.6 \text{ MHz}$

On the flanks of the fluorescence line of figure (6.10), for a detuning of $\pm 1 \text{ MHz}$ for instance, we can notice that the modulation generates locally a sin function which amplitude (or RMS value) is *proportional to the local derivative* of the line. This is why is it interesting to have a look at the derivative of this curve: a dispersion-type function is recovered which exhibits a monotonic part, crossing the zero. This null value corresponds precisely to the top of the atomic line, at the exact Cs transition ν_0 i.e. the amplitude of the sin is zero. So we can obviously use this configuration to **build a signed error signal equivalent to the absolute shift from the atomic frequency**. Unlike the usual frequency discriminators, it is the local (deterministic) modulation that allows to point out on the local slope of the Cs line. If one demodulates this signal, the slope can be measured and the absolute position of the frequency is deduced. With frequency noise, this reasoning still holds: the operation point will change randomly but the state of the frequency is known.

Quantitatively, if h is the global time-domain transfer function of the atomic line and the fluorescence detection (global measurement system), it generates a voltage signal $v(t)$ with $\nu(t) =$

$\bar{\nu}_l + \Delta\nu_m(t) = \bar{\nu}_l + \tilde{\nu}_m \sin(\omega_d t)$, then with a first order Taylor expansion:

$$v(t) = h(\nu) = h(\bar{\nu}_l + \Delta\nu_m) \quad (6.19)$$

$$\approx h(\bar{\nu}_l) + \Delta\nu_m \left. \frac{dh}{d\nu} \right|_{\bar{\nu}} = h(\bar{\nu}_l) + \tilde{\nu}_m \sin(\omega_d t) \left. \frac{dh}{d\nu} \right|_{\bar{\nu}} \quad (6.20)$$

Then, a demodulation operation allows to retrieve the RMS value of this signal at the point $\bar{\nu}_l$, that is the function:

$$\mathcal{D}(\nu) = \frac{\tilde{\nu}_m}{\sqrt{2}} \left. \frac{dh}{d\nu} \right|_{\bar{\nu}} \quad (6.21)$$

This technique is called *dither-locking*. In practice, the *synchronous demodulation* principle is used to retrieve this signal, which can be realized practically with a lock-in amplifier (analog or embedding a Digital Signal Processor for instance). This apparatus, together with the atomic resonator, handles completely the generation of the error signal to lock the laser frequency on the reference (in the block-diagram of figure (6.3), the comparator between $X = \nu_0$ and the input after H is actually the whole modulation-demodulation process described above).

6.3.3 Dither-lock setup from a servo point of view

The aim of the zone A of the clock setup in [1.2.2.1] is to keep the frequency of the laser close to the atomic transition ν_0 with a small enough spectral broadening to ensure a good overlap with the Cs lineshape. Indeed, this will yield a high interaction of light with atoms in the zone A' where full atomic pumping in one of the ground state is needed (if some un-pumped atoms leave this zone to the third detection zone B, they will induce a strong noise that will degrade the SNR of the clock).

Figure (6.11) depicts the dither-lock loop with the several elements of the system. For the sake of clarity, the underlying block diagram is also represented. Several cutoff frequencies are present in this system. **The dominant pole comes from the lock-in amplifier**, of $f_c \in [1 \text{ Hz}, 1 \text{ kHz}]$ which behaves like a 1st to 2nd order before the second pole $f_c \simeq 10 \text{ kHz}$ of the measurement system is reached. Two different questions must be addressed in the servo loop conception:

1. What is the maximum correction gain allowed before instability, given the global transfer function of the servo ?
2. What is the minimal correction gain to apply regarding the technical targets to achieve on the laser in-loop linewidth and the related pumping efficiency of the atomic beam, servo breaking limit...?

The first question is rather simple: the answer depends on the transfer functions of the elements of the loop. The second point is more tricky because it deals with the control of random fluctuations: criteria based on probabilities have to be introduced.

6.3.3.1 Maximal gain condition

With ideal models of nth order low-pass for each element of (6.11), it is possible to predict the stability of the dither-lock scheme. We describe here their main characteristics.

A/ Loop elements

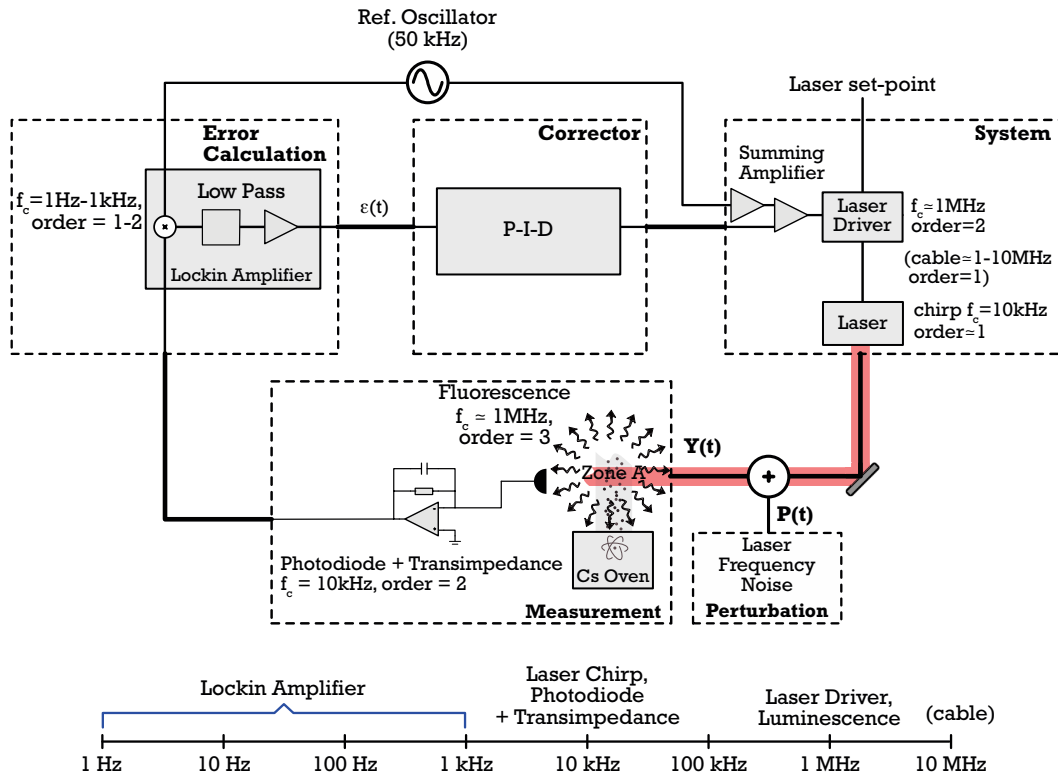


Figure 6.11: Complete block diagram of the dither-locking on a Cs line. The cutoff frequency of the sub-elements of the systems are spotted on a frequency scale. Input data with the courtesy of Thales Electron Devices

* Lock-in amplifier

The lock-in transfer function is a first order low-pass of the form (6.22):

$$H(f) = \frac{H_i}{1 + j \frac{f}{f_{c_i}}} \tag{6.22}$$

There is some flexibility on the lock-in parameters (H_i, f_{c_i}) tuning. This apparatus can be seen as a pure integrator for $f \gg f_{c_i}$. It is thus very efficient to correct the low-frequency perturbations.

* Detection system

The detection system comprises a photodiode (detection of the fluorescence) and the photocurrent transimpedance amplifier (figure (6.12)). Playing with the value of the capacitor C_f , a well-designed transimpedance circuit can be equivalent to a simple 2nd order Butterworth filter with no resonance. The given amplifier has always a limited *Gain-Bandwidth product* GBP (product of the gain at DC with the -3 dB cutoff frequency f_{-3dB}). In the configuration we are looking for, it can be shown that $GPB = 2\pi \times f_{-3dB}^2 \times R_f C_s$ where R_f and C_s are respectively the charge resistance (defining the gain) and the photodiode capacitance [Instrument 2009]. That is:

$$f_{-3dB} \propto \frac{1}{\sqrt{R_f C_s}} \tag{6.23}$$

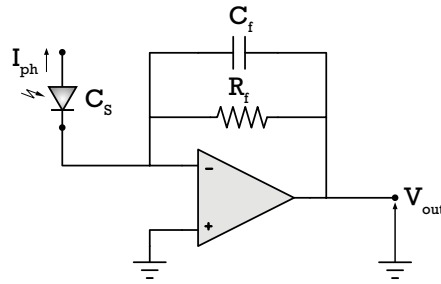


Figure 6.12: Typical circuit of a detector made of a photodiode and a transimpedance amplifier. In good operation conditions, this system is of 2nd order

The clock configuration and the atomic transitions used (three-level) produce a low level of fluorescence. This is counteracted in practice by increasing the surface of the photodiode (thus increasing its capacitance C_s) and the gain R_f on the output photocurrent. We see that it is bound to reduce the transfer function bandwidth. In practice, we estimate a $f_c = f_{-3dB} \sim 10 \text{ kHz}$. Increasing the fluorescence level detected could repel this limit, and thus repel the dominant pole of the detection, which is a very limiting element of the dither loop.

* Laser chirp

The chirp is the response function of the laser frequency with relation to the input current modulation. Until now, we have used the fact that the DC response was on the order of $\partial\nu_l/\partial I \simeq 1 \text{ GHz.mA}^{-1}$, arising essentially from Joule heating effects. The characteristic time of the thermal conduction being relatively low, we can expect the response function to be a 1st order low-pass with a cutoff frequency on the order of $f_c \sim 10 \text{ kHz}$. It is on the same order as for the detection system, so there is, for the moment, no interest in optimizing this value by an *ad-hoc* laser design.

* Laser driver

The laser driver in current has at least a 2nd order transfer function (for structural reasons of its design). The manufacturer specifies that the response is flat until $f_c \simeq 1 \text{ MHz}$.

* Cesium fluorescence response

In section [6.3.1], the small signal frequency response of a two-levels system was written explicitly. It appeared that it is a 3rd order non-resonant system, providing that we remain in the linearity zone of the discriminator. The cutoff frequency corresponds to the cesium excited state lifetime: $f_c \simeq 2 \text{ MHz}$.

B/ Global transfer function

The open-loop transfer function of the dither-lock set-up is shown in figure (6.13), based on a the previous analysis. It is clear, regarding the total phase function, that the detection system and the laser chirp set the limit to an arbitrary increase of the gain (-180° crossing after the dominant pole). So, in order to avoid any instability, the method is to set first the gain of the complete system **without the lock-in** to 0 dB on the flat part of the response at DC. This sets the constraint to have -3 dB at the critical frequency of the crossing-point of -180° . Then, it is possible to increase the gain of the lock-in function until the total gain effectively reaches the 3 dB previous limit. It defines the total gain margin at 3 dB.

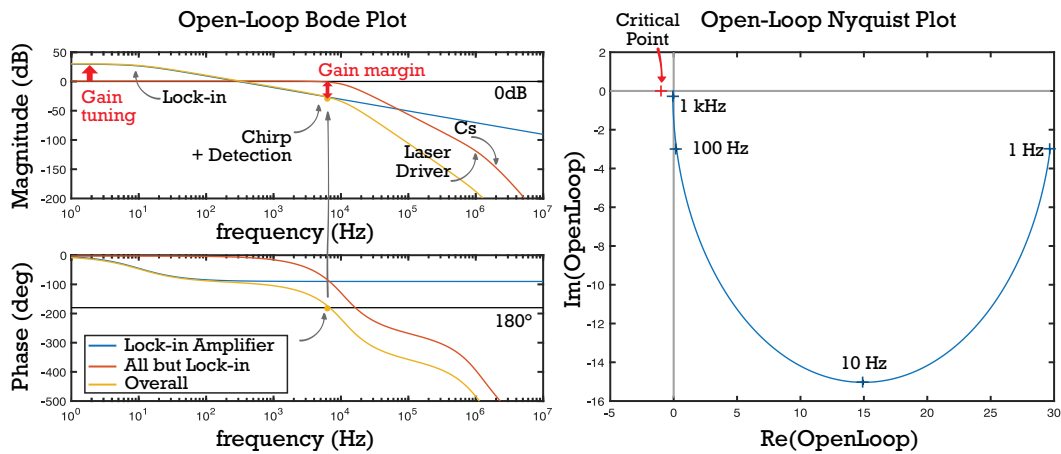


Figure 6.13: Bode plots (left) and Nyquist plot (right) of several transfer functions. The cutoff frequency of the lock-in has been arbitrary set to $f_c = 10 \text{ Hz}$ (to correspond to the laboratory configuration of TED). The Nyquist plot indicates that the closed-loop transfer function is stable provided the gain is below the gain margin at the phase critical point

From this analysis, we deduce that the maximum *proportional* gain (of constant magnitude over its bandwidth) that can be injected before instability is $G_{max} = H_{max} \simeq 700$ (6.14). The Nyquist representation allows to see that the global transfer function in the Nyquist domain has always the critical point to its left in the Nyquist domain provided that $H_i \leq H_{max}$.

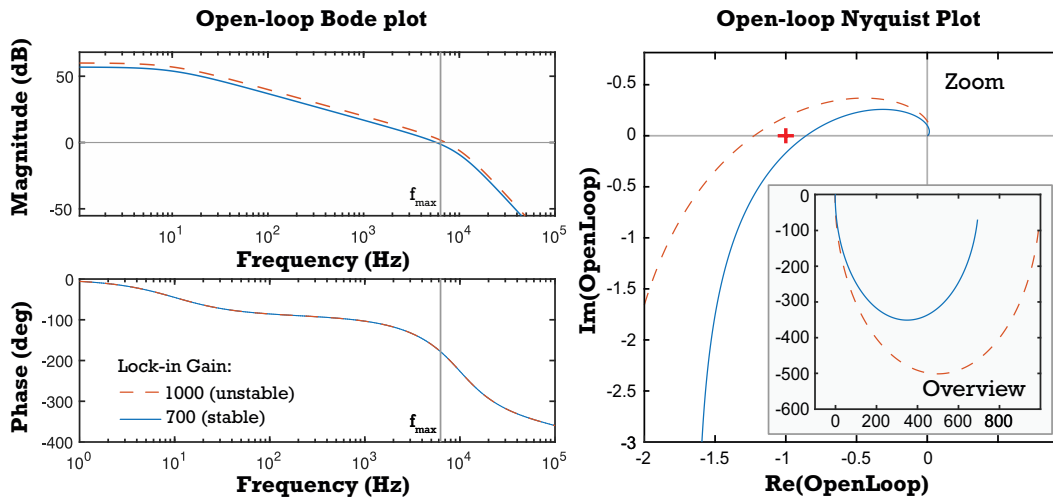


Figure 6.14: Bode plots (left) and Nyquist plot (right) of the complete open-loop dither-lock transfer function. The Nyquist plot indicates that the loop is stable provided that $H_i \leq 700$ (point $(-1, 0)$ is at the left of the blue curve $H_i = 700$)

6.3.3.2 Minimum gain condition

The minimum gain to add to the servo depends on what is to be optimized. We have retained two main requirements:

- To keep the laser locked in-loop for a given time τ_0 (we have chosen 10 years which corresponds to the lifetime of the commercial system)
- To ensure a good overlap between the in-loop laser linewidth and the cesium line

Thus, a numerical analysis has to be performed on the frequency noise as well as the linewidth when the laser is in the locking configuration.

A/ Laser locking stability on the long term

Let assume that the PSD of the free-running laser frequency noise $S_{\delta\nu}$ has a non-limited low-frequency component of $1/f^\alpha$. Over time, the (growing) random excursions of the frequency may exceed the range of the discriminator linearity (or are least the range where it is monotonic), causing the servo loop breaking. It is thus required that the **amplitude** $\tilde{\nu}_l$ of the **locked laser fluctuations** at a given time τ_0 (defining consequently a lifetime for the servo) should not exceed the range of the useful bandwidth of $\Delta\nu_{lin} \sim 2.6 \text{ MHz}$ (remember figure (6.10)). Additionally, the dither amplitude $\tilde{\nu}_m$ imposes a more stringent condition: $\tilde{\nu}_l + \tilde{\nu}_m < \Delta\nu_{lin}$. So finally, we end up with the representation (6.15) of these constraints.

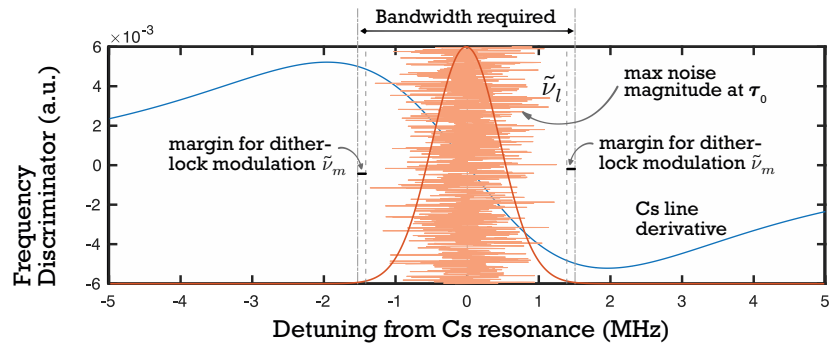


Figure 6.15: Frequency discrimination function against the detuning from the Cs resonance. The fluctuations of frequency noise and their Gaussian statistical distribution are represented in red. The frequency excursions must remain in the monotonic range of the discriminator to keep the frequency locking on the Cs line. Additionally, the constant modulation of the dithering frequency increases the range of the frequency excursions by a constant amount $\tilde{\nu}_m$

A common experimental laboratory configuration is to set a current dither modulation depth of $\tilde{i}_m = 1 \mu A$ for a dither frequency of $f_d = 50 \text{ kHz}$. Given the laser chirp low-pass response, this modulation is well-attenuated (around 25% of the DC response): $\tilde{\nu}_m = 1 \text{ GHz} \cdot \text{mA}^{-1} \times 25\% \times 1 \mu A = 0.25 \text{ MHz}$. So the final condition is:

$$\tilde{\nu}_l < 2.3 \text{ MHz} \quad (6.24)$$

Now, it is assumed that the fluctuations have a Gaussian distribution of zero mean and variance σ^2 as in chapter 4, (4.9) (it is not necessarily the case for $1/f$ noise, but it is a common hypothesis [Milotti 2002]). In this model, σ is also the RMS value of the frequency excursions. If we want (6.24) to be satisfied with a 6σ interval of confidence (less than 0.3% of chances to observe a frequency shift

over 2.3 MHz), the following condition must be satisfied:

$$6\sigma < 2.3 \text{ MHz} \quad (6.25)$$

$$\Rightarrow \sqrt{\int_{f_0}^{+\infty} S_{\delta\nu}^{\text{locked}}(f) df} < \frac{2.3}{6} \text{ MHz} = 380 \text{ kHz} \quad (6.26)$$

where the frequency noise of the **locked** laser $S_{\delta\nu}^{\text{locked}} = S_Y$ is integrated between $f_0 = 1/\tau_0$ and all the upper frequencies. **The above inequality defines a minimum statical gain H_{min} to avoid laser de-locking on an horizon of τ_0 .**

B/ Laser linewidth versus the Cs line: overlap efficiency

A general criterion of this condition can be constructed if we consider the overlap η_{Cs} of the FWHM laser linewidth $\Delta\nu_l$ with the FWHM $\Delta\nu_{Cs}$ of the Cs line. It is computed as:

$$\eta_{Cs} = \frac{\int_{-\infty}^{+\infty} \mathcal{L}_{Cs}(\nu) \times \mathcal{L}_l(\nu) d\nu}{\int_{-\infty}^{+\infty} \mathcal{L}_l(\nu) d\nu} \quad (6.27)$$

where \mathcal{L}_{Cs} and \mathcal{L}_l (no unit) are respectively the Cs fluorescence lineshape and the laser spectrum lineshape. Figure (6.16) shows a plot of this parameter as a function of the laser FWHM linewidth for the case of a strict Lorentzian and a strict Gaussian spectrum with the atomic line computed in figure (6.10) which has $\Delta\nu_{Cs} \simeq 4.6 \text{ MHz}$. It can be interpreted as a probability of interaction between the Cs atomic population and the laser beam (in the classic theory). This overlap η_{Cs} makes a simple equivalence between the contribution from the laser noise and the optical power to use to increase atom-light interaction: if the value of η_{Cs} is not enough, doubling the power (which is still acceptable given the range of operation of the laser diode) will compensate for the laser linewidth. We can notice that there is a small correction of 15% to apply from the Lorentzian case to the Gaussian one. From

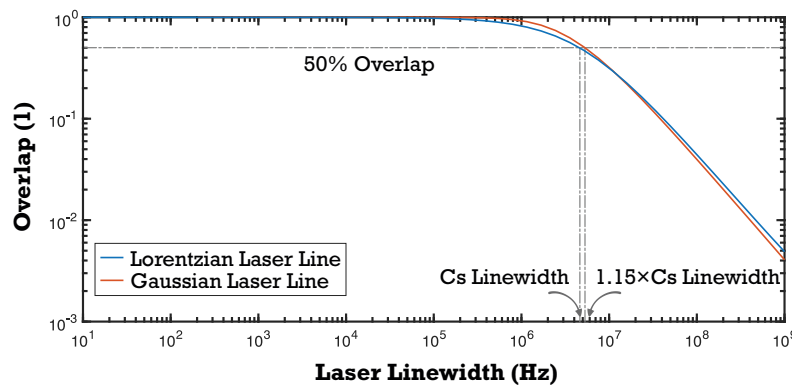


Figure 6.16: Overlap η_{Cs} for the Cs transition of figure (6.10) as a function of the laser linewidth for a Lorentzian (blue line) and a Gaussian (red line) lineshape. Here, $\Delta\nu_{Cs} \simeq 4.6 \text{ MHz}$. For a $\eta_{Cs} = 50\%$, the laser linewidth needed in the case of a Gaussian shape is slightly higher than for the Lorentzian case

now on, we set $\eta_{Cs} = 50\%$. This sets a limit for the in-loop laser linewidth to achieve, thus another constraint on the servo minimal gain.

6.3.4 Investigation of the servo requirements with a β -separation line analysis

Once the locking criteria defined, a simple reasoning based on the β -separation line (see chapter 5) allows to get more insight on the servo constraints to stabilize the laser on the Cs line and to compute the in-loop gain conditions.

To begin with, let consider a model for the laser frequency noise:

$$S_{\delta\nu}(f) = \frac{A}{f^\alpha} + B \quad (6.28)$$

which is the sum of a white noise and a low-frequency noise component. In chapter 5, we measured typical coefficients of $B = S_0 \sim 10^5 \text{ Hz}^2 \cdot \text{Hz}^{-1}$, $A = S_{-1} \sim 5 \times 10^{10} \text{ Hz}^{\alpha+2} \cdot \text{Hz}^{-1}$ and $\alpha \in [1, 1.4]$ with variations depending on the laser geometry and technology. Also, the principle of the β -separation line was presented. According to [Di Domenico 2010], the useful noise bandwidth that really affects the FWHM linewidth of the laser can be identified by the domain where $S_{\delta\nu}(f) > \beta f$, with $\beta = 8 \ln 2 / \pi^2$. The crossing frequency f_β of the two curves defines an upper limit to which the frequency noise counts. The FWHM linewidth estimation is then given by $\Delta\nu = \sqrt{8 \ln 2 \times \mathcal{A}}$ where \mathcal{A} is the surface below $S_{\delta\nu}$ between the lower frequency of observation f_0 and the upper ' β point'. A graphical illustration is given in figure (6.17)(a). It has been assumed in particular that $f_0 = 1 \text{ Hz}$ (lower frequency of linewidth observation) and $\alpha = 1$.

Several locking configurations are represented versus the β -separation. Because of the -1 slope of the $1/f$ noise, the 1st-order low-pass correction (6.8) (which has a $+2$ slope in the PSD diagram) yields a $+1$ slope global transfer function, which is precisely the tendency of the β -line. Thus, this servo order is enough to correct efficiently the low-frequency noise here. It is not necessary to correct any fluctuation above f_β so we can set the gain to be around -3 dB at this cross-point. Then, with a varying H_i parameter of the lock-in amplifier, we observe in graph (6.17)(b) that the laser linewidth, given by this theory, barely varies until H_i is high enough to decrease the in-loop $1/f$ noise below the β -line. **This limits the integration area from f_0 to $\sim f_c$ and yields a brutal suppression of the noise.** The transition gain is $H_c = 1.37 \times 10^3$ for this profile of laser frequency noise. In this model, it is also pointed out that the white noise level does have a non-negligible influence on the final in-loop linewidth.

We should also bear in mind that it highlights too distinct definitions of the linewidth: the **short-term** one, linked to the servo correction bandwidth (from f_c to f_β) and the **long-term** one, which adds the uncorrected low-frequency noise (contribution from f_0 to f_c). Fortunately, because of the log-scale, one has to 'wait a very long time at low frequencies' so that the latter contribution becomes significant, even if the noise magnitude rises with a slope of $+1$ towards the DC (the noise contribution in one decade of frequency is constant, wherever it is taken on the frequency axis).

It is worth to add that rigorously, the noise brought by the modulation at the dither frequency appears through a peak at $f_d = 50 \text{ kHz}$ with a total RMS energy of $\tilde{\nu}_m = 250 \text{ kHz}$. In theory, it contributes to the short-term linewidth when it is above the β -line. It has been neglected here. Also, the wave generator at 50 kHz associated to the dither-lock do have its own frequency noise which may add further unwanted frequency excursions on the discriminator useful range of operation. It has also been neglected here.

★ *Conclusion*

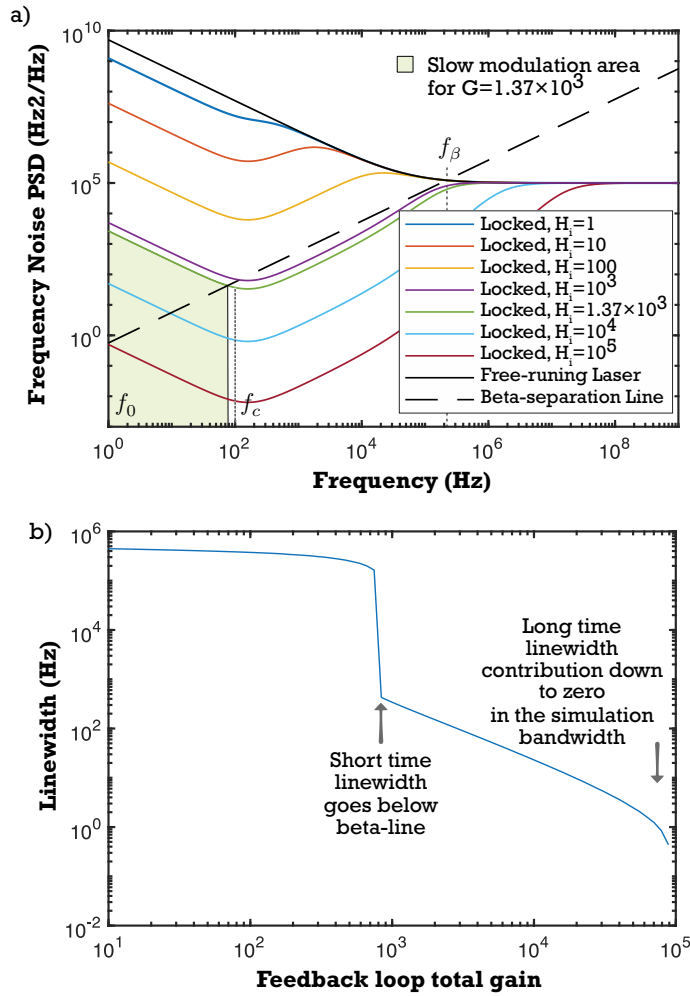


Figure 6.17: Top: Laser frequency noise rejection versus the β -line. Bottom: Computation of the in-loop laser linewidth as a function of the feedback loop gain

To recap, we have determined in [6.3.3.1] the maximum gain $H(f_{max}) = H_{max} = 700$ of the locking to inject in the loop before it gets unstable at the frequency f_{max} of the crossing of the -180° phase point. Then, in [6.3.3.2], the minimum gain H_{min} of the lock-in parameter to achieve the desired short-term and long-term linewidth was linked to the requirements for the servo stability and efficiency regarding the Cs line pumping. We set the corner frequency f_c of the lock-in to an 'arbitrary' value of 10 Hz. There still remain many possibilities for the choice of the (H_i, f_{c_i}) of (6.22). Indeed, all the couples such that $H_i \times f_{c_i} = H_{max} \times f_{max}$ (when $f_{c_i} \ll f_{max}$) are eligible for the minimum requirements. In particular, it is interesting to reduce f_{c_i} to achieve maximum *integral* correction at low frequencies, to decrease further the long-term linewidth of the laser. This is what is illustrated in figure (6.18).

6.4 LAMA lasers in-loop: case studies

The experimental PSD of frequency noise shows deviations from the ideal 1/f law. An α low-frequency exponent greater than one will call for a more stringent condition on the gain to reduce efficiently the linewidth. Here, several cases are studied: for each, the corrected in-loop (theoretical) PSD is

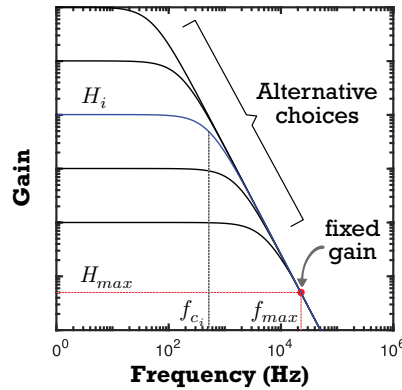


Figure 6.18: Plot of the lock-in transfer function $H(f)$ gain versus the frequency with the constraint $H(f_{max}) = H_{max}$, for several different couples of (H_i, f_{c_i})

computed and a β -analysis of the noise is performed versus the criteria we have retained for the servo performances. For that, the lower linewidth observation time of $\tau_0 = 1$ s has been chosen, to interpret more easily the graphs. Also, for a given form of the frequency noise (α exponent), the gain to respect fully the criteria of the 10 years lifetime (i.e. $\tau_0 = 10$ years) of the servo (no de-locking) is given for the couples of white and flicker magnitude parameters. Thus, we can see quickly which lasers are eligible for the atomic clock application.

6.4.1 LAMA 852 nm modules

The results of the study for the 852 nm LAMA lasers of the 1st run of fabrication are given in graph (6.19) and (6.20). Given the parameters measured for these lasers in chapter 4, for which it was found a white noise parameter of $S_0 = 10^5 \text{ Hz}^2 \cdot \text{Hz}^{-1}$, a flicker coefficient of $S_{-1} = 5 \cdot 10^{11} \text{ Hz}^{\alpha+2} \cdot \text{Hz}^{-1}$ and a flicker exponent of $\alpha \sim 1.1$, **it is found that the loop gain to inject is on the order of $H_i \simeq 70$ to achieve the locking** in the conditions described. The condition on the overlap with the Cs line is well fulfilled, as-well as the maximum gain condition of stability.

6.4.2 LAMA 894 nm modules

The results of the study for the 894 nm LAMA lasers of the 1st run of fabrication are given in graph (6.21) and (6.22). Given the parameters measured for these lasers in chapter 4, for which it was found a white noise parameter of $S_0 = 10^5 \text{ Hz}^2 \cdot \text{Hz}^{-1}$, a flicker coefficient of $S_{-1} = 5 \cdot 10^{11} \text{ Hz}^{\alpha+2} \cdot \text{Hz}^{-1}$ and a flicker exponent of $\alpha \sim 1.4$, **it is found that the loop gain to inject is on the order of $H_i \simeq 100$ to achieve the locking** in the conditions described. The condition on the overlap with the Cs line is again well fulfilled, as-well as the maximum gain condition of stability.

6.4.3 LAMA 894 nm modules under feedback

The results of the study for the 894 nm LAMA lasers of the 1st run of fabrication under external optical feedback are given in graph (6.23) and (6.24). Given the parameters measured for these lasers and the noise levels induced by the mechanical perturbations in chapter 4, the mapping, realized for a fixed $S_0 = 10^5 \text{ Hz}$, indicates that the in-loop lasers are broadly resistant to the feedback. Indeed, for $H_i = 100$, the servo can bear a large amount of external perturbations before delocking.

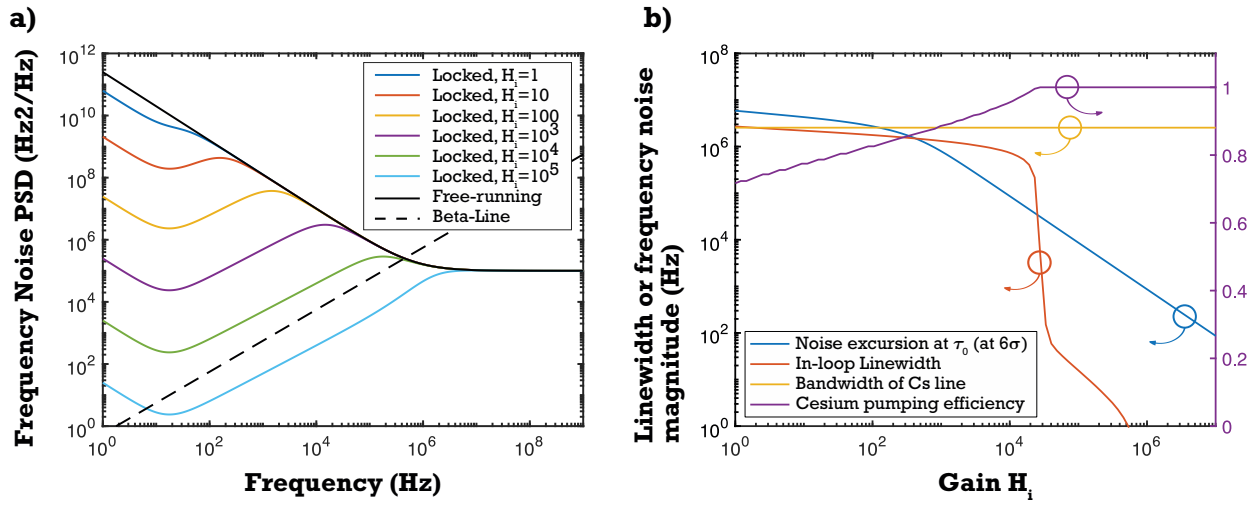


Figure 6.19: β -separation line analysis of the in-loop laser frequency noise of the 852 nm LAMA lasers (1st run of fabrication). (a) Locked-laser frequency noise as a function of the Fourier frequency for several values of the lock-in H_i parameter ($f_c = 10$ Hz) versus the β -line. The lower observation time is $\tau_0 = 1$ s. (b) Red curve: Laser linewidth (as given by the β -line theory) as a function of the lock-in H_i gain parameter, Purple curve: overlap efficiency η_{Cs} of the laser linewidth and the Cs line as a function of H_i , Yellow curve: total allowed noise bandwidth for the Cs discriminator operation (condition (6.24)), Blue curve: maximum frequency noise excursions on an horizon of $\tau_0 = 1$ s (with a 6σ interval of confidence)

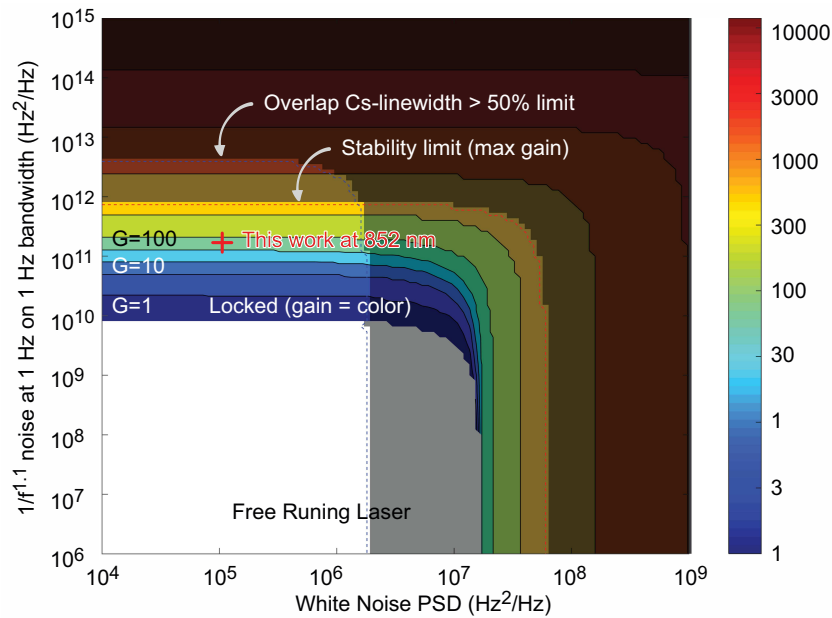


Figure 6.20: Mapping of the required loop gain to achieve the 852 nm LAMA lasers frequency locking at $\tau_0 = 10$ years on the Cs line (with a 6σ interval of confidence), given a white noise level and a $1/f^{1.1}$ flicker noise level of the laser. The maximum gain limit before loop instability is in gray shaded area. The minimum overlap condition η_{Cs} on the cesium line is the darker gray shaded area

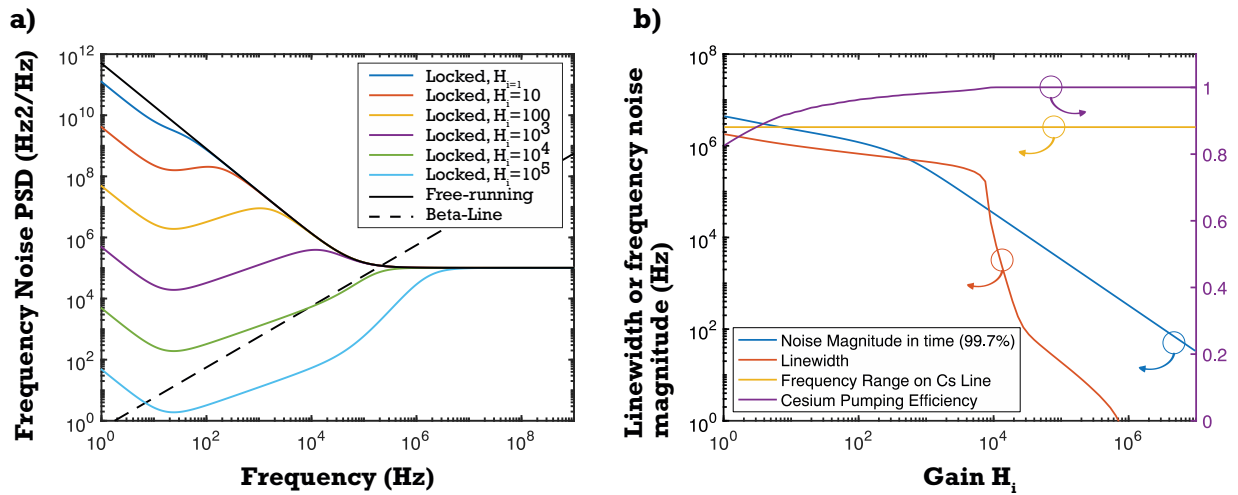


Figure 6.21: β -separation line analysis of the in-loop laser frequency noise of the 894 nm LAMA lasers (1st run of fabrication). (a) Locked-laser frequency noise as a function of the Fourier frequency for several values of the lock-in H_i parameter ($f_c = 10$ Hz) versus the β -line. The lower observation time is $\tau_0 = 1$ s. (b) Red curve: Laser linewidth (as given by the β -line theory) as a function of the lock-in H_i gain parameter, Purple curve: overlap efficiency η_{Cs} of the laser linewidth and the Cs line as a function of H_i , Yellow curve: total allowed noise bandwidth for the Cs discriminator operation (condition (6.24)), Blue curve: maximum frequency noise excursions on an horizon of $\tau_0 = 1$ s (with a 6σ interval of confidence)

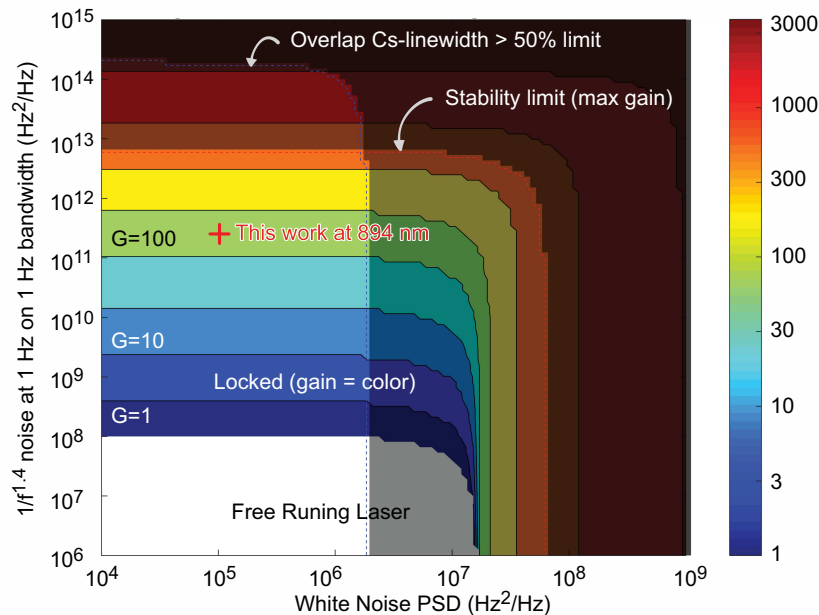


Figure 6.22: Mapping of the required loop gain to achieve the 894 nm LAMA lasers frequency locking at $\tau_0 = 10$ years on the Cs line (with a 6σ interval of confidence), given a white noise level and a $1/f^{1.4}$ flicker noise level of the laser. The maximum gain limit before loop instability is in gray shaded area. The minimum overlap condition η_{Cs} on the cesium line is the darker gray shaded area

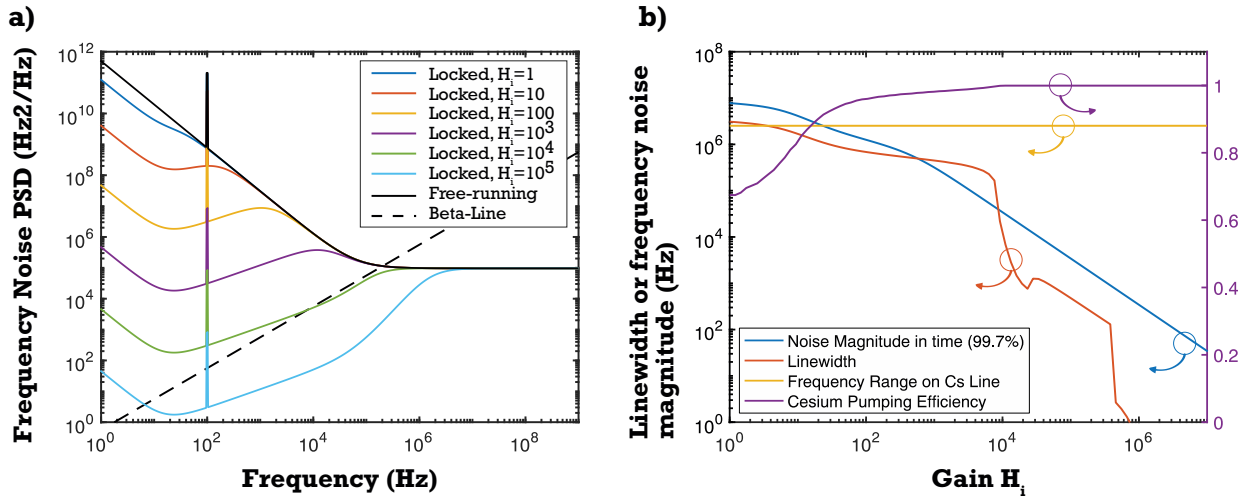


Figure 6.23: β -separation line analysis of the in-loop laser frequency noise of the 894 nm LAMA lasers under feedback. (a) Locked-laser frequency noise as a function of the Fourier frequency for several values of the lock-in H_i parameter ($f_c = 10$ Hz) versus the β -line. The lower observation time is $\tau_0 = 1$ s. (b) Red curve: Laser linewidth (as given by the β -line theory) as a function of the lock-in H_i gain parameter, Purple curve: overlap efficiency η_{Cs} of the laser linewidth and the Cs line as a function of H_i , Yellow curve: total allowed noise bandwidth for the Cs discriminator operation (condition (6.24)), Blue curve: maximum frequency noise excursions on an horizon of $\tau_0 = 1$ s (with a 6σ interval of confidence)

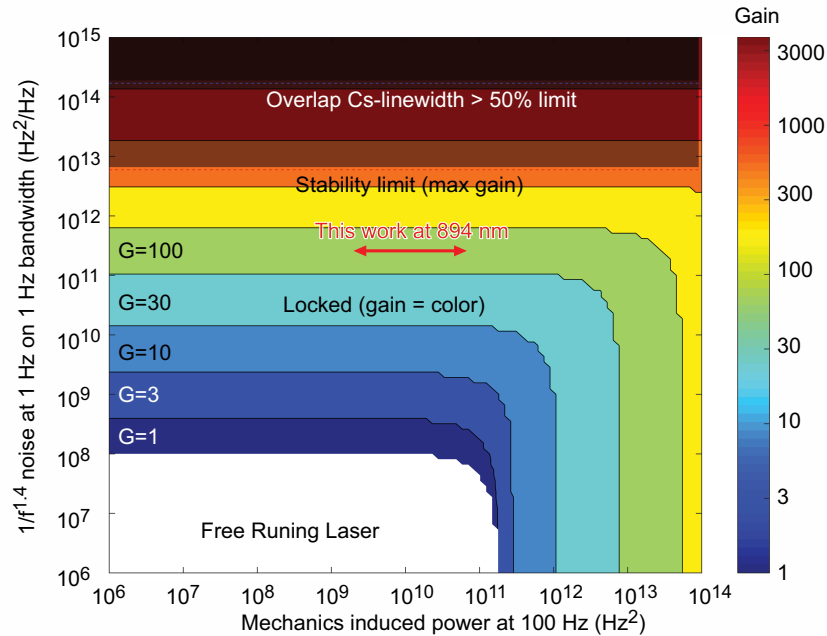


Figure 6.24: Mapping of the required loop gain to achieve the 894 nm LAMA lasers frequency locking under feedback at $\tau_0 = 10$ years on the Cs line (with a 6σ interval of confidence), given a white noise level and a $1/f^{1.4}$ flicker noise level of the laser. The maximum gain limit before loop instability is in gray shaded area. The minimum overlap condition η_{Cs} on the cesium line is the darker gray shaded area

6.5 Conclusion and perspectives

To conclude this theoretical study of the laser modules stabilization on cesium lines, we can mention the limits of this model. It has been built in the small-signal regime around the permanent state, but we cannot rule out a non-linear behavior in the initial transient regime that would lead to an unstable system. It is unlikely though, provided that the laser free-running linewidth is a bit lower than the Cs linewidth, and that the laser is not saturated by the optical power. Also, based on a limited set of data provided by a laboratory set-up of Thales Electron Devices, the noise of the electronic circuits has not been taken into account. It is the same for the atomic discriminator itself and the fluctuations brought by the atomic shot of the beam or the partition noise of the detector. As bold as these assumptions may seem, in practice, these elements do not prevent an efficient locking, as proved by the experimentation: the noise brought by these elements is then negligible in front of the noise of the in-loop laser, falling that the atomic clock would just not work!

Again, the final goal of this part of the clock is to pump efficiently the Cs beam: given the initial specification of our lasers, we are in a comfortable area of the noise-gain map. This is due to both the combination of a low white noise level of the components and an acceptable flicker magnitude. Also, the simulation of a laser spectrum perturbed by unwanted optical feedback confirms the possibility of easy de-locking of the source: if the laser is brought in the coherent collapse regime (see chapter 3), it loses all of its coherence properties and the servo breaks out. Our lasers being relatively more resistant to feedback than other commercial components already tested in this setup, the white noise level is still low even under strong perturbation, which makes them suitable for a safe operation without any optical isolator. If the perturbation arises only locally in the mechanics frequency range, there is still a chance that the servo will survive, provided a minimum level of loop gain: the servo has indeed strong capabilities of noise reduction at these frequencies, because of its high integral correction.

For further optimization, we can imagine to add a *derivative* gain to the loop to correct more efficiently the short-time linewidth. It should be done carefully though: this additional function must remain below the β -line. Concerning the integral gain, there is, in theory, no limit to realize ideal integrators with very high gain at very low frequencies, with passive components.

6.6 Summary

In this chapter, the **in-loop properties of the laser frequency noise** in a servo configuration have been studied. In the atomic clock, the locking of the laser central frequency on a cesium atomic transition is realized by 'dither-locking'. It consists in deriving a frequency discriminator function out of the fluorescence line by modulating locally the laser frequency with a small amplitude. At the top of the line, the amplitude of this response is zero: thus, **it is possible to retrieve an error function calibrated on zero that mirrors the absolute distance of the laser frequency to the atomic transition frequency**. In practice, such scheme can be realized by synchronous demodulation of the modulated current of the laser.

Regarding the loop properties, the frequency noise of the laser in the dither-locking loop can be theoretically rejected, all the more so since the gain magnitude injected in the servo is high. This works until the noise floor brought by the measurement process (fluorescence detection and interpretation) is reached. However, this physical limit is not necessarily reached because increasing the gain will bring the servo close to its **limit of instability**. This point is reached when the phase of the open-loop transfer function of the system reaches -180° for a unitary gain. Thus, the design of the servo has to take into account the mathematical orders and cutoff frequencies of the several components of the loop. Generally, one has better to ensure that the system is (a low-pass filter) of 1st order on the maximum possible bandwidth to repel the critical frequency of the instability point at the highest possible value. In the dither-loop, we have identify that this point corresponds to the cutoff of the detection electronic of the measurement process (photodiode and transimpedance amplifier) which induces a phase change at around $f_c = 10 \text{ kHz}$. So further optimization of the setup would require, for instance, to **enhance the photon collection process out of the cesium beam**: it would induce a higher frequency cutoff (by decreasing the amplifier gain required, for instance) and allow more gain to be injected. In the current configuration, we estimate that the maximum gain allowed is on the order of $G_{max} \simeq 700$, based on the laboratory configuration of Thales Electron Devices.

On the other hand, there exists a minimum gain to inject to ensure a good performance of the setup: the first criterion is to keep the locking on the Cs line for 10 years at least, in spite of the random frequency excursion of the laser, the second is the minimum in-loop linewidth of the laser to reach to have good pumping efficient of the Cs beam. With these constraints, we found the range of laser (intrinsic) noise characteristics that are suitable for the application. It is pointed out, thanks to an analysis based on the β -separation line, that **both the laser white noise level (linked to the Schawlow-Townes limit) and the laser flicker noise magnitude have to be taken into account**. Especially, the LAMA lasers have enough low white noise to stand very comfortably in the security margins of operation. When some unwanted optical feedback perturbs the laser, the class of devices allowed for the application is reduced, but the components developed in this thesis are still eligible for an operation without any optical isolator.

The study has inherent limits in the model used: for instance, the noise in the fluorescence of the Cs brought by the other parts of the setup (atomic shot-noise) has not been taken into account, as well as the noise of the electronics. Though, the experimental evidences (Thales Electron Devices setup) proves that the scheme works, so these perturbations can be neglected in front of the laser intrinsic noise contributions in a first analysis. This clarifies the somewhat ambiguous specifications asked by the final users (originally based on empirical observations) on the linewidth required for the application: on a servo point of view, not all the noise components of the source are equivalent in

the system performances. The low-frequency ones directly impact the long-term lifetime of the servo –it can be enhanced by adding more **integral gain at low-frequencies**– while the high frequency white noise part impacts the short-term linewidth, so the pumping efficiency of the atomic beam. This later part could be better addressed by adding a reasonable amount of **derivative gain at higher frequencies**.

Bibliography

- [Di Domenico 2010] Gianni Di Domenico, Stéphane Schilt et Pierre Thomann. *Simple approach to the relation between laser frequency noise and laser line shape*. Applied optics, vol. 49, no. 25, pages 4801–4807, 2010.
- [Instrument 2009] Texas Instrument. *Transimpedance Considerations for High-Speed Amplifiers - Application report SBOA122*. Rapport technique, 2009.
- [Lucas-Leclin 1998] Gaelle Lucas-Leclin. *Importance des propriétés spectrales des lasers pour les performances des horloges atomiques à pompage optique*. PhD thesis, Université Paris-Sud XI, Orsay, 1998.
- [Milotti 2002] Edoardo Milotti. *1/f noise: a pedagogical review*. arXiv preprint physics/0204033, 2002.
- [Sellahi 2011] M. Sellahi. *Etude et réduction du bruit de fréquence dans les vecsels en cavité externe*. Master's thesis, Université Montpellier II, 2011.
- [Tannoudji 1973] Cohen Claude Tannoudji, Diu Bernard et Laloë Franck. *Quantum mechanics. volume i*. Hermann, 1973.

Epilogue

This part presents the most up-to-date results of stability regarding the performances of the Optical Cesium Frequency Standard (OCFS) described in Chapter 1. The data refers to the study of [Schmeissner 2016] and is reproduced with the courtesy of R. Schmeissner of Thales Electron Devices.

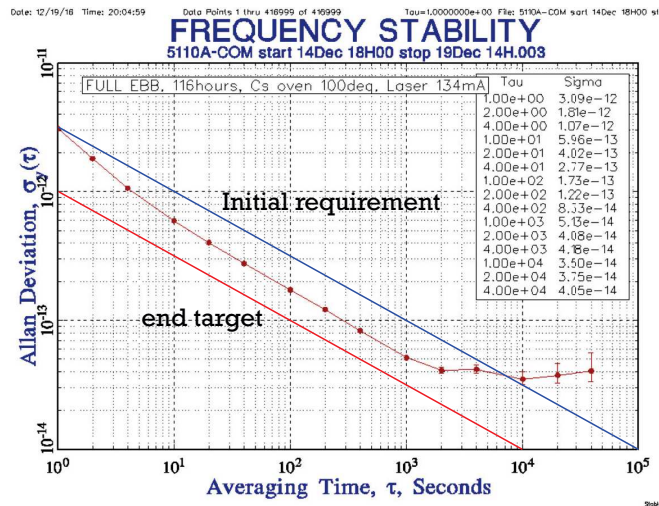


Figure 6.25: Allan Deviation trace of the spatial prototype of the OCFS running with a 894 nm LAMA laser source. It as been recorded by a comparison with a more stable Hydrogen maser. Source: Thales Electron Devices

Figure (6.25) is the Allan Deviation plot of the OCFS prototype of Thales Electron Devices of on-board atomic clocks for the Galileo constellation. The trace was recorded thanks to a sampling operated by a very stable Hydrogen maser of the SYRTE (Paris Observatory). The clock runs with a 894 nm LAMA laser of the 1st run of fabrication. It shows that the initial specifications of the *OSCC* project for the stability where met at the beginning of year 2017. The performances were also better than expected in the mid-term range, allowing to get close to the long-term end-target of the project ($\sigma(\tau = 1 s) = 10^{-12}$). Regarding the long-term stability, further improvements will try to better stabilize the clock at $\tau = 10^4 s$, where the setup is mostly affected by thermal perturbations.

Nevertheless, the proof of concept has been validated for the application, thanks to the development made with these laser sources. Of course, considerable improvements on the stability, either from the use of the source or on the electronics of the setup itself, have to be awaited with this scheme in the coming years. Alternative interrogation schemes (Coherent Population Trapping interrogation on a thermal Cs beam or multi-lines interrogation with a D_1 and a D_2 source) will certainly allow to simplify deeply the current configuration to gain on the manufacturing costs.

Bibliography

- [Schmeissner 2016] R Schmeissner, A Douahi, I Barberau, P Dufreche, N Mestre, M Baldy, N von Bandel, O Parillaud, M Garcia, M Krakowski *et al.* *Towards an engineering model of Optical Space Cs Clock*. In 2016 European Frequency and Time Forum (EFTF), pages 1–4. IEEE, 2016.

Conclusion

The bottom line of this work was to explore the possibilities offered by a single-mode Distributed-Feedback (DFB) semiconductor laser electrically-pumped to address the needs of the high-end technology of the Optical Cesium Frequency Standard. This type of atomic clock has demanding specifications in terms of the spectral purity of the laser source used.

This led us first to consider the building parameters of the laser cavity and their relations with the photon noise in the output beam. It was underlined that this fundamental spontaneous emission noise on the optical frequency, known as the Schawlow-Townes limit, increases with the resonator losses, be they from the internal absorption of the gain medium or because of the outgoing flux of coherent photons. In the meantime, the laser linewidth also decreases with the amount of coherent energy stored in the cavity. In semiconductor media, additional factors broaden this parameter, the most famous being Henry's phase-to-amplitude coupling factor, which accounts for the perturbation of the electrically-pumped medium by the field itself. On the other side, we recognized other 'technical' sources of perturbations of the laser carrier frequency, the strongest one being the internal modulation of the electronic transport in the diode junction. This source, driven by Hooke's crystal lattice parameter, can be contained partially by a very good fabrication quality of the device.

Regarding the technical aspects of the realization of the laser modules, the full conception, from the very beginning of the vertical epitaxial structure definition to the laser chip packaging, was addressed. In practice, we obtained in the first realization single-mode lasers at the D_1 line (894 nm), operating at 70°C, with a high Single-Mode Suppression-Ratio, a good efficiency and an output power above 40 mW. Operation at ambient temperature will be achieved when the new run of epitaxial fabrication, with recalibrated materials of the structure, will be realized. It is worth to point out that the DFB diode lasers, although well-described theoretically since the 1980's, are complex devices that couple tightly many optical, electrical and thermal parameters, which is bound to have consequences on the noise dynamics in the device.

To study the frequency noise of the lasers, we set up a comparative study of some techniques of the literature to measure either the laser heterodyne linewidth or directly the Spectral Density of frequency noise using an optical frequency discriminator. It was shown that this traditional metrology, beyond its difficulty to set up properly, is not suitable to evaluate fully and accurately the laser noise. Indeed, for the sources affected by strong technical perturbations (relatively to the white noise), the related laser linewidth depends on the observation time. Thus, we have developed a new method to measure all the noise parameters at once and in an absolute manner, taking into account this limit. Because of its simplicity of use (it is based on a beat note of two equivalent lasers and a numerical treatment) and its accuracy, it is especially appropriate as an on the shelf method to characterize sources in an industrial context. Finally, using these considerations, we evaluated the linewidths of the first batch of sources to be at 1 MHz for a few ms of observation time, which abide by the specifications of the manufacturers of the clock. We also gave hints to reduce further this value by acting on devices parameters.

Still, we attached a great importance to the link between the 'free-running' laser noise and its performances in an active servo loop that stabilizes its frequency on the cesium lines in the atomic clock. This is why, helped by the control loop theory and a simplified scheme of this 'dither-locking'

system, we proved that the lasers fabricated during this work were suitable for the application, provided a sufficient amount of electronic gain, compatible with the stability of the system, in injected in the servo. We also specified more generally to which extent a laser can be used in the clock setup, regarding its frequency noise characteristics.

We hope that the bird-eye-view of the component to the system outlined in this manuscript will help to find levers of further optimizations of the atomic clock setup.

Publications

- [1] N. von Bandel, M. Myara, M. Sellahi, T. Souici, R. Dardaillon, and P. Signoret. Time-dependent laser linewidth : beat-note digital acquisition and numerical analysis. **Optics Express**, 24(24):27961, November 2016.
- [2] N. von Bandel, M. Garcia, M. Lecomte, A. Larrue, Y. Robert, E. Vinet, O. Driss, O. Parillaud, M. Krakowski, F. Gruet, R. Matthey, and G. Mileti. DFB-ridge laser diodes at 894 nm for cesium atomic clocks. **In the proceedings of SPIE OPTO**, pp. 97552K, March 2016.
- [3] N. von Bandel, M. Garcia, M. Lecomte, A. Larrue, Y. Robert, E. Vinet, O. Driss, O. Parillaud, M. Krakowski, F. Gruet, R. Matthey, and G. Mileti. Al-free active region laser diodes at 894 nm for compact cesium atomic clocks. **In the proceedings of SPIE OPTO**, pp. 93820L, March 2015.
- [4] R. Matthey, F. Gruet, C. Affolderbach, G. Mileti, N. von Bandel, M. Garcia, M. Krakowski, and P. Berthoud. Development and spectral characterization of ridge-DFB laser diodes for Cs optical pumping at 894 nm. **In the 2016 European Frequency and Time Forum (EFTF)**, April 2016
- [5] R. Schmeissner, A. Douahi, I. Barberau, P. Dufreche, N. Mestre, M. Baldy, N. von Bandel, O. Parillaud, M. Garcia, M. Krakowski, et al. Towards an engineering model of optical space Cs clock. **In the 2016 European Frequency and Time Forum (EFTF)**, April 2016

Article I

Time-dependent laser linewidth :
beat-note digital acquisition and numerical analysis

N. von Bandel, M. Myara, M. Sellahi, T. Souici, R. Dardaillon, and P. Signoret.

in Optics Express, November 2016.

Time-dependent laser linewidth : beat-note digital acquisition and numerical analysis

NICOLAS VON BANDEL,^{1,2} MIKHAËL MYARA,^{1,*} MOHAMED SELLAHI,³ TAHAR SOUCI,¹ RÉMI DARDAILLON,¹ PHILIPPE SIGNORET¹

¹IES-UMR5214, 34090 Montpellier, France

²III-V Lab, 91767 Palaiseau, France

³UMR ITAP-IRSTEA, 34196 Montpellier, France

*mikhael.myara@umontpellier.fr

Abstract: We revisit and improve the optical heterodyne technique for the measurement of the laser coherence, by digital acquisition of the beat-note and numerical analysis of the resulting signal. Our main result is that with the same experimental setup we reach the very "short-time linewidth" with the highest accuracy as well as the frequency noise spectrum.

© 2016 Optical Society of America

OCIS codes: (140.0140) Lasers and laser optics; (030.1640) Coherence; (300.6310) Spectroscopy, heterodyne.

References and links

1. A. Schawlow and C. Townes, "Infrared and optical masers," *Phys. Rev.* **112**, 1940–1949 (1958).
2. C. H. Henry, "Theory of the phase noise and power spectrum of a single mode injection laser," *IEEE J. Quantum Electron.* **19**, 1391–1397 (1983).
3. C. H. Henry, "Theory of the linewidth of semiconductor lasers," *IEEE J. Quantum Electron.* **18**, 256–263 (1982).
4. P. Gallion and G. Debarge, "Quantum phase noise and field correlation in single frequency semiconductor laser systems," *IEEE J. Quantum Electron.* **20**, 343–349 (1984).
5. J. Wang and K. Petermann, "Noise analysis of semiconductor lasers with coherence collapse regime," *IEEE J. Quantum Electron.* **27** (1991).
6. J.-P. Tourrenc, P. Signoret, M. Myara, M. Bellon, J.-P. Perez, J.-M. Gosalbes, R. Alabedra, and B. Orsal, "Low-frequency fm-noise-induced lineshape : A theoretical and experimental approach," *IEEE J. Quantum Electron.* **41**, 549–553 (2005).
7. K. Petermann, *Laser Diode Modulation and Noise* (Kluwer Academic Publishers, 1988).
8. L. A. Coldren and S. Corzine, *Diode Lasers and Photonic Integrated Circuits* (Wiley, 1995).
9. A. Yariv, *Quantum Electronics* (Wiley, 1989).
10. K. Iga and H. E. Li, *Vertical-cavity Surface-emitting Laser Devices* (Springer, 2002).
11. D. Derickson, *Fiber Optic Test and Measurements* (Prentice-Hall, 1998), isbn : 0-13-534330-5 ed.
12. J. L. Gimlett and N. K. Cheung, "Effects of phase to intensity noise conversion by multiple reflections on gigabit-per-second dfb laser transmission systems," *J. Lightwave Technol.* **7**, 888–895 (1989).
13. D. M. Baney, P. Gallion, and R. S. Tucker, "Theory and measurement techniques for the noise figure of optical amplifiers," *Opt. Fiber Technol.* **6**, 122–154 (2000).
14. M. Okai, T. Tsuchiya, K. Uomi, N. Chimone, and T. Harada, "Corrugation-pitch-modulated mqw-dfb laser with narrow spectral linewidth (170 khz)," *IEEE Photonics Technol. Lett.* **2**, 529–534 (1990).
15. H. Yamazaki, M. Yamaguchi, and Kitamura, "Spectral linewidth rebroadening in mqw-dfb lds caused by spontaneous emission noise in sch/barrier layers," *IEEE Photonics Technol. Lett.* **2**, 529–534 (1990).
16. M. Ohtsu, M. Murata, and M. Kourogi, "FM noise reduction and subkilohertz linewidth of an algaas laser by negative electrical feedback," *IEEE J. Quantum Electron.* **26**, 231–241 (1990).
17. G. H. Duan and P. Gallion, "Drive current noise induced linewidth in tunable multielectrode lasers," *IEEE Photonics Technol. Lett.* **3**, 302–304 (1991).
18. J.-M. Verdiell, U. Koren, and T. L. Koch, "Linewidth and alpha-factor of detuned-loaded dbr lasers," *IEEE Photonics Technol. Lett.* **4**, 302–305 (1992).
19. W. A. Hamel, M. P. van Exter, and J. P. Woerdman, "Coherence properties of a semiconductor laser with feedback from a distant reflector: Experiment and theory," *IEEE J. Quantum Electron.* **28**, 1459–1469 (1992).
20. H. Ishii, F. Kano, Y. Tohmori, Y. Kondo, T. Tamamura, and Y. Yoshikuni, "Narrow spectral linewidth under wavelength tuning in thermal tunable super-structure-grating (ssg) dbr lasers," *IEEE J. Sel. Top. Quantum Electron.* **1**, 401–407 (1995).
21. R. W. Tkach and A. R. Chraplyvy, "Phase noise and linewidth in an inaaasp dfb laser," *J. Lightwave Technol.* **4**, 1711 (1996).

22. P. Signoret, F. Marin, S. Viciani, G. Belleville, M. Myara, J.-P. Tourrenc, B. Orsal, A. Plais, F. Gaborit, and J. Jacquet, "3.6-mhz linewidth 1.55 μm monomode vertical-cavity surface-emitting laser," *IEEE Photonics Technol. Lett.* **13**, 269–271 (2001).
23. S. Viciani, M. Gabrysch, F. Marin, F. M. di Sopra, M. Moser, and K. H. Gulden, "Lineshape of a vertical cavity surface emitting laser," *Opt. Commun.* **206**(1), 89–97 (2002).
24. P. Signoret, M. Myara, J.-P. Tourrenc, B. Orsal, M.-H. Monier, J. Jacquet, P. Leboudec, and F. Marin, "Bragg section effects on linewidth and lineshape in 1.55 μm dbr tunable laser diodes," *IEEE Photonics Technol. Lett.* **25**, 1429–1431 (2004).
25. C. Lauer and M.-C. Amann, "Calculation of the linewidth broadening in vertical-cavity surface-emitting lasers due to temperature fluctuations," *Appl. Phys. Lett.* **86** (2005).
26. M. W. Fleming and A. Mooradian, "Spectral characteristics of external-cavity controlled semiconductor lasers," *IEEE J. Quantum Electron.* **17** (1981).
27. T. Laurila, T. Joutsenoja, R. Hernberg, and M. Kuittinen, "Tunable external cavity diode laser at 650 nm based on a transmission diffraction grating," *Appl. Opt.* **41**, 5632 (2002).
28. S. Foster and A. Tikhomirov, "Pump-noise contribution to frequency noise and linewidth of distributed-feedback fiber lasers," *IEEE J. Quantum Electron.* **46**, 734–741 (2010).
29. C. Spiegelberg, J. Geng, Y. Hu, Y. Kaneda, S. Jiang, and N. Peyghambarian, "Low-noise narrow-linewidth fiber laser at 1550 nm (june 2003)," *J. Lightwave Technol.* **22**, 57–62 (2004).
30. A. Laurain, M. Myara, G. Beaudoin, I. Sagnes, and A. Garnache, "Multiwatt-power highly-coherent compact single-frequency tunable vertical external cavity surface emitting semiconductor laser," *Opt. Express* **14**, 14631 (2010).
31. M. Myara, M. Sellahi, A. Laurain, A. Garnache, A. Michon, and I. Sagnes, "Noise properties of nir and mir vessels (invited paper)," in *IEEE Proceedings of International Conference on Noise and Fluctuations (IEEE)*, (2013).
32. B. Abbott, R. Abbott, T. Abbott, M. Abernathy, F. Acernese, K. Ackley, C. Adams, T. Adams, P. Addesso, and R. Adhikari, "Observation of gravitational waves from a binary black hole merger," *Phys. Rev. Lett.* **116**, 061102 (2016).
33. S. P. Smith, F. Zarinetchi, and S. Ezekiel, "Narrow-linewidth stimulated brillouin fiber laser and applications," *Opt. Lett.* **16**, 393–395 (1991).
34. T. M. Taczak and D. K. Killinger, "Development of a tunable, narrow-linewidth, cw 2.066- μm Ho:YLF laser for remote sensing of atmospheric CO₂ and H₂O," *Appl. Opt.* **37**, 8460–8476 (1998).
35. S. M. Melle, A. T. Alavie, S. Karr, T. Coroy, K. Liu, and R. M. Measures, "A bragg grating-tuned fiber laser strain sensor system," *IEEE Photonics Technol. Lett.* **5**, 263–266 (1993).
36. F. M. di Sopra, H. P. Zappe, M. Moser, R. Hövel, H.-P. Guggel, and K. G. Gulden, "Near-infrared vertical-cavity surface emitting lasers with 3-mhz linewidth," *IEEE Photonics Technol. Lett.* **11**, 1533–1535 (1999).
37. A. Tikhomirov and S. Foster, "DFB FL sensor cross-coupling reduction," *J. Lightwave Technol.* **25**, 533–538 (2007).
38. J. Morville, D. Romanini, M. Chenevri er, and A. Kachanov, "Effects of laser phase noise on the injection of a high-finesse cavity," *Appl. Opt.* **41** (2002).
39. "8 hints for better spectrum analysis," Agilent Application Note 1286-1.
40. D. Halford, "Infrared-microwave frequency synthesis design : Some relevant conceptual noise aspects," in *Seminar on Frequency Standards and Metrology - Quebec*, (1971), pp. 431.
41. G. Di Domenico, S. Schilt, and P. Thomann, "Simple approach to the relation between laser frequency noise and laser line shape," *Appl. Opt.* **49**, 4801–4807 (2010).
42. N. Bucalovic, V. Dolgovskiy, C. Schori, P. Thomann, G. Di Domenico, and S. Schilt, "Experimental validation of a simple approximation to determine the linewidth of a laser from its frequency noise spectrum," *Appl. Opt.* **51**, 4582–4588 (2012).
43. F. Hooge, T. G. M. Kleinpenning, and L. K. J. Vandamme, "Experimental studies on 1/f noise," *Rep. Prog. Phys.* **44**, 479 (1981).
44. R. J. Fronen and L. K. J. Vandamme, "Low-frequency intensity noise semiconductor lasers," *IEEE J. Quantum Electron.* **24**, 724–736 (1988).
45. L. B. Mercer, "1/f frequency noise effects on self-heterodyne linewidth measurements," *J. Lightwave Technol.* **9**, 485–492 (1991).
46. N. Von Bandel, M. Garcia, M. Lecomte, A. Larrue, Y. Robert, O. Driss, O. Parrilaud, M. Krakowski, F. Gruet, and R. Matthey, "Dfb-ridge laser diodes at 894 nm for cesium atomic clocks," in *SPIE OPTO*, (ISOP, 2016), pp. 97552K.
47. M. Myara, P. Signoret, J.-P. Tourrenc, J.-P. Perez, B. Orsal, and J. Jacquet, "Strongly sub-poissonian electrical noise in 1.55 μm dbr tunable laser diodes," *IEEE J. Quantum Electron.* **40**, 852–857 (2004).
48. C. K. Boggs, A. D. Doak, and F. Walls, "Measurement of voltage noise in chemical batteries," in *49th Proceedings of the 1995 IEEE International Frequency Control Symposium (IEEE, 1995)*, pp. 367–373.
49. C. Ye, *Tunable External Cavity Diode Lasers* (World Scientific, 2004).
50. F. W. King, *Hilbert transforms*, vol. 2 (Cambridge University Press Cambridge, 2009).
51. B. Boashash, "Estimating and interpreting the instantaneous frequency of a signal. i. fundamentals," *Proc. IEEE* **80**, 520–538 (1992).
52. W. H. Press, S. A. Teukolsky, W. T. Vetterling, and B. P. Flannery, *Numerical Recipes in C - The Art of Scientific Computing - Second Edition*, 3rd ed. (Cambridge University Press, 2007).

53. G. Heinzel, A. Rüdiger, and R. Schilling, "Spectrum and spectral density estimation by the discrete fourier transform (dft-fft), including a comprehensive list of window functions and some new flat-top windows." Tech. rep., Albert Einstein Institut (2002).
54. A. E. Siegman, G. Nemes, and J. Serna, "How to (maybe) measure laser beam quality," in *Diode Pumped Solid State Lasers: Applications and Issues (DLAI)*, M. Dowley, ed. (Optical Society of America, 1998), pp. MQ1.
55. L. Mandel and E. Wolf, *Optical Coherence and Quantum Optics* (Cambridge University Press, 1995).
56. B. Saleh and M. C. Teich, *Fundamentals of Photonics* (Wiley Interscience, 1991).
57. A. McLean, C. Mitchell, and D. Swanston, "Implementation of an efficient analytical approximation to the voigt function for photoemission lineshape analysis," *J. Electron Spectrosc.* **69**, 125–132 (1994).
58. J. Olivero and R. Longbothum, "Empirical fits to the voigt line width: A brief review," *J. Quant. Spectrosc. Rad.* **17**, 233–236 (1977).
59. C. Azeredo-Leme, Clock jitter effects on sampling: a tutorial, *IEEE Circuits Syst. Mag.* **11**, 26–37 (2011).
60. R. Boudot and E. Rubiola, "Phase noise in rf and microwave amplifiers," *IEEE Trans. Ultrason Ferr.* **59**, 2613–2624 (2012).
61. O. Llopis, P. Merrer, H. Brahim, K. Saleh, and P. Lacroix, "Phase noise measurement of a narrow linewidth cw laser using delay line approaches," *Opt. Lett.* **36**, 2713–2715 (2011).
62. H. Tsuchida, "Laser frequency modulation noise measurement by recirculating delayed self-heterodyne method," *Opt. Lett.* **36**, 681–683 (2011).
63. M. Myara, N. Von Bandel, and M. Sellahi, "LaserCoherenceAnalyser - DOI:10.5281/zenodo.162952," <https://doi.org/10.5281/zenodo.162952> (2016).

1. Introduction

It is a well known fact that the fundamental linewidth limit of most lasers originates from the spontaneous emission coupled to the lasing mode. This limit is called the "Shawlow-Townes linewidth" [1], enhanced by Henry in the case of semiconductor lasers [2, 3]. This topic of research has been widely discussed in the scientific literature during the 1980-2000 years [4–6] thanks to the development of single frequency laser diodes [7–10], encouraged itself by the rise of fiber optic telecommunications for the world-wide internet network [11]. The laser diodes linewidth is indeed a crucial parameter for the optical fiber telecommunication systems themselves, as it obviously impacts the purity of the signal phase, as well as the intensity noise at the optical receiver [12, 13].

But beyond that, in a more fundamental perspective, these laser components exhibit strong advantages for studying the linewidth, compared to other laser technologies. First of all, they do not exhibit mode-hopping in time, making practical, for the first time, the experimental study of this fundamental limit of laser noise. Moreover, in many cases, their spontaneous emission level is strong, masking the contributions of most other technical fluctuations (cavity length or index variations) to the linewidth. This motivated the production of a large set of studies and data on these devices [14–25].

As a result, because the noise of these components originates mainly from the spontaneous emission, which is theoretically a pure white noise, the value of the linewidth is usually considered to be stable whatever the time during which its measurement occurs. However, lasers emitting a small amount of spontaneous emission (such as edge-emitting extended cavity lasers [26, 27], fiber lasers [28, 29], vertical external cavity surface emitting lasers [30, 31], and other kinds ...) lead to laser spectra dominated by other sources of noise (that we call here "technical noise sources": these are typically mechanical, thermal or carrier-induced).

Unfortunately, in that case, the linewidth depends strongly on the observation time. This fact raises theoretical problems as well as experimental ones, which are usually incompletely addressed in the literature. Nowadays, this issue has to be addressed regarding the increasing number of narrow linewidth lasers developed, motivated by new kinds of applications, mainly in the field of optical sensors [32–38].

In this paper, we intend to provide a better understanding as well as experimental techniques to overcome the limitations of the standard metrology.

2. Limits of the standard metrology of the linewidth

Concerning the experimental techniques, the metrology of the linewidth classically relies on the so-called heterodyne set-up: the beams of two identical lasers are superimposed spatially, and the frequency of the lasers is adjusted to generate a beating at a frequency which is low enough to be observable with radio-frequency (RF) instrumentation. The resulting beam then falls on a photodiode that generates a beat-note in the radio-frequency domain which is in turn analyzed thanks to a sweeping (superheterodyne) RF spectrum analyzer [39] (see Fig.1).

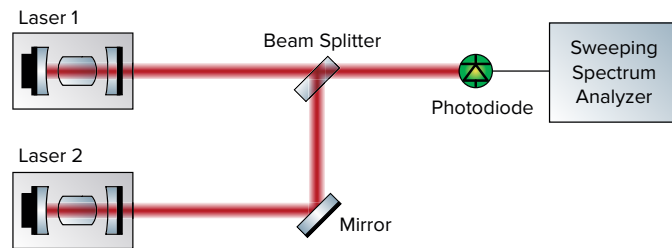


Fig. 1. Basic Heterodyne Set-up.

Unfortunately, these spectrum analyzers do not allow to study easily the time dependency of the linewidth, because of the time required to sweep across the RF spectrum, which cannot usually be quicker than 1 ms in practical cases. There is an additional problem: using this device, the data obtained cannot be considered to be a snapshot of the laser spectrum, because all the points of such spectrum are not evaluated accurately at the same time due to the sweeping of the resolution filter [39] (Fig. 2).

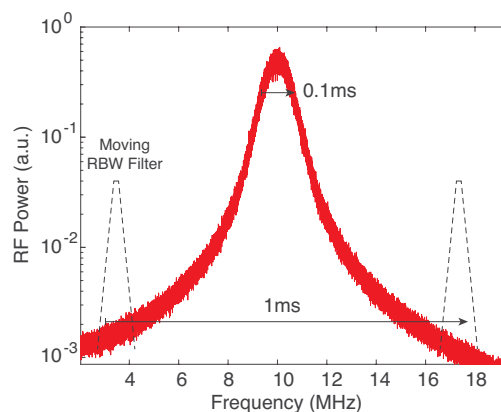


Fig. 2. Sweeping (superheterodyne) RF spectrum analyzer at work: the resolution filter sweeps in time across all the frequencies to obtain the whole spectrum. The spectrum does not reflect a specific timeframe.

This comes from the fact that acquisitions obtained with this kind of analyzer assume that the spectrum remains stable during the whole sweeping, which is not true with laser lines perturbed by technical noise sources. Thus, the profile acquired is distorted by the highly non-linear transfer function of the spectrum analyzer, losing accuracy on the spectral shape itself.

Finally, it is clear that in some cases, the time-limited linewidth may change at each acquisition, even for a constant timeframe. A telling example is the case of frequency fluctuations originating

from mechanical vibrations, which are typically sine-wave shaped in time (they usually find their origin in mechanical resonances). One will easily see that the linewidth is not constant between repeated experiments, given that the RMS frequency fluctuation intercepted in the corresponding time window changes, as depicted in Fig. 3.

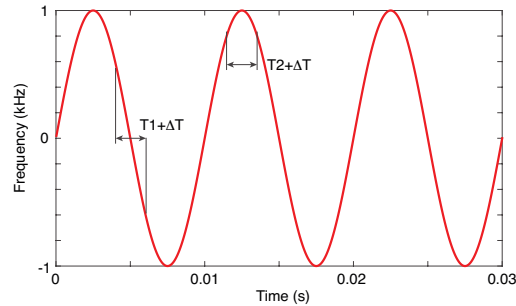


Fig. 3. Frequency variations induced by typical mechanical noise. In this case, the RMS value is not stable as a function of the starting time T_i of the experiment.

Formally written, the value of:

$$\sqrt{\frac{1}{\Delta T} \int_{T_i}^{T_i+\Delta T} \sin^2(2\pi f_M t) dt} \quad (1)$$

is obviously not constant as a function of T_i nor as a function of ΔT (Here, T_i is the time at the beginning of the experiment, ΔT the duration of the experiment, and f_M the frequency of the considered mechanical oscillation). For that reason, such linewidth can only be given in statistical terms over repeated measurements, such as average value and standard deviation.

Due to these metrological limits, the experimenters try to estimate the laser linewidth from frequency noise measurements. It is an interesting idea because thanks to a frequency noise spectrum, they can pinpoint the characteristic time associated with each noise source and obtain much more information than with a single-shot heterodyne measurement. In this field, various works are reported [7, 40], but the most useful and interesting one, to our knowledge, has been performed by Di Domenico et al. by applying the β -separation line theory to the study of the laser linewidth [41, 42]. This is a method of calculating a time-dependent linewidth from a power density spectrum of frequency noise. Whereas it is reliable in many practical cases, this approach has two drawbacks: first of all, it relies on frequency noise measurements, which require quite complex set-ups and are not so easy to calibrate accurately. Secondly, the computation of the linewidth through this process requires approximations that can lead to inaccurate results.

This can be explained by the fact that linewidth metrology and the associated signal analysis were imagined when the available RF instrumentation was far less developed than they are today. It is now possible to acquire the heterodyne beat-note in the time domain thanks to the emergence of high-speed data acquisition systems at quite low cost (compared to RF spectrum analyzers). This beat-note contains obviously all the noise information traditionally obtained by indirect ways. In the work described here, we propose to use modern widespread data acquisition systems (high performance samplers) and numerical signal analysis to perform a more accurate and more powerful study of the beat-note obtained with the heterodyne set-up (Fig. 4), enabling to overcome the already-discussed drawbacks of the methods proposed in the state-of-the-art.

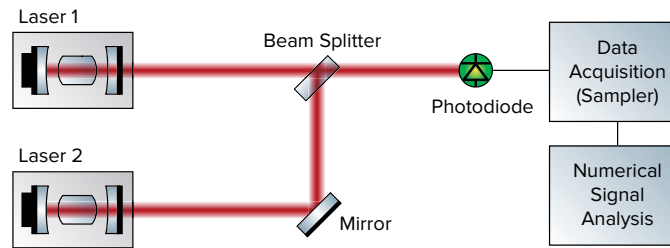


Fig. 4. Heterodyne Set-up proposed in this work: use of a sampler and numerical signal analysis.

3. Data treatment through signal analysis: an overview

In contrast to what is usually reported in the scientific literature, our approach consists in performing numerical processing to the acquired time-domain beat-note signal in order to extract the phase fluctuation information in terms of power spectral density and linewidth. The associated theoretical description is summarized in Fig. 5, that displays the attainable physical quantities as well as the mathematical relationships that exist between them. The numerical acquisition of the time-domain beat-note is the central entry point. These mathematical relationships are not new and are very well understood in the signal analysis literature. However, in the context of laser study, they are generally taken as a pure theoretical basis and not used in practice under their numerical form in order to be applied directly on recorded signals: this is precisely what we intend to propose here.

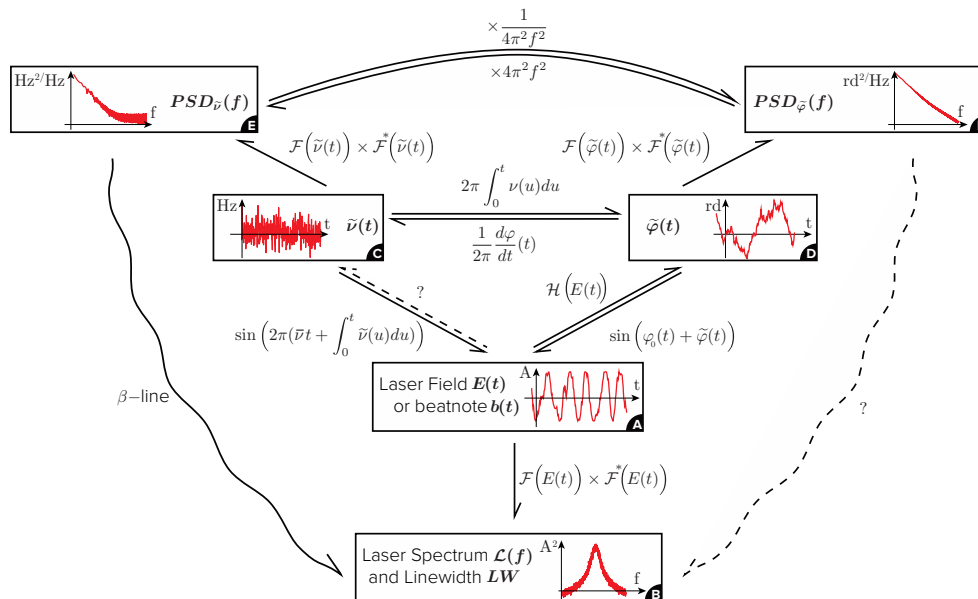


Fig. 5. Summary of the relevant signals and the mathematical relationships between them. No arrow is for no possible path. Dashed arrow is for no conceptual impossibility but not reported in literature. Wavy arrow is for possible path with approximations.

Frequency Noise: By sampling the beat-note, it is possible to extract the instantaneous phase in the time-domain thanks to the numerical Hilbert transform \mathcal{H} . It opens the study of the frequency noise and related spectral densities with the classical approach, by following the path A→D→C→E in Fig. 5. Thanks to this procedure, we get more comfortable experimental conditions than with traditional frequency noise measurement systems, because the heterodyne set-up offers all the benefits of a coherent detection: we work with a high magnitude signal (the beat-note), which is weakly sensitive to the background noise of the instrumentation or to the RIN (Relative Intensity Noise) of the laser itself, which are usual limits of the methods exploiting frequency discriminators. Moreover, the calibration of the frequency noise spectrum does not rely anymore on the evaluation of the frequency discriminator slope, and there is thus no requirement for any calibration process.

Time-Dependent Linewidth: Beyond that, the acquisition of the beat-note opens the access to a range of meaningful information. The laser spectrum may now be assessed over different timeframes, simply by computing the Fourier transform \mathcal{F} over sub-samples of various lengths. Now it is simply the A→B path in Fig. 5 that we have to follow. This triggers the extraction of valuable statistics about the linewidth, which may now be calculated from various sub-samples, as depicted in Fig. 6. In particular, the average, as well as the associated standard deviation, can be brought to light.

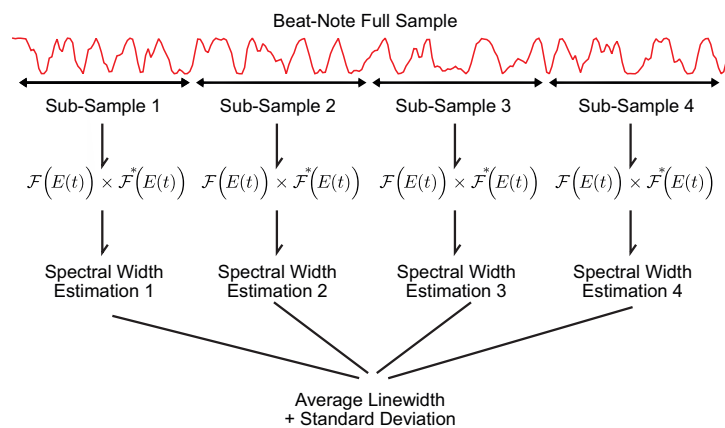


Fig. 6. Beat-note sampling and short-time linewidth estimation. Thanks to the change of the length of the sub-sample, a time-dependent linewidth study is possible.

Such way of exploiting signal analysis on the same beat-note sample makes available in one go various informations that would normally require different experimental set-ups. Moreover, because all these processings are performed on the same data source, the results can only be consistent between them.

About the acquisition of the beat-note itself, in numerous practical cases, it is difficult to maintain the beating of two lasers over long durations in a too-confined spectral span. Thus, the sampled beat-note must be set at a quite high frequency, which requires a high sampling frequency, typically in the $100 \text{ MHz} - 1 \text{ GHz}$ range. To access the statistical studies (averages of power-spectral densities, average and standard deviation of the linewidth, etc), long duration time-samples are required. For that reason, a wide amount of memory is mandatory, usually 10^8 to 10^9 samples, which is possible today with a modern desktop computer embedding some *Go* of RAM.

4. Experimental work: configurations under study

4.1. Configuration 1: DFB-SC for atomic-clock systems

The first configuration used to check the validity of our approach consists in studying the beating of two similar "Distributed FeedBack Semiconductor laser diodes (DFB-SC)". The noise profile of the optical field emitted by these devices is generally affected by two main components.

The first one is linked to the –cold– optical cavity linewidth through the Schawlow-Townes limit, enhanced by a multiplying factor α_H known as the Henry factor [2, 3]. This correction arises from the perturbation of the refractive index of the gain medium through the gain change with carrier density fluctuations in this medium. The resulting laser lineshape is Lorentzian [1].

The second component of the noise spectral density is related to the electrical nature of the pumping process. A very fundamental consequence of this is the existence of a carrier noise occurring in various locations of the component. The most fundamental part of this noise (which is thermal noise due to the equivalent electrical resistance of the device) does not impact the optical field. Unfortunately, some additional transport mechanisms, due to inhomogeneities in the semiconductor crystal, impact the noise at low frequencies [43]. Even with the cleanest fabrication processes, the "1/f type" noise seems to be unavoidable and is always observed [44]. Its contribution to the linewidth is known to be Gaussian [7, 45]. The laser spectrum resulting from these two contributions has a "Voigt Profile", which is the result of the convolution between a Lorentzian and a Gaussian spectrum.

As a case study, compact modules emitting at 894nm – which corresponds to the *D1* transition line of the Cesium 133 – can be used to realize the Optical Cesium Frequency Standard, a type of compact atomic clock which allows better short-term stability than its magnetic counterpart [46]. In such apparatus, the stability of the clock is known to depend on the noise characteristics of the pumping laser. In the present case, the GaAs DFB-SC of 2 mm–long cavities are used at a 40 mW output at the Cesium *D1* line. The measurements are done on a packaged version of the diodes that includes thermal monitoring and regulation. In particular, the beat-note is realized with two lasers of equivalent first-order characteristics.

During the experiments, the two laser diodes are biased using a set of batteries and low-noise resistors to perform the voltage to current conversion. The noise of the resulting laser driver is much lower than the intrinsic electrical noise of the laser diode itself [47, 48]: this ensures that the noise sources observed during the experiments are intrinsic to the laser components and are not due to some environmental perturbations. The noise analysis coming from these components is thus designed to give a reference measurement using a class of components which is well known in the literature. Also, it enables an accurate estimation of the impact of the 1/f noise on the linewidth.

4.2. Configuration 2: DFB-FL and ECDL

To expand this study, we investigated the noise coming from the beating between a DFB Fiber Laser (DFB-FL) [28] and a single-frequency External Cavity Diode Laser (ECDL) [49], both operating in the telecommunication window (1530 nm – 1560 nm for the ECDL, 1553 nm for the DFB-FL). Here, the DFB-FL spectrum can be identified as a Dirac peak compared to the ECDL, as its frequency noise is known to be ultra low, exhibiting FWHM (Full Width Half Maximum) linewidth close to 10 kHz.

The DFB-FL involved here is a commercial device by IxFiber. It is ≈ 5 cm long and is pumped by a battery-biased low power EDFA (Erbium-Doped Fiber Amplifier) pump (< 300 mW); the emitted power is close to 100 μ W for 150 mW pump power launched. The packaging ensures a very small contribution of mechanical vibrations on the linewidth.

The ECDL is a refurbished OSICS ECL Model 1560 biased through the electricity network. It is an interesting kind of laser to study because its spontaneous emission noise is known to be

quite low (compared to DFB-SC) but due to its external cavity, it may experience some cavity length fluctuations originating from mechanical noise, leading to frequency variations in time. The emitted power is in the 10 mW range over the whole tuning capability of the laser.

4.3. Configuration 3: two DFB-FL

Some additional results are obtained with the beating of two DFB-FL identical to the one described in the previous section. Once again, the pumps of these two lasers were biased using the set of low-noise batteries and resistors already described in section 4.1.

5. Frequency noise

The first part of the study is the frequency noise of each laser configuration, obtained from the beat-note and the application of the process described in §3.

5.1. Theoretical Background

As mentioned above, the starting point is the time domain sample of the beat-note signal, $b(t)$. It is a real-valued function and can be written as:

$$b(t) = a(t) \times \cos(\varphi(t)) \quad (2)$$

where, $a(t)$ and $\varphi(t)$ are the instantaneous amplitude and phase of the signal.

The so-called analytic signal associated with the real-valued signal $b(t)$ can be constructed using the Hilbert transform \mathcal{H} as follows [50]:

$$b_a(t) = b(t) + j\mathcal{H}[b(t)] \quad (3)$$

the quantities $a(t)$ and $\varphi(t)$, accounting for the demodulated magnitude and phase of $b(t)$, are then given by, respectively: $a(t) = \sqrt{b(t)^2 + \mathcal{H}[b(t)]^2}$ and $\varphi(t) = \arctan[\mathcal{H}[b(t)]/a(t)]$. Using this representation, the rate of change of $\varphi(t)$ is the instantaneous frequency of the beat-note. Without loss of generality, it can be written as [51]:

$$\nu(t) = \frac{1}{2\pi} \times \frac{d\varphi(t)}{dt} \quad (4)$$

$$= \bar{\nu} + \tilde{\nu}(t) \quad (5)$$

where $\bar{\nu}$ is the central frequency of the beat-note, and $\tilde{\nu}(t)$ represents the noise contribution. Hence, the power spectral density (PSD) of the frequency noise of the laser can be calculated thanks to the Fourier transform of the autocorrelation function:

$$PSD_{\nu}(f) = \mathcal{F} \left(\lim_{T \rightarrow \infty} \frac{1}{2T} \int_{-T}^{+T} \tilde{\nu}^*(t) \tilde{\nu}(t + \tau) dt \right) \quad (6)$$

For computation time reasons, it may be better not to evaluate the autocorrelation function directly. Fortunately, this expression can find another form, entirely based on the Fourier transform [52]:

$$PSD_{\nu}(f) \propto \mathcal{F}(\tilde{\nu}(t)) \times \mathcal{F}^*(\tilde{\nu}(t)) \quad (7)$$

where $*$ is the conjugate complex operator. This expression behaves well in the numerical world, as the time required for the autocorrelation computation (Eq. 6) is proportional to N^2 for a N -samples long signal, while the one required for the Fast-Fourier-Transform (FFT) based expression in (Eq. 7) is only proportional to $N \times \log_2(N)$ [52] for the same signal length. Averaging a given amount of such spectra with a properly scaled FFT transform [53] leads to the expected $PSD_{\nu}(f)$ estimation with the required magnitude accuracy.

5.2. Experimental validation of our technique

In order to validate our approach, we compared the results obtained with our technique to the ones recorded through a direct demodulation interferometer, here a fiber optic Michelson, depicted in Fig. 7. The experiments were carried out with the two DFB-SC lasers (configuration 1) developed for the Cesium atomic clock.

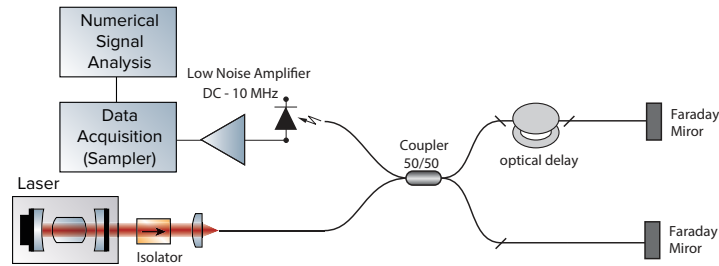


Fig. 7. Michelson-Based Frequency Noise set-up.

As the beat-note contains the noise contributions of the two lasers, the frequency noises of the two DFB-SC sources were measured directly and then added to be compared to the output given by the Hilbert demodulation. The result is shown in Fig. 8. A very good matching between the two techniques is observed.

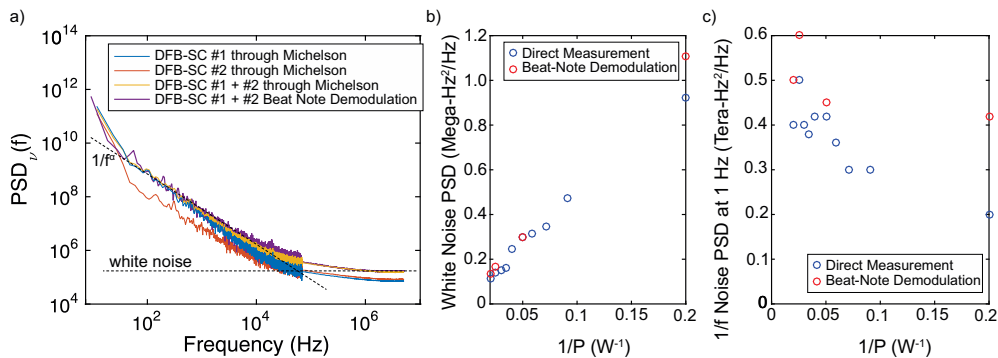


Fig. 8. Frequency noise spectrum obtained from Michelson experiments and beating experiments for the DFB-SC (each close to $40mW$). The $1/f^\alpha$ noise part usually comes from electrical transport phenomena [43], whereas the white noise part comes from the spontaneous emission (Shawlow-Townes-Henry).

5.3. ECDL and DFB-FL results

The result of the beat-note demodulation process for these lasers is given in Fig. 9. Beyond the fact that this operation can be done on a variety of lasers, these data will be useful for a better understanding of the linewidth results to come.

As expected, the strongest contribution in the case of DFB-FL is the low-frequency $1/f^\alpha$ noise originating from the thermal fluctuations induced by the pump intensity noise, with some feeble mechanical contributions in the $100 Hz - 1 kHz$ range.

In the case of the ECDL/DFB-FL beating, the noise levels exhibited lead to the expected conclusion that the DFB-FL noise level can be neglected, and that the beating is representative

of the ECDL alone. Concerning the ECDL, Fig. 9 shows that the strongest contribution to the noise is due to mechanical variations in the $100\text{ Hz}-1\text{ kHz}$ range. Additional pollution comes in the $10\text{ kHz}-1\text{ MHz}$ range from the switching power supply. At higher frequencies, the white noise coming from spontaneous emission is quite low ($\approx 10^4\text{ Hz}^2/\text{Hz}$).

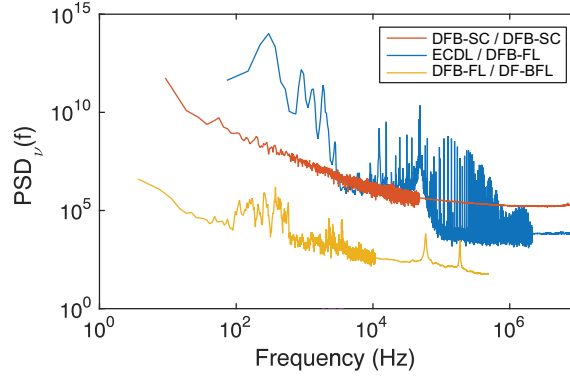


Fig. 9. Frequency Noise spectra obtained from DFB-SC, ECDL and DFB-FL beating.

6. Time dependent linewidth of the beat-note

6.1. Theoretical background

The linewidth is obtained from the power spectrum of the beat-note, and computed thanks to the Fourier transform of the autocorrelation function:

$$\mathcal{L}(f) = \mathcal{F} \left(\lim_{T \rightarrow \infty} \frac{1}{2T} \int_{-T}^{+T} b^*(t)b(t + \tau) dt \right) \quad (8)$$

This spectrum is only defined for an infinite observation time, which is not compatible with realistic experimental conditions. We define then a short-time spectrum, computed from a beat-note $b_{T_i, \Delta T}(t)$ existing over a time-window ΔT starting at the time T_i :

$$\mathcal{L}_{T_i, \Delta T}(f) = \mathcal{F} \left(\lim_{T \rightarrow \infty} \frac{1}{2T} \int_{-T}^{+T} b_{T_i, \Delta T}^*(t)b_{T_i, \Delta T}(t + \tau) dt \right) \quad (9)$$

Again, as it is better to avoid the evaluation of the autocorrelation function numerically, we use another form of this expression:

$$\mathcal{L}_{T_i, \Delta T}(f) = \mathcal{F} \left(b_{T_i, \Delta T}^*(t) \right) \times \mathcal{F} \left(b_{T_i, \Delta T}(t) \right) \quad (10)$$

We now have to find an estimator for the spectral width. Unfortunately, exploiting the FWHM, as it is very usual in the literature, is not relevant here. Indeed, if we have a look to Fig. 10(b) showing the spectrum of an ECDL obtained over a quite long integration time ($\approx ms$), we can easily assert that the strongest part of the laser line fluctuation is not contained in the FWHM but certainly in the pedestal, and thus the FWHM indicator does not accurately report the real size of this signal in the Fourier space.

The question of the quantification of the width of a signal has been very often considered in the scientific literature, and in various domains. In the field of lasers, we can notice that A.E. Siegman examines the problem of the width of the spatial (transverse) modes in a very interesting document [54]. At the end of his article, Siegman concludes that it is "maybe" relevant

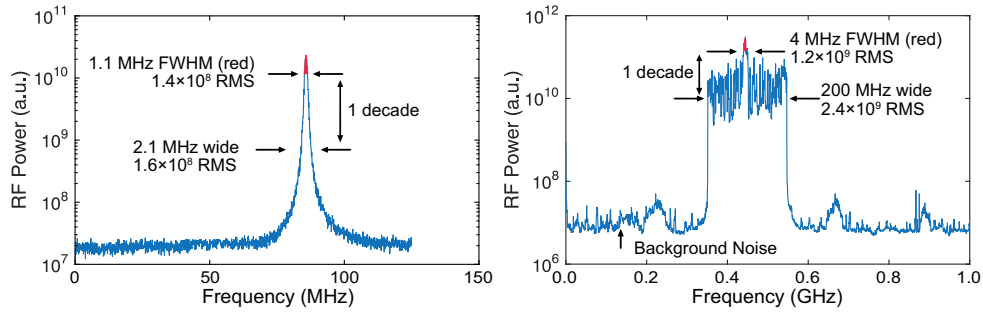


Fig. 10. Relevance (a) and irrelevance (b) of the FWHM depending on the spectral shape. a) case of a semiconductor DFB: the width and the associated RMS value do not change too much over one decade of magnitude. b) case of an ECDL: the width and associated RMS value changes dramatically in the same conditions.

to use the second order momentum instead of the FWHM. In the case of spatial modes, which are usually combinations of Gaussian distributions, it works very well. Unfortunately, in the case of laser spectra, such a definition cannot be used. Indeed, a laser lineshape has always a Lorentzian contribution [22] and none of the high order moments (>1) can be evaluated for such case.

As the goal is to compare very different laser technologies, we propose here to use the spectral width definition derived from the coherence time, as described in the fundamental work of Mandel and Wolf on the optical coherence [55, 56] :

$$\Delta\nu_{T_i, \Delta T} = \frac{\left(\int_0^{+\infty} \mathcal{L}_{T_i, \Delta T}(f) df \right)^2}{\int_0^{+\infty} \mathcal{L}_{T_i, \Delta T}^2(f) df} \quad (11)$$

Contrary to the FWHM, this definition depends on the whole spectrum and does not neglect the impact of some spectral components. Moreover, it shows sturdiness because it is defined for all the usual spectral shapes (Lorentzian, Gaussian, Voigt, Rectangular, ...).

In the numerical treatment performed here, we compute, for each targeted ΔT , the average :

$$\overline{\Delta\nu_c} = \frac{1}{M} \sum_{i=1}^M \Delta\nu_{T_i, \Delta T} \quad (12)$$

over the M available sub-samples, as well as the uncertainty using the standard-deviation:

$$\Delta\nu_c = \overline{\Delta\nu_c} \pm \frac{1}{2} \sqrt{\frac{1}{M} \sum_{i=1}^M (\Delta\nu_{T_i, \Delta T} - \overline{\Delta\nu_c})^2} \quad (13)$$

by exploiting all the possible sub-samples from the signal $b(t)$. To facilitate the comparisons with existing data, Table 1 links $\Delta\nu_c$ to the FWHM for usual spectral shapes.

6.2. Experimental Results

We display in Fig. 11 the evolution of $\Delta\nu_c$ calculated thanks to the process described in §6.1 for the beating between an ECDL and a DFB-FL. This experiment is the most iconic of our work because the ECDL noise contains all the usual contributions (mechanical, $1/f$ and white noise) to the linewidth (Fig. 9).

This graph shows three main trends:

Table 1. Relations between standard FWHM and $\Delta\nu_c$

Shape	FWHM
Lorentzian	$\pi\Delta\nu_{T_i,\Delta T}$
Gaussian	$\Delta\nu_{T_i,\Delta T}/\sqrt{2\ln 2\pi}$
Rectangular	$\Delta\nu_{T_i,\Delta T}$
sinc^2	$\approx \Delta\nu_{T_i,\Delta T}/1.7$

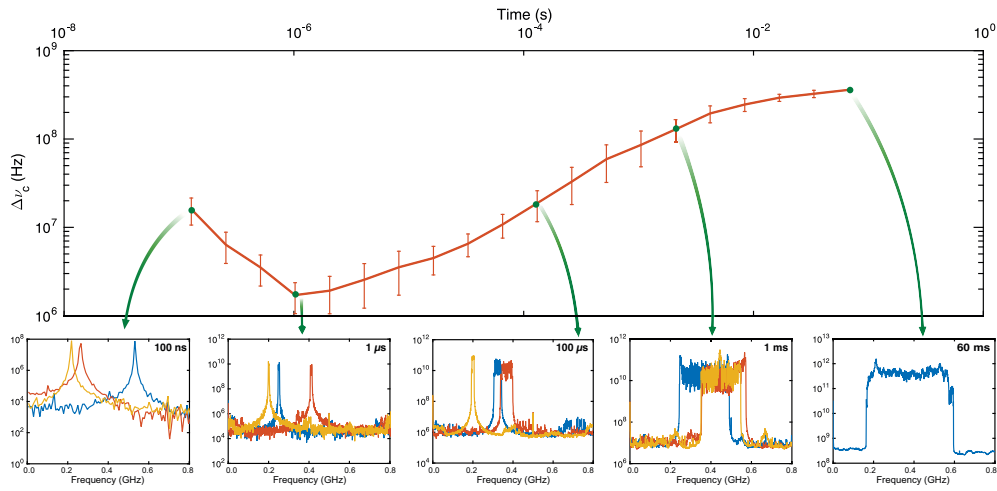


Fig. 11. Estimated $\Delta\nu_c$ for the ECDL/DFB-FL experiments as a function of the beat-note time sample length. The main curve is the average value and the error bars are the standard deviation over 128 samples up to 1 ms. Above this duration, the beat-note sample size imposes the amount of averages to decrease, down to a single full-size sample for the last point at 60 ms. In the insets, various spectra have been displayed to show the instability of the central frequency and of the linewidth due to mechanical fluctuations; the vertical scale of the insets is the RF power in arbitrary unit.

- for the shortest integration times ($< 1 \mu\text{s}$), the linewidth estimation is dominated by the Fourier limit: the time window is small and the contribution of the frequency noise is much lower than the Fourier uncertainty. In that case, all the linewidth spectra are intrinsically convoluted with a sinc^2 which $\Delta\nu_c$ width evolves like $1.77/\Delta T$, where ΔT is the sample length in time. As the time window increases, the associated linewidth decreases.
- for longer times, the frequency noise of the laser becomes much more significant. The linewidth increases quickly up to the $\sim 0.1 \text{ ms}$ observation time, mainly because this time window allows to integrate an increasing part of the $1/f$ and mechanical contributions, which characteristic time is also in the ms range (see Fig. 9). This behavior can be understood from the insets: for times below $10 \mu\text{s}$, the lineshape is always Lorentzian, demonstrating that the spontaneous emission noise dominates. Starting at $100 \mu\text{s}$, the lineshape contains some top-hat contribution, which renders the strong mechanical fluctuations. In fact, this shape is close to the one of the Fourier Transform of the sum of Bessel functions of the first kind. Such form arises from the fact that the laser sine wave function

is modulated in frequency by additional mechanical sine waves:

$$b(t) = A \cos(2\pi f_b t + \beta \sin(2\pi f_M t)) = A \sum_{n=-\infty}^{+\infty} J_n(\beta) \cos(2\pi(f_p + n f_M)t).$$

where f_b is the beating frequency and $J_n(\beta)$ the n^{th} Bessel function of the first kind.

- Then, for times > 0.1 ms, the huge mechanical contribution is fully integrated and the linewidth begins to saturate as a function of the integration time. For even longer times, the linewidth may keep on increasing due to $1/f$ noise (due to memory limitations in the data acquisition card, we were not able to explore further).

To explore the impact of $1/f$ noise, we also focused on the DFB-SC beating configuration, as shown in Fig. 12. For these experiments, we calculated Δv_c and extracted from the same data the Lorentzian and Gaussian linewidth FWHM (resp. Δv_L and Δv_G) thanks to a robust automated fitting process exploiting an analytical accurate approximation of the Voigt function to reduce the computation time [57]. Just as for Δv_c , the average and standard deviation over a large number of samples were performed. The corresponding Voigt profile FWHM was calculated thanks to the empirical formula: $\Delta v_V \approx 0.5346\Delta v_L + \sqrt{(0.2166\Delta v_L^2 + \Delta v_G^2)}$ according to [58].

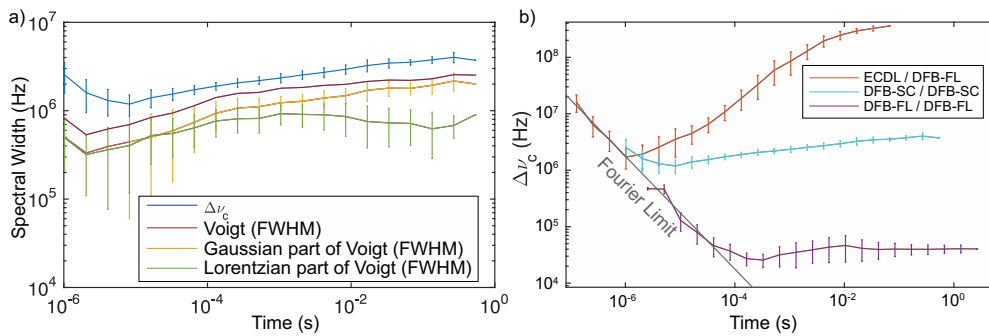


Fig. 12. a) Spectral width of the DFB-SC beating and comparison of the Δv_c criterion with the Voigt profile fitting. b) Δv_c for configurations 1, 2 and 3.

The global tendency is the increase of the Gaussian linewidth as a function of time, which is expected since an increasing part of $1/f$ noise is integrated with increasing times.

Finally, if we add the data measured on DFB-FL, we end with the results shown in Fig. 12(b). It states that a wide variety of lasers can be explored using this method, from low to high coherence.

6.3. Discussion: comparison with β -separation line approach

To our knowledge, the most interesting work concerning the short-time linewidth was published by Di Domenico et al. [41], who used the β -separation line theory to the laser linewidth computation. It is a process that defines which part of the noise spectrum has a significant contribution to the FWHM linewidth. It is based upon the identification of the "slow modulation area", defined by comparing the noise level to the β -separation line for each frequency of the spectrum, as shown on an example in Fig. 13(a). Among the points discussed in his article, Di Domenico's work confronts a very challenging problem: the time-dependence of the linewidth in the case of $1/f^\alpha$ ($1 < \alpha < 2$) noise, and more generally in [42], the time-dependence due to any noise of arbitrary shape. In this approach, the main source of inaccuracy is due an approximation.

But this approximation was unavoidable because there was no other way than introducing there an assumption to obtain the convergence of the analytical calculus in the case of $1/f^\alpha$ noise. The assumption is that, to estimate the linewidth over a duration ΔT , the lowest frequency integrated in the noise spectrum is chosen to be $1/\Delta T$, and thus any event faster than ΔT is not taken into account. Unfortunately, for the reasons illustrated by Eq. 1 and Fig. 3, this choice may lead to strong inaccuracies in the linewidth computation in the case of strong spectral components in the low frequency domain. Following this idea, we compare our numerical approach - which is not based on such an approximation - to the results obtained by the β -line analytical approach, in the case of the three previous and already discussed experimental configurations. This is what is shown in Fig. 13: in part a), the frequency noise spectra and the "slow modulation area" (filled areas) for a fixed ΔT as described in [42] ; part b), the corresponding time-dependent linewidths according to the β -separation line, as well as the one obtained with our numerical treatment.

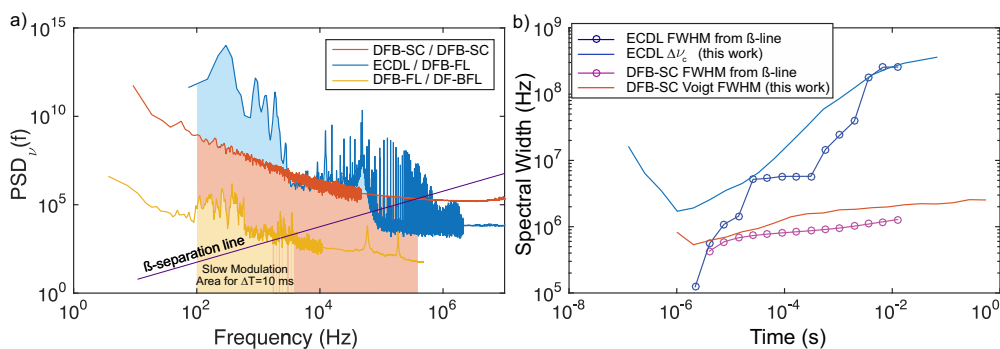


Fig. 13. a) β -separation line illustration, the slow modulation area (filled) is represented for $\Delta T = 1 \text{ ms}$. b) Time-dependent linewidth computed thanks to the numerical methods proposed here, compared to the β -separation line approach.

If the β -line computation leads globally to a good estimation of the laser FWHM, we observe three main drawbacks:

- The β -separation line does not take into account the Fourier Limit, and gives quite optimistic results in the case of the shortest times.
- Also, it can lead to strong inaccuracies in the case of lasers dominated by mechanical noise. An example of this fact is given by the ECDL results in Fig. 13(b). In this plot, the $\Delta\nu_c$ and FWHM values can be directly compared for times $> 1 \text{ ms}$ (according to Table 1) because the lineshape is close to a top-hat in this range. In this context, we notice that at 0.3 ms , the estimation made by the β -separation line process is at least 5 times more optimistic compared to the one obtained with our approach.
- Finally, observing the DFB-SC results in Fig. 13(b) leads to the conclusion that the FWHM estimation through the β -separation line process in the case of lasers dominated by $1/f$ noise leads also to quite optimistic results, with a factor close to 2 on the linewidth.

7. Sensitivity limit

In this section we want to discuss the ultimate sensitivity limits of this set-up. Of course, because it is based on RF instrumentation, it demonstrates ultra-low absolute noise limits compared to usual optical sources.

Firstly, the set-up is limited by the jitter of the acquisition card clock [59]. The main impact is a contribution to the magnitude of the background noise. One of the contributions of this

jitter-originated noise is frequency-dependent, and may thus lead to choose optimised conditions for the data acquisition. This noise occurs like an additive noise $\epsilon^\bullet(f)$ appearing on the sampled data. Its spectrum is given by the convolution between the clock jitter spectrum $\Delta T(f)$ and the spectrum of the signal to be sampled :

$$\epsilon^\bullet(f) = j2\pi f \mathcal{F}(b(t)) * \Delta T(f) \quad (14)$$

Because of the proportionality with f , we should choose the smallest possible beating frequency (but of course high enough to contain the total laser frequency drift during the time-window of the measurement), and thus avoid to work beyond the Shannon frequency. This contribution to background noise of course limits a few the dynamics of the beat-note spectrum.

Secondly, the full span background noise may be a limit for the frequency noise measurement at high Fourier frequencies. According to [60], background intensity noise appears like additional phase noise. For a white background voltage noise, the resulting frequency noise is given by :

$$PSD_f^\bullet = 4\pi f^2 \frac{PSD_\epsilon^\bullet}{V_0^2} \quad (15)$$

where PSD_f^\bullet is the frequency noise (in Hz^2/Hz) due to the voltage noise PSD_ϵ^\bullet (in V^2/Hz), and V_0 the RMS value of the beating voltage. So, the full span background voltage noise spectrum contributes to the measured frequency noise spectrum at high frequencies whatever its origin (laser RIN, amplifier noise, data acquisition card jitter). We have to notice that this limit can be overtaken by the means of a large amount of averages.

Nevertheless, all these expected limits needed to be checked up. That is why we performed additional experiments by using an Agilent 33220A sine wave voltage source working at $1 MHz$, which frequency modulation input was seeded with an amplified DC-150 Hz white noise source. This signal was injected into the Agilent U1084A-001 sampler that was used for the acquisition of most of the data exploited in this work. The result is depicted in Fig. 14 .

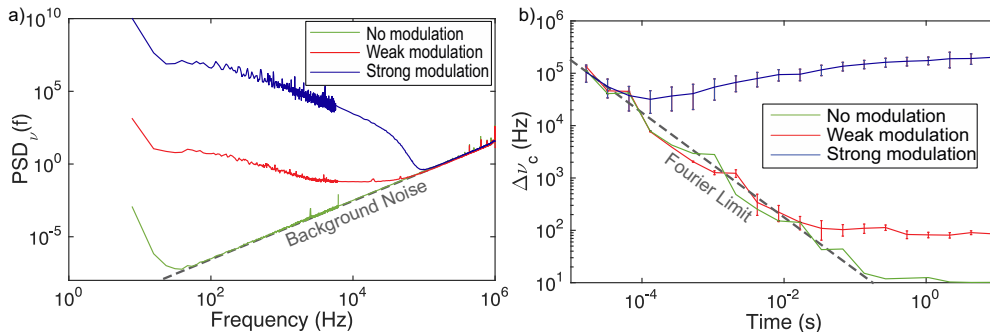


Fig. 14. a) Frequency noise limit measured b) Linewidth limit measured.

These measurements exhibit that the limits are very low compared to available lasers: frequency noise values as low as $1 Hz^2/Hz$ can be measured over frequency spans as wide as $100 kHz$, while linewidth values as narrow as $10 Hz$ can be extracted. Concerning this last limit, we believe that it is due to the frequency generator and not to the sampler, which time jitter is said to be below $1 ps$ for $10 \mu s$ record length.

8. Extension: intrinsic time dependent linewidth

In the previous experiments, all the results presented were the sum of the frequency noises of two lasers, because they were based on the heterodyne set-up. However, it is often interesting to

have access to the intrinsic linewidth of a single laser, which cannot be reached in a rigorous way through the β -separation line approach in some cases, as discussed above. In order to compute this quantity, the frequency noise set-up of Fig. 7 was used, but instead of computing the power spectral density of the frequency noise, we performed only the acquisition of the frequency fluctuations as a function of the time. Then, we followed the path $C \rightarrow D \rightarrow A \rightarrow B$ from Fig. 5 to retrieve the laser spectrum as a function of the time. For this purpose, a "virtual" beat-note was generated by injecting the phase fluctuations in time on a deterministic numerical sine wave-shaped carrier, and then the same process as above was carried out to obtain the laser spectrum from the beat-note. The results, grounded on one of the DFB-SC studied in this paper, are displayed in Fig. 15, and illustrate again the spectral broadening due to $1/f$ noise.

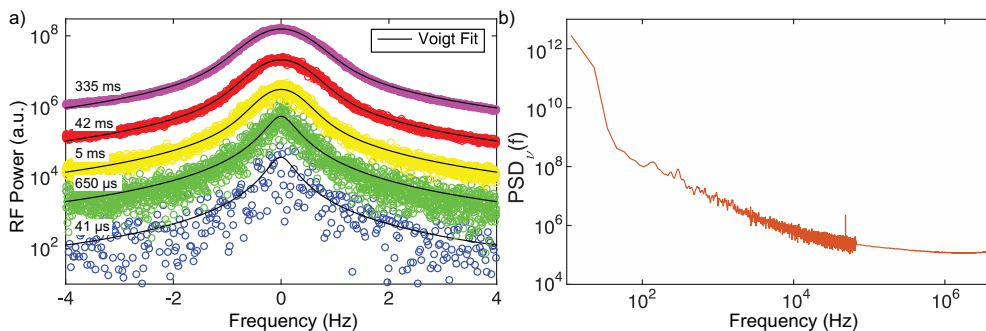


Fig. 15. a) Intrinsic linewidth computed from time-domain frequency noise signal using "virtual" carrier. b) Frequency noise spectrum computed from the time domain frequency noise signal.

9. Conclusion

We have demonstrated in this article the possibilities brought by the sampling of the beat-note obtained from the heterodyne beating interferometry. This process, based on a very simple and low-cost experimental set-up, is associated to a set of numerical processings in order to offer numerous possible derivations, as well as a high accuracy in the analysis of laser lines fluctuations, which have never been developed in the literature to our knowledge. It overcomes the capabilities of more traditional or more complex measurement set-ups, and opens the access to the very "short-time linewidth" that is so often required.

As discussed above, we encourage the reader to use the spectral width indicator $\Delta\nu_c$ associated with Mandel and Wolf's definition of the coherence time, instead of the more basic FWHM, as it can lead to significant errors in the case of lasers dominated by technical noise contributions. We also addressed the complex topic of low frequency noise, including the $1/f^\alpha$ noise, and demonstrated for the first time a method that can really take into account, with the highest accuracy, the impact of these noise sources on the linewidth.

We also mention that other original techniques explored in the scientific literature [61,62], and which rely on more complex RF instrumentation, could take benefit from acquisition systems as simple as the one used in this paper. With adequate signal analysis, it could make them much more available than today, as they depend on so specific instruments.

Finally, we want to mention that the Matlab code that is necessary to reproduce this set-up is open source and available under BSD licence, as additional material associated to this paper (Code 1, Ref. [63]). It takes advantage of the Matlab FFT multiple-core implementation to reduce computation times. For example, computing $\Delta\nu_c$ over a 2×10^8 points sample requires a few minutes on a Xeon E5-1603 2.8 GHz with 32 Go RAM.

Funding

Euripides-Eureka LAMA project (grant EM 12-1307); Direction Générale des Entreprises (DGE, France) (grant 122930229); Commission pour la Technologie et L'Innovation (CTI, Switzerland) (grant 14750.1)

Acknowledgments

The authors would like to thank Odile Verdure-Labeille of ECOSTRATEGIE, for her kind and valuable help in translating this paper to English.

Article II

DFB-ridge laser diodes at 894 nm for cesium atomic clocks

N. von Bandel, M. Garcia, M. Lecomte, A. Larrue, Y. Robert, E. Vinet, O. Driss, O. Parillaud,
M. Krakowski, F. Gruet, R. Matthey, and G. Mileti.

in the proceedings of SPIE OPTO, March 2016.

DFB-ridge laser diodes at 894 nm for Cesium atomic clocks

N. Von Bandel¹, M. Garcia¹, M. Lecomte¹, A. Larrue¹, Y. Robert¹, E. Vinet¹, O. Driss¹,
O. Parillaud¹, M. Krakowski¹, F. Gruet², R. Matthey², G. Mileti²

¹ III-V Lab, Campus de Polytechnique, 1 av. Augustin Fresnel, 91767 Palaiseau, France

² Laboratoire Temps - Fréquence (LTF), Institut de Physique, Université de Neuchâtel
Avenue de Bellevaux 51, 2000 Neuchâtel, Switzerland

* nicolas.vonbandel@3-5lab.fr

** michel.krakowski@3-5lab.fr

ABSTRACT

Time & Frequency applications are in need of high accuracy and high stability clocks. Optically pumped compact industrial Cesium atomic clocks are a promising approach that could satisfy these demands. However, the stability of these clocks relies, among others, on the performances of the laser diodes that are used. This issue has led the III-V Lab to commit to the European Euripides-LAMA project that aims to provide competitive compact optical Cesium clocks for ground applications. This work will provide key experience for further space technology qualification. III-V Lab is in charge of the design, fabrication and reliability of Distributed-Feedback diodes (DFB) at 894 nm (D1 line of Cesium) and 852 nm (D2 line). LTF-Unine is in charge of their spectral characterisation. The use of D1 line for pumping will provide simplified clock architecture compared to the D2 line pumping thanks to simpler atomic transitions and a larger spectral separation between lines in the 894 nm case. Also, D1 line pumping overcomes the issue of unpumped “idle states” that occur with D2 line. The modules should provide narrow linewidth (<1 MHz), very good reliability in time and, crucially, be less sensitive to optical feedback. The development of the 894 nm wavelength is grounded on III-V Lab results for 852 nm DFB. We show here results from Al-free active region with InGaAsP quantum well Ridge DFB lasers. We obtain the D1 Cs line (894.4 nm) at 67°C and 165 mA (optical power of 40 mW) with a high side mode suppression ratio. The wavelength evolution with temperature and current are respectively 0.06 nm/K and 0.003 nm/mA. The laser linewidth is less than 1 MHz. The Relative Intensity Noise (RIN) and the frequency noise are respectively less than $10^{-12} \text{ Hz}^{-1} @ f \geq 10 \text{ Hz}$ and $109 \text{ Hz}^2/\text{Hz} @ f \geq 10 \text{ Hz}$.

Keywords: DFB laser, 894nm, 852nm, narrow linewidth, relative intensity noise, atomic clocks, Cesium, D1 line, D2 line, time metrology.

1. INTRODUCTION

1.1 The optically-pumped Cesium beam Frequency Standard

Accurate and stable time-frequency standards are needed for a range of applications: definition of a universal time, synchronization of modern telecommunication systems, fundamental experiments or communication with and between satellites, including the use of the Global Positioning System (GPS). In the latter case, space environment constraints have led to build compact and reliable clocks based on various physical paradigm that could stand long spatial missions. Several different technologies are competing: for instance, the Passive Hydrogen Maser (PHM) exhibits a stability – measured by the Allan deviation $\sigma_y(\tau)$ – of $\sigma_y(\tau) \sim 5 \cdot 10^{-13}$ for short-term ($1 \text{ s} > \tau > 10^4 \text{ s}$), and $\sigma_y(\tau) = 10^{-14}$ for long term ($\tau > 10^4 \text{ s}$), for a volume ranging between 20 dm^3 to 80 dm^3 and a weight of 10 to 20 kilograms. Another type of clock is the Rubidium Atomic Frequency Standard (RAFS) which current characteristics are a short-term $\sigma_y(\tau) \sim 5 \cdot 10^{-12}$, a long-term $\sigma_y(\tau) \sim 6 \cdot 10^{-14}$, for a volume of a few liters and a weight $\sim 6 \text{ kg}^1$. These clocks already take part in the first generation of the Galileo constellation, the European equivalent of the GPS or the GLONASS. For the two latest positioning systems, the Cesium Frequency Standard (CFS) has been widely used through the magnetic selection Cesium atomic clock, where the preparation and interrogation process is realized with magnetic field gradients².

However, another approach to realize the Cesium standard is to optically pump and interrogate a thermal Cesium beam. Proof of this concept³ has led to predict a short-term stability as low as $\sigma_y(\tau) = 1 \cdot 10^{-12}$, which overcomes the current limit of around $\sigma_y(\tau) = 1 \cdot 10^{-11}$ for the clock with magnetic selectors, for a 10-years lifetime (Galileo positioning system requires

a stability $\sigma_y(\tau) < 3 \cdot 10^{-12}$). Also, the simpler optical setup allows easier and cheaper fabrication. While the ultimate performance in the magnetic CFS relies on the intensity of the Cesium beam flux –it improves with higher flux–, the lifetime of the clock decreases due to a faster consumption of the Cs, which compromises long operation. In optically pumped CFS, laser pumping uses more efficiently the atomic beam, which allows to gain on clock’s stability, for a given lifetime.

To achieve atomic preparation and interrogation, one can consider the transition lines between the ground state $6^2S_{1/2}$ and the two following excited states of the fine structure of Cesium: $6^2P_{1/2}$ (D1 line around 894nm) and $6^2P_{3/2}$ (D2 line around 852nm⁵), see figure 1. These levels are again subdivided in the hyperfine structure, where the transition F=4 to F=3 at 9.19 GHz in the ground state coincides with the resonant frequency of the Ramsey cavity and is used for the definition of the second. For the preparation process, which consists in storing the atomic population in the same hyperfine level of the ground state, one can either use the D2:44’ σ transition at 852 nm or the D1:34’ π at 894 nm, where σ and π are the type of atomic transitions controlled by the polarization of the incident light. It is, first, pumping transition (3-level systems) but it has also been demonstrated to maximize the efficiency of the process⁶. On the contrary, lines D2:32’ and D2:45’ are cycling transitions (2-levels system) that cannot be used at this step. Also, in the case of the D2 line, the existence of so-called “idle-states” in the presence of a weak magnetic field (Hanle effect) may hinder the pumping efficiency, and ultimately degrade the clock performance. This phenomenon does not exist for the D1 line, which calls *a priori* for its use, though the issue can be overcome with the D2 line by acting on the polarization properties of the beam⁷. For the detection process, one can use either pumping or cycling transitions, but it has also been shown that the cycling transitions of D2 line produces more fluorescence photons that enhance the signal detection⁴. Finally, the use of the two D1 and D2 lines is worth to maximize clock’s efficiency.

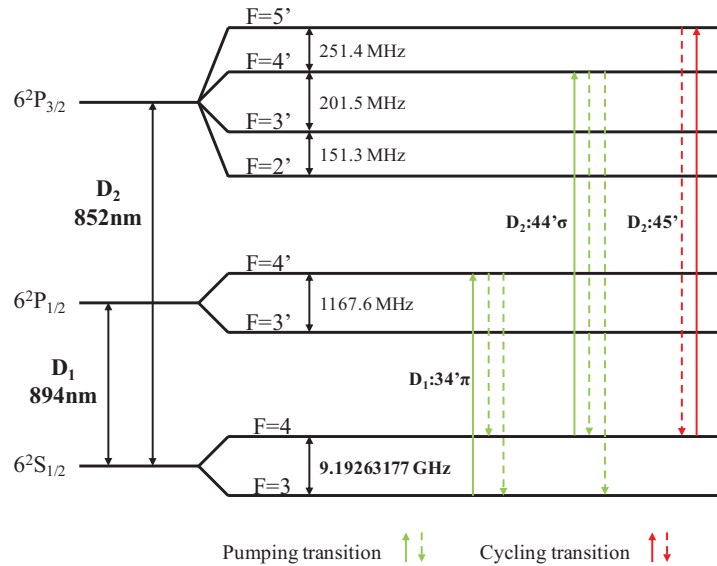


Figure 1: Hyperfine structure of Cesium in air and useful pumping and cycling transitions. Zeeman level splitting is not shown.

1.2 Laser chips requirements

Until now, several attempts of industrial optical CFS prototypes have shown success^{8, 9}, but the quality of sources used for pumping has rapidly appeared to be a crucial limiting factor of the setup. In many experiments, and for further development, Distributed-Feedback (DFB) or Distributed Bragg Reflector (DBR) semiconductor lasers have been used for their compactness, reliability in time and low power consumption against extended-cavity diode laser (ECDL) that is more complex to implement for an industrial clock, but may have also, for the time being, lower reliability for space applications.

However, the spectral purity of the laser is of crucial importance to recover a high clock signal-to-noise ratio (SNR) that leads to high clock stability. Laser linewidth (and fundamentally laser frequency noise) should be as low as possible so not to become the dominant term in the noise budget of the overall clock setup⁹. A low laser linewidth and high spectral

purity also enables one to use less optical power to achieve the same atomic population inversion which, in turn, reduces spurious light noise in the detectors. Typically, a sub-MHz linewidth will overcome these current limitations.

Secondly, the laser should provide excellent key parameters stability over time (more than 10 years). Especially, wavelength stability is of key importance to operate the atomic transitions without ranging out of the scope of the frequency-locking electronics in the long term. Therefore, the laser should have stable threshold current and stable operating current through ageing.

Finally, the laser chip is required to remain insensitive to external environment, especially to external optical feedback that can occur in the optical pumping setup. Until now, many commercial diodes have proved to be non-operable in the latest optical CFS experiments due to either high sensitivity to optical feedback, too broad linewidth or poor reliability.

It is worthwhile mentioning that the developed DFB laser diodes may find application in other types of atomic frequency standards (such as Cs vapor cell standards based on coherent population trapping or microwave-optical double resonance, cold Cs atomic fountains, etc.) and high precision sensors (atomic magnetometers, atomic gyroscopes, etc.).

1.3 The LAMA project

All the above mentioned requirements have led III-V Lab (joint laboratory of Thales R&T, Nokia-Alcatel-Lucent Bell Labs and CEA Leti) to commit to the European Euripides-LAMA project¹⁰ (LAsER diode Modules for compact Atomic clocks) that aims to provide reliable laser modules at 852 nm and 894 nm for pre-industrialization of an optical CFS. The other partners are Laboratoire Temps-Fréquence (University of Neuchâtel) which has longstanding expertise in design and evaluation of atomic clocks, along with characterization of laser diodes for atomic pumping¹¹, Oscilloquartz S.A. (ADVA Optical Networking) a clock manufacturer designing the optical CFS and Thales Electron Devices (subdivision of Thales Group) which will supply the Cesium tube.

III-V Lab results on Aluminum-free based DFB laser diodes at 852 nm have shown to compel with almost all previous requirements for a clock application: low threshold current (50 mA at 25°C), high differential external efficiency (around 1.1 W/A at 25°C), high power output without noticeable thermal roll-over (110 mW at bias current of 150 mA and 25°C). The Cesium D2 line was obtained at 30°C and a current of 200 mA, for which the Side Mode Suppression Ratio (SMSR) was higher than 50 dB and the linewidth at -3dB equal to $\Delta\nu=300$ kHz for white noise part and $\Delta\nu=400$ kHz for low frequency noise component, with an overall $\Delta\nu<500$ kHz at 200 mA bias¹². In addition, ageing tests of DFB lasers have shown long-term reliability (more than 10 years) with no significant degradation of the key parameters mentioned before¹³. Finally, the laser diode enables to operate the new optical CFS prototype without optical feedback issue.

In conclusion, III-V Lab goals are to reproduce comparable results for the Cesium D1 line at the wavelength of 894 nm and make further improvements on laser design through the experimental feedback of prototype testing.

2. LASER STRUCTURE

The vertical laser heterostructure is realized by Metal Organic Vapour Phase Epitaxy (MOVPE) growth on an n-doped (100) GaAs buffer wafer. The active zone is composed of a 8 nm compressive-strained (+1%) InGaAsP quantum well embedded in a ~ 1 μm GaInP Large Optical Cavity (LOC). The LOC is surrounded by AlGaInP confining layers providing the refractive index gap for effective optical confinement (Figure 2). Also, a ~ 50 nm InGaAsP grating layer is inserted between the cladding and the LOC in a second-step regrowth (see below).

The analysis of the photoluminescence wavelength of the quantum well on a calibration structure (2 inches wafer) showed that the emission is spectrally centered at 885 nm.

AlGaInP	p-doped Cladding
GaInP	0.5 μm Optical Confinement
InGaAsP	8nm Quantum Well
GaInP	0.5 μm Optical Confinement
AlGaInP	n-doped Cladding

Figure 2: Laser structure. Active region is Al-free.

In the meantime, the DFB single mode wavelength is given by Bragg's law (figure 5). For an emission at 894.4 nm and an effective index of $n_{\text{eff}}=3.27$ at 25°C, a Bragg pitch of $\Lambda=273.5$ nm is computed. In practice, several Λ values are tested on the same wafer, given the uncertainty on the n_{eff} computation. In the meantime, the DFB should work at around 65°C given the gain detuning mentioned above. The effective index rise with temperature has then to be taken into account to obtain good accordance between the Bragg wavelength and the gain peak for effective lasing action at 65°C.

4. RIDGE LASER AND BRAGG GRATING PROCESSING TECHNOLOGY

After a first step of epitaxial growth of the heterostructure including the quantum well, a second-order Bragg grating with a period ranging from 272 nm to 275 nm is defined by ebeam lithography in the grating layers, followed by pattern etching by means of Reactive Ion Etching. A second step of regrowth burries the nanostructure up to the highly doped top GaAs contact layer. Figure 6 is a typical scanning electronic microscope (SEM) picture of a cut of the epitaxial structure. Good grating definition and layers planarity after regrowth of material are noticeable. The mean opening factor of the corrugation is approximately $a=0.33$ (figure 7).

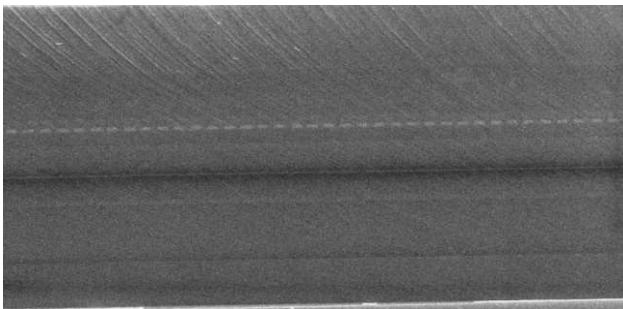


Figure 6 : SEM view of the total structure.

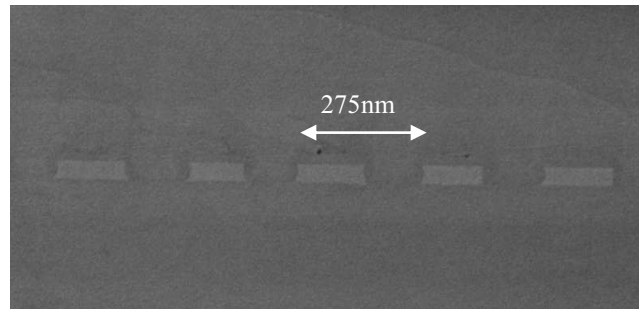


Figure 7 : SEM view detail of the grating layer.

By standard photolithography, a double-trench waveguide of 3.5-4 μm wide is defined at the top of the heterostructure to maintain a single transverse mode in the cavity (figure 8 and 9). This etch step is done by Inductively Coupled Plasma. An insulating SiO_2 layer is deposited on the surface by Plasma Enhanced Chemical Vapor Deposition. On the top of the mesa, SiO_2 is removed to enable localized current injection. Top p-type Ohmic contact is made of Ti/Pt/Au deposit. After reduction of the GaAs substrate thickness down to 100 μm , the Au/Ge/Ni/Au bottom n-type contact is deposited. Following an annealing at 400°C, a new deposit of Ti/Pt/Au is realized.

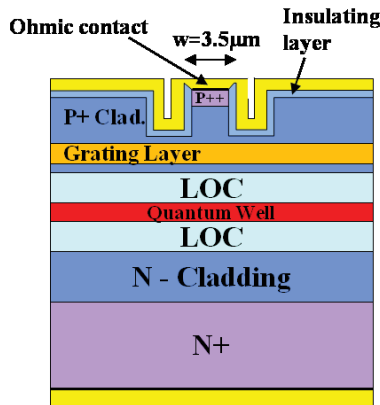


Figure 8 : Schematic of the ridge DFB laser structure.

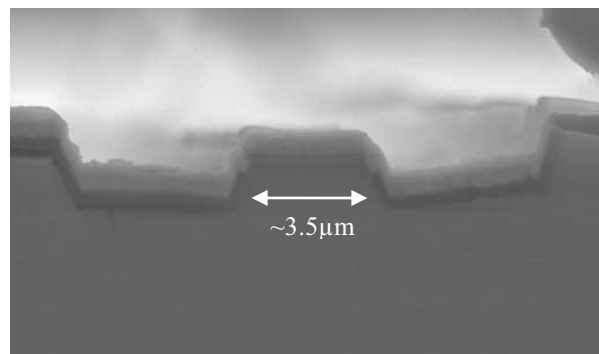


Figure 9 : SEM view of the top double-trench ridge waveguide.

At the end of the process, the wafer is cleaved in bars of length $L=1.5$ mm and $L=2$ mm cavities. The facets are coated with dielectric mirrors. Standard 3% (front facet) and 95% (rear facet) reflectivity are achieved. The individual chips are separated and mounted p-side up on C-mount, equipped with a CuW heat dissipator, for lab characterisation.

5. RESULTS OF RIDGE DFB LASER CHARACTERIZATIONS

5.1 Characterization procedure description

In a first step, basic measurements of the optical power versus injection current (L-I curve) and rough spectral investigations (use of a 10 pm resolution optical spectrum analyzer) were performed on C-mounted lasers right after fabrication. At this stage, around 88% of the devices showed good apparent DFB single mode lasing (first batch test of 62 devices). In a second step, in-depth characterization both in III-V Lab and LTF premises were conducted on the devices that passed the first screening.

A dedicated test bench was assembled in the latter site with particular emphasis on spectral parameters. The C-mount packaged laser under test is installed on a thermally controlled platform (see Figure 10) which temperature can be freely adjusted and stabilized. This platform and the associated thermal controller were developed on purpose, as no commercially available C-mount holder could be found, which proposed sufficient thermal stability (around 10 μ K) for laser diode free-running mode. Beside measurements of the L-I curve, yielding current threshold and slope efficiency values, the evaluation of the frequency tuning coefficients versus current or temperature is realized by means of a precision wavemeter (10 MHz resolution). SMSR measurements rely on an optical spectrum analyzer, while the relative intensity noise (RIN) and the frequency noise are measured with a fast Fourier transform (FFT) spectrum analyzer.



Figure 10: Platform onto which a laser packed on a C-mount is fixed. Thermal adjustment and stabilization is obtained by a Peltier element placed below the platform and a temperature controller. A cap (not shown) ensures proper protection against air fluxes.

As the primary goal of the laser diodes is to officiate as light source for Cesium-based research set-ups or application apparatuses, each laser diode is controlled to operate at Cesium D1 line at 894 nm using a Cesium vapour gas cell to record the Cesium spectrum in a sub-Doppler absorption scheme based on atom velocity selection. The vapour gas cell is not heated and stands at ambient temperature. An example of recorded spectrum is presented in Figure 11. The temperature T_{Cs} at which a laser diode reaches the Cesium wavelength (corresponding more precisely to the transition from the ground state $F=4$) while delivering 40 mW of optical output power is determined. This condition serves as benchmark for comparison between the various devices – it shall be noticed that the RIN and the SMSR are determined when the laser under test is operating at T_{Cs} , the SMSR being recorded for various current values. The same Cesium cell is used as frequency discriminator for the measurement of the frequency noise spectrum. In this case, the laser frequency is tuned to one of the slopes of the $F = 4 \rightarrow F' = 3$ transition.

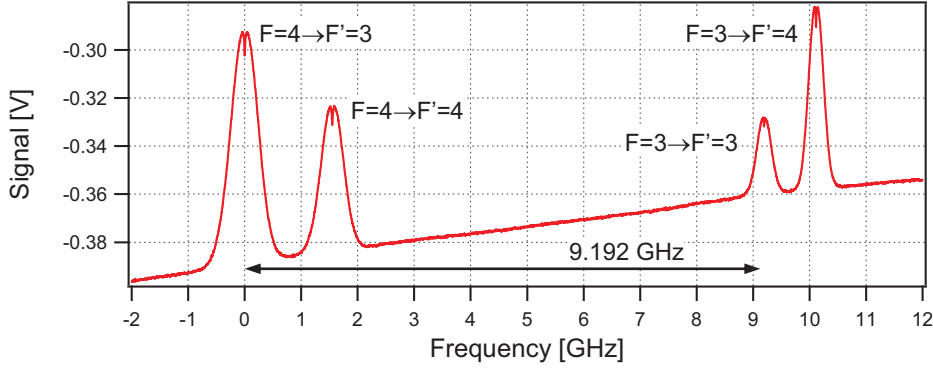


Figure 11: Spectrum of Cesium D1 line at 894nm as obtained when sweeping the DFB laser current and monitoring the transmission signal through an evacuated gas cell filled with Cs. The hyperfine levels F associated to the total angular momentum of the atom are indicated for each optical transition from the ground state $6^2S_{1/2}$ to the excited $6^2P_{1/2}$; see Figure 1. The slope of the baseline is due to the variation of the emitted optical power with respect to the current.

Two different types of laser noises may limit the performance of a system like an optically-pumped atomic clock, and are therefore measured: optical power fluctuations (given by the RIN), and frequency fluctuations (also known as frequency noise). The laser linewidth at 894 nm is derived from the frequency noise spectrum and the β -separation line formalism¹⁵. This method was applied because no narrow-linewidth laser was available for this wavelength to create a beat note with the device under test in a heterodyne configuration. However, the results from the β -separation line method were compared to linewidth measurements in a heterodyne set-up built around an external cavity diode laser in the case of DFB lasers emitting at 852 nm. Both methods fit into agreement within the error bars (10%-40%) of the heterodyne method, confirming that the β -separation line method provides trustful linewidth values.

5.2 Characterization results

At 25°C, the current threshold and the slope efficiency are in average 58 mA and 0.59 W/A, respectively, for laser chips of 1.5 mm length, while they amount to 70 mA and 0.53 W/A, respectively, for laser chips of 2.0 mm length. When operating the lasers at higher temperatures, the current threshold increases, while the slope efficiency diminishes in accordance to the expectations. For the case of a 2.0 mm length laser chip running at a temperature of 67°C, the current threshold and slope efficiency amount to 91.8 mA and 0.43 mW/mA, respectively, as illustrated in Figure 12. In average, the frequency tuning coefficients equal -1.2 GHz/mA and -20.5 GHz/K for current and temperature, respectively.

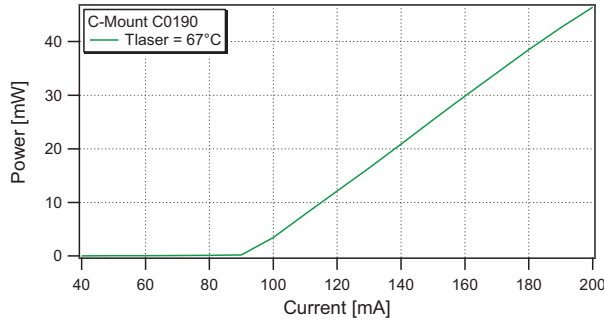


Figure 12: L-I characteristic for a laser operated at 67°C to reach the Cesium D1 line.

Depending on the samples, the fabricated DFB lasers reach the Cs D1 wavelength at a temperature between 66.4 and 70.3°C for an injection current of 160-185 mA settled to deliver 40 mW of optical power. The grating pitch used for these results is $\Lambda=275$ nm. Such temperatures values of operation, higher than expected, enables laser gain to match Bragg condition, as explained before. For those parameters, SMSR values always larger than 45 dB are observed, as

illustrated in Figure 13. Also, the linewidth at 4 ms equivalent observation time and Full Width Half Maximum (FWHM) lies between 640 kHz and 1.0 MHz and therefore meets the target value of 1 MHz or less. It is retrieved from frequency noise spectral densities (see Figure 14), whose flicker noise mostly fits the function (in Hz^2/Hz) $2 \cdot 10^{10}/f^{1.08}$, f being the Fourier frequency. The relative intensity noise is always less than 10^{-12} Hz^{-1} at $f > 10 \text{ Hz}$. More precisely, it remains below $1 \cdot 10^{-11}/f \text{ Hz}^{-1}$ for f between 10 Hz and 1 kHz and less than 10^{-14} Hz^{-1} above 1 kHz for all evaluated DFB lasers, as shown in Figure 15.

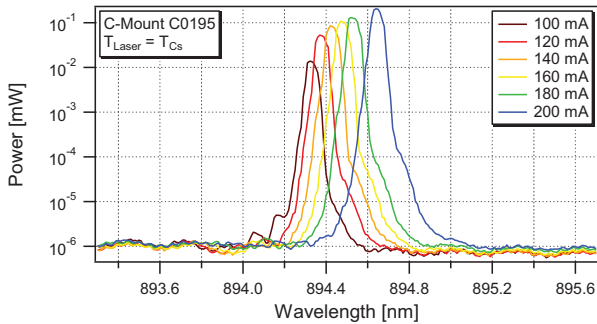


Figure 13: Typical emission spectra of one of the 894 nm DFB lasers as measured for various current values with an optical spectrum analyzer when the laser is operating at a temperature T_{Cs} of 70.3°C. Cs D1 line is reached at a current of 182 mA and an optical power of 40 mW. The corresponding SMSR is larger than 49 dB.

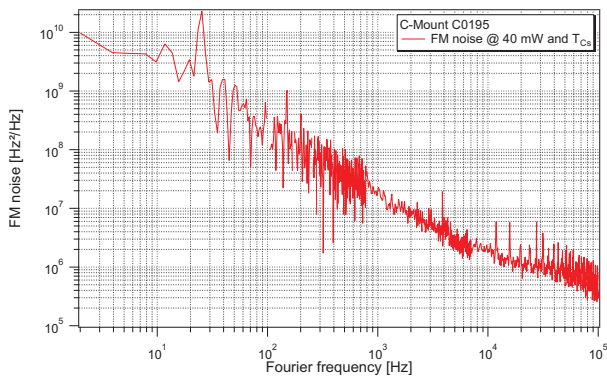


Figure 14: Example of frequency noise spectrum for one of the 894 nm DFB lasers, operated at a temperature T_{Cs} of 70.3°C and a current of 186 mA to deliver 40 mW at Cs D1 wavelength.

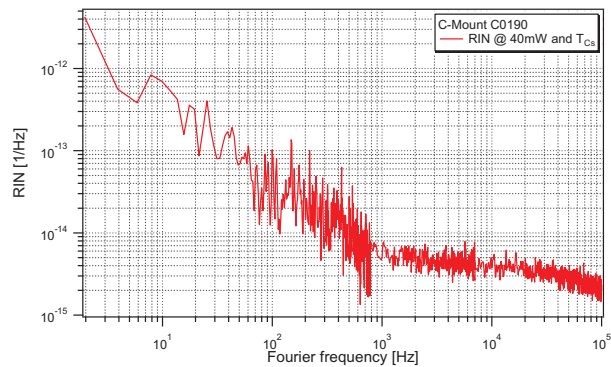


Figure 15: Example of RIN for one of the 894 nm DFB lasers, operated at a temperature T_{Cs} of 67.5°C and a current of 186 mA to deliver 40 mW at Cs D1 wavelength.

6. PACKAGING IN TO3

For the purpose of laboratory characterisation, the lasers were mounted on C-mount. As for the use in compact atomic clock setup, lasers have been integrated to a standard TO3-can equipped with a CTN and Peltier element for temperature sensing and control. Such assembly is a ready-to-use device for the clock's manufacturer (figure 16).



Figure 16: Example of TO3 packaged laser for direct use in atomic clock setup

CONCLUSION

The aim of the LAMA project is to provide reliable laser modules at 852 nm and 894 nm for pre-industrialization of an optical CFS. Therefore, we have designed DFB lasers emitting at 894 nm. A first batch of such lasers was produced. They were fully characterized using, in particular, Cs spectroscopic techniques. For these devices, laser emission at 894 nm was achieved for 1.5 mm and 2 mm cavities, with the required output power (40 mW), low threshold current (70 mA), good external efficiency (0.5 W/A), low linewidth (<1 MHz) and operational temperature of 66-70°C. Special attention was attached to measurements of noise properties like intensity and frequency noises. The RIN stays below $1 \cdot 10^{-11}/f$ Hz⁻¹ for Fourier frequencies f between 10 Hz and 1 kHz, and less than 10^{-14} Hz⁻¹ for f above 1 kHz, while the flicker noise component of the frequency noise shows an upper fit function of $2 \cdot 10^{10}/f$ Hz²/Hz. These values are in line with the requirement of the clock's manufacturer. Current and further on-going work is focused on producing reliable modules reaching 894 nm at room temperature, by epitaxial recalibration and recomputing of the effective refractive index of the structure.

ACKNOWLEDGMENTS

The authors gratefully acknowledge the support of Euripides (grant 12-1307), the French DGE and the Swiss CTI agencies for the partial funding of LAMA project. The authors would like to thank F. van Dijk and C. Affolderbach for fruitful discussions.

REFERENCES

- [1] Droz, F., et al., "The On-board Galileo Clocks: Rubidium Standard and Passive Hydrogen Maser -Current Status and Performance-", 20th European Time and Frequency Forum, (2006).
- [2] Lutwak, R., et al., "Standard for GPS-III Optically-pumped cesium beam frequency," 33rd Annual Precise Time and Time Interval (PTTI) meeting, (2001).
- [3] Lecomte, S., et al., "Performance demonstration of a compact, single optical frequency Cesium beam clock for space applications," Frequency Control Symposium, 2007 Joint with the 21st European Frequency and Time Forum. IEEE International, (2007).
- [4] Dimarcq, N., Giordano, V., Cérez, P., Théolbald, G., "Analysis of the Noise Sources in an Optically Pumped Cesium Beam Resonator," J. Appl. Phys. 69 (3), p. 1158-1162 (1991).
- [5] Steck, D. A., "Cesium D Line Data", available online at <http://steck.us/alkalidata> (revision 2.1.4), (2010).
- [6] Dimarcq, N., Giordano, V., Théolbald, G., Cérez, P., "Comparison of pumping a cesium beam tube with D1 and D2 lines," J. Appl. Phys. 69 (3), p. 1158-1162 (1991).
- [7] Shirley, J. H., Drullinger, R. E., "Zeeman coherences and dark states in optically pumped cesium frequency standards," IEEE Proc. Electromagn. Meas., (1994).
- [8] Hermann, V., et al., "OSCC project : A space Cs beam optically pumped atomic clock for Galileo," Frequency Control Symposium, 2007 Joint with the 21st European Frequency and Time Forum. IEEE International, (2007).
- [9] Sallot, C., et al., " $3 \cdot 10^{-12} \tau^{-1/2}$ On industrial prototype optically pumped cesium beam frequency standard," Frequency Control Symposium and PDA Exhibition Jointly with the 17th European Frequency and Time Forum, 2003. IEEE International, (2003).
- [10] http://lama_euripides.eu
- [11] Matthey, R., Affolderbach, C., Mileti, G., "Methods and evaluation of frequency aging in DFB laser diodes for Rubidium atomic clocks," Optics Letters, 36 (17), p. 3311-3313 (2011).
- [12] Cayron, C., et al., "Very narrow linewidth of high power DFB laser diode for Cs pumping," CLEO EUROPE/EQEC, 2011 Conference on and 12th European Quantum Electronics Conference, (2011).
- [13] Cayron, C., et al., "High-power, high-reliability, narrow-linewidth, Al-free DFB laser diode, for Cs pumping (852 nm)," Proc. SPIE 7230, (2009).
- [14] Von Bandel, N., et al., "Al-free active region laser diodes at 894 nm for compact Cesium atomic clocks," Proc. SPIE 9382, (2015).
- [15] Di Domenico, G., Schilt, S., Thomann, P., "Simple approach to the relation between laser frequency noise and laser line shape", Applied Optics, 49 (25), p. 4801-4807, (2010).

Article V

Towards an engineering model of optical space Cs clock

R. Schmeissner, A. Douahi, I. Barberau, P. Dufreche, N. Mestre, M. Baldy, N. von Bandel,
O. Parillaud, M. Garcia, M. Krakowski, et al.

In the 2016 European Frequency and Time Forum (EFTF), April 2016

Towards an Engineering Model of Optical Space Cs Clock

R.Schmeissner, A.Douahi,
I.Barberau, P.Dufreche, N.Mestre
M.Baldy
Department of Atomic Clocks
Thales Electron Devices
Vélizy, France

N. von Bandel, O.Parillaud,
M.Garcia, M.Krakowski
III-V Lab
Palaiseau, France

K.Kudielka, F.Loiseau, A.Romer,
C.Roth, W.W.Cooppolse
RUAG AG
Zurich, Switzerland

Abstract— Thales Electron Devices and RUAG currently develop the engineering model of the Optical Space Cs Clock (OSCC) in the framework of an ESA/CNES project. Recent progress of the project is reported. Emphasis is put on the performance tests using new laser sources delivered by III-V Lab. The implementation of an isolator-free optics subsystem and the space evaluation of the laser and photodiode are discussed.

Keywords *Optically pumped Cs clock, DFB laser diodes, space evaluation*

I. INTRODUCTION

The optical pumping of the Cs hyperfine state was identified many years ago as a suitable technology candidate for an atomic clock to operate in GNSS, and in particular in Galileo. Related industrial activities currently develop this technology with focus on ground applications [1, 2]. Based on their heritage in the domains of Cs clock development and space electronics, Thales Electron Devices (TED) and RUAG currently develop the engineering model (EM) of the Optical Space Cs Clock (OSCC). The current project phase started in 2015 and will end in 2017.

II. FORMER DEVELOPMENTS AND DESIGN TARGET

In end of the previous development phase in 2013, a short-term frequency stability of $3E-12\tau^{-1/2}$ was demonstrated. The target of the present phase is $1E-12\tau^{-1/2}$. Further new design constraints are: 12 liter volume, 10kg mass, 30W power consumption and 12 years lifetime in medium earth orbit.

III. PRELIMINARY DESIGN

The preliminary design of the engineering model has been completed in spring 2016.

A. Functional Architecture

The functional architecture was consolidated in former development phases. As shown in Fig. 1, the clock is composed by the Laser and Optics (L&O) sub-system (s/s), the Atomic Resonator (AR) s/s and the Electronic Package (EP) s/s.

The preliminary design of the housing of the engineering model is shown in Fig. 2. It demonstrates the theoretical feasibility of a highly integrated clock. Small size AR (target

The Cs clock development is supported by the European Space Agency under European GNSS Evolution Program (activity ID-98) and CNES under contract n° 150920. The DFB laser diode development project LAMA is supported by Euripides/CTI grant No. 14750.1 PFNM-NM

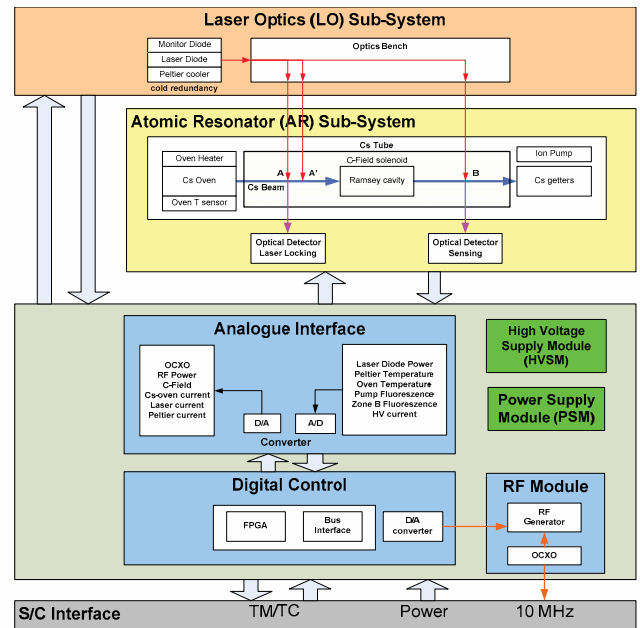


Fig. 1. Functional Architecture of the optically pumped Cs clock

5kg, 6 liters) and L&O s/s (target 500g, 1liter) were re-designed to fit with weight and volume constraints. The concept of the EP was modified using multiplexing technologies to reduce the number of components. Oversampling approaches are implemented to reach the necessary signal conversion resolutions while maintaining low power consumption through low bit-number AD/DA converters. The over-all housing is optimized in order to withstand the vibrational constraints at satellite launch while still providing the necessary thermal conductivity.

IV. TEST OF A NEW DFB LASER DIODE SOURCE

During the former development phase of the industrial, optically pumped Cs clock, the laser diode has been evaluated as the most critical technology. The reach of optimal linewidths below 1 MHz [6] was historically linked to the use of external cavity diode lasers. Although this technology is well known, it appears to add a significant amount of complexity to a commercial clock. Today, even two European suppliers provide T03 packaged DFB sources with a specified

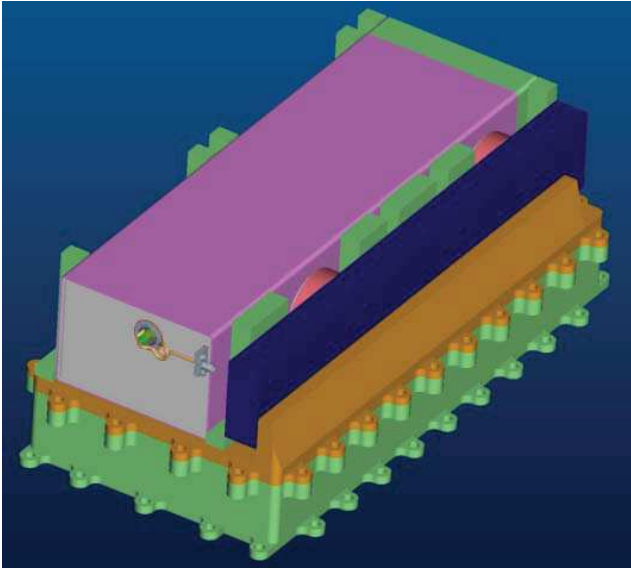


Fig. 2. Preliminary design of the housing of the engineering model. The Atomic Resonator is on the top, the Laser and Optics s/s on the right, the Electronics Package is integrated in the housing below.

linewidth below 2 MHz as a standard product. They can be readily implemented in a clock. Nevertheless, a clock performance comparison using these sources was so far not available and will be presented here.

A. Suitable atomic transitions

The theoretically achievable clock performance is proportional to the product of the signal to noise ratio of the detected Rabi-Ramsey Signal Fringe. The following table recalls the optical pumping/read-out transitions which are theoretically the most suitable for clock operation and highest SNR [3]. Therein, the value Δn is the theoretically achievable Cs atom hyperfine level population difference which can be achieved by optical pumping. All the mentioned transitions are subject to the Hanle effect [5]. This coherent population trapping during pumping is circumvented by the known principle of spatial depolarization of the laser beam. In the ideal case, the highest product of population difference Δn and photons per atom will provide the highest SNR. In conclusion, the D1 4-3' and the D2 3-3' transitions are theoretically the most suitable for clock operation. In the previous phase of OSCC, the D2 4-4' transition has been used according to the exclusive availability of a Cs D2 DFB laser source.

TABLE I. RECALL OF SUITABLE CS TRANSITIONS

Line	Transition	Δn in %	Photons/atom
D1	4-3' σ	16.5	4
D2	3-3' σ	12.2	4
D2	4-4' σ	15.5	2,4

B. Performance comparison to former developments

The following table II summarizes former developments of optically pumped Cs clocks in single optical frequency configuration. The value Q is the quality factor of the atomic resonator and $1/Q \cdot \text{SNR}$ is proportional to the theoretical achievable clock stability assuming $\sigma(t) \sim [Q \cdot \text{SNR}]^{-1} t^{1/2}$.

TABLE II. COMPARISON OF SIMILAR FORMER DEVELOPMENTS

Clock (year)	Oven temp °C	Transition	Laser	SNR (typ)	$1/Q \cdot \text{SNR}$
Tekelec (2000)	110	D2 3-3' σ	DBR	> 4500	< 1E-11
Cs4 (2000)	90	D2 3-3' σ	DBR	11800	6E-12
PHACS	110	D1 3-4' π	ECDL	9200	2.5E-11
ECO	95	D2 4-4'dp	DFB	13500	6.1E-12
OSCC (2013)	95	D2 4-4'dp	DFB	17000	4.8E-12

dp...depolarized,

Indeed, the Cs D1 transition has not been studied so far using a readily applicable DFB laser. In addition, the quality factor of the PHACS atomic resonator did not permit to reach the OSCC target stabilities.

C. Test of a new DFB laser diode

For Cs clock application and in the frame of the European Euripides LAMA project, III-V Lab has recently developed an active region Aluminum-free DFB laser diode emitting at Cs D1 line 894nm. The implementation is based on previous results at Cs D2 line 852nm [4]. The laser is a Separate Confinement Heterostructure (SCH) made of a single compressive-strain 8 nm thick GaInAsP quantum-well embedded in a GaInP 1 μm wide cavity, surrounded by AlGaInP cladding layers, see Fig. 3. Such structure has low transparency current density $J_0=93\text{A}/\text{cm}^2$ and low internal losses $\alpha_i=2\text{cm}^{-1}$. The cavity single transverse mode behavior is enabled by etching a few μm wide ($\sim 3.5\mu\text{m}$) ridge waveguide in the layers. On the other side, the single longitudinal mode operation is ensured by definition -with Ebeam lithography- and etching of a second-order Bragg grating above the active zone, followed by an epitaxial regrowth to bury the diffraction pattern up to the top contact layer. When the two laser facets are coated with, respectively, antireflective and high reflectivity dielectric mirrors

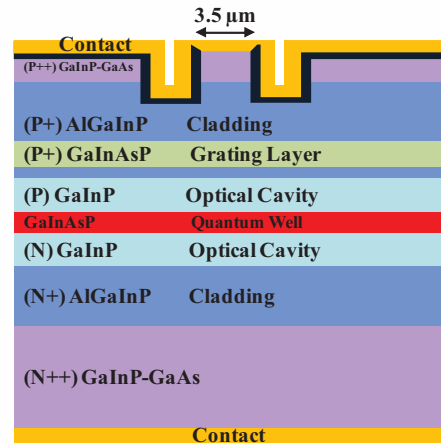


Fig. 3. III-V Lab laser structure. The active region is Al free.

(3%-95%), the laser shows single mode behavior at Cs D1 line with more than 45dB Side Mode Suppression Ratio (SMSR), at the operation temperature of $\sim 65^\circ\text{C}$. For a 2 mm laser bar, the threshold current at such temperature is in the range of 90 mA, with 0.5W/A of external efficiency. An output power of 40mW at 185 mA bias is obtained in such conditions. The laser linewidth was measured by two different methods: with the self-heterodyne setup (2 km delay line and 4 ms integration time) and by derivation from the frequency noise characteristic from 250Hz to the high frequencies [4]. Both methods show that the linewidth lies in the range of 0.7 to 1MHz. Ongoing developments aim at DFB Cs D1 line at ambient chip temperature. They modify the design in order to improve the threshold current and the external laser diode efficiency. All chips are integrated into a TO3 can, monitored and controlled in temperature. Table III compares the III-V Lab laser diode to the eagleyard [8]. Although the electro-optical tuning coefficients are nearly identical, the III-V provides a significantly smaller linewidth.

TABLE III. LASER DIODE COMPARISON – TYPICAL PERFORMANCES

DFB Laser	GHz/K	GHz/mA	$\Delta\nu$ MHz	SMSR dB
eagleyard	24	1.2	2	> 30
III-V Lab	25	1.1	0.7 to 0.9	> 45

D. Signal To Noise Ratio Measurements

Table IV shows the measured SNR performance of the OSCC Cs tube using three different laser sources, an eagleyard DFB at 852nm and two III-V Labs DFB emitting at 852nm and 894nm respectively. They key results of the present paper. All measurements were carried out with a HP35670A FFT Spectrum Analyzer. All three laser diodes were packaged in TO3. They were implemented on a dedicated optics test bench seeding the Cs Atomic Resonator with identical geometric properties independent to the laser used. The beam intensities were optimized for each laser. This approach permits a quantitative comparison of the maximum achievable SNR. An impact of the optical linewidths on the SNR is expected according to [6], but its level is driven by the part of un-pumped Cs atoms in the signal detection [7].

TABLE IV. CS-CLOCK/LASER DIODE COMPARISON – TYPICAL PERFORMANCES

SNR in $1/\text{Hz}^{1/2}$ on OSCC tube at 96°C Cs oven measurement uncertainty $500\text{Hz}^{-1/2}$			
DFB Laser	D1 4-3'	D2 4-4'	D2 3-3'
eagleyard	n/a	15000	15500
III-V Lab	20000	15000	16500

The ratio un-pumped atoms for the experiments considered here is lower than $5\text{E-}3$. At this level, a small impact of the laser diode linewidth on the detected noise level is expected. This is confirmed by the measurement shown in table IV. In line with the theoretical expectation, the highest SNR is obtained with the D1 4-3' transition.

V. SMALL SIZE LOW WEIGHT OPTICS BENCH

A key design challenge on the design of the OSCC clock are the mass and volume constraints. In order to minimize the respective budgets of the laser and optics s/s (500g, 1liter), a simplified optics bench has been designed. Despite a cold laser diode redundancy, it contains only the minimum number of optical elements and no optical isolator.

A. Prototype implementation

In order to verify the functionality of this optics design, a partially representative prototype was implemented together with a dedicated Cs tube. The latter is nearly identical to the OSCC one. It uses the concept of tilted optical windows in order to reduce the amount of back-reflected light into the laser diode. Both tubes show the same SNR performances on the optics test bench.

B. Performance validation

With this new atomic resonator and optics bench, a typical SNR of 24500 is measured using the III-V lab DFB laser diode on the Cs D1 4-3' transition, at 100°C Cs oven temperature and under optimization of all optical beam properties. This level of SNR corresponds to a theoretical clock stability of better than $2\text{E-}12\tau^{-1/2}$. The maximum Cs oven temperature for OSCC is 100°C in order to limit the Cs consumption over 12 years target lifetime.

The Fig. 4 shows the clock stability when measured against an OSCILLOQUARTZ BVA 8607BM quartz reference oscillator and using the electronics hardware from previous OSCC breadboard development. A short term stability of better than $2.8\text{E-}12\tau^{-1/2}$ is measured at 20s integration time. The slight stability degradation for longer integration times might be due to thermal drift of the reference oscillator. The discrepancy to the expected $2\text{E-}12\tau^{-1/2}$ is attributed to non optimal parameters of the clock electronics. In summary, the stability shown in Fig. 3 demonstrates the applicability of the III-V Lab 894nm DFB laser diodes for optical clock application. Their functionality is validated in a setup without an optical isolator.

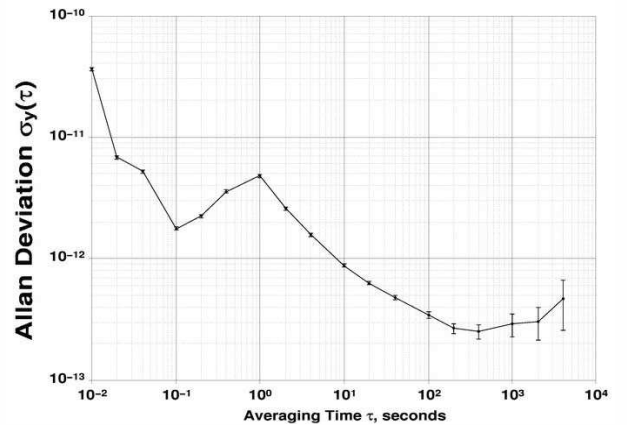


Fig. 4. Validation of the simplified optics bench using Cs D1 4-3' transition. The clock loop resonance is at 1Hz. The Quartz reference oscillator limits the measurement precision above 200s. Data obtained with a Timing Solutions TSC5110A time interval counter.

TABLE V. CS-CLOCK NOISE BUDGET AND TYPICAL CONTRIBUTIONS

Typical noise levels in $\mu\text{Vrms}/\text{Hz}^{1/2}$ at 40Hz (pre-amplified signal)			
Clock Signal at Full Width Half Peak Valley Ramsey Fringe	Photodiode dark noise and pre-amplifier	Stray Light	Atomic Signal Noise
54	21	30	41

Table V shows the over all noise budget of the measurement. The detected noise is limited by the noise in the atomic fluorescence signal. This is in line with the consolidated design of the photodetector signal amplification and the optimized properties of the interrogating laser beam. Nevertheless, improvements in the atomic resonator optics design can still reduce the amount stray light and improve clock performance.

VI. SPACE EVALUATION OF OPTOELECTRONIC COMPONENTS

Being conceived for a lifetime of 12 years in medium earth orbit, all components of the clock will have to be space qualified at a later development phase. The current project phase aims to reduce the associated risk. The latter is essentially driven by the space-qualification of the optoelectronic components: the laser diode and the light detecting photodiode. In a pre-evaluation phase in 2015, the most critical properties and degradation modes of the two components were identified based on supplier heritage and expertise of THALES, CNES and ESA. To reduce the remaining qualification risks, a respective space-evaluation program was defined and will be implemented starting-2016.

A. Laser Diode

The design baseline is a TO3 packaged DFB laser diode as an off-the-shelf product with modifications. Lifetime, and component construction have been identified as most critical issues. They will be evaluated in detail in the current project phase. In contrast and based on return on experience from former laser diode qualifications, radiation induced damage (100krad over 12years) was evaluated to be a minor risk. The same holds for the hermeticity of the TO3 packaging which benefits from longstanding industrial heritage.

B. Photodiode

The OSCC development was so far based on a Hamamatsu S1337 large area, low noise photodetector. Former CNES evaluations demonstrated that this off-the-shelf detector cannot be space qualified mostly due to hermeticity issues of the packaging. In early 2016 TED conceived with First Sensor a customized detector for a space evaluation. It is an off-the-shelf product with modifications and shall even slightly increase the detected clock signal level (clock stability) due to a higher light collection efficiency. The foreseen detector chip is similar to a quadrant detector which is currently qualified for the use in a space sun-sensor application. Indeed, the photodetector dark noise could be increased by the total

ionizing dose above the acceptable margins. This aspect will be verified in the space-evaluation program 2016-2017. A dedicated test campaign will be implemented concerning the photodiode substrate types (n-type or p-type). The impact of ionizing radiation is known to depend on this parameter. The customized TO packaging will benefit from supplier heritage on a similar packaging for EUCLID mission.

VII. CONCLUSIONS

The preliminary design of the OSCC engineering model is reported. In addition to mechanical and electronic design improvements, a new laser diode source and a new optics bench were developed and tested successfully. Using a III-V Lab 894nm DFB laser diode on the Cs D1 4-3' transition, a clock stability of better than $3\text{E-}12\tau^{-1/2}$ was demonstrated. The implemented optics s/s is of minimized complexity and does not contain an optical isolator. As a first step towards space qualification, possible degradation modes of the laser diode and the photodiodes were evaluated. To reduce the remaining qualification risks, a dedicated space evaluation program was developed and will be implemented starting 2016.

Acknowledgment

The authors acknowledge European Space Agency (ESA), the Centre National d'Etudes Spatiales (CNES), EURIPIDES and Thales Electron Devices for financial support of the project. The authors are grateful for helpful discussion and technical support to V.Hermann, G.Corrador and G.Gauthier at Thales Electron Devices, S.Guérandel at SYRTE, Paris, and G.Baily and L.Morvan at Thales Research and Technology, Palaiseau, G.Guibaud at Thales Communication and Security, Toulouse, J.Delporte, F-X Esnault, O.Gilard and J.Mekki at CNES, Toulouse, C.Bringer and P.Waller at ESA-ESTEC, Noordwijk. The authors acknowledge support from the suppliers First Sensor and eagleyard Photonics.

References

- [1] Progress in the Development of Commercial Optically Pumped Cs Atomic Clock, Yuanhong Cao, et al., International Frequency Control Symposium IFCS 2014
- [2] Development of a transportable optically pumped atomic Cs beam clock, P.Berthoud et al. EFTF 2015
- [3] Comparison of pumping a cesium beam tube with D1 and D2 lines, N. Dimarcq, V. Giordano, G. Theobald, and P. Cérez, J.Appl Phys 69 (3), 1991
- [4] N. Von Bandel et al., SPIE Photonics West 2016, Quantum Sensing and Nano Electronics and Photonics XIII, paper 9755-90
- [5] G.Théobald, N.Dimarcq, V.Giordano, P.Cérez, Ground state zeeman coherence effects in an optically pumped cesium beam, Opt.Comm. 71 (5) 1989
- [6] N.Dimarcq, V.Giordano, P.Cérez, G.Théobald, Analysis of the Noise sources in an optically Pumped Cesium Beam resonator, IEEE Trans. Instr. and Meas., 42 (2) 1993
- [7] G.Lucas-Leclin, P.Cérez, N.Dimarcq, Laser-induced noise contribution due to imperfect atomic state preparation in an optically pumped caesium beam resonator. J.Phys.B, At. Mol. Opt. Phys 32 (1999)
- [8] Part No. EYP-DFB-0852-00150-1500-TOC03-0005

Abstract : This PhD work deals with the design, the fabrication and the study of high-coherence semiconductor laser sources emitting at 894 nm, for application to compact, optically-pumped cesium atomic clocks in an industrial context. We are particularly interested in the electrically pumped "Distributed-Feedback" in-plane laser diodes (DFB). The aim is to obtain a low-threshold, single-mode laser with high optical efficiency and a linewidth of less than 1 MHz. We first deal with the design and first-order characterization of the DFB diodes until they are put into modules for the clock. We then carry out an in-depth study of the physical properties of the laser emission in terms of the coherence time. For that purpose, a new universal method for characterizing the optical frequency noise is introduced. Finally, we look further into the spectral properties of the emission in a servo configuration on a fluorescence line of the cesium ("Dither-Locking"). We show that the intrinsic properties of the component satisfy the requirements of the industrial system as defined in the study.

Keywords : Laser diodes, low noise, 894nm, cesium atomic clocks, frequency noise metrology, linewidth in servo

Titre: Développement et étude de diodes laser à faible bruit émettant à 894 nm pour horloges atomiques compactes au césium

Résumé : Ce travail de thèse porte sur la conception, la réalisation et l'étude de sources laser à semi-conducteur de haute cohérence, émettant à 894 nm, pour application aux horloges atomiques césium compactes, pompées optiquement. Nous nous intéressons plus particulièrement aux lasers à émission par la tranche, dits "Distributed-Feedback" (DFB), pompés électriquement. L'objectif est d'obtenir un laser monomode en fréquence, à faible seuil, à rendement optique élevé et de largeur de raie inférieure à 1 MHz. Nous traitons d'abord de la conception et de la caractérisation au premier ordre des diodes DFB, jusqu'à leur mise en modules pour horloge, puis nous effectuons une étude approfondie des propriétés physiques de l'émission laser en terme de cohérence temporelle, en introduisant une nouvelle méthode universelle de caractérisation du bruit de fréquence optique. Enfin, nous nous intéressons aux propriétés spectrales de l'émission en configuration d'asservissement sur une raie de fluorescence du césium ("Dither-Locking"). Nous montrons que les propriétés intrinsèques du composant satisfont aux exigences du système industriel tel qu'il a été défini lors de l'étude.

Mots-clés : Diodes laser, faible bruit, 894nm, horloges atomiques au césium, métrologie du bruit de fréquence, largeur de raie en asservissement
